COLLECTED PAPERS

ON

NANO/ATOM PHOTONICS

Volume 16

August 2000－July 2001

Professor

Motoichi OHTSU

TOKYO INSTITUTE OF TECHNOLOGY

Interdisciplinary Graduate School of Science and Engineering

4259 Nagatsuta-cho, Midori-ku, Yokohama, Kanagawa 226-8502, JAPAN

TEL：＋81－45－924－5455

FAX：＋81－45－924－5599

E-mail：ohtsu @ ae. titech. ac. jp

PREFACE

In order to realize the ultimate status of light and matter, M. Ohtsu tries to control the spatial properties of light. The approach he has used is through the research of near-field optics and its application to nano-structure fabrication and atom manipulation. This will open up a new era of nano/atom photonics. It should be pointed out that the nano/atom photonics is closely related to quantum optics, atom optics, high density optical storage, nano-structure fabrication technology, and so on (see the figures on the next pages). And for this relationship of near-field optics with a variety of fields, nano/atom photonics exhibits rapid progress. Further research will be done to realize novel nanometric materials and devices.

Ohtsu-Saiki group, which is executed in Kanagawa Academy of Science and Technology(KAST) and directed by Ohtsu and Saiki, has started from April, 2001 in order to transfer the results of the research of the previous "PHOTON CONTROL" project to industry so as to produce commercial near field optical spectrometers, optical memories, fiber probes, and so on(*). From October, 1998, a "LOCALIZED PHOTON" project, which is supported as ERATO (Exploratory Research for Advanced Technology) by Japan Science and Technology Corporation and directed by Ohtsu, has started for exploring a novel theory of optical near-field, for studying nano-photonics and atom-photonics.(+) Results of the recent research carried out by Ohtsu are reviewed in this issue of the COLLECTED PAPERS.

August 2001

Motoichi OHTSU
大津　元一

(*) Address: Ohtsu-Saiki group,
Kanagawa Academy of Science and Technology
KSP East, Rm. 408, 3-2-1 Sakado, Takatsu-ku,
Kawasaki-shi, Kanagawa 213-0012, JAPAN
Phone: +81-44-819-2075
Fax: +81-44-819-2072
〒213-0012　神奈川県川崎市高津区坂戸３－２－１

ＫＳＰ東棟４０８号室
（財）神奈川科学技術アカデミー，光科学重点研究室
大津・斎木グループ
(+) Address: Localized photon project,
Japan Science and Technology
4th-floor, Tenko Building #17
687-1 Tsuruma, Machida-shi, Tokyo 194-0004
Phone: +81-42-788-6030
Fax: +81-42-788-6031
〒194-0004　東京都町田市鶴間 687-1
第１７天幸ビル４階
科学技術振興事業団　「局在フォトン」プロジェクト

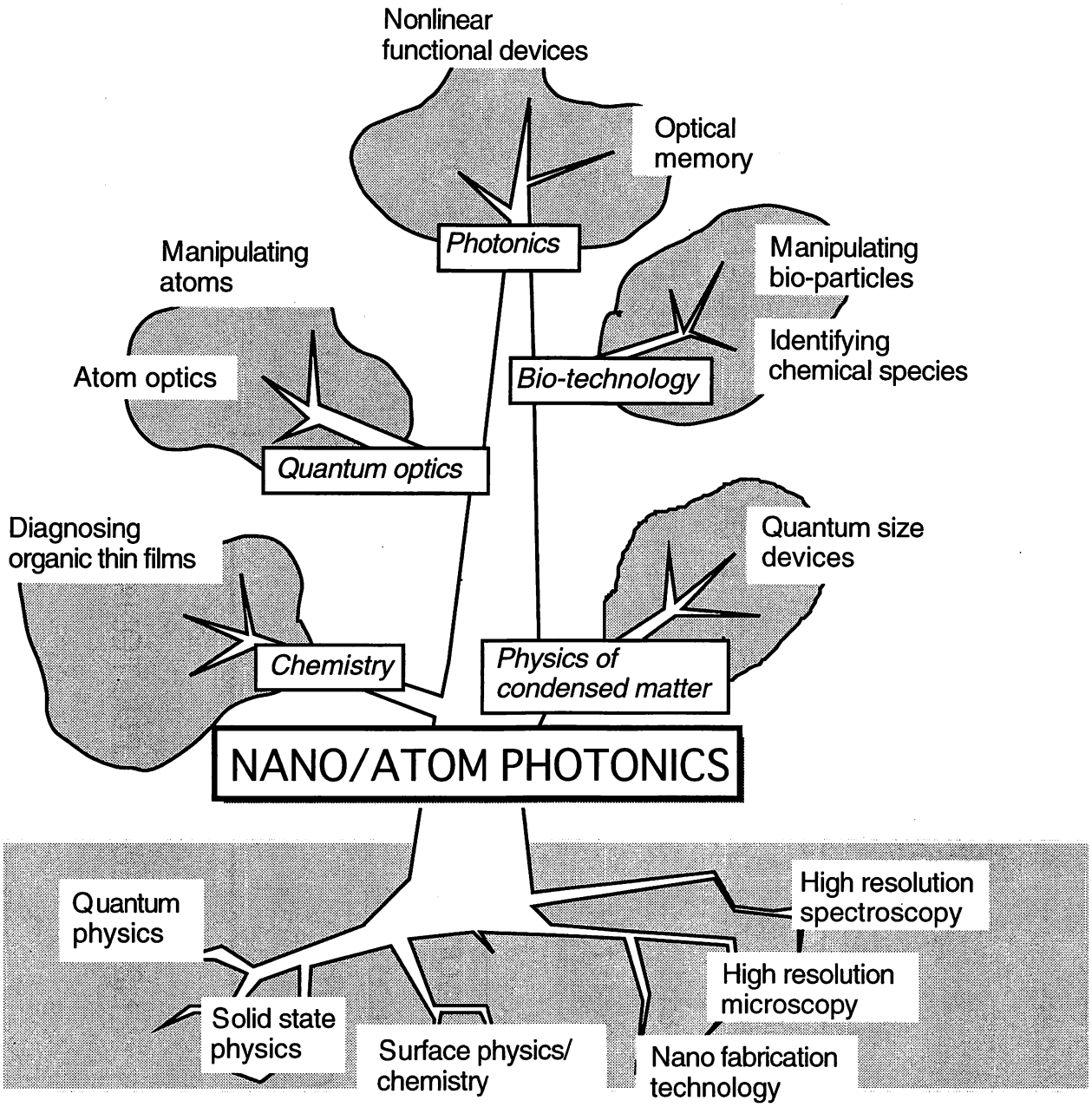

Nano/atom photonic tree with its roots and leaves covering a wide range of fields

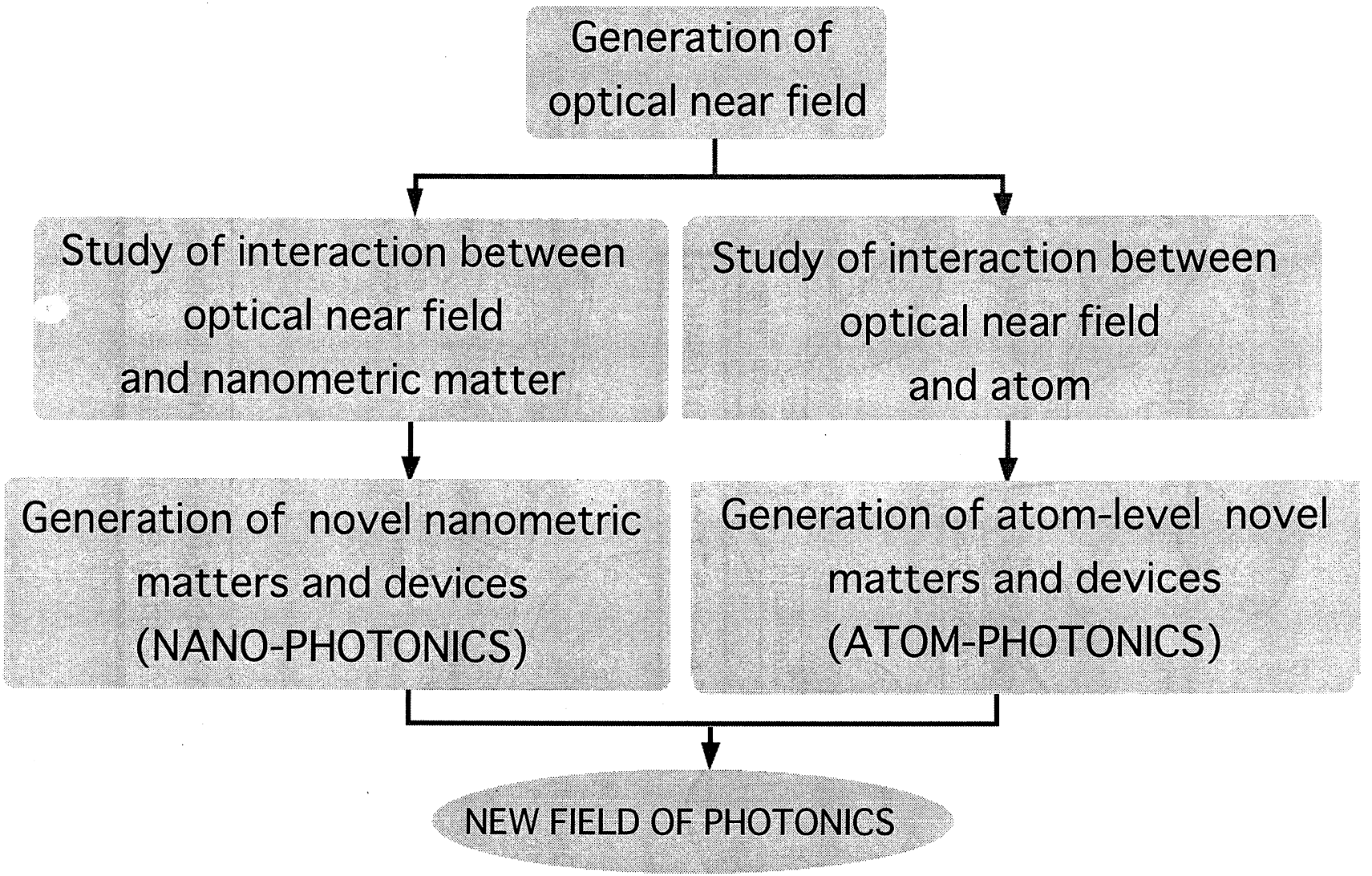
Generation of optical near field
Study of interaction between optical near field and nanometric matter
Study of interaction between optical near field and atom
Generation of novel nanometric matters and devices (NANO-PHOTONICS)
Generation of atom-level novel matters and devices (ATOM-PHOTONICS)
NEW FIELD OF PHOTONICS

MEMBERS

(From April 1, 2001)

[I] TOKYO INSTITUTE OF TECHNOLOGY

Professor

Motoichi OHTSU[a,b] (Dr. Eng.)

Associate Professor

Haruhiko ITO[c] (Dr. Sci.)

Research Associate

Motonobu KOUROGI[c,d] (Dr. Eng.)

Graduate Students (Doctor Candidates)

Akifumi TAKAMIZAWA
Shuko KOGISO

Graduate Students (Master Course)

Tokiya ABE
Minoru UEDA
Masakazu YAMAGIWA
Nobuo SASAKI
Kazuhiko YAMADA
Kazutaka ITSUMI
Satoru TAKUBO
Jung-Shik LIM
Yuji ECHIGO
Shungo YAMADA
Kazuhiro YAMAMOTO

Undergraduate Students

Wataru NOMURA
Masanori KOSUGI

Visiting Scientists

Seok-Jeong LEE [e]	(PhD.)
Bambang Widiyatmoko	(Dr. Eng.)
Osamu NAKAMOTO	
Yoshinobu NAKAYAMA[f]	(Dr. Eng.)
Nariyoshi MISAWA[f]	(Dr. Eng.)
Takashi YATSUI [g]	(Dr. Eng.)

Secretaries

Chikako ISHIDA
Kaoru OGURA

a) Also with Kanagawa Academy of Science and Technology
(Director, Ohtsu-Saiki group)
b) Also with ERATO, Japan Science and Technology Corporation
(Director, "Localized photon" project)
c) Also with "Localized photon" project, ERATO,
Japan Science and Technology Corporation
d) Also with Kanagawa Academy of Science and Technology
(Part-time researcher, Ohtsu-Saiki group)
e) Permanent affiliation: Korea Maritime University
f) Permanent affiliation: RICOH Co.Ltd.
g) Permanent affiliation: "Localized photon" project, ERATO,
Japan Science and Technology Corporation

[II] "LOCALIZED PHOTON" PROJECT, ERATO, JAPAN SCIENCE AND TECHNOLOGY CORPORATION

Researchers

Theory Group

Kiyoshi KOBAYASHI[h]	(Dr. Sci.) (Group Leader)
Suguru SANGU	(Dr. Eng.)

Nano-photonics Group

Tadashi KAWAZOE	(Dr. Sci.)
Takashi YATSUI	(Dr. Eng.)
Hemantkumar N. AIYER	(Ph.D.)

Atom-photonics Group

Kouki TOTSUKA	(Dr. Sci.)
S. M. IFTIQUAR	(Ph.D.)

Visiting Researchers

Guen-Hyoung LEE[i]	(Dr. Eng.)

Managers

Akiyoshi ORIDE[j]
Takaaki MORIYAMA

Secretaries

Fumiko OHTA
Tomoko OHTA

h) Permanent affiliation: Japan IBM Co. Ltd.
i) Permanent affiliation: Dong-Eui University, Korea
j) Permanent affiliation: RICOH Co.Ltd.

[III] KANAGAWA ACADEMY OF SCIENCE AND TECHNOLOGY

Full-Time Researchers

Shuji MONONOBE (Dr. Eng.)

Part-Time Researchers

Motonobu KOUROGI[k] (Dr. Eng.)

Secretary

Tomoko NAKAMURA

k) Permanent affiliation: Tokyo Institute of Technology

LIST OF PAPERS

[(pp.XX-XX); pages in this issue of the COLLECTED PAPERS]

[I] PAPERS IN NANO/ATOM PHOTONICS

[I-1] PAPERS IN ATOM PHOTONICS

(a) Journal Papers

(b) International Conferences

[3] S.M. Iftiquar, H. Ito, and M. Ohtsu, "Tunable doughnut light beam for a near-field optical funnel of atoms", Technical Digest of the 4th Pacific Rim Conference on Lasers and Electro-Optics(CLEO/PR01), July 16-19, 2001, Makuhari Messe, (paper number WJPD1-5)(Post-deadline paper)

(pp.20-21)

[4] K. Totsuka, H. Ito, T. Kawamura, T. Yatsui, and M. Ohtsu, "A slit-type near-field optical detector for neutral atoms with high sensitivity and nanometric resolution", Technical Digest of Quantum Electronics and Laser Science Conference, May 6-11, 2001, Baltimore, MA, pp. 110-111 (paper number QTuG2)

(pp.22-23)

[5] K. Kobayashi, S. Sangu, H. Ito and, M. Ohtsu, "Near-field optical potential generated by a nanometric tip", Abstract of Condensed Matter and Materials Physics Conference, December 12-21, 2000, Bristol, UK, pp.128-129 (paper number ASp.P3.14)

(pp.24-25)

[6] K. Kobayashi, S. Sangu, H. Ito, and M. Ohtsu, "Effective probe-sample interaction: Toward atom deflection and manipulation", in Near-Field Optics: Principles and Applications, Proceedings of the Second Asia-Pacific Workshop on Near Field Optics, ed. by X. Zhu and M. Ohtsu, World Scientific, Singapore, 2000, pp.82-88

(pp.26-32)

[7] H. Ito, A. Takamizawa, H. Tanioka, H. Totsuka, and M. Ohtsu, "Toward Near-Field Optical Manipulation of Atoms Using a Nanometric Fiber Probe", Conference Digest of 2000 International Quantum Electronics Conference, September 10-15, 2000, Nice, France, paper number QWD38

(p.33)

[8] K. Totsuka, A. Takamizawa, H. Tanioka, H. Ito, and M. Ohtsu, "Experimental progress of atom deflection with a fiber-probe using an atomic funnel with optical near field", Abstracts of the 6th International Conference on Near Field Optics and Related Techniques, August 27-31, 2000, Enschede, the Netherland, p.158 (paper number TuO8)

(p.34)

[I-2] PAPERS IN NANO PHOTONICS

(a) Journal Papers

selective fiber optodes", BUNSEKI KAGAKU, vol.49, no.12, December 2000, pp.961-967

【栗原一嘉、大津元一、久本秀明、鈴木孝治、「超微細化イオン選択性オプトード」、分析化学、第４９巻、第１２号、２０００年１２月、pp.961-967】

(pp.62-68)

[7] M. Ohtsu, K. Kobayashi, H. Ito, and G.H. Lee, "Nanofabrication and Atom Manipulation by Optical Near-Field and Relevant Quantum Optical Theory", Proc. IEEE, vol.88, no.9, September 2000, pp.1499-1518

[Invited paper]

(pp.69-88)

[8] Takashi Yatsui, Motonobu Kourogi, Kazuo Tsutsui, Jun-ichi Takahashi, and Motoichi Ohtsu, "High-density-speed optical near-field recording-reading with a pyramidal silicon probe on a contact slider," Optics Letters, vol.25, no.17, September 2000, pp. 1279-1281

(pp.89-91)

(b) International Conferences

[1] K. Kobayashi and M. Ohtsu, "Near-field Quantum Optical Theory towards Nano/atom Photonics", Proceedings of Pogress In Electromagnetic Research Symposium (PIERS 2001), July 18-22, 2001, Osaka, p.650

(p.92)

[2] K. Kobayashi, T. Kawazoe, S. Sangu, and M. Ohtsu, "Proposal for a near-field optical nano-switch", Technical Digest of the 4th Pacific Rim Conference on Lasers and Electro-Optics(CLEO/PR01), July 16-19, 2001, Makuhari Messe, pp. I192-I193 (paper number MH2-3)

(pp.93-94)

[3] T. Kawazoe, K. Kobayashi, J. Lim, Y. Narita, and M. Ohtsu, "Verification of principle for nano-matter size optical near-field switch by using CuCl quantum cubes", Technical Digest of the 4th Pacific Rim Conference on Lasers and Electro-Optics(CLEO/PR01), July 16-19, 2001, Makuhari Messe, pp. I194 - I195 (paper number MH2-4)

(pp.95-96)

[4] Y. Yamamoto, T. Kawazoe, G.H. Lee, T. Shimizu, M. Kourogi, and M. Ohtsu, "In-situ lateral fabrication of Zinc and Aluminum nanodots by near field optical chemical vapor deposition", Technical Digest of the 4th Pacific Rim Conference on Lasers and Electro-Optics(CLEO/PR01), July 16-19, 2001, Makuhari Messe, pp. I520 – I521 (paper number TuH2-5)

(pp.97-98)

[5] T. Yatsui, T. Shimizu, Y. Yamamoto, G.H. Lee, M. Kourogi, and M. Ohtsu, "Spatially and spectrally resolved imaging of a polycrystalline ZnO dots using near field optical technique", Technical Digest of the 4th Pacific Rim Conference on Lasers and Electro-Optics(CLEO/PR01), July 16-19, 2001, Makuhari Messe, pp. I522 – I523 (paper number TuH2-6)

(pp.99-100)

[6] S. Sangu, K. Kobayashi, and M. Ohtsu, "Optical near-field sample-probe interaction depending on excitation energy of matter", Technical Digest of the 4th Pacific Rim Conference on Lasers and Electro-Optics(CLEO/PR01), July 16-19, 2001, Makuhari Messe, pp. II352-II353 (paper number P2-62)

(pp.101-102)

[7] T. Kawazoe, Y. Yamamoto, and M. Ohtsu, "Deposition of nano-meter size Zn dot by near-field optical CVD with nonresonant light", Technical Digest of the 4th Pacific Rim Conference on Lasers and Electro-Optics(CLEO/PR01), July 16-19, 2001, Makuhari Messe, pp. II362-II363 (paper number P2-67)

(pp.103-104)

[8] H.N. Aiyer, T. Kawazoe, J. Lim, T. Shimizu, and M. Ohtsu, "Mercury treatment of near field fiber probes for overcoming light leakage", Technical Digest of the 4th Pacific Rim Conference on Lasers and Electro-Optics(CLEO/PR01), July 16-19, 2001, Makuhari Messe, pp. II366-II367 (paper number P2-69)

(pp.105-106)

[9] S. Mononobe and M. Ohtsu, "Characterization of Silica Optical Fibers Based on Chemical Etching", Technical Digest of the 4th Pacific Rim Conference on Lasers and Electro-Optics(CLEO/PR01), July 16-19, 2001, Makuhari Messe, pp. II454-II455 (paper number WH2-5)

(pp.107-108)

[10] K. Kobayashi, T. Kawazoe, S. Sangu, J. Lim, and M. Ohtsu, "Theoretical and experimental study on a near-field optical nano-switch", Technical Digest of Photonics Switching, OSA/IEEE LEOS Meeting, Monterey, CA, June 13-15, 2001, pp.27-29, (paper number PThB4)

(pp.109-111)

[11] K. Kobayashi, T. Kawazoe, S. Sangu, J. Lim, and M. Ohtsu, "Nanometric quantum dots controlled by optical near fields: theoretical and experimental study", Abstract of the 2001 JRCAT-CERC Workshops on Phase Control on Correlated Electron System", Maui Is, Hawaii, June 6-9, 2001, p.23

(p.112)

[12] M. Ohtsu, "Nanotechnology and nano/atom photonics by optical near-field", Proceedings of SPIE, vol.4416, International Conference on Optical Engineering for Sensing and Nanotechnology (ICOSN 2001), June 6-8, 2001, Yokohama, pp.1-13

[Plenary presentation]

(pp.113-125)

[13] M. Ohtsu, "Photochemical vapor deposition by optical near field toward nanometric photonic integration", Abstracts of Tokyo-2001: Scanning Probe Microscopy, Sensors, and Nanostructures, May 27-31, 2001, Makuhari, p.10
[Invited presentation]

(p.126)

[14] T. Yatsui, M. Kourogi, and M. Ohtsu, "A pyramidal silicon probe with an extremely high throughput and resolution for optical near field technology", Technical Digest of Quantum Electronics and Laser Science Conference, May 6-11, 2001, Baltimore, MA, pp. 51-52 (paper number QMN5)

(pp.127-128)

[15] T. Yatsui, M. Ueda, M. Kourogi, and M. Ohtsu, "High throughput capability of a microfabricated hollow probe for near field microscopy in ultraviolet region", Technical Digest of Quantum Electronics and Laser Science Conference, May 6-11, 2001, Baltimore, MA, pp. 79-80 (paper

number QTuE1)

(pp.129-130)

[16] T. Kawazoe, T. Shimizu, and M. Ohtsu, "Second Harmonic Generation in Aluminum Coated Near-Field Fiber Probe", Technical Digest of Quantum Electronics and Laser Science Conference, May 6-11, 2001, Baltimore, MA, pp. 80-81 (paper number QTuE3)

(pp.131-132)

[17] M. Ohtsu, "Overview", in "Near-Field Optics: Principles and Applications", The Second Asia-Pacific Workshop on Near Field Optics, ed.by X. Zhu and M. Ohtsu, World Scientific, Singapore, 2000, pp.1-8

[Introductory talk]

(pp.133-140)

[18] S. Mononobe and M. Ohtsu, "Fabrication of a near-field optical probe based on electroless plating", Abstracts of the 6th International Conference on Near Field Optics and Related Techniques, August 27-31, 2000, Enschede, the Netherland, p.115 (paper number MoP48)

(p.141)

[19] Y. Yamamoto, G.H. Lee, V.V. Polonski, T. Shimizu, M. Kourogi, and M. Ohtsu, "Chemical vapor deposition of Zn and ZnO dots with optical near field", Abstracts of the 6th International Conference on Near Field Optics and Related Techniques, August 27-31, 2000, Enschede, the Netherland, p.177 (paper number TuP1)

(p.142)

[20] H. Fukuda and M. Ohtsu, "Near-field photocurrent measurements of reverse-biased Si p-n junction", Abstracts of the 6th International Conference on Near Field Optics and Related Techniques, August 27-31, 2000, Enschede, the Netherland, p.178 (paper number TuP2)

(p.143)

[21] N. Toyoshima, T. Kawasaki, M. Ohtsuka, J. Takahashi, T. Yatsui, M. Kourogi, and M. Ohtsu, "Recording/readout/erasing on phase-change optical media with apertured fiber-probe", Abstracts of the 6th International Conference on Near Field Optics and Related Techniques, August 27-31, 2000, Enschede, the Netherland, p.179 (paper number TuP3)

(p.144)

[22] S. Sangu, K. Kobahashi, and M. Ohtsu, "Optical near fields as photon-matter interacting systems", Abstracts of the 6th International Conference on Near Field Optics and Related Techniques, August 27-31, 2000, Enschede, the Netherland, p.202 (paper number TuP26)

(p.145)

[I-3] REVIEW PAPERS

[1] M. Ohtsu, "Progress In Near-field Optical Microscopy", Optical and Electro-Optical Engineering Contact, vol.39, no.4, April 2001, pp.202-211
【大津元一、「近接場光学顕微鏡の進展」、光技術コンタクト、第３９巻、第４号、２００１年４月、pp.202-211】

(pp.147-156)

[2] M. Ohtsu, "Nano-photonics and Its Overlook", J. Inst. Electronics, Information and Communication Eng., vol.84, no.1, January 2001, pp.26-32
【大津元一、「ナノフォトニクスとその展望」、電子情報通信学会誌、第８４巻、第１号、２００１年１月、pp.26-32】

(pp.157-163)

[3] M. Ohtsu, "Optical-nano-technology for IT", O plus E, vol.23, no.1, January 2001, pp.49-52
【大津元一、「ITのハードウエア技術を支える光ナノテクノロジー」、O plus E、第２３巻、第１号、２００１年１月、pp.49-52】

(pp.164-167)

[4] G.H. Lee, Y. Yamamoto, M. Kourogi, and M. Ohtsu, "Deposition of nanometric matters by optical near-field", J. Appl. Phys. Jpn., vol.69, no.10, October 2000, pp.1222-1223
【李謹炯、山本洋、興梠元伸、大津元一、「近接場光によるナノ領域堆積」、応用物理、第６９巻、第１０号、２０００年１０月、pp.1222-1223】

(pp.168-169)

[5] S. Mononobe and M. Ohtsu, "Selective chemical etching of optical fibers and its applications", New Glass, vol.15, no.2, 2000, pp.47-50
【物部秀二、大津元一、「光ファイバーの選択エッチングとその応用」、ニューガラス、第１５巻、第２号、２０００，pp.47-50】

(pp.170-173)

[II] PAPERS IN OTHER FIELDS

(b) International Conferences

[1] M. Kourogi, B. Widiyatmoko, S.-J. Lee, and M. Ohtsu, "Ultra-high scanning speed optical coherence tomography using optical frequency comb generators", Technical Digest of Conference on Lasers and Electro-Optics, May 6-11, 2001, Baltimore, MA, p. 368 (paper number CWN3)

(p.175)

[2] M. Kourogi and M. Ohtsu, "Past, Present, and future of optical comb generation", Proceedings of SPIE, vol.4269, Conference on Laser Frequency Stabilization, Standards, Measurement, and Applications, January 24-26, 2001, San Jose, CA, pp.59-71

[Invited presentation]

(pp.176-188)

(c) Review Papers

[1] M. Kourogi, K. Imai, B. Widiyatmoko, and M. Ohtsu, "Generation of Expanded Optical Frequency Combs", in *Frequency Measurement and Control*, ed. by A.N. Luiten, Topics Appl. Phys., vol.79, 2001, pp.315-335

(pp.189-209)

[2] M. Ohtsu, "Reviewing the Dr. M. Kourogi's paper for Jpn. J. Optics Award", Jpn. J. Optics, vol.30, no.4, April 2001, p.278
【大津元一、「興梠元伸氏の論文紹介」、光学、第 30 巻、第 4 号、2001 年 4 月、p.278】

(p.210)

[III] PUBLISHED BOOKS

[1] M. Ohtsu (ed.), *Optical and Electronic Process of Nano-matters*, KTK Scientific Publishers/Tokyo, Kluwer Academic Publishers/Dordrecht, 2001 (334 pages)

(pp.211-217)

[2] X. Zhu and M. Ohtsu, *Near-Field Optics: Principles and Applications*, The Second Asia-Pacific Workshop on Near Field Optics, World Scientific, Singapore, 2000

[IV] PRESENTED PH.D THESIS

[1] H. Fukuda, "Study on diagnosing silicon semiconductor devices by an optical near field microscope", January 2001
【福田浩章、「近接場光学顕微鏡を用いたシリコン半導体デバイスの評価に関する研究」、2001年1月】

[2] Y. Yamamoto, "Study on photochemical vapor deposition by optical near field", January 2001
【山本洋、「近接場光学手法による光化学気相堆積法に関する研究」、2001年1月】

[3] T. Murashita, "Development of a collection-mode electron tunneling emission probe microscope and its application to diagnose nano-structures"
【村下達、「探針集光型トンネル電子発光顕微鏡の開発とナノ構造評価への応用に関する研究」、2001年1月】

[4] N. Takachio, "Increasing the capacity of optical transmission system by suppressing nonlinear optical effects in optical fiber and compensation of wavelength-dispersion", January 2001
【高知尾昇、「光ファイバの非線形光学効果抑圧と波長分散補償による光伝送システム大容量化に関する研究」、2001年1月】

[I] PAPERS IN NANO/ATOM PHOTONICS

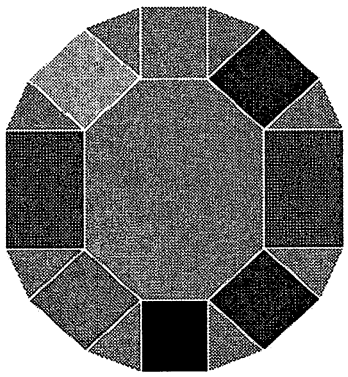

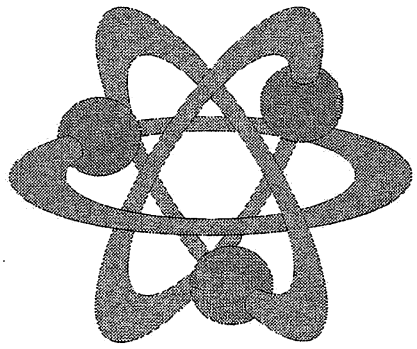

[I-1] PAPERS IN ATOM PHOTONICS

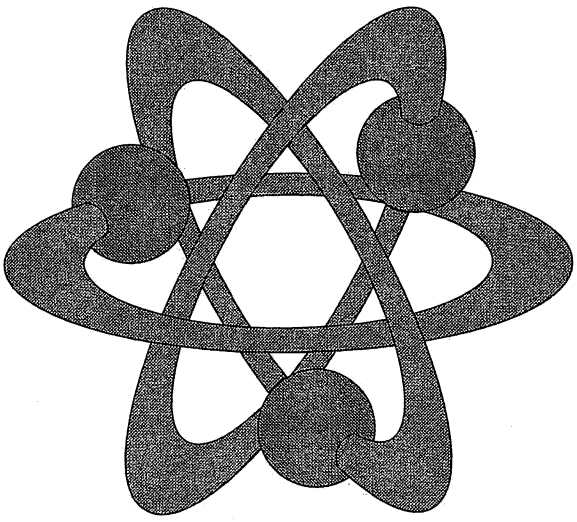

PHYSICAL REVIEW A, VOLUME 63, 013806

Near-field optical potential for a neutral atom

K. Kobayashi* and S. Sangu
ERATO Localized Photon Project, Japan Science and Technology Corporation, 687-1 Tsuruma, Machida, Tokyo 194-0004, Japan

H. Ito and M. Ohtsu†
Interdisciplinary Graduate School of Science and Engineering, Tokyo Institute of Technology, 4259 Nagatsuta-cho, Midori-ku, Yokohama, Kanagawa 226-8502, Japan

(Received 19 April 2000; published 11 December 2000)

We study an effective interaction potential between a neutral atom and a nanometric probe tip in optical near-field systems. The wave-number dependence of the coupling coefficients of exciton polaritons is described with the effective-mass approximation, where massive virtual photons are exchanged between the atom and the probe tip. The near-field optical potential is shown as the sum of the Yukawa functions with several kinds of effective masses or interaction ranges, and is characterized in terms of detuning for the resonance energies of the atom and the probe tip. Consequently, we find that a potential minimum is produced for a blue detuning case. This result indicates that an atom can be trapped in the near-field optical potential well. Furthermore, we numerically investigate deflection and trapping of a single atom by means of optical near fields generated from a nanometric probe tip. The dependence on the probe-tip size, the kinetic energy of the cold atom, and the excitation energies of both probe tip and atom is clarified.

DOI: 10.1103/PhysRevA.63.013806 PACS number(s): 42.50.Ct, 32.80.Pj

I. INTRODUCTION

Optical near-field techniques are considered promising as enabling technologies for nanostructure fabrication with arbitrary shapes and high spatial accuracy far beyond the diffraction limit [1]. As a result of the development of a highly efficient probe tip for optical near-field systems [2–4], local excitation of a nanometric quantum dot [4–6] and photochemical deposition of, for example, Zn [7,8] and ZnO [1] on a sub-100-nm scale have become possible. The ultimate goal of such fabrication is to make atomic-scale crystal growth by manipulating individual atoms with optical methods [2,9–11]. In fact, an optical near-field probe tip with a diameter of less than 10 nm has been developed and is expected to be used in atom manipulation experiments [2]. Microscopic or quantum-mechanical treatment [12–16] of the interaction between such a nanometric probe tip and an atom is essential for describing the atom manipulation with optical near fields. In particular, it is important to consider the nanometric tip and the atom as an interacting system through the coupling to a macroscopic bath system made up of incident photons, substrate, and/or fiber probe. It should be noted that the conventional theories in near-field optics, which deal with the tip and the atom independently, have been developed in order to analyze scanning-microscope images with *macroscopic* quantities such as refractive indices. Therefore they are not suitable for formulating *microscopic* phenomena associated with optical near-field techniques.

In this paper we concentrate on the theoretical derivation and evaluation of effective interaction potentials between a neutral atom and a nanometric probe tip. We follow the well-known approach of describing atomic behavior in terms of the optical potential, by which we can obtain a clear physical image. This kind of treatment also allows us to quantitatively discuss the interacting system. The near-field optical potential, however, has not been derived yet in a microscopic way. That is the chief reason why we try to microscopically derive the potential.

Although the existing theories have predicted the possibility of atom trapping, they have never included a microscopic and consistent discussion on the near-field optical potential since a nanometric probe tip has not been employed to produce optical near fields. Let us take an example illustrating this point clearly. An approach for atom trapping by evanescent fields has been proposed; it employs two laser beams that propagate through totally internal reflection by a flat prism [17], or by the wall of a microsphere [18]. In this scheme, the blue-detuned beam has a larger incident angle than the red-detuned beam, so that two different evanescent fields with two different penetration depths are produced in a vacuum side. The fundamental idea is based on the potential balance due to the existence of these two fields. This kind of trapping is usually explained with reference to the *far-field* optical potential [19] qualified by the dressed atom theory [20], which is applied to a wide range of phenomena, from atom-photon interaction in general to laser cooling [21]. The optical near field, however, is a highly mixed state with material excitation rather than the propagating light field. This viewpoint becomes more and more important as we consider a tiny generator of the optical near field, whose size is much smaller than the wavelength of light. It has therefore remained an open question whether atomic behavior in near-field optical systems can be adequately expressed by the optical potential borrowed from the far-field theory.

We develop a consistent theory appropriate for investigating the near-field optical manipulation of an atom. The atom is considered to interact with the nanometric probe tip via an

*Electronic address: kkoba@ohtsu.jst.go.jp
†Also at ERATO Localized Photon Project, Japan Science and Technology Corporation.

elementary excitation mode of real photons and the macroscopic matter system. We discuss the possibility of trapping a single atom, giving a numerical estimation of the near-field optical potential. The paper is organized as follows. Section II presents a formulation for the derivation of a near-field optical potential with the help of the projection-operator method. Section III clarifies the fundamental features of the near-field optical potential. In Sec. IV a numerical analysis of atom deflection and trapping is performed. Section V offers some concluding remarks.

II. FORMULATION

It is reasonable to use classical electromagnetic theories for macroscopic descriptions of the behavior of light and matter. However, when the size of the probe tip or aperture becomes nanometric, that is, comparable to an atomic scale, there is no guarantee that we can use classical theories to correctly formulate optical near-field problems such as interactions between atoms or nanometric samples and the probe tip. We therefore try to study the problems within a quantum theoretical framework, paying special attention to the hierarchical structure of optical near-field systems [1,16]. Our formulation is general, but hereafter we focus on an effective interaction between a probe tip and a neutral atom. On the basis of the projection-operator method, the effective interaction can be exactly expressed by using a small number of bases after renormalizing the effects of the other degrees of freedom [see Eqs. (7a) and (7b)]. The renormalizing effects may include cavity quantum-electrodynamic (QED) effects, energy shift and mixing of the ground and higher-level states of the atom, and the probe tip. It is noted that the nanometric probe tip has discrete energy levels. If we employ static or steady states as the bases, the effective interaction corresponds to an effective potential for the relevant system from quantum-field theoretical consideration. The potential picture is very appropriate for investigating atomic behavior, and will be adopted in the following discussion.

In order to derive an effective potential $V_{\rm eff}(r)$, where r is the atom's position measured from an arbitrary point ($\vec{r}_2$) inside a probe tip, we divide an optical near-field system into two subsystems: (i) incident propagating light consisting of real photons that interact with a macroscopic matter system, typically a prism in the collection mode or a fiber probe in the illumination mode [2], and (ii) a nanometric probe tip and an atom. Figure 1 illustrates the division considered here. These two subsystems interact with each other, and consequently produce the interaction between the probe tip and the atom in the subsystem (ii). The interaction originates from the exchange of virtual exciton polaritons, as we will see in the following.

The starting point is that the eigenvalues and eigenstates of the total Hamiltonian $\hat{H}$ for the optical near-field system are written as E_λ and $|\Psi_\lambda\rangle$, respectively; that is,

$$\hat{H}|\Psi_\lambda\rangle=(\hat{H}_0+\hat{V})|\Psi_\lambda\rangle=E_\lambda|\Psi_\lambda\rangle, \tag{1}$$

where $\hat{H}_0$ consists of the Hamiltonians $\hat{H}_{\rm bath}$ for the subsystem (i) and $\hat{H}_A+\hat{H}_B$ for the subsystem (ii), while $\hat{V}$ denotes the interaction between the two subsystems. It is noted that the Hamiltonian $\hat{H}_A$ ($\hat{H}_B$) describes the states of the atom (the probe tip) as an isolated quantum-mechanical system. The suffix λ distinguishes each eigenstate. Defining the projection operators P and $Q=1-P$ in the usual manner as

$$|\Psi_\lambda^{(1)}\rangle=P|\Psi_\lambda\rangle, \quad |\Psi_\lambda^{(2)}\rangle=Q|\Psi_\lambda\rangle, \tag{2a}$$

$$P^2=P, \quad PQ=QP=0, \tag{2b}$$

$$[P,\hat{H}_0]=[Q,\hat{H}_0]=0, \tag{2c}$$

we divide the eigenstates $|\Psi_\lambda\rangle$ into two groups, $|\Psi_\lambda^{(1)}\rangle$ in P space and $|\Psi_\lambda^{(2)}\rangle$ in Q space. By using Eqs. (2a)–(2c), Eq. (1) is then rewritten as a set of equations

$$(E_\lambda-\hat{H}_0)P|\Psi_\lambda^{(1)}\rangle=P\hat{V}P|\Psi_\lambda^{(1)}\rangle+P\hat{V}Q|\Psi_\lambda^{(2)}\rangle, \tag{3a}$$

$$(E_\lambda-\hat{H}_0)Q|\Psi_\lambda^{(2)}\rangle=Q\hat{V}P|\Psi_\lambda^{(1)}\rangle+Q\hat{V}Q|\Psi_\lambda^{(2)}\rangle. \tag{3b}$$

From the above equation Eq. (3b), it is possible to formally express $Q|\Psi_\lambda^{(2)}\rangle$ by $P|\Psi_\lambda^{(1)}\rangle$ as

$$\begin{aligned} Q|\Psi_\lambda^{(2)}\rangle&=(E_\lambda-\hat{H}_0-Q\hat{V})^{-1}Q\hat{V}P|\Psi_\lambda^{(1)}\rangle \\ &=\hat{J}(E_\lambda-\hat{H}_0)^{-1}Q\hat{V}P|\Psi_\lambda^{(1)}\rangle, \end{aligned} \tag{4a}$$

$$\hat{J}=[1-(E_\lambda-\hat{H}_0)^{-1}Q\hat{V}]^{-1}, \tag{4b}$$

and the eigenstates $|\Psi_\lambda\rangle$ for the total Hamiltonian can then be expressed in terms of the eigenstates in P space as

$$|\Psi_\lambda\rangle=(P+Q)|\Psi_\lambda\rangle=\hat{J}P|\Psi_\lambda^{(1)}\rangle. \tag{5}$$

Since both of the states satisfy the normalization condition, we can rewrite this as

$$|\Psi_\lambda\rangle=\hat{J}P(P\hat{J}^\dagger\hat{J}P)^{-1/2}|\Psi_\lambda^{(1)}\rangle. \tag{6}$$

Using the projection operators, we can thus consistently treat the interaction as follows [1,16]:

$$\langle\Psi_\mu|\hat{V}|\Psi_\lambda\rangle=\langle\Psi_\mu^{(1)}|\hat{V}_{\rm eff}|\Psi_\lambda^{(1)}\rangle, \tag{7a}$$

$$\hat{V}_{\rm eff}=(P\hat{J}^\dagger\hat{J}P)^{-1/2}(P\hat{J}^\dagger\hat{V}\hat{J}P)(P\hat{J}^\dagger\hat{J}P)^{-1/2}, \tag{7b}$$

where the bare interaction $\hat{V}$ operates on exact states $|\Psi\rangle$ of the total system, while $\hat{V}_{\rm eff}$ operates on a small number of states $|\Psi^{(1)}\rangle$ of the subsystem (ii).

In order to proceed further in evaluating Eq. (7a), we need explicit forms of $\hat{V}$ and $\hat{J}$ as well as P. First the interaction $\hat{V}$ between the two subsystems is described by the multipolar QED Hamiltonian [22]. We employ, for simplicity, its dipole approximation as

$$\hat{V}=-\sum_\alpha \theta(z_\alpha)\hat{\vec{\mu}}_\alpha\cdot\hat{\vec{D}}(\vec{r}_\alpha), \tag{8}$$

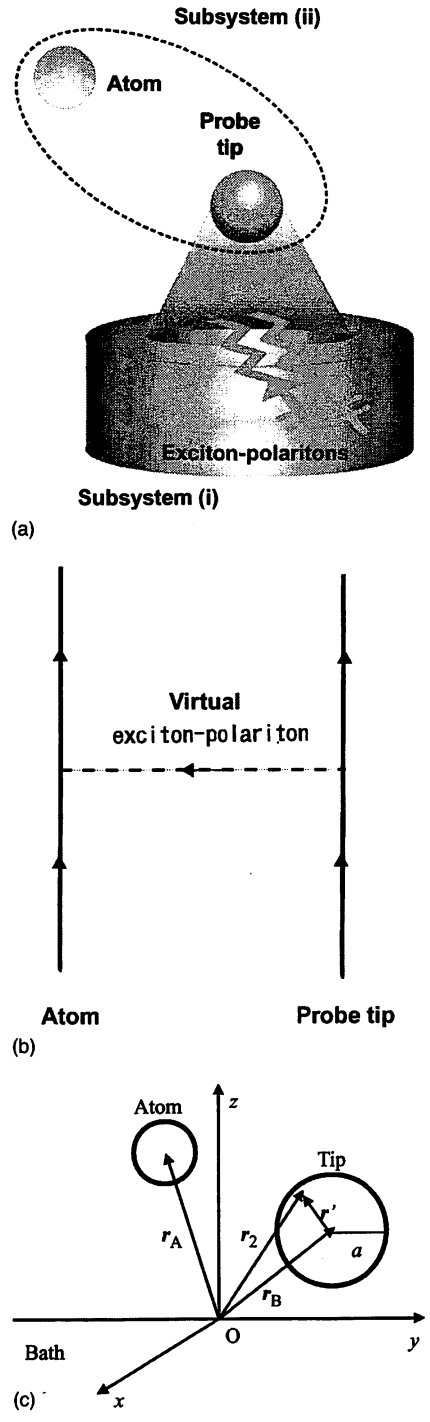

FIG. 1. Schematic illustration of how to divide a near-field optical system. A nanometric probe tip and an atom, referred to as subsystem (ii), are extracted from the total system, while the remaining part is regarded as subsystem (i). These two subsystems interact with each other via an elementary excitation mode, or exciton-polaritons as shown in wavy lines. As a result, the probe tip and the atom also interact by exchanging virtual exciton polaritons. Geometry of the model is also inserted. The vectors $\vec{r}_A$ and $\vec{r}_B$ denote the center of the atom and the center of the tip sphere with a radius of a, respectively. An arbitrary position inside the tip sphere is represented by $\vec{r}_2$ measured from the origin of the coordinates system, and $\vec{r}'$ measured from the center of the tip sphere, respectively.

where $\theta(z)$ and $\hat{\vec{\mu}}(\vec{r})$ are the step function and the dipole operator, respectively. The displacement field operator is denoted as $\hat{\vec{D}}(\vec{r})$, and is given by the conjugate momentum operator $\hat{\vec{\Pi}}(\vec{r})$ of the vector potential operator $\hat{\vec{A}}(\vec{r})$. Then it is necessary to find out an explicit form of the operator $\hat{J}$ that can be handled. Noting that the state $P|\Psi_\lambda^{(1)}\rangle$ satisfies the following equation:

$$(E_\lambda - \hat{H}_0)P|\Psi_\lambda^{(1)}\rangle = P\hat{V}\hat{J}P|\Psi_\lambda^{(1)}\rangle, \tag{9}$$

with the help of Eqs. (3a) and (4a) we can then write down the equation to be solved as

$$[\hat{J},\hat{H}_0]P = (E-\hat{H}_0)\hat{J}P - \hat{J}(E-\hat{H}_0)P = \hat{V}\hat{J}P - \hat{J}P\hat{V}\hat{J}P, \tag{10}$$

where we used Eqs. (1), (5), and (9). If we expand the operator $\hat{J}$ as

$$\hat{J} = \sum_{n=0}^{\infty} g^{(n)}\hat{J}^{(n)} = P + \sum_{n=1}^{\infty} g^{(n)}\hat{J}^{(n)}, \tag{11}$$

we have the following perturbative solutions in the order of $\hat{V}$:

$$\hat{J}^{(0)} = P, \quad \hat{J}^{(1)} = Q(E_P^0 - E_Q^0)^{-1}\hat{V}P, \ldots, \tag{12}$$

where E_P^0 and E_Q^0 are the eigenvalues of the unperturbed Hamiltonian $\hat{H}_0$ in P and Q space, respectively. Finally let us comment on the selection of a small number of bases in the P space, or construction of the projection operator P. Since we are mainly interested in the interaction potential between the atom and the probe tip, it is preferable to choose the bases so that the degrees of freedom of the subsystem (i) are eliminated. We assume, for simplicity, that eigenstates and eigenenergies of $\hat{H}_\alpha$ ($\alpha = A$ or B) are known as $|\alpha\rangle$, $|\alpha^*\rangle, \ldots$, and E_α^0, $E_{\alpha^*}^0 \ldots$. In addition, let the bath system, or the subsystem (i), be a set of excitons, photons, and their interactions, by assuming that the induced electric polarization in the macroscopic matter system is represented as excitons [23]. It is well known that such a system has characteristic elementary excitation modes, that is, exciton-polariton modes, or so-called "dressed" states of photons and excitons [24–26]. These eigenstates and eigenenergies are well determined. If we rewrite the photon operators in $\hat{\vec{D}}(\vec{r})$ [Eq. (8)] as exciton-polariton operators, we can obtain the bare interaction $\hat{V}$ in the exciton-polariton picture. Now let us choose a combination of the five states $|A\rangle$, $|A^*\rangle$, $|B\rangle$, $|B^*\rangle$, and $|0\rangle$ as the P-space bases. Here the ground state of $\hat{H}_{\text{bath}}$, including no exciton polaritons, is expressed as $|0\rangle$.

By using Eqs. (7a) and (12), the effective potential in the lowest order [27] can be written as

$$V_{\mathrm{eff}}(r)=-\frac{4\pi}{(2\pi)^3}\sum_{\alpha\neq\alpha'}^{(A,B)}\int d^3k\left[\frac{K'_\alpha(\vec{k})K'^{*}_{\alpha'}(\vec{k})}{\Omega(\vec{k})-\Omega(\alpha')}+\frac{K'_{\alpha'}(\vec{k})K'^{*}_{\alpha}(\vec{k})}{\Omega(\vec{k})+\Omega(\alpha)}\right]. \quad (13)$$

Here the eigenenergy of the elementary excitation modes of the subsystem (i), that is, of the massive virtual photons, is denoted as $\hbar\Omega(k)$. The electronic excitation energies of the atom and the probe tip in the second subsystem are denoted as $E_A=\hbar\Omega(A)$ and $E_B=\hbar\Omega(B)$ ($\alpha,\alpha'=A$ or B). Note that the center-of-mass motion of the atom is not considered here. The coefficients $K'_\alpha(\vec{k})$ and its complex conjugate $K'^{*}_\alpha(\vec{k})$ represent the coupling strength of the elementary excitation modes to the atom and the probe tip, and one can obtain the explicit form of $K'_\alpha(\vec{k})$ to define the coupling coefficient $f(k)$ as

$$K'_\alpha(\vec{k})=\sum_{\lambda=1}^{2}\theta(z_\alpha)\mu_\alpha[\vec{e}\cdot\vec{e}_\lambda(\vec{k})]f(k)e^{i\vec{k}\cdot\vec{r}_\alpha}, \quad (14a)$$

$$f(k)=\frac{ck}{\sqrt{\Omega(k)}}\frac{\sqrt{\Omega^2(k)-\Omega^2/4}}{\sqrt{2\Omega^2(k)-\Omega^2/4-c^2k^2}}, \quad (14b)$$

where the wave-number dependence of $f(k)$ characterizes a typical interaction range of exciton polaritons coupled to the subsystem (ii). Here the jth component of the dipole moment and the unit polarization vector for photons are, respectively, designated as $\mu_\alpha\vec{e}_j$ and $\vec{e}_\lambda(\vec{k})$. The quantities c and $E_m=\hbar\Omega/2$ stand for the speed of light and the electronic excitation energy of the macroscopic matter in the subsystem (i).

On the basis of the dispersion relation of an exciton-polariton with effective mass m_p ($E_p=m_pc^2$), we perform the usual effective-mass approximation as follows:

$$\hbar\Omega(k)=\frac{\hbar\Omega}{2}+\frac{(\hbar k)^2}{2m_p}. \quad (15)$$

Substituting this expression into Eqs. (13), (14a), and (14b) we can rewrite the effective potential $V_{\mathrm{eff}}(r)$ as

$$\begin{aligned}V_{\mathrm{eff}}(r)&=-\frac{4\mu_A\mu_B\hbar E_p}{3i\pi r(\hbar c)^2}\int dkkf^2(k)e^{ikr}\left\{\frac{1}{k^2+2E_p(E_m+E_A)(\hbar c)^{-2}}+\frac{1}{k^2+2E_p(E_m-E_A)(\hbar c)^{-2}}\right.\\&\left.+\frac{1}{k^2+2E_p(E_m+E_B)(\hbar c)^{-2}}+\frac{1}{k^2+2E_p(E_m-E_B)(\hbar c)^{-2}}\right\}\\&=\frac{2\mu_A\mu_BE_p^2}{3i\pi r(\hbar c)^2}\int_{-\infty}^{\infty}dkkF(k)e^{ikr}, \end{aligned}\quad (16)$$

where we average the summation over λ as 2/3, and define $F(k)$ as

$$F(k)\equiv\left(\frac{A_+}{k^2+\Delta_{A_+}^2}-\frac{A_-}{k^2+\Delta_{A_-}^2}\right)+\left(\frac{B_+}{k^2+\Delta_{B_+}^2}-\frac{B_-}{k^2+\Delta_{B_-}^2}\right)+\left(\frac{C_+}{k^2+\Delta_{C_+}^2}-\frac{C_-}{k^2+\Delta_{C_-}^2}\right). \quad (17)$$

Finally, as the sum of the Yukawa functions with several kinds of masses, we obtain the following near-field optical potential:

$$V_{\mathrm{eff}}(r)=\frac{2\mu_A\mu_BE_p^2}{3(\hbar c)^2}\{A_+Y(\Delta_{A_+}r)-A_-Y(\Delta_{A_-}r)+B_+Y(\Delta_{B_+}r)-B_-Y(\Delta_{B_-}r)\}, \quad (18a)$$

$$Y(\mu r)\equiv\frac{\exp(-\mu r)}{r}. \quad (18b)$$

The four kinds of effective masses of the Yukawa function are denoted as Δ_{A_+}, Δ_{B_+}, Δ_{A_-}, and Δ_{B_-}, of which the first two are heavier and thus have shorter interaction ranges. Two constants Δ_{C_+} and Δ_{C_-}, omitted in Eq. (18a), mainly give the periodic functions related to the property of the macroscopic matter, not the Yukawa function related to the microscopic subsystem. Here, we use the following explicit expression for the effective masses:

$$\Delta_{A_\pm}=\frac{\sqrt{2E_p(E_m\pm E_A)}}{\hbar c}, \quad \Delta_{B_\pm}=\frac{\sqrt{2E_p(E_m\pm E_B)}}{\hbar c}, \quad (19)$$

assuming a blue detuning case [$\hbar\Omega(k)>E_m>E_A$ and E_B]. Note that the positive ones (Δ_{A_+} and Δ_{B_+}) are kept for a red detuning case [$E_m<\hbar\Omega(k)<E_A$ and E_B]. The first and second pairs of terms in Eq. (17) come from the coupling between the exciton polaritons and the subsystem (ii), while the third pair of terms originates from the macroscopic matter. The weight factors in Eq. (18a), that is, the numerators of each term in Eq. (17), are functions of E_A, E_B, E_p, and E_m.

Depending on whether the weight factor is positive or negative, it contributes to a repulsive or an attractive part of the effective potential $V_{\rm eff}(r)$.

III. PROPERTIES OF THE NEAR-FIELD OPTICAL POTENTIAL

Let us examine the features of the effective potential described by Eq. (18a). The potential is formally symmetric in terms of $A_\pm$ and $B_\pm$, and thus the discussion on one of the pairs is applicable to the other, though they are not necessarily the same in sign and magnitude. In the following, we will abbreviate $A_\pm$ or $B_\pm$ to $G_\pm$ unless otherwise stated. The sign and magnitude of $G_\pm$ depend on the detuning $\hbar\delta \equiv E_m - E_G$ and E_m. We consider a case where the detuning is large and the natural linewidth and saturation are negligible. The difference between G_+ and G_- is written as

$$G_+ - G_- \cong G_+\left[1-\frac{9}{5}\left(\frac{\hbar\delta}{E_m}+\frac{E_m}{2\hbar\delta}\right)^{-1}\right], \qquad (20)$$

when $\hbar\delta$ stays between 0 and E_m in blue detuning. This detuning dependence is qualitatively consistent with that of the usual far-field optical potential in the large detuning limit [19,20]. Spontaneous emission and radiation pressure are also negligible in this limit [28]. If G_+ is positive, that is, blue detuned, and if the detuning $\hbar\delta$ is chosen so that the difference between G_+ and G_- is positive, the total potential then becomes repulsive, because the repulsive G_+ term is larger than the attractive G_- term. Note that the decay length of the repulsive G_+ term is shorter than that of the attractive G_- term.

As an example, we assume a typical alkali-metal atom with $E_A = 1.6$ eV, where infrared and/or visible excitations of a macroscopic matter system and a probe tip are taken as $E_m = 1-1.8$ eV and $E_B = 1.0-1.2$ eV, respectively. Figure 2 represents several examples of the effective potentials. In Fig. 2(a) we use $E_A = 1.6$ eV, $E_B = 1.2$ eV, and $E_m = 1.0$ eV for a red-detuning case. Then G_+ is negative for red detuning and results in the attractive Yukawa potential. The solid line shows the total potential, while the dotted and dashed lines represent the attractive potentials with light and heavy effective masses, respectively. In contrast to red detuning, Fig. 2(b) shows a blue-detuning case, where we employ $E_A = 1.6$ eV, $E_B = 1.0$ eV, and $E_m = 1.8$ eV. This set of parameters leads to a repulsive potential for the $A_\pm$ term and an attractive potential for the $B_\pm$ term; the $(A_+ - A_-)$ term, in addition, is smaller than the $(B_+ - B_-)$ term; as a result, the attractive Yukawa potential occurs, as similar to Fig. 2(a). If a value of E_B is carefully chosen, it is possible to have a potential well for blue detuning. We show such an example in Fig. 2(c), where excitation energy of the probe tip is taken as $E_B = 1.2$ eV, while the other conditions are the same as in Fig. 2(b). In this case, the $(A_+ - A_-)$ term is larger than the $(B_+ - B_-)$ term, and thus the total potential forms a well as shown in the solid line. Figures 2(b) and 2(c) show how the difference in the balance between the $(A_+ - A_-)$ and $(B_+ - B_-)$ terms affects the final potential shapes.

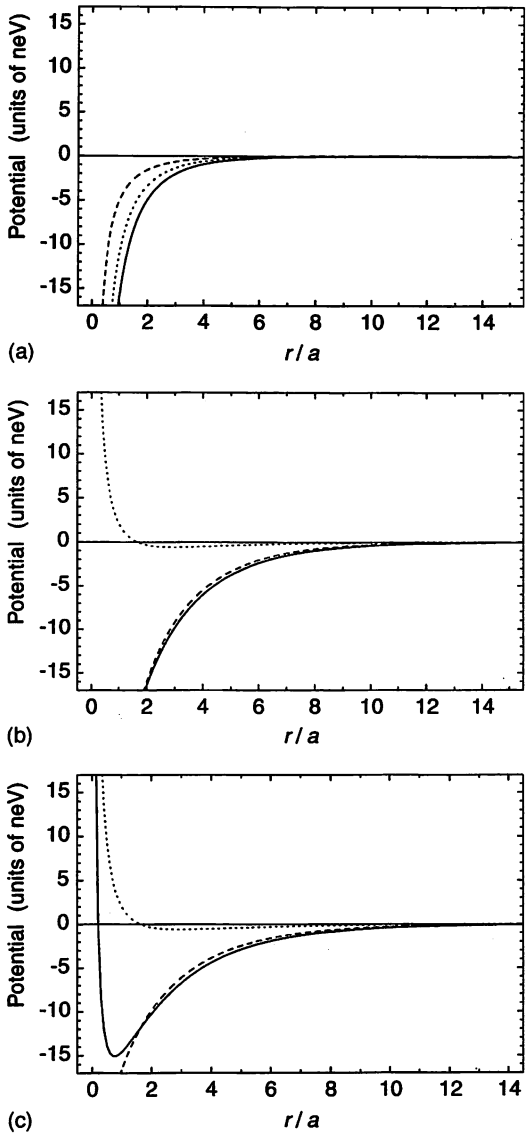

FIG. 2. Examples of the near-field optical potentials. (a) An attractive Yukawa potential in a red-detuning case. The resonance energy of an atom is assumed as $E_A = 1.6$ eV. The electronic excitation energies $E_B = 1.2$ eV and $E_m = 1.0$ eV are used for a probe tip and a macroscopic matter system, respectively. The solid line shows the total potential, while the dotted and dashed lines represent the attractive potentials with light and heavy masses. (b) An attractive Yukawa potential in a blue-detuning case. The excitation energies of the probe tip and the macroscopic matter system are chosen as $E_B = 1.0$ eV and $E_m = 1.8$ eV, respectively. The dotted, dashed, and solid lines represent the repulsive, attractive, and total potentials, respectively. (c) A potential well in a blue-detuning case. The excitation energy of the probe tip is chosen as $E_B = 1.2$ eV, while the other conditions are the same as in (b).

We can simply explain the detuning dependence of the near-field optical potential discussed above, on the basis of the wave-number dependence of the coupling coefficient $f(k)$ in Eq. (14b). It follows from Fig. 3 that $f(k)$ is constant when k is larger than the lower cutoff $k_c \approx 2\sqrt{m_p\Omega/\hbar} = 2\sqrt{2E_pE_m}/(\hbar c)$, while it is approximately proportional to k below k_c. The solid and dashed lines represent two cases

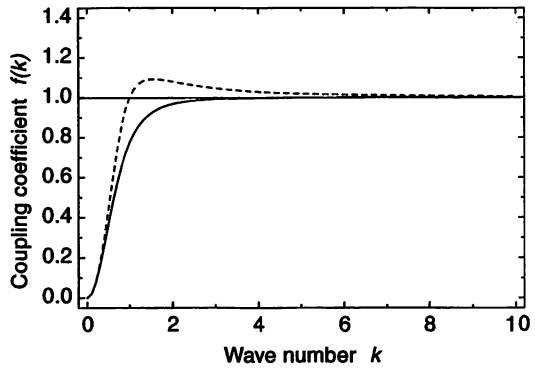

FIG. 3. Wave-number dependence of the coupling coefficient $f(k)$. The horizontal and vertical axes are measured in units of $\sqrt{E_m E_p}/\hbar c$ and $\sqrt{E_p}/\hbar$. The solid and dotted lines represent two cases of $E_p=E_m$ and $E_p=2E_m$, respectively.

of $E_p=E_m$ and $E_p=2E_m$, respectively. The coefficient $f(k)$ in the case of $E_p=E_m$ is always smaller than the asymptotic value, while in the case of $E_p=2E_m$ it becomes larger than the asymptotic value near the cutoff k_c. Simple estimation [29] yields $k_c \approx 1/100$ nm, which characterizes the interaction range of the exciton polaritons or massive virtual photons coupled to the subsystem (ii). It also shows that the coupling coefficient $f(k)$ is almost constant for a large red-detuning case and thus the Yukawa potential becomes attractive. For a blue-detuning case, the nonconstant term is not negligible and contributes to the repulsive potential.

As mentioned above, we can control the polarities and the interaction ranges of the Yukawa potentials, changing the detuning and material properties. It is thus possible to find the condition for forming a potential well due to the balance between the attractive and the repulsive potentials. Figure 4 illustrates such a condition. The solid curve shows how the weight factor of $B_- - B_+$ depends on the excitation energy E_B of a probe tip. The dashed line, which is independent of E_B, represents the weight factor $A_+ - A_-$ when the detuning and the resonance energies of both an atom and a macroscopic matter are fixed. The shaded area corresponds to the condition that the repulsive $A_+ - A_-$ term for blue detuning becomes larger than the attractive $B_+ - B_-$ term, that is, the condition that the total potential has a minimum. If we

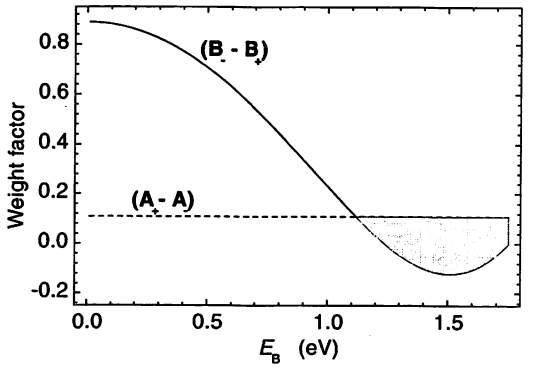

FIG. 4. Weight factor dependence on the excitation energy of a probe tip. If we take one of the excitation energies E_B in the shaded area, we can obtain a potential well as shown in Fig. 2(c).

choose a smaller value than $E_B=1.12$ eV, the smallest value in the shaded area, the $B_+ - B_-$ term becomes larger than the $(A_+ - A_-)$ term and the total potential results in an attractive Yukawa potential as shown in Fig. 2(b). Both Figs. 2 and 4 indicate that a near-field optical potential can have a minimum if we employ an appropriate detuning and material of a probe tip for the relevant system.

IV. NUMERICAL ANALYSIS

In the preceding sections we microscopically described the near-field optical potential as the sum of the Yukawa functions with several kinds of effective masses, and discussed the fundamental features of the potential. As an example of the application of the near-field optical potential, let us consider two cases of single-atom manipulation using optical near fields generated by a nanometric probe tip: (1) atom deflection, where an atom is cooled down on the order of millikelvins, and (2) atom trapping, where an atom is further cooled down on the order of microkelvins. Our intention is to provide an experimental guideline as well as to deepen the physical understanding of optical near fields and related phenomena. The cases considered involve experimentally unique techniques that will be essential for carrying an atom to a desired point on a substrate with high spatial accuracy far beyond the diffraction limit.

In order to take the size of a probe-tip sphere explicitly into account, we simply integrate $V_{\rm eff}(r)$ in Eq. (18a) within the sphere (variable radius: a) as

$$V(r)=\frac{1}{4\pi a^3/3}\int V_{\rm eff}(|\vec{r}_A-(\vec{r}'+\vec{r}_B)|)d^3r'$$

$$=\frac{\mu_A\mu_B E_P^2}{(\hbar c)^2 a^3}\left[\sum_{G,j=\pm}\frac{jG_j}{\Delta_{Gj}^3}\{(1+a\Delta_{Gj})\right.$$

$$\left.\times\exp(-\Delta_{Gj}a)-(1-a\Delta_{Gj})\exp(\Delta_{Gj}a)\}Y(\Delta_{Gj}r)\right], \quad (21)$$

redefining the argument r of the potential V as $r=|\vec{r}|=|\vec{r}_A-\vec{r}_B|$. Thus the total potential $V(r)$ is expressed as a function of the distance between the center of the tip sphere and the atomic center. Here we assume that the atom is pointlike with discrete energy levels, while the Yukawa sources are homogeneously distributed within the probe-tip sphere [30]. The total potential $V(r)$ is used in the following simulation of atom deflection and trapping. As a test case, let us use a ^{85}Rb atom with $E_A=1.59$ eV and $\mu_A=7.5$ debye. For the effective mass of the exciton polaritons, $E_p=m_p c^2=\hbar\Omega$ is employed.

First we discuss Rb-atom deflection by the effective potential $V(r)$. It is formulated as a potential scattering problem in the first Born approximation. As the velocity of the atom decreases, the first Born approximation becomes invalid. It is known, however, that the breakdown of the first Born approximation occurs when the incident velocity is

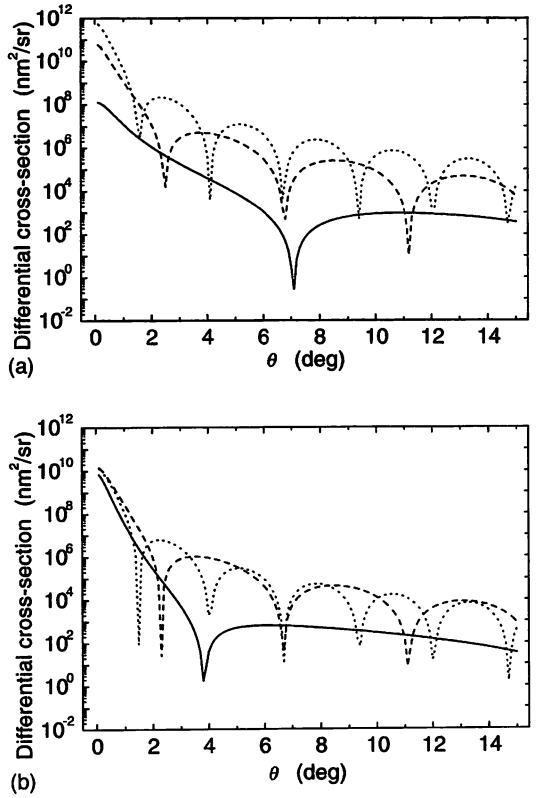

FIG. 5. Differential scattering cross section of ^{85}Rb with an incident velocity of 1 m/s in the first Born approximation. The near-field optical potential is generated by a probe tip with a radius of 10–50 nm for (a) a red-detuning case and (b) a blue-detuning case. Solid: $a=10$ nm; dashed: $a=30$ nm; and dotted: $a=50$ nm.

close to the sub-meter-per-second range or the kinetic energy is in the submillikelvin range [29]. Figure 5 represents the differential scattering cross section, or angular distribution of ^{85}Rb with an incident velocity of 1 m/s, or 10 mK in terms of temperature, as the radius a of the probe tip varies from 10 to 50 nm. The solid, dashed, and dotted lines show the results for $a=10$ nm, $a=30$ nm, and $a=50$ nm, respectively. Figure 5(a) is calculated with the red-detuned potential similar to that in Fig. 2(a), while Fig. 5(b) is calculated with the blue-detuned potential similar to that in Fig. 2(c). The periodic structure seen in the figures results from the finite size of the probe tip. From the analytic expression it follows that the periodic length is inversely proportional to the tip size: the larger the tip size is, the shorter the period is. Both figures show that a smaller probe tip can deflect the atom more strongly, though an optimum size should be determined from a discussion on the de Broglie wavelength of the atom. The difference between Figs. 5(a) and 5(b) can be understood as follows: In Fig. 5(a), two components with the same signs of the effective potential $V(r)$ constructively contribute to the scattering amplitude, $\int r \sin(qr)V(r)dr$, where q is the transferred momentum. On the other hand, in Fig. 5(b), two components with opposite signs of $V(r)$, the repulsive and attractive, are destructively summed up in the scattering amplitude. This reduces the deflection angle θ in Fig. 5(b) in comparison with those in Fig. 5(a).

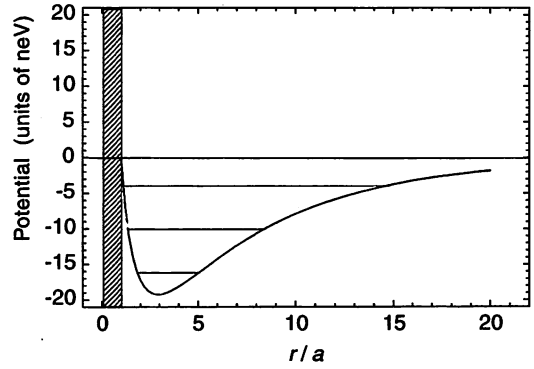

FIG. 6. Example of near-field optical potential for ^{85}Rb (resonance energy of 1.59 eV), represented by the solid line. The probe tip is assumed to have a radius of 10 nm and an electronic excitation energy of 1.51 eV. The probe tip and atom system is coupled with a macroscopic matter system with $E_m=2.0$ eV. Approximating it by a harmonic-oscillator potential around the minimum point, vibrational levels with the labels $n=0$, 1, and 2 are shown. The shaded area shows the probe-tip size.

Next let us consider an example of a near-field optical potential for atom trapping. Figure 6 shows a case for the system of a ^{85}Rb atom with an excitation energy $E_A=1.59$ eV and a probe tip with a radius $a=10$ nm, a transition dipole moment $\mu_B=1.5$ debye, and an excitation energy $E_B=1.51$ eV. They are coupled with a macroscopic matter with $E_m=2.0$ eV. In order to determine the value of the excitation energy E_B, we perform a similar analysis developed in Fig. 4 by means of the total potential $V(r)$. As a result, the smallest value of 1.51 eV is chosen from the possible values giving a potential well in the case of $a=10$ nm. This condition would be satisfied if we choose, for example, a III-V compound of $Al_xGa_{1-x}As$. It follows from Fig. 6 that the potential has a minimum, -20 neV, near the position $r=2a$ from the probe-tip surface. Approximating it by a harmonic-oscillator potential around the minimum point, we find that two or three vibrational levels can be supported; the lowest vibrational energy with the label $n=0$ corresponds to 3.1 neV, or equivalently 35 μK. This result suggests the possibility of a single Rb-atom trapping at this level.

It may be interesting to compare the depth of the above potential well with the ones obtained for an atom and a microsphere system, where the radius of the sphere is much larger than ours. The potential depth for a Rb atom semiclassically calculated in Ref. [31] is the same order of magnitude, or a little shallower, as our results. However, their minimum position of the potential depends on the wavelength used and is different from ours. This is because they use a microsphere with a dielectric constant of 6 and a radius of about 1 μm for visible light. The potential for a Cs atom quantum-mechanically calculated with a 50-μm sphere shows the similar tendency [32]. It follows that the nonresonant term neglected in Ref. [31], which is the optical near field leading to the size-dependent effect, becomes important as a tip sphere becomes smaller. The effect of an ideally conducting conical surface on an atom was also classically estimated [33], and an energy shift of the atom in the region

of interest seems to be a similar order of magnitude though the details of the parameters used are not known.

V. CONCLUSIONS

We have microscopically derived an effective interaction potential between a neutral atom and a nanometric probe tip in optical near-field systems. The near-field optical potential consists of the sum of the Yukawa functions with several kinds of effective masses, which is attractive or repulsive, depending on the detuning and material properties. This approach succeeds in quantitatively analyzing the probe-tip size and material dependence of the potential. It also can be applied to a variety of phenomena inherent to optical near-field techniques.

Recent experiments in atom manipulation and nanostructure fabrication [34] have made remarkable progress. An atomic mirror [35–37] and an atomic guide with a hollow fiber and blue-detuned optical near field [38,39] have been experimentally demonstrated. An atomic guide using magnetic forces has been recently reported [40,41]. A beam of laser-cooled atoms was also guided by a pair of parallel wires produced on a glass substrate by photolithography and subsequent electroplating [42]. In addition to these methods, atom deflection and trapping with a nanometric tip will greatly advance the manipulation techniques. In fact, we have shown the possibilities of such atom deflection and trapping. These analyses also illustrate the usefulness of the microscopic theory developed in this paper. The probe-tip size and potential shape are quantitatively shown as key parameters of atom deflection. The difference in the deflection angles for the attractive and the repulsive potentials is explained by the Yukawa potentials with two kinds of effective masses. Besides, by choosing appropriate detuning and material properties, it is numerically shown that a potential well is generated to be suitable for Rb-atom trapping. It means that we can form a well in the near-field optical potential with single blue-detuned light, though the methods based on the existing far-field theories mentioned in Sec. I require both red- and blue-detuned laser beams. Moreover, we expect that we can apply the near-field optical potential method to atom deposition [43] and nanostructure fabrication. These microscopic analyses will provide useful information for the future experimental demonstration.

[1] M. Ohtsu, K. Kobayashi, H. Ito, and G.H. Lee, Proc. IEEE **88**, 1499 (2000).

[2] *Near-Field Nano/Atom Optics and Technology*, edited by M. Ohtsu (Springer-Verlag, Berlin, 1998).

[3] T. Yatsui, M. Kourogi, and M. Ohtsu, Appl. Phys. Lett. **73**, 2090 (1998).

[4] T. Saiki and K. Matsuda, Appl. Phys. Lett. **74**, 2773 (1999).

[5] Y. Toda, S. Shinomori, K. Suzuki, and Y. Arakawa, Appl. Phys. Lett. **73**, 517 (1998).

[6] T. Matsumoto, M. Ohtsu, K. Matsuda, T. Saiki, H. Saito, and K. Nishi, Appl. Phys. Lett. **75**, 3246 (1999).

[7] V.V. Polonski, Y. Yamamoto, M. Kourogi, H. Fukuda, and M. Ohtsu, J. Microsc. **194**, 545 (1999).

[8] Y. Yamamoto, M. Kourogi, M. Ohtsu, V. Polonski, and G.H. Lee, Appl. Phys. Lett. **76**, 2173 (2000).

[9] H. Hori, in *Near Field Optics*, edited by D.W. Pohl and D. Courjon (Kluwer, Dordrecht, 1993), pp. 105–114.

[10] M. Ohtsu, S. Jiang, T. Pangaribuan, and M. Kozuma, in *Near Field Optics*, edited by D.W. Pohl and D. Courjon (Kluwer, Dordrecht, 1993), pp. 131–139.

[11] M. Ohtsu and H. Hori, *Near-Field Nano-Optics* (Kluwer/Plenum, New York, 1999).

[12] C. Girard, O.J.F. Martin, and A. Dereux, Phys. Rev. Lett. **75**, 3098 (1995).

[13] K. Cho, Y. Ohfuti, and K. Arima, Surf. Sci. **363**, 378 (1996).

[14] O. Keller, Ultramicroscopy **71**, 1 (1998).

[15] K. Kobayashi, Appl. Phys. A: Mater. Sci. Process. **66**, S391 (1998).

[16] K. Kobayashi and M. Ohtsu, J. Microsc. **194**, 249 (1999), and references therein.

[17] Yu.B. Ovchinnikov, S.V. Shul'ga, and V.I. Balykin, J. Phys. B **24**, 3173 (1991).

[18] H. Mabuchi and H.J. Kimble, Opt. Lett. **19**, 749 (1994).

[19] J.P. Dowling and J. Gea-Banacloche, in *Advances in Atomic, Molecular, and Optical Physics*, edited by B. Bederson and H. Walther (Academic Press, San Diego, 1996), Vol. 37.

[20] J. Dalibard and C. Cohen-Tannoudji, J. Opt. Soc. Am. B **2**, 1707 (1985).

[21] C. Cohen-Tannoudji, *Atoms in Electromagnetic Fields* (World Scientific, Singapore, 1994).

[22] D.P. Craig and T. Thirunamachandran, *Molecular Quantum Electrodynamics* (Dover, New York, 1998).

[23] H. Haken, *Quantum Field Theory of Solids* (Elsevier, Amsterdam, 1983).

[24] J.J. Hopfield, Phys. Rev. **112**, 1555 (1958).

[25] J. Knoester and S. Mukamel, Phys. Rev. A **40**, 7065 (1989).

[26] B. Huttner and S.M. Barnett, Phys. Rev. A **46**, 4306 (1992).

[27] Since we are primarily interested in interactions between a neutral atom and a nanometric probe tip originated from optical near fields, we assume the situation that the neutral atom interacts with the probe tip only if incident light comes into a macroscopic matter system. In other words, of *P*-space bases, we employ eigenstates of an unperturbed Hamiltonian, where the neutral atom and the probe tip are isolated from each other. If one is interested in atomic interactions between a neutral atom and probe-tip atoms as well as optical near-field interactions, one can use appropriate eigenstates of an unperturbed Hamiltonian, including such interactions as *P*-space bases.

[28] G. Grynberg, B. Lounis, P. Verkerk, J.-Y. Courtois, and C. Salomon, Phys. Rev. Lett. **70**, 2249 (1993).

[29] K. Kobayashi, S. Sangu, H. Ito, and M. Ohtsu, in *Near-Field Optics: Principles and Applications*, edited by X. Zhu and M. Ohtsu (World Scientific, Singapore, 2000).

[30] In Sec. II we assume that we know eigenstates of a probe tip when it is isolated, for example, confined states in a sphere with a radius of a. Then the effective interaction potential be-

tween two arbitrary points with energy levels (one is located in the probe tip and the other is located at the center of the neutral atom) is derived as Eq. (18a). If we assume that the tip is made up of such linearly independent points, then the total potential is given as an integration of Eq. (18a) over the sphere.

[31] V. Klimov, V.S. Letokhov, and M. Ducloy, Eur. Phys. J. D **5**, 345 (1999).

[32] D.W. Vernooy and H.J. Kimble, Phys. Rev. A **55**, 1239 (1997).

[33] V.V. Klimov and Ya.A. Perventsev, Quantum Electron. **29**, 847 (1999).

[34] W.R. Anderson, C.C. Bradley, J.J. McClelland, and R.J. Celotta, Phys. Rev. A **59**, 2476 (1999).

[35] V.I. Balykin, V.S. Letokhov, Yu.B. Ovchinnikov, and A.I. Sidorov, Phys. Rev. Lett. **60**, 2137 (1988).

[36] C.G. Aminoff, A.M. Steane, P. Bouyer, P. Desbiolles, J. Dalibard, and C. Cohen-Tannoudji, Phys. Rev. Lett. **71**, 3083 (1993).

[37] A. Landragin, J.-Y. Courtois, G. Labeyrie, N. Vansteenkiste, C.I. Westbrook, and A. Aspect, Phys. Rev. Lett. **77**, 1464 (1996).

[38] M.J. Renn, E.A. Donley, E.A. Cornell, C.E. Wieman, and D.Z. Anderson, Phys. Rev. A **53**, R648 (1996).

[39] H. Ito, T. Nakata, K. Sakaki, M. Ohtsu, K.I. Lee, and W. Jhe, Phys. Rev. Lett. **76**, 4500 (1996).

[40] E.A. Hinds, M.G. Boshier, and I.G. Hughes, Phys. Rev. Lett. **80**, 645 (1998).

[41] J. Denschlag, D. Cassettari, and J. Schmiedmayer, Phys. Rev. Lett. **82**, 2014 (1999).

[42] D. Müller, D.Z. Anderson, R.J. Grow, P.D.D. Schwindt, and E.A. Cornell, Phys. Rev. Lett. **83**, 5194 (1999).

[43] H. Ito, K. Sakaki, M. Ohtsu, and W. Jhe, Appl. Phys. Lett. **70**, 2496 (1997).

Jpn. J. Appl. Phys. Vol. 39 (2000) pp. 6737–6742
Part 1, No. 12A, December 2000

High Efficiency Excitation of Cylindrical Optical Near Fields for Atom Guidance

Akifumi TAKAMIZAWA[1], Haruhiko ITO[1] and Motoichi OHTSU[1,2]

[1]*Interdisciplinary Graduate School of Science and Engineering, Tokyo Institute of Technology, 4259, Nagatsuta, Midori-ku, Yokohama 226-8502, Japan*
[2]*ERATO, Japan Science and Technology Corporation, 687-1 Tsuruma, Machida 194-8502, Japan*

(Received June 2, 2000; accepted for publication August 18, 2000)

We describe coupling of light beams to a micron-sized hollow fiber used for atom guidance. In particular, we deal with an annular light beam produced by means of a hollow fiber. The coupling efficiency of the annular light beam to the LP_{01} mode with a cylindrical optical near field is compared to that of a Gaussian light beam. Next, we examine optical pumping and heating effects of the light beams on atoms before they enter the hollow fiber. From these results, we find that the use of the annular light beam is more advantageous than the use of the Gaussian light beam for both high efficiency excitation of the LP_{01} mode and suppression of the preinteraction between atoms and leaked light at the entrance. The spatial intensity distribution of an annular light beam is measured with a protrusion-type fiber probe. This method is useful for observing fine structures of light beams with high spatial resolution.

KEYWORDS: optical near field, atom guidance, hollow fiber, annular light beam, coupling efficiency, LP_{01} mode, optical pumping, heating, fiber probe

1. Introduction

The use of optical near fields enables us to overcome the diffraction limit of light waves. This characteristic is highly advantageous for optical control of neutral atoms. Indeed, the development of relevant techniques including fiber probes is opening a way for the application of the optical near fields to atom manipulation with high spatial accuracy in the range of nanometers, and furthermore, in atomic size.[1)] As the first step in the near-field optical control, the mirror reflection of atoms was performed with a blue-detuned planar optical near field produced on a prism.[2)] A leap in this field has been enabled using a hollow fiber.[3,4)] The blue-detuned cylindrical optical near field, which works as a tunnel to guide atoms, excited in the hollow region successfully sends atoms through the glass fiber. This guiding technique is expected to be used for atomic-scale crystal growth as well as studies of quantum mechanical phenomena such as cavity quantum electrodynamical effects.[1,5,6)]

For the atom guidance, an optical near field is produced in the micron-sized hollow region by coupling of a laser beam to the core. Figure 1 schematically shows the cross-sectional structure of the hollow fiber. When the light frequency is slightly higher than that of the atomic resonant frequencies, the optical near field exerts a repulsive dipole force on an atom.[7)] In the blue-detuning case, if the light intensity is sufficiently strong, an atom entering the hollow region is reflected whenever it approaches the inner-wall surface, and is then guided through the hollow fiber without adhesion.

Compared to the method of using a propagating light beam with a doughnut mode,[8)] this type of atom guidance has several advantages in addition to the fact that one can guide atoms species- and state-selectively by virtue of the resonant characteristic of the dipole force to reflect atoms. First, it is possible to control the atomic position with high accuracy of less than one wavelength. In fact, guiding of Rb atoms has been demonstrated with a hollow fiber having a hollow diameter of 300 nm which is smaller than the guide wavelength of 780 nm.[1)] Second, since the optical fiber is flexible, one can carry atoms to an arbitrary point with a bent hollow fiber. Furthermore, since the optical near field is localized in a narrow region near the inner-wall surface, one can suppress unfavorable interaction between atoms and intense light inside the hollow fiber, that is, heating and optical pumping effects on atoms. These effects reduce the guide efficiency.

In our previous work,[4)] we stimulated the optical near field by directly irradiating the core with a high power laser beam inside a vacuum chamber with a pressure of less than 10^{-6} Pa. However, we were not able to completely focus the laser beam on the core with a thickness of a few microns using a lens system, because a hollow fiber was placed at a point about 10 cm off from an optical window. Note that it is inconvenient to use commercial objectives to focus a laser beam on the small

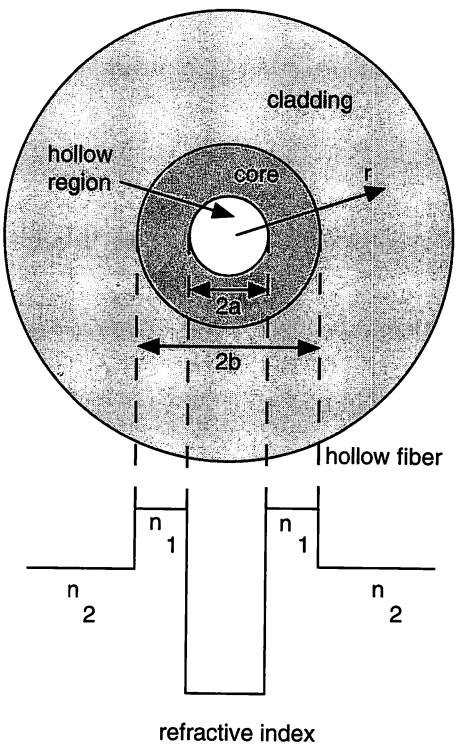

Fig. 1. Cross-sectional structure of a step-index hollow fiber with a micron-sized hollow diameter. The propagating modes are approximately described by the LP modes owing to the small refractive index difference between the core n_1 and the cladding n_2. The fundamental mode is the LP_{01} mode, in which the optical near field produced near the inner-wall surface has a homogeneous cylindrical distribution without nodes.

core inside the high vacuum chamber because they are too large and usually contain air increasing the vacuum pressure. The imperfect focusing gives rise to the occurrence of unnecessary light in front of the fiber facet on the incidence side of atoms. Such light exercise influence, for example, heating and optical pumping on atoms entering the hollow fiber. In particular, the latter transfers atoms to nonresonant energy levels having less interaction with the optical near field, so that the optical potential reflecting the atoms decreases: it is in inverse proportion to the frequency detuning.

In this paper, we describe a method of high efficiency coupling of a guide-light beam to a micron-sized hollow fiber. In order to eliminate the undesirable preinteraction before atoms enter the hollow region, we can use an annular light beam whose shape and diameter are approximately the same as those of the core. The use of the annular light beam also makes it feasible to excite the LP_{01} mode with a power of 10 mW sufficiently to reflect atoms.[9,10] The optical near field produced with the LP_{01} mode has a cylindrical shape around the inner-wall surface without nodes, and consequently it is suitable for the atom guidance.

First, in §2, we present the measurement of the coupling efficiency of a Gaussian light beam to a hollow fiber. Next, in §3, we show a method of producing an annular light beam by means of a hollow fiber and examining its intensity profile with a fiber probe, including measurement of the coupling efficiency. In §4, we discuss the influence of leaked light on atoms before they enter the hollow fiber, based on the results obtained in the previous sections. As a result, it is found that the use of the annular light beam not only increases the coupling efficiency to the LP_{01} mode but also decreases the unfavorable interaction such as optical pumping. Finally, we give the conclusions in §5.

2. Coupling of a Gaussian Light Beam to a Hollow Fiber

In the atom guidance experiment, we use a hollow fiber with a hollow diameter and a core thickness of a few microns. The micron-sized hollow fiber is put inside a vacuum chamber and a guide-light beam which produces an optical near field in the hollow region is coupled to the hollow fiber by using a tunnel mirror with a small hole to pass an atomic beam. Figure 2 is a sketch of the coupling system. The atomic beam is introduced into the hollow fiber placed coaxially, while the guide-light beam is introduced from the direction perpendicular to the fiber and focused on the core after being reflected by the tunnel mirror placed at an angle of 45° to the center axis of the fiber.

As mentioned earlier, the guide-light beam is not completely focused on the core using the coupling system without objectives, so that a part of the light beam illuminates the cladding and the hollow area in the fiber facet. In the configuration shown in Fig. 3, we measured the coupling efficiency of a Gaussian light beam with the TEM_{00} mode to the LP_{01} mode supported by a hollow fiber. The spotsize s_0, which is twice as large as the beam waist, indicates the fullwidth at the e^{-2} maximum light intensity, and the displacement x_0 indicates the distance of the light beam axis from the fiber axis. The coupling efficiency, which is defined as the ratio of the output light power from the hollow fiber to the incident light power, depends on the values of s_0 and x_0.

Figure 4 shows the maximum coupling efficiency plotted as

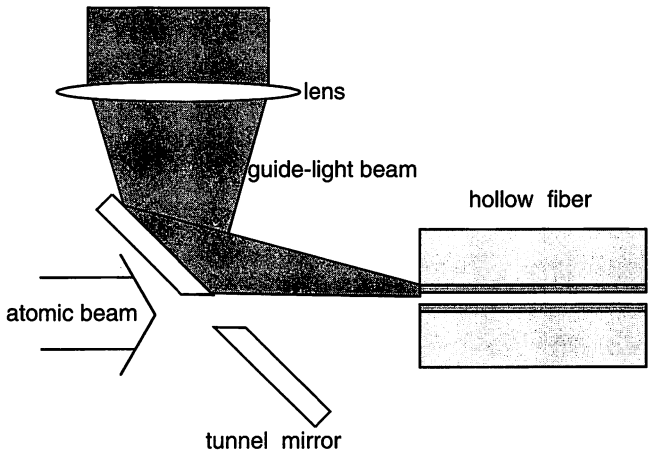

Fig. 2. Configuration of light coupling to a hollow fiber in the atom guidance experiment. An atomic beam is introduced into a hollow fiber coaxially placed through a small hole on a tunnel mirror, while a guide-light beam which excites the LP_{01} mode accompanied with a cylindrical optical near field is focused on the core with a thickness of a few microns from the direction perpendicular to the fiber axis by using a lens-tunnel mirror system without objectives. Note that the wavelength of the guide light is 780 nm for guiding of Rb atoms.

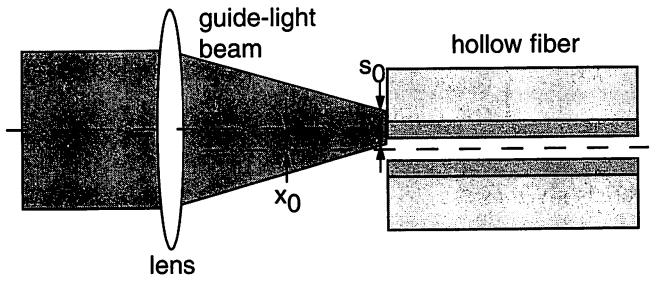

Fig. 3. Coupling of a Gaussian light beam to a hollow fiber. The Gaussian light beam is focused on an area in the vicinity of the core, where s_0 and x_0 are the spotsize and the displacement from the center axis, respectively. In this configuration, the spotsize is larger than the core thickness.

a function of s_0, where a Gaussian light beam with a power of 100 mW is coupled to a 7-μm hollow fiber with a core thickness of 3.8 μm, a length of 3 m, and a relative refractive index difference between core and cladding of 0.18%. The wavelength of the Gaussian light beam from a Ti:sapphire laser is tuned to a resonant wavelength of 780 nm for the guidance of Rb atoms. As shown in Fig. 4, the excitation efficiency of the LP_{01} mode has the maximum value of 59% at $s_0 = 17\,\mu$m. We did not observe any modes propagating through the hollow region. The coupling loss, therefore, results mainly from scattering at the fiber facet.

In a cylindrical coordinate system (r, θ, z), the coupling efficiency η is given by[11]

$$\eta = \frac{\left|\int_0^{2\pi}\int_0^{\infty} F(r,\theta)G(r,\theta)r\,\mathrm{d}r\,\mathrm{d}\theta\right|^2}{\left|\int_0^{2\pi}\int_0^{\infty} F^2(r,\theta)r\,\mathrm{d}r\,\mathrm{d}\theta\right|\left|\int_0^{2\pi}\int_0^{\infty} G^2(r,\theta)r\,\mathrm{d}r\,\mathrm{d}\theta\right|}, \tag{2.1}$$

where the r–θ plane indicates the fiber facet whose center is taken to be $r = 0$ and the z axis corresponds to the propagating direction of the light beam. The electric field $F(r, \theta)$ for the LP_{01} mode excited in the hollow fiber is given as[9,10]

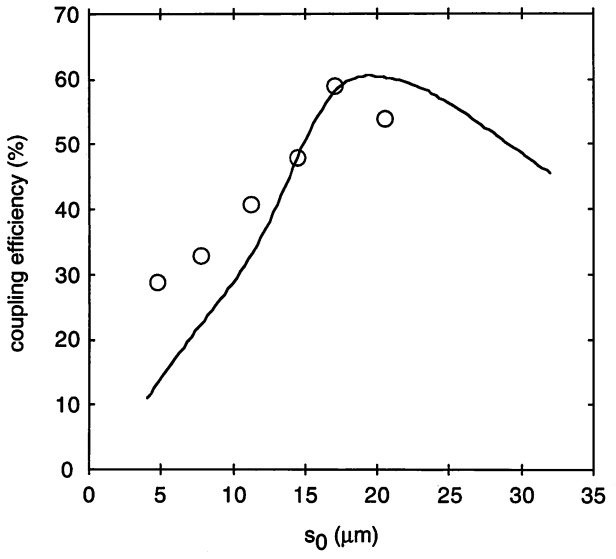

Fig. 4. Maximum coupling efficiency of a Gaussian light beam with a wavelength of 780 nm and a power of 100 mW to a 7-μm hollow fiber with a core thickness of 3.8 μm, a relative refractive index difference of 0.18%, and a length of 3 m. The experimental values indicated with open circles are plotted as a function of the spotsize s_0 together with a theoretical result drawn as a solid curve, where the LP_{01} mode is excited.

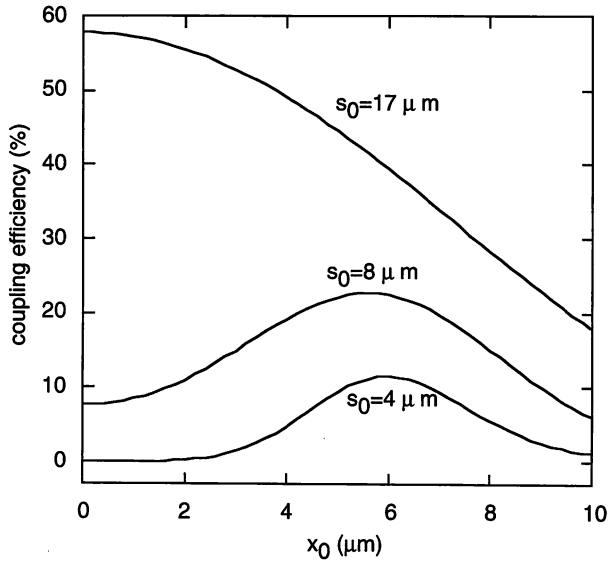

Fig. 5. Coupling efficiency of a Gaussian light beam to the 7-μm hollow fiber numerically calculated. Three cases of $s_0 = 4$, 8, and 17 μm are plotted as a function of the displacement x_0.

$$F(r) = \begin{cases} AI_0(vr) & (r \le a), \\ BJ_0(ur) + CN_0(ur) & (a < r < b), \\ DK_0(wr) & (r \ge b), \end{cases} \quad (2.2)$$

while the electric field $G(r, \theta)$ for the incident Gaussian light beam is given as[12]

$$G(r, \theta) = E \exp\left\{ -\frac{(r\cos\theta - x_0)^2 + r^2 \sin^2\theta}{(s_0/2)^2} \right\}, \quad (2.3)$$

where a is the radius of the hollow region and b is the radius of the core + hollow region (see Fig. 1). Here, J_0 and N_0 are the Bessel functions of the first and second kinds with the 0th order, and I_0 and K_0 are the modified Bessel functions of the first and second kinds with the 0th order, respectively. The coefficients A, B, C, and D are determined by the light power coupled to the hollow fiber and the boundary conditions at $r = a$ and b, while the coefficient E is determined by the incident light power. The transverse propagating constants u in the core, and the transverse decay constant v in the hollow region and w in the cladding are respectively given by[9,10]

$$u = \sqrt{n_1^2 k^2 - \beta^2}, \quad (2.4)$$

$$v = \sqrt{\beta^2 - k^2}, \quad (2.5)$$

$$w = \sqrt{\beta^2 - n_2^2 k^2}, \quad (2.6)$$

where k is the wave number of the incident light and β is the propagating constant of the LP_{01} mode, depending on the boundary conditions at $r = a$ and b.

The solid curve drawn in Fig. 4 shows the theoretical value of the maximum coupling efficiency obtained using eq. (2.1). They are in good agreement with the experimental values for large s_0. Figure 5 shows the coupling efficiency η of the LP_{01} mode numerically calculated using eq. (2.1) in the three cases of $s_0 = 4$, 8, and 17 μm as a function of the displacement x_0. In Fig. 5, we find that η is maximum at $x_0 = 0$ for $s_0 = 17$ μm and around $x_0 = 6$ μm for $s_0 = 4$ and 8 μm, respectively.

The coupling efficiency of a Gaussian light beam to a hollow fiber is almost the same even if a tunnel mirror is added as shown in Fig. 2. In the atom guidance experiment, however, the guide-light beam is introduced at an incidence angle so that it avoids the hole of the tunnel mirror (see Fig. 2). Since the guide-light beam is focused on the core at an angle determined by the focal length of the lens used, the incidence angle has to be greater than the focusing angle. In this case, the effective numerical aperture NA_{eff} of the incident light beam to the hollow fiber is twice as large as the numerical aperture given by the focusing angle, and is estimated to be 0.31, 0.15, and 0.056 for $s_0 = 4$, 8, and 17 μm, respectively. On the other hand, the numerical aperture NA of the 7-μm hollow fiber is estimated to be 0.087. Accordingly, in the two cases of $s_0 = 4$ and 8 μm, the value of NA_{eff} is larger than that of NA. This implies that the coupling efficiency is lower than the value given in Fig. 4: a part of the incident light beam leaks from the core of the hollow fiber without undergoing total-internal reflection. In fact, we experimentally obtained a very small value of $\eta = 1.6\%$ in the case where the incidence angle is 5° [$\simeq \tan^{-1}(0.15/2)$] for $s_0 = 8$ μm. It follows that we need an intense light beam with a high power of 600 mW to excite the LP_{01} mode up to a power level of 10 mW in the 7-μm hollow fiber.

Let us consider the relationship between coupling efficiency and influence of the incident light on atoms before entering the hollow fiber. In the case of $s_0 = 17$ μm, although the guide-light beam can be efficiently coupled to the hollow fiber, the intense light beam illuminates the entire hollow area. Consequently, it gives rise to a strong interaction between atoms and the incident light at the entrance. On the other hand, for $s_0 = 4$ and 8 μm, if an appropriate value of x_0 is chosen, we can couple the guide-light beam to the hollow fiber without irradiating the hollow area with the intense light. In these cases, while the preinteraction is negligible, the guiding efficiency of atoms is significantly low because the optical near field produced in the hollow region is very weak.

3. Coupling of an Annular Light Beam to a Hollow Fiber

In order to solve some problems occurring while using a Gaussian light beam, we can use an annular light beam for excitation of a cylindrical optical near field. This scheme not only improves the coupling efficiency but also suppresses the preinteraction. One of the simple methods for obtaining an annular light beam is to use a hollow fiber.[13] Figure 6 shows the experimental setup. A Gaussian light beam coupled to a hollow fiber excites the LP_{01} mode. The output light beam from the hollow fiber, which has an annular shape just after exiting the hollow fiber, is collimated and condensed with two convex lenses. Then, an annular light beam with the same intensity profile as that of the LP_{01} mode is reproduced at the focal point behind the second lens. Note that the hollow region disappears as it moves away from the focal point.

We performed measurements of the spatial intensity distribution of the annular light beam using a protrusion-type fiber probe. Figure 7 schematically shows the experimental configuration. The cross section of the annular light beam is scanned with the fiber probe. The signal picked up by the fiber probe is sent to a powermeter. This novel fiber-probe method of examining beam-profiles makes it possible to obtain high spatial-resolution measurement of light beams with special distribution. Note that it is inconvenient to use a commercial beam-profiler with a slit-type head: Although only the hollow region of the annular light beam with a small hollow diameter of a few microns needs to be observed, the beam profiler is unable to do this task.

The solid curve in Fig. 8 shows the cross-sectional intensity distribution of an annular light beam produced by coupling of a Gaussian light beam with a wavelength of 780 nm and a beam waist of 17 μm to the 7-μm hollow fiber. Here, two convex lenses with a focal length of 25.2 mm are placed at a distance of 500 mm from each other for collimating and condensing of the light beam. For the measurement, we used a gold-coated protrusion-type fiber probe with a foot diameter of 3 μm, which is fabricated by chemical etching.[1] The broken curve in Fig. 8 shows the intensity distribution of the LP_{01} mode supported by the 7-μm hollow fiber. From Fig. 8,

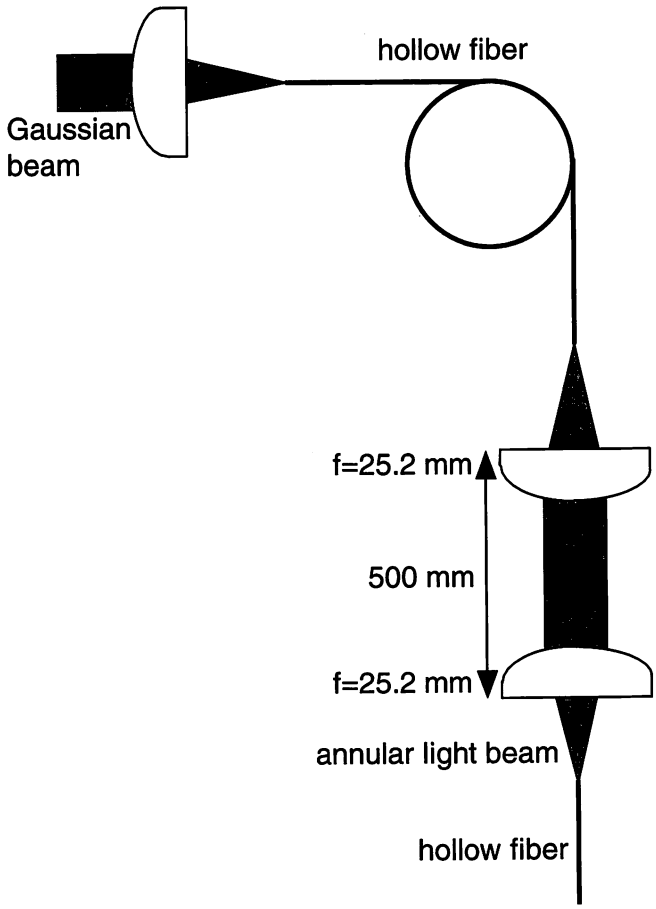

Fig. 6. Conversion of a Gaussian light beam to an annular light beam using a hollow fiber. An annular light beam exiting out of the hollow fiber is gathered and recoupled to another hollow fiber with two convex lenses. The typical values of the focal length and the distance of the two convex lenses are 25.2 mm and 500 mm, respectively.

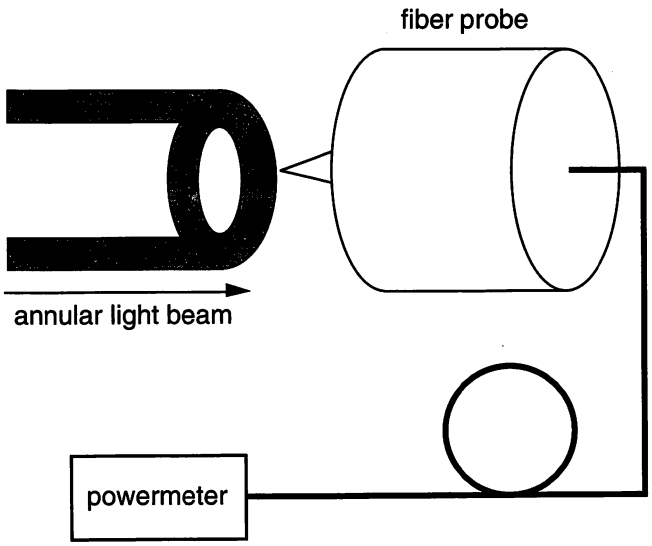

Fig. 7. Setup for measurement of intensity profile of an annular light beam with a protrusion-type fiber probe. In the experiment, a gold-coated fiber probe with a foot diameter of 3 μm is employed. The fiber probe is placed after the second convex lens in Fig. 6 instead of the hollow fiber. The signal picked up by the fiber probe is sent to a powermeter.

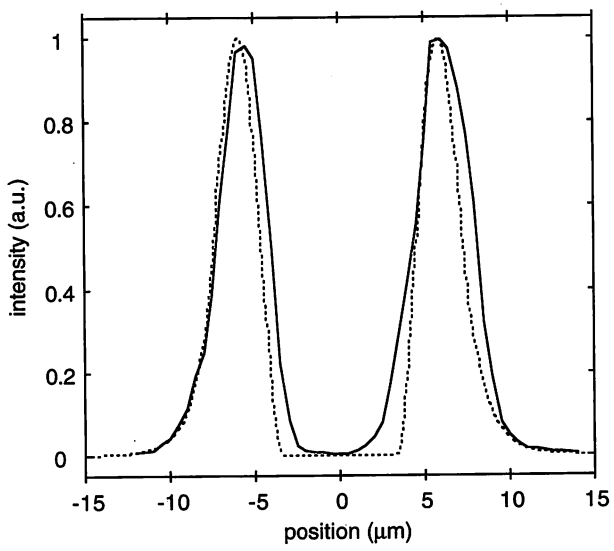

Fig. 8. Cross-sectional intensity distribution of an annular light beam produced through the 7-μm hollow fiber. The broken curve shows the theoretical value of the spatial intensity distribution of the LP_{01} mode supported by the 7-μm hollow fiber.

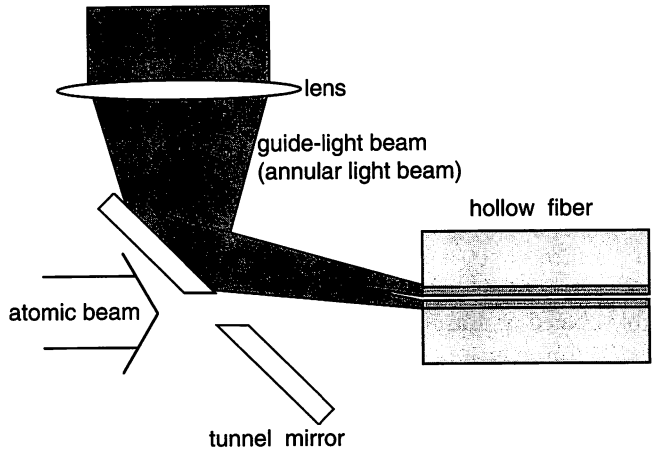

Fig. 9. Coupling of an annular light beam to a hollow fiber in the atom guidance experiment.

it is found that the intensity profile of the annular light beam is almost the same as that of the LP_{01} mode. The intensity at the center of the annular light beam is negligible: the ratio to the maximum intensity is 1.8×10^{-3}.

As expected, the coupling efficiency of the annular light beam to the hollow fiber is higher than that of the Gaussian light beam mentioned in §2. In fact, we obtained the coupling efficiency of 75%. This result is reasonable because $F(r, \theta) \simeq G(r, \theta)$ in eq. (2.1).

Similar to a Gaussian light beam, an annular light beam has to be introduced into a hollow fiber at an angle in the atom guidance experiment as shown in Fig. 9. In the case of using the annular light beam given in Fig. 8, the effective numerical aperture NA_{eff} is estimated to be 0.11, which is somewhat higher than the numerical aperture $NA = 0.087$ of the 7-μm hollow fiber. Accordingly, the coupling efficiency decreases compared with the case of normal incidence. In fact, when the incident angle is 3° ($\simeq \tan^{-1}(0.11/2)$), we still get a high coupling efficiency of 55%.

4. Discussion

In the configuration of atom guidance experimantal setup shown in Fig. 2 or 9, preinteraction between atoms and incident light is inevitable. In this section, we estimate the two dominant effects, optical pumping and heating, on Rb atoms at the entrance of a hollow fiber. As concrete examples, we deal with three cases of coupling to the 7-μm hollow fiber under excitation of the LP_{01} mode with a power of 10 mW: (a) coupling of a Gaussian light beam with $s_0 = 17\,\mu$m at an incidence angle of 3° for $x_0 = 0$, (b) coupling of a Gaussian light beam with $s_0 = 8\,\mu$m at an incidence angle of 5° for $x_0 = 6\,\mu$m, and (c) coupling of the annular light beam mentioned in §3 at an incidence angle of 3° for $x_0 = 0$. We consider the case where the incident light beam interacts with atoms moving along the center axis of the hollow fiber between a tunnel mirror and the fiber facet on the entrance side, where the distance is taken to be 1 cm.

Let us consider optical pumping of ^{85}Rb atoms with two hyperfine ground states labeled as $F = 2$ and 3, whose separations are about 3 GHz. To this end, we calculate the probability P_i ($i = 1, 2$) of spontaneous transition, which means that the Rb atom is excited from one of the hyperfine ground states to the excited state by absorbing a photon and then spontaneously decays; this is given by[14]

$$P_i = 1 - \exp\left(-\frac{1}{3}\int \Gamma S_i dt\right), \tag{4.1}$$

where P_1 and P_2 correspond to the spontaneous transitions from the $F = 2$ and 3 levels, respectively. With the Rabi frequency $\Omega_i = \sqrt{I/2I_i^s}\Gamma_i$, the saturation parameter S_i is defined as[14]

$$S_i = \frac{\Omega_i^2/2}{\Delta^2 + \Gamma_i^2/4}, \tag{4.2}$$

where $I = I(r, \theta, z)$ is the light intensity and $\Delta = \omega_L - \omega_0 - kv$ is the detuning between the light frequency ω_L and the resonant atomic one ω_0 including the Doppler shift kv for the atomic velocity v. For ^{85}Rb, the natural linewidth Γ and the saturation intensity I^s are $2\pi \times 6.1$ MHz and 1.6 mW/cm^2, respectively, and the mean branching coefficients q_1 and q_2 from the $F = 2$ and 3 levels are 0.75 and 0.25, respectively.[14] It follows that $\Gamma_1 = q_1\Gamma$, $\Gamma_2 = q_2\Gamma$, $I_1^s = q_1 I^s$, and $I_2^s = q_2 I^s$.

Figure 10 shows the two spontaneous transition probabilities P_1 and P_2 plotted as a function of Δ which is the detuning from the transition frequency between the $5S_{1/2}$, $F = 2$ lower ground state and the $5P_{3/2}$ excited state. Here, we assume a Rb atomic beam following a Maxwell-Boltzmann distribution with a mean temperature of 250°C. In Fig. 10, the solid curves are obtained for the cases of (b) and (c), while the broken curves are obtained for the case of (a). The spontaneous transition probabilities for the two cases of (b) and (c) are almost the same and lower than the case of (a). This is in good

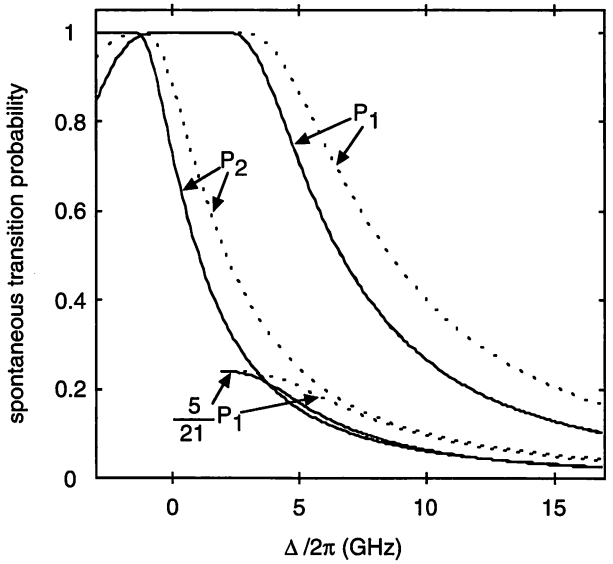

Fig. 10. Spontaneous transition probability of ^{85}Rb between a tunnel mirror and the entrance facet of the 7-μm hollow fiber plotted as a function of the frequency detuning Δ from the transition frequency between the $5S_{1/2}$, $F = 2$ lower ground state and the $5P_{3/2}$ excited state, where P_1 and P_2 are the transition probabilities from the $F = 2$ and 3 ground states, respectively. The solid curve shows the two cases of a Gaussian light beam with $s_0 = 8\,\mu$m and $x_0 = 6\,\mu$m at an incidence angle of 5°, and the annular light beam given in Fig. 8 with $x_0 = 0$ at an incidence angle of 3°. The broken curve shows the case of a Gaussian light beam with $s_0 = 17\,\mu$m and $x_0 = 0$ at an incidence angle of 3°. The plot of $5/21P_1$ is also shown. When the condition $P_2 = 5/21P_1$ is satisfied, optical pumping effects are not significant.

agreement with the qualitative consideration made in the previous sections. Note that the annular beam keeps its shape in the region of about 100 μm before reaching the fiber facet. Even in the case of (c), therefore, the spontaneous transition can take place with the same degree as in the case of (b).

It should be noted that the ratio of the thermal population occupying the $F = 2$ level to the $F = 3$ one is 5 : 7. If the spontaneous transition from the $F = 2$ level with the probability P_1 occurs, atoms are pumped to the $F = 3$ level. Then, if the transition from the $F = 3$ level occurs succeedingly with the probability $P_2 = 5/21P_1$, the initial population is conserved. The condition $P_2 = 5/21P_1$ estimated with $q_1 : q_2 = 3 : 1$ is also shown in Fig. 10 with a solid curve for the cases of (b) and (c), and with a broken curve for the case of (a). The condition that the optical pumping does not take place is satisfied by $\Delta/2\pi > +3$ GHz for the cases of (b) and (c), but $\Delta/2\pi > +7$ GHz for the case of (a). Since the dipole force to guide atoms is in inverse proportion to the frequency detuning in the region greater than +3 GHz under the low coupling power of 10 mW, the former is more advantageous than the latter. If we take into account the fact that the case of (c) has the highest coupling efficiency, we find that the use of an annular light beam is superior to that of a Gaussian one.

Next, let us consider heating of atoms by the incident light. The heating principally occurs due to acceleration by the spontaneous force of the light beam illuminating an atomic beam. The increase in atomic velocity dv during the time interval dt is given by[15]

$$dv = \frac{\hbar k\Gamma}{2m}\frac{I/I^s}{1 + I/I^s + 4\Delta^2/\Gamma^2}dt, \qquad (4.3)$$

where $\hbar$ and m are the Planck constant and the atomic mass, respectively. For simplicity, we assume the two-level atom without a hyperfine structure.

To illustrate the heating effect, we examine the case where an atomic beam with a low longitudinal mean energy of 100 mK in terms of temperature is employed as a source of the atom guidance. When the frequency detuning $\Delta/2\pi$ is +3 GHz, by numerically integrating eq. (4.3), the atomic beam is estimated to be heated up to 180 mK, 210 mK, and 190 mK just before entering the 7-μm hollow fiber for the cases of (a), (b), and (c), respectively. On the other hand, the transverse heating due to the light incidence at an angle is estimated to be less than 1 mK for the three cases, which is much lower than the dipole force potential to reflect atoms inside the hollow region. This indicates that the heating effect on the atomic beam with a longitudinal temperature of more than 100 mK is negligible. The heating effect will be crucial for a cold atomic beam.

5. Conclusion

We examined two types of light couplings to a micron-sized hollow fiber. The scheme of using a Gaussian light beam is experimentally simple. However, if we try to increase the coupling efficiency, it also increases the optical pumping effect of the leaked light illuminating the hollow area on atoms before entering the hollow fiber. On the other hand, the use of an annular light beam is more advantageous for increasing the coupling efficiency and simultaneously suppressing the optical pumping effect. In both cases, the heating effect is trivial for a thermal atomic beam. Elimination of the heating effect due to the spontaneous force pushing atoms will be more beneficial when employing a cold atomic beam for precise control.

The atom guidance technique with a hollow fiber is expected to be applied to a gravitational atom trap,[16] matter-wave interferometry and atom-laser cavity,[17] and measurement of the Casimir-Polder force.[1,6] For these applications, undesirable interaction between atoms and lights before atoms enter a hollow fiber should be removed. The preinteraction also caused problems in the study itself for the atom guidance. In the case of the light coupling from the forward direction to a hollow fiber, the problem of preinteracton cannot be completely eliminated. An artifice such as the light coupling from the backward direction is essential for further improvement.

1) H. Ito and M. Ohtsu: *Near-Field Nano/Atom Optics and Technology*, ed. M. Ohtsu (Springer, Tokyo, 1998) Chap. 11.
2) V. I. Balykin, V. S. Letokhov, Yu. B. Ovchinnikov and A. I. Sidorov: Phys. Rev. Lett. **60** (1988) 2137.
3) M. J. Renn, E. A. Donley, E. A. Cornell, C. E. Wieman and D. Z. Anderson: Phys. Rev. A **53** (1996) R648.
4) H. Ito, T. Nakata, K. Sakaki, M. Ohtsu, K. I. Lee and W. Jhe: Phys. Rev. Lett. **76** (1996) 4500.
5) H. Ito, K. Sakaki, W. Jhe and M. Ohtsu: Appl. Phys. Lett. **70** (1997) 2496.
6) H. Ito, K. Sakaki, W. Jhe and M. Ohtsu: Proc. SPIE **2995** (1997) 138.
7) J. P. Dowling and J. Gea-Banacloche: *Advances in Atomic, Molecular, and Optical Physics*, eds. B. Bederson and H. Walther (Academic Press, San Diego, 1996) Vol. 37, p. 1.
8) N. Schiffer, M. Rauner, S. Kuppens, M. Zinner, K. Sengstock and W. Ertmer: Appl. Phys. B **67** (1998) 705.
9) H. Ito, K. Sakaki, T. Nakata, W. Jhe and M. Ohtsu: Opt. Commun. **115** (1995) 57.
10) H. Ito, K. Sakaki, T. Nakata, W. Jhe and M. Ohtsu: Ultramicroscopy **61** (1995) 91.
11) G. P. Agrawal: *Nonlinear Fiber Optics* (Academic Press, San Diego, 1989) Chap. 7.
12) A. Yariv: *Optical Electronics* (Holt-Saunders, New York, 1985) 3rd ed., Chap. 2.
13) J. Yin, H.-R. Noh, K.-I. Lee, K.-H. Kim, Y.-Z. Wang and W. Jhe: Opt. Commun. **138** (1997) 287.
14) J. Söding, R. Grimm and Yu. B. Ovchinnikov: Opt. Commun. **119** (1995) 652.
15) W. D. Phillips: *Fundamental Systems in Quantum Optics*, eds. J. Dalibard, J.-M. Raimond and J. Zinn-Justin (North-Holland, Amsterdam, 1992) Course 2.
16) D. J. Harris and C. M. Savage: Phys. Rev. A **51** (1995) 3967.
17) G. M. Moy, J. J. Hope and C. M. Savage: Phys. Rev. A **55** (1997) 3631.

Generation of a cold atomic beam with a near-field optical funnel

A. Takamizawa
Interdisciplinary Graduate School of Science and Engineering, Tokyo Institute of Technology, 4259 Nagatsuta, Midori-ku, Yokohama 226-8502, Japan, Tel : +81 45-924-5459, Fax : +81 45-924-5588, takami@ae.titech.ac.jp

H. Ito[a], and M. Ohtsu[a,b]
[a]Interdisciplinary Graduate School of Science and Engineering, Tokyo Institute of Technology, 4259 Nagatsuta, Midori-ku, Yokohama 226-8502, Japan, Tel : +81 45-924-5459, Fax : +81 45-924-5588
[b]ERATO, Japan Science and Technology Corporation, Tenko building 17-4, 687-1 Tsuruma, Machida 194-0004, Japan, Tel : +81 42-788-6030, Fax : +81 42-788-6031

Abstract: A cold Rb atomic beam with a low velocity of 0.10 m/s and a dense flux of 8.3×10^{12} atom·cm^2/s can be generated from a magneto-optical trap by an atom funnel.

The use of optical near fields enables us to precisely control the spatial position of neutral atoms beyond the diffraction limit [1]. The atom manipulation is based on the resonant mechanical interaction between a vapor atom and the optical near field, i.e. the dipole force: when the light frequency is higher than the atomic resonant frequency (blue detuning), the dipole force is repulsive. In order to efficiently and frequently have the interaction with the nanometric optical near field, the vapor atoms have to be very slow and high dense. A cold atomic beam fulfills the conditions. Here, we report the experimental progress of making a cold Rb atomic beam by means of an atom funnel [2] with a hollow prism.

Figure 1 schematically shows the atom funnel. A dense ensemble of cold atoms is produced by a magneto-optical trap (MOT) [3] and a polarization-gradient cooling (PGC) [4] inside the hollow prism with a small exit hole at the bottom. A blue-detuned doughnut laser beam shone upward excites the optical near field reflecting atoms on the inner wall surface of the prism. The cold atoms released from the MOT divergently fall into the prism, being accelerated by gravity. Then, they are repeatedly reflected by the repulsive optical near field on the inner wall surface. Moreover, in the process of the reflection, they are recooled by the Sisyphus cooling mechanism [5] with the help of a repumping laser beam shone downward. Therefore, the atoms are collected at the bottom and go out of the exit hole as a cold atomic beam.

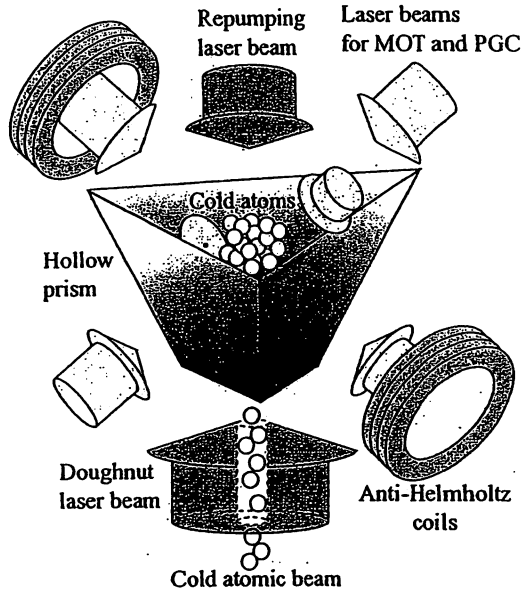

Fig. 1. Sketch of the atom funnel

Figure 2 shows a CCD camera image of the fluorescence from the cold ^{87}Rb atoms with a resonant wavelength of 780 nm. The cold atom cloud with a diameter of 1.5 mm is produced inside the hollow prism under the vacuum pressure of 10^{-8} torr by the MOT composed of a pair of anti-Helmholtz coils and orthogonal six laser beams with circular polarizations and a red-detuning of −10 MHz. The center of the cloud is at 4 mm above the exit hole. The number and mean temperature of the atomic ensemble are estimated to be 10^8 and 140 μK, respectively. Then, to cool down further the cold ^{87}Rb atoms, we perform the PGC by turning off the quadrupole magnetic field

and making a red-detuning of about –100 MHz as well as reducing the laser power. Figure 3 shows a time-of-flight (TOF) signal measured at a position of 10 cm below the MOT by irradiating a weak probe laser beam, where the prism is taken off. The intensity of fluorescence radiated from the cold ^{87}Rb atoms is plotted as a function of the time from the release. From the time variance of this signal, we estimate the velocity variance of the cooled atoms, and then find that the mean temperature is 8 μK.

From the Monte-Carlo simulations, we evaluate that a cold ^{87}Rb atomic beam with a mean velocity of 0.10 m/s and a flux of 8.3×10^{12} atom·cm^2/s is generated from the cold atomic source. In the simulations, we assume the hollow prism with an exit hole diameter of 10 μm and the doughnut laser beam with a blue detuning of +1 GHz, a power of 1 W, a beam waist (full width of $1/e^2$ maximum) of 5 mm, and an incidence angle of 45 degree. The result indicates that 8.3 atoms per a second are sent to a small volume (an optical near-field region) of 10^3 nm^3. In this case, the dipole interaction takes place ~200 times during the atom is in the optical near-field with a detuning of +1.5 GHz and an intensity of 3×10^5 mW/cm^2.

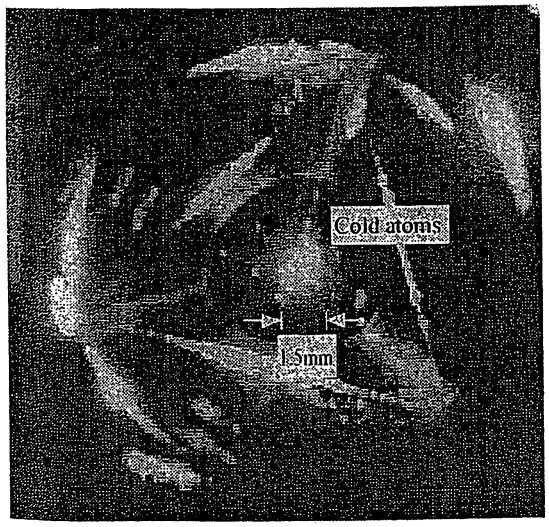

Fig. 2. Top view of the ensemble of cold ^{87}Rb atoms produced inside the prism for the funnel.

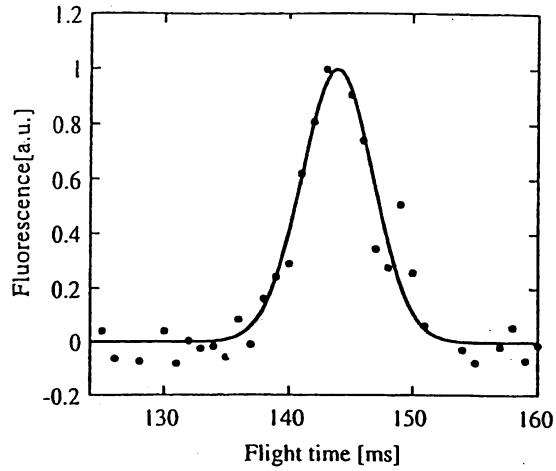

Fig. 3. TOF signal (filled circles) measured at 10cm below the MOT. A solid line shows a Gaussian fitting.

[1] M. Ohtsu (ed.), Near-Field Nano/Atom Optics and Technology, Chap. 11, (Springer, Tokyo, 1998).
[2] H. Ito, K. Sakaki, W. Jhe, and M. Ohtsu, "Atomic funnel with evanescent light," Phys. Rev. A 56, 712-718 (1997).
[3] E. L. Raab, M. Prentiss, A. Cable, S. Chu, and D. E. Pritchard, "Trapping of Neutral Sodium Atoms with Radiation Pressure," Phys. Rev. Lett. 59, 2631-2634 (1987).
[4] J. Dalibard and C. Cohen-Tannoudji, "Laser cooling below the Doppler limit by polarization gradients: simple theoretical models," J. Opt. Soc. Am. B 6, 2023-2045 (1989).
[5] J. Söding, R. Grimm, Yu. B. Ovchinnikov, "Gravitational laser trap for atoms with evanescent-wave cooling," Opt. Commun. 119, 652-662 (1995).

TuH2-2

Near-field optical detection of atoms with high sensitivity and high spatial resolution

Haruhiko Ito[1,2], Kouki Totsuka[2], Tomoto Kawamura[1], Takashi Yatsui[2], Motoichi Ohtsu[1,2]

[1]*Interdisciplinary Graduate School of Science and Engineering, Tokyo Institute of Technology, 4259 Nagatsuta-cho, Midori-ku, Yokohama 226-8502, Japan*

[2]*ERATO, Japan Science and Technology Corporation, Tenko building 17-4, 687-1 Tsuruma, Machida 194-0004, Japan*

Abstract: We describe an atom detector with two-color optical near fields designed for deflection experiments. The sensitivity is estimated to be about 10 % for both photoionization and resonant excitation schemes using a slit-type probe.

1. Introduction

The precise control of neutral atoms with optical near fields can be applied to fabrication of nano-scale matter. To this end, we are working at deflection of atoms with a nanometric fiber probe [1]. In the experiment, a Rb atom with a slow velocity of 10 m/s can be deflected with a displacement of about 10 μm from the incident axis. To detect the atom with a spatial accuracy of 1 %, we are planning to use a slit-type probe with a width of 100 nm. Here, we report two kinds of preliminary experiments to show the feasibility of the atom detection.

2. Methods

As the atom detector, we use a slit-type probe inducing two-color optical near fields [2-4]. Figure 1 (a) shows the scheme of detecting atoms. The slit is built on a silicon-on-insulator substrate. The two-color optical near fields are excited on the slit by illuminating the V-shape trench on the reverse side with two laser beams. The atoms approaching the slit are ionized or excited species- and state-selectively by the two-color optical near fields. Figure 1 (b) shows a SEM image of a slit-type probe with a width of 100 nm and a length of 100 μm.

There are two kinds of methods of detecting the atoms. The first one is two-step photoionization. The Rb atoms in the $5S_{1/2}$ ground state are excited to the $5P_{3/2}$ state by the first optical near field from a diode-laser beam with a resonant wavelength of 780 nm and then ionized by the second optical near field from an Ar-ion laser beam with a wavelength of 476.5 nm (see Fig. 2). The ionized atoms are detected by a channel electron multiplier biased negatively. The second one is two-step resonant excitation. The Rb atoms in the $5S_{1/2}$ ground state are excited to the $5D_{5/2}$ state via the $5P_{3/2}$ state by the two-color optical near fields from two diode-laser beams whose wavelengths are 780 nm and 775 nm, respectively. The excited Rb atoms spontaneously decay from the $5D_{5/2}$ state to the $5S_{1/2}$ state via the $6P_{3/2}$ state (see Fig. 3). By observing the blue fluorescence with a wavelength of 420 nm, we can detect the Rb atoms.

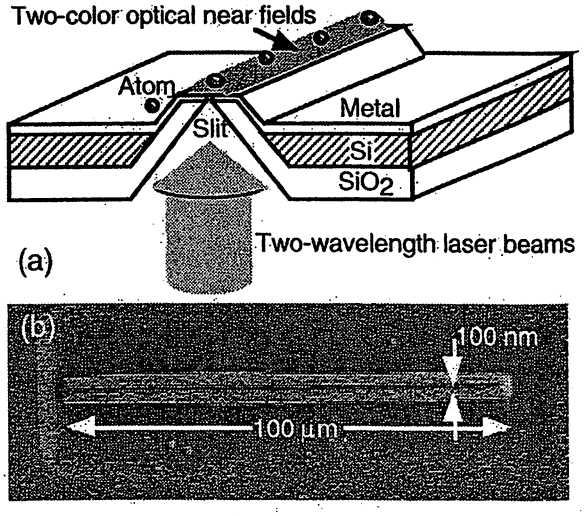

Fig. 1 (a) Atom detection with two-color optical near fields, and (b) SEM image of a slit-type probe.

3. Estimation of detection efficiency

In order to show the feasibility of the near-field optical detection, we examine the detection efficiency for the two methods. Figure 2 shows a two-step photoionization spectrum plotted as a function of the diode-laser detuning from the resonant frequency. Here, a thermal Rb atomic beam from an oven heated up to 150℃ is sent down to a prism with the optical near field excited by the Ar-ion laser. The Rb atoms entering the near-field region are ionized by illuminating the prism with the diode laser. From the ion count, it is estimated that the detection efficiency can be about 10 % if we use the slit-type probe.

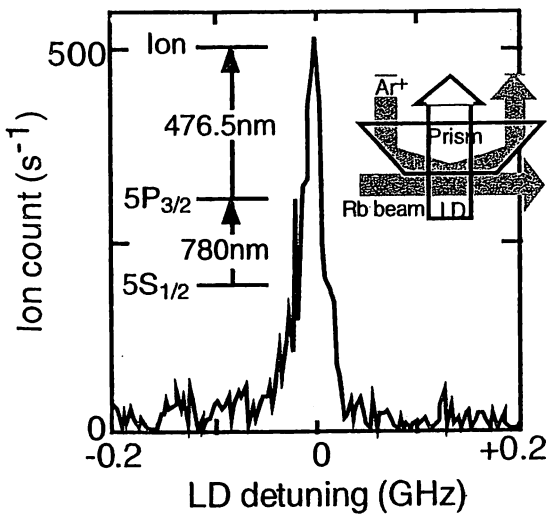

Fig. 2 Two-step photoionization spectrum.

On the other hand, Figure 3 shows the resonant blue-fluorescence from the Rb atoms in the $6P_{3/2}$ state plotted as a function of the detuning from the $5P_{3/2}$--$5D_{5/2}$ transition frequency. Here, we perform the two-step resonant excitation using the two-color optical near fields through a prism attached on a Rb vapor cell heated up to 200℃. As seen in Fig. 3, a Doppler-free spectrum is obtained due to the two counter-propagating laser beams: the FWHM is 80 MHz. From the fluorescence intensity, it is roughly estimated that the detection efficiency can be also about 10 % if we use the slit-type probe.

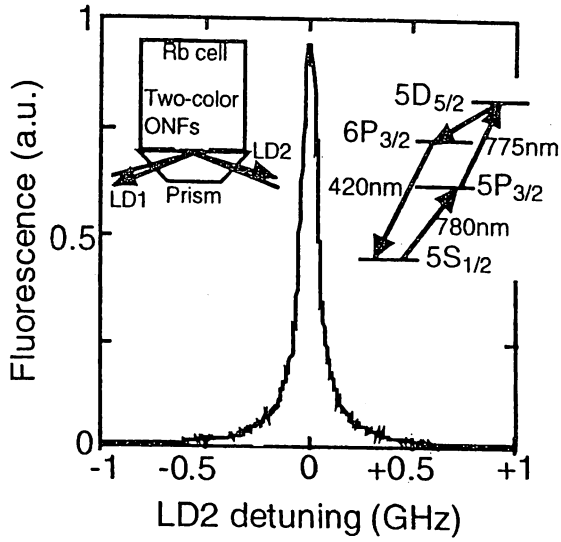

Fig. 3 Fluorescence from the $6P_{3/2}$ state in two-step resonant excitation.

4. Conclusion

We have fabricated a slit-type probe with a width of 100 nm and a length of 100 μm for the near-field optical detection of atoms. By using the slit-type probe, we can detect Rb atoms with a high efficiency of about 10 % as well as with a high spatial resolution of 100 nm.

References

[1] Near-Field Nano/Atom Optics and Technology, M. Ohtsu (ed.), Chap. 11 (Springer, Tokyo, 1998).

[2] K. Totsuka, H. Tanioka, H. Ito, M. Ohtsu, QELS 2000 Technical Digest, p.18 (OSA, San Francisco, 2000).

[3] K. Totsuka, A. Takamizawa, H. Tanioka, H. Ito, M. Ohtsu, NFO-6, p.158 (University of Twente, 2000).

[4] H. Ito, A. Takamizawa, H. Tanioka, K. Totsuka, M. Ohtsu, 2000 IQEC Conference Digest, p.106 (IEEE, Nice, 2000).

WJPD1-5

Tunable doughnut light beam for a near-field optical funnel of atoms

S. M. Iftiquar[A], H. Ito[A,B], and M. Ohtsu[A,B]

[A] ERATO Localized Photon Project, Japan Science and Technology Corporation, 687-1-17/4F Tsuruma, Machida-shi, Tokyo 194-0004, Japan. Tel: +81-42-788-6038, Fax: +81-42-788-6031, E-mail: iftiquar@ohtsu.jst.go.jp

[B] Interdisciplinary Graduate School of Science and Engineering, Tokyo Institute of Technology, 4259 Nagatsuta, Kanagawa 226-8502, Japan

Abstract

A doughnut-shaped Laguerre-Gaussian (LG) beam has been generated through interference of two spherical waves. The beam has a 5 mm bright ring and a 250-microns dark center suitable for our atom funnel experiment. The power conversion efficiency from a Gaussian mode to the LG mode is about 50 %.

A cold atomic beam is required for precise manipulation of neutral atoms with optical near fields localized in a nanometric region. To make the cold atomic beam from a magneto-optical trap, we have been developing an atom funnel with an optical near field [1,2]. In the atom funnel [2], a blue-detuned doughnut light beam with a radius of the dark center of around 250 micron and a ring thickness of 5 mm excites the repulsive optical near field, which reflects and cools the atoms, on the inner wall of a hollow prism. In this paper, we report a new method of generating the doughnut light beam with interference. Figure 1 shows the experimental layout. A light beam from a Ti:sapphire laser is divided into two beams and they are overlapped after the phase delay with PZT actuators. Figure 2 shows a cross-sectional image of a generated beam, while Figure 3 shows the intensity profile. As shown in Fig. 3, the doughnut beam converted from a Gaussian beam with a power of 800 mW has a dark center with a diameter of 250 microns and a bright ring of 3 mm with the intensity of 360 mW.

This method has a great advantage of controlling the shape through interference of two spherical-wave light beams. In fact, we observed the various LG modes (see Table 1) and various shape of doughnut beam by tuning optical delay of the two beams as shown in Table 2, Fig. 4 and Fig. 5. Here, a 260-nm optical delay tunes the bright-ring diameter from 3.3 mm to 2.6 mm with a variation of the beam diameter from 5.6 mm to 4.9 mm and the dark diameter changes from 1.2 mm to almost zero.

It is also advantageous to power conversion. The efficiency depends on the selected mode of the output beam. We observed the 50 % conversion in the case of the perfect doughnut shape. The conversion efficiency at narrower dark center becomes more than 50 %. In table 3, the ratios of output beam power to reflected beam power are given in the two cases of pump beam power, with a wavelength of 780 nm for the Rb funnel.

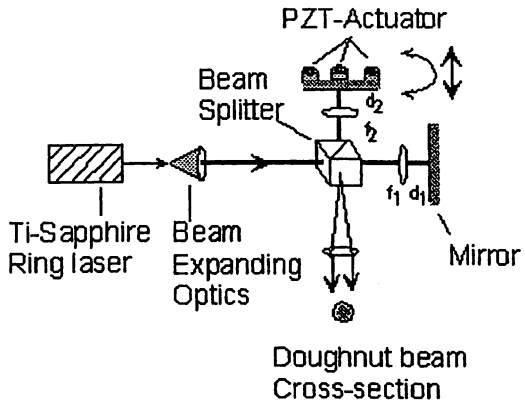

Figure 1: Doughnut beam generation setup

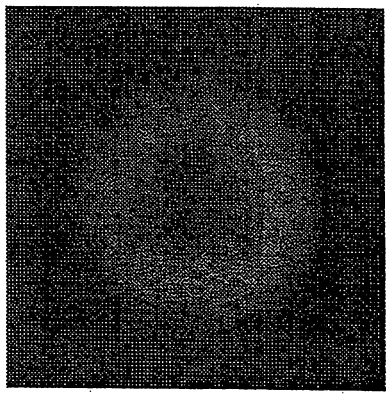

Figure 2: CCD image of generated doughnut beam

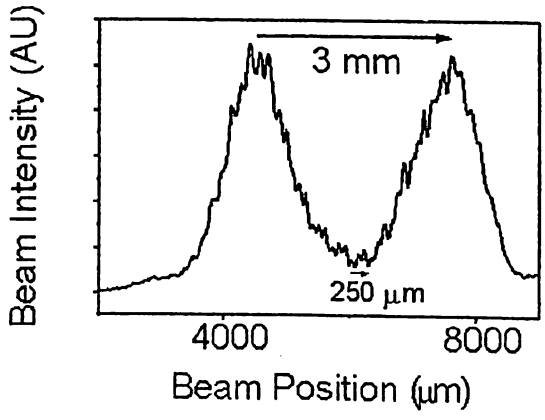

Figure 3: Intensity profile of generated doughnut beam

References

[1] H. Ito, K. Sakaki, W. Jhe, and M. Ohtsu, Phys. Rev. A 56, 712 (1997)

[2] H. Ito, A. Takamizawa, H. Tanioka, H. Totsuka, M. Ohtsu, Conference Digest 2000 Intl. Q. Electronics Conf. (Nice, France), QWD38

Table 1: Various Laguerre-Gaussian mode, LG_p^l, formation, with dark center $p = l - 1$, where $l\pi$ is the phase change for one round trip along the ring and $p+1$ is the number of annular rings

Beam dia. (mm)	f_1 (mm)	f_2 (mm)	d_1 (mm)	d_2 (mm)	p
1.5	250	200	45	58	0
1.5	400	200	45	58	5
7.5	250	250	25	25	0
7.5	300	300	25	25	5

Table 2: Tuning of doughnut beam shape or LG_0^1 mode for different beam diameter and size of its dark center through various optical delay.

Optical delay (nm)	Total beam diameter (mm)	Diameter of dark center (μm)
0	4.9	0
25	4.92	negligible
80	4.96	< 50
145	5.00	250
190	5.30	900
260	5.55	1200

Table 3: Output and reflected beam intensity ratio at various pump power. P_o output beam intensity, P_r reflected beam (towards the laser) intensity.Gauss: Airy type flat top near Gaussian, H-G: half Gaussian with very small dark center, D-N: doughnut. It has been noticed that a part of the beam power is lost to the optics.

Pump (780 nm) beam power, mW	Output Beam mode	Output Beam Power (mW)	$P_o : P_r$
250	Gauss	147	2.26 : 1
	H-G	125	1.45 : 1
	D-N	107	1 : 1
900	Gauss	619	2.2 : 1
	H-G	460	1.5 : 1
	D-N	380	1 : 1

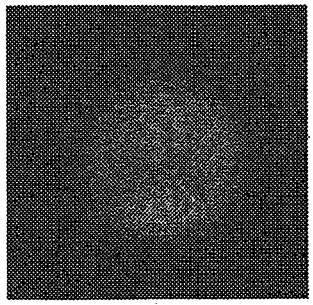

Figure 4(a): CCD image of two spherical beam interference pattern with circular cross section. The Airy disk has near uniform intensity distribution.

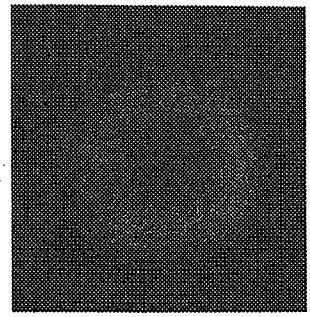

Figure 4(b): CCD image of the two spherical beam interference pattern having doughnut shape LG mode.

Figure 4(a) and 4(b): Transition of 'near Gaussian' beam mode into doughnut shape through tuning of optical delay by 260 nm. It may be noted that while the near Gaussian beam is transformed into a doughnut shaped LG mode, the beam size increases

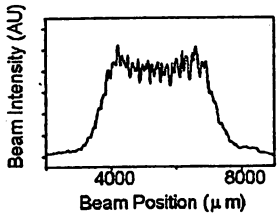

Figure 5(a): Intensity distribution of beam, shown in figure 4(a), measured with beam profiler.

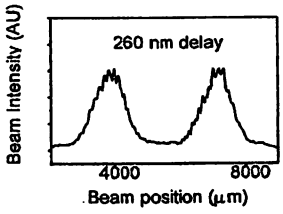

Figure 5(b): Intensity distribution of doughnut beam, as shown in figure 4(b).

Figure 5(a), 5(b): Intensity profile measurement shows the transformation of the output beam from near Gaussian into a doughnut shape. Associated beam diameter changes from 4.9 mm to 5.55 mm for the 260 nm optical delay between the two interfering spherical waves.

QTuG2 **3:00 pm**

A slit-type near-field optical detector for neutral atoms with high sensitivity and nanometric resolution

K. Totsuka*, H. Ito*,**, T. Kawamura**, T. Yatsui*, M. Ohtsu,*,**, **ERATO Localized Photon Project, Japan Science and Technology Corporation, 684-1 Tsuruma, Machida, Tokyo, 194-0004, Japan; Email: ktotsu@ohtsu.jst.go.jp; **Interdisciplinary Graduate School of Science and Engineering, Tokyo Institute of Technology, 4259 Nagatsuta, Midori-ku, Yokohama, Kanagawa 226-8502, Japan*

We have proposed deflection by an optical near field on a fiber probe to control atoms with high spatial accuracy.[1,2] In this case, the deflection angle is estimated to be 0.1 degree for a Rb atom with an incident velocity of 10 m/s. It leads to the deviation of 10 μm from the incident axis at 1 cm in the downstream. To detect the deflected atoms with an accuracy of 1%, we need the spatial resolution of 100 nm. However, a commercial detector such as MCP has a low resolution of 50 μm at most and the highest resolution that has been reported is 1 μm to our knowledges.[3] In addition, these are applied to metastable atoms and have less detection efficiency for ground state atoms we manipulate. For drastic improvement, we present here a slit-type atom detector with a nanometric lateral resolution. Since the number of atoms deflected by the optical near field is very small, it is important to detect atoms with high efficiency. For this purpose, we use photoionization with two-color optical near fields.

Figure 1 (a) shows a scheme for detecting neutral Rb atoms in the ground state. Two-color optical near fields are generated on the slit by irradiation of a diode-laser beam (780 nm) and an Ar-ion-laser beam (476.5 nm) from the rear. As shown in Fig. 1 (b), the Rb atoms approaching the slit are ionized from the $5S_{1/2}$ ground state via the $5P_{3/2}$ excited state by the two-color optical near fields in two steps. The ionized atoms are detected by a channel electron multiplier (CEM) biased with a voltage of –3 kV.

Figure 2 shows SEM images and the cross-sectional profile of the silicon-based slit-type detector fabricated through photolithography and etching.[4] A SiO_2 layer and a V-groove structure prevent the strong absorption of the Ar-ion-laser beam by silicon. A slit with a width of 100 nm is fabricated on the top whose height is 10 μm. To increase the ionization efficiency, we took a length as long as 100 μm. Since the optical near-field distribution has almost the same size as the slit, we expect that the lateral spatial resolution reaches 100 nm. Moreover, since there is no cut-off diameter for the light beam with the polarization perpendicular to the slit direction, the probe has a high throughput.[5] Since the throughput as high as 1% is expected, the ionization efficiency of the Rb atom with a velocity of 10 m/s is estimated to be up to 20% in the case where the light powers of the diode laser and the Ar-ion laser are 100 W/cm^2 and 1 kW/cm^2, respectively. This is sufficiently high for our purpose.

As a preliminary experiment, we observe a Doppler-free blue-fluorescence spectrum of Rb atoms in the 6P state (Fig. 3). In this case, the Rb atoms are excited to the 5D state via the 5P state by two-color planar optical near fields and transferred to the 6P state. This scheme is used as an al-

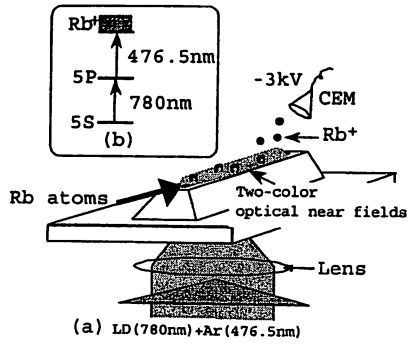

QTuG2 Fig. 1. Sketch of counting the number of atoms with a slit-type detector. Two-color optical near fields are generated on the slit by irradiation of a diode-laser beam and an Ar-ion laser beam from the rear. Rb atoms entering the near-field region are ionized in two-steps as shown in (b).

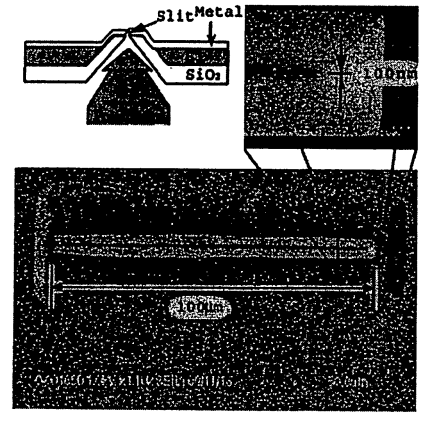

QTuG2 Fig. 2. Scanning electron microscope images and the cross-sectional profile of a slit-type detector. The width and the length of the slit are 100 nm and 100 μm, respectively.

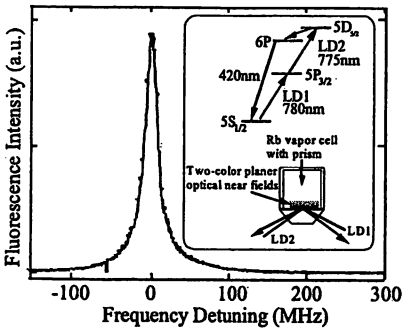

QTuG2 Fig. 3. Doppler-free blue-fluorescence spectrum (420 nm) of Rb plotted as a function of the frequency detuning with respect to the transition between the 5P state and the 5D state. The Rb atoms are pumped to the 6P state with the two-step excitation by two-color planar optical near fields.

ternative method of detecting Rb atoms with the slit-type detector.

1. H. Ito and M. Ohtsu, in *Near-Field Nano/ Atom Optics and technology,* M. Ohtsu, ed. (Springer, Tokyo, 1998), Chap. 11.
2. K. Kobayashi *et al.,* "Near-field optical potential for a neutral atom," Phys. Rev. A 63 (2001).
3. Ch. Kurtsiefer and J. Mlynek, "A 2-dimensional detector with high spatial and temporal resolution for metastable rare gas atoms," Appl. Phys. B 64, 85 (1997).
4. T. Yatsui *et al.,* "High-density-speed optical near-field recording-reading with a pyramidal silicon probe on a contact slider," Opt. Lett. 25, 1279 (2000).
5. H.U. Danzebrink *et al.,* "Nano-slit probes for near-field optical microscopy fabricated by focused ion beams," Journal of Microscopy 194, 335 (1999).

ASp.P3.14

Near-field optical potential generated by a nanometric tip

K Kobayashi, S Sangu, H Ito*, M Ohtsu*
Japan Science and Technology Corporation, Japan
**Tokyo Institute of Technology, Japan*

Optical near-field techniques are considered promising as enabling technologies for nano-structure fabrication with arbitrary shapes and high spatial accuracy far beyond the diffraction limit [1]. The ultimate goal of such fabrication is to make atomic-scale crystal growth by manipulating individual atoms with optical methods, and microscopic or quantum mechanical treatment of the interaction between a nanometric probe-tip and an atom is essential. In this report, we show novel and microscopic derivation of an effective interaction potential between such a nanometric probe-tip and sample. With the help of the projection-operator method, we develop a consistent theory appropriate for investigating near-field optical manipulation of an atom [2]. The atom is considered to interact with the probe tip in optical near-field systems via an elementary excitation mode of real photons and the macroscopic matter system. We find that the effective potential consists of the sum of the Yukawa functions with several kinds of effective masses, or interaction ranges. Each term is characterized in terms of detuning for resonance energies of the atom and probe tip, and shown to be attractive or repulsive,

depending on the detuning and material properties. Recent experimental results [3] support such a situation though a probe tip is not employed. Besides, choosing appropriate detuning and material properties, we can numerically show that a quasi- three dimensional potential well is generated to be suitable for a single atom trapping. It is noted that we can form a well in the near-field optical potential with single blue-detuned light.

[1] M. Ohtsu, K. Kobayashi, H. Ito, and G. H. Lee, Proc. IEEE 88(9), 2000, in press.
[2] K. Kobayashi, S. Sangu, H. Ito, and M. Ohtsu, Phys. Rev. A, 2000, in press.
[3] H. Failache, S. Saltiel, M. Fichet, D. Bloch, and M. Ducloy, Phys. Rev. Lett. 83, 5467, 1999.

EFFECTIVE PROBE-SAMPLE INTERACTION: TOWARD ATOM DEFLECTION AND MANIPULATION

K. KOBAYASHI [1], S. SANGU [1], H. ITO [1),2)], AND M. OHTSU [1),2)]

1) ERATO Localized Photon Project, Japan Science and Technology Corporation, 687-1 Tsuruma, Machida, Tokyo 194-0004, Japan
E-mail: kkoba@ohtsu.jst.go.jp

2) Interdisciplinary Graduate School of Science and Engineering, Tokyo Institute of Technology, 4259 Nagatsuta-cho, Midori, Yokohama, Kanagawa 226-8502, Japan

In this paper we discuss effective interactions between a probe tip and sample in optical near-field systems, focusing particularly on functional forms of the interactions. By analyzing the wave number dependence of the coupling coefficients of a probe/sample coupled to virtual photons or exciton-polaritons, we find that the Yukawa potential accounts for the main part of the interactions. We also examine the deviations from the Yukawa potential, which depend on a variety of parameters such as the size and material properties (excitation energy, effective mass, and so on). If the Yukawa potential is repulsive, the deviations may produce the potential minimum, which indicates the possibility of atom trapping by optical near fields. In order to demonstrate the application of our formulation with effective interactions, we show an example of atom deflection and manipulation by optical near fields as a quantum-mechanical problem.

1 Introduction

Recent experimental progress [1] encourages theoretical investigation of the quantum-mechanical aspects of near field optics. Using the projection-operator method, we have proposed a microscopic formulation of optical near-field systems that can be viewed as a hierarchical combination of two subsystems: (1) macroscopic matter and incident light, and (2) a microscopic probe-tip and sample [2-4]. Such a formulation enables us to analyze the quantum theoretical behavior or cavity QED effects of an atom, a molecule, and a quantum dot interacting with optical near fields, as well as the fundamental properties of optical near-field microscopy and spectroscopy [3,4].

The next section briefly outlines our approach, and describes the characteristic behavior of effective probe-sample interaction. In section 3, we discuss atom deflection and manipulation by optical near fields within our framework, and finally we offer some concluding remarks in section 4.

2 Effective Potential for Probe tip-Sample Systems

2.1 *Derivation of the Potential by the Projection-Operator Method*

Following Refs. [3,4], we briefly outline the derivation of an effective interaction $V_{\text{eff}}(\text{AB})$ between a probe tip and sample system. First, we divide an optical near-field system into two subsystems, as mentioned in the introduction. Using the projection operators (P and $Q = 1 - P$), we can then consistently treat the interaction between these two subsystems as follows:

$$\langle \Psi_\mu | \hat{V} | \Psi_\lambda \rangle = \langle \Psi_\mu^{(1)} | \hat{V}_{\text{eff}} | \Psi_\lambda^{(1)} \rangle, \quad \hat{V}_{\text{eff}} = (PJ^+JP)^{-1/2} (PJ^+\hat{V}JP)(PJ^+JP)^{-1/2},$$

where the bare interaction $\hat{V}$ operates on exact states of the total system, $|\Psi\rangle$, while $\hat{V}_{\text{eff}}$ operates on a small number of states of subsystem (2), $|\Psi^{(1)}\rangle$. If we expand the operator J perturbatively, the effective potential can be written in an analytic form, and the expression in the lowest order is given as

$$V_{\text{eff}}(\text{AB}) = -\frac{4\pi}{(2\pi)^3} \int d^3k \left[\frac{K_{\text{A}}(\bar{k}) K_{\text{B}}^*(\bar{k})}{\Omega(\bar{k}) - \Omega(\text{B})} + \frac{K_{\text{B}}(\bar{k}) K_{\text{A}}^*(\bar{k})}{\Omega(\bar{k}) + \Omega(\text{A})} \right],$$

where the coefficient and eigenenergy of elementary excitation modes of subsystem (1), that is, the virtual photons, are denoted as $K'(\bar{k})$ and $\Omega(\bar{k})$, respectively. The excitation energies of subsystem (2) are designated as $\Omega(\text{A})$ and $\Omega(\text{B})$.

2.2 *Wave Number Dependence of Coupling Coefficients f(k) via Exciton-Polaritons*

Let us adopt the dipole approximation of the multipolar QED Hamiltonian to represent the bare interaction $\hat{V}$, and consider exciton-polaritons as elementary excitation modes of subsystem (2). Rewriting the photon operators in $\hat{V}$ as exciton-polariton operators, we obtain the bare interaction in the exciton-polariton picture. We then define the coupling coefficient $f(k)$ through $K'(\bar{k})$ as

$$K'_{\alpha j}(\bar{k}) = \sum_{\lambda=1}^{2} \mu_\alpha (\bar{e}_j \cdot \bar{e}_\lambda(\bar{k})) f(k) e^{i\bar{k}\cdot\bar{r}_\alpha}, \quad f(k) = \frac{ck}{\sqrt{\Omega(k)}} \frac{\sqrt{\Omega^2(k) - \Omega^2/4}}{\sqrt{2\Omega^2(k) - \Omega^2/4 - (ck)^2}},$$

and discuss the wave number dependence of $f(k)$ that characterizes a typical interaction range of exciton-polaritons coupled to the probe tip and sample system. Here the j-th component of the dipole moment (α =A or B) and the unit vector for photon polarization are respectively designated as $\mu_\alpha \bar{e}_j$ and $\bar{e}_\lambda(\bar{k})$, while c and Ω stand for the speed of light and the excitation energy of the macroscopic matter. In

Fig. 1 the coupling coefficient $f(k)$ is shown by approximating the dispersion curve of exciton-polaritons as parabolic with effective mass m_p. The horizontal and vertical axes in Fig. 1 are measured in units of $\sqrt{m_p\Omega/\hbar}$ and $\sqrt{2m_pc^2/\hbar}$, respectively. It thus follows that the coupling coefficients of the exciton-polariton modes (virtual photons) to the nanometric subsystem (2) are constant when the wave number is larger than the lower cutoff $k_c \sim 2\sqrt{m_p\Omega/\hbar}$, while they are approximately proportional to k below k_c. Simple estimation gives $k_c \sim$ (1/100 nm) if the excitation energy and effective mass are taken as $\hbar\Omega \sim 1$ eV and $m_pc^2 \sim 1$ eV.

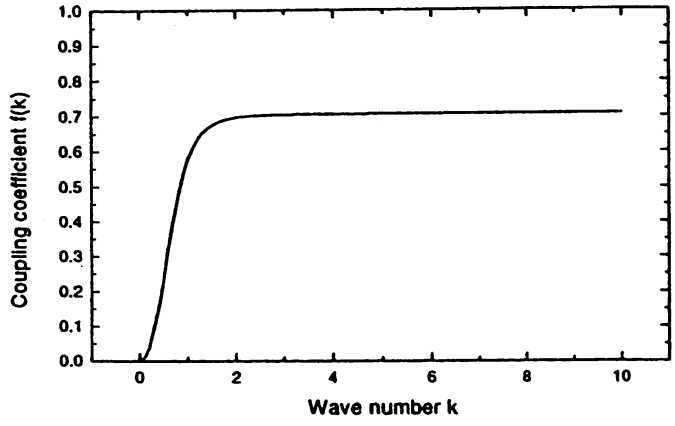

Figure 1. Wave number dependence of the coefficient $f(k)$, which characterizes a typical interaction range of exciton-polaritons coupled to a probe-tip and sample subsystem.

2.3 Characteristics of the EffectivePotential

Following the procedure discussed above, we examine the characteristic behavior of the effective potential $V_{eff}(r)$, where r is the sample position measured from the probe tip. As shown in Fig. 2, $V_{eff}(r)$ is an attractive Yukawa potential when $k_c/m_{eff} \sim 0$, while it becomes repulsive when $k_c/m_{eff} \sim 2$. Here m_{eff} is the effective mass of the Yukawa potential, and is found as

$$m_{eff} = \sqrt{2m_p\Omega(A)/\hbar + m_p\Omega/\hbar}\,.$$

Our analysis shows that the constant term of $f(k)$ gives the Yukawa potential, while the non-constant term contributes to the repulsive potential as k_c/m_{eff} comes close to 2. As is easily shown, the parameter $k_c/m_{eff} = 0$ corresponds to large red detuning ($\Omega(A)>\Omega(k)$), and $k_c/m_{eff} = 2$ corresponds to large blue detuning ($\Omega(A)<\Omega(k)$). This situation resembles the dipole potential in dressed-atom theory [6].

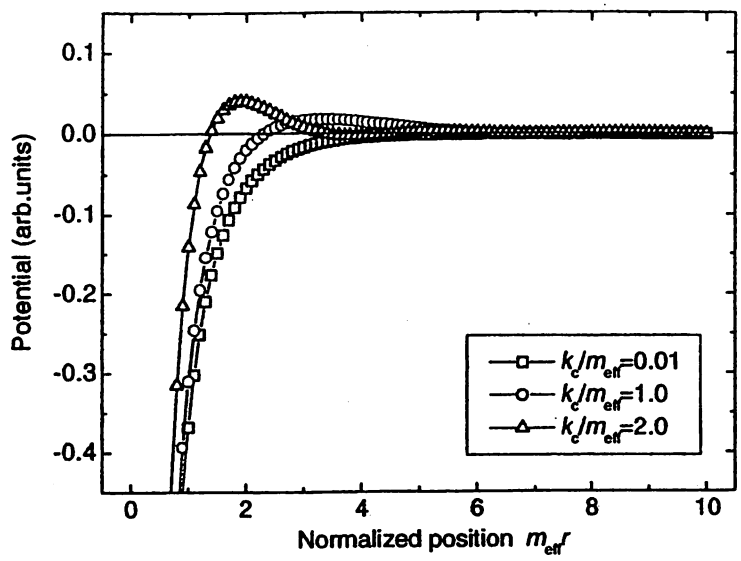

Figure 2. Effective potential $V_{eff}(r)$ as a function of the position r of the sample measured from the probe tip. The position is normalized by the effective mass m_{eff}. The potential forms depend on the parameter k_c/m_{eff}.

In the above discussion we approximated $f(k)$ as a linear + constant function in order to obtain the effective potential. Numerical evaluation, however, shows a very complex behavior of $f(k)$ close to k_c, which strongly depends on the material properties. Therefore, more rigorous analysis of $f(k)$ may produce a potential minimum around $1/m_{eff}$, indicating the possibility of atom trapping by the potential minimum.

3 Atom Deflection and Manipulation

3.1 Formulation

We formulate atom deflection or trapping by optical near fields [5,7] as a potential scattering problem. Since we have obtained $V_{eff}(r)$ as a potential generated between two arbitrary points in a probe tip and sample from a microscopic point of view, we can calculate the total potential $V(r)$ generated from a whole probe-tip sphere with radius a by integrating $V_{eff}(r)$ within the sphere. Note that $V(r)$ is also given as the Yukawa function when we keep only the Yukawa part from $V_{eff}(r)$.

The differential cross-section, or angular distribution is given by

$$\frac{d\sigma}{d\Omega} = |f(K)|^2 = \left| -\frac{1}{4\pi} T(K) \right|^2 ,$$

where $f(K)$ and $T(K)$ are the scattering amplitude and T-matrix as functions of the transferred momentum K, respectively. Here K is connected with the mass (M) and

incident speed (v) of the atom and the scattering angle (θ) by the equation $K=2(Mv/\hbar)\sin(\theta/2)$. We estimate it, as a first step, in the first Born approximation as

$$T^{(1)}(K)=\left(\frac{8\pi MV_0}{K\hbar^2}\right)\int_a^\infty dr\, rV(r)\sin(Kr)=\left(\frac{8\pi MV_0}{K\hbar^2}\right)\int_a^\infty dr\exp(-m_{\text{eff}}r)\sin(Kr)$$

$$=\left(\frac{8\pi MV_0}{K\hbar^2}\right)\frac{K\cos(Ka)+m_{\text{eff}}\sin(Ka)}{K^2+m_{\text{eff}}^2}.$$

From the above equation, it follows that the denominator with $m_{\text{eff}} = 0$ gives a similarity to Rutherford scattering, and that a periodic structure appears on account of the numerator. The validity of the first-order approximation can be simply evaluated by comparing it with that given by the second Born approximation:

$$T^{(2)}(K)=T^{(1)}(K)-\left(\frac{2}{\pi}\right)\left(\frac{2MV_0}{\hbar^2}\right)^2 S,\quad k=Mv/\hbar,$$

$$S=\frac{2\pi^2}{KA}\left\{\tan^{-1}\left[\frac{m_{\text{eff}}K}{2A}\right]-\left(\frac{i}{2}\right)\ln\left[\frac{A-kK}{A+kK}\right]\right\},\quad A=\sqrt{m_{\text{eff}}^4+k^2\left(4m_{\text{eff}}^2+K^2\right)},$$

where we have kept only the Yukawa part from $V_{\text{eff}}(r)$.

3.2 *Numerical Results*

Let us simulate a situation in which atoms cooled in an atomic funnel [8] are led to a potential (i.e., optical near-field) region generated by a fiber probe tip or planar apertured probe arrays [9], and are carried to a desired point on a substrate with high spatial accuracy far beyond the diffraction limit. Following the above equations, we calculate the angular distribution of ^{85}Rb with incident speed v = 1 m/s and transition dipole moment $\mu=0.3\left(\text{eV}\cdot\text{nm}^3\right)^{1/2}$ [10], where the atoms are deflected by optical near fields generated from a probe-tip sphere with variable radius a. We approximately employ only the Yukawa part of $V_{\text{eff}}(r)$.

Figure 3 shows an example of such results. As the radius of the probe tip decreases from a = 50 nm to 10 nm, the deflection angle θ (HWHM) increases from 1 degree to 5 degrees, while the cross-section decreases by 7 orders of magnitude. It is not shown in the figure, but it follows that the deflection angle decreases as the speed and mass of the atom increase. These parameters should be optimized for each experimental situation.

3.3 *Discussion*

Owing to the functional form of the Yukawa potential, we can analytically estimate the angular distribution in the second Born approximation. It depends on the mass, velocity, energy levels, and transition dipole moment of the atom, and the size, material properties, and energy levels of the probe tip and macroscopic matter, that

is, the optical near fields. In the simulated range of the parameters, the second Born approximation makes a very small contribution to the differential cross-section, as shown in Fig. 4. It is thus reasonable to use the first Born approximation in the process of designing atom guidance and manipulation systems.

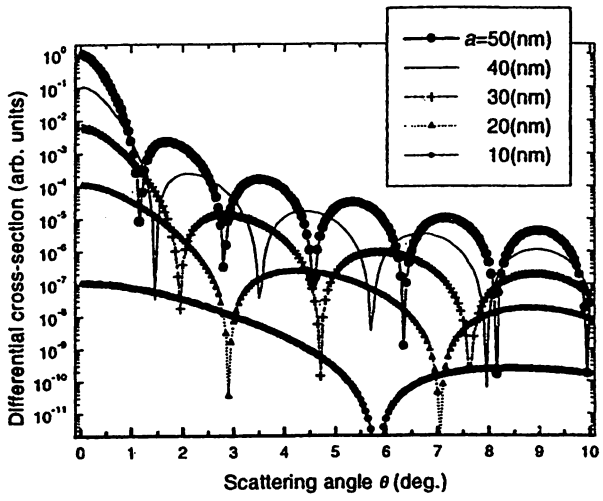

Figure 3. Angular distribution of ^{85}Rb atoms deflected by an optical near field when the incident speed of the atom is assumed to be v = 1 m/s. Each curve is calculated in the first Born approximation when the size of the tip varies from a = 10 nm to 50 nm.

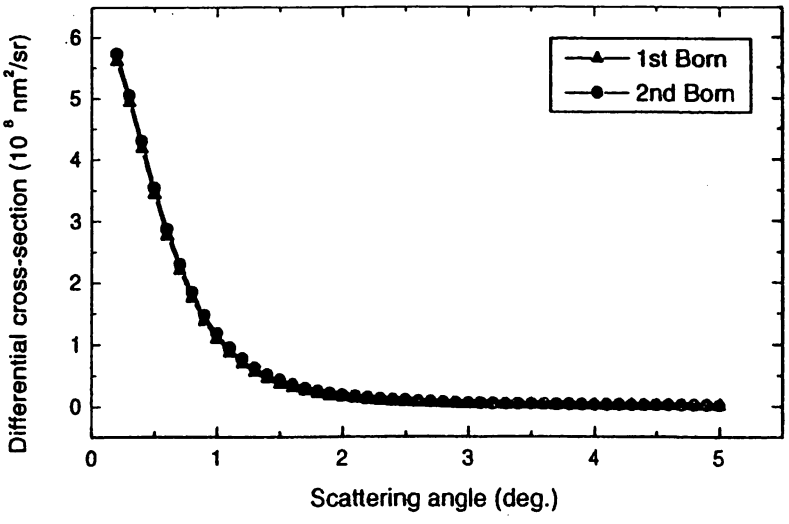

Figure 4. Comparison of the angular distribution of ^{85}Rb atoms calculated in the first and second Born approximations. The incident speed of the atom is assumed to be v = 1 m/s, and the size of the tip is assumed to be a = 50 nm. The transition dipole moments of the atom and probe tip are assumed to be 0.3 and 0.025 (eV nm^3) $^{1/2}$, respectively.

As explained in the previous section, $V_{eff}(r)$ consists of a repulsive part as well as the attractiveYukawa part in the blue detuning case (see Fig. 2). It should be clarified how the deviation from the Yukawa potential contributes to atom deflection and manipulation. In particular, it would be interesting to investigate the case in which $V_{eff}(r)$ has a minimum, since we may expect the possibility of atom trapping in such a case. It would also be intriguing to examine the effects of QED on the effective transition dipole moments and energy level shifts of an atom caused by the optical near field.

4 Concluding Remarks

We have derived an effective potential for a probe-sample system from microscopic theory. The potential is the attractive Yukawa potential in the red detuning case, and the Yukawa plus additional repulsive potential in the blue detuning case. Using the effective potential derived, we discussed the atom deflection cross-section within the Born approximation, and clarified the validity of our approach and future issues.

References

1. See for example, Ohtsu M. (ed.), *Near-Field Nano/Atom Optics and Technology*, (Springer-Verlag, Tokyo, 1998).
2. Ohtsu M. (ed.), *Near-Field Nano/Atom Optics and Technology*, (Springer-Verlag, Tokyo, 1998) Chap. 12.
3. Kobayashi K. and Ohtsu M., Quantum theoretical approach to a near-field optical system, *J. Microscopy* **194** (1999) pp. 249–254.
4. Kobayashi K. and Ohtsu M., Quantum theory and virtual photon model of near field optics, *Proc. SPIE* **3791** (1999) pp.10–20.
5. Ohtsu M. (ed.), *Near-Field Nano/Atom Optics and Technology*, (Springer-Verlag, Tokyo, 1998) Chap. 11.
6. Dalibard J. and Cohen-Tannoudji C., Dressed-atom approach to atomic motion in laser light: the dipole force revisited, *J. Opt. Soc. Am. B* **2** (1985) pp. 1707–1720.
7. Ohtsu M. and Hori H., *Near-Field Nano-Optics*, (Kluwer Academic/Plenum, New York, 1999) Chap. 7.
8. Ito H., Sakaki K., Jhe W., and Ohtsu M., Atomic funnel with evanescent light, *Phys. Rev. A* **56** (1997) pp. 712–718.
9. Yatsui T., Kourogi M., Tsutsui K., Takahashi J., and Ohtsu M., Subwavelength-sized phase change recording with a silicon planar apertured probe, *Proc. SPIE* **3791** (1999) pp.76–84.
10. Krainov V. P, Reiss H. R., and Smirnov B. M., *Radiative Processes in Atomic Physics*, (John Wiley & Sons, New York, 1997) p. 84.

QWD38

Toward near-field optical manipulation of atoms using a nanometric fiber probe

Haruhiko Ito[1], Akifumi Takamizawa[1], Hideaki Tanioka[1], Hiroki Totsuka[2], Motoichi Ohtsu[1,2]
[1]Interdisciplinary Graduate School of Science and Engineering, Tokyo Institute of Technology,
4259 Nagatsuta, Midori-ku, Yokohama, Kanagawa 226-8502, Japan
Phone: +81-45-924-5459, Fax: +81-45-924-5487
[2]ERATO Localized Photon Project, Japan Science and Technology Corporation,
684-1 Tsuruma, Machida, Tokyo 194-0004, Japan; Phone: +81-42-788-6030, Fax: +81-42-788-6031

The conventional atom-manipulation techniques with propagating light are limited in spatial accuracy by diffraction effects of light waves In order to overcome the diffraction limit and increase the manipulation accuracy, we can use the optical near field localized in a nanometer region Such an optical near field is produced by a fiber probe with a nanometric aperture [1] We consider manipulating atoms by means of the dipole force from the localized optical near field In this paper, we report the experimental progress toward the realization of atom manipulation with the nanometric fiber probe

There are two principal factors for the experiment One is to fabricate a fiber probe suitable for the atom used and estimate the dipole-force potential which depends on light intensity, frequency detuning, atomic natural linewidth, and so on In fact, we made a fiber probe with a small aperture and measured the near-field light intensity distribution produced by the fiber probe The other is to prepare cold atoms Since the interaction region is very narrow, the atomic velocity has to be sufficiently small In addition, the high atomic density is required for the efficient detection in the experimental demonstration For this purpose, a cold atomic beam is suitable To create the cold atomic beam, we use an atom funnel composed of an optical near field [2]

The measurement of the near-field light intensity profile in the close vicinity of the aperture is carried out in a probe-to-probe configuration controlled by the shear-force technique with an optical feedback system In this scheme, another fiber probe with a smaller aperture is approaching the fiber probe placed face to face and picks up the scattered light signal Figure 1 shows the typical result plotted as a function of the distance r from the aperture surface The inset photograph is a SEM image of the fiber probe with a 200-nm aperture used here The intensity change can be fitted by the Yukawa-type function $I(r) \sim \exp(-cr/a)/r$,[1] where a is the radius of the aperture and c has the value between 0 32 and 2 10 depending on the distance From this result, we estimated the trap potential made up of the repulsive dipole-force and attractive van der Waals potentials [1] For example, Rb atoms cooled down to 30 μK can be trapped near the tip of a fiber probe if the aperture size is reduced to 20 nm

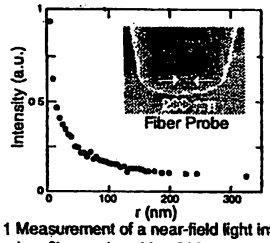

Fig 1 Measurement of a near-field light intensity in a fiber probe with a 200-nm aperture

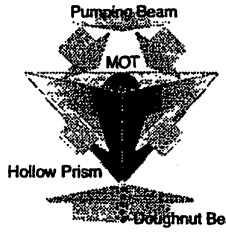

Fig 2 Near-field optical funnel

Figure 2 shows the near-field optical funnel which collects cold atoms released from an MOT In this funnel, the atoms are reflected by the optical near field produced by the total-internal reflection of a blue-detuned doughnut-shaped light beam shone upward In addition, the atoms are recooled through the Sisyphus cooling induced by a weak pumping light beam shone downward As shown in Fig 2, we use an inverse triangular-pyramid hollow prism to couple the light beams for the MOT with the funnel The collected atoms go out of the small exit hole at the bottom In the experiment, Rb atoms are trapped by the MOT and cooled down to about 5 μK by PGC inside the prism The funneled atoms are detected by a time of flight method The created cold atomic beam can be used for deflection and trap experiments with the fiber probe [1]

1 M Ohtsu (ed), *Near-field nano/atom optics and technology* (Springer, Tokyo, 1998)
2 H Ito, K Sakaki, W Jhe, M Ohtsu, Phys Rev A 56, 712 (1997)

EXPERIMENTAL PROGRESS OF ATOM DEFLECTION WITH A FIBER-PROBE USING AN ATOMIC FUNNEL WITH OPTICAL NEAR FIELD

K. Totsuka[1], A. Takamizawa[2], H. Tanioka[2], H. Ito[2], M. Ohtsu[1,2]

[1]ERATO Localized Photon Project, Japan Science and Technology Corporation, 684-1 Tsuruma, Machida, Tokyo, 194-0004, Japan; email: ktotsu@ohtsu.jst.go.jp
[2]Interdisciplinary Graduate School of Science and Engineering, Tokyo Institute of Technology, 4259 Nagatsuta, Midori-ku, Yokohama, Kanagawa 226-8502, Japan

Atom manipulation using the propagating light is restricted by the diffraction limit. On the other hand, if we use optical near field we can manipulate an atom being free from this limitation. In this paper, we report the experimental progress toward the manipulation of an atom by a nanometric sized sharpened fiber-probe. To manipulate an atom by a fiber-probe, there are two fundamental factors. One is to fabricate a suitable fiber-probe for an atom. The other is to create a cold atoms. Since, the optical near field is localized in a nanometric size, we have to use cold atoms to get enough interaction. For this purpose, a cold atomic beam is suitable for the experimental demonstration.

We consider to manipulate an atom by the dipole force. By the rapidly decreasing characteristic of the optical near field intensity distribution, strong dipole force is affected on an atom when we use the slightly detuned laser light from its transition frequency. In a certain condition, a trap potential is calculated for an atom at a balance between the repulsive dipole force and the attractive van der Waals force.[1] This potential depends on the intensity distribution of the optical near field, detuning from the transition frequency, atomic natural linewidth, etc. We measured the intensity distribution of the optical near field on an apertured fiber-probe by a probe-to-probe configuration. Figure 1 shows the result as a function of the distance r from the surface of the tip. This distribution can be fitted by the Yukawa-type function $\exp(-cr/a)$, where a is the radius of the aperture and c has the value between 0.4 and 3 depending on the distance. From this result, we estimate a trap potential near the tip that Rb atoms with several tens of micro kelvin can be trapped if we reduce the aperture size to 20 nm. To create a cold atomic beam, we collect cold atoms from a magneto-optical trap(MOT) by an atomic funnel using an optical near field. Figure 2 shows an inverse triangular-pyramid hollow prism which is shone upwards by a blue-detuned doughnut-shaped light beam to create the optical near field on the surface to reflect cold atoms. The reflected cold atoms are recooled by the Sisyphus cooling. The collected atoms exit from the hole at the bottom. In this method, the cold atoms are created by the MOT and the polarization gradient cooling(PGC) methods in the prism. We measured the time of flight of the Rb atoms 10 cm below the trapped position. Figure 3 shows the fluorescence of the Rb atoms as a function of the time which is released from a MOT and further cooled by PGC. From this result, it is estimated that the Rb atoms are cooled to 10 μK by the MOT and PGC. From the result of a Monte Carlo simulation, this temperature is found to be low enough to perform the funneling. The created cold atomic beam can be used for deflection and trapping with the fiber-probe.

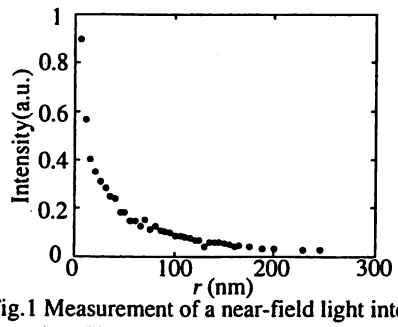

Fig.1 Measurement of a near-field light intensity in a fiber probe with a 200nm aperture

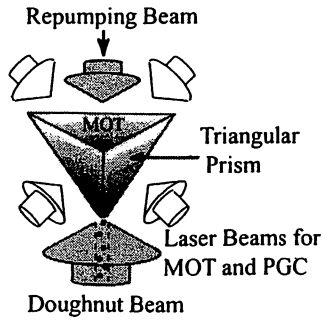

Fig.2 Atomic funnel by optical near field

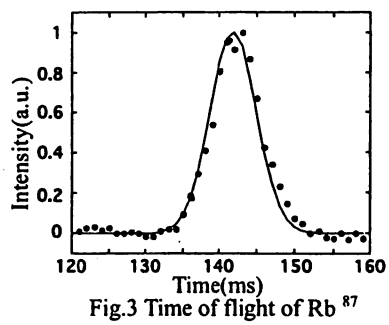

Fig.3 Time of flight of Rb ^{87}

[1] M. Ohtsu(ed.), Near-Field nano/atom optics and technology,Springer, Tokyo, 1998.

NEAR-FIELD QUANTUM OPTICAL THEORY APPLIED TO ATOM MANIPULATION

K. Kobayashi [1], S. Sangu [1], H. Ito [2] and M. Ohtsu [1], [2]

(1) ERATO Localized Photon Project, Japan Science and Technology Corporation, 687-1 Tsuruma, Machida, Tokyo 194-0004, Japan
e-mail: kkoba@ohtsu.jst.go.jp

(2) Interdisciplinary Graduate School of Science and Engineering, Tokyo Institute of Technology 4259 Nagatsuta-cho, Midori, Yokohama, Kanagawa 226-8502, Japan

Optical near-field techniques are expected as a candidate of enabling technologies for nano-structure fabrication and atom manipulation [1]. As a first step in this direction, we report a numerical estimation of a single atom deflection and manipulation by using optical near fields. It is formulated as an atom scattering by an effective potential generated between a nanometric probe tip and neutral atom. We use the effective near-field optical potential derived microscopically [2], that is, the sum of the Yukawa potentials with several kinds of effective masses, or interaction ranges. We numerically clarify how the angular distributions of deflected atoms depend on the tip size, incident speed (kinetic temperature) of atoms, and the detuning.

We simulate a situation in which atoms cooled in an atomic funnel are led to the potential region generated by a fiber probe tip or planar apertured probe arrays, and are carried to a desired point on a substrate with high spatial accuracy [3]. Figure 1 shows an example of the angular distribution of ^{85}Rb with an incident speed of 1 m/s and transition dipole moment of 7.5 debye, where the atoms are deflected by optical near fields generated by a probe tip sphere with variable radius a=10 – 50 nm. It shows that a smaller probe tip can deflect the atom more strongly. We will also discuss the dependence of the scattering angle on the shape of the optical potential that is governed by the detuning and the resonance energies of the atom, probe tip, and macroscopic matter.

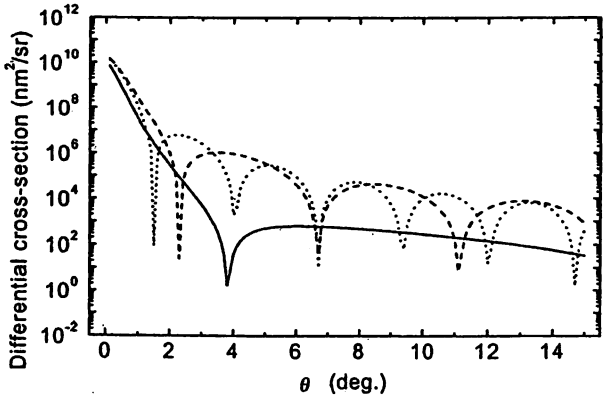

Fig. 1 *Differential cross-section of ^{85}Rb calculated with the blue detuned potential. Solid: a=10 nm, dashed: a=30 nm, and dotted: a=50 nm.*

References

[1] M. Ohtsu, K. Kobayashi, H. Ito, and G. H. Lee, *Proc. IEEE*, in press.
[2] K. Kobayashi and M. Ohtsu, "Quantum theoretical approach to a near-field optical system," *J. Microscopy* **194**, 249-254 (1999).
[3] H. Ito, A. Takamizawa, H. Tanioka, and M. Ohtsu, "Precise control of atoms with optical near fields: deflection and trap," *Proc SPIE* **3791**, 2-9 (1999).

[I-2] PAPRES IN NANO PHOTONICS

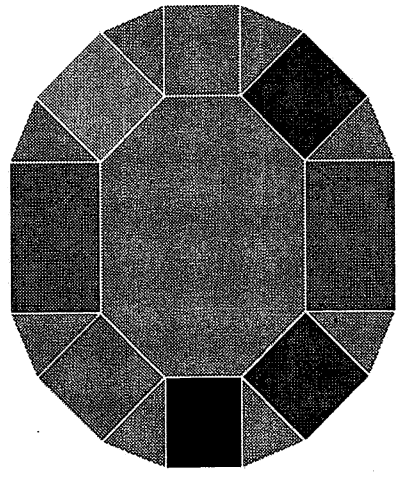

Journal of Microscopy, Vol. 202, Pt 2, May 2001, pp. 279–285.
Received 28 August 2000; accepted 11 October 2000

Optical near fields as photon-matter interacting systems

S. SANGU*, K. KOBAYASHI* AND M. OHTSU*†
**ERATO Localized Photon Project, Japan Science and Technology Corporation, 687-1 Tsuruma, Machida, Tokyo 194-0004, Japan*
†Interdisciplinary Graduate School of Science and Engineering, Tokyo Institute of Technology, 4259 Nagatsuta-cho, Midori-ku, Yokohama, Kanagawa 226-8502, Japan

Key words. Effective probe–sample interaction, optical near field, optical near-field microscopy, polarization, signal intensity, size–resonance effect, taper angle, virtual exciton-polariton, Yukawa function.

Summary

A quantum theoretical formulation of an optical near-field system developed using the projection operator method is shown to be applicable to conventional problems in the optical near field in a unified way, and also addresses different quantum mechanical issues such as atom manipulation and nano-fabrication. To gain a clear insight, the effective mass of exciton-polaritons is introduced; this depends on the sizes of the probe tip and sample. We calculate the optical near-field intensity detected by (a) a probe sphere and (b) tapered probe modelled by two spheres. The results show that the size of the probe tip determines the spatial resolution, while the contribution of the tapered part causes degradation of the signal contrast. A size–resonance effect between the probe and sample is predicted. Furthermore, enhancement of the signal intensity is observed at the edges of a circular aperture perpendicular to incident polarization. These results are consistent with those obtained from different methods. The approach employed is shown to be a valuable tool in physical understanding and analysis of the near-field optical phenomena as well as experimental situations.

Introduction

Recent endeavour in the field of photonics has been devoted to the study of the realization of optical functional devices on the nanometre scale. For example, optical near-field photochemical deposition of Zn and ZnO on a sub-100-nm scale has been experimentally demonstrated (Ohtsu *et al.*, 2000; Yamamoto *et al.*, 2000), as one of the promising technologies for nanostructure fabrication.

Correspondence: S. Sangu. Tel: + 81 42 788 6043; fax: + 81 42 788 6031; e-mail: sangu@ohtsu.jst.go.jp

Theoretical studies of optical near fields have mainly focused on high-resolution imaging analysis of a near-field optical microscope, on the basis of the macroscopic Maxwell equations, or of classical electrodynamics. Consequently, probe–sample interactions via incident light and macroscopic matter systems have not been explicitly formulated, though we realize from the experimental progress mentioned above that the interactions play an important role in theoretical treatments. Under the experimental circumstances such as nanostructure fabrication, optical near fields might be mixed states consisting of photons and matter excitation. Recognizing these points, we have developed a quantum theoretical formulation of optical near field systems with the help of the projection-operator method (Kobayashi & Ohtsu, 1999a), and applied our approach to atom deflection, trapping, and manipulation in order to clarify key parameters for experimental demonstration (Kobayashi *et al.*, 2000, 2001).

In this paper, we show that our formulation is also applicable to conventional problems on optical near fields in a unified way, as well as to the quantum mechanical issues mentioned above. We calculate optical near-field intensity in idealized probe-sample systems, and analyse fundamental properties of detected signals in such systems. An important idea is introduced here; virtual exciton-polaritons are supposed to mediate between the nanometric probe and the sample to produce effective interactions between them. Effective mass of the exciton-polaritons, determined from the dispersion relation, also depends on the sizes of the probe tip and the sample and hence on their energy levels. It thus follows that the detected signals show characteristic size dependence.

A number of theoretical and numerical studies on similar problems have been presented by using various methods based on the Maxwell equations: for example, self-consistent approach (Girard & Courjon, 1990; Girard & Bouju, 1992; Berntsen *et al.*, 1993), the method using multiple multipole

expansion (Novotny *et al.*, 1994), diffraction theory modified in optical near-field regime (Leviatan, 1986; Roberts, 1991; Jang & Jhe, 1996) and coupled dipole approximation (Taubenblatt & Tran, 1993; Keller *et al.*, 1993; Kobayashi & Watanuki, 1996, 1997; Saiki & Ohtsu, 1998). The present theoretical and numerical calculations show that we can easily obtain new results or equivalent ones predicted by these conventional optical near-field theories. Furthermore, our approach can give an intuitive understanding of optical near fields without solving complex boundary value problems.

The paper is organized as follows. In Section 2, theoretical derivation of the effective probe–sample interactions is briefly summarized. In order to have a clear insight, effective mass approximation is made in Section 3. Using the effective interaction thus derived, we calculate near-field intensity for both a probe sphere–sample sphere system and a tapered probe–sample sphere system in Section 4. The polarization dependence of the detected signals is also discussed. Finally, concluding remarks are presented in Section 5.

2. Theoretical derivation of effective probe–sample interaction

Theoretical formulation and the effective probe–sample interactions are briefly outlined for use in the following sections. Details have been published elsewhere (Kobayashi & Ohtsu, 1999b).

Using the projection-operator method (Fulde, 1995; Kobayashi & Ohtsu, 1999a,b), we exactly renormalize the effects of the other degrees of freedom than that of a probe–sample system. Then the probe–sample system can be considered to be isolated from the other systems (bath systems), although the bare interactions $\hat{V}$ between the probe and sample are transformed into the effective interactions $\hat{V}_{\mathrm{eff}}$.

Noting that the bare interaction $\hat{V}$ can be described by the multipolar QED Hamiltonian (Craig & Thirunamachandran, 1998), we employ, for simplicity, its dipole approximation as

$$\hat{V} = -\sum_{\alpha=A}^{B} \theta(z_\alpha)\hat{\boldsymbol{\mu}}_\alpha \cdot \hat{\boldsymbol{D}}(\boldsymbol{r}_\alpha), \tag{1}$$

where the index α denotes the sample (A) and probe (B), and $\theta(z)$ and $\hat{\boldsymbol{\mu}}$ stand for the step function and the dipole operator, respectively. The displacement field operator is denoted as $\hat{\boldsymbol{D}}(\boldsymbol{r})$, and is given by the conjugate momentum operator $\hat{\boldsymbol{\Pi}}(\boldsymbol{r})$ of the vector potential operator $\hat{\boldsymbol{A}}(\boldsymbol{r})$.

Let the bath systems be a set of excitons, photons, and their interactions, by assuming that the induced electric polarization in the macroscopic matter system, such as a prism in the collection mode or a fibre probe in the illumination mode, is represented as excitons (Haken, 1983). It is well known that such systems have characteristic elementary excitation modes, or exciton-polariton modes, that is, so-called 'dressed' states of photons and excitons (Hopfield, 1958; Knoester & Mukamel, 1989; Huttner & Barnett, 1992). If we rewrite the photon operators in $\hat{\boldsymbol{D}}(\boldsymbol{r})$ as exciton-polariton operators, we can convert the bare interaction $\hat{V}$ into the exciton-polariton representation as follows:

$$\hat{V} = -i\sqrt{\frac{2\pi\hbar}{V_0}}\sum_{\alpha=A}^{B}\theta(z_\alpha)[\hat{b}^\dagger(\boldsymbol{r}_\alpha) + \hat{b}(\boldsymbol{r}_\alpha)] \cdot \sum_{\boldsymbol{k}}[K'_\alpha(\boldsymbol{k})\hat{\xi}(\boldsymbol{k}) - K'^{*}_\alpha(\boldsymbol{k})\hat{\xi}^\dagger(\boldsymbol{k})], \tag{2}$$

where $(\hat{b}^\dagger, \hat{b})$ and $(\hat{\xi}^\dagger, \hat{\xi})$ denote the creation and annihilation operators of electronic excitation of the microscopic probe-sample system and the exciton-polaritons, respectively. The coefficient $K'_\alpha(\boldsymbol{k})$ and its complex conjugate $K'^{*}_\alpha(\boldsymbol{k})$ represent the coupling strength of exciton-polaritons to the probe–sample system and one can obtain the explicit form of $K'_\alpha(\boldsymbol{k})$ to define the coupling coefficient $f(k)$ as

$$K'_\alpha(\boldsymbol{k}) = \sum_{\lambda=1}^{2}\sum_{j=1}^{3}\mu_{\alpha j}[\boldsymbol{e}_j \cdot \boldsymbol{e}_\lambda(\boldsymbol{k})]f(k)e^{i\boldsymbol{k}\cdot\boldsymbol{r}\alpha}, \tag{3}$$

$$f(k) = \frac{ck}{\sqrt{\Omega(k)}}\,\frac{\sqrt{\Omega^2(k) - \Omega^2/4}}{\sqrt{2\Omega^2(k) - \Omega^2/4 - c^2k^2}}, \tag{4}$$

where the jth component of dipole moment and the unit polarization vector for photons are designated as $\mu_{\alpha j}\boldsymbol{e}_j$ and $\boldsymbol{e}_\lambda(\boldsymbol{k})$, respectively. The wavenumber dependence of $f(k)$ characterizes a typical interaction range. The quantities c, $\hbar\Omega/2$, and $\hbar\Omega(k)$ stand for the speed of light, the electronic excitation energy of the macroscopic matter system, and the eigenenergy of the exciton-polaritons.

As shown by Kobayashi & Ohtsu (1999b), we can finally write down the effective probe–sample interaction in the lowest order as

$$V(r) = -\frac{4\pi}{(2\pi)^3}\int\left[K'_B(\boldsymbol{k})K'^{*}_A(\boldsymbol{k})\left\{\frac{1}{\Omega(k)+\Omega_A} + \frac{1}{\Omega(k)-\Omega_A}\right\} + K'_A(\boldsymbol{k})K'^{*}_B(\boldsymbol{k})\left\{\frac{1}{\Omega(k)+\Omega_B} + \frac{1}{\Omega(k)-\Omega_B}\right\}\right]d^3k, \tag{5}$$

where r represents the distance between two arbitrary points in the probe–sample system, and the electronic excitation energies of the sample and probe tip are denoted as $\hbar\Omega_A$ and $\hbar\Omega_B$, respectively. From the above, it follows that the effective interactions are produced by mediation of virtual exciton-polaritons. In addition, it should be noted that the non-resonant terms are readily accounted in the effective interactions, which are neglected in the rotating wave approximation.

3. Effective probe–sample interaction based on effective mass approximation

Virtual exciton-polariton exchange between a probe and

sample was shown to be an source of the effective probe–sample interaction in the preceding section. From the dispersion relation of the exciton-polaritons, it follows that they are massive, with an effective mass which is usually determined from $\hbar k|d\Omega(k)/dk|^{-1}_{k=0}$. Here we should note that the electrons in a nanometric probe or sample are locally confined and that electron wavenumbers are also localized around $k_0 = \pi/a_\alpha$, depending on the size of the probe-sample system a_α. Then the wavenumber or momentum of the exciton-polariton virtually exchanged between the probe and sample is expected to close to the wavenumber k_0. Thus we define the effective mass of the exciton-polaritons at $k = k_0$ instead of $k = 0$ and is expressed as

$$\frac{1}{m_\alpha} = \left[\frac{1}{\hbar k}\left|\frac{d\Omega(k)}{dk}\right|\right]_{k=k_0} \approx \frac{a_\alpha c}{\pi\hbar}. \tag{6}$$

where $\Omega(k_0)$ is approximated as ck_0. This is because the eigenfrequency $\Omega(k)$ is close to the frequency of free photons at $k = k_0$, when the size of the probe–sample system corresponds to a several tens of nanometres. Using the above approximation, we can write the eigenfrequency of the exciton-polaritons as follows:

$$\begin{aligned}\Omega(k) &\equiv \Omega(k, a_\alpha) = \frac{\hbar k^2}{2m_\alpha} + \frac{\Omega}{2} \\ &= \frac{a_\alpha c}{2\pi}\left(k^2 + \frac{\pi^2}{a_\alpha^2}\right).\end{aligned} \tag{7}$$

By substituting Eq. (7) into Eq. (5), and using the following relation,

$$K'_\alpha(\boldsymbol{k})K'^{*}_\beta(\boldsymbol{k}) = \sum_{i,j=1}^{3}\mu_{\alpha i}\mu_{\beta j}\left(\delta_{ij} + \frac{1}{k^2}\nabla_i\nabla_j\right)f^2(k, a_\alpha)e^{i\boldsymbol{k}\cdot(\boldsymbol{r}_\alpha - \boldsymbol{r}_\beta)}, \tag{8}$$

with $f(k) \equiv f(k, a_\alpha)$, the effective interaction potential can be obtained as

$$\begin{aligned}V(r) = &\sum_{i,j=1}^{3}\mu_{Ai}\mu_{Bj} \\ &\times \sum_{\substack{\alpha,\beta=A \\ \alpha\neq\beta}}^{B}\left\{w^{(+)}_{\alpha\beta}\left(\delta_{ij} - \frac{1}{\Delta^{(+)2}_{\alpha\beta}}\nabla_i\nabla_j\right)\frac{e^{-\Delta^{(+)}_{\alpha\beta}r}}{r}\right. \\ &+ w^{(-)}_{\alpha\beta}\left(\delta_{ij} - \frac{1}{\Delta^{(-)2}_{\alpha\beta}}\nabla_i\nabla_j\right)\frac{e^{-\Delta^{(-)}_{\alpha\beta}r}}{r} \\ &+ w^{(1)}_{\alpha\beta}\left(\delta_{ij} - \frac{1}{\Delta^{(1)2}_{\alpha\beta}}\nabla_i\nabla_j\right)\frac{e^{-\Delta^{(1)}_{\alpha\beta}r}}{r} \\ &\left.+ w^{(2)}_{\alpha\beta}\left(\delta_{ij} - \frac{1}{\Delta^{(2)2}_{\alpha\beta}}\nabla_i\nabla_j\right)\frac{e^{-\Delta^{(2)}_{\alpha\beta}r}}{r}\right\},\end{aligned} \tag{9}$$

where $w^{(\pm,1,2)}_{\alpha\beta}$ is the weight coefficients. Note that each term in Eq. (9) has a different decay constant and/or frequency as follows:

$$\Delta^{(\pm)}_{\alpha\beta} = \frac{\pi}{a_\beta}\sqrt{1 \pm \frac{2a_\beta\Omega_\alpha}{\pi c}}, \tag{10}$$

$$\Delta^{(1)}_{\alpha\beta} = \Delta^{(2)*}_{\alpha\beta} = 2^{-3/4}(-1+i)\frac{\pi}{a_\beta}. \tag{11}$$

The first two terms in Eq. (9) represent the Yukawa functions with different decay constants, including their gradients. They originate from the direct coupling of the exciton-polariton to the probe–sample system and the decay constants show the dependence on size of the probe–sample system. This is one of the characteristics of optical near fields. A similar result has been reported by Hori (1993), who assumes the size dependence from the uncertainty principle. The last two terms in Eq. (9) show far-field propagating, or oscillating behaviour with a frequency independent of the probe (sample) resonance frequency. In the following calculations we restrict ourselves to the first two terms, as we are mainly interested in the direct coupling. In particular, when $2a_\beta\Omega_\alpha/\pi c \ll 1$ in Eq. (10), the effective interaction given in Eq. (9) is much simplified and becomes the sum of Yukawa functions with two different decay lengths:

$$\begin{aligned}V(r) \approx &\sum_{i,j=1}^{3}\frac{8\mu_{Ai}\mu_{Bj}}{9} \\ &\times\left\{\left(\frac{\pi^2}{a_A^2}\delta_{ij} - \nabla_i\nabla_j\right)\frac{e^{-\pi r/a_A}}{r}\right. \\ &\left.+\left(\frac{\pi^2}{a_B^2}\delta_{ij} - \nabla_i\nabla_j\right)\frac{e^{-\pi r/a_B}}{r}\right\}\end{aligned} \tag{12}$$

The detailed discussion on the behaviour of this effective interaction is quite involved and will be published elsewhere (Kobayashi *et al.*, 2001). For the present discussion, we note that the effective probe–sample interaction can be either mechanically attractive or repulsive, depending on the internal energy levels of both the probe–sample and macroscopic systems and the detuning of light from their energy levels. It also depends on the distance between the probe and sample. This feature will be particularly vital for atom manipulation and nano-fabrication as well as for the understanding of the fundamental properties of optical near fields.

4. Signal intensity detected by an optical near-field probe

On the basis of the preceding sections, let us discuss the fundamental properties of the signal intensity in a typical nanometric probe–sample system. As shown in Fig. 1, we consider two cases: (a) a probe sphere with a radius of a_1 is scanned above a sample sphere with a radius of a_s on a plane of constant height, where the height of h is the

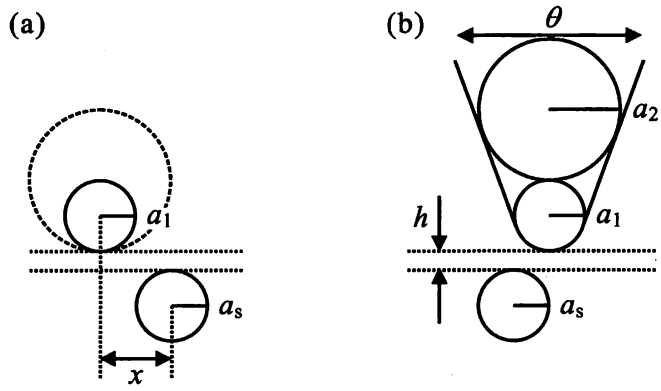

Fig. 1. Illustration of models for an optical near-field probe and sample system: (a) a spherical probe with a radius of a_1, and (b) a tapered probe consisting of two spheres with radii of a_1 and a_2.

shortest distance between the top of the sample sphere and the bottom of the probe sphere. (b) A tapered probe with angle θ, modelled by two spheres with radii of a_1 and a_2, is scanned above the sample sphere as same in the first case. From Eq. (12), the Yukawa potential as the effective interaction is generated between two arbitrary points (r_i, r_s) in the probe and sample spheres. Thus, the pickup signal I obtained from the entire probe sphere can be written as

$$I(r_{sp}) \equiv \sum_{i=1}^{2}\left|\int\int \nabla_{r_i} V(|r_i - r_s|)dr_s dr_i\right|^2$$

$$\propto \sum_{i=1}^{2}\left[a_i^3\left\{\frac{a_s}{a_i}\cosh\left(\frac{\pi a_s}{a_i}\right) - \frac{1}{\pi}\sinh\left(\frac{\pi a_s}{a_i}\right)\right\}\right.$$

$$\left.\times\left(\frac{1}{r_{sp}} + \frac{a_i}{\pi r_{sp}^2}\right)e^{-\pi r_{sp}/a_i}\right]^2, \qquad (13)$$

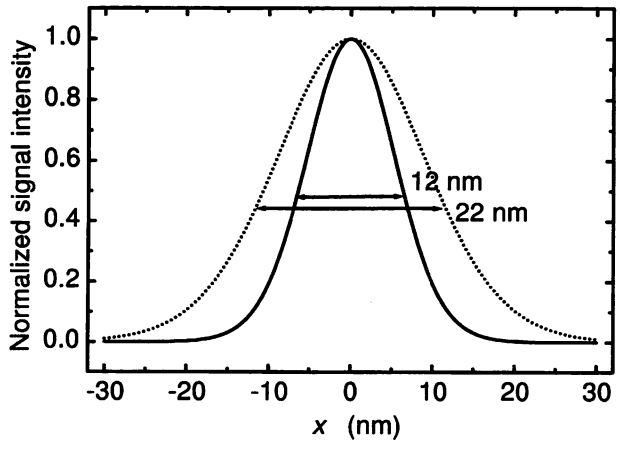

Fig. 2. Spatial distribution of signal intensity scanned with probe-tip sizes of $a_1 = 10$ nm (solid line) and 20 nm (dotted line), where the probe-tip height and sample size are fixed at $h = 1$ nm and $a_s = 10$ nm, respectively. Vertical axis is normalized by the signal intensity at the centre of the sample sphere ($x = 0$).

where r_{sp} denotes the distance between the centre of the probe and sample. From Eq. (13), it follows that the signal intensity decays in a similar manner to the Yukawa function. Using this expression, we present the results for the case (a) in Figs 2 and 3 and those for the case (b) in Figs 4 and 5.

Figure 2 shows the signal intensity from the sample with $a_s = 10$ nm detected by the probe with $a_1 = 10$ nm or 20 nm which is scanned in lateral direction with constant height $h = 1$ nm. It follows that each full width at half maximum determining the lateral resolution of the system is nearly equal to the size of each probe tip. In Fig. 3, we present the signal intensity normalized by the volume of both probe and sample spheres when the probe radius is varied with the radius of the sample sphere fixed at $a_s = 10$ nm or 20 nm. It shows that the signal remains the highest when the probe size is comparable to the sample size. This is called the size–resonance effect. These results are consistent with numerical ones obtained from the different methods (Jang & Jhe, 1996; Saiki & Ohtsu, 1998).

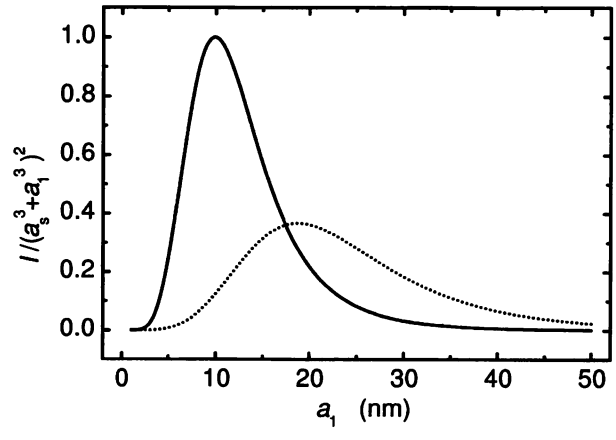

Fig. 3. Dependence of the signal intensity on the probe-tip size. The solid and dotted curves represent the results for the sample sizes $a_s = 10$ nm and 20 nm, respectively.

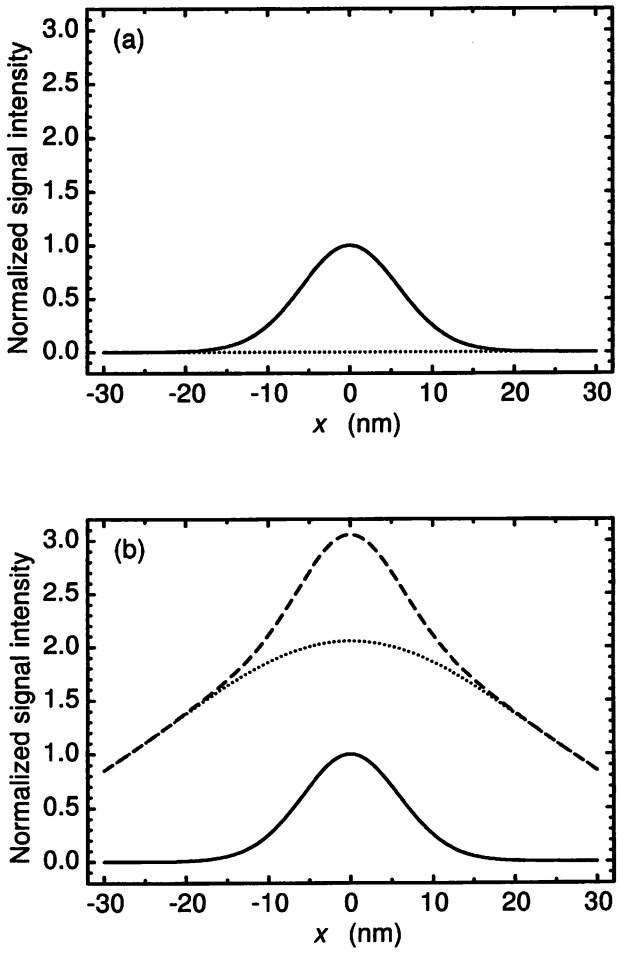

Fig. 4. Spatial distribution of signal intensity detected by a tapered probe with the taper angles (a) $\theta = 20°$ and (b) 80°. The sizes of probe tip and sample are set as $a_1 = 10$ nm and $a_s = 10$ nm, the probe height being $h = 5$ nm. The solid, dotted and dashed curves represent the contributions from the probe tip, the taper, and their sum, respectively. The vertical axis is normalized by the maximum value of the signal intensity detected by the probe tip.

In Fig. 4, we plot the signal intensity as a function of the probe position, varying the taper angle θ. When the taper angle is as small as $\theta = 20°$, as shown in Fig. 4(a), the signal intensity originating from the tapered part is negligibly small and the net signal is determined by the apex contribution. This means that the lateral resolution is dominated by the apex part. By contrast, as the taper angle becomes as large as $\theta = 80°$, the taper contribution to the signal intensity becomes significantly large. This broadens the width of the net signal (see Fig. 4(b)), leading to the degradation of the contrast, that is, the ratio of the signal intensity from the apex part to that from the tapered part. Figure 5 shows the dependence of this contrast on θ. It illustrates how the approach distance of the probe affects the contrast of the image. For approach distance as small as $h = 1$ nm, interaction between the apex and sample

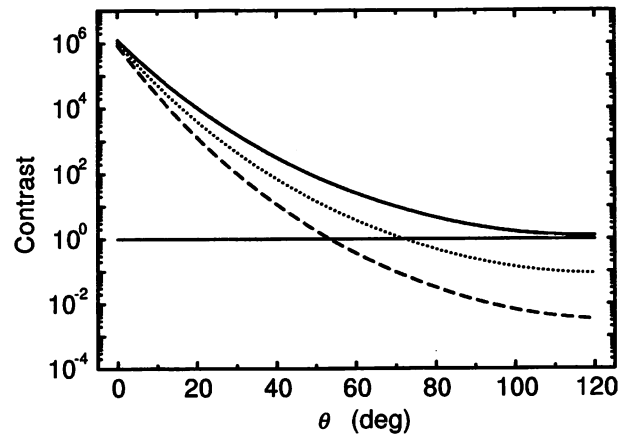

Fig. 5. Variation of the ratio of signal intensity from the apex part to that from the tapered part as a function of taper angle, θ. The solid, dotted and dashed curves represent the results for the different heights, $h = 1$, 5 and 10 nm, respectively. The region above the horizontal line, the ratio 1, indicates that the contrast can be determined from the probe tip, not the taper part. By contrast, the tapered part governs the contrast in the region below the ratio 1.

spheres is stronger than that between the taper and sample spheres. Thus, the apex sphere is the main factor determining the contrast as well as lateral resolution. As the approach distance becomes as large as $h = 10$ nm, interaction between apex and the sample reduces in contrast with that between taper and the sample. This can be understood by noticing the fact that interaction range of a larger sphere is longer than that of a smaller sphere (see Eq. (12)). Therefore, in such a case, the tapered part gradually determines the contrast with increasing taper angle. At taper angle as large as 60°, the contrast degrades again. It is worth noting here that we could improve the contrast, and accordingly, lateral resolution of the system by screening the tapered part by some kind of metallic aperture, which would reduce the interaction between the taper and sample.

At the end of the section, we comment on the polarization dependence of the signal intensity. It follows from Eq. (12) that the polarization effect manifests itself near the edge of a sample. As an example, we show the signal intensity from a circular aperture in Fig. 6, where the incident polarization relative to the aperture is fixed in the x-direction while all polarization components of the probe are detected. The signal intensity is enhanced near both sides of the aperture that are perpendicular to the incident polarization direction. In Fig. 6(b) the dependence of the signal intensity on the approach distance of the probe is plotted. The enhancement of the signal at the aperture edges disappears, as the probe is located at a higher position. Such polarization dependence of the signal intensity has been explained theoretically and numerically by using macroscopic electromagnetic theory.

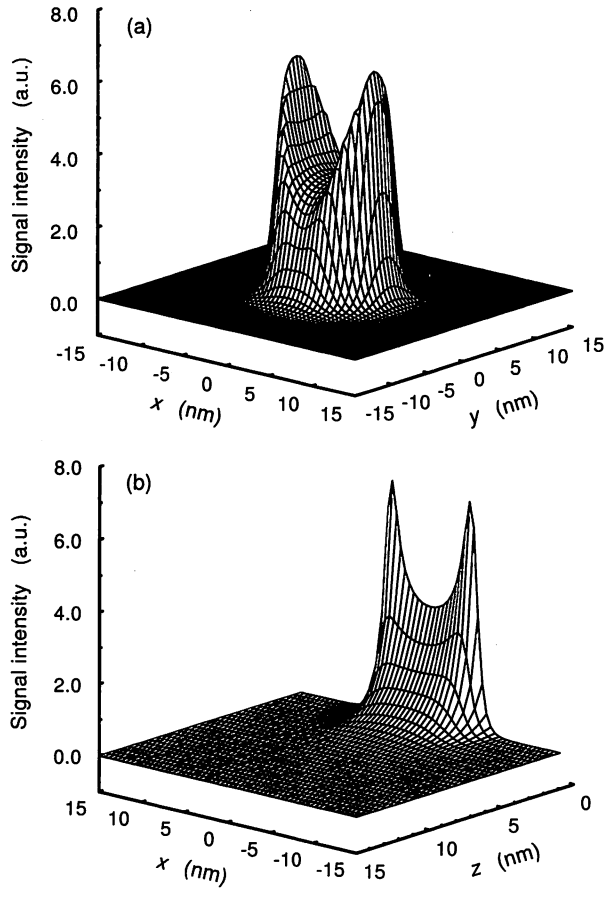

Fig. 6. Spatial distribution of signal intensity on the (a) xy-plane and (b) xz-plane. The circular aperture with a radius of $a_s = 10$ nm is chosen as a sample, and the polarization of incident light is parallel to the x-axis. The probe height is fixed at $h = 1$ nm for the lateral scan.

Exact solutions of optical near fields have been obtained for an infinitely thin conducting plane with a small aperture by Leviatan (1986) and for a relatively thick one by Roberts (1993). Novotny *et al.* (1994) have shown similar results numerically by means of multiple multipole method. Our results are qualitatively consistent with these previous studies.

5. Conclusions

Effective interactions between a nanometric probe and a sample have been discussed on the basis of a quantum theoretical formulation. After renormalizing effects of the bath system, the probe–sample system can be treated to be isolated from the other systems and the effective probe–sample interactions can be expressed in terms of the sum of Yukawa functions with different decay lengths. The Yukawa function indicates that the optical near fields are localized around the probe–sample system and have decay constants inversely proportional to the size of the probe or sample.

In order to test the applicability of our formulation to conventional optical near-field problems in a unified way, as well as to quantum theoretical issues, we analysed the fundamental properties of the detected signals in two idealized probe–sample systems. For such systems, first, the so-called size–resonance effect is predicted, which was previously obtained by numerical calculations based on the diffraction theory. Second, the polarization dependence that emphasizes the signal intensity at the aperture edges is shown numerically. These are consistent with the previous studies. Finally the taper angle dependence of the signal intensity, contrast, and thus, the lateral resolution of the system, are numerically analysed for situations where the results are in reasonable agreement with experimental observations. Present results establish that our approach is applicable to the diverse issues of optical near-field problems with a low computational cost. Moreover, analysis improves the physical understanding of near-field optical phenomena as well as the experimental situations. At the same time, it should be noted that the present formulation is quite valuable for design and analysis of atom manipulation and nano-fabrication systems, where interactions between a probe tip and neutral atoms would play important roles.

References

Berntsen, S., Bozhevolnaya, E. & Bozhevolnyi, S. (1993) Macroscopic self-consistent model for external-reflection near-field microscopy. *J. Opt. Soc. Am. A*, **10**, 878–885.

Craig, D.P. & Thirunamachandran, T. (1998) *Molecular Quantum Electrodynamics*. Dover, New York.

Fulde, P. (1995) Electron Correlations in Molecules and Solids. 3rd edn. *Springer Series in Solid-State Science*. **Vol. 100**. Springer-Verlag, Berlin, pp. 83–100.

Girard, C. & Bouju, X. (1992) Self-consistent study of dynamical and polarization effects in near-field optical microscopy. *J. Opt. Soc. Am. B*, **9**, 298–305.

Girard, C. & Courjon, D. (1990) Model for scanning tunneling optical microscopy: a microscopic self-consistent approach. *Phys. Rev. B*, **42**, 9340–9349.

Haken, H. (1983) *Quantum Field Theory of Solids*. Elsevier, Amsterdam.

Hopfield, J.J. (1958) Theory of the contribution of excitons to the complex dielectric constant of crystals. *Phys. Rev.* **112**, 1555–1567.

Hori, H. (1993) Quantum optical picture of photon STM and proposal of single atom manipulation. *Near Field Optics* (ed. by D. W. Pohl and D. Courjon), pp. 105–114. Kluwer, Dordrecht.

Huttner, B. & Barnett, S.M. (1992) Quantization of the electromagnetic field in dielectrics. *Phys. Rev. A*, **46**, 4306–4322.

Jang, K. & Jhe, W. (1996) Nonglobal model for a near-field scanning optical microscope using diffraction of the optical near field. *Opt. Lett.* **21**, 236–238.

Keller, O., Xiao, M. & Bozhevolnyi, S. (1993) Configurational resonances in optical near-field microscopy: a rigorous point-dipole approach. *Surf. Sci.* **280**, 217–230.

Knoester, J. & Mukamel, S. (1989) Nonlinear optics using the multipolar Hamiltonian: the Bloch–Maxwell equations and local fields. *Phys. Rev. A*, **39**, 1899–1914.

Kobayashi, K. & Ohtsu, M. (1999a) Quantum theoretical approach to a near-field optical system. *J. Microsc.* **194**, 249–254.

Kobayashi, K. & Ohtsu, M. (1999b) Quantum theory and virtual photon model of near-field optics. *Proc. SPIE*, **3791**, 10–20.

Kobayashi, K., Sangu, S., Ito, H. & Ohtsu, M. (2000) Effective probe–sample interaction: toward atom deflection and manipulation. *Near-Field Optics: Principles and Applications* (ed. by X. Zhu and M. Ohtsu), pp. 82–88. World Scientific, Singapore.

Kobayashi, K., Sangu, S., Ito, H. & Ohtsu, M. (2001) Near-field optical potential for a neutral atom. *Phys. Rev. A*, **63**, in press.

Kobayashi, K. & Watanuki, O. (1996) Characteristics of photon scanning tunneling microscope read-out. *J. Vac. Sci. Technol. B*, **14**, 804–808.

Kobayashi, K. & Watanuki, O. (1997) Polarization-dependent contrast in near-field optical microscopy. *J. Vac. Sci. Technol. B*, **15**, 1966–1970.

Leviatan, Y. (1986) Study of near-zone fields of a small aperture. *J. Appl. Phys.* **60**, 1577–1583.

Novotny, L., Pohl, D.W. & Regli, P. (1994) Light propagation through nanometer-sized structures: the two-dimensional-aperture scanning near-field optical microscope. *J. Opt. Soc. Am. A*, **11**, 1768–1779.

Ohtsu, M., Kobayashi, K., Ito, H. & Lee, G.H. (2000) Nanofabrication/atom-manipulation by optical near field and relevant quantum optical theory. *Proc. IEEE*, **88**, 1499-1519.

Roberts, A. (1991) Small-hole coupling of radiation into a near-field probe. *J. Appl. Phys.* **70**, 4045–4049.

Roberts, A. (1993) Theoretical considerations associated with near-field scanning by subwavelength apertures. *Near Field Optics* (ed. by D. W. Pohl and D. Courjon), pp. 221–228. Kluwer. Dordrecht.

Saiki, T. & Ohtsu, M. (1998) *Near-Field Nano/Atom Optics and Technology* (ed. by M. Ohtsu), pp. 15–29. Springer-Verlag, Tokyo.

Taubenblatt, M.A. & Tran, T.K. (1993) Calculation of light scattering from particles and structures on a surface by the coupled-dipole method. *J. Opt. Soc. Am. A*, **10**, 912–919.

Yamamoto, Y., Kourogi, M., Ohtsu, M., Polonski, V. & Lee, G.H. (2000) Fabrication of nanometric zinc pattern with photodissociated gas-phase diethylzinc by optical near field. *Appl. Phys. Lett.* **76**, 2173–2175.

ELSEVIER

Thin Solid Films 386 (2001) 117–120

thin solid films

www.elsevier.com/locate/tsf

Blue shift in room temperature photoluminescence from photo-chemical vapor deposited ZnO films

G.H. Lee[a,*], Y. Yamamoto[b], M. Kourogi[a,b], M. Ohtsu[a,b]

[a] *Japan Science and Technology Corporation, 687-1 Tsuruma, Machida, Tokyo 194-0004, Japan*
[b] *Interdisciplinary Graduate School and Engineering, Tokyo Institute of Technology 4259 Nagatsuda, Midori-ku, Yokohama, Kanagawa 226-8508, Japan*

Received 18 August 2000; received in revised form 3 December 2000; accepted 15 December 2000

Abstract

Highly transparent ZnO films were deposited on (001) α-Al_2O_3 at substrate temperature in the range of room temperature to 300°C by photo-chemical vapor deposition. This enabled selective deposition of ZnO films on the selected substrate area irradiated by the light source. With the descending substrate temperature as low as 100°C, band gap widening of the films has been observed, which resulted in the shift of room temperature ultraviolet photoluminescence of ZnO from 380 nm to the shorter wavelength of 360 nm. It implies that in situ patterning of ZnO with different wavelength emission characteristics is possible on the same substrate by controlling the deposition temperature.

Keywords: Zinc oxide; Chemical vapor deposition; Luminescence; Optical properties

1. Introduction

ZnO is a very promising material for optical devices due to its non-linear optical property and room temperature ultraviolet emission. Its band gap of 3.37 eV at room temperature and the exciton binding energy of 60 meV, which is larger than the room temperature energy of 24 meV, give rise to the excitonic stimulated ultraviolet (UV) emission even at room temperature [1–3].

In n-type semiconductors, an important phenomenon known as the Burstein–Moss effect has been observed [4,5], which is that the Fermi level moves into the conduction band due to the filling of the conduction band by electrons. ZnO is also an n-type semiconductor in which the donor is associated with oxygen vacancies and interstitial zinc atoms. Therefore, by adjusting carrier concentration with donor, its band gap energy can be controlled [6–10], and of which must influence on the luminescence spectra. So far, there has been no report of the investigation of the Burstein–Moss effect on the room temperature photoluminescence (PL) for ZnO. In the room temperature PL of ZnO, it should be noted that the free exciton emission is dominant [1–3]. But in case of the Burstein–Moss effect, the band–band transition is expected to be enhanced, and so shift toward higher energy. However, room temperature UV emission with wavelength shorter than that from free exciton is not yet reported.

Photo-enhanced chemical vapor deposition (PE-CVD) is a versatile technique which allows in-situ patterning and offers the possibility for the lateral integration (i.e. side by side) of different structures, related to different sequence of layers, materials, thickness and dopants, without any lithography or etching steps [11–13]. Besides, PE-CVD has an inherent potential to change the lateral pattern during growth, thus it

* Corresponding author. Department of Advanced Materials Engineering, Dong-Eui University, Gaya-Dong 24, Pusanjin-Ku, Pusan, South Korea, 614-714. Tel.: +81-42-788-6030; fax: +81-42-788-6031.
E-mail address: ghl@ohtsu.jst.go.jp (G.H. Lee).

0040-6090/01/$ - see front matter
PII: S0040-6090(01)00764-7

is expected to become a key technology in the optoelectronic fabrication. Recently, in situ patterning of nanometric Zn with the size smaller than 100 nm has been accomplished by PE-CVD of diethylzinc gas using optical near field with controlled size and position [14,15]. In addition, it was demonstrated that this method can be applied to the in situ fabrication of ZnO nano-dot [16]. The observation of room temperature emission of ZnO grown by PE-CVD would be also interesting in the point of the applications such as in-situ patterning of nanometric UV luminescent elements for optoelctronic devices.

In this paper, we report not only the first observation of the room temperature UV emission from ZnO deposited by PE-CVD, but also its control by regulating the substrate temperature, which promises in situ fabrication of ZnO patterns with different emission spectra.

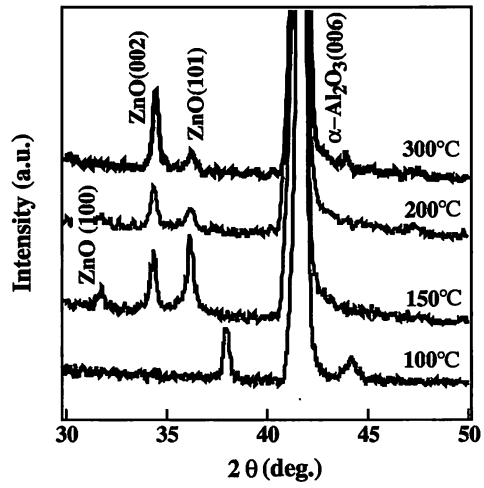

Fig. 1. The XRD spectra of ZnO thin films grown at different substrate temperatures between 100 and 300°C.

2. Experimental details

ZnO thin films were grown on (001) α-Al_2O_3 substrates. PE-CVD is employed as a very useful method for the in-situ patterning. In our experiments, the photo-irradiation effect on the deposition rate was clearly observed for all substrates. Diethyzinc [DEZ/$Zn(C_2H_5)_2$] and oxygen were used as the sources of Zn and O, respectively. The second harmonic light ($\lambda = 244$ nm) of an Ar laser, which was generated by transmitting the Ar laser beam through a built-up cavity with a BBO crystal, was used as the light source for the photo-decomposition of DEZ. The reaction chamber was initially evacuated to pressures in the low 10^{-5} or 10^{-7} torr range, then filled with the reactant gases with the ratio of DEZ/O of 1:10 at a working pressure of 10 mtorr. The chamber pressure was maintained constantly at 10 mtorr during the film growth. The experiments were carried out at various substrate temperatures from room temperature to 300°C. The power and the spot size of the light beam were 10 mW and 600 μm, respectively. The crystallinity and the stoichiometry were characterized by X-ray photoelectron spectroscopy (XPS) using Al Kα X-ray and X-ray diffraction (XRD) using Cu Kα radiation, while the optical transmissions were measured by a double beam monochromator in an ambient atmosphere from $\lambda = 300$ nm to 1000 nm, from which the optical band gaps of the films were estimated. The PL spectra were measured using a continuous wave He–Cd laser ($\lambda =$ 325 nm).

3. Results and discussion

Fig. 1 shows XRD patterns of ZnO films deposited at substrate temperatures between 100 and 300°C. The thicknesses of the films were 140, 150, 170 and 140 nm for each temperature, respectively. Films were deposited only on the substrate area irradiated by UV light. No XRD refection lines were observed for the film grown at room temperature, indicating its amorphous nature. Crystalline diffraction patterns were recorded from the films prepared at the substrate temperature of 100°C. But the diffraction peaks observed for the film grown at 100°C were located between peaks of ZnO with hexagonal structure and those of Zn with hexagonal closed packed structure, suggesting the imperfect oxidation of Zn and presence of excess Zn in ZnO crystal. At substrate temperatures above 150°C, however, *c*-axis oriented films exhibiting the (002) XRD lines were obtained. With increasing the substrate temperature, X-ray peaks from (002) planes evolved strongly while other peaks such as the (101) peak diminished in intensity. The peak from (002) planes is located at $2\theta = 34.46°$, which agrees well with the one from the bulk ZnO.

The stoichiometry of the films was confirmed from the XPS spectrum. For the films deposited at substrate temperatures higher than 200°C, the atomic ratio of Zn/O was 1.00:1.03 within the accuracy of a few percent, whereas it increased to 1.32:1.00 for the film grown at 100°C, which confirmed the excess Zn in ZnO crystal giving higher free electron carrier concentration with decreasing the temperatures.

Fig. 2 shows the transmittance spectra of the films. For the substrate temperatures over 150°C, transmittance of grown films fell off steeply at $\lambda = 380$ nm, which is characteristic of high quality ZnO films [17–19]. On the other hand, in case of 100°C deposition, the absorption edge of the film was approximately 360 nm. For the films deposited at temperatures above 100°C, transmittance in the visible region was over 80% and films were highly transparent. From the obtained transmittance spectra, by plotting $(\alpha h\nu)^2$ vs. $h\nu$, in which α is the absorption coefficient and $h\nu$ is the photon

energy, and extrapolating the straight line portion of this plot to the energy axis, the optical band gaps ranging from 3.26 to 3.44 eV were estimated (the change of the optical bandgap as a function of substrate temperature shown in the inset of Fig. 2). For stoichiometric ZnO films, the optical band gap is known to be 3.24 eV [18]. It is noteworthy that with the lower deposition temperatures, the band gap widens while Zn content in the crystal also increases. This band gap widening can be thus be interpreted as a Burstein–Moss effect which is supported by the observed XPS and XRD data.

Fig. 3 shows the PL spectra of ZnO films measured at room temperature. For the films deposited at > 200°C, the position of the emission peak is close to the reported energy of 3.26 eV ($\lambda = 380$ nm) for the free exciton in high quality ZnO thin films [2,20,21], and thus the emission is attributed to free excitons. The FWHM of PL spectra at room temperature is approximately 120 meV, which is comparable with the 117 meV of ZnO film grown (001) α-Al_2O_3 substrate by molecular beam epitaxy [20]. With decreasing the temperature, the position of the peak of the PL spectrum shifts to higher energy. Even for the film grown at a temperature as low as 100°C, an ultraviolet room temperature PL was observed. Surprisingly, the peak position shifted to a shorter wavelength, which correlates well with the shift of the absorption edge up to 180 meV. The PL intensity could be observed by naked eyes. This emission is most likely to be due to the band–band transition of free electrons rather than by free exciton. Thus, significantly shorter wavelength emission was successfully achieved by lowering the deposition temperature.

The stability of the PL of these films has been examined. The intensity, position and full width at half maximum (FWHM) of the PL peaks were the same as the initial values even after 9 months aging in the laboratory. This implies that ZnO is very stable in the air due to its oxide.

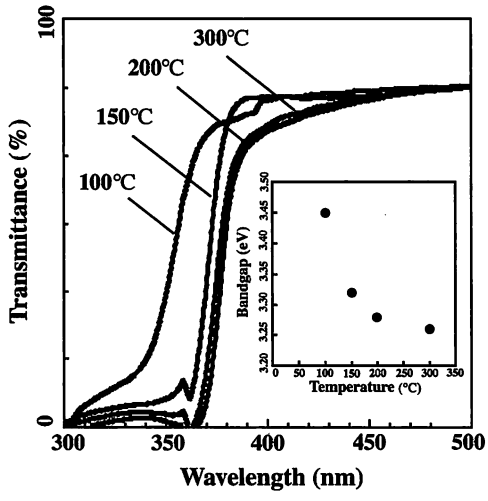

Fig. 2. Optical transmittance spectra of ZnO thin films deposited at different substrate temperatures. Inset: the change of the optical band gap determined from the obtained transmittance spectra.

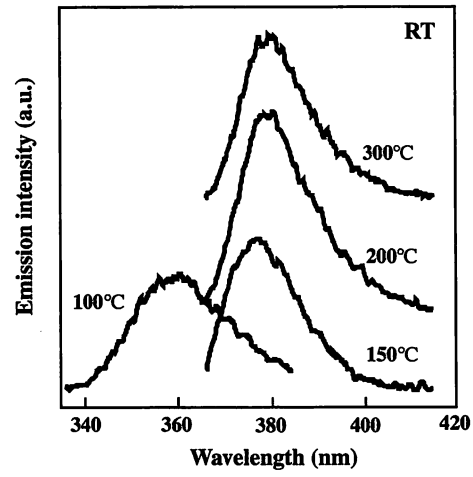

Fig. 3. Room temperature PL spectra of ZnO thin films for various substrate temperatures.

On the other hand, it is known that the Burstein–Moss effect in ZnO thin film would not disappear until the film was annealed at a temperature > 737 K by oxygen chemisorption [10,22]. Thus this suggests that blue shift in room temperature PL properties of ZnO films observed in this experiment can be observed at least till the temperature of 737 K.

4. Conclusions

Highly transparent ZnO films with the optical band gaps in the range of 3.26 ($\lambda = 380$ nm) to 3.44 eV ($\lambda = 360$ nm) were deposited by PE-CVD by controlling only the deposition temperature. All the films grown above 100°C exhibited room temperature visible photoluminescence in accordance with the band gaps. Furthermore, ZnO films were deposited selectively on laser beam irradiated substrate areas. This allows in-situ patterning of light emission elements with different wavelengths on the same substrate only by changing the substrate temperature. Further experiments are currently in progress on the band gap widening with respect to the various conditions of deposition.

Acknowledgements

We would like to thank Dr K. Matsuda of Kanagawa Academy of Science and Technology for PL measurement and useful discussions.

References

[1] Z.K. Tang, G.K.L. Wong, P. Yu, M. Kawasaki, A. Ohtomo, H. Koinuma, Y. Segawa, Appl. Phys. Lett. 72 (1998) 3270.
[2] D.M. Bagnall, Y.F. Chen, Z. Zhu, T. Yao, M.Y. Shen, T. Goto, Appl. Phys. Lett. 73 (1998) 1038.

[3] S. Cho, J. Ma, Y. Kim, Y. Sun, G.K. Wong, J.B. Ketterson, Appl. Phys. Lett. 75 (1999) 2761.
[4] M.K. Hudait, P. Modak, S.B. Krupamdai, Mater. Sci. Eng. B 56 (1999) 1.
[5] N.Y. Lee, K.J. Lee, C. Lee, J.E. Kim, H.Y. Park, D.H. Kwak, H.C. Lee, H. Lim, J. Appl. Phys. 78 (1995) 3367.
[6] D.H. Zhang, R.W. Gao, H.L. Ma, Thin Solid Films 295 (1997) 83.
[7] A.P. Roth, D.F. Williams, J. Appl. Phys. 52 (1981) 6685.
[8] A.P. Roth, J.B. Webb, D.F. Williams, Phys. Rev. B 25 (1982) 7836.
[9] B.E. Sernelius, K.F. Berggren, Z.C. Jin, I. Hamberg, C.G. Granqvist, Phys. Rev. B 37 (1988) 10244.
[10] D.H. Zhang, D.E. Brodie, Thin Solid Films 213 (1992) 109.
[11] E. Maayan, O. Kreinin, G. Bahir, J. Salzman, A. Eyal, R. Beserman, J. Cryst. Growth 135 (1994) 23.
[12] S.M. Bedair, J.K. Whisnant, N.H. Karam, D. Griffis, N.A. El-Masry, H.H. Stadelmaier, J. Cryst. Growth 77 (1986) 229.
[13] Y. Aoyagi, M. Kanazawa, A. Doi, S. Iwai, S. Namba, J. Appl. Phys. 60 (1986) 3131.
[14] Y. Yamamoto, M. Kourogi, M. Ohtsu, V. Polonski, G.H. Lee, Appl. Phys. Lett. 76 (2000) 2173.
[15] V. Polonski, Y. Yamamoto, M. Kourogi, M. Ohtsu, J. Microscopy 194 (1999) 545.
[16] G.H. Lee, Y. Yamamoto, M. Kourogi, M. Ohtsu, SPIE's 44th annual meeting, Denver, U.S.A., July 1999, Proceedings of SPIE 3791 (1999) 132.
[17] V. Craciun, J. Elders, J.G.E. Gardeniers, W. Boyd, Appl. Phys. Lett. 65 (1994) 2963.
[18] D.H. Zhang, D.E. Brodie, Thin Solid Films 298 (1994) 95.
[19] W.W. Wenas, A. Yamada, K. Takahashi, M. Yoshino, M. Konagai, J. Appl. Phys. 70 (1991) 7113.
[20] Y. Chen, D.M. Bagnall, H.J. Ko, K.T. Park, K. Hiraga, Z. Zhu, T. Yao, J. Appl. Phys. 84 (1998) 3912.
[21] D.M. Bagnall, Y. Chen, M.Y. Shen, Z. Zhu, T. Goto, T. Yao, J. Cryst. Growth 184/185 (1998) 605.
[22] T. Minami, H. Nanto, S. Shooji, T. Takata, Thin Solid Films 111 (1984) 167.

Jpn. J. Appl. Phys. Vol. 40 (2001) pp. L286–L288
Part 2, No. 3B, 15 March 2001

Near-Field Photocurrent Measurements of Si p-n Junction under the Reverse-Bias Condition

Hiroaki FUKUDA[1,2,*] and Motoichi OHTSU[1]

[1]*Interdisciplinary Graduate School of Science and Engineering, Tokyo Institute of Technology, 4259 Nagatsuda, Midori-ku, Yokohama 226-8502, Japan*
[2]*Research and Development Center, RICOH Co., Ltd., 16-1 Shineicho, Tsuzuki-ku, Yokohama 224-0035, Japan*

(Received August 25, 2000; accepted for publication February 2, 2001)

We measured the near-field photocurrent of the p-n junction on a Si substrate under the reverse-bias condition in order to estimate the dopant concentration of the p-n junction. The full-width at half maximum (FWHM) of the cross-sectional profile of the near-field photocurrent signal varied on changing the applied reverse-biased voltage according to the resulting change in the thickness of the depletion region. From the measured reverse-bias dependence of the FWHM of the cross-sectional profile, the local dopant concentration of the Si substrate was estimated as $3.5 \pm 0.4 \times 10^{16}\,\mathrm{cm}^{-3}$. This result shows good agreement with the value of dopant concentration ($3.1 \times 10^{16}\,\mathrm{cm}^{-3}$) evaluated from the device fabrication conditions.

KEYWORDS: near-field optical microscope, near-field photocurrent, p-n junction, Si semiconductor device, fiber probe, dopant concentration

Recently, the nondestructive and direct characterization of the micro-structure of semiconductor devices in actual operation has emerged as an important approach for understanding and improving the performance of semiconductor devices. Many existing analysis tools are able to yield the measured parameter averaged over a large area. Thus, the local characteristics of the device structure are usually estimated by computer simulation based on the results of the macroscopic electrical characterization of devices. The dopant concentration is an important issue in semiconductor devices because it directly affects the device characteristics. Secondary ion mass spectroscopy (SIMS), which is widely used to measure the dopant profile of semiconductor devices, can damage the sample. We have investigated the local dopant concentration of the p-n junction using near-field techniques.

The near-field optical microscope has been developed to realize subwavelength spatial resolution for imaging nanometric biological specimens, spectroscopy of semiconductor devices, high-density optical storage, atom manipulation, and nanostructure fabrication.[1)] The near-field photocurrent measurements carried out with a near-field optical microscope have revealed useful information on semiconductor p-n junctions.[2–5)]

In this letter, we report our results of near-field photocurrent measurements of the reverse-biased p-n junction on the Si substrate and estimate the local dopant concentration of the p-n junction from such measurements for the first time.

Figure 1(a) shows a schematic of the experimental setup and sample structure. After removing the mold package of the bipolar transistor with a known structure, the passivation layer and local oxidation of the Si layer were etched away by reactive ion etching. The sample was made by a collaboration of one of the authors (H. F.). The surface of the p-n junction on the Si substrate was exposed by wet etching. The electrode configuration for near-field photocurrent measurements of the Si p-n junction under the reverse-bias condition was also depicted in Fig. 1(a). The depth of the p-n junction in the substrate was 0.6 μm. The dopant concentration in the n-type region evaluated from the device fabrication condition was $3.1 \times 10^{16}\,\mathrm{cm}^{-3}$. The shear-force technique[6,7)] was employed to maintain the separation between the fiber probe and the sample surface constant at 20 nm. All measurements were

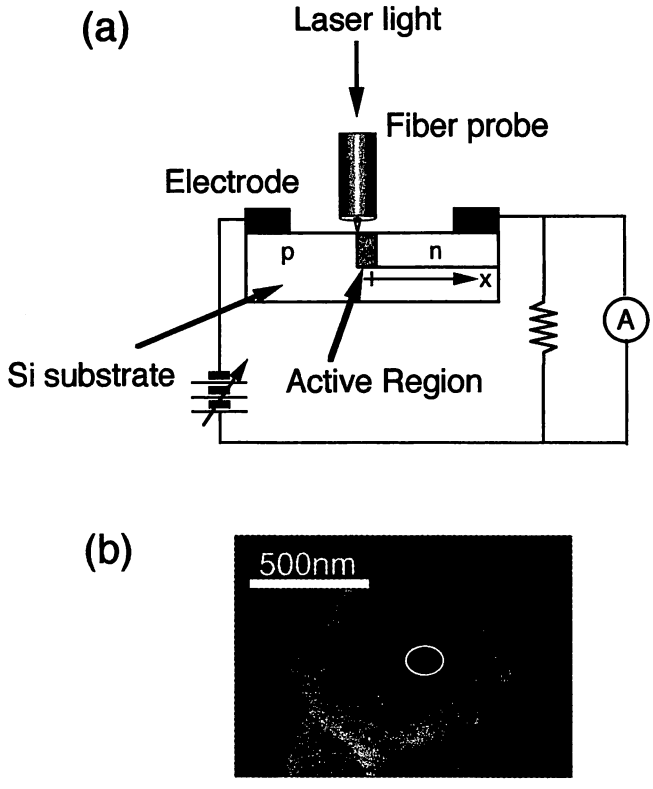

Fig. 1. (a) Schematic of the experimental setup and the cross-sectional sample structure. (b) Scanning electron micrograph of the fiber probe with an aperture diameter of 150 nm. A white circle represents the position of the aperture.

carried out under ambient conditions. For excitation, the light from an Ar^+ laser ($\lambda = 458$ nm) was coupled to the fiber probe. The penetration depth of this light into the Si substrate is estimated to be about 277 nm.[8)] When the optical near-field of the fiber probe tip generates the electron-hole pair in the sample, the respective minority carriers diffuse away over an average diffusion length before the recombination. The induced near-field photocurrent signal is thus proportional to the number of carriers sweeping the p-n junction and that collected at the electrodes. The signal is amplified with a current injection preamplifier, and synchronously detected with a lock-in amplifier as a function of the position of the fiber probe across the surface of the p-n junction.

Figure 1(b) shows the scanning electron micrograph of the

*E-mail address: fukuda@rdc.ricoh.co.jp

fiber probe used for the measurements. The optical fiber with a germanium-dioxide-(GeO_2) doped core was used to fabricate the fiber probe. The core diameter of this fiber was 2 μm and the clad diameter was 125 μm. The fiber probe was fabricated by a two-step etching method.[9] The fiber was etched for 60 min in a buffered hydrogen fluoride (BHF) solution containing NH_4F (40% weight), HF (50% weight) and H_2O with the volume ratio of 1.7 : 1 : 1. Next, the fiber was etched for 40 min in NH_4F, HF and H_2O with the respective volume ratio of 10 : 1 : 1. The temperature of the BHF solution was maintained at 25 ± 0.1°C. The sharpened fiber probe was coated with 300-nm-thick Au. A subwavelength aperture was fabricated by pounding the metal-coated fiber probe on a Si substrate and suqeezing the Au off to the side.[10] The diameter of the fabricated aperture was 150 nm. The efficiency of optical near-field generation was 5.0×10^{-3}, as estimated by collecting the far-field throughput with a 0.4 numerical aperture objective lens.

Figures 2(a)–2(c) show the near-field photocurrent images for the applied reverse-biased voltage of 0 V, 3 V, and 5 V, respectively. The distribution of evanescent modes is determined by the aperture radius a of the fiber probe. The cutoff wave vector of the evanescent mode distribution is $\pi/2a$.[3] If the aperture diameter $2a$ is less than half the wavelength $\lambda/2$, the evanescent modes occupy the region $k_{//} > 2\pi/\lambda$. When the aperture of the probe is close to optically dense material, a part of the evanescent mode is present in the region $k_{//} < n(2\pi/\lambda)$, where n is the refractive index of the material. For the case of a 150 nm aperture and $n = 4.58$ (refractive index of Si at the wavelength $\lambda = 458$ nm), almost all the evanescent modes from the fiber probe are coupled with the propagating ones. The propagating beam spread angle into Si is 20°, which is determined by the aperture diameter. The propagation modes are governed by the bulk absorption characteristics of a substrate material. Therefore, the resolution is limited by the size of the aperture radius, the penetration depth of the semiconductor material and the diffusion length of photoexcited minority carriers. Figure 3 shows the cross-sectional profiles of the near-field photocurrent intensities. The uniformity of the decay length of the near-field photocurrent signals is clearly observed under the various reverse-bias conditions along the length of the p-n active region. The cross-sectional profiles of the near-field photocurrent intensities are averaged over the measurement area. The clear peak of the cross-sectional profiles of the near-field photocurrent signals can be observed by locating the aperture over the depletion region. The full-width at half maximum (FWHM) of the cross-sectional profiles of the near-field photocurrent signal increases with increasing reverse-biased voltage, as shown in Fig. 3. Also shown in Fig. 3 is the slower rise of the near-field photocurrent signals in the p region than in the n region, which reveals the difference in the diffusion lengths for holes and electrons.

The thickness of the depletion region increased with increasing reverse-biased voltage, which widens the observed width of the cross-sectional profile of the near-field photocurrent signal. Because the decay length of the near-field photocurrent signals is constant under the various reverse-bias conditions, the relationship between the FWHM of the cross-sectional profile of the near-field photocurrent $W(V_R)$ and the thickness of the depletion region $D(V_R)$ under the

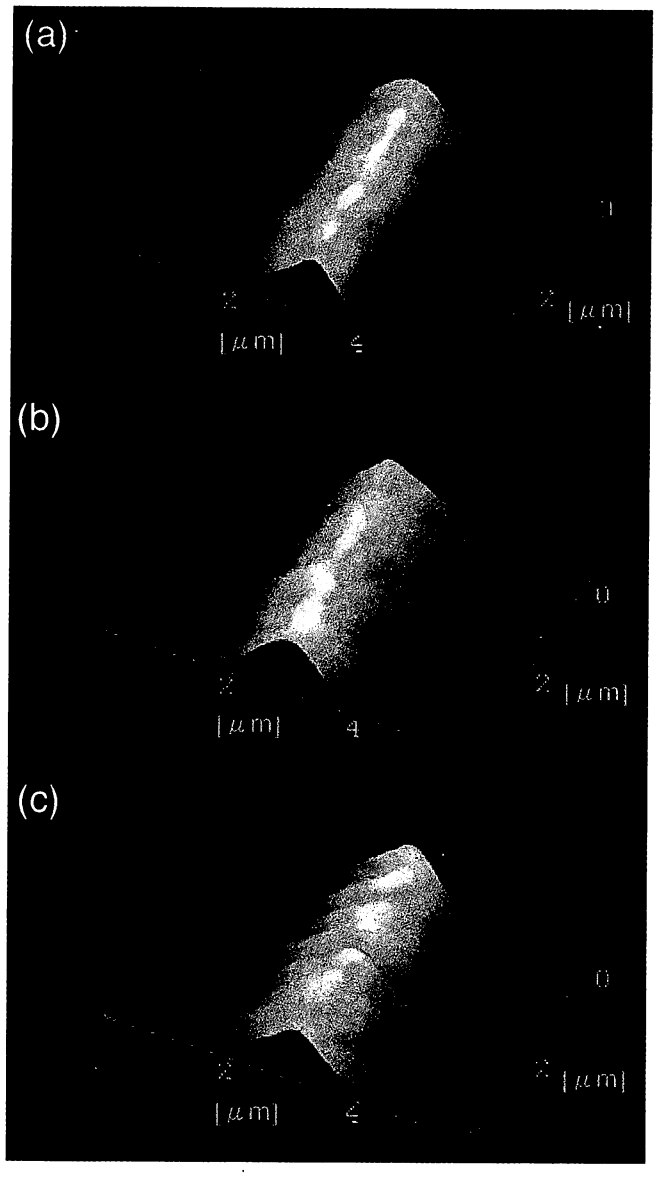

Fig. 2. Perspective views of the near-field photocurrent images under the reverse-biased voltage at (a) 0 V, (b) 3 V, and (c) 5 V. The image size is 6 μm × 4 μm.

reverse-biased voltage V_R is described by

$$W(V_R) = D(V_R) + C, \tag{1}$$

where C is a constant. For the shallow junction, the thickness of the depletion region is described by the one-sided step junction approximation and is expressed as

$$D(V_R) = \sqrt{2\varepsilon \frac{(V_R + \phi_B)}{q \cdot N_D}}, \tag{2}$$

where N_D is the dopant density in the n-type sample, ε is the dielectric constant of Si, $\phi_B = 0.7$ V is the built-in voltage, and q is the electron charge.[11] From eqs. (1) and (2), the difference in the FWHM of the cross-sectional profile of the near-field photocurrent between the reverse-bias condition and the no-bias condition is represented by

$$W(V_R) - W(0) = \sqrt{\frac{2\varepsilon}{q \cdot N_D}} \cdot [\sqrt{V_R + \phi_B} - \sqrt{\phi_B}]. \tag{3}$$

From this equation, the dopant density N_D in the Si substrate

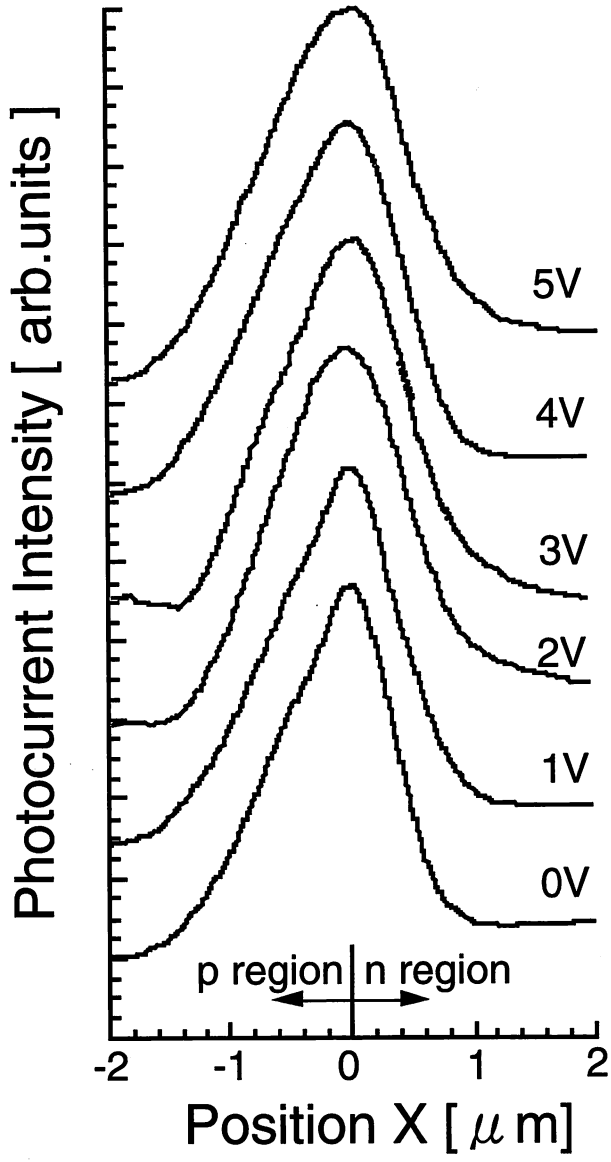

Fig. 3. Cross-sectional profiles of the near-field photocurrent signals under various reverse-biased voltages.

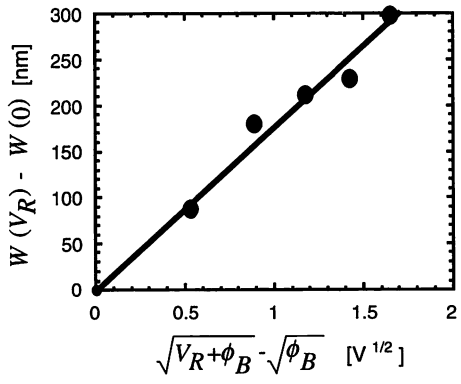

Fig. 4. Plot of the reverse-biased voltage vs the differential of the FWHM of the cross-sectional profile of the near-field photocurrent signals.

can be determined. Figure 4 shows the dependence of the FWHM of the cross-sectional profile of the near-field photocurrent signals under the reverse-bias conditions obtained from Fig. 3. The reverse-bias voltage was varied from 0 V to 5 V. By increasing the reverse-biased voltage, the FWHM of the cross-sectional profiles of the near-field photocurrent signal increases. From the slope of the line fitted to the measured values in this figure, the value of N_D in the n-type region is estimated as $3.5 \pm 0.4 \times 10^{16}\,\mathrm{cm}^{-3}$. This is consistent with the value of the dopant concentration ($3.1 \times 10^{16}\,\mathrm{cm}^{-3}$) evaluated from the device fabrication conditions. This result establishes a simple relationship between the FWHM of the cross-sectional profiles of the near-field photocurrent signal and the applied reverse-biased voltage. Thus, such measurement can be utilized as a simple nondestructive and local method for estimating the dopant concentration of semiconductor substrates and devices. Discussion of the influence of the surface band bending and surface recombination on the near-field photocurrent is very complicated based on the present results. The carrier dynamics in the transition region and the surface region are future problems to be addressed.

In summary, we have carried out near-field photocurrent measurements of the p-n junction on a Si substrate under the reverse-bias condition in order to estimate the dopant concentration of the p-n junction. By increasing the reverse-biased voltage of the p-n junction, the FWHM of the cross-sectional profile of the near-field photocurrent signal becomes wider according to the extent of the depletion region. From these results, the local dopant concentration N_D in the n-type region was estimated as $3.5 \pm 0.4 \times 10^{16}\,\mathrm{cm}^{-3}$. This result is consistent with the value of the dopant concentration ($3.1 \times 10^{16}\,\mathrm{cm}^{-3}$) evaluated from the device fabrication conditions.

The authors wish to express their thanks to Mr. Y. Kadota of RICOH Co., Ltd., for supplying the Si p-n junction sample. They are also grateful to Dr. T. Saiki of the Kanagawa Academy of Science and Technology for valuable discussion and comments.

1) M. Ohtsu: *Near-Field Nano/Atom Optics & Technology* (Springer-Verlag, Tokyo, 1998).
2) S. K. Buratto, J. W. P. Hsu, E. Betzig, J. K. Trautman, R. B. Bylsma, C. C. Bahr and M. J. Cardillo: Appl. Phys. Lett. **65** (1994) 2654.
3) M. S. Ünlü, B. B. Goldberg, W. D. Hrzog, D. Sun and E. Towe: Appl. Phys. Lett. **67** (1995) 1862.
4) T. Saiki, N. Saito, J. Kusano and M. Ohtsu: Appl. Phys. Lett. **69** (1996) 644.
5) H. Fukuda, Y. Kadota and M. Ohtsu: Jpn. J. Appl. Phys. **38** (1999) L571.
6) E. Betzig, P. L. Finn and J. S. Weiner: Appl. Phys. Lett. **60** (1992) 2484.
7) R. Toledo-Crow, P. C. Yang, Y. Chen and M. Vaez-Iravani: Appl. Phys. Lett. **60** (1992) 2957.
8) E. D. Palik: *Handbook of Optical Constants of Solids* (Academic Press, Orlando, 1985).
9) T. Saiki, S. Mononobe, M. Ohtsu, N Saito and J. Kusano: Appl. Phys. Lett. **68** (1996) 2612.
10) T. Saiki and K. Matsuda: Appl. Phys. Lett. **64** (1999) 2773.
11) A. S. Grove: *Physics & Technology of Semiconductor Devices* (John Wiley & Sons Inc., New York, 1967).

ELSEVIER

Analytica Chimica Acta 426 (2001) 11–18

ANALYTICA CHIMICA ACTA

www.elsevier.com/locate/aca

Micrometer-sized lithium ion-selective microoptodes based on a "tailed" neutral ionophore and a fluorescent anionic dye

Kazuyoshi Kurihara[a], Motoichi Ohtsu[a,b], Takeo Yoshida[c], Toshihito Abe[c], Hideaki Hisamoto[c], Koji Suzuki[a,c,*]

[a] *Kanagawa Academy of Science and Technology, 3-2-1 Sakado, Takatsu-ku, Kawasaki 213-0012, Japan*
[b] *Interdisciplinary Graduate School of Science and Engineering, Tokyo Institute of Technology, 4259 Nagatsuta, Midori-ku, Yokohama 226-8502, Japan*
[c] *Department of Applied Chemistry, Faculty of Science and Technology, Keio University, 3-14-1 Hiyoshi, Kohoku-ku, Yokohama 223-8522, Japan*

Received 6 April 2000; received in revised form 31 July 2000; accepted 15 August 2000

Abstract

The preparation and response features of a micrometer-sized lithium ion-selective optode based on a liquid membrane were examined. The optode membrane was a plasticized poly(vinyl chloride) (PVC)-based copolymer incorporating a lipophilic 14-crown-4 derivative as the neutral lithium ionophore and a dibromofluorescein derivative as the fluorescent anionic dye. The detection mode was a fluorescence change based on the ion-pair extraction/ion exchange principle caused by the fluorescent anionic dye and the lithium ionophore. The 5-μm-sized microoptode was prepared by the micropipette fabrication method and characterized by measuring the optical responses to Li^+ concentrations with the time-resolved photon counting method. The microoptode responded to lithium ion concentrations of ~0.5 to ~500 mM. The micrometer-sized lithium ion-selective microoptode was successfully obtained when a tailed ionophore was used. The anchor effect of the tailed ionophore was useful for the lithium ion-selective microoptode to resolve leaching of the ionophore, which is a significant problem in a microoptode based on a liquid membrane. This demonstration indicates that other ion-selective microoptodes can be obtained simply by replacing the tailed ionophore.

Keywords: Microoptode; Ion optode; Micropipette fabrication; Tailed ionophore; Lithium ion; Liquid membrane

1. Introduction

Recent improvement of a miniature optode (microoptode) as an alternative to a microelectrode has been triggered by the development of a fabrication technique for the optical fiber probes of scanning near-field optical microscopy (SNOM), whose spatial resolution is much higher than the diffraction limit approximating half of the optical wavelength, λ/2 (λ = 0.38–0.78 μm) [1–3]. The optical fiber probe of SNOM has played a critical role in a transducer of the microoptode with a small size of the optical wavelength. A pioneering study of the microoptode using the SNOM fiber probe has been carried out by Kopelman and his colleagues [4–6]. Their immobilization method was based on a photoinitiated polymerization using a water-soluble polymer of acrylamide-methylenbis(acrylamide) copolymer including an indicator molecule.

* Corresponding author. Tel.: +81-45-563-1141/42355; fax: +81-45-564-5095.
E-mail address: suzuki@applc.keio.ac.jp (K. Suzuki).

0003-2670/01/$ – see front matter
PII: S0003-2670(00)01148-X

As a new immobilization method, we have recently proposed a micropipette fabrication method for producing a micrometer-sized microoptode from the SNOM fiber probe [2,7,8]. Our demonstration has meant that miniaturization of the optode into optical wavelength size brings about significant difficulties in the immobilization method and the sensing membrane. In our method, a sensing membrane is immobilized on the tip of the fiber probe using a micropipette controlled by a micromanipulator system. The size of the immobilized membrane is controllable to the precision of a micrometer. The micropipette fabrication method is applicable to a liquid membrane-based optode whose sensing membrane consists of a plasticized poly(vinyl chloride) (PVC)-based copolymer including a neutral ionophore and an anionic dye. A major advantage in using the liquid membrane-based optode as the sensing membrane is flexibility in ion selectivity, because a large number of ionophores can be used for ion detection selective for Li^+, Na^+, K^+, NH_4^+, Mg^{2+}, Ca^{2+}, Zn^{2+}, Ag^+, Hg^+, Pb^{2+}, Al^{3+} and so on [9,10]. Simple replacement of an ionophore in the liquid membrane enables changing the ion selectivity of the microoptode.

In previous papers [7,8], we demonstrated a micrometer-sized sodium ion-selective microoptode based on a liquid membrane incorporating a 16-crown-5 derivative as the neutral sodium ionophore. The micrometer-sized optode membrane was immobilized by the micropipette fabrication method. On the way to develop a successful micrometer-sized microoptode membrane, we faced a significant problem: the ionophore containing a sensed ion in the cavity leached from the membrane phase into the water phase. After careful examination, we understood that the leaching of the ionophore was substantially reduced by using a tailed ionophore that possesses a highly liphophilic long alkyl chain. The mechanism of this solution in relation to the leaching problem was not explained simply by the lipophilicity, which is a criterion of leaching at bulk size but by the anchor effect of the tailed ionophore. The tail of the tailed ionophore functions as an "anchor", which prevents the ionophore itself from leaching into the water phase because of its hydrophobic interaction.

The present paper describes a micrometer-sized lithium ion-selective microoptode, which was prepared on the basis of knowledge obtained in a previous study [8]. The optode membrane was a liquid membrane incorporating a tailed 14-crown-4 derivative as the neutral lithium ionophore and a dibromofluorescein derivative as the fluorescent anionic dye. The micrometer-sized lithium ion-selective optode has been simply accomplished using a tailed ionophore selective for the lithium ion. In this case, the anchor effect of the tailed ionophore also prevents the ionophore from leaching into the water phase because of its hydrophobic interaction, one of the opposing forces to constructing self-association of amphiphilic molecules. Our results indicate that other ion-selective microoptodes can be obtained simply by replacing the tailed ionophore for other objective ions.

2. Principle of response theory

An optode membrane is a liquid membrane incorporating a cation-selective neutral ionophore, S, and a fluorescent anionic dye, AH. Its chemical response mechanism is based on the ion exchange principle given by

$$S_o + i_w^+ + AH_o \Leftrightarrow SiA_o + H_w^+ \quad (1)$$

where the subscripts 'o' and 'w' represent the existence of a chemical species in the organic phase (liquid membrane) and in the water phase, respectively, i^+ is the ion to be sensed, SiA the produced association (ion-pair) and H^+ is the hydrogen ion. By transforming the ion-exchange equilibrium shown in Eq. (1) with the relative portion of the deprotonated anionic dye, α, the total ionophore concentration, $[S_{tot}]$, and the total anionic dye concentration, $[A_{tot}]$, the chemical response equation is described as follows:

$$[i^+] = \frac{[H^+]\alpha}{K_{exch}(1-\alpha)([S_{tot}] - [A_{tot}]\alpha)} \quad (2)$$

where K_{exch} is the ion-exchange equilibrium constant, and $[H^+]$ the hydrogen ion concentration. In the fluorescence intensity measurement using a single-emission fluorescent dye, α is given by

$$\alpha = \frac{F - F_N}{F_A - F_N} \quad (3)$$

where F_N and F_A are theoretical values for the fluorescence intensity when all the dyes are in a neutral form

and an anionic form, respectively, and F the observed value of the fluorescence intensity from dyes excited by the light source. By substituting Eq. (3) into Eq. (2), the optode response equation is finally given by

$$[i^+] = \frac{[H^+](F - F_N)(F_A - F_N)}{K_{exch}(F_A - F)\{[S_{tot}]F_A + ([A_{tot}] - [S_{tot}])F_N - [A_{tot}]F\}} \quad (4)$$

In a special case where $[A_{tot}] = [S_{tot}]$, Eq. (4) is simplified as

$$[i^+] = \frac{[H^+]}{K_{exch}[S_{tot}]} \frac{(F - F_N)(F_A - F_N)}{(F_A - F)^2} \quad (5)$$

Eq. (5) helps us to understand qualitative behavior of the response equation, Eq. (4). In usual measurement conditions, the pH in the water phase, $[H^+]$, is kept constant by a buffer solution. Also, the total ionophore concentration, $[S_{tot}]$, and the equilibrium constant, K_{exch}, are maintained constant in each measurement. Then, the target ion concentration, $[i^+]$, can be determined by the fluorescent intensity, F. The response curve of F versus $\log[i^+]$ is a S-type curve, whose shape theoretically determines the dynamic range of the optodes. On the other hand, Eq. (5) tells us that the detection limit is shifted in proportion to the factor $[H^+]/K_{exch}[S_{tot}]$. It means that the detection limit is affected by the pH of the external solution, $[H^+]$, but can be controlled by the factors K_{exch} and $[S_{tot}]$, where $[S_{tot}] = [A_{tot}]$. In the usual case where $[H^+]$ is constant due to the buffer solution, the detection limit of the optodes can be improved by increasing the equilibrium constant, K_{exch}, and/or the concentrations of chemical components, $[S_{tot}]$ and $[A_{tot}]$. Of these two methods, the former is practical because K_{exch} is easily increased by a factor of more than 100 using an anionic dye with a lower acidity (pK_a) value. However, the concentrations of $[S_{tot}]$ and $[A_{tot}]$ are difficult to increase even by 10 due to limits in the sensing membrane. Although fluorescence measurements are effective for miniature optodes in high-performance detection, their intensity measurements have several problems such as fluorescence distortion caused by optical systems and indicator dyes. The sensing performance is lowered by instabilities in the power intensity of light sources and by the mechanical mounting of optical elements such as lenses. Fluorescence intensity of the indicator dyes changes according to photobleaching due to a strong excitation, solvent effects in the sensing membrane and leaching from the sensing membrane. These problems can be resolved using fluorescence ratiometric measurement, which is described in the previous paper [8].

At last, we comment on the influence of ionic strength, which is known as an important factor in the theory of ion-selective electrodes. In the present theory, the influence of ionic strength does not appear as a term in the equation because the equilibrium constant, K_{exch}, includes it. Under usual measurement conditions using buffer solutions, the ionic strength is supposed to be constant at all the target ion concentrations; then, the equilibrium equation is valid. In a more strict expression, the effect of ionic strength should be expressed as an activity in the equilibrium constant, K_{exch}.

3. Experimental

3.1. Micropipette fabrication method

The fabrication of a micrometer-sized microoptode using a micropipette is described. Other detailed descriptions of this fabrication method were reported in our previous papers [2,8]. Fig. 1a shows a schematic diagram of this method. Micrometer-sized immobilization using a micropipette was done using micromanipulator system, which consists of two micromanipulators (Shimazu MMS-77, Kyoto, Japan) and an optical microscope (Olympus BX60, Tokyo, Japan). The optical fiber probe of SNOM was held on the holder of one micromanipulator while a micropipette filled with the optode membrane cocktail was set on the holder of the other. The fiber probe was fabricated from a quartz-core optical fiber with a micropipette puller (Sutter Instrument Co. P-2000, CA, USA) by the heat-pulling process. No further modifications, such as metal coating and silanization, were done to the fiber probe. The micropipette was fabricated from a glass tube using a micropipette puller (Narishige Scientific Instrument Lab., PP-83, Tokyo, Japan). The micropipette had an inner diameter of ~5 μm and was filled with the cocktail using a syringe, whose needle was put into the glass tube at the other side of the micropipette. By controlling the micromanipulators under visual observation through

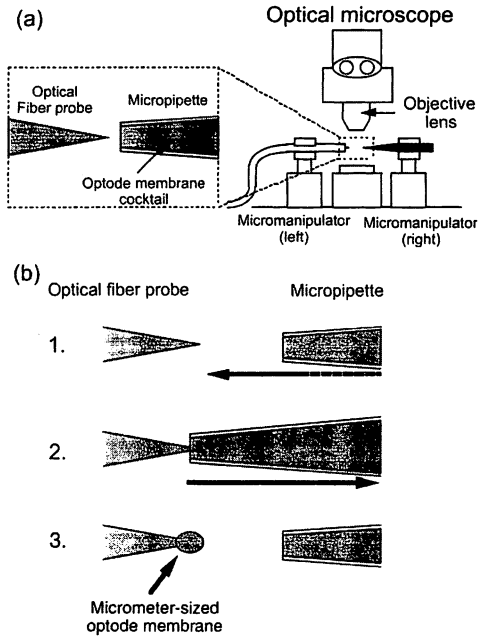

Fig. 1. Schematic explanation of the micropipette fabrication method. (a) Diagram of the micromanipulator system which consists of two micromanipulators and an optical microscope. (b) Immobilization procedure to fabricate the micrometer-sized microoptode. (1) The micropipette and the optical fiber probe of SNOM are aligned coaxially. (2) The micropipette is made to approach the probe until the tip of the probe is inserted into the optode membrane cocktail in the micropipette. (3) The micropipette is removed from the probe, which consequently has a micrometer-sized optode membrane on the tip.

the optical microscope, the cocktail was immobilized on the tip of the fiber probe (Fig. 1b). The final microoptode was obtained by evaporating the solvent tetrahydrofuran (THF) of the cocktail in a vacuum container.

3.2. Preparation of the optode membrane

The optode membrane, prepared as described above, incorporated a neutral ionophore selective for Li^+ and a fluorescent anionic dye introduced into the liquid membrane using a THF solution (Wako Pure Chemical Industries Ltd., Osaka, Japan, Type Infinity Pure). The liquid membrane consisted of 66 wt.% bis-(2-ethylhexyl)sebacate (BEHS) (Tokyo Chemical Industry, Tokyo, Japan) with a lipophilicity of 10.3 [11] and 33 wt.% copolymer (OH-PVC) of 90 wt.% vinyl chloride, 6 wt.% vinyl alcohol and 4 wt.% vinyl acetate (Aldrich Chemical Co., Inc., Milwaukee, WI, USA). By using OH-PVC instead of PVC, which is normally used in the liquid membrane, micrometer-sized immobilization using the micropipette fabrication method was accomplished. Hydroxyl groups of the OH-PVC allow many hydrogen bonds to strengthen the adhesion of the optode membrane to the glass surface of the fiber probe. Fig. 2 shows the chemical structures of two ionophores selective for Li^+. The tailed ionophore (Fig. 2a) is 2,2,3,3-tetramethyl-9-tetradecyl-1,4,8,11-tetraoxacyclotetradecane (TTD14C4) (Dojindo Lab., Kumamoto, Japan) with a lipophilicity of 14.0 ± 0.2, which was designed and synthesized by the authors according to the previous report [12]. The non-tailed ionophore (Fig. 2b) is 2,6,9,13-tetraoxatricyclo(12.4.4.03,4)docosane (D14C4) with a lipophilicity of 5.1 ± 0.3. The fluorescent anionic dye is 4′,5′-dibromofluorescein-octadecyl-ester (Fluka Chemical Corp., Ronkonkoma, NY, USA). The optode membrane contained the anionic dye at 2.9 wt.% relative to the liquid membrane and the ionophore at two times the molar concentration of the anionic dye. The optode components were mixed uniformly with more than 20 times their amount of THF.

3.3. Optical measurements

Fig. 3 shows a schematic diagram of the experimental setup. The measurement system was constructed chiefly from an inverted optical microscope (Olympus IX70, Tokyo, Japan). The microoptode was vertically held on an *xyz*-stage and immersed in a Tris–HCl buffer solution of pH 7.4, which was kept in a culture dish on the inverted optical microscope. The beam of a 514.5-nm single-mode cw Ar^+ laser (Coherent, Inc., CA, USA) was coupled with a fiber coupler (Newport Corp., CA, USA) into the optical fiber at the back side of the microoptode. The fluorescent dye in the optode membrane was excited by a ~1 μW laser light propagating through the optical fiber. The fluorescence peaking at ~540 nm wavelength was collected with a 10× objective lens of the inverted optical microscope. The collected fluorescence passed through a holographic notch-plus filter (Kaiser Optical Systems, Inc., MI, USA) to reject the laser light by a factor of 10^6. Finally, the fluorescence was detected by a photo-

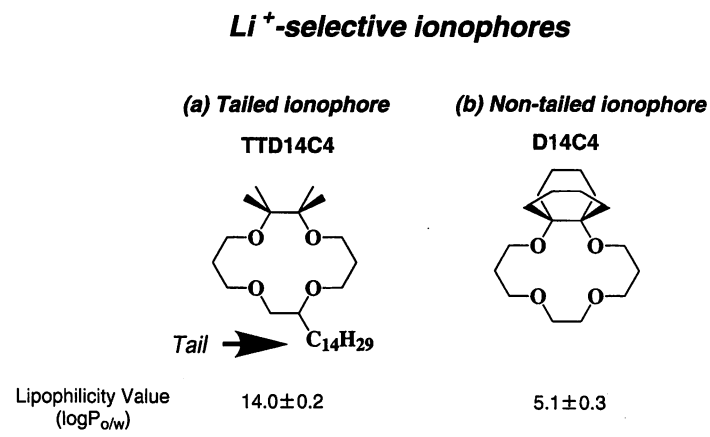

Fig. 2. Chemical structure of Li^+-selective ionophores. (a) The tailed ionophore of tetramethyl-tetradecyl-14-crown-4 (TTD14C4) and (b) the non-tailed ionophore of decalino-14-crown-4 (D14C4).

multiplier tube (PMT) (Hamamatsu R464, Shizuoka, Japan) by means of the photon counting method with an accumulation time of 1 s. Data were stored on a personal computer through a photon counting board (Hamamatsu M3949, Shizuoka, Japan) and a photon counting unit (Hamamatsu C3866, Shizuoka, Japan). The Li^+ concentration in the sample solution was varied by adding droplets of LiCl solution (10^{-3}–1 M) into the culture dish using a syringe. To check visually whether the droplets fell into the culture dish, we used a light flash, whose light intensity was recorded in the sensor response profiles as a signal of the point when the Li^+ concentration was varied.

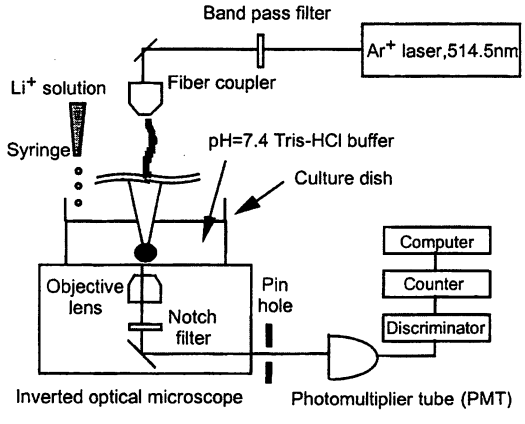

Fig. 3. Schematic diagram of the experimental setup for measuring the sensor response of the micrometer-sized microoptode. The lithium ion concentration is monitored by the fluorescence intensity of the microoptode.

4. Results and discussion

The micrometer-sized Li^+-selective microoptodes were prepared by the micropipette fabrication method and characterized by fluorescence intensity measurement. Fig. 4a shows a micrograph of the microoptode with a size of 5 μm. On the tip of the optical fiber probe of SNOM, the optode membrane with a diameter of 5 μm was immobilized. Fig. 4b shows typical dynamic responses of the microoptode for changes in Li^+ concentration in the sample solution. The upper profile was obtained with the microoptode based on the non-tailed ionophore, D14C4, while the lower profile resulted from that based on the tailed ionophore, TTD14C4. The peaks accompanying the arrow with a number in the profiles indicate the time when the Li^+ concentration was changed. Those peaks were caused by a light flash to check the Li^+ droplets falling into the culture dish. In the lower profile, the microoptode based on the tailed ionophore successfully responded to changes in the Li^+ concentration. Contrariwise, in the upper profile, the microoptode based on the non-tailed ionophore did not respond to any Li^+ concentration changes. The difference in experimental conditions between the two microoptodes was only selection of the ionophore in the chemical compo-

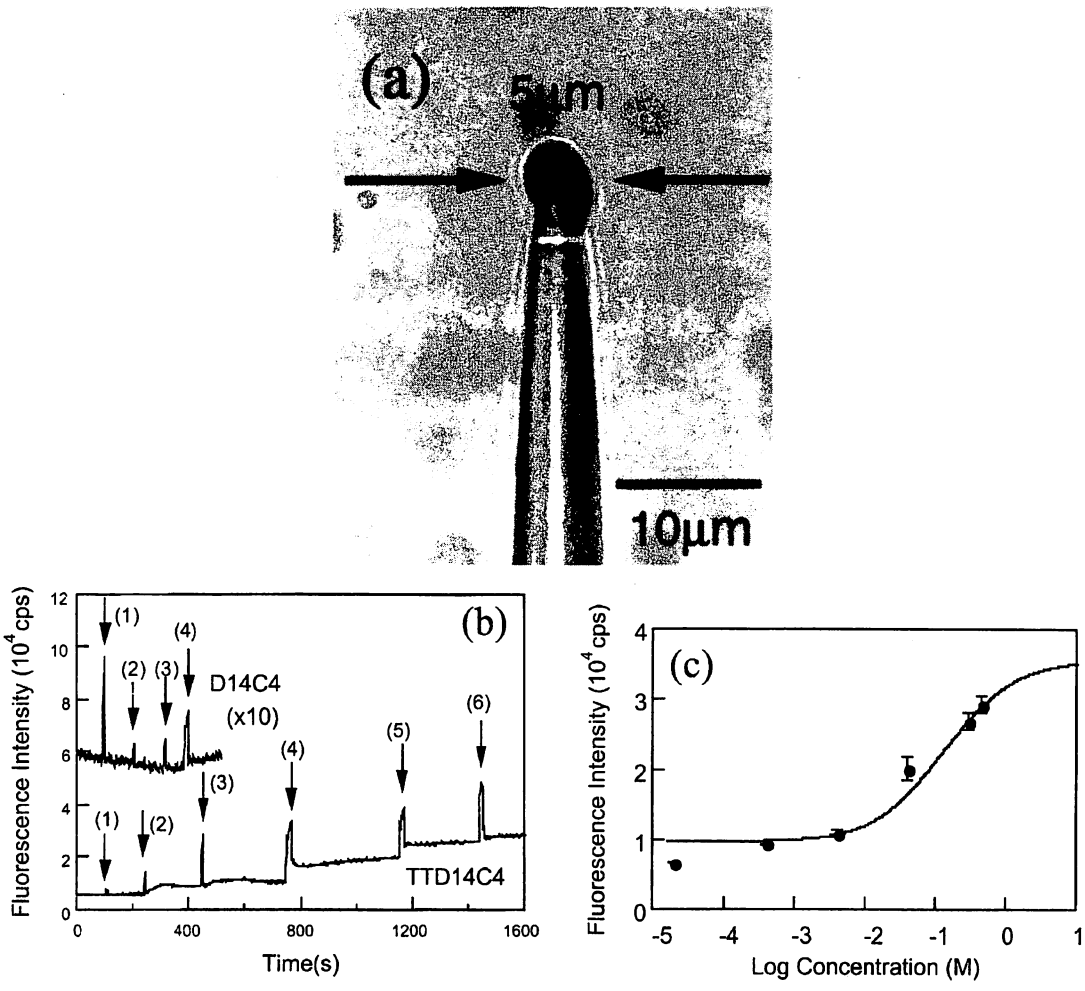

Fig. 4. Characterization of the micrometer-sized Li^+-selective microoptode. (a) The micrograph of a 5-μm-sized microoptode. (b) The dynamic response profiles of the microoptode with respect to Li^+ concentrations. The upper profile resulted from the microoptode based on the non-tailed ionophore, D14C4, while the lower profile came from the microoptode based on the tailed ionophore, TTD14C4. The upper profile did not respond to any Li^+ concentrations because the ionophore, including a lithium ion, leached from the membrane to the water. Arrows with numbers indicate the time when Li^+ droplets were added. Peaks accompanying the marks are due to a light flash to check the droplets falling into the culture dish. Li^+ concentrations of the upper profile are: initial state 0 M; (1) 3.9×10^{-4} M; (2) 4.1×10^{-3} M; (3) 4.0×10^{-2} M; (4) 4.4×10^{-1} M, while those of the lower profile are: initial state 0 M; (1) 2.4×10^{-4} M; (2) 3.9×10^{-4} M; (3) 4.1×10^{-3} M; (4) 4.0×10^{-2} M; (5) 2.9×10^{-1} M; (6) 4.4×10^{-1} M. (c) Plots of the sensor response and their response curve calculated by theoretical Eq. (4).

nents. There are two major differences between two ionophores, D14C4 and TTD14C4: the existence of a lipophilic "tail" and the lipohilicity value. No response of the microoptode in the upper profile can be explained by the leaching of the non-tailed ionophore, D14C4, into the water phase. The response of the microoptode in the lower profile means that the tailed ionophore is an effective solution to the leaching problem of the ionophore. The tail of the tailed ionophore increases the lipophilicity value of the ionophore to reduce leaching. The tail prevents the ionophore from leaching because of the anchor effect due to its high hydrophobic interaction, to which theoretical consideration is given later. In our case, it is also quite natu-

ral that the leaching problem of fluorescent dyes was resolved by using a fluorescent dye with a long alkyl chain. It is, however, noted that our optodes have an intrinsic problem about leaching from the sensing membrane because the plasticizer, BEHS, in the membrane has a relatively low lipophilicity of 10.3 [11]. In the lower profile of Fig. 4b, the response time of the microoptode based on the tailed ionophore is estimated to be approximately 100 s. This response profile shows that the microoptode had a detection minimum concentration of 4×10^{-4} M, a detection maximum concentration of 4×10^{-1} M and a signal-to-noise (S/N) ratio of 11 dB. Fig. 4c shows the sensor response of the lower profile in Fig. 4b. The response curve of the solid line in Fig. 4c was obtained by fitting the plots of the sensor response with theoretical Eq. (4) using the computer software, Igor Pro (WaveMetrics, Inc.). In this fitting, $F_N = (1.0 \pm 0.3) \times 10^4$, $F_A = (3.6 \pm 0.2) \times 10^4$, and $\log_{10} K_{exch} = -5.4 \pm 0.4$ were obtained as parameters of Eq. (4). The response curve agreed well with the plots of the sensor response, but the fluorescence intensity measurement has an intrinsic problem of being weak in fluorescence distortion so that the obtained parameters were varied between measurements. In fact, the sensor response of Fig. 4c was obtained from one of the most sensitive microoptodes we prepared and measured under the same conditions. Reproducibility of the sensor response between optodes was low at Li^+ concentrations higher than 4.0×10^{-2} M, where the baseline was also sloping up together with the time in Fig. 4b. The low reproducibility between optodes is mainly due to the leaching of the sensing membrane that includes all the components. The leaching was sometimes observed under an optical microscope as a reduction in size after the measurement. The sloping baseline is mainly due to the solvent effect on the fluorescent dye in the membrane. In addition, the reproducibility was made lower by the photobleaching that depends on excitation power. In order to obtain higher reproducibility, fluorescence ratiometric measurement is applicable [8].

We comment on the anchor effect of the tailed ionophore that resolves the leaching problem. The anchor effect results from the size effect due to miniaturization, which cannot be understood by the simple idea of hydrophobic interaction as we proposed in the previous papers [7,8] as a reason to prevent the tailed ionophore, which includes a target ion, from leaching into the water phase. A proper discussion about the anchor effect is based on self-association theory of amphiphilic molecules, which deals with chemistry in a small space. The tailed ionophore, including a target ion, is classified as an amphiphilic molecule because the tail and ion parts of the tailed ionophore, including a target ion, correspond to the hydrophobic and hydrophilic groups of the amphiphilic molecule, respectively. As examples of the self-association of amphiphilic molecules, the phenomena of micelles, vesicles and bimolecular membranes are well known. A driving force to construct self-association is a set of opposing forces at the interface; that is, an attractive force due to the hydrophobic group and a repulsive force due to the hydrophilic group. This discussion indicates that the hydrophobic interaction of the tailed ionophore causing the anchor effect should be recognized as one of the opposing forces to constructing self-association, and also suggests that the anchor effect can be quantitatively understood using self-association theory.

In summary, the present paper demonstrated a micrometer-sized lithium ion-selective optode based on a liquid membrane using a tailed neutral ionophore, TTD14C4. The micrometer-sized lithium ion-selective optode was easily obtained by replacing the tailed ionophore in the sodium ion-selective microoptode reported in the previous papers [7,8]. This demonstration indicates that other ion-selective microoptodes are obtained simply only by replacing the tailed ionophore.

Acknowledgements

One of the authors, K. Kurihara, thanks Nissan Science Foundation for financial support. This study was partially supported by a Grant-in-Aid for Scientific Research from the Ministry of Education, Science, Sports and Culture.

References

[1] M. Ohtsu, J. Lightwave Technol. 13 (1995) 1200.
[2] M. Ohtsu (Ed.) Near-Field Nano/Atom Optics and Technology, Springer, Tokyo, 1998.
[3] M. Ohtsu, H. Hori, Near-Field Nano-Optics, Plenum Press, New York, 1999.

[4] W. Tan, Z.-Y. Shi, R. Kopelman, Anal. Chem. 64 (1992) 2985.
[5] W. Tan, Z.-Y. Shi, D. Birnbaum, R. Kopelman, Science 258 (1992) 778.
[6] Z. Rosenzweig, R. Kopelman, Anal. Chem. 67 (1995) 2650.
[7] K. Kurihara, M. Ohtsu, T. Yoshida, T. Abe, H. Hisamoto, K. Suzuki, Proc. Europt(r)ode IV (1998) 49.
[8] K. Kurihara, M. Ohtsu, T. Yoshida, T. Abe, H. Hisamoto, K. Suzuki, Anal. Chem. 71 (1999) 3558.
[9] P. Buhlmann, E. Pretsch, E. Bakker, Chem. Rev. 98 (1998) 1593.
[10] H. Hisamoto, K. Suzuki, Trends Anal. Chem. 18 (1999) 513.
[11] H. Hisamoto, K. Watanabe, E. Nakagawa, D. Siswanta, Y. Shichi, K. Suzuki, Anal. Chim. Acta 299 (1994) 179.
[12] K. Suzuki, H. Yamada, K. Sato, K. Watanabe, H. Hisamoto, Y. Tobe, K. Kobiro, Anal. Chem. 65 (1993) 3404.

OPTICAL REVIEW Vol. 7, No. 6 (2000) 486–488

Letter

Fabrication of an Ultraviolet Light-Emitting Functional Probe of Sub-Micron Size by Photochemical Vapor Deposition

Yoh YAMAMOTO,[1] Guen-hyoung LEE,[2,4] Kazunari MATSUDA,[3] Takashi SHIMIZU,[1] Motonobu KOUROGI[1,2] and Motoichi OHTSU[1,2]

[1]*Interdisciplinary Graduate School of Science and Engineering, Tokyo Institute of Technology, 4259, Nagatsuta, Midori-Ku, Yokohama, Kanagawa, 226-8508 Japan,* [2]*Japan Science and Technology Corporation, 671-1, Tsuruma, Machida, Tokyo, 194-0004 Japan,* [3]*Kanagawa Academy of Science and Technology, Takatsu-Ku, 3-2-1, Sakado, Kanagawa, 213-0012 Japan*

(Received July 13, 2000; Accepted September 6, 2000)

We report a new fabrication technique of a sub-micron sized probe consisting of functional material on the aperture of a metal coated optical fiber probe tip for near field optical microscopy. The selective fixation of sub-micron size functional material has been achieved by photochemical vapor deposition. Here, we demonstrate for the first time the selective fixation of zinc oxide, a wide gap semiconductor with ultraviolet emission ability, on such probe tips. Results reveal the efficient excitonic emission of 372 nm even at room temperature, which is characteristic of high quality zinc oxide.

Key words: near field optical microscopy, functional probe, photochemical vapor deposition, zinc oxide, excitonic emission

With the progress of near field optical microscopy, various optical fiber probes have been developed for different applications such as a highly sensitive probe for spectroscopy, a high resolution probe for imaging and a high transmittance probe for the ultraviolet region.[1)] By attaching functional material like dye molecules or semiconductor particles of micro- or sub-micro- meter size to the tip of optical fiber probes, functional probes with localized function down to a sub-micro-meter scale can be realized. Applications such as energy transfer, optical nonlinearity and chemical/biological sensing are feasible with such functional probes.

To date, these functional probes have been typically fabricated by fixing functional material onto the tip of an optical fiber probe using techniques which involve photoinitiated polymerization[2)] and a micropipette.[3)] While photoinitiated polymerization offers excellent spatial selectivity, it is limited in its applicable materials. The micropipette can fix various materials but fixation of those of sub-micron size is difficult. Both approaches additionally suffer from poor crystallinity of fixed material and adhesion to a probe due to the use of chemical adsorption for the fixation.

In this letter, we propose and demonstrate a new technique of fabrication of a functional probe by photochemical vapor deposition (photo-CVD). Photo-CVD with an optical fiber probe yields localized deposition by selective photo-dissociation of molecules in the irradiated region. This is applicable to the deposition of various materials, such as metals, semiconductors and insulators, by varying the reaction gases and photon energy of the light source. Thus, this approach can easily fix various materials of sub-micron size on the tip of an optical fiber probe selectively. Crystal growth on the tip of the probe by photochemical reaction allows this method to firmly fix materials with high crystallinity.

We describe the fabrication of light-emitting functional probe with zinc oxide (ZnO) as an example. ZnO is a wide-gap semiconductor which has attracted a great deal of attention for its efficient UV emission and lasing even at room temperature, due to a large exciton binding energy of 60 meV.[4.5)] Another interesting property that has been reported is the second harmonic generation from ZnO.[6)] We believe that a fabricated probe with ZnO can find potential application as an UV point light source with convertible photon energy.

The fixation of ZnO was performed using the photochemical reaction between diethylzinc (Zn $(C_2H_5)_2$: DEZ) and oxygen (O_2) during the irradiation of UV light.[7)] Figure 1 shows a schematic diagram of our experimental setup for the fixation. Second harmonic (SH) light ($\lambda = 244$ nm) of an argon ion laser was used as a UV light source. The built-up cavity with the BBO crystal generated 10% of highly efficient SH light. This light was coupled with the optical fiber and delivered to the fiber probe tip through the fiber. We employed an aluminum-coated UV triple-tapered probe[8)] with an aperture diameter of 250 nm as shown in Fig. 2(a). This probe was prepared by chemically etching the multi-index fiber consisting of fluorine doped claddings, a pure silica core and a germanium dioxide (GeO_2) doped core. Transmission loss of the pure silica core in the UV-visible region was very low (1.1d B/m@wavelength: 244 nm), and transmission efficiency at the triple-tapered probe tip was high (1×10^{-4}@aperture diameter: 100 nm). The aperture of the probe was created using a focused ion beam, with a size controllable from 30 nm to more than a micrometer. The probe tip and the heater were located within a vacu-

[4]Present address: Department of Advanced Materials Engineering, Dong-Eui University, Gaya-dong 24, Pusanjin-ku, Pusan, 614-714, Korea
E-mail: yoh@ae.titech.ac.jp

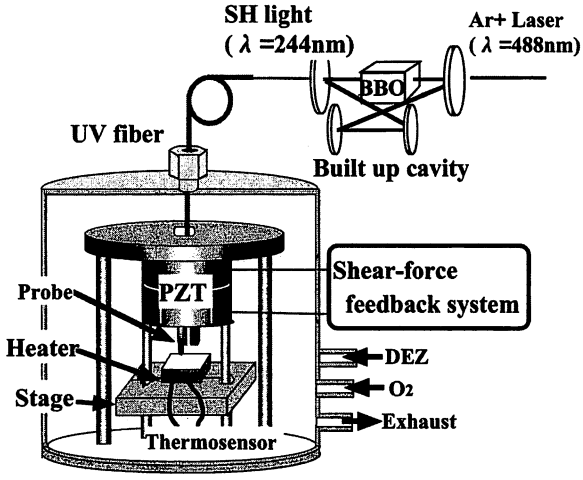

Fig. 1. Experimental setup for the fixation.

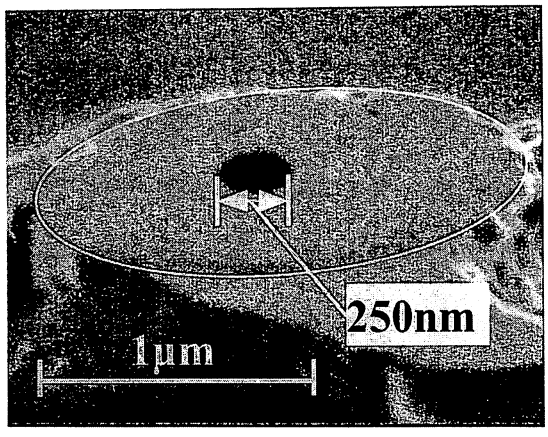

(a)

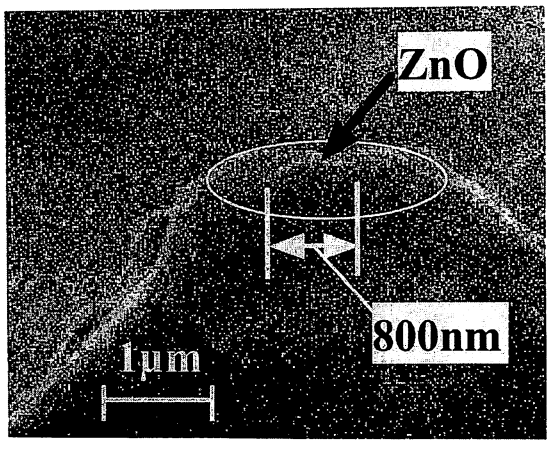

(b)

Fig. 2. SEM images of fabricated functional probe with ZnO (a) before and (b) after the fixation of ZnO, respectively. In (a) and (b), the white circle defines the flattened tip area of the fiber probe.

um chamber filled with reactant gases in a ratio of DEZ:O_2=1:10. In our earlier reports, we discussed the characteristics of films fabricated by far field light and

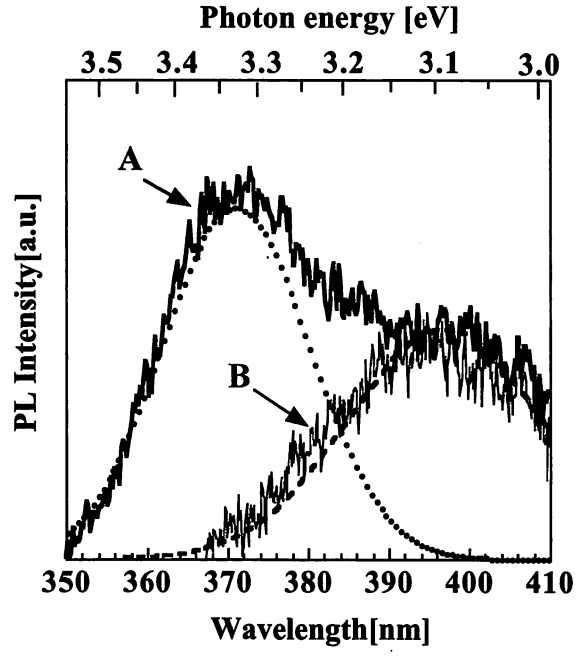

Fig. 3. Light emission of the probe: Curves A and B show the emission characteristics from the functional probe and bare fiber, respectively. Dotted and dashed curves show the Gaussian fits to the 372 nm and 395 nm peaks of curve A, respectively.

the fabrication of sub-micron sized dots by optical near field.[9] Through such optimization, we confirmed that high quality ZnO films (in terms of crystalline quality and optical property) were obtained at the substrate temperatures above 150°C. Measurements on these films showed a free excitonic emission even at room temperature with a peak ranging from 375 nm to 380 nm. Thus, to accelerate the growth of high quality ZnO on the probe tip, fixation was carried out under identical conditions to that of the film deposition, i.e., optical fiber probe was brought within a few nanometers of the heater at 200°C by shear-force technique during the fixation.

Figures 2(a) and (b) show SEM (scanning electron microscopy) images of the probe before and after the fixation of ZnO, respectively. The fixation time was 30 min by 5 mW SH light. As evident from Fig. 2 (b), we were able to selectively fix ZnO with a diameter of 800 nm on the aperture at the flattened tip of the optical fiber probe by photo-CVD. Next, we measured the emission spectrum from the ZnO fixed fiber probe to investigate its qualities. This measurement was conducted using a 325 nm line of He-Cd laser as an excitation light. The laser light was coupled to the optical fiber at the end of the fiber probe. The emission from the probe was detected by a cooled CCD through a monochromator, and this measurement was performed at room temperature. In Fig. 3, curves A and B show the emission spectra from the fabricated probe and a bare fiber, i.e., a fiber without ZnO on the tip. Dotted and dashed curves in the figure represent the Gaussian fits of 372 nm and 395 nm peaks, respectively. The peak around 395 nm was ob-

served in the emission spectra from both fibers and originated from the fluorescence of GeO_2 in the fiber core. The peak around 372 nm, however, was seen only in the emission spectrum from the ZnO fixed fiber probe, and therefore it could be attributed to the fixed ZnO on the aperture of the probe tip. The emission peak position of 372 nm correlates well with the room temperature band gap energy of 3.37 eV for bulk ZnO crystal,[10] which is characteristic of high quality ZnO material. This indicates that high crystallinity ZnO was fixed on the aperture.

In conclusion, we have proposed and demonstrated a new technique of functional probe fabrication by selective photochemical vapor deposition. Fixation of ZnO with sub-micron diameter on the aperture of the optical fiber probe was examined and confirmed for the first time. This technique offers a simple way to fix functional materials of sub-micron size on the tip of the optical fiber probe. Photoluminescence measurements showed the efficient excitonic emission of 372 nm even at room temperature, which reflects high crystalline quality of fixed ZnO on the aperture of the optical fiber probe. Accordingly, this functional probe has potential application as an UV point light source with convertible photon energy. With the adoption of different fixing materials, a wide variety of functional probes can be realized by this approach.

Acknowledgments

The authors would like to thank Dr. S. Mononobe of Kanagawa Academy of Science and Technology for his invaluable help and advice in the art of making fiber probes. They are also grateful to Drs. H. N. Aiyer and T. Kawazoe of the Japan Science and Technology Corporation for useful discussions.

References

1) M. Ohtsu, ed.: *Near-Field Nano/Atom Optics and Technology* (Springer-Verlag, Tokyo, 1998)
2) W. Tan, Z. -Y. Shi, S. Smith, D. Birnbaum and R. Kopelman: Science **258** (1992) 778.
3) K. Kurihara, T. Yoshida, T. Abe, H. Hisamoto, K. Suzuki and M. Ohtsu: Anal. Chem. **71** (1999) 3558.
4) Z. K. Tang, G. K. L. Wong, P. Yu, M. Kawasaki, A. Ohtomo, H. Koinuma and Y. Segawa: Appl. Phys. Lett. **72** (1998) 3270.
5) D. M. Bagnall, Y. F. Chen, Z. Zhu, T. Yao, S. Koyama, M. Y. Shen and T. Goto: Appl. Phys. Lett. **70** (1997) 2230.
6) H. Cao, J. Y. Wu, H. C. Ong, J. Y. Dai and R. P. H. Chang: Appl. Phys. Lett. **73** (1998) 572.
7) M. Shimizu, H. Kamei, M. Tanizawa, T. Shiosaki and A. Kawabata: J. Cryst. Growth. **89** (1988) 365.
8) S. Mononobe, T. Saiki, T. Suzuki, S. Koshihara and M. Ohtsu: Opt. Commun. **146** (1998) 45.
9) G. H. Lee, Y. Yamamoto, M. Kourogi and M. Ohtsu: Proc. SPIE **3791** (1999) 132.
10) C. Klingshirn: Phys. Status Solidi B **71** (1975) 547.

BUNSEKI KAGAKU Vol. 49, No. 12, pp. 961–967 (2000)

報　文

超微細化イオン選択性オプトード

栗原　一嘉[*1]，大津　元一[*1,*2]，久本　秀明[*3,*4]，鈴木　孝治®[*1,*3]

Ultrasmall ion-selective fiber optodes

Kazuyoshi KURIHARA[*1], Motoichi OHTSU[*1,*2], Hideaki HISAMOTO[*3] and Koji SUZUKI[*1,*3]

[*1] Kanagawa Academy of Science and Technology, 3-2-1, Sakado, Takatsu-ku, Kawasaki 213-0012
[*2] Interdisciplinary Graduate School of Sceience and Engineering, Tokyo Institute of Technology, 4259, Nagatsuta Midori-ku Yokohama 226-8502
[*3] Department of Applied Chemistry, Keio University, 3-14-1, Hiyoshi, Kohoku-ku, Yokohama 223-8522

(Received 7 August 2000, Accepted 24 August 2000)

The preparation and response features of a micrometer-sized sodium ion-selective fiber optode based on a liquid membrane were described. The sensing membrane is a plasticized poly (vinyl chloride)-based copolymer with a neutral ionophore and an anionic dye. In order to fabricate a micrometer-sized fiber optode, a "micropipette fabrication method" was newly proposed to fix a liquid membrane-based optode on the small tip of an optical fiber probe. At the first stage of the investigation, it was found that the ionophore including a sodium ion in its cavity leached from the membrane phase. However, we have discovered that the problem can be resolved by using a "tailed" ionophore, which is an ionophore possessing a lipophilic long alkyl chain. The "tail" of the ionophore functions as an "anchor", which prevents leaching of the ionophore from the membrane phase into the water phase. The anchor effect of the tailed ionophore was clearly demonstrated with 6 μm-sized sodium ion-selective optodes. In addition, the problem of fluorescence distortion due to photobleaching and solvent effect was resolved by a ratiometric calibration in which the sensor response is monitored by the spectral shift of the dual-emission fluorescence. The sensor response of an 8 μm-sized fiber optode having ratiometric calibration was examined and successfully explained by response theory. Our method gives a general preparation for ultrasmall ion-selective fiber optodes because other ion-selective optodes can be obtained simply by replacing the tailed ionophore.

Keywords : microoptode; ion-selective optode; fiber optode; tailed ionophore; liquid membrane.

1 緒　　言

オプトードと呼ばれている光検出型の化学センサーは，1980年代中ごろに始まる近接場光学顕微鏡[1)2)]（アメリカではNSOM，ヨーロッパではSNOMと略される）の研究に強い影響を受け，急速に微細化が進み，現在，サブミクロン寸法の超微細化が可能になっている．その先駆的な研究は，米国ミシガン大学のコッペルマン教授ら[3)~5)]によって行われ，超微細化されたオプトードは，「ナノオプトード」と呼ばれ，ナノテクノロジーの一つに位置付けされる．ナノオプトードは，今まで以上に微小な空間の化学センシングを可能とし，その最も重要な応用の一つは，生きた細胞中の生化学センシングである[6)]．ヒトゲノムが全解読され，今後，ヒトゲノム研究が発現と機能の解明に向かうことを考えると，ナノオプトードはヒトゲノム研究において重要なツールになる可能性がある．

[*1] (財)神奈川科学技術アカデミー：213-0012　神奈川県川崎市高津区坂戸3-2-1
[*2] 東京工業大学総合理工学研究科：226-8502　神奈川県横浜市緑区長津田町4259
[*3] 慶應義塾大学理工学部：223-8522　神奈川県横浜市港北区日吉3-14-1
[*4] 現在所属　東京大学大学院工学系研究科：113-8656　東京都文京区本郷7-3-1

今までに確立したナノオプトード作製法の一つは，コッペルマン教授らによるもので，近接場光学顕微鏡プローブ先端の微小開口部に，光重合法を使って化学センシング材料を固定化するものである[3)~5)]．親水性ポリマーとして知られているポリアクリルアミドゲルを担体として，イオン感応性蛍光色素などのセンシング分子を固定化する．光重合による固定化法は，サブミクロン寸法の固定化を可能とし，オプトードの微細化に優れた方法である．しかし，光重合法に使える市販のセンシング分子が限られており，はん用性に欠ける問題があった．

この解決法の一つに，脂溶性液膜型のイオン選択性オプトード膜を利用することがあげられる[7)~9)]．このオプトード膜は，1990年ごろ，脂溶性液膜型イオン選択性電極の技術の延長線上に，鈴木ら[10)11)]やスイスETHのシモンら[12)]が提案をしたものである．その膜の成分は，可塑化ポリ塩化ビニルなどの脂溶性液膜にイオン選択性分子とpH感応型蛍光色素を保持したもので，イオン共同抽出/イオン対交換の原理により，イオン濃度を吸光/蛍光などの光信号として応答を示す．このオプトードの利点は，イオン選択性電極における技術資産を受け継いでいるため，Li^+，Na^+，K^+，NH_4^+，Mg^{2+}，Ca^{2+}，Zn^{2+}，Ag^+，Hg^+，Pb^{2+}，Al^{3+}などに対するイオン選択性分子が既に市販されており，はん用性が確保されていることである．

本稿は，上記の脂溶性液膜型イオン選択性オプトード膜を，近接場光学顕微鏡の光ファイバープローブの先端へ固定化し，マイクロメートル寸法にまで微細化したことについて述べる．特に，Na^+に対して選択性があるオプトードの微細化について詳しく研究をした．固定化法として，オプトード膜の溶媒溶液をマイクロピペット中に注入し，光学顕微鏡下でマイクロマニュピュレーターを操作しながら，光ファイバープローブの先端へ固定する新しい方法を開発した．また，微細化によって，イオン選択性分子（イオノホア分子）が溶出する問題に直面し，長アルキル鎖のテイルを持つイオノホア分子を使うと，溶出の問題を解決できることを見いだした．このように作製したオプトードを，高感度な光子計数法により蛍光測定した．更に，光退色や溶媒効果などによる蛍光強度変動の問題を，蛍光スペクトル測定により解決した．以上により，目的イオン濃度10^{-3}～10^{-1}の範囲で，高感度に応答を示すマイクロメートル寸法の超微細化オプトードを作製することができた．

2 理　論

2・1 イオン選択性オプトードの原理

イオン選択性オプトードは，可塑化ポリ塩化ビニル（PVC）などの脂溶性液膜を担体とし，中性イオノホア（S）などのイオン選択性分子と陰イオン性蛍光色素（AH）などのpH感応型蛍光色素を保持したもので，イオン対抽出/イオン交換の原理に基づいて，イオンを検出する．具体的には，次式の関係として与えられる．

$$S_o + i_w^+ + AH_o \Leftrightarrow SiA_o + H_w^+ \qquad (1)$$

ここで，添え字のoとwは，それぞれ，油相と水相に存在していることを意味し，i^+は目的イオン，H^+は水素イオンを示している．関係式（1）は，熱力学的平衡の式により，定量的に扱える．

$$K_{exch} = \frac{[SiA_o][H_w^+]}{[S_o][i_w^+][AH_o]} \qquad (2)$$

脱プロトン色素の割合をα，脂溶性膜中のイオノホア濃度を$[S_{tot}]$，陰イオン性蛍光色素濃度を$[A_{tot}]$とすると，水相の目的イオン濃度$[i_w^+]$は，

$$[i_w^+] = \frac{[H_w^+]}{K_{exch}(1-\alpha)([S_{tot}]-[A_{tot}]\alpha)} \qquad (3)$$

で与えられる．水相の水素イオン濃度$[H_w^+]$は，緩衝溶液により一定に保たれるので，脱プロトン色素の割合αを蛍光の測定で評価することにより，目的イオン濃度$[i_w^+]$が決められる．脱プロトン色素の割合αを蛍光測定で評価する方法は，主に二つある．一つは蛍光強度測定であり，もう一つは蛍光スペクトル測定である．蛍光強度測定の場合，脱プロトン色素の割合αは，

$$\alpha = \frac{F - F_N}{F_A - F_N} \qquad (4)$$

で与えられる．ここで，Fが測定される蛍光強度，F_NとF_Aは，オプトード膜中の陰イオン性蛍光色素すべてがそれぞれ，中性形と陰イオン形の場合の蛍光強度を示す．一方，蛍光スペクトル測定の場合，二つの波長における蛍光強度F_1とF_2の比$R = F_1/F_2$を測定することにより，脱プロトン色素の割合αが与えられる．

$$\alpha = \frac{RF_{2max} - F_{1min}}{(F_{1max} - F_{1min}) + R(F_{2max} - F_{2min})} \qquad (5)$$

ここで，F_{1min}とF_{1max}は蛍光強度F_1の最小と最大を示し，同様に，F_{2min}とF_{2max}は蛍光強度F_2の最小と最大を示す．一般に，蛍光強度測定よりも，蛍光スペクトル測定のほうが安定に，脱プロトン色素の割合αを決められる．特にオプトードを微細化する場合，蛍光色素の光退色や溶媒効果による蛍光強度変動が問題となり，蛍光スペクトル測定が有力な検出法となる．

3　実　　験

3·1　マイクロピペット固定化法

脂溶性液膜型のイオン選択性オプトードを，近接場光学顕微鏡の光ファイバープローブ先端に固定化するには，コッペルマン教授らの光重合による方法[3)~5)]は使えないため，新しい固定化方法を開発する必要がある．単に，光ファイバープローブ先端に塗布するのであれば，ディップコーテイングの方法も使えるが，寸法を制御することが難しい．著者らが開発した方法は，Fig. 1 に示すように，マイクロマニュピュレーターで制御されたマイクロピペットを使って，光ファイバープローブ先端に，マイクロメートル寸法でイオン選択性オプトードを固定化するものである．

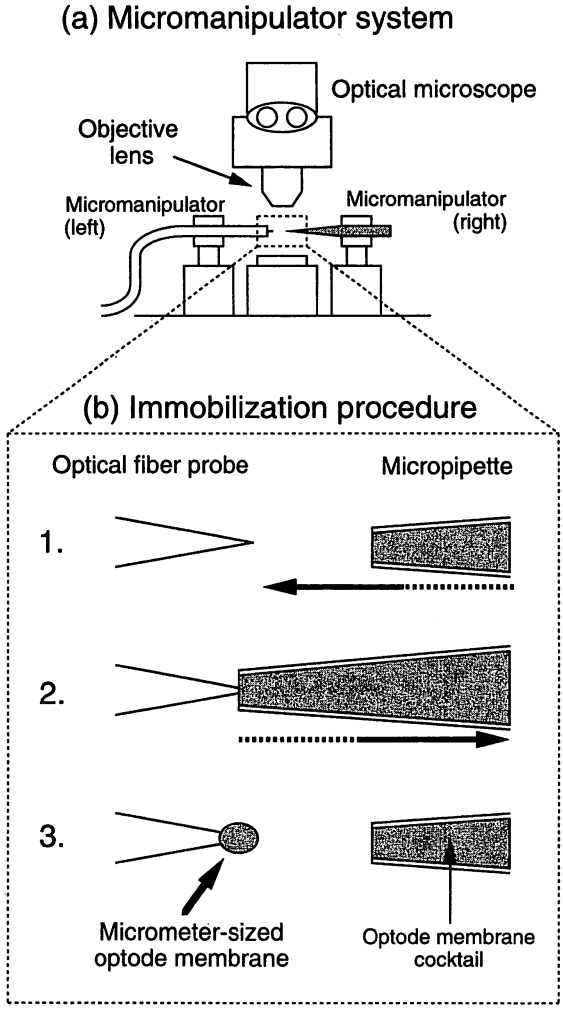

Fig. 1　Schematic diagram of the micromanipulator system and illustration of the micropipette fabrication method

(a) The system consists of two micromanipulators and an optical microscope. (b) Immobilization procedure to fabricate the micrometer-sized microoptode. 1) The micropipette and the optical fiber probe of SNOM are aligned coaxially. 2) The micropipette is made to approach the probe until the tip of the probe is inserted into the optode membrane cocktail in the micropipette. 3) The micropipette is removed from the probe, which consequently has a micrometer-sized optode membrane on the tip.

光学顕微鏡下で観察をしながら，光ファイバープローブ先端をマイクロピペット中のセンシング材料へ突っ込み，化学吸着によりセンシング材料を固定化する．光ファイバープローブは，近接場光学顕微鏡の技術として知られている，マイクロピペットプラーを使った加熱引伸法により作製した．加熱引伸法は，レーザーをガラス光ファイバーに照射加熱しながら，光ファイバー両端を引っ張り，引き伸ばし，先鋭化する方法である．このように作製した光ファイバープローブに，金属コーティングやシラン化処理によるガラス表面の改質は行っていない．一方，センシング材料の脂溶性液膜型イオン選択性オプトードは，ガラス表面への化学吸着力を増強するために，担体の脂溶性液膜のポリマーとして通常使われている PVC に代わって，親水基を含む塩化ビニルのコポリマー（OH-PVC）を使用した．コポリマーのヒドロキシル基とガラス表面のシラノール基の間に水素結合相互作用が働き，化学吸着力を増強すると考えられる．このマイクロピペット固定化法は，脂溶性液膜型イオン選択性オプトードを，1 から 10 μm 以上の広範囲の寸法で，しかも 1 μm 寸法の精度で，光ファイバープローブ先端に固定化することを可能にする．イオン選択性オプトード膜を固定化した光ファイバープローブは，簡易な真空装置で，オプトード膜中のテトラヒドロフラン（THF）溶媒を蒸発させて成膜し，性能を評価した．

3·2　イオン選択性オプトードの化学成分

本実験で使用したイオン選択性オプトードは，イオノホアと陰イオン性蛍光色素を，無水 THF を溶媒として，脂溶性液膜に混合したものである．脂溶性液膜は，ビス(2-エチルヘキシル)セバケート（BEHS）を可塑剤とし，ビニルアルコール 6 wt% とビニルアセテート 4 wt% と塩化ビニル 90 wt% からなるコポリマー（OH-PVC）を，BEHS : OH-PVC = 2 : 1 の重量比で混合したものである．陰イオン性蛍光色素は，蛍光強度測定の場合に，ジブロモフルオレセイン誘導体 {Fig. 2(a)} を使い，蛍光スペクトル測定の場合に，ヒドロキシクマリン誘導体 {Fig. 2(b)} を使った．陰イオン性蛍光色素の混合量は，脂溶性液膜に対し，ジブロモフルオレセイン誘導体の場合に 1.7 wt%，ヒドロキシクマリン誘導体の場合に 1.4 wt% とした．また，イオノホアは，陰イオン性蛍光色素の 2 倍のモル濃度の量になるように混合した．イオノホアは，Na^+ に対して高い選択性があるクラウンエーテル型のイオノホア（DD16C5，C-14DTM16C5，ODM16C5）を用いた．イオノホアは長鎖アルキル基によるテイル構造の有無で 2 種類に分類される．その化学構造式は，Fig. 3 の中に示した．

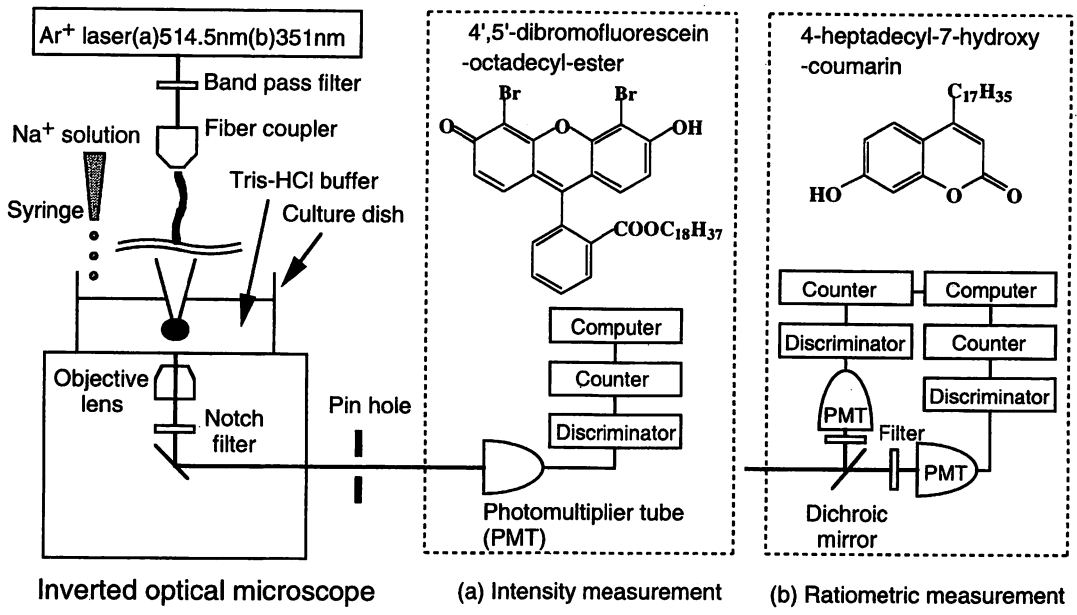

Fig. 2 Experimental setups of the miniature optode for (a) intensity measurement using a single-emission dye of 4',5'-dibromofluorescein-octadecyl-ester and (b) ratiometric measurement using a dual-emission dye of 4-heptadecyl-7-hydroxy-coumarin

The miniature optode is excited by the light of an Ar^+ laser system, and its fluorescence is measured with the time-resolved photon counting method. The optode is immersed in a buffer solution, whose Na^+ concentration is changed by adding droplets of NaCl solution into the culture dish with a syringe.

3・3 測定配置

Fig. 2 に，超微細化イオン選択性オプトードの目的イオンに対するセンサー応答を評価する測定系を示す．測定系は，溶液系と光学系に分けられる．

溶液系は，微細化オプトードのセンシング部が，pH が一定に制御された Tris-HCl 緩衝溶液中に保持され，同時に蛍光測定を行えるように，倒立光学顕微鏡を使って構成した．目的イオン（Na^+）濃度の制御は，緩衝溶液を入れたカルチャーディッシュの容器に，スポイトで NaCl 溶液を滴下することにより行った．

光学系は，光源として連続発振 Ar^+ レーザーを使い，シングルモードで発振した単色光を，ファイバーカップラーにより，超微細化オプトードの光ファイバーに導入した．レーザー光は，光ファイバー中を伝播し，μm 寸法のオプトード膜に達し，オプトード膜中の陰イオン性蛍光色素を励起する．陰イオン性蛍光色素は目的イオン濃度に応じた蛍光を発し，その蛍光を倒立光学顕微鏡の対物レンズにより集光する．集光した光は，ノッチフィルターによりレーザー光だけを分離した後，光子計数法により微弱な蛍光を高感度に検出する．

蛍光強度測定 {Fig. 2(a)} の場合は，蛍光の全強度を検出するのに対し，蛍光スペクトル測定 {Fig. 2(b)} の場合は，蛍光をダイクロイックミラーにより等蛍光点でスペクトルを 2 分割し，各蛍光強度を同時に検出し，コンピュータ上で二つの蛍光強度の比を計算する．蛍光強度測定の場合は，陰イオン性蛍光色素としてジブロモフルオレセイン誘導体を用いたため，励起波長を 514.5 nm とし，そのとき蛍光最大波長は約 540 nm であった．

一方，蛍光スペクトル測定の場合は，ヒドロキシクマリン誘導体を用い，励起波長を 351 nm，等蛍光点が約 400 nm であった．緩衝溶液の pH は，蛍光強度測定の場合に pH = 7.4 とし，蛍光スペクトル測定の場合に pH = 9 とした．

4 結果と考察

超微細化イオン選択性オプトードの応答特性を二つの方法により改善した．

4・1 イオノホアによる改善

オプトードの微細化に伴う問題の一つに，センシング膜中の化学成分の溶出がある．オプトードが微細化すると，体積に対する表面積の割合が大きくなるため，バルク寸法では問題とならない溶出の問題が顕著に現れてくる．

Fig. 3 はイオノホアの溶出に関するデータである．6 μm 寸法のオプトード {Fig. 3(a)} を使い，イオノホアの成分だけを変え，蛍光強度測定で目的イオン（Na^+）に対する光学応答を観測した {Fig. 3(b)}．分子構造に長いアルキル鎖のテイルを持つイオノホア C14-DTM16C5 と

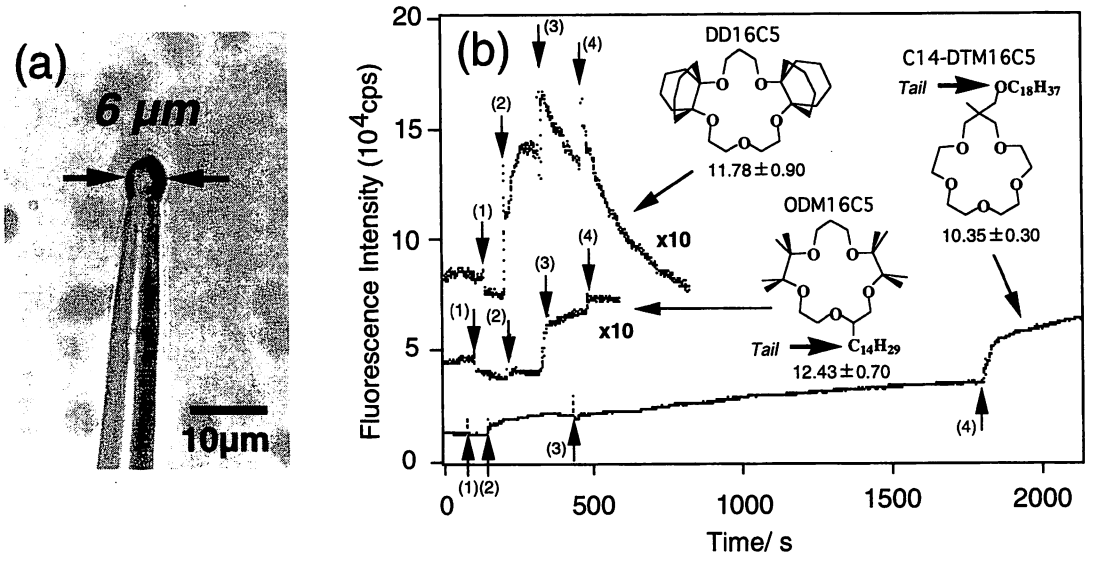

Fig. 3 Comparison of dynamic response profiles of 6-μm-sized optodes based on different types of ionophores: a non-tailed ionophore of DD16C5 and two tailed ionophores of C14-DTM16C5 and ODM16C5

Their lipophilicities are given below their chemical structures as values of log $P_{o/w}$, where $P_{o/w}$ is the distribution coefficient between the organic liquid and water. (a) A micrograph of the 6 μm-sized optode and (b) dynamic responses of three kinds of optodes. The arrows with numbers indicate when Na^+ droplets were added. The peaks accompanying the marks are due to a light flash to check the droplets falling into the culture dish. Na^+ concentrations in the solution were: initial state 0 M; (1) 3.8×10^{-4} M; (2) 4.1×10^{-3} M; (3) 4.0×10^{-2} M; (4) 2.9×10^{-1} M

ODM16C5 を使ったオプトードでは，目的イオン濃度に応じて安定した蛍光強度を示している．それに対し，テイルがないイオノホア DD16C5 のオプトードでは，瞬時に目的イオン濃度の増加に応じて蛍光強度は増加するが，その後その蛍光強度は指数関数的に減衰する．減衰の速さは，目的イオン濃度が高いほど速い．この結果は，超微細化オプトードでは，テイルのあるイオノホアを使わなければならない，という実用的に重要な結論を与える．

もう一つの重要なことは，テイル効果の化学的原因の解明である．バルク寸法において，使用した三つのイオノホアに基づくオプトードは，目的イオンに対してどれも再現性の良い応答を示す．通常，イオノホアの溶出は脂溶性値により判断されるが，使った三つのイオノホアの脂溶性値は，Fig. 3(b) の化学構造式の下に数値を示したようにほとんど同じである．しかも，溶出したテイルなしのイオノホア DD16C5 の脂溶性値（11.78）は，溶出しないテイルありのイオノホア ODM16C5 の脂溶性値（10.35）よりも，脂溶性値が高い．テイルを持つイオノホアが目的イオンを包接した状態は，分子構造の点で，界面活性剤などの両親媒性分子に分類されることに注目すると，ミセル，二分子膜，ベシクルなどの自己会合のミクロ構造から，テイル効果のメカニズムが類推される．自己会合の重要な概念は，疎水性引力と親水性疎力の相反するきっ（拮）抗力が，自己会合の形成を促進することである．この概念の導入により，イオノホアのテイルは脂溶性度を高める疎水性引力を起こすだけでなく，自己会合の推進力となる拮抗力を生み出し，その結果，微細化に伴う溶出を低く抑えられることになると理解できる．このように，イオノホアのテイル効果は，脂溶性値による巨視的な量ではなく，分子構造を考慮した微視的立場に基づいて説明する必要がある．この現象は，微小空間化学の一つの好例といえる．

4・2　光学測定系による改善

オプトードの微細化に伴う重要な問題に，蛍光色素の蛍光強度の変動に関する問題がある．一般的に，蛍光強度の変動には，光学系が由来のものと蛍光色素が由来のものと，2 種類がある．

光学系由来の原因は，レンズなどの光学素子が不安定なことである．しかし，この光学系由来の蛍光強度変動は，微細化オプトードでは本質的でない．一方，蛍光色素由来の例は，強励起による蛍光色素の光退色やセンシング膜の溶媒効果などである．これらの問題は，微細化オプトードに本質的なものである．

光退色の問題は，微小化寸法の 3 乗に比例して蛍光色素の量が減少するため，バルク寸法の場合と比べ，微細化すると顕著に現れる．また，溶媒効果の問題は，微細化に伴って体積に対する表面積の割合が増加するために，蛍光色素周りの環境が不均一になり，溶媒の効果だけで蛍光強

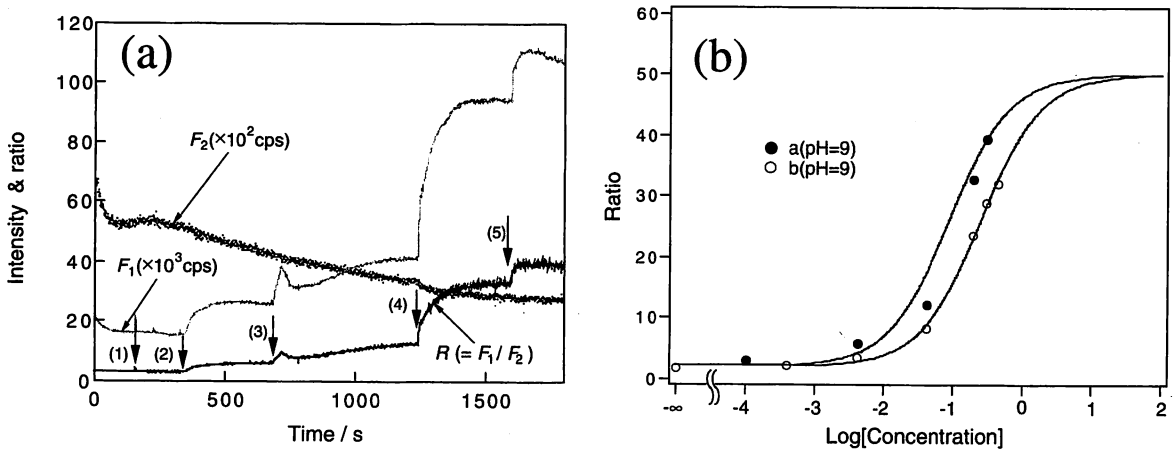

Fig. 4 Characterization of a 8-μm-sized optode having ratiometric calibration based on the tailed ionophore C14-DTM16C5 and the dual-emission dye 4-heptadecyl-7-hydroxy-coumarin

(a) Dynamic responses of the 8-μm sized optode. The profile of R is the dynamic response of the optode based on the ratiometric measurement. The profiles of F_1 and F_2 were obtained by measuring fluorescence intensities from the dual-emission dye at two different wavelengths. The profile of R is calculated by dividing the profile of F_1 by that of F_2. Arrows with a number indicate the point of a change in the Na^+ concentration: initial state 0 M; (1) 1.0×10^{-4} M; (2) 4.1×10^{-3} M; (3) 4.0×10^{-2} M; (4) 1.9×10^{-1} M; (5) 2.9×10^{-1} M. (b) Sensor responses and their response curve calculated by the theoretical equation. Data a denoted by closed circles result from the dynamic response of the profile R in Fig. 4 (a). Data b denoted by open circles were obtained from another optode.

度が増加したり減少したりする．このような蛍光強度の変動に対しては，蛍光スペクトルの変化を測定する方法が有効である．

Fig. 4は，蛍光スペクトル測定 {Fig. 2(b)} によって蛍光強度変動を補正し，超微細化オプトードの感度を向上した測定結果である．イオン選択性オプトード膜は，イオノホアにC14-DTM16C5，陰イオン性蛍光色素にヒドロキシクマリン誘導体を使用し，8 μm寸法のオプトードで測定した．Fig. 4(a) は，オプトードの目的イオン (Na^+) に対する光学応答を示している．F_1 は420から約500 nmの範囲の蛍光強度を示しているのに対し，F_2 は約360から385 nmの範囲の蛍光強度を示している．蛍光強度比 $R = F_1/F_2$ の計算により，蛍光強度の変動を補正できる．蛍光スペクトル測定が成果を上げていることが次の点で確認できる．すなわち，Fig. 4(a) おいて，F_1 と F_2 両方とも0～70秒の間に急速に減少し，70～340秒の間に緩やかな増加と減少をしているが，強度比 $R = F_1/F_2$ は常に一定である点である．

Fig. 4(a) のセンサー応答は，Fig. 4(b) の黒丸に示した．データ点は，実線で示した理論曲線と良い一致を示している．Fig. 4(b) の白丸は，ほぼ同じ寸法を持つ別の微細化オプトードのデータである．同じ測定条件でありながら，センサー応答が高濃度側に少し移動している．二つのセンサー応答の違いは，本実験の微細化オプトードの再現性の程度を示している．再現性を下げている原因として，オプトード膜中の化学成分の溶出が依然として考えられる．

各種イオン選択性を容易に実現できる高脂溶性液膜型イオン選択性オプトード膜を，近接場光学顕微鏡の光ファイバープローブ先端に固定化したマイクロメートル寸法の超微細化オプトードの作製に成功した．はん用イオン選択性オプトードでは，現状で，最も微細である．開発の過程において，マイクロピペットを使った新しい固定化法を確立し，微細化に伴うイオノホアの溶出の問題を解決した．溶出の問題は，長いアルキル鎖のテイル構造を持つイオノホアを使うと解決することを見いだした．また，光退色などの微細化に伴う蛍光強度の変動の問題を蛍光スペクトル測定により解決した．蛍光スペクトル測定によるセンサー応答の理論を展開し，得られた理論曲線は実験結果と良い一致を示した．以上の結果は Na^+ 選択性分子を用いたオプトードの実験から得られたものであるが，ほかのイオン選択性分子を用いることにより，はん用性のあるイオン選択性オプトードの微細化を実現できる[13]．

本研究の遂行に当たり，(財)日産科学振興財団の助成に感謝を致します．

文　献

1) 大津元一，河田　聡編："近接場ナノフォトニクスハンドブック", (1997), (オプトロニクス社).

2) M. Ohtsu (Ed.): "*Near-field nano/atom optics and technology*", (1998), (Springer-Verlag, Tokyo).
3) W. Tan, Z.-Y. Shi, R. Kopelman: *Anal. Chem.*, **64**, 2985 (1992).
4) W. Tan, Z.-Y. Shi, S. Smith, D. Birnbaum, R. Kopelman: *Science* (Washington, D.C.), **258**, 778 (1992).
5) Z. Rosenzweig, R. Kopelman: *Anal. Chem.*, **67**, 2650 (1995).
6) W. Tan, R. Kopelman, S. L. R. Barker, M. T. Miller: *Anal. Chem.*, **71**, 606A (1999).
7) M. Shortreed, E. Bakker, R. Kopelman: *Anal. Chem.*, **68**, 2656 (1996).
8) I. Koronczi, J. Reichert, G. Heinzmann, H. J. Ache: *Sens. Actuators B*, **51**, 188 (1998).
9) K. Kurihara, M. Ohtsu, T. Yoshida, T. Abe, H. Hisamoto, K. Suzuki: *Anal. Chem.*, **71**, 3558 (1999).
10) K. Suzuki, K. Tohda, Y. Tanada, H. Ohzora, S. Nishihara, H. Inoue, T. Shirai: *Anal. Chem.*, **61**, 382, (1989).
11) K. Suzuki, H. Ohzora, K. Tohda, K. Miyazaki, K. Watanabe, H. Inoue, T. Shirai: *Anal. Chim. Acta*, **237**, 155 (1990).
12) W. E. Molf, K. Seiler, B. Rusterholz, W. Simon: *Anal. Chem.*, **62**, 738 (1990).
13) K. Kurihara, M. Ohtsu, T. Yoshida, T. Abe, H. Hisamoto, K. Suzuki: *Anal. Chim. Acta*, in press.

要　旨

光検出型化学センサーの一つである光ファイバー型イオン・オプトードにおいて，新しい微細化の方法を確立した．イオン選択性分子（イオノホア分子）とpH感応性蛍光色素を保持した脂溶性液膜からなるイオン選択性オプトード膜を，近接場光学顕微鏡の光ファイバープローブ先端にマイクロメートル寸法で固定化して，超微細化イオン選択性オプトードを実現した．マイクロピペットによる新しい固定化方法を開発し，微細化に伴う溶出の問題を，長アルキル鎖のテイル構造を持つイオノホア分子を用いることにより解決した．このテイル効果は，微小空間化学の現象であり，分子構造に基づいた微視的な説明を必要とする．また，光退色などの微細化に伴う蛍光強度変動の問題を，蛍光スペクトル測定により解決した．以上の方法を用いるセンサーデバイスは，センシング膜中のイオノホア分子を交換するだけで目的のイオン選択性を容易に実現できることから，超微細化イオン選択性オプトードに関して一般的な方法を提供する．その例として，本稿は，Na^+ イオノホア分子に基づく，ナトリウムイオン選択性オプトードの超微細化について，プローブの作製と応答特性を詳細に検討した．

Nanofabrication and Atom Manipulation by Optical Near-Field and Relevant Quantum Optical Theory

MOTOICHI OHTSU, SENIOR MEMBER, IEEE, KIYOSHI KOBAYASHI, MEMBER, IEEE, HARUHIKO ITO, AND GEUN-HYOUNG LEE

Recent progress on application of interactions between optical near-field and nanoscale materials and atoms is reviewed. Photochemical vapor deposition of Zn dots and lines with the size of sub-100 nm has been realized by using an ultraviolet optical near field. Deposition of nanoscale ZnO is also revealed. Manipulation of atoms is then described to control the thermal motion of atoms in high vacuum. Experimental and theoretical results of manipulation by using optical near field generated on a prism surface, hollow fiber, and fiber probe are presented. Finally, quantum theoretical treatment of optical near field is given.

Keywords*—*Atom manipulation, nanostructure, optical near fields, quantum theory.

I. INTRODUCTION

Basic process governing near-field optics is the short-range electromagnetic interaction between the probe tip and sample in the optical frequency region. In the case when this interaction is sufficiently strong, the sample structure and conformation can be optically modified, and, thus, this modification can open new applications, such as fabrication of nanometric materials and manipulation of atoms. Based on this consideration, this paper reviews the recent progress of authors' works on fabricating nanometric materials and manipulating atoms by optical near field. Further, novel theory is also reviewed, which can be used for designing experimental systems on nanofabrication and atom manipulation, and to analyze experimental results.

Manuscript received September 20, 1999; revised February 7, 2000.

M. Ohtsu is with the Interdisciplinary Graduate School of Science and Technology, Tokyo Institute of Technology, Yokohama 226-8502, Japan, and also with the ERATO Localized Photon Project, Japan Science and Technology Corporation, Tokyo 194-0004, Japan (e-mail: ohtsu@ae.titech.ac.jp).

K. Kobayashi and G. H. Lee are with the ERATO Localized Photon Project, Japan Science and Technology Corporation, Tokyo 194-0004, Japan (e-mail: kkoba@ohtsu.jst.go.jp; ghl@ohtsu.jst.go.jp).

H. Ito is with the Interdisciplinary Graduate School of Science and Technology, Tokyo Institute of Technology, Yokohama 226-8502, Japan, and also with PRESTO, Japan Science and Technology Corporation, Okayama 700-0904, Japan, and the Kanagawa Academy of Science and Technology, Kawasaki 213-0012, Japan. (e-mail: ito@ae.titech.ac.jp).

Publisher Item Identifier S 0018-9219(00)08973-8.

In Section II, we review experimental results on depositing nanometer-sized metallic Zn pattern by photochemical vapor deposition induced by the optical near field. Results on depositing ZnO, a semiconductor emitting a blue light, will be also presented. To explore the new field of atom manipulation, controlling thermal motion of Rb atoms by optical near field is reviewed in Section III. In order to analyze the local interaction between optical near field and matter or atoms, Section IV reviews the theoretical formalism on Yukawa potential model. Section V summarizes the main results presented by this paper.

II. NANOMETRIC FABRICATION

In order to realize the photonic devices composed of nanometric-sized elements, experiments on the fabrication of nanostructure by photoenhanced chemical vapor deposition (PE-CVD) under illumination by optical near field have been carried out.

So far, lithographic technology has been widely utilized for the fabrication of submicrometer structures. However, with the complexity of the process and with the damage of substrate and film by etchants, it has a lot of problems that still need to be solved. As a technology to solve those problems, the PE-CVD method has been attracting attention. Based on photochemical reaction, PE-CVD offers not only the possibility for the lateral integration of different structures (different sequence of layers, materials, thickness, and dopants) in a truly single growth run [1], [2] but also the option of chemical selective growth by varying the wavelength of used light source.

On the other hand, optical near field is a light with its energy concentrated within nanometric dimension smaller than the wavelength of light [3], [4], which enables us to deposit various materials on nanometric dimension by utilizing in photodecomposition of chemical gases. In addition, optical near field has been applied in a microscopy to break out the diffraction limit of light, resulting in nanometric resolution [5]–[7]. Also, on account of the nanometric resolution, it has been employed for measuring the optical properties of nanostructures [8]–[10]. Therefore, the combination

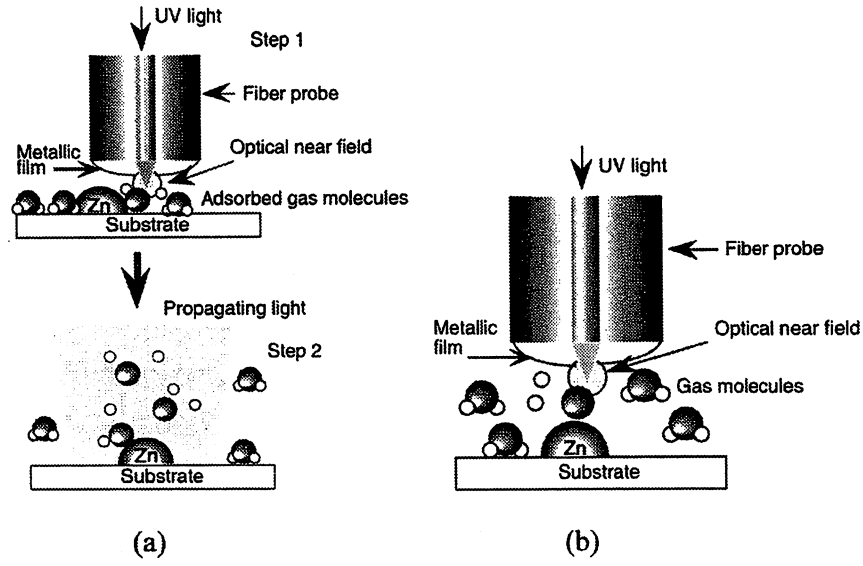

Fig. 1. Principles of NFO-CVD. (a) Prenucleation method: Step 1: formation of nuclei by the photodecomposition of adsorbed molecules, Step 2; growth of prenucleated area by propagating far field light. (b) Gas phase direct photodecomposition method.

of near-field optical technology with the PE-CVD process appears to be the most suitable technology for the integration of nanometer-scale elements because it not only allows us to fabricate nanostructures, but also gives a dual advantage of the *in situ* measurement of the optical properties of the fabricated nanostructures.

A. Principle and Method

The PE-CVD combined with optical near field, i.e., near-field optical-CVD (NFO-CVD), was carried out by utilizing the optical near field generated from the subwavelength aperture at the tip of a probe introduced into vacuum chamber. The scanning of the probe was performed by typical near-field optical microscope system.

As NFO-CVD is based on photodissociation reaction; for deposition it is necessary for reactant molecules to adsorb photons with higher energy than its dissociation energy. Hence, as the light source, light with higher energy than dissociation energy of reactant molecule should be used.

The deposition mechanisms using optical near field are represented in Fig. 1, which demonstrates two methods. One is prenucleation method to fabricate prenuclei by decompositing only adsorbed molecules on the substrate with optical near field [Fig. 1(a)] [11]. The process consists of two steps. In the first step, metalorganic gas is filled into the vacuum chamber for a few minutes and then evacuated, which leaves a few adsorbed monolayers on the surface of substrate. By decomposing the adsorbed molecules with optical near field, nuclei for growth are formed when patterning of the prenuclei is executed by scanning of the probe. In the second step, conventional propagating light is directed onto the prenucleated area in the presence of a parent gas, and then the decomposed metal atoms are selectively deposited on the preexisting nuclei. This technique has the advantage of being free from the deposition at the probe tip; otherwise, it has the drawback that the lateral integration of various materials is not easy due to using the propagating light in the second step.

The other method is to directly deposit metal atoms by gas phase photodissociation of metalorganic gas with optical near field [Fig. 1(b)] [12]. The advantage lies in the possibility of selective deposition of various materials by changing parent gases, which is useful for lateral integration.

B. Depositing Zinc

Now, let us discuss the deposition of Zn as an example of NFO-CVD by using a diethylzinc (DEZ) as a parent gas. This molecule adsorbs a light with photon energy higher than 4.76 eV (wavelength below $\lambda = 260$ nm), and photodissociation reaction occurs as follows:

$$Zn(C_2H_5)_2 + 2.256\ \text{eV} \rightarrow ZnC_2H_5 + C_2H_5$$
$$ZnC_2H_5 + 0.9545\ \text{eV} \rightarrow Zn + C_2H_5.$$

Thus, the second harmonic light (SH light) of Ar^+ laser ($\lambda = 244$ nm) and ArF excimer laser ($\lambda = 193$ nm) were used as the light source for photodissociation of DEZ gas. Fig. 2(a) shows the schematic diagram of the experimental setup. SH light was generated in BBO crystal placed in the built-up cavity. For the purpose of generating the optical near field with sufficient power density to decompose DEZ gas, an ultraviolet (UV) fiber with transmission loss as low as 1.1 dB/m at 244 nm was developed to fabricate the probe. The UV probe coated with 200-nm-thick Al film after being tapered by chemical etching [13]. The shape of this probe is shown in Fig. 2(b). The throughput of the fiber probe was 1×10^{-4}, and the power density at the tip of the fiber probe with a sub-100-nm aperture for 1 mW of UV light was as high as 1 kW/cm^2. The separation between the probe and the substrate was maintained within several nanometers by shear-force technique using a tuning-fork-based probe [14].

Fig. 3 shows the shear-force image of the loop-shaped Zn pattern on glass substrate produced by the prenucleation

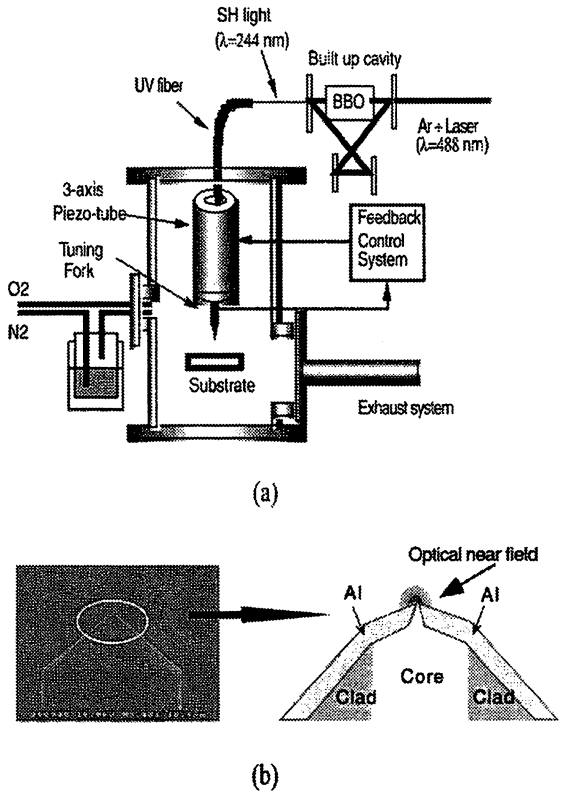

Fig. 2. (a) Schematic diagram of the experimental setup. (b) SEM and cross sectional images of the tip of the fiber probe for UV light.

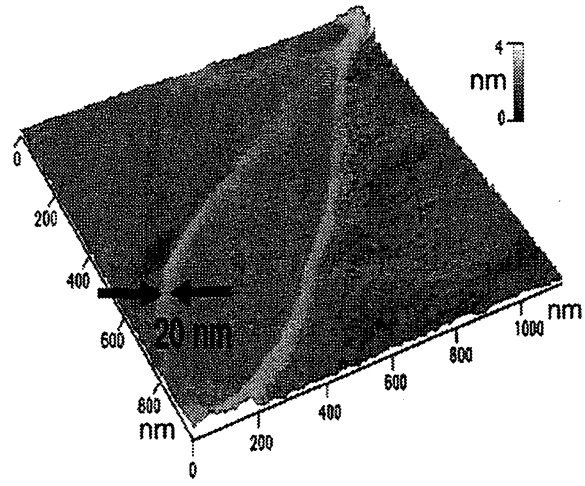

Fig. 3. Shear force image of a loop shaped Zn deposit on glass produced by prenucleation method.

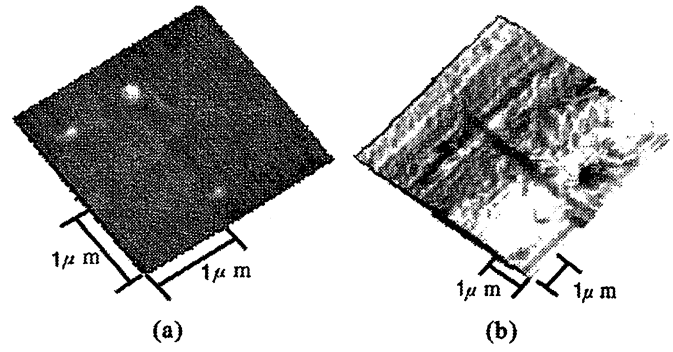

Fig. 4. Shear force image of (a) Zn nanodots and (b) T-shaped pattern fabricated on glass by direct photodecompostion in gas phase.

method [11]. The vacuum chamber was evacuated to below 10^{-5} torr prior to the prenuclei fabrication stage, then filled with about 10 torr of DEZ gas, maintaining at this pressure for 20 min. Next, the chamber was reevacuated to the pressure of 10^{-5} torr, which leaves an adsorbed layer of a few monolayers on the surface of substrate. Prenucleation was performed by delivering the SH light on the substrate covered with adsorbed molecules using a fiber probe. Nuclei of Zn were formed by the decomposition of DEZ gas adsorbed on the substrate with the optical near field at the tip of the fiber probe. In the growth stage after nuclei fabrication, DEZ gas was refilled in the chamber with a few torr, and an unfocused ArF excimer laser with the maximum energy of 10 mJ was directly irradiated on the prenucleated substrate. Then the growth proceeded only on the preexisting nuclei.

As seen in Fig. 3, the minimum width of the pattern is as small as 20 nm. The width achieved here is two orders smaller than the minimum width so far reported by conventional PE-CVD using far-field light [15]. Since the measured width includes the resolution of a shear-force microscope depending on the shape of the used probe, the intrinsic width can be smaller than the value estimated from Fig. 3.

Next, we discuss the results from the direct gas phase photodissociation method. Fig. 4(a) and (b) shows the shear-force images of deposited Zn dots and a T-shaped pattern. The gas pressure and the input power of SH light were 1 mtorr and 10 mW, respectively. In the fabrication of dots, optical near field on the probe tip was illuminated over five spots at the interval of 800 nm on the substrate for a few seconds. As shown in Fig. 4(a), the positions of dots are spaced by 800 nm in excellent agreement with the spacings of the illuminated points, which establishes high controllability of the positioning in fabricating nanostructures by this technique. The T-shaped pattern was prepared by scanning the substrate at a speed of 10–50 nm/s. A glance at Fig. 4(b) is sufficient to explain that NFO-CVD makes it possible to fabricate subwavelength-scale structures with control of their size and position. One disadvantage of this method is that the probe tip is also gradually covered with depositing material while fabricating a nanostructure on the substrate. In our experience, however, this only became a problem after a few hours of operation, while only a few seconds are necessary to fabricate a nanostructure. Therefore, it is not a serious problem. The NFO-CVD technique also allows us to fabricate nanostructures of oxides and semiconductors as well as metals containing Zn, Al, Cr, and W.

In order to examine the effect of optical near-field energy on the growth, an experiment was performed by varying illumination time at a constant gas pressure of 1 mtorr and input SH light power of 15 mW. The substrate was kept at room temperature, and SH light power at the probe tip was estimated to be 300 nW by a broad-area Si photodiode (sensor area: 5.8 × 5.8 mm^2) at a distance of a few millimeters apart

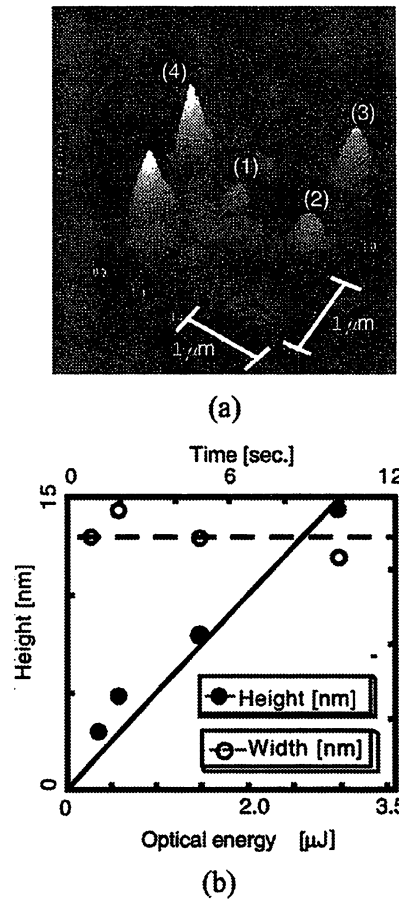

Fig. 5. (a) Shear force image of Zn dots fabricated at different optical near field energies. (b) Variation of the height and diameter of the deposited Zn dots.

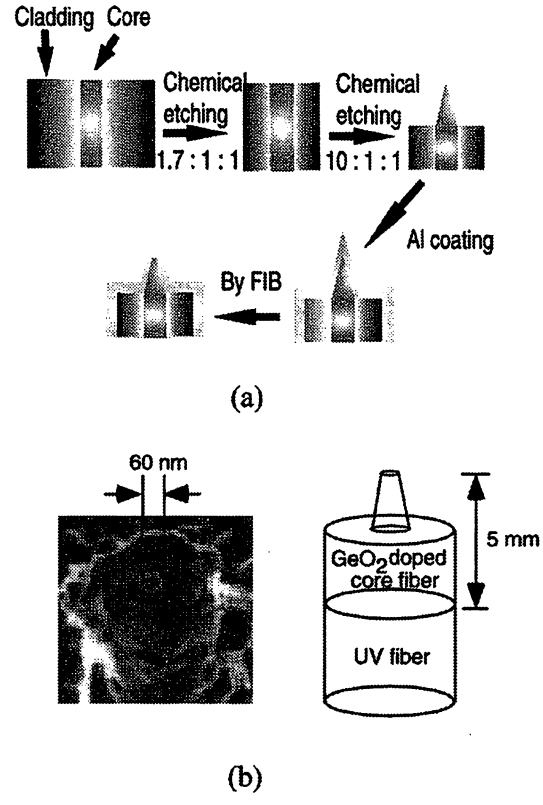

Fig. 6. (a) Fabrication method of a fiber probe. (b) SEM image of the tip region of the fabricated fiber probe.

from the tip. The value of the optical near-field energy was evaluated by measured SH light power × illumination time.

Fig. 5(a) and (b) represents the shear-force images of deposited dots and the variation of height and diameter of the shear-force image of the dots as a function of optical near-field energy, respectively. The optical near-field energies corresponding to fabrication of dots (1), (2), (3), and (4) were 0.3, 0.6, 1.5, and 3.0 μJ (illumination time: 1, 2, 5, 10 s), respectively. The diameter was almost constant with respect to the optical near-field energy, whereas the height increased linearly at the rate of about 5 nm/μJ in proportion to the increase of the energy. This shows that the size of dots depends on the spatial distribution of optical near field in the direction lateral to the substrate surface, while relying on the energy of optical near field in the normal direction. Thus, the aspect ratio of the dot, i.e., the ratio of its height to diameter, increased proportionally with the increase of optical near-field energy at a ratio of about 0.03/μJ.

One of the most attractive features of this technique is its high spatial resolution. The lateral size of a fabricated pattern depends on the spatial distribution of the optical near field, and its reproducibility also depends on the reproducibility of fabricating probes. Currently used probes are made of optical fiber with GeO_2 doped core and have shown high resolution and high reproducibility. But the transmission loss for the light of 244 nm (96 dB/m) is so high that the fiber cannot be used in UV region. To increase the reproducibility and spatial resolution of UV fiber probe, we spliced fiber probe with GeO_2 doped core to the tip of UV fiber. With the fiber probe, the tip was prepared by a two-step etching process [16]. Fig. 6(a) shows a schematic diagram of the fabrication method. During the first step, the cladding diameter was reduced by immersing in BHF with a volume ratio of [40 wt.%NH_4F aqueous solution] : [50 wt.%HF acid] : [deionized water] = 1.7 : 1 : 1. In the next step, the fiber was selectively etched in the same kind of solution with a volume ratio of 10 : 1 : 1, while the temperature was kept at 25 °C to obtain a single-tapered profile. After completing the etching process, the fiber was coated with 200-nm-thick Al by vacuum evaporation. In order to form an aperture, the Al film was removed from the tip of the probe by focused ion beam. Fig. 6(b) shows a scanning electron microscope (SEM) image of a fabricated probe with an aperture of 60 nm. This probe is fabricated with highly reproducible aperture size less than 100 nm. Fig. 7(a) and (b) shows the shear-force image of deposited dots by using a probe with an aperture diameter of 60 nm and cross sectional profile along the dashed line, respectively. Two dots with a diameter of 60 and 70 nm (full width at the half-maximum of the cross sectional profile) were fabricated at a very close distance of 100 nm. The diameter of the dots was comparable with aperture diameter of the used probe, which suggests that the smaller patterns can be fabricated by using a fiber probe with smaller aperture. Since the measured diameter of the dot image includes the resolution of the shear-force microscopy depending on the shape of the

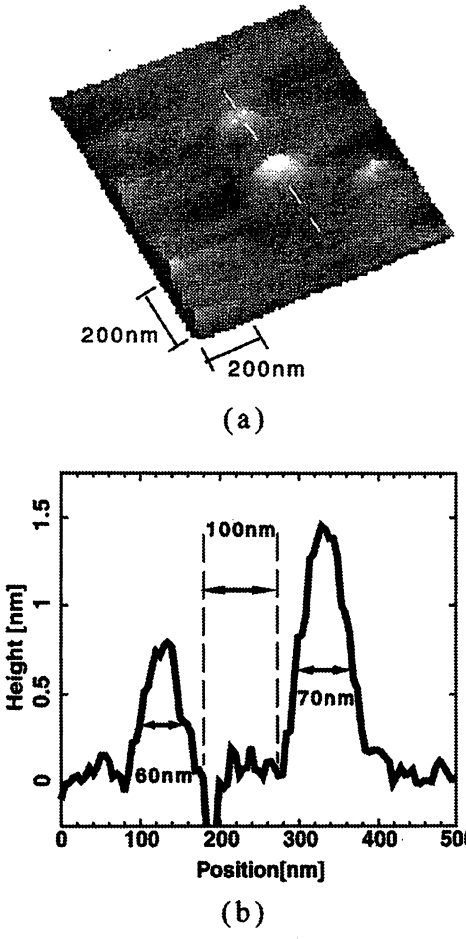

Fig. 7. (a) Shear force image of Zn dots fabricated by using a spliced fiber probe with the aperture size of 60 nm. (b) Cross sectional profile of the dots along the dashed line in (a).

used probe, intrinsic diameter can be smaller than the value estimated from Fig. 7.

C. Depositing Zinc Oxide

One of the advantages in this NFO-CVD is that there is no limitation in regard to substrate and film materials. Another technique in which CVD is combined with scanning tunneling microscopy (STM) has been reported to successfully produce a nanostructure with dimensions close to the atomic level [17]. However, the main drawback comes from the impossibility of using nonconductive substrates and growing nonconductive films. The limitation is eliminated by using optical near field. As an example, let us demonstrate the nanofabrication of ZnO on α-Al_2O_3 substrate as an insulator [18].

As a preliminary experiment, ZnO films were deposited by PE-CVD method using a propagating far-field light. Here, we used the reaction between oxygen and DEZ conveyed by a carrier gas (Ar) into the chamber during the irradiation by the second harmonic light ($\lambda = 244$ nm) of Ar^+ laser. We selected (0001) α-Al_2O_3 as the substrate for the epitaxial growth of ZnO. The reaction chamber was initially evacuated to pressures in the low 10^{-5} or 10^{-7} torr range, then filled with the reactant gases with the ratio of DEZ : O of 1 : 10 at a working pressure of 10 mtorr. The chamber pressure was maintained constantly at 10 mtorr during growth. In

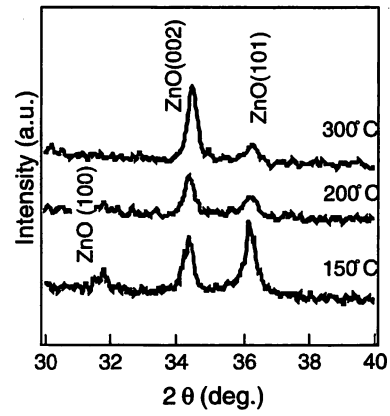

Fig. 8. X-ray diffraction patterns of ZnO films grown at the substrate temperatures of 150 °C, 200 °C, and 300 °C.

order to find the optimal growth conditions, the crystallinity, stoichiometry, optical transmission, and photoluminescence were evaluated. The crystallinity and the stoichiometry were evaluated by X-ray diffraction (XRD) measurement using Cu Kα radiation and X-ray photoelectron spectroscopy (XPS) using Al Kα X-ray. The optical transmission measurements were carried out by a double-beam monochromator in atmospheric ambient at wavelengths from 300 to 1000 nm to measure the optical energy bandgap of the films. The photoluminescence was measured at room temperature using a continuous-wave (CW) He–Cd laser as an excitation light source.

The PE-CVD of ZnO was carried out for 10 min within a range of the substrate temperature from room temperature to 300 °C. The energy density of the laser source and the spot size were 10 mW and 600 μm, respectively. The films were grown on only irradiated area, and the photoirradiation effect for the deposition rate was clearly observed for all substrates.

Fig. 8 shows X-ray diffraction patterns of ZnO films deposited at various substrate temperatures. The rise in the surface temperature of the substrate from UV light was negligible, for the light power was as low as 0.2 mW/cm^2, which means that the deposition resulted from photochemical reaction between DEZ and oxygen. The film deposited at room temperature exhibits no XRD reflection lines, which implies that it is essentially amorphous. Crystalline films were grown at substrate temperature over 100 °C, and the films with c-axis oriented crystalline, exhibiting the (002) XRD lines, were grown at substrate temperature above 150 °C. With the increase of substrate temperature above 150 °C, the intensity of X-ray peak from (002) planes became stronger, and other peaks such as the (101) peak became weaker. The c-axis lattice constant was estimated to be 0.5207 nm from the peak position of the (002) line, which is comparable to the c-axis value of 0.5206 nm reported for bulk ZnO [19]. It indicates that these films have a high-quality crystalline structure. The stoichiometry was confirmed from the XPS spectrum for the planar films. For the films deposited at the substrate temperature above 150 °C, the atomic ratios of Zn : O were also 1.00 : 1.00 within an accuracy of a few percent.

The optical properties were also investigated. Fig. 9 shows the optical transmission spectra of films deposited at substrate temperatures from 150 °C to 300 °C. Transmission fell

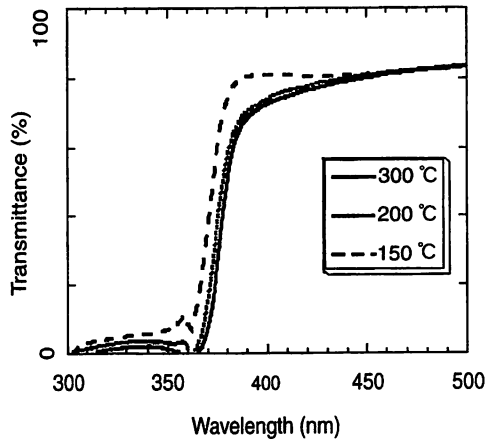

Fig. 9. Transmittance spectra of ZnO films measured at room temperature.

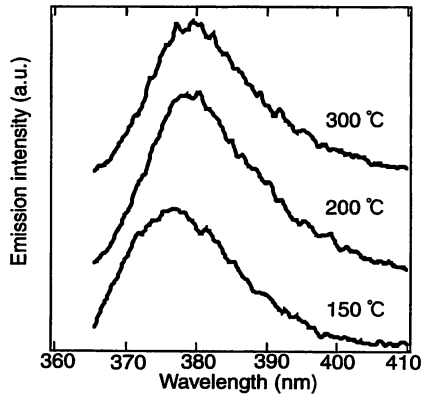

Fig. 10. Photoluminescence spectra taken at room temperature for the ZnO films deposited at substrate temperature of 150 °C, 200 °C, and 300 °C.

off steeply at around 380 nm, characteristic of high-quality ZnO films. From the plot of wavelength versus the absorption coefficient, optical bandgap energies ranging from 3.26 to 3.31 eV were estimated, which is identical to the value recorded for high-quality ZnO films [20].

The photoluminescence spectra were measured using the 325-nm line of a CW He–Cd laser. Fig. 10 shows the emission spectra measured at room temperature from the films deposited at the substrate temperature from 150 °C to 300 °C. The emission peak position is coincident with the expected energy of the free exciton, and even at room temperature a strong free exciton emission at 380 nm is clearly observed [21], [22]. This confirms that if we use the PE-CVD method at a low temperature, ZnO film emitting UV light at room temperature can be fabricated. This is the first observation of room-temperature UV from the ZnO films deposited by PE-CVD.

Under the growth conditions found by the preliminary experiment described above, the ZnO nanostructure fabrication was carried out by NFO-CVD. The fabrication was performed by introducing the SH light of Ar^+ laser onto the α-Al_2O_3 substrate surface through the fiber probe, which is shown by Fig. 6(b). The maximum power of the SH light was 10 mW, which means that the light power density at the probe

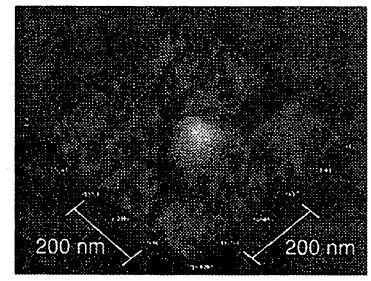

Fig. 11. Shear force image of ZnO dot deposited on the (0001) α-Al_2O_3 substrate.

tip was on the order of several kW/cm^2. During the deposition, sample-probe tip separation was maintained at 10 nm by shear-force technique.

Fig. 11 shows the shear-force image of fabricated nanometric scale ZnO. The dot was 200 nm diameter and 5 nm height. The diameter is smaller than the wavelength of the irradiating light source. However, because this value includes the broadening due to the resolution of the shear-force microscopy, the real diameter should be much smaller than that observed. We have actually succeeded in making Zn dots and wires below 100 nm with the same probe by optimizing the growth conditions, as shown in Fig. 7.

We demonstrated that with using optical near field, we can realize the fabrication of ZnO nanostructures with the sizes below the wavelength of the light, emitting the UV light even at room temperature by fabricating under proper growth conditions.

D. Future Outlook

The NFO-CVD constitutes a very promising tool for *in situ* patterning of nanostructures. Nanoscale Zn dots and lines with the size of sub-100 nm have been successfully realized in a single growth step. We also revealed that ZnO nanostructures with various shapes, emitting the room-temperature UV light, can be actualized. In addition, the controllability and reproducibility of the technique in fabricating nanostructures at desired positions is much higher than any other conventional self-organized growth technique of semiconductor nanostructures. What is better, as it is based on photodissociation reaction, selective growth of various materials (i.e., metals, oxides, insulators, and semiconductors) can be accomplished by the choice of light source, which allows us to realize a nano-photonic integrated circuit composed of nanostructures. Optical near-field technology offers the opportunity to modify surfaces and develop new nanostructures that may exhibit quantum effect due to their extremely small size.

III. Manipulation of Atoms

Fabrication of nanometric substances described in the previous section leads to atomic-scale manipulation and processing as an ultimate technique. Much attention has been devoted, for the past two decades, to control of atomic motion with laser light [23]. Moreover, the possibility of manipulating a single atom, ion, and molecule has opened up with the development of near-field optical techniques [3],

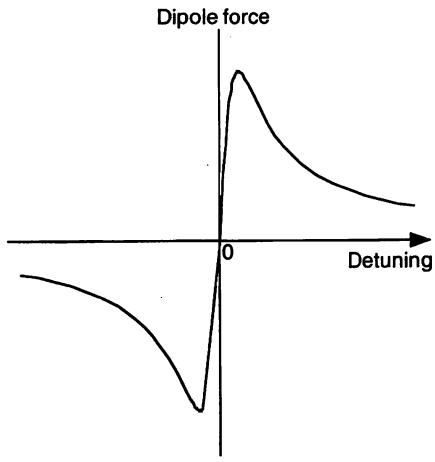

Fig. 12. Dipole force plotted as a function of the detuning of a light frequency from a resonant atomic one. The dipole force is repulsive in the region where the detuning is positive (blue detuning), while attractive in the region where the detuning is negative (red detuning).

[4], [24]–[27]. Since the optical near field is not affected by diffraction in contrast to propagating light, we can expect to use the optical near field localized in a nanometric region for controlling atoms with pinpoint accuracy much beyond the diffraction limit.

In principle, we deal with the dipole force of an optical near field on atoms [27], [28]. When the light frequency is slightly detuned from an atomic resonant frequency, the dipole force works in the direction where the light intensity changes. It should be noted that the direction of the dipole force depends on the frequency detuning. Fig. 12 shows the dispersion-like character of the dipole force with respect to an atomic resonant frequency. If the light frequency is higher than the atomic resonant one, which is called blue-detuning, the dipole force acts in the direction where the light intensity weakens: i.e., the dipole force becomes repulsive in a region where the detuning is positive. In the opposite case, the dipole force becomes attractive. On the other hand, the strength of the dipole force is in proportion to the gradient of light intensity as well as the intensity itself. Therefore, the optical near field whose intensity exponentially decays exerts the dipole force enough to greatly change the thermal atomic motion with a velocity of more than 100 m/s. Incidentally, by virtue of the resonant character, we can manipulate atoms species- and state-selectively.

In this section, we present several schemes of atom manipulation by means of optical near fields. First, glancing at reflection of atoms by a planar optical near field, we introduce the method of guiding atoms through a hollow optical fiber, including a photoionization spectroscopic experiment. Second, we consider atom deflection and trap with a fiber probe. These possibilities are shown from estimations of the deflection angle and the trap potential based on the Yukawa-type intensity distribution of the optical near field. In addition, we touch upon the measurement of the spatial intensity distribution of an optical near field in the vicinity of the tip of a fiber probe. Finally, we present a method of generating a cold atomic beam required for the demonstration of the atom manipulation experiments with fiber probes.

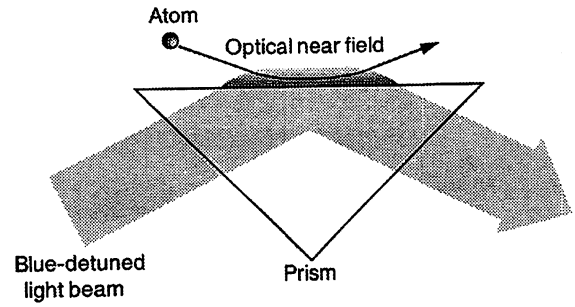

Fig. 13. Atom reflection with a prism. An optical near field induced on a prism surface by total-internal reflection of a blue-detuned light beam reflects an atom approaching the prism surface.

To this end, an atom funnel technique can be used, involving the Sisyphus cooling of atoms.

A. Atom Reflection with a Prism

Atoms can be reflected by the optical near field with a blue detuning [27]. Fig. 13 shows an atom mirror induced on a plane surface of a prism. When the total-internal reflection of a light beam takes place, an optical near field, which is often called an evanescent wave in this case, filters out of the surface in a region of less than a wavelength. Under a blue-detuning condition, the optical near field works as a mirror to reflect atoms approaching the prism surface if the light intensity is sufficiently strong.

The first demonstration of the atom reflection was performed by Balykin *et al.* with an Na atomic beam [28]. Afterward, Aminoff *et al.* reported that Cs atoms repeatedly bounced on a prism surface with the blue-detuned optical near field as if on a trampoline [29].

As is well known, the van der Waals force acts on an atom near a dielectric surface. Contrary to the case of a Rydberg state atom [30], there has been no effective method of measuring the van der Waals force on a ground state atom so far. Aspect *et al.* estimated the strength of the van der Waals force on an atom in a hyperfine ground state by using the atom reflection technique [31]: they scanned the light frequency and examined the threshold frequency where the reflection cannot take place because of balance between the repulsive dipole force and the attractive van der Waals force. This is based on the fact that the strength of the dipole force also depends on the frequency detuning.

B. Atom Guidance With a Hollow Fiber

The atom reflection by an optical near field can be applied to an atom guidance scheme with a hollow optical fiber [32]–[34]. Fig. 14 shows the outline of the atom guidance. When a light beam is coupled to the core of a hollow fiber, an optical near field appears in the hollow region as surrounding the inner wall surface. Under a blue-detuning condition, an atom entering the hollow region is reflected by the optical near field whenever it approaches the inner wall and then guided through the hollow fiber with few losses, if the light intensity is sufficiently strong.

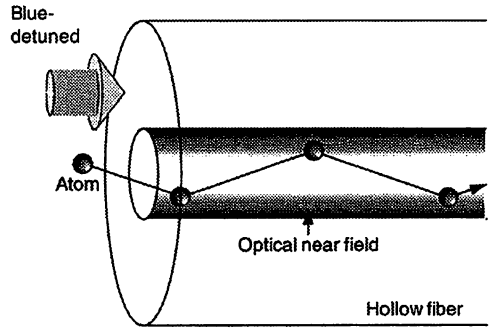

Fig. 14. Atom guidance with a hollow fiber. An optical near field produced in a hollow region by coupling of a blue-detuned light beam to the core reflects atoms approaching the inner wall surface and guides them through the hollow region.

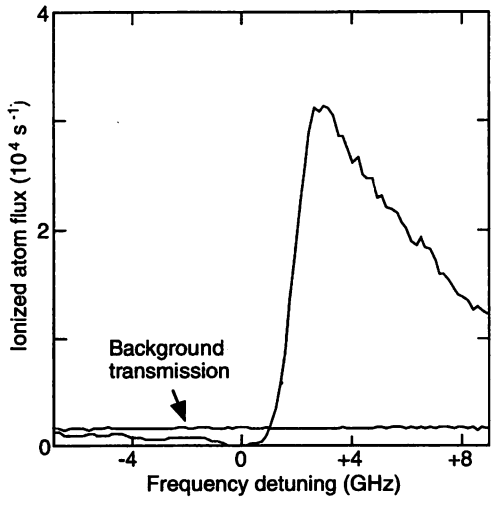

Fig. 15. Two-step photoionization spectrum on ^{85}Rb atoms guided through a hollow fiber with a length of 3 cm and a hollow diameter of 7 μm. The ionized atom flux is plotted as a function of the frequency detuning measured with respect to the $5S_{1/2}$, $F = 3$ upper ground state. The two-step photoionization is carried out with a diode laser tuned to the $5S_{1/2}$, $F = 3 \rightarrow 5P_{3/2}$, $F = 4$ transition and a high-power Ar–ion laser with a wavelength of 476.5 nm. The background transmission signal is obtained in the case without guide light from a Ti : Sapphire laser.

The intensity distribution of the optical near field in the hollow region depends on the propagating mode excited in the hollow fiber. The fundamental mode is approximately given as the LP_{01} mode [34]. Since the optical near field originating from the LP_{01} mode has a homogeneous intensity distribution without node around the inner wall, the LP_{01} mode is suitable for the atom guidance. In fact, we can selectively excite the LP_{01} mode by adjusting the incident angle in coupling a light beam to the core.

The experimental demonstrations were performed with Rb atoms whose resonant wavelength is 780 nm [35], [36]. Fig. 15 shows a photoionization spectrum of the ^{85}Rb atoms guided through a hollow glass fiber with a length of 3 cm and a hollow diameter of 7 μm [36], in which the ionized atom flux is plotted as a function of the frequency detuning measured with respect to the $5S_{1/2}$, $F = 3$ hyperfine ground state. The photoionization was carried out in two steps: a diode laser excites the ^{85}Rb atoms in the $5S_{1/2}$, $F = 3$ hyperfine ground state to the $5P_{3/2}$, $F = 4$ excited state, and

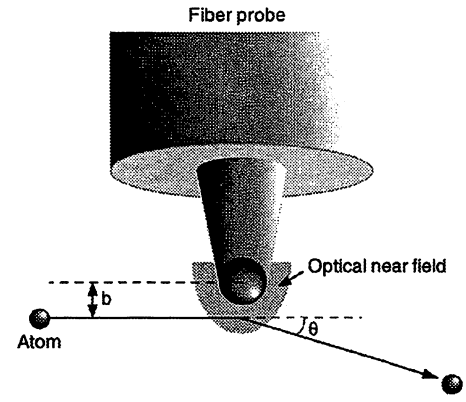

Fig. 16. Atom deflection with a fiber probe. An atom ballistically flying is deflected by the dipole force from the optical near field produced near the tip of a fiber probe. θ and b are the deflection angle and the impact parameter shown in Fig. 6, respectively.

then a high power Ar–ion laser with a wavelength of 476.5 nm excites them to the ionization level at 4.18 eV above the $5S_{1/2}$ ground state. These two lasers were overlapped behind the exit facet of the hollow fiber coaxially placed along a Rb atomic beam in a vacuum chamber with a typical pressure of 10^{-8} torr. The ionized atoms were detected with a channel electron multiplier biased by -3 kV.

As shown in Fig. 15, the guided atom flux is greatly increased in the blue-detuning region. This result reflects the dispersion-like character of the dipole force straightforward. Comparing the maximum flux obtained at a detuning of $+3$ GHz with the background transmission level without the guide light from a Ti : Sapphire laser, we get an enhancement factor of about 20 times. The atom guidance experiment using a hollow fiber with a hollow diameter of 300 nm, which is smaller than the wavelength of 780 nm, has been also performed [3].

In this scheme, thanks to the resonant character of the dipole force, we can guide atoms species- and state-selectively by choosing the light frequency. In fact, we tried the separation between two isotopes of ^{85}Rb and ^{87}Rb whose resonant frequencies are different by about 1 GHz, using the atom guidance technique [36]. This technique can be also applied to a new scheme of atom deposition [37]. It should be noted that the deposition rate can be precisely controlled by the frequency detuning, except for the thermal fluctuation. Considering the above advantages, we can expect to perform atom deposition with high deposition-rate control and high purity. On the other hand, enhancement of the cavity quantum electrodynamical effects can be expected inside a hollow fiber with a small hollow diameter. The effects will be observed by using the atom guidance technique [3], [38].

C. Atom Deflection and Trap With a Fiber Probe

1) Atom Deflection: The optical near field localized in a nanometer region can be generated near the nanometric tip of a fiber probe. In this section, we present two types of atom manipulation, deflection and trap, with such a fiber probe [3]. First, let us consider deflection of an atom with a fiber probe as shown in Fig. 16. When an atom ballistically flying is passing through the near-field region produced near the tip,

it feels the dipole force and the van der Waals force. Under a blue-detuning condition, if the light intensity is sufficiently strong, the repulsive dipole force becomes stronger than the attractive van der Waals force, so that the atom can be deflected in the direction shown in Fig. 16.

In order to estimate the deflection angle θ, we have to know the intensity distribution of the optical near field near the nanometric tip. As is well known, the optical near field is determined by the Maxwell equations. However, the numerical analysis often needs a long computational time. In addition, it gives us poor physical perspective. Therefore, we here introduce a phenomenological model with the Yukawa-type potential to describe the intensity distribution of the optical near field. The Yukawa-type potential is written as [24], [26], [39] (see also Section IV)

$$\phi(r) = \iint \frac{\exp(-r/a)}{r}\, dS \tag{1}$$

where a is a radius of curvature of the tip and r is a distance from the tip surface. From the Yukawa-type potential, we obtain the optical near-field intensity distribution $I(r)$ given by [24], [26]

$$I(r) \sim |\nabla\phi(r)|^2 + \frac{1}{a^2}|\phi(r)|^2. \tag{2}$$

This simple analytical formula enables us to directly handle some experimental parameters: light power, frequency detuning, tip radius, and so on. When the shape of the tip is hemispherical, the two components of $\phi(r)$ and $|\nabla\phi(r)|$ can be approximately written as

$$\phi(r) = \frac{2\pi a^2}{r}\left[\exp\left(-\frac{r-a}{a}\right) - \exp\left(-\frac{\sqrt{r^2+a^2}}{a}\right)\right] \tag{3}$$

$$|\nabla\phi(r)| = 2\pi\left[\left(\frac{a}{r}+\frac{a^2}{r^2}\right)\exp\left(-\frac{r-a}{a}\right) - \left(\frac{a}{\sqrt{r^2+a^2}}+\frac{a^2}{r^2}\right)\exp\left(-\frac{\sqrt{r^2+a^2}}{a}\right)\right] \tag{4}$$

where r is measured from the center of the hemispherical tip.

Using the Yukawa-type intensity distribution, we can estimate the optical potential resulting from the dipole force. The optical potential is given by [27], [28]

$$U_{\text{opt}}(r) = \frac{\hbar\delta}{2}\ln\left\{1 + \frac{\gamma^2}{4\delta^2+\gamma^2}\frac{I(r)}{I_{\text{sat}}}\right\} \tag{5}$$

where $\delta = \omega - \omega_0$ is the detuning of a light frequency ω from a resonant atomic frequency ω_0, γ is the natural linewidth of an atomic excited state, and I_{sat} is a saturation intensity of the corresponding atomic transition. On the other hand, the van der Waals potential is written as [40]–[42]

$$U_{\text{vdw}}(r) = -\frac{1}{16r^3}\sum_j \frac{n_j^2-1}{n_j^2+2}\frac{\hbar\gamma_j}{k_j^3} \tag{6}$$

where n_j and k_j are a refractive index and a wave number, respectively. The summation is carried out about the possible dipole transitions. For example, assuming the optical near-field power P_{onf} of 50 nW for $a = 50$ nm, we find that the repulsive optical potential can be comparable to the attractive van der Waals potential between $a = 10$ nm and $a = 50$ nm for a Rb atom, under a condition of $\delta/2\pi = +1$ GHz [3]. The total potential on an atom in the near-field region is given as the sum of the optical potential and the van der Waals potential.

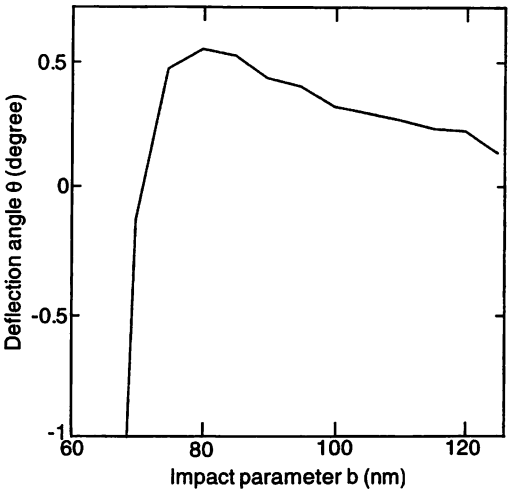

Fig. 17. Deflection angle θ of a Rb atom with a velocity of 10 m/s plotted as a function of the impact parameter b. In this calculation, we assume $a = 50$ nm, $\delta/2\pi = +2$ GHz, and $P_{\text{onf}} = 50$ nW.

Fig. 17 shows the deflection angle θ plotted as a function of the impact parameter b, which is defined as the distance between the center of the hemispherical tip and the incident direction. In this calculation, we assume a moderate slow Rb atom with a velocity of 10 m/s under a condition of $a = 50$ nm, $\delta/2\pi = +2$ GHz, and $P_{\text{onf}} = 50$ nW. The slow Rb atom can be supplied from an atomic beam with a mean temperature of 200 mK.

As shown in Fig. 17, the deflection angle is about 0.5° at $b = 80$ nm. From this value, we find that the displacement of the atom from the incident axis is about 100 μm at a distance of 10 cm downstream the fiber tip. This result indicates that the atom can be easily detected with a commercial detector such as a microchannel plate.

2) Atom Trap: Next, let us consider trap of an atom with a fiber probe. The original idea proposed by Hori and Ohtsu *et al.*dealt with the balance of three forces: the attractive dipole force, the enhanced spontaneous force, and the centrifugal force [25]–[27]. On the other hand, Letokhov *et al.* calculated a spatial distribution of an optical near field for trap of atoms [43]. Here, we describe a more static trap based on a balance between the repulsive dipole force and the attractive van der Waals force as shown in Fig. 18 [3]. In this scheme, an atom is trapped at the minimum point of the total potential produced near the tip of a fiber probe.

As mentioned above, the optical potential can be comparable to the van der Waals potential under a suitable condition. Fig. 19 shows the trap potential on a ^{85}Rb atom composed of the repulsive optical potential and the attractive van der Waals potential. Two potential curves for the two hyperfine ground states $F = 2$ and $F = 3$ are plotted as a func-

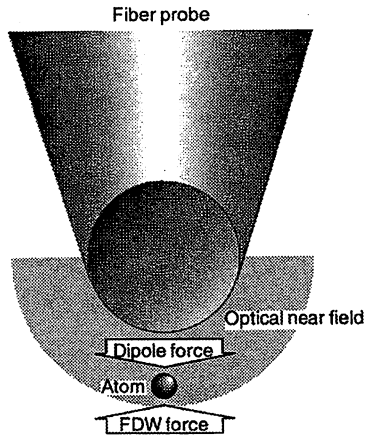

Fig. 18. Atom trap with a fiber probe. An atom can be trapped by balancing the repulsive dipole force with the attractive van der Waals force.

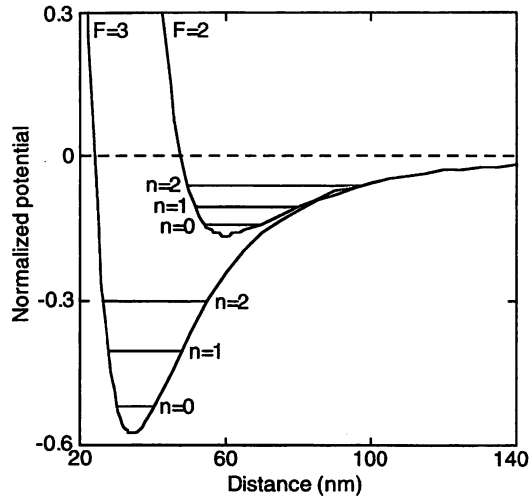

Fig. 19. Trap potentials on a ^{85}Rb atom for two hyperfine ground states $F = 2$ and $F = 3$ produced near the hemispherical tip with $a = 20$ nm. The total potential composed of the repulsive optical potential and the attractive van der Waals potential is plotted as a function of the distance from the tip surface, where $\delta/2\pi = +2$ GHz with respect to the $F = 2$ lower ground state and $P_{\rm onf} = 600$ nW. The horizontal lines labeled by the number n indicate the quantized vibrational levels.

tion of the distance from the hemispherical tip surface, where $a = 20$ nm and $P_{\rm onf} = 600$ nW. The frequency detuning δ is taken to be $+2\pi \times 2$ GHz with respect to the $F = 2$ lower ground state at about 3 GHz below the $F = 3$ upper ground state. The ^{85}Rb atom can be trapped in one of the quantized vibrational levels indicated by the horizontal lines with the label n. For example, the lowest level with $n = 0$ for the $F = 3$ upper ground state corresponds to a temperature of 30 μK, at which the de Broglie wavelength of the ^{85}Rb atom is the order of 10 nm.

3) Measurement of Optical Near-Field Intensity: For experimental demonstrations of the atom manipulation presented here, it is fundamentally important to fabricate a fiber probe suitable for the atom used. There are several factors to be considered: a shape of the tip, a radius of curvature, light intensity, frequency detuning, and so on. First of all, we measured the intensity distribution of the optical near field produced near the tip of a fiber probe in a probe-to-probe configuration [44], [45]. Although this method is a destructive measurement of an optical near field, we can get a lot of information about the fiber fabrication.

Fig. 20 shows the outline of the experimental setup. An optical near field is induced near the tip of a fiber probe whose position is controlled with a piezoelectric transducer (PZT). Another gold-coated fiber probe placed tip to tip approaches the fiber probe and then picks up the scattered light signal with high efficiency. The gold-coated fiber probe with a PZT is controlled by the shear-force technique with an optical feedback system composed of a diode laser (LD) and a photodiode (PD). The signal picked up by the gold-coated fiber probe is recorded as a function of the distance r from the tip of the fiber probe.

Fig. 21 shows a result obtained from a measurement of the light field produced near the tip of a fiber probe with $a = 200$ nm, where a light beam with a wavelength of 780 nm is coupled to the fiber probe and a gold-coated fiber probe with a radius of curvature of 40 nm is used. The light intensity is normalized to the value at a distance of 10 nm. In Fig. 21, the signal in a region of less than 100 nm, we think, reflects the intensity change of the optical near field, while the signal in a region of more than 100 nm contains the far-field components. The intensity distribution of the near-field component can be approximately fitted by an expression $I(r) = I_0 \exp(-1.85r/a)$. This approaches the Yukawa-type intensity distribution. If we estimate a trap potential from applying this experimental expression to the case of $a = 20$ nm, we find again that an atom with an energy of 30 μK in terms of temperature can be trapped.

D. Atom Funnel With a Hollow Prism

Conventional schemes with propagating light often use an atomic beam as a source of atoms for manipulation. It should be noted that a thermal atomic beam has a mean velocity of more than 100 m/s. This velocity is too fast to manipulate with a nanometric fiber probe, because such atoms go through the near-field region in a very short time. In addition, the thermal atomic density is very low. Therefore, the optical near field has few occasions to interact with the atoms. In order to improve these drawbacks, we consider the use of a cold atomic beam. In fact, such a cold atomic beam can be generated by an atom funnel composed of an optical near-field mirror [46].

Fig. 22 shows a cross section of the atom funnel. In this scheme, the optical near-field mirror to reflect atoms is excited on the inner wall surface by way of total-internal reflection of a blue-detuned doughnut-shaped light beam shone upward from the bottom of a hollow prism. Cold atoms released from a magneto-optical trap [47] fall into the prism and are reflected whenever they approach the inner wall surface. The key point is that atoms are cooled down in the process of the reflection, which is called Sisyphus cooling [48]–[50]. The atoms accelerated by gravity are recooled due to the cooling mechanism and collected to the bottom. Consequently, they are going out of a small exit hole as a cold atomic beam. In

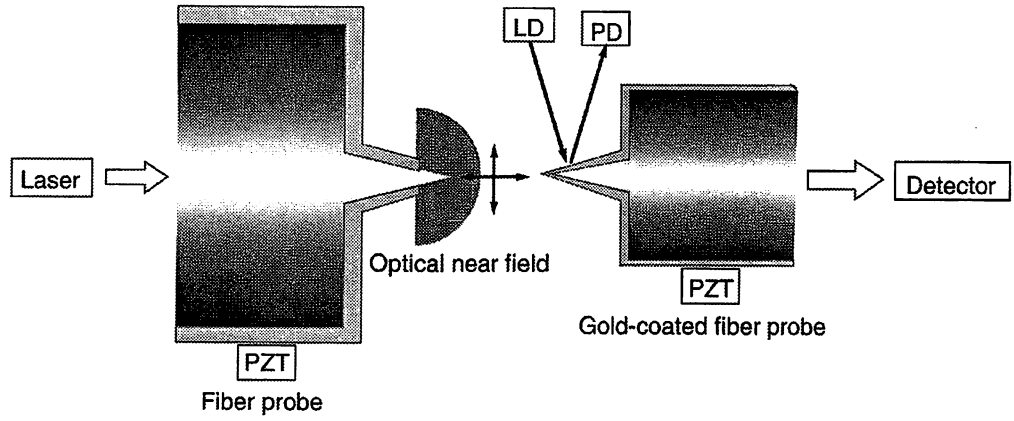

Fig. 20. Experimental setup with a probe-to-probe configuration. An optical near field produced near the tip of a fiber probe is measured with another gold-coated fiber probe. They are positioned with piezoelectric transducers (PZT). In addition, the gold-coated fiber probe is controlled by means of the shear-force technique with an optical feedback system composed of a diode laser (LD) and a photodiode (PD).

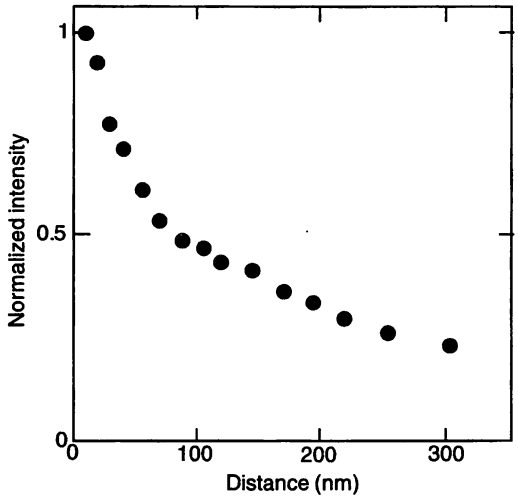

Fig. 21. Measurement of the light intensity near the tip of a fiber probe with $a = 200$ nm. Another gold-coated fiber probe with $a = 40$ nm is used for measurement. The light intensity normalized to the value at a distance of 10 nm is plotted as a function of the distance from the tip of the fiber probe.

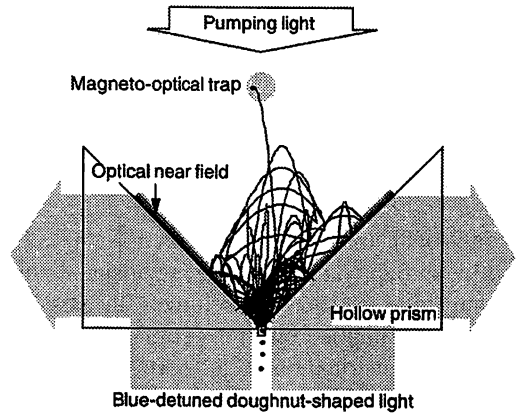

Fig. 22. Atom funnel with a hollow prism. Cold atoms supplied from a magneto-optical trap are reflected by the optical near field excited on the inner wall surface via total-internal reflection of a blue-detuned doughnut-shaped light beam shone upward. The reflected atoms are cooled down through the Sisyphus cooling process, which is reiterated by a weak pumping light shone downward. The collected atoms go out of a small exit hole as a cold atomic beam. In addition, a trajectory is obtained from a Monte Carlo simulation performed for a Rb atom falling from a magneto-optical trap with a mean temperature of 10 μK.

Fig. 22, as an example, a trajectory of a Rb atom falling from a magneto-optical trap with a Maxwell–Boltzmann distribution whose mean temperature of 10 μK is drawn based on a result from a Monte Carlo simulation, where the center of the magneto-optical trap is assumed to be at 5 mm above the exit hole.

The cooling process is induced by a weak pumping light shone downward. Fig. 23 shows the principle of the Sisyphus cooling with the dressed atom picture [51] under a blue-detuning condition. Each atomic energy level is spatially modulated as a result of the interaction with the optical near field. The energy shift is equivalent to the optical potential, which is in proportion to the light intensity but in inverse proportion to the frequency detuning. It should be noted that the frequency of the doughnut-shaped light indicated by an arrow A is detuned for both hyperfine ground states $|g1\rangle$ and $|g2\rangle$. In this case, the energy shift becomes larger as approaching the surface because the optical near-field intensity becomes stronger, while the energy shift for the lower ground state $|g1\rangle$ is larger than that for the upper ground state $|g2\rangle$ because the frequency detuning for $|g1\rangle$ is smaller than that for $|g2\rangle$. If an atom in $|g1\rangle$ is transferred to $|g2\rangle$ in the process of reflection as indicated by an arrow T, the atom loses its kinetic energy by an amount of the difference between both energy shifts. This process can be repeated by optical pumping from $|g2\rangle$ to $|g1\rangle$ indicated by an arrow P, which is induced by pumping light tuned to the transition indicated by an arrow B. The funnel experiment is now in progress.

E. Future Outlook

In this section, we reviewed methods of reflecting and guiding atoms with optical near fields. Then, we examined the possibility of precise control of neutral atoms with a

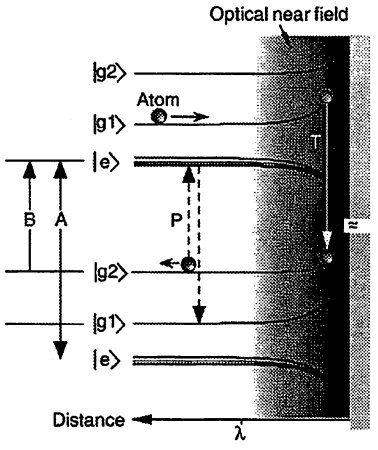

Fig. 23. Sisyphus cooling induced by the blue-detuned optical near field in the process of reflection. If an atom in the lower ground state $|g1\rangle$ is transferred to the upper ground state $|g2\rangle$, as shown by an arrow T, the atom loses its kinetic energy by an amount of the difference between the energy shifts for both ground states. This process is repeated by optical pumping from $|g2\rangle$ to $|g1\rangle$ as shown by an arrow P. In this scheme, the frequency detuning of doughnut-shaped light and the frequency of pumping light are shown by arrows A and B, respectively.

nanometric fiber probe based on numerical analyses with the Yukawa-type intensity distribution. When a fiber probe customized for Rb atoms is used, a cold Rb atom can be not only deflected at a large deflection angle but also captured by an trap composed of the repulsive dipole force and the attractive van der Walls force. The possibility of the trap was also implied by an experimental measurement of the intensity distribution of an optical near field in a probe-to-probe configuration. In addition, a cold atomic beam appropriate for the near-field optical manipulation can be generated by means of an atom funnel involving the Sisyphus cooling.

Using the atom guidance or/and deflection techniques, we can carry atoms to an arbitrary point on a substrate. Moreover, if the atom trap technique, which will enable us to realize single-atom manipulation, is used together, we can expect to make a small structure such as quantum dots atom by atom and species-selectively.

The deflection technique with a fiber probe is also useful for the study of optical near fields. Measurements of the optical near field have been made in a destructive way so far. Using an atom as a probe, we can perform nondemolition measurements of the optical near field. The nondemolition measurement will be important for the test of the Yukawa-type intensity distribution model. In addition, the deflection technique can be used for the study of the cavity quantum electrodynamic effects, including the van der Waals force in a near-field region.

Few exact theories to describe the interaction between an atom and an optical near field have been derived so far. It should be noted that the dressed atom picture used for the atom funnel is based on the far-field theory. However, this dressed atom picture is not necessarily suitable to handle the interaction with the optical near field, because the photon number must be well defined: an optical near field has no real photon. The near-field optical atom-manipulation methods presented here will be powerful tools for the study of such open questions.

IV. Theory

In this section, we will develop a new theoretical formulation of optical near-field systems within the quantum theoretical framework. Taking note of the hierarchical structure of near field optics, namely, the existence of two subsystems, we apply the projection-operator method to it. The effective interaction between a nanometric probe tip and a sample system is then derived from the mediation of exciton-polaritons (massive virtual photons). It is shown to result in the Yukawa potential, which is an empirical assumption of the virtual photon model as an intuitive model. The effective probe tip-sample interaction is essential for describing such phenomena as atom guidance and manipulation, or local excitation of a single quantum dot and nanometric structure. On the basis of our formulation and the virtual photon model, we discuss both conventional and quantum theoretical aspects of optical near-field problems, and finally we offer a summary of the section and future outlook.

A. Background

High-resolution imaging beyond the diffraction limit is now available for a variety of samples and materials by using optical near fields [3]. Local excitation with similar precision is also possible for a nanometric quantum dot [52] or a single molecule [53]. From the spectroscopic observations thus obtained, we can learn about details of the internal structure of an object, such as its energy level structure, relaxation mechanism, and transition dynamics. Photochemical reaction as well as transition has been demonstrated on a sub-100-nm scale [11] (refer also to Section II), and has opened up a new way of developing nanometric photonics components, since optical near-field recording in both thermal [54], [55] and photon modes [56] has been reported to be feasible on a sub-100-nm scale. As an ultimate component, an atom is also utilized in this context. For example, neutral atoms have been guided [35], [36] through a micrometer-sized hollow fiber by using a blue-detuned optical near field. Moreover, atomic deposition with nanometric precision using very-low-energy atom deflection or manipulation has been proposed [46] (refer also to Section III).

These experimental advances imply that a quantum theoretical approach should be pursued even in near-field optics. In addition, we should preserve the connection with an intuitive model such as the virtual photon model [24], [26], because such a connection plays a very important role as a bridge between conventional theories and recent and future experimental achievements. There are two alternative quantum theoretical approaches to near-field optics. In one, called the semiclassical approach, electromagnetic fields are treated as classical, while matter fields are described by the Schrödinger equation with local [57]–[59] or nonlocal [60], [61] susceptibility. Near-field spectroscopic problems, in fact, have been discussed by using the semiclassical

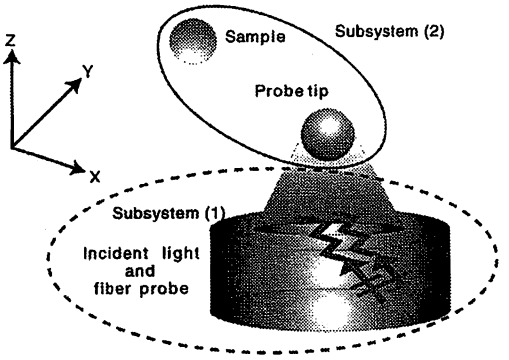

Fig. 24. Schematically illustrated optical near-field system consisting of two subsystems: 1) an incident light and macroscopic matter system and 2) a microscopic probe tip and sample system.

approach. In the other, called the full quantum approach, both fields are quantized. When we quantize the field, we usually employ a plane wave basis (propagating modes) for infinite systems, but we have to consider how to include nonpropagating modes, that is, optical near fields [62], [63]. In relation to cavity QED problems [64], [65], electromagnetic field has been quantized with spherical bases in atom-trapping by a microsphere [66]. From the elementary excitation point of view, exciton-polariton modes have been extensively studied both with [67]–[71] and without [72] matter absorption. Four-wave mixing experimental results have been analyzed from the exciton-polariton scattering picture, and the validity of boson expansion has been revisited [73]. In the optical near-field area, a quantum theoretical approach was proposed [39], [74] on the basis of effective interaction by virtual mediation of exciton-polaritons. This approach provides a foundation for the massive virtual photon model—an intuitive model based on experimental results—that empirically assumes Yukawa interaction between a probe tip and a sample.

B. Formulation

Depending on our viewpoint as regards to optical near-field systems, we may expect to reach a different formulation, as previously mentioned. It is appropriate to use classical electromagnetic theories for macroscopic descriptions of the behavior of light and matter such as a fiber probe. However, when the size of the probe tip or aperture is nanometric as used in recent experiments [4], there is no guarantee that we can use the classical theories to correctly formulate optical near-field problems such as interactions between atom/nanometric samples and the probe. We, therefore, try to describe such problems within a quantum theoretical framework, paying special attention to the hierarchical structure of optical near-field systems.

1) Hierarchical Structure in Near-Field Optics: The optical near-field system, as illustrated in Fig. 24, has characteristic structure in scale. There are two subsystems: in (1), incident propagating light consisting of real photons interacts with a macroscopic matter system (typically a prism in collection mode or a fiber probe in illumination mode). The other subsystem, (2), consists of a nanometric probe tip and quantum-mechanical objects (atoms, molecules, and/or quantum dots). These two subsystems interact with each other, and their interactions should be treated consistently. This kind of problem can be formulated in a unified and systematic way by using the projection-operator method.

2) Projection-Operator Method: The projection-operator method is very appropriate for extracting an arbitrary number of degrees of freedom (P-space) from the many degrees of freedom of the system and for renormalizing the effects of the other degrees of freedom (Q-space). Even if we are, for example, not able to obtain all of the exact states for the total system, we can derive the exact effective interaction in terms of a few states for the subsystems. In the following discussion, we can more generally obtain an effective operator $\hat{O}_{\text{eff}}$ in the P-space, which is equivalent to an arbitrary operator $\hat{O}$ in the full space, corresponding to physical observables.

We follow the projection-operator method for steady states [75], [76], but readers interested in the relationship to the resolvent or time evolution of the operators may consult the publications listed in [51] and [77]–[80]. The starting point is that the eigenvalues and eigenstates of the total Hamiltonian $\hat{H}$ for the optical near-field system are written as E_λ and $|\Psi_\lambda\rangle$, respectively; i.e.,

$$\hat{H}|\Psi_\lambda\rangle = \left(\hat{H}_0 + \hat{V}\right)|\Psi_\lambda\rangle = E_\lambda|\Psi_\lambda\rangle \tag{7}$$

where $\hat{H}_0$ consists of the Hamiltonians $\hat{H}_{\text{bath}}$ for the subsystem (1) and $\hat{H}_A + \hat{H}_B$ for subsystem (2), while $\hat{V}$ denotes the interaction between the two subsystems. Defining the projection operators P and $Q = 1 - P$ in the usual manner as

$$\left|\Psi_\lambda^{(1)}\right\rangle = P|\Psi_\lambda\rangle, \qquad \left|\Psi_\lambda^{(2)}\right\rangle = Q|\Psi_\lambda\rangle \tag{8}$$

$$P^2 = P, \qquad PQ = QP = 0 \tag{9}$$

$$\left[P, \hat{H}_0\right] = \left[Q, \hat{H}_0\right] = 0 \tag{10}$$

we divide the eigenstates $|\Psi_\lambda\rangle$ into two groups, $|\Psi_\lambda^{(1)}\rangle$ in P-space and $|\Psi_\lambda^{(2)}\rangle$ in Q-space. By using (8)–(10), (7) is then rewritten as a set of equations

$$\left(E_\lambda - \hat{H}_0\right) P\left|\Psi_\lambda^{(1)}\right\rangle = P\hat{V}P\left|\Psi_\lambda^{(1)}\right\rangle + P\hat{V}Q\left|\Psi_\lambda^{(2)}\right\rangle \tag{11}$$

$$\left(E_\lambda - \hat{H}_0\right) Q\left|\Psi_\lambda^{(2)}\right\rangle = Q\hat{V}P\left|\Psi_\lambda^{(1)}\right\rangle + Q\hat{V}Q\left|\Psi_\lambda^{(2)}\right\rangle. \tag{12}$$

From (12), it is possible to formally express $Q|\Psi_\lambda^{(2)}\rangle$ by $P|\Psi_\lambda^{(1)}\rangle$ as

$$Q\left|\Psi_\lambda^{(2)}\right\rangle = \left(E_\lambda - \hat{H}_0 - Q\hat{V}\right)^{-1} Q\hat{V}P\left|\Psi_\lambda^{(1)}\right\rangle = J\left(E_\lambda - \hat{H}_0\right)^{-1} Q\hat{V}P\left|\Psi_\lambda^{(1)}\right\rangle \tag{13}$$

$$J = \left[1 - \left(E_\lambda - \hat{H}_0\right)^{-1} Q\hat{V}\right]^{-1} \tag{14}$$

and the eigenstates $|\Psi_\lambda\rangle$ for the total Hamiltonian can then be expressed in terms of the eigenstates in P-space as

$$|\Psi_\lambda\rangle = (P+Q)|\Psi_\lambda\rangle = JP\left|\Psi_\lambda^{(1)}\right\rangle. \tag{15}$$

Since both of the states satisfy the normalization condition, we can rewrite this as

$$|\Psi_\lambda\rangle = JP(PJ^\dagger JP)^{-1/2}\left|\Psi_\lambda^{(1)}\right\rangle. \tag{16}$$

We, thus, obtain the effective operator $\hat{O}_{\text{eff}}$ in the P-space as follows:

$$\langle\Psi_\mu|\hat{O}|\Psi_\lambda\rangle = \left\langle\Psi_\mu^{(1)}\right|\hat{O}_{\text{eff}}\left|\Psi_\lambda^{(1)}\right\rangle \tag{17}$$

$$\hat{O}_{\text{eff}} = (PJ^\dagger JP)^{-1/2}\left(PJ^\dagger\hat{O}JP\right)(PJ^\dagger JP)^{-1/2}. \tag{18}$$

From (17) and (18), it follows that relevant quantities such as the probe tip-sample interaction and transition dipole moments can be exactly expressed by using a small number of bases in P-space after renormalizing the effects from Q-space. This is one of the advantages of the method and is desirable from the computational viewpoint.

3) Elementary Excitation—Exciton-Polariton: In Section IV-B3 and IV-B4, components of the unperturbed Hamiltonian $\hat{H}_0$ for the two subsystems (1) and (2) will be discussed. There are basically no restrictions on the Hamiltonian, but for simplicity we assume that its eigenvalues and eigenstates are known.

Subsystem (1) can be viewed as a set of 1) excitons; 2) real photons; and 3) their interactions, if the induced electric polarization in three-dimensional infinite matter or macroscopic matter is represented as excitons with energy $\hbar\Omega$. Such a system has characteristic elementary excitation modes, i.e., exciton-polariton modes, and we can obtain the modes with energy $\hbar\Omega(\vec{k})$ and momentum $\hbar\vec{k}$ as

$$\left[\hat{\xi}\left(\vec{k}\right), \hat{H}_{\text{bath}}\right] = \hbar\Omega\left(\vec{k}\right)\hat{\xi}\left(\vec{k}\right) \tag{19}$$

where the creation and annihilation operators of the exciton-polaritons $(\hat{\xi}^\dagger, \hat{\xi})$ are a linear combination of those of photons $(\hat{a}^\dagger, \hat{a})$ and excitons $(\hat{B}^\dagger, \hat{B})$ as follows:

$$\hat{\xi}\left(\vec{k}\right) = \sum_{\lambda=1}^{2}\left\{w_\lambda\left(\vec{k}\right)\hat{a}_\lambda\left(\vec{k}\right) + y_\lambda\left(\vec{k}\right)\hat{a}_\lambda^\dagger\left(-\vec{k}\right)\right\} + \sum_{\lambda'=1}^{3}\left\{x_{\lambda'}\left(\vec{k}\right)\hat{B}_{\lambda'}\left(\vec{k}\right) + z_{\lambda'}\left(\vec{k}\right)\hat{B}_{\lambda'}^\dagger\left(-\vec{k}\right)\right\}. \tag{20}$$

Here, w, x, y, and z denote the mixing amplitude. This means that the states determined by the exciton-polariton modes are so-called "dressed" states of photons and excitons. The Hamiltonian $\hat{H}_{\text{bath}}$ is now given by

$$\hat{H}_{\text{bath}} = \sum_{\vec{k}}\sum_{\lambda=1}^{2}\hbar\omega\left(\vec{k}\right)\hat{a}_\lambda^\dagger\left(\vec{k}\right)\hat{a}_\lambda\left(\vec{k}\right) + \sum_{\lambda'=1}^{3}\int d^3r\hbar\Omega\hat{B}_{\lambda'}^\dagger(\vec{r})\hat{B}_{\lambda'}(\vec{r}) - \int d^3r\hat{\vec{\mu}}(\vec{r})\cdot\hat{\vec{D}}(\vec{r}) \tag{21}$$

$$= \sum_{\vec{k}}\hbar\Omega\left(\vec{k}\right)\hat{\xi}^\dagger\left(\vec{k}\right)\hat{\xi}\left(\vec{k}\right) \tag{22}$$

where the photon energy is denoted as $\hbar\omega(\vec{k}) = \hbar c|\vec{k}|$. The third term in (21) represents the interactions between photons and excitons in a multipolar QED Hamiltonian [81], where $\hat{\vec{\mu}}(\vec{r})$ is the dipole operator of matter and $\hat{\vec{D}}(\vec{r})$ is the displacement field operator that is given by the conjugate momentum operator $\hat{\vec{\Pi}}(\vec{r})$ of the vector potential operator $\hat{\vec{A}}(\vec{r})$ expanded in terms of plane wave bases as

$$\hat{\vec{D}}(\vec{r}) = -4\pi c\hat{\vec{\Pi}}(\vec{r}) \tag{23}$$

$$= \sum_{\vec{k}}\sum_{\lambda=1}^{2} i\sqrt{\frac{4\pi\hbar\omega\left(\vec{k}\right)}{2V_0}}\vec{e}_\lambda\left(\vec{k}\right) \times\left\{\hat{a}_\lambda\left(\vec{k}\right)e^{i\vec{k}\cdot\vec{r}} - \hat{a}_\lambda^\dagger\left(\vec{k}\right)e^{-i\vec{k}\cdot\vec{r}}\right\}. \tag{24}$$

Here the speed of light in vacuum, the normalization volume, and the unit vector for photon polarization are designated as c, V_0, and $\vec{e}_\lambda(\vec{k})$, respectively. This Hamiltonian can be easily extended to include the absorption effects of matter. Moreover, it is possible to treat infinite matter (two-dimensional) with a boundary at $z = 0$ by using the step function $\theta(-z)$ as follows:

$$\hat{H}_{\text{bath}} = \sum_{\vec{k}}\sum_{\lambda=1}^{2}\hbar\omega\left(\vec{k}\right)\hat{a}_\lambda^\dagger\left(\vec{k}\right)\hat{a}_\lambda\left(\vec{k}\right) + \sum_{\lambda'=1}^{3}\int d^3r\theta(-z)\hbar\Omega\hat{B}_{\lambda'}^\dagger(\vec{r})\hat{B}_{\lambda'}(\vec{r}) - \int d^3r\theta(-z)\hat{\vec{\mu}}(\vec{r})\cdot\hat{\vec{D}}(\vec{r}). \tag{25}$$

Noting that the step function can be written as

$$\theta(-z) = \frac{1}{2}\int\delta(k_z)e^{ik_z z}\,dk_z + \frac{i}{2\pi}\int\frac{1}{k_z}e^{ik_z z}\,dk_z \tag{26}$$

we find that the second term in (26) produces an infinite series of couplings with respect to k_z in the second and third terms of (25). If the effect is negligible, as in the case where there is no absorption, however, we can rewrite (25) in a similar form to (21)

$$\hat{H}_{\text{bath}} = \sum_{\vec{k}}\sum_{\lambda=1}^{2}\hbar\omega\left(\vec{k}\right)\hat{a}_\lambda^\dagger\left(\vec{k}\right)\hat{a}_\lambda\left(\vec{k}\right) + \frac{1}{2}\sum_{\vec{k}}\sum_{\lambda'=1}^{3}\hbar\Omega\hat{B}_{\lambda'}^\dagger\left(\vec{k}\right)\hat{B}_{\lambda'}\left(\vec{k}\right) - \frac{1}{2}\sum_{\vec{k}}\hat{\vec{\mu}}\left(-\vec{k}\right)\cdot\hat{\vec{D}}\left(\vec{k}\right). \tag{27}$$

If the effect is not negligible, we have to choose some of the eigenstates of (27) as P-space, and to handle an effective Hamiltonian in order to renormalize the Q-space, as explained in the previous section. In all of the above cases, therefore, a probe tip can be considered as interacting with nanometric samples or quantum-mechanical objects via exciton-polariton (massive virtual photon, or dressed photon) mediation.

4) Nanometric Probe Tip-Sample System: The Hamiltonian describing subsystem (2) depends, of course, on what kinds of material (atoms, molecules, nanometric samples, etc.) are taken into consideration. Instead of adopting specific Hamiltonians for $\hat{H}_\alpha$ ($\alpha = A, B$), i.e., specific atomic or molecular Hamiltonians, let us choose ones in which electrons with effective mass m_e and wave number k_α are confined in an infinite well potential of size $a(b)$. This not only can represent a characteristic situation in which the electrons are confined within a small area, but also can give a diagonalized form of the Hamiltonians as follows:

$$\hat{H}_\alpha = \sum_n E_n(\alpha)\hat{c}^\dagger_{n\alpha}\hat{c}_{n\alpha} \tag{28}$$

$$E_n(\alpha) = \frac{\hbar^2 k_\alpha^2}{2m_e} = \frac{\hbar^2}{2m_e}\left(\frac{n\pi}{a}\right)^2 \quad \text{or} \quad \frac{\hbar^2}{2m_e}\left(\frac{n\pi}{b}\right)^2 \tag{29}$$

where the relevant energy levels are designated as $E_n(\alpha)$ for a positive integer n, the creation and annihilation operators are denoted as $\hat{c}^\dagger_{n\alpha}$ and $\hat{c}_{n\alpha}$, and electric dipole transitions between those levels are allowed.

5) Effective Interaction Between Probe Tip and Sample System: Yukawa Potential: The interaction $\hat{V}$ between the two subsystems described in the previous sections is written as

$$\hat{V} = -\sum_{\alpha=A}^{B} \theta(z_\alpha)\hat{\vec{\mu}}_\alpha \cdot \hat{\vec{D}}(\vec{r}_\alpha) \tag{30}$$

by assuming the dipole approximation of the multipolar QED Hamiltonian. Rewriting the photon operators as exciton-polariton operators, we can obtain the bare interaction in the exciton-polariton (elementary excitation mode) picture. Note that the word "bare" means that the interaction is not renormalized yet, or that the effects of the Q-space are not consistently included yet

$$\hat{V} = -i\sqrt{\frac{2\pi\hbar}{V_0}}\sum_{\alpha=A}^{B}\theta(z_\alpha)\sum_{j=1}^{3}\left(\hat{b}^\dagger_j(\vec{r}_\alpha) + \hat{b}_j(\vec{r}_\alpha)\right) \cdot \sum_{\vec{k}}\left[K'_{\alpha j}\left(\vec{k}\right)\hat{\xi}\left(\vec{k}\right) - K'^{*}_{\alpha j}\left(\vec{k}\right)\hat{\xi}^\dagger\left(\vec{k}\right)\right] \tag{31}$$

$$K'_{\alpha j}\left(\vec{k}\right) = \sum_{\lambda=1}^{2}\mu_\alpha\left(\vec{e}_j \cdot \vec{e}_\lambda\left(\vec{k}\right)\right)f(k)e^{i\vec{k}\cdot\vec{r}_\alpha} \tag{32}$$

$$f(k) = \frac{ck}{\sqrt{\Omega(k)}}\frac{\sqrt{\Omega^2(k) - \Omega^2/4}}{\sqrt{2\Omega^2(k) - \Omega^2/4 - c^2k^2}} \tag{33}$$

where we used (19) and (27) to calculate the eigenvalue $\Omega(k)$. The coupling coefficients between the probe (sample) and exciton-polaritons are denoted as $K'_{\alpha j}$ and $K'^{*}_{\alpha j}$, and $\hat{b}^\dagger_j$ and $\hat{b}_j$ are the creation and annihilation operators leading to electric dipole transitions of the sample-probe system, relating to (28). The unit vector $\vec{e}_j$ in (32) gives the direction of the dipole moment μ_α. It is worth reminding ourselves that there is no direct interaction between sample and probe tip in this Hamiltonian.

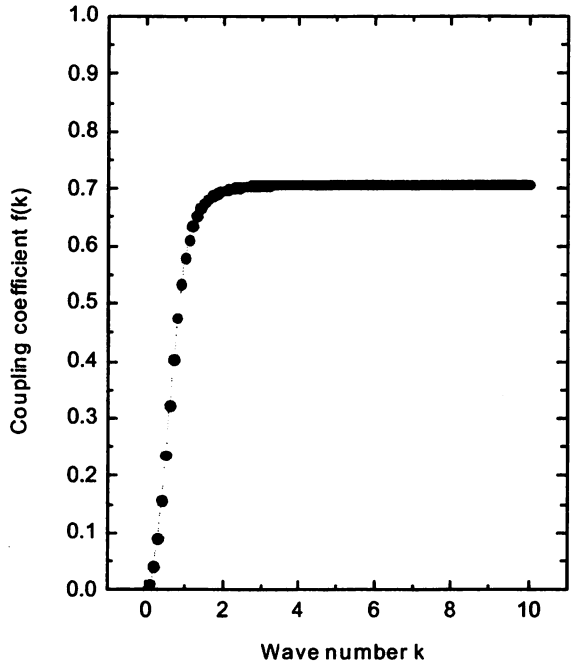

Fig. 25. Dependence of the coupling coefficient $f(k)$ on the wave number k of incident light.

On the basis of the dispersion relation of an exciton-polariton (effective mass: m_p) obtained from (19), we make the usual effective mass approximation as

$$\Omega(k) = \frac{\Omega}{2} + \frac{\hbar k^2}{2m_p}. \tag{34}$$

From (32) and (33), the dependence of the coupling coefficient $f(k)$ on the wave number k of the incident light can be obtained as shown in Fig. 25. The horizontal and vertical axes in Fig. 25 are measured in units of $\sqrt{m_p\Omega/\hbar}$ and $\sqrt{2m_pc^2/\hbar}$, respectively. It, thus, follows that the coupling coefficients of the exciton-polariton modes to the nanometric subsystem (2) are constant when the wave number is larger than $k_c \sim 2\sqrt{m_p\Omega/\hbar}$. Simple estimation gives $k_c^{-1} \sim 100$ nm by putting the excitation energy and effective mass as $\hbar\Omega \sim 1$ eV, $m_pc^2 \sim 1$ eV.

Now let us discuss the effective interaction $\hat{V}_{\text{eff}}$ according to the method described in Section IV-B2. As explained in that section, the relevant interaction can be exactly expressed by using the bare interaction $\hat{V}$ and a small number of bases in the P-space, after renormalizing the effects from the Q-space. We then choose a combination of the five states, $|A\rangle, |A^*\rangle, |B\rangle, |B^*\rangle$, and $|0\rangle$, as the P-space bases. Here, the ground and excited states of $\hat{H}_\alpha$ ($\alpha = A$ or B) are designated as $|A\rangle, |A^*\rangle$ and $|B\rangle, |B^*\rangle$, while the ground state of $\hat{H}_{\text{bath}}$ is expressed as $|0\rangle$. In order to evaluate the effective sample-probe interaction $V_{\text{eff}}(AB)$ from (17) and (18), we set $|\Psi^{(1)}_\lambda\rangle = |A\rangle|B^*\rangle|0\rangle, |\Psi^{(1)}_\mu\rangle = |A^*\rangle|B\rangle|0\rangle$, and have

$$V_{\text{eff}}(AB) \equiv \left\langle\Psi^{(1)}_\mu\right|\hat{V}_{\text{eff}}\left|\Psi^{(1)}_\lambda\right\rangle = \left\langle\Psi^{(1)}_\mu\right|\left(PJ^\dagger JP\right)^{-1/2}\left(PJ^\dagger\hat{V}JP\right) \times \left(PJ^\dagger JP\right)^{-1/2}\left|\Psi^{(1)}_\lambda\right\rangle. \tag{35}$$

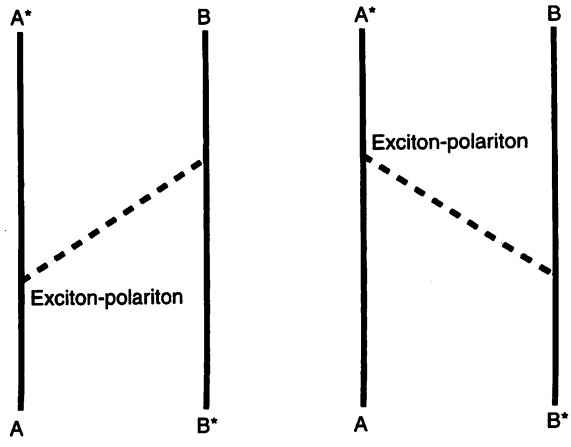

Fig. 26. Elementary process in the second order: A virtual exciton-polariton, or a massive virtual photon, mediating between probe tip and sample.

The remaining task is to find an explicit form of the operator J that can be handled. Note that the state $P|\Psi_\lambda^{(1)}\rangle$ satisfies the following equation:

$$\left(E_\lambda - \hat{H}_0\right) P\left|\Psi_\lambda^{(1)}\right\rangle = P\hat{V}JP\left|\Psi_\lambda^{(1)}\right\rangle \tag{36}$$

with the help of (11) and (13). Using (7), (15), and (36), we can then write down the equation to be solved as

$$\begin{aligned}\left[J, \hat{H}_0\right] P &= \left(E - \hat{H}_0\right) JP - J\left(E - \hat{H}_0\right) P \\ &= \hat{V}JP - JP\hat{V}JP. \end{aligned} \tag{37}$$

If we expand J as $J = P + \sum_{n=1}^{\infty} g^{(n)} J^{(n)}$ and obtain perturbative solutions of it, we can determine $V_{\text{eff}}(AB)$ perturbatively in the order of $\hat{V}$. Since there are no contributions in the lowest order of $\hat{V}$, because $P\hat{V}P = 0$, the nonzero contributions to $V_{\text{eff}}(AB)$ come from the second order of $\hat{V}$ (see Fig. 26) as

$$\begin{aligned} V_{\text{eff}}(AB) &= \langle A^*|\langle B|\langle 0|\left[P\hat{V}Q\left(E_P^0 - E_Q^0\right)^{-1}\hat{V}P\right. \\ &\quad \left. + P\hat{V}\left(E_P^0 - E_Q^0\right)^{-1} Q\hat{V}P\right]|A\rangle|B^*\rangle|0\rangle \\ &= -\frac{4\pi}{(2\pi)^3}\int d^3k \left[\frac{K'_A(\vec{k})K'^*_B(\vec{k})}{\Omega(\vec{k}) - \Omega_0(B)}\right. \\ &\quad \left. + \frac{K'_B(\vec{k})K'^*_A(\vec{k})}{\Omega(\vec{k}) + \Omega_0(A)}\right]. \end{aligned} \tag{38}$$

Here, the summation of $\vec{k}$ is replaced by integrating $\vec{k}$, and $\hat{H}_0$ in the denominators with respect to the corresponding eigenvalues. The excitation energies $\hbar\Omega_0(A)$ and $\hbar\Omega_0(B)$ are

$$\begin{aligned}\hbar\Omega_0(A) &= \frac{3\hbar^2}{2m_e}\left(\frac{\pi}{a}\right)^2 \\ \hbar\Omega_0(B) &= \frac{3\hbar^2}{2m_e}\left(\frac{\pi}{b}\right)^2 \end{aligned} \tag{39}$$

from (29). We can similarly show how $\langle\Psi_\lambda^{(1)}|\hat{V}_{\text{eff}}|\Psi_\mu^{(1)}\rangle$ contributes to the effective sample-probe interaction $V_{\text{eff}}(BA)$.

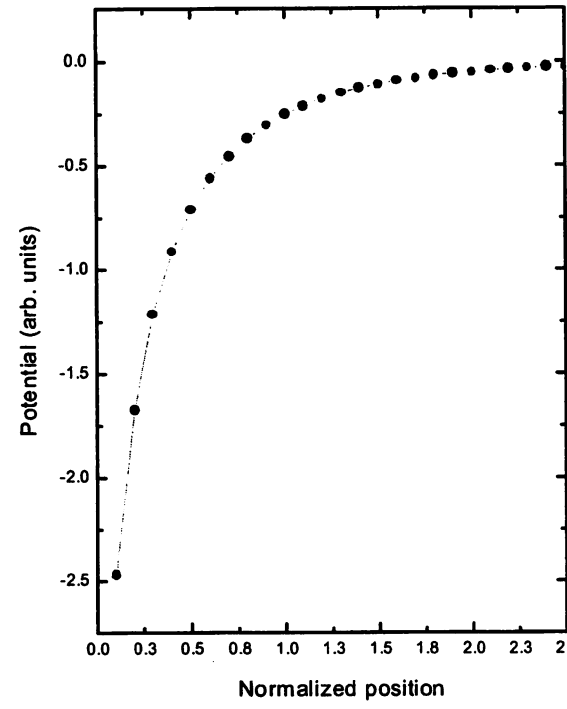

Fig. 27. Yukawa potential: Theoretical position dependence of the potential is shown.

Using the effective mass approximation of the exciton-polaritons given in (34) and the fact that $f(k) \sim$ constant, we obtain the explicit function form of

$$\begin{aligned} &V_{\text{eff}}(AB) + V_{\text{eff}}(BA) \\ &\quad \propto \frac{\exp[(i\gamma\pi r)/b]}{r} + \frac{\exp[-(\gamma\pi r)/a]}{r} \\ &\qquad + \frac{\exp[(i\gamma\pi r)/a]}{r} + \frac{\exp[-(\gamma\pi r)/b]}{r} \\ &r = |\vec{r}_A - \vec{r}_B| \end{aligned} \tag{40}$$

where γ is the effective mass ratio for exciton-polaritons and electrons in the probe tip and sample system and is defined as $\gamma = (3m_p/m_e)^{1/2}$. This gives the effective sample-probe interaction derived from microscopic consideration, and the second and fourth terms are the Yukawa function (see Fig. 27), which was empirically assumed in the virtual photon model. The numerical estimation also shows that contributions to the effective interaction from $f(k) \neq$ const are negligible for typical cases. Therefore, we find that the Yukawa potential as the effective sample-probe interaction plays, in particular, an important role in the near-field region, typically less than $k_c^{-1} \sim 100$ nm. The formula also shows that optical near field is effectively localized near the sample-probe system and that the decay length is proportional to the inverse of the probe (sample) size and consistent with the experimental results.

C. Application of the Theory

In the previous section, we formulated optical near-field problems, emphasizing the quantum theoretical viewpoint. It was shown that the Yukawa potential describes the effective interaction between the nanometric sample-probe system in

the optical near-field region as a result of renormalizing or screening. This is the empirical assumption of the virtual photon model. We will take advantage of the characteristics of the model in order to develop applications of our theory for both the conventional and the quantum-mechanical aspects of optical near-field problems.

1) Size Resonance in the Probe-Sample System: Let us investigate the contrast of signals picked up by a nanometric probe sphere (or aperture) interacting with a nanometric sample sphere (or aperture). We examine, in particular, how the contrast depends on the sizes (a_p for the probe and a_s for the sample). In the following we use the term "sphere," but the results are also applicable to the "aperture." Let the probe sphere scan above the sample sphere on a plane of constant height, where the height of d is the shortest distance between the top of the sample sphere and the bottom of the probe sphere. From (40), the Yukawa potential as the effective interaction is generated between the two arbitrary points $(\vec{r}_p, \vec{r}_s)$ on the surfaces of the probe and sample spheres. Thus, the pickup signal obtained from the whole of the probe sphere can be written as

$$I \propto \left| \int d\vec{r}_p \int d\vec{r}_s \, V_{\text{eff}}(r_{\text{ps}}) \right|^2, \quad r_{\text{ps}} = |\vec{r}_p - \vec{r}_s|. \quad (41)$$

This might be regarded as showing that the Yukawa sources are distributed on both the spheres. Note that (41) corresponds to (1) and (2) used in Section III-C. Since we are interested in the effect of the existence of the probe sphere close to the sample sphere, we define the contrast as the signal I divided by the geometrical cross-section $\pi(a_s^2 + a_p^2)$, which corresponds to the case in which each sphere is individually located. Such a example is illustrated in Fig. 28, which shows that the contrast remains the highest when the probe size a_p is comparable or slightly less than the sample size a_s. This result is called the size-resonance effect and has been obtained by numerical calculation based on classical electromagnetics [82], but our approach is more convenient with respect to the computation time and applicability to an arbitrary shape.

2) Atom Deflection as Potential Scattering: As an example of a quantum-mechanical system, we discuss the possibility of applying the formulation to atom deflection and manipulation with a fiber probe (refer to Section III-C). These techniques are unique and will be essential for carrying an atom to a desired point on a substrate with high spatial accuracy far beyond the diffraction limit [83]. Suppose that an incident atom with momentum $\hbar\vec{k}$ is deflected into momentum $\hbar\vec{k}'$ by an optical near field V_{eff}. Then the differential cross-section or angular distribution of the deflected atom is given by

$$\frac{d\sigma}{d\Omega} = \left| \frac{M}{2\pi\hbar^2} \left\langle \vec{k}' \right| V_{\text{eff}} \left| \vec{k} \right\rangle \right|^2 \quad (42)$$

where M is the mass of the atom and the Born approximation is assumed. Fig. 29 shows an example that Rb atom is deflected by optical near field generated from the tip sphere with variable radius a. This kind of evaluation and thorough investigation will be required in the design of atom guidance and manipulation systems using the optical near field, as well as in the discussion of basic experimental results. The above treatment is based on the Yukawa potential scattering of an atom, and it is an interesting issue to take into consideration

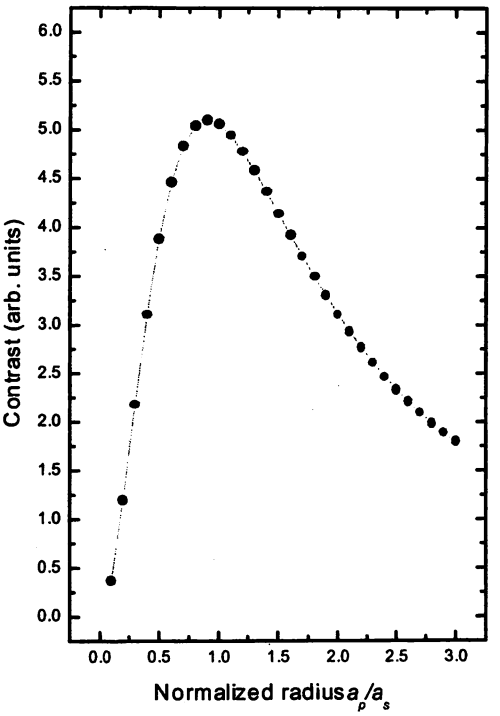

Fig. 28. Size-resonance effect in the probe-sample system calculated by using the Yukawa potential.

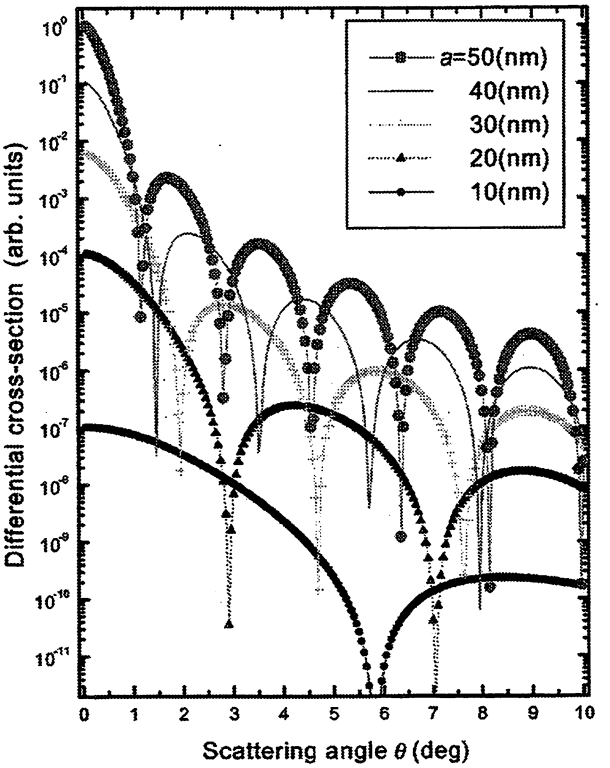

Fig. 29. Angular distribution of Rb atom deflected by optical near fields. Dependence on the size of the probe tip is shown for 1) a = 50 nm; 2) a = 40 nm; 3) a = 30 nm; 4) a = 20 nm; and 5) a = 10 nm, when the incident velocity of the atom is assumed as v = 1 m/s.

the effect of effective dipole transition and energy-level shift caused by the optical near field. It is also important for future study to apply the theory to local excitation of a molecule or an artificial atom/molecule (quantum dot) in order to discuss quantum coherence, nonlinear response, photochemical reactions, and so on.

D. Future Outlook

We have pointed out the need for quantum theoretical treatment and an intuitive model of optical near-field problems. Paying special attention to the hierarchical structure of optical near-field systems, we have developed a quantum theoretical formulation on the basis of the projection-operator method and discussed the virtual photon model from the elementary excitation and effective interaction point of view. As an example of the application of the theory, we have numerically shown the so-called size-resonance effect and outlined problems involving atom deflection and manipulation by using optical near fields.

In our theory, optical near fields can be viewed as real photons and matter excitation simultaneously, i.e., massive virtual photons. Thus, it is fascinating to investigate problems and/or phenomena (energy-level and size dependence, quantum coherence, dimensionality, etc.) inherent in quantum objects such as atoms, molecules, and quantum dots interacting with optical near fields. Atom deflection and manipulation/nano fabrication, as mentioned in the previous section, would provide very appropriate examples involving a variety of challenges from fundamental physics to nano/atom photonics.

V. Summary

This paper reviewed the recent progress of the application of interactions between optical near field and nanoscale materials and atoms. Photochemical vapor deposition of Zn dots and lines with a size of sub-100 nm has been realized by using an ultraviolet optical near field. Deposition of nanoscale ZnO was also revealed. Manipulation of atoms was also described to control the thermal motion of atoms in high vacuum. Experimental and theoretical results of manipulation by using optical near field generated on a prism surface, hollow fiber, and fiber probe were presented. Quantum theoretical treatment of optical near field was given, and intuitive model of Yukawa potential was presented.

Acknowledgment

The authors would like to thank Prof. M. Konagai and Prof. A. Yamada (Tokyo Institute of Technology) for useful advice for the development of the instrument, and S. Mononobe (Kanagawa Academy of Science and Technology) and H. Fukuda (Ricoh Co. Ltd.) for their useful comments on fibers and experiments. They express special thanks to Dr. V. Polonski (Japan Science and Technology Corp.) and Y. Yamamoto (Tokyo Institute of Technology) for their devoted collaboration.

They acknowledge Dr. S. Sudo and Dr. Y. Sakai (NTT Opto-Electronic Laboratory) for useful discussion on hollow optical fibers. They also thank Prof. W. Jhe (Seoul National University) for his efficient collaboration.

The authors gratefully acknowledge fruitful conversation with Prof. H. Hori and Dr. I. Banno (Yamanashi University), Dr. S. Sangu (Japan Science and Technology Corporation), and Dr. M. Kourogi (Tokyo Institute of Technology). They also appreciate valuable suggestions from Prof. T. Kohmura (University of Tsukuba).

References

[1] E. Maayan, O. Kreinin, G. Bahir, J. Salzman, A. Eyal, and R. Beserman, "Selective growth of GaAs/InGaP heterostructures by photo-enhanced organometallic chemical vapor deposition," *J. Crystal. Growth*, vol. 135, pp. 23–30, 1994.

[2] D. Bauerle, "Laser-chemical processing: Recent developments," *Appl. Surf. Sci.*, vol. 106, pp. 1–10, 1996.

[3] M. Ohtsu, Ed., *Near-Field Nano/Atom Optics and Technology*. Berlin, Germany: Springer-Verlag, 1998.

[4] M. Ohtsu, "Progress of high-resolution photon scanning tunneling microscope due to a nanometric fiber probe," *J. Lightwave Technol.*, vol. 13, pp. 1200–1221, 1995.

[5] R. U. Maheswari, H. Tatsumi, Y. Katayama, and M. Ohtsu, "Observation of subcellular nanostructure of single neurons with an illumination mode photon scanning tunneling microscopy," *Opt. Commun.*, vol. 120, pp. 325–334, 1995.

[6] R. U. Maheswari, S. Mononobe, H. Tatsumi, Y. Katayama, and M. Ohtsu, "Observation of subcellular structure of neurons by an illumination mode near-field optical microscope under an optical feedback control," *Opt. Rev.*, vol. 3, pp. 463–467, 1996.

[7] M. Naya, R. Micheletto, S. Mononobe, R. U. Maheswari, and M. Ohtsu, "Near-field optical imaging of flagellar filaments of salmonella in water with optical feedback control," *Appl. Opt.*, vol. 36, pp. 1681–1683, 1997.

[8] H. F. Hess, E. Betzig, T. D. Harris, L. N. Pfeiffer, and K. W. West, "Near-field spectroscopy of the quantum constituents of a luminescent system," *Science*, vol. 264, pp. 1740–1745, 1994.

[9] Y. Toda, M. Kourogi, M. Ohtsu, Y. Nagamune, and Y. Arakawa, "Spatially and spectrally resolved imaging of GaAs quantum-dot structures using near-field optical technology," *Appl. Phys. Lett.*, vol. 69, no. 6, pp. 827–829, 1996.

[10] T. Saiki, K. Nishi, and M. Ohtsu, "Low temperature near-field photoluminescence spectroscopy of InGaAs single quantum dots," *Jpn. J. Appl. Phys.*, vol. 37, no. 3B, pp. 1638–1642, 1998.

[11] V. V. Polonski, Y. Yamamoto, M. Kourogi, H. Fukuda, and M. Ohtsu, "Nanometric patterning of zinc by optical near-field photochemical vapor deposition," *J. Microscopy*, vol. 194, no. 2/3, pp. 545–551, 1999.

[12] Y. Yamamoto, V. V. Polonski, G. H. Lee, M. Kourogi, and M. Ohtsu, "Photochemical vapor deposition by optical near field," in *Proc. SPIE 44th Annu. Meeting, 3791-18*, Denver, CO, July 18–23, 1999.

[13] S. Mononobe, T. Saiki, T. Suzuki, S. Koshihara, and M. Ohtsu, "Fabrication of a triple tapered probe for near-field optical spectroscopy in UV region based on selective etching of a multistep index fiber," *Opt. Commun.*, vol. 146, pp. 45–48, Jan. 15, 1998.

[14] G. T. Ruiter, "Dynamic behavior of tuning fork shear-force feedback," *Appl. Phys. Lett.*, vol. 71, no. 1, pp. 28–30, 1997.

[15] D. J. Ehrlich, R. M. Osgood Jr., and T. F. Deutsch, "Photodeposition of metal films with ultraviolet laser light," *J. Vac. Sci. Technol.*, vol. 21, pp. 23–32, 1982.

[16] T. Pangaribun, K. Yamada, S. Jiang, H. Ohsawa, and M. Ohtsu, "Reproducible fabrication technique of nanometric tip diameter fiber probe for photon scanning microscope," *Jpn. J. Appl. Phys.*, pt. 2, vol. 31, pp. L1302–L1304, 1992.

[17] R. Wiesendanger, "Fabrication of nanometer structures using STM," *Appl. Surf. Sci.*, vol. 54, pp. 271–277, 1992.

[18] G. H. Lee, Y. Yamamoto, M. Kourogi, and M. Ohtsu, "Fabrication of ZnO nanostructure using near-field optical technology," in *Proc. SPIE 44th Annu. Meeting, 3791-19*, Denver, CO, July 18–23, 1999.

[19] O. Madelung, *Landolt-Bornstein New Series*. Berlin, Germany: Springer-Verlag, 1982, vol. 17b.

[20] T. Y. Ma, G. C. Park, and K. W. Kim, "Substrate temperature dependence of ZnO films prepared by ultrasonic spray pyrolysis," *Jpn. J. Appl. Phys.*, vol. 35, no. 12A, pp. 6208–6211, 1996.

[21] Z. T. Tang, G. K. L. Wong, and P. Yu, "Room-temperature ultraviolet laser emission from self-assembled ZnO microcrystallite thin films," *Appl. Phys. Lett.*, vol. 72, no. 25, pp. 3270–3272, 1998.
[22] D. B. Bagnall, Y. F. Chen, Z. Zhu, and T. Yao, "Optically pumped lasing of ZnO at room temperature," *Appl. Phys. Lett.*, vol. 70, no. 17, pp. 2230–2232, 1997.
[23] V. I. Balykin and V. S. Letokhov, *Atom Optics with Laser Light*. Chur: Harwood, 1995.
[24] M. Ohtsu and H. Hori, *Near-Field Nano-Optics*. New York: Kluwer/Plenum, 1999.
[25] M. Ohtsu, S. Jiang, T. Pangaribuan, and M. Kozuma, "Nanometer resolution photon STM and single atom manipulation," in *Near-Field Optics*, D. W. Pohl and D. Courjon, Eds. Dordrecht, The Netherlands: Kluwer, 1993, pp. 131–139.
[26] H. Hori, "Quantum optical picture of photon STM and proposal of single atom manipulation," in *Near Field Optics*, D. W. Pohl and D. Courjon, Eds. Dordrecht, The Netherlands: Kluwer, 1993, pp. 105–114.
[27] J. P. Dowling and J. Gea-Banacloche, "Evanescent light-wave atom mirrors, resonators, waveguides, and traps," in *Advances in Atomic, Molecular, and Optical Physics*, B. Bederson and H. Walther, Eds. San Diego, CA: Academic, 1996, vol. 37, pp. 1–94.
[28] V. I. Balykin, V. S. Letokov, Yu. B. Ovchinnikov, and A. I. Sidorov, "Quantum-state-selective mirror reflection of atoms by laser light," *Phys. Rev. Lett.*, vol. 60, no. 21, pp. 2137–2140, 1988.
[29] C. G. Aminoff, A. M. Steane, P. Bouyer, P. Desbiolles, J. Dalibard, and C. Cohen-Tannoudji, "Cesium atoms bouncing in a stable gravitational cavity," *Phys. Rev. Lett.*, vol. 71, no. 19, pp. 3083–3086, 1993.
[30] V. Sandoghdar, C. I. Sukenik, E. A. Hinds, and S. Haroche, "Direct measurement of the van der Waals interaction between an atom an its images in a micron-sized cavity," *Phys. Rev. Lett.*, vol. 68, no. 23, pp. 3432–3435, 1992.
[31] A. Landragin, J.-Y. Courtois, G. Labeyrie, N. Vansteenkiste, C. I. Westbrook, and A. Aspect, "Measurement of the van der Waals force in an atomic mirror," *Phys. Rev. Lett.*, vol. 77, no. 8, pp. 1464–1467, 1996.
[32] S. Marksteiner, C. M. Savage, and P. Zoller, "Coherent atomic waveguides from hollow optical fibers: Quantized atomic motion," *Phys. Rev. A*, vol. 50, no. 3, pp. R2680–R2690, 1994.
[33] H. Ito, K. Sakaki, T. Nakata, W. Jhe, and M. Ohtsu, "Optical potential for atom guidance in a cylindrical-core hollow fiber," *Opt. Commun.*, vol. 115, pp. 57–64, 1995.
[34] ——, "Optical guidance of neutral atoms using evanescent waves in a cylindrical-core hollow fiber: Theoretical approach," *Ultramicroscopy*, vol. 61, pp. 91–97, 1995.
[35] M. J. Renn, E. A. Donley, E. A. Cornell, C. E. Wieman, and D. Z. Anderson, "Evanescent-wave guiding of atoms in hollow optical fibers," *Phys. Rev. A*, vol. 53, no. 2, pp. R648–R651, 1996.
[36] H. Ito, T. Nakata, K. Sakaki, M. Ohtsu, K. I. Lee, and W. Jhe, "Laser spectroscopy of atoms guided by evanescent waves in micron-sized hollow optical fibers," *Phys. Rev. Lett.*, vol. 76, no. 24, pp. 4500–4503, 1996.
[37] H. Ito, K. Sakaki, M. Ohtsu, and W. Jhe, "Evanescent-light guiding of atoms through hollow optical fiber for optically controlled atomic deposition," *Appl. Phys. Lett.*, vol. 70, no. 19, pp. 2496–2498, 1997.
[38] H. Ito, K. Sakaki, W. Jhe, and M. Ohtsu, "Atom guidance using evanescent waves in small hollow optical fibers and its applications," in *Proc. SPIE*, vol. 2995, 1997, pp. 138–145.
[39] K. Kobayashi and M. Ohtsu, "Quantum theoretical approach to a near-field optical system," *J. Microscopy*, vol. 194, no. 2/3, pp. 249–254, 1999.
[40] M. Chevrollier, M. Fichet, M. Oria, G. Rahmat, D. Bloch, and M. Ducloy, "High resolution selective reflection spectroscopy as a probe of long-range surface interaction: Measurement of the surface van der Waals attraction exerted on excited Cs atoms," *J. Phys. France II*, vol. 2, pp. 631–657, 1992.
[41] W. Jhe and J. W. Kim, "Atomic energy-level shifts near a dielectric microsphere," *Phys. Rev. A*, vol. 51, no. 2, pp. 1150–1153, 1995.
[42] H. Nha and W. Jhe, "Cavity quantum electrodynamics between parallel dielectric surface," *Phys. Rev. A*, vol. 54, no. 4, pp. 3505–3513, 1996.
[43] V. V. Klimov and V. S. Letokhov, "New atom trap configurations in the near field of laser radiation," *Opt. Commun.*, vol. 121, pp. 130–136, 1995.
[44] T. Yatsui, M. Kourogi, and M. Ohtsu, "Increasing throughput of a near-field optical fiber probe over 1000 times by the use of a triple-tapered structure," *Appl. Phys. Lett.*, vol. 73, no. 15, pp. 2090–2092, 1998.
[45] H. Ito, A. Takamizawa, H. Tanioka, and M. Ohtsu, "Precise control of atoms with optical near fields: Deflection and trap," in *Proc. SPIE*, vol. 3791, 1999, pp. 1–8.
[46] H. Ito, K. Sakaki, W. Jhe, and M. Ohtsu, "Atomic funnel with evanescent light," *Phys. Rev. A*, vol. 56, no. 1, pp. 712–718, 1997.
[47] "Laser cooling and trapping of atoms," *J. Opt. Soc. Amer. B*, vol. 11, pp. 2019–2278, 1989.
[48] J. Söding, R. Grimm, and Yu. B. Ovchinnikov, "Gravitational laser trap for atoms with evanescent-wave cooling," *Opt. Commun.*, vol. 119, pp. 652–662, 1995.
[49] P. Desbiolles, M. Arndt, P. Szriftgiser, and J. Dalibard, "Elementary Sisyphus process close to a dielectric surface," *Phys. Rev. A*, vol. 54, no. 5, pp. 4292–4298, 1996.
[50] N. Nha and W. Jhe, "Sisyphus cooling on the surface of a hollow-mirror atom trap," *Phys. Rev. A*, vol. 56, no. 1, pp. 729–736, 1997.
[51] C. Cohen-Tannoudji, J. Dupont-Roc, and G. Grynberg, *Atom-Photon Interactions*. New York: Wiley, 1992.
[52] T. Saiki and K. Matsuda, "Near-field optical fiber probe optimized for illumination-collection hybrid mode operation," *Appl. Phys. Lett.*, vol. 74, no. 19, pp. 2773–2775, 1999.
[53] J. Trautmann and W. P. Ambrose, "Near-field optical imaging and spectroscopy of single molecules," in *Single Molecule Optical Detection, Imaging and Spectroscopy*, T. Basché, W. E. Moerner, M. Orrit, and U. P. Wild, Eds, Weinheim, Germany: Wiley-VCH, 1997, pp. 191–222.
[54] E. Betzig, J. K. Trautman, R. Wolfe, E. M. Gyorgy, and P. L. Finn, "Near-field magneto-optics and high density data storage," *Appl. Phys. Lett.*, vol. 61, no. 2, pp. 142–144, 1992.
[55] S. Hosaka, T. Shintani, M. Miyamoto, A. Kikukawa, A. Hirotsune, M. Terao, M. Yoshida, K. Fujita, and S. Kämmer, "Phase change recording using a scanning near-field optical microscope," *J. Appl. Phys.*, vol. 79, no. 10, pp. 8082–8086, 1996.
[56] S. Jiang, J. Ichihashi, H. Monobe, M. Fujihira, and M. Ohtsu, "Highly localized photochemical process in LB films of photochromic material by using a photon scanning tunneling microscope," *Opt. Commun.*, vol. 106, pp. 173–177, 1994.
[57] C. Girard, O. J. F. Martin, and A. Dereux, "Molecular lifetime changes induced by nanometer scale optical fields," *Phys. Rev. Lett.*, vol. 75, no. 16, pp. 3098–3101, 1995.
[58] O. Keller, "Toward a microscopic theory of spatial confinement of light," *Ultramicroscopy*, vol. 71, pp. 1–9, Mar. 1, 1998.
[59] K. Kobayashi, "Spin polarization in near-field optical microscopy," *Appl. Phys. A*, vol. 66, no. 7, pp. S391–S395, 1998.
[60] K. Cho, "Nonlocal theory of radiation-matter interaction: Boundary-condition-less treatment of Maxwell equations," *Prog. Theor. Phys. Suppl.*, vol. 106, pp. 225–233, 1991.
[61] K. Cho, Y. Ohfuti, and K. Arima, "Theory of resonant SNOM (scanning near field optical microscopy): Breakdown of the electric dipole selection rule in the reflection mode," *Surf. Sci.*, vol. 363, pp. 378–384, 1996.
[62] C. K. Carniglia and L. Mandel, "Quantization of evanescent electromagnetic waves," *Phys. Rev. D*, vol. 3, pp. 280–296, 1971.
[63] J. M. Vigoureux, L. D'Hooge, and D. V. Labeke, "Quantization of evanescent electromagnetic waves: Momentum of the electromagnetic field very close to a dielectric medium," *Phys. Rev. A*, vol. 21, no. , pp. 347–355, 1980.
[64] P. R. Berman, Ed., *Cavity Quantum Electrodynamics*. San Diego, CA: Academic, 1994.
[65] H. Cao, S. Pau, Y. Yamamoto, and G. Bjork, "Exciton-polariton ladder in a semiconductor microcavity," *Phys. Rev. B*, vol. 54, no. 11, pp. 8083–8086, 1996.
[66] D. W. Vernooy and H. J. Kimble, "Quantum structure and dynamics for atom galleries," *Phys. Rev. A*, vol. 55, no. 2, pp. 1239–1261, 1997.
[67] M. Orrit, C. Aslangul, and P. Kottis, "Quantum-mechanical-model calculations of radiative properties of a molecular crystal. I. Polaritons and abnormal decays of excitons in one- and two-dimensional systems," *Phys. Rev. B*, vol. 25, pp. 7263–7280, 1982.
[68] J. Knoester and S. Mukamel, "Intermolecular forces, spontaneous emission, and superradiance in a dielectric medium: Polariton-mediated interactions," *Phys. Rev. A*, vol. 40, no. 12, pp. 7065–7080, 1989.
[69] B. Huttner and S. M. Barnett, "Quantization of the electromagnetic field in dielectrics," *Phys. Rev. A*, vol. 46, no. 7, pp. 4306–4322, 1992.
[70] G. Juzeliūnas and D. L. Andrews, "Quantum electrodynamics of resonant energy transfer in condensed matter," *Phys. Rev. B*, vol. 49, no. 13, pp. 8751–8763, 1994.
[71] M. S. Yeung and T. K. Gustafson, "Spontaneous emission near an adsorbing dielectric surface," *Phys. Rev. A*, vol. 54, no. 6, pp. 5227–5242, 1996.

[72] J. J. Hopfield, "Theory of the contribution of excitons to the complex dielectric constant of crystals," *Phys. Rev.*, vol. 112, pp. 1555–1567, 1958.
[73] M. Kuwata-Gonokami, S. Inouye, H. Suzuura, M. Shirane, and R. Shimano, "Parametric scattering of cavity polaritons," *Phys. Rev. Lett.*, vol. 79, no. 7, pp. 1341–1344, 1997.
[74] K. Kobayashi and M. Ohtsu, "Quantum theory and virtual photon model of near field optics," in *Proc. SPIE*, vol. 3791, 1999, pp. 10–20.
[75] H. Hyuga and H. Ohtsubo, "Breakdown of the Siegert theorem and the many-body charge density operators," *Nucl. Phys. A*, vol. 294, pp. 348–356, 1978.
[76] K. Kobayashi and T. Kohmura, "Momentum-transfer dependence of nuclear spin-isospin transitions," *Prog. Theor. Phys.*, vol. 71, pp. 327–338, 1984.
[77] R. Zwanzig, "On the identity of three generalized master equations," *Physica*, vol. 30, pp. 1109–1123, 1964.
[78] H. Mori, "Transport, collective motion, and Brownian motion," *Prog. Theor. Phys.*, vol. 33, pp. 423–455, 1965.
[79] C. R. Willis and R. H. Picard, "Time-dependent projection-operator approach to master equations for coupled systems," *Phys. Rev. A*, vol. 9, pp. 1343–1358, 1974.
[80] P. Fulde, *Electron Correlations in Molecules and Solids*, 3rd ed. Berlin, Germany: Springer-Verlag, 1995.
[81] D. P. Craig and T. Thirunamachandran, *Molecular Quantum Electrodynamics*. London, U.K.: Academic, 1984.
[82] K. Jang and W. Jhe, "Nonglobal model for a near-field scanning optical microscope using diffraction of the optical near field," *Opt. Lett.*, vol. 21, pp. 236–238, 1996.
[83] H. Ito, K. Otake, and M. Ohtsu, "Near-field optical guidance and manipulation of atoms," in *Proc. SPIE*, vol. 3467, 1998, pp. 250–257.

Motoichi Ohtsu (Senior Member, IEEE) was born in Kanagawa, Japan, on October 5, 1950. He received the B.E., M.E., and D.E. degrees in electronics engineering from the Tokyo Institute of Technology, Tokyo, Japan, in 1973, 1975, and 1978, respectively.

In 1978, he was appointed as a Research Associate and in 1982, he became an Associate Professor at the Tokyo Institute of Technology. From 1986 to 1987, while on leave from Tokyo Institute of Technology, he joined AT&T Bell Laboratories, Holmdel, NJ, as a Member of Technical Staff. In 1991, he became a Professor at the Tokyo Institute of Technology. From 1993 to 1998, he has been the leader of the "Photon Control" project at the Kanagawa Academy of Science and Technology (KAST), Kanagawa, Japan. Since April 1998, he has been the leader of the "Near-Field Photonics" research group of KAST. Since October 1998, he has been the leader of the "Localized Photon" project for the Exploratory Research for Advanced Technology (ERATO) at the Japan Science and Technology Corporation (JST). He has written more than 150 papers and has received a number of patents. He is author and coauthor of 20 books, including *Near-Field Nano/Atom Optics and Technology* (Berlin, Tokyo: Springer-Verlag, 1998) and *Near Field Nano-Optics* (New York: Kluwer/Plenum, 1999). He is currently President of LEOS Japan Chapter, IEEE. He has been a tutorial Lecturer of the SPIE and the OSA. His main fields of interest are near-field optics and its application to nano/atom photonics.

Dr. Ohtsu is a Member of the Institute of Electronics, Information and Communications Engineering of Japan, the Institute of Electrical Engineering of Japan, the Japan Society of Applied Physics, the Optical Society of America, and the American Physical Society. He has been awarded ten prizes from academic institutions, including the Issac Koga Gold Medal of URSI in 1984, the Japan IBM Science Award in 1988, two awards from the Japan Society of Applied Physics in 1982 and 1990, and the Inoue Science Foundation Award in 1999.

Kiyoshi Kobayashi (Member, IEEE) was born in Okayama, Japan, on November 25, 1953. He received the D.S. degree in physics from the University of Tsukuba, Tsukuba, Japan, in 1982.

After graduating from the University of Tsukuba, he joined IBM Japan as a Research Staff Member at Tokyo Research Laboratory. Since 1998, he has been the theoretical group leader of the "Localized Photon" project for the Exploratory Research for Advanced Technology (ERATO) at the Japan Science and Technology Corporation (JST), Tokyo. His main fields of interest are theory on near-field optics and its application to nano/atom photonics.

Dr. Kobayashi is a Member of the Physical Society of Japan, the Japan Society of Applied Physics, the Optical Society of America, and the American Physical Society.

Haruhiko Ito was born in Yokkaichi, Japan, in 1961. He received the Ph.D. degree from Kyoto University, Kyoto, Japan, in 1994.

He joined the Kanagawa Academy of Science and Technology, Japan, in 1994. Since 1999, he has been an Associate Professor with the Interdisciplinary Graduate School of Science and Engineering, Tokyo Institute of Technology, Yokohama, Japan. His current research interests include atom optics and near-field optics.

Geun-Hyoung Lee was born in Seoul, Korea, on February 12, 1965. He received the B.E. and M.E. degrees in material science engineering from the Yonsei University, Seoul, in 1987 and 1990, respectively, and the Ph.D. degree in material science engineering from the Tokyo Institute of Technology, Tokyo, Japan, in 1998.

Since 1998, he has been a Researcher at the Japan Science and Technology Corporation, Tokyo. His main interests are the fabrication of nano-structure using optical near-field technology.

Dr. Lee received the excellent research presentation award from the Japan Society of Applied Physics and the Outstanding student research award at the 4th International Conference on Laser Ablation, USA, both in 1997.

High-density–speed optical near-field recording–reading with a pyramidal silicon probe on a contact slider

Takashi Yatsui

Interdisciplinary Graduate School of Science and Engineering, Tokyo Institute of Technology, 4259 Nagatsuta, Midori-ku, Yokohama 226-8502, Japan

Motonobu Kourogi

Interdisciplinary Graduate School of Science and Engineering, Tokyo Institute of Technology, 4259 Nagatsuta, Midori-ku, Yokohama 226-8502, Japan, and Kanagawa Academy of Science and Technology, 3-2-1 Sakado, Takatsu-ku, Kawasaki, Kanagawa 213-0012, Japan

Kazuo Tsutsui

Interdisciplinary Graduate School of Science and Engineering, Tokyo Institute of Technology, 4259 Nagatsuta, Midori-ku, Yokohama 226-8502, Japan

Motoichi Ohtsu

Interdisciplinary Graduate School of Science and Engineering, Tokyo Institute of Technology, 4529 Nagatsuta, Midori-ku, Yokohama 226-8502, Japan, and Kanagawa Academy of Science and Technology, 3-2-1 Sakado, Takatsu-ku, Kawasaki, Kanagawa 213-0012, Japan

Jun-ichi Takahashi

Research and Development Center, Ricoh Company, Ltd., 16-1 Shin-eichou, Tsuzuki-ku, Yokohama Kanagawa 224-0035, Japan

Received April 27, 2000

We demonstrate high-density–speed phase-change recording–reading by use of a pyramidal silicon structure. The contact slider, which has a pyramidal silicon probe array with height dispersion of less than 10 nm, is fabricated by use of a silicon-on-insulator wafer. By illumination with a laser beam (λ = 830 nm) of one element of the probe array, we find the shortest phase-change mark length and the carrier-to-noise ratio to be 110 nm and 10 dB, respectively, corresponding to a data transmission rate of 2.0 MHz. This rate can be increased to 200 MHz by use of all elements of the probe array. © 2000 Optical Society of America

OCIS codes: 210.0210, 220.4000.

The use of an optical near field for realization of a high-density optical storage system has attracted a great deal of attention. The development of a metallic sharpened optical fiber probe with a subwavelength aperture has made it possible to realize high recording density beyond the diffraction limit.[1–3]

Recently it was reported that the interference characteristics of the guided modes in the metallic tapered fiber probe result in the maximum electric field intensity and the minimum spot size at each cutoff diameter of the modes.[4] By optimization of the interference characteristics, an increase in the throughput of 1000 times was achieved. Thus it becomes possible to realize optical near-field recording–reading with a data transmission rate as high as or even higher than 100 Mbits/s. However, since precise mechanical tracking of a single fiber probe while maintaining a probe–medium separation within 10 nm by conventional actuators is difficult, reading is limited to extremely low speed.

For realization of a high data trnasmission rate a superresolution near-field structure[5] and a planar probe mounted on an optical slider[6] were proposed recently. Since these methods do not require shear-force feedback, reading speed is increased without technical difficulties. However, since the incident light is focused by a lens in these systems, the intensity of the optical near field generated on the subwavelength aperture might be low.

In this Letter we propose and demonstrate a new contact slider with a high throughput ratio of near-field intensity for realization of high recording density and fast readout to the phase-change medium. Schematics of the slider structure and the data storage system are illustrated in Fig. 1. A pyramidal silicon probe array is arranged on the rear pad of the slider. The advantages of such a slider are as follows:

(1) The high refractive index of the silicon (n = 3.67 at λ = 830 nm) leads to a short effective wavelength inside the probe, which results in higher throughput and smaller spot size than those of conventional fiber probes made from silica glass.[7]

(2) The height of the pyramidal silicon probe array is fabricated to be less than 10 μm so that sufficiently low propagation loss in the silicon is

0146-9592/00/171279-03$15.00/0

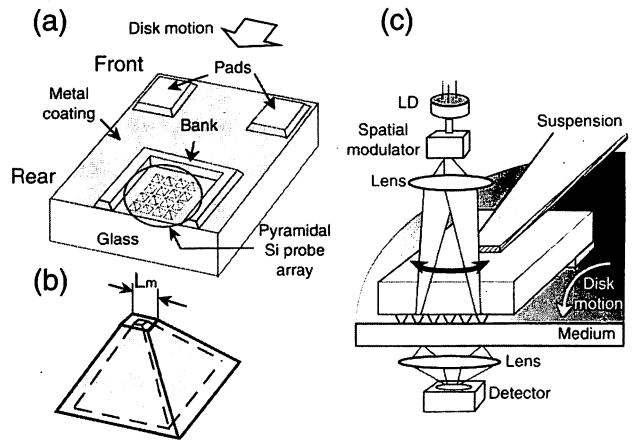

Fig. 1. (a) Contact slider with a pyramidal silicon probe array. (b) Pyramidal silicon probe (L_m mesa length). (c) Schematic of the data storage system with the slider: LD, laser diode.

maintained. Furthermore, the probe array has high durability because it is bonded to a thick glass substrate.

(3) Compared with those of previously reported pyramidal probes fabricated by use of a focused ion beam[8] or by the transfer mold technique in a pyramidal silicon groove,[9] ultrahigh homogeneity in the heights of the probes and the pads can be obtained, since the flatness of the probe tip and of the upper surface of the pad is determined by the uniformity of the thickness of the silicon wafer.

(4) Use of a probe array with many elements increases the total data transmission rate by parallel readout.[9–11] In this system the incident light is spatially modulated by an electro-optic method, and the scattered light from a different probe can be read out as a time-sequential signal.

Since the key issue in realizing a pyramidal silicon probe array is high homogeneity in the heights of the probes, the probe array is fabricated from a (100)-oriented silicon-on-insulator (SOI) wafer:

(i) The SOI wafer is bonded to the glass substrate by anodic bonding (300 V, 350 °C, 10 min)[12] [see Fig. 2(a)].

(ii) After removal of the silicon substrate from the SOI wafer by means of wet etching, the SiO_2 layer is patterned by photolithography.

(iii) The probe array, the bank, and the pads are fabricated by means of anisotropic etching (40 g · KOH + 60 g · H_2O + 40 g · isopropyl alcohol, 80 °C) [see Fig. 2(b)]. Note that height homogeneity is maintained by the remaining the SiO_2 layer [Fig. 2(c)].

(iv) The slider is quarried with a dicing saw.

(v) After removal of the SiO_2 layer, the slider is coated with 30-nm-thick aluminum for enhanced efficiency of light scattering.

Figures 2(d) and 2(e) show an optical image of the contact slider and a scanning electron microscopic image of the pyramidal silicon probe array fabricated on the slider, respectively. The height dispersions of the probes and pads should be less than 10 nm, because these dispersions are determined by the uniformity of thickness of the SOI wafer. Here the slider is designed by use of the design criteria[13] for a contact-type hard-disk head so that its jumping height over the phase-change medium is maintained at less than 10 nm. Furthermore, since the phase-change medium is fragile, we designed the bank so that the contact stress becomes 100 times weaker than the yield stress of the magnetic disk at a constant linear velocity (CLV) of 0.3 m/s, corresponding to a data transmission rate of 10 MHz for a data density of 1 Tbit/in.^{2}. To increase the readout speed 100 times, i.e., to realize a 1-Gbit/s data transmission rate for data density of 1 Tbit/in.^{2}, we fabricated 100 probe elements on the inner part of the bank for parallel readout.

In recording and readout experiments with the fabricated contact slider, we compared signals transmitted through phase-change marks recorded with

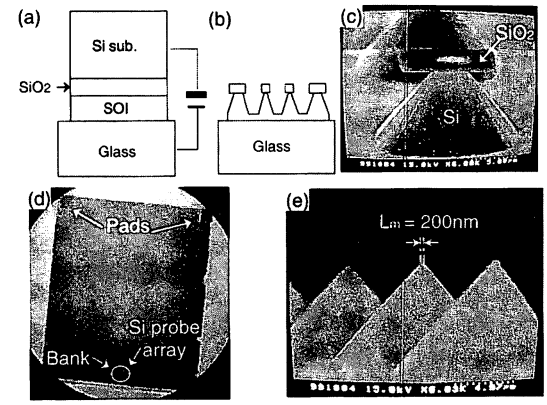

Fig. 2. Schematic of the process of fabrication of a contact slider with a pyramidal silicon probe array: (a) anodic bonding [step (i)]; (b) anisotropic etching for fabrication of the probe array, the bank, and the pads [step (ii)]; (c) result of step (ii); (d) result of step (iv). (e) Magnified scanning electron microscopic image of the fabricated pyramidal silicon probe array. sub., substrate.

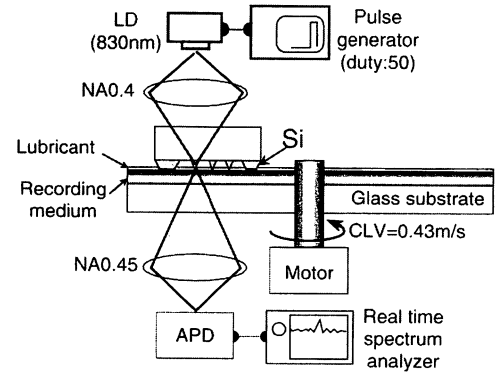

Fig. 3. Schematic of the experimental setup for phase-change recording–reading by the contact slider. APD, avalanche photodiode; LD, laser diode; NA's, numerical apertures.

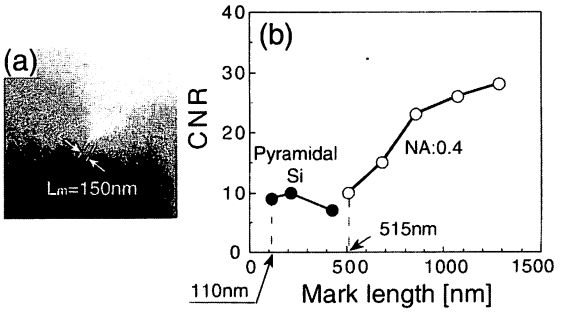

Fig. 4. (a) Magnified scanning electron microscopic image of the pyramidal silicon probe tip used for optical near-field recording–reading. (b) Dependence of the CNR on mark length for (filled circles) the optical near field with the pyramidal silicon probe and (open circles) propagating light focused by an object lens.

a single element of the probe array and focused propagating light. The experimental setup is shown in Fig. 3. The contact slider was glued to a suspension. The slider was in contact with a phase-change medium coated with a thin lubricant film (Fomblin Z-DOL). A laser beam (λ = 830 nm) was focused on one element of the probe array on the slider, where the rectangularly modulated frequency with a duty of 50% was changed from 0.16 to 2.0 MHz at a CLV of 0.43 m/s. Then the light transmitted through the recording medium was detected with an avalanche photodiode. We used an as-deposited AgInSbTe film as a recording medium. The optical recording powers for a pyramidal silicon probe with a mesa length L_m of 150 nm [see Figs. 1(b) and 4(a)] and a focused propagating light with an object lens (N.A., 0.4) were 200 mW and 15 mW, respectively, which in both cases is the lowest recording power of which we are aware. The optical throughput of the pyramidal silicon probe with a 30-nm-thick aluminum coating was 7.5×10^{-2}, which we estimated from the ratio of the optical powers for near- and far-field recordings. Readout was carried out at a CLV of 0.43 m/s, and the constant reading optical powers for the pyramidal silicon probe and the focused propagating light were 20 mW and 3.6 mW, respectively. The resolution bandwidth was fixed at 30 kHz.

The dependence of the carrier-to-noise ratio (CNR) on mark length is shown in Fig. 4(b). In this figure one can see that shorter crystalline phase-changed marks beyond the diffraction limit were recorded and read out by an optical near field generated on the pyramidal silicon probe. The shortest mark length was 110 nm at a CLV of 0.43 m/s, corresponding to a data transmission rate of 2.0 MHz. This is, to our knowledge, the first phase-change recording–reading with a contact slider. Since this slider has 100 elements in the probe array, we expect a 100-fold increase in the data transmission rate by parallel readout. Furthermore, a higher CLV can be expected, since we did not observe any damage on the probe tip or the recording medium after a series of experiments. The constant CNR of the pyramidal silicon probe seen in Fig. 4(b) might be due to the small spot size for recording–reading and the narrow recorded mark width, which are as small as L_m of the pyramidal silicon probe. These results indicate that an increased CNR and decreased mark length will be achieved by means of tracking during readout. Furthermore, it is expected that the recording density can be increased to as high as 1 Tbit/in.^{2} by optimization of the interference characteristics of the guided modes in the pyramidal silicon probe.[4]

In summary, we have proposed and fabricated a new contact slider with a pyramidal silicon probe array, with high homogeneity in the heights of the probes for realization of high recording density and a high data transmission rate. Furthermore, we demonstrated, for what is believed to be the first time, phase-change recording–reading with a slider. By illuminating one element of the silicon probe array with a laser beam (λ = 830 nm), we obtained a shortest mark length and a carrier-to-noise ratio of 110 nm and 10 dB, respectively, corresponding to a data transmisison rate of 2.0 MHz. This rate can be increased to 200 MHz by parallel readout with all elements of the probe array.

Valuable discussions with H. Ishiwara and E. Tokumitsu of the Tokyo Institute of Technology are greatly appreciated. T. Yatsui's e-mail address is yatsui@ohtsu.jst.go.jp.

References

1. E. Betzig, J. K. Trautman, R. Wolfe, E. M. Gyorgy, P. L. Finn, M. H. Kryder, and C. H. Chang, Appl. Phys. Lett. **61,** 142 (1992).
2. S. Jiang, J. Ichihashi, H. Monobe, M. Fujihira, and M. Ohtsu, Opt. Commun. **106,** 173 (1994).
3. S. Hosaka, T. Shintani, M. Miyamoto, A. Hirotsune, M. Terao, M. Yoshida, K. Fujita, and S. Kammer, Jpn. J. Appl. Phys. **35,** 443 (1996).
4. M. Kourogi, T. Yatsui, and M. Ohtsu, Proc. SPIE **3791,** 68 (1999).
5. J. Tominaga, T. Nakano, and N. Atoda, Appl. Phys. Lett. **73,** 2078 (1998).
6. H. Yoshikawa, Y. Andoh, M. Yamamoto, K. Fukuzawa, T. Tamamura, and T. Ohkubo, Opt. Lett. **25,** 67 (2000).
7. H. U. Dangebrink, T. Dziomba, T. Sulzbach, O. Ohlsson, C. Lehrer, and L. Frey, J. Microsc. (Oxford) **194,** 335 (1999).
8. F. Isshiki, K. Ito, and S. Hosaka, Appl. Phys. Lett. **76,** 804 (2000).
9. Y. J. Kim, K. Kurihara, K. Suzuki, M. Nomura, S. Mitsugi, M. Chiba, and K. Goto, Jpn. J. Appl. Phys. **39,** 1538 (2000).
10. T. Yatsui, M. Kourogi, K. Tsutsui, J. Takahashi, and M. Ohtsu, Proc. SPIE **3791,** 76 (1999).
11. D. W. Pohl, IBM J. Res. Dev. **39,** 701 (1995).
12. T. R. Anthony, J. Appl. Phys. **58,** 1240 (1998).
13. M. Yanagisawa, A. Sato, K. Ajiki, and F. Watanabe, in *Tribology of Contact/Near-Contact Recording for Ultra High Density Magnetic Storage*, C. S. Bhatia and A. K. Menon, eds., TRIB Vol. 6 (American Society of Mechanical Engineers, New York, 1996), p. 25.

Near-field Quantum Optical Theory towards Nano/atom Photonics

K. Kobayashi [1] and M. Ohtsu [1), 2)]
1) ERATO Localized Photon Project, Japan Science and Technology Corporation
2) Interdisciplinary Graduate School of Science and Engineering,
Tokyo Institute of Technology
687-1 Tsuruma, Machida, Tokyo 194-0004, Japan
Telephone: 042-788-6036, Fax: 042-788-6031, E-mail: kkoba@ohtsu.jst.go.jp

Quantum-mechanical behavior of a single atom, molecule and quantum dot (QD) has been explored experimentally by using optical near-field techniques that can allow nano-structure fabrication with arbitrary shapes and high spatial accuracy far beyond the diffraction limit [1]. In those situations, microscopic or quantum-mechanical treatment of the interaction between a nanometric probe-tip and sample is essential.

In this report, we show novel and quantum-mechanical derivation of an effective interaction potential between such a nanometric probe-tip and sample [2]. With the help of the projection-operator method, we develop a consistent theory appropriate for investigating both near-field optical manipulation of an atom and the excitation energy transfer process between nanometric quantum dots (QDs). The atom/QD is considered to interact with the probe tip in optical near-field systems via an elementary excitation mode of real photons and the macroscopic matter system.

We find that the effective potential consists of the sum of the Yukawa functions with several kinds of effective masses, or interaction ranges. Each term is characterized in terms of detuning for resonance energies of the atom/QD and probe tip, and shown to be attractive or repulsive, depending on the detuning and material properties. Recent experimental results support our predictions [3].

As an application of our approach, we discuss atom deflection and manipulation by optical near field generated by a nanometric probe-tip. Moreover, a novel scheme for optical switch is proposed, on the basis of near-field optical interactions responsible for signal transmission through confined states of nanometric QDs.

References

[1] M. Ohtsu, K. Kobayashi, H. Ito, and G. H. Lee, Proc IEEE **88**, 1499 (2000).
[2] K. Kobayashi and M. Ohtsu, J. Microsc. **194**, 249 (1999); K. Kobayashi, S. Sangu, H. Ito, and M. Ohtsu, Phys. Rev. A **63**, 0138xx (2001).
[3] H. Failache, S. Saltiel, M. Fichet, D. Bloch, and M. Ducloy, Phys. Rev. Lett. **83**, 5467 (1999).

MH2-3

Proposal for a near-field optical nano-switch

K. Kobayashi, T. Kawazoe, S. Sangu, and M. Ohtsu [(1),(2)]

(1) ERATO Localized Photon Project, Japan Science and Technology Corporation, 687-1 Tsuruma, Machida, Tokyo 194-0004, Japan
Telephone: +81 42-788-6036, fax: +81 42-788-6031, e-mail: kkoba@ohtsu.jst.go.jp

(2) Interdisciplinary Graduate School of Science and Engineering, Tokyo Institute of Technology, 4259 Nagatsuta-cho, Midori-ku, Yokohama, Kanagawa 226-8502, Japan

Abstract: A novel approach towards a nano-switch is proposed. Yukawa interaction allows signal transmission through confined states of nanometric quantum dots. Switching time, which is controlled by another dot locally excited/de-excited, is estimated at sub-nanosecond.

1. Introduction

Miniaturization and higher speed of photonic devices ultimately require overcoming of the diffraction limit of light. Near-field optical technique combined with photochemical deposition is a promising solution of the problem because it permits highly controllable nanostructure (nanometric quantum dots, or QDs) fabrication both in size and position [1]. Taking advantage of optical near fields, we propose a new scheme for an optical nano-switch using such QDs to discuss its principle and performance.

2. Near-field optical switch

A switch device based on localized optical near fields has the following major advantages: it does not suffer from the size restriction to miniaturization faced in current interferometer-type devices and it also relieves the so-called *electronic bottleneck*. Here, we present theoretical investigation of such a device. Experimental status is reported in an accompanying paper [2].

2.1 Theoretical background

Basic idea of our approach relies on the Yukawa interaction as an effective two-body interaction between nanometric objects via optical near fields. It is responsible for excitation energy transfer, or population transfer between the objects such as QDs, as is dipole-dipole interaction in the Förster process [3] of molecular system. We briefly outline the derivation using the projection operator method [4-5]. When nanometric QDs are excited by optical near fields, the total system may be divided into two subsystems. One is the relevant subsystem of QDs, and the other is the irrelevant subsystem consisting of all the remaining degrees of freedom. A few eigenstates $|\psi_\lambda^{(1)}\rangle$ (P-space) of the relevant subsystem are selected from among all eigenstates of the total optical near-field system, by using the projection operator P defined as

$$|\psi_\lambda^{(1)}\rangle = P|\psi_\lambda\rangle.$$

Then the bare interaction between two subsystems, which is described by the multipolar QED interaction between transverse photons and matter as $\hat{V} = -\hat{\vec{\mu}} \cdot \hat{\vec{D}}(\vec{r})$ [6], is transformed into the effective interaction $\hat{V}_{\text{eff}}$ that only operates on the P-space:

$$\begin{cases} \langle \psi_\mu | \hat{V} | \psi_\lambda \rangle = \langle \psi_\mu^{(1)} | \hat{V}_{\text{eff}} | \psi_\lambda^{(1)} \rangle, \\ \hat{V}_{\text{eff}} = \left(P\hat{J}^\dagger JP\right)^{-1/2} \left(P\hat{J}^\dagger V\hat{J}P\right)\left(P\hat{J}^\dagger JP\right)^{-1/2}. \end{cases}$$

This means that the effective near-field optical interaction $\hat{V}_{\text{eff}}$ exerts on QDs as if they were isolated from the other subsystem. It can be reduced to the Yukawa interaction, as discussed in the literature [1, 4-5].

2.2 Principle

Figure 1 illustrates the proposed device schematic showing the discrete energy levels of each dot that are described as

$$E_n = E_B + \frac{\pi^2\hbar^2}{2Ma^2}\left[n_x^2 + n_y^2 + n_z^2\right], \quad (n_x, n_y, n_z = 1,2,3\cdots).$$

When the sizes of dot 1, 2, and 3 are respectively chosen as $a/2$, $a/\sqrt{2}$, and a, two neighboring dots with the distance r_{ij} $(i, j = 1,2,3)$ have the same excited energies denoted as E_1, E_2, and E_3 in Fig. 1. Dot 1 is coupled to the input light that is transmitted by the Yukawa coupling, as described above, to dot 2 connected to the output light. Dot 3 is coupled to the control light that governs the switching mechanism. When the control light is on, level E_1 of dot 3 is occupied and near-field interactions of dot 3 with other dots are forbidden. In contrast, when it is off,

those interactions are active. This results in population difference in dot 2 producing a difference in the transmission signal.

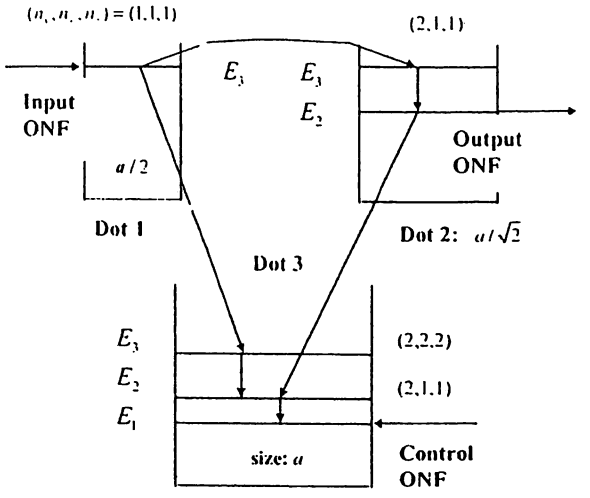

Fig. 1 Schematic diagram of a proposed device. Optical near fields are abbreviated to ONF.

2.3 Switching time

In order to analyze dynamic properties of the device, we employ the following master equation:

$$\begin{cases} \dfrac{\partial P_n^j(t)}{\partial t} = -\left[\dfrac{1}{\tau_{n-1,n}} + U_n^{ij}\right] P_n^j(t) + U_n^{jk} P_n^k(t), \\ U_n^{ij} = \dfrac{\gamma_0}{\hbar} \dfrac{\exp\left[-m_{\mathrm{eff}}(n) r_{ij}\right]}{m_{\mathrm{eff}}(n) r_{ij}}, \end{cases}$$

where $P_n^j(t)$ represents the population of dot j to remain in the excited states E_n at time t. The intra-dot relaxation time from E_n to E_{n-1} level is denoted as $\tau_{n-1,n}$ while U_n^{ij} shows the transfer rate due to the inter-dot Yukawa interaction. Effective mass $m_{\mathrm{eff}}(n)$ determines the interaction range between E_n levels of the neighboring dots i and j, whose excitation energy is transferred. Under the initial condition as

$$\begin{cases} P_n^j(0) = 1 \text{ for } n = 3 \text{ and } j = 1, \\ P_n^j(0) = 0 \text{ for otherwise}, \end{cases}$$

we obtain time evolution of $P_{n=2}^{j=2}(t)$ of dot 2. An example of the time evolution is plotted in Fig. 2, where we assume CuCl dots [7] with $a = r_{ij} = 10\,\mathrm{nm}$ and $\tau_{n-1,n} = 1$ psec. The line with circles represents the ON condition while the line with triangles shows the OFF condition. We estimate from Fig. 2 that a near-field nano-switch can be operated within a few hundred picoseconds, and expect that it would be, in principle, applicable to other material systems like GaAs and ZnO.

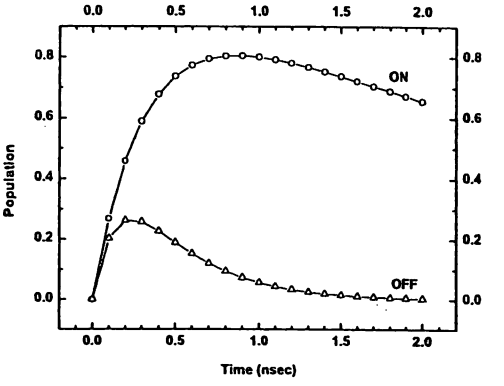

Fig. 2 Time evolution of population for E_2 state of dot 2, $P_{n=2}^{j=2}(t)$.

3. Summary and future issues

On the basis of an effective interaction picture for optical near fields, we have proposed a new scheme for an optical nano-switch, and discussed switching time of such a device. We have employed master equation with incoherent population transfer process between nanometric quantum dots, triggered by optical near fields. It would be intriguing to derive more rigorous equations including coherent dynamics, which will provide us with a more powerful tool to analyze and improve the switching performance.

References

[1] Y. Yamamoto et al., Appl. Phys. Lett. **76**, 2173 (2000); M. Ohtsu et al., Proc. IEEE **88**, 1499 (2000).
[2] T. Kawazoe et al., submitted to this conference.
[3] H. Haken, *Quantum Field Theory of Solids* (Elsevier, Amsterdam, 1983).
[4] K. Kobayashi et al., J. Microsc. **194**, 249 (1999).
[5] K. Kobayashi et al., Phys. Rev. A **63**, 013806 (2001); S. Sangu et al., J. Microsc. **201**, Jan/Feb (2001).
[6] D. P. Craig and T. Thirunamachandran, *Molecular Quantum Dynamics* (Dover, New York, 1998).
[7] N. Sakakura et al., Phys. Rev. B **56**, 4051 (1997).

Verification of principle for nano-meter size optical near-field switch by using CuCl quantum cubes

Tadashi Kawazoe[1], Kiyoshi Kobayashi[1], Jungshik Lim[2], Yoshihito Narita[3] and Motoichi Ohtsu[1),2)]

[1)]*Exploratory Research for Advanced Technology (ERATO), Japan Science and Technology Corporation (JST), 687-1 Tsuruma, Machida, Tokyo 194-0004, Japan*
Telephone:+81-42-788-6039, fax:+81-42-788-6031, e-mail: kawazoe@ohtsu.jst.go.jp

[2)]*Interdisciplinary Graduate School of Science and Engineering, Tokyo Institute of Technology, 4259 Nagatsuta, Midori-ku, Yokohama 226-8502, Japan*

[3)]*JASCO Corporation, 2967-5, Ishikawa-cho, Hachioji, Tokyo, 192-8537, Japan*

Abstract: We propose a near-field optical nano-switch. The switching mechanism is based on the near-field energy transfer among sub-levels in quantum cubes. To inspect the switching, we observed the size-selected spatial distribution of CuCl quantum cubes.

Optical near field gives us not only high-resolution microscope but also a novel scheme for nano-size optical switch [1,2]. We have been researching the optical nano-switch using near-field interaction among quantum cubes (QCs).

Figure 1 shows a schematic mechanism of the proposed near-field optical switch. The cubes 1, 2, and 3 play roles of input, output and control ports, respectively. In CuCl QC with side lengths less than 10 nm, we can observe the discrete exciton energy sublevels described by the quantum numbers (n_x, n_y, n_z) [3]. Assuming the three QCs with side lengths $L/2$ (cube 1), $L/\sqrt{2}$ (cube 2), and L (cube 3), respectively, the exciton energy sublevels (2,2,2) in cube 3, (2,1,1) in cube 2, and (1,1,1) in cube 1 become resonant with each other. When the separations among cubes are less than 10 nm, the resonant levels in each cube are coupled with the optical near-field. Thus, the excitation at the energy level (1,1,1) in cube 1 is transferred to the energy level (2,1,1) in cube 2 or to (2,2,2) in cube 3 within the transition time, τ_n. If the relaxation time τ_i between the sublevels of about 1ps [4] is much faster than τ_n and the lifetime of the excitation, the output (shown in Fig.1) can be controlled by quenching the transfer of excitation to the cube 3 by incorporating the control light.

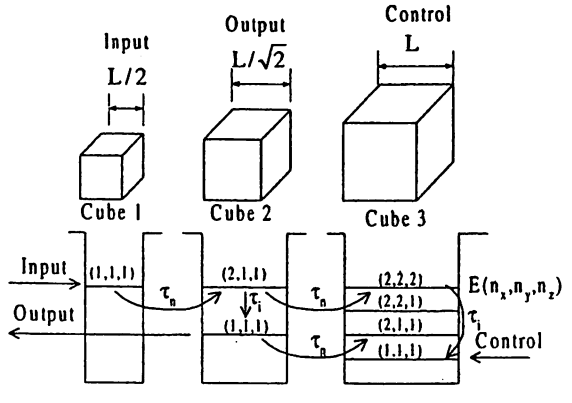

Fig.1. Schematic mechanism of the proposed near-field optical switch using quantum cubes. Arrows input, output, and control mean interface of the switching system. τ_n and τ_i correspond to the inter- and intra- cubes energy transfer time, respectively.

We prepared and employed the CuCl QCs embedded in NaCl matrix as components for realization of the near-field optical switching system as CuCl QC offers the similar discrete energy levels of exciton as shown in Fig.1 [3]. The CuCl QCs in NaCl matrix has large size distribution. We have to search the *trio* which satisfy the conditions of the sizes and the distances among the cubes by using the near-field spectroscopy. The curve A of Fig. 2 shows the far-field luminescence spectrum of this sample, which was recorded with 1μm distance between the near-field optical probe and the sample

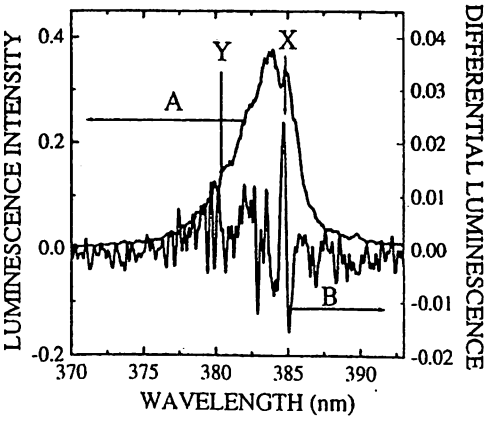

Fig.2. Luminescence and differential luminescence spectra of CuCl quantum cubes embedded in NaCl matrix at 15 K.

for the collection-mode operation of the near-field optical microscope (NOM) at 18K. He-Cd laser with wavelength of 325 nm was used as a light source. This curve gives the collective luminescence from several CuCl QCs, and is inhomogeneously broadened owing to the size distribution of the QCs. However, the near-field optical switch (Fig.1) demands luminescence from individual QC. The curve B represents the differential luminescence which is the intensity difference between luminescence measured with the probe-sample separations of 1μm and less than 10 nm. This curve consists of many fine structures. The fine structures in this curve correspond to contribution of the cubes near the aperture of the probe because the measured luminescence from the cubes near the probe increases, for the probe-sample separation below 10nm.

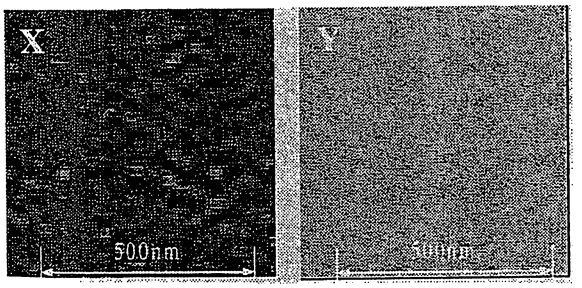

Fig.3. The spatial distributions of the differential luminescence peaks X and Y marked in Fig.2. The spatial distributions for peak X and peak Y correspond to the spatial distributions of the quantum cubes with side lengths of 4.8 nm and 3.4 nm, respectively.

Figure 3 shows the spatial distribution of the peaks X and Y marked on the curve B. These spatial distributions, i.e. NOM images, for peaks X and peak Y correspond to the spatial distributions of the QCs with side lengths of 4.8 nm and 3.4 nm, respectively [3]. Their sizes are equivalent to cube 3 (L) and cube 2 ($L/\sqrt{2}$) in Fig.1. The spatial resolution of about 50 nm observed in Fig.3 is reasonable considering the aperture diameter of 70 nm. The distributions of size-selected QCs are clearly observed. The coincident position where observed strong luminescence form the size-different QC *trio* ($L/2$, $L/\sqrt{2}$, L) may satisfy the configuration condition in Fig.1. This approach gives a method to search the QC *trio* for realizing the proposed near-field switch from the CuCl QCs with large size distribution.

In our presentation, we would like to explain the near-field switching mechanisms and the experimental procedure of the inspection and the demonstration of the optical near-field switch in detail.

References

1. M. Ohtsu, *Near-Field Nano/Atom Optics and Technology* (Springer, Tokyo, Berlin, Heidelberg, New York, 1998).
2. K. Kobayasi, T. Kawazoe, S. Sangu, and M. Ohtsu, "Proposal for a near-field optical nano-switch" Proceedings of CLEO/PR01, this issue (2001).
3. N. Sakakura and Y. Masumoto, "Persistent spectral-hole-burning spectroscopy of CuCl quantum cubes" Phys. Rev. **B56**, 4051-4055 (1997).
4. T. Suzuki, T. Mitsuyu, K. Nishi, H. Ohyama, T. Tomimasu, S. Noda, T. Asano, A. Sasaki, "Observation of ultrafast all-optical modulation based on intersubband transition in n-doped quantum wells by using free electron laser" Appl. Phys. Lett. **69**, 4136-4138 (1996).

In-situ lateral fabrication of Zinc and Aluminum nanodots by near field optical chemical vapor deposition

Y. Yamamoto [a], T. Kawazoe[b], G. H. Lee [b], T. Shimizu [a], M. Kourogi [a,b], *M. Ohtsu [a,b]

a. Interdisciplinary Graduate School of Science and Engineering, Tokyo Institute of Technology, 4259 Nagatsuta, Midori-ku, Yokohama, 226-8502, Japan
Phone: +81-45-924-5476, Fax: +81-45-924-5599, *E-mail: ohtsu@ae.titech.ac.jp
b. Japan Science and Technology Corporation, 687-1 Tsuruma, Machida, Tokyo, 194-0004, Japan

Abstract: Nanometric Zn and Al dots were deposited on a sapphire substrate with the space of 100nm. Minimum diameter of fabricated Zn and Al dots were 37nm and 25nm, respectively.

Recently, chemical vapor deposition technique combined with optical near field has been proved to be a valuable nano-fabrication tool [1]. This novel method underpins the eventual realization of nano-photonic integration, as it is capable of nano-scale precise positioning and selective thin film growth. Lateral fabrication of various nano-structure (sequence of layers, materials, size and dopant) in a single growth run can be achieved, at the same time avoiding etching step to cause deterioration.

In this work, we demonstrate for the first time the deposition of nanoscale Zn and Al dots on the same substrate and the high controllability of the deposited position and dot size.

Deposition of Zn was performed by using photodissociation reaction of diethylzinc (DEZ) with the second harmonic (SH) light (wavelength: 244nm) of argon ion laser. SH light of a few mW was coupled with UV fiber probe [2]. The fiber probe generated optical near field was inserted into the deposition chamber and controlled by conventional scanning near field optical microscope system. During the deposition, the distance between the substrate and the probe was maintained within several nanometers by shear-force feedback technique. The substrate was kept at room temperature. Figure 1 shows the shear-force image of two nanometric Zn dots deposited on the sapphire substrate. The partial pressure of DEZ and carrier gas (Ar) were 10mTorr and 270mTorr, respectively. The deposition time was 60s. Full width at half maximum (FWHM) of two dots are 52nm and 37nm, which is comparable with apex diameter of the used thin Al-coated probe. The distance between the two dots is 45nm, which is close to the FWHM of the dots. This result establishes the capability of this technique for nanometric deposition with controlling their size and position.

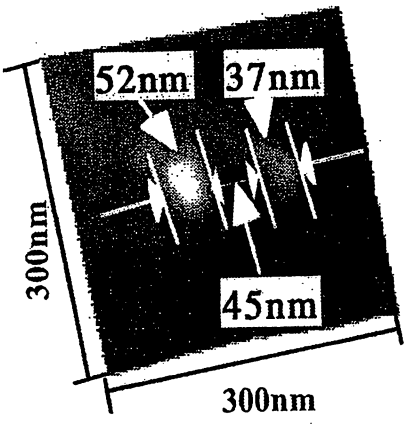

Fig.1 Shear-force image of two nanometric Zn dots deposited on a sapphire substrate

Figure 2 shows shear-force image of five Al dots deposited on a sapphire. The deposition of

Al was performed by the photodissociation of trimethylaluminun (TMA) using SH light. The TMA partial pressure and the incident SH light power were 10mTorr and 1mW, respectively. The FWHM of the dots are 27nm, which is also comparable with apex diameter of the used probe. This is the first report to deposit nanometric Al dots by this technique.

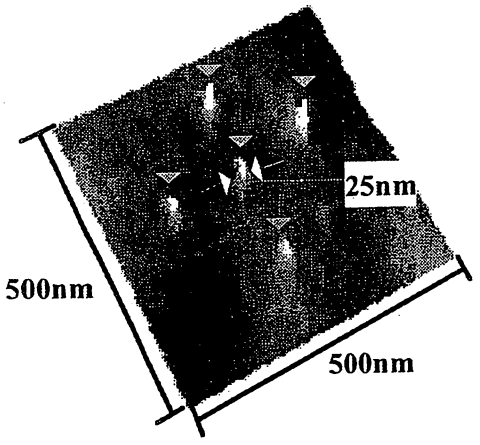

Fig.2 Shear force image of five Al dots deposited on a sapphire substrate (Gray arrows indicate the Al dots)

As shown in the deposition of Zn and Al, various materials can be deposited selectively by only changing the reactant gases. Furthermore, there is no limitation in regard to substrate and deposit materials. Zn and Al were deposited on an insulator substrate like sapphire. These are the advantage of this technique.

Another of the most attractive points of this technique is the possibility for in-situ lateral integration of nano-scale structures of different materials with ease, which is difficult in conventional techniques. Figure 3 shows the possibility. Shear-force image of deposited Zn and Al dots at closely position on a sapphire substrate is represented in Fig.3. First, Zn dots were deposited under DEZ pressure of 10mTorr, and then the deposition chamber was evaporated to the pressure of 5×10^{-6}Torr. Next, Al dot was deposited under TMA pressure of 10mTorr. The distance between the Zn dot and the Al dot was 100nm.

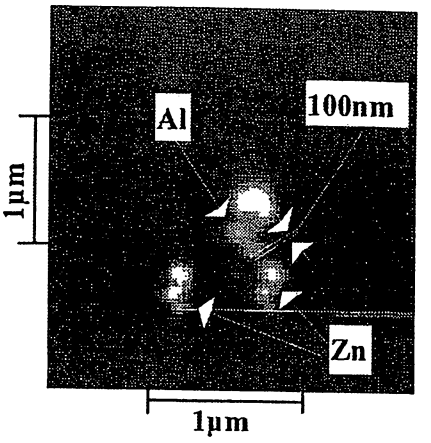

Fig.3 Zn and Al dots deposited closely on a sapphire substrate

This technique gives us the possibility for the fabrication of nanoscale electro-luminescence(EL) devices. As an example, we have demonstrated the deposition of n-type zinc oxide(ZnO) with a blue light emission ability using this technique[3][4], therefore, we can produce a nanoscale EL device by fabricating metallic Al wires and ZnO nanoscale dots on a p-type semiconductor substrate. In addition, this technique is applicable to not only Zn, Al and ZnO, but also various metals, semiconductors and insulators. Therefore, this technique enables fabrication and integration of various nano-photonic device.

References

[1] V. V. Polonski, et al, J. Microscopy, 194, (1999) 545
[2] M. Ohtsu (Ed.) *Near-Field Nano/Atom Optics and Technology*, Springer-Verlag, Berlin (1998)
[3] G. H. Lee, et al, Proc. SPIE, 3791(1999) 132
[4] G. H. Lee, et al, Thin Solid Films (2001) in Press

Spatially and spectrally resolved imaging of a polycrystalline ZnO dots using near field optical technique

T. Yatsui*, T. Shimizu**, Y. Yamamoto**, G. H. Lee***, M. Kourogi**, and M. Ohtsu*,**

*Ohtsu Project, ERATO, Japan Science and Technology Corporation
687-1 Tsuruma, Machida, Tokyo, Japan 194-0004
+81 42-788-6040, +81 42-788-6031, yatsui@ohtsu.jst.go.jp

** Interdisciplinary Graduate School of Science and Engineering, Tokyo Institute of Technology

***Department of Advanced Materials Engineering, Dong-Eui University

Abstract: By applying an optical near field technique, the two-dimensional identification of optical properties and crystallinity in polycrystalline ZnO dots is obtained at room temperature for the first time.

ZnO is a very promising material for ultraviolet (UV) light emitting devices at room temperature due to its wide band gap of 3.37 eV and much larger exciton binding energy (60 meV) than the thermal energy at room temperature (26 meV) [1,2]. Thus, nanocrystalline ZnO has been paid attention as a light emitting source in nanometric opto-electronic device. Recently, we have realized nanometric ZnO dots by near-field optical chemical vapor deposition (NFO-CVD) [3]. On the other hand, their optical properties and crystallinity have been evaluated by conventional techniques such as far field photoluminescence (PL) spectroscopy and Raman spectroscopy. However, they measure an ensemble of dots with size and shape fluctuations due to its poor spatial resolution. For applying single ZnO dots to opto-electronic device, the measurement of the optical properties of nanometric ZnO structure is required. For realizing a single ZnO dot spectroscopy and investigation of their individual cristallinity, we demonstrate here high spatial resolution capability of the near field PL spectroscopy.

Figure 1 shows the schematics of experimental setup for spatially and spectrally resolved PL spectroscopy at room temperature by using an UV single-tapered fiber probe [4], where the separation between the sample and the probe was maintained within several nanometers.

Polycrystalline ZnO dots were fabricated by the following steps.

(i) Zn thin film was grown with thickness of 200 nm by optical CVD on sapphire (0001) substrate [5].

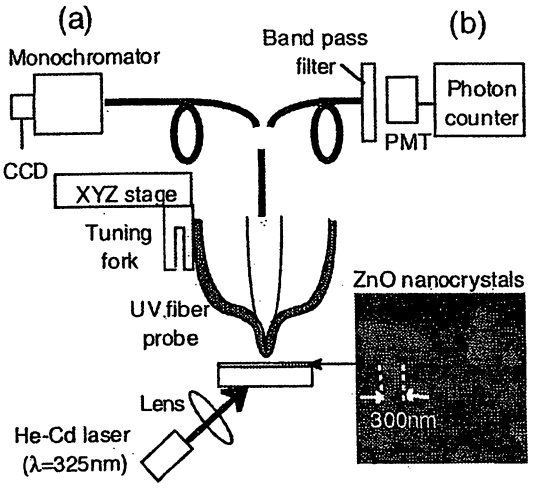

Fig. 1. Schematics of experimental setup for near field spatially and spectrally resolved PL spectroscopy [(a) and (b)]. Inset: topographic image of the polycrystalline ZnO dots. Image size is 2.5 μm×2.5 μm.

(ii) Thermal oxidation was carried out in 1 atm oxygen ambient at temperature of 750 °C for 60 minutes [6].

As shown in the inset of Fig. 1, the grain sizes were in the range of 250-330 nm and their surface roughness was within several nanometers, which was estimated by shear-force microscope with an UV single-tapered fiber probe with 50-nm-thick aluminum coating.

Using the apertured UV single-tapered probe with aperture diameter (D) of 80 nm [see Fig. 2 (a)], we obtained the near field PL spectra of polycrystalline ZnO dots [see Fig. 2(b)]. It can be found that the position of the emission peak is close to the reported energy of 3.26 eV (λ = 380 nm) corresponding to spontaneous emission from the free exciton in the high quality ZnO thin films [2], which implies that fabricated dots is ZnO dots.

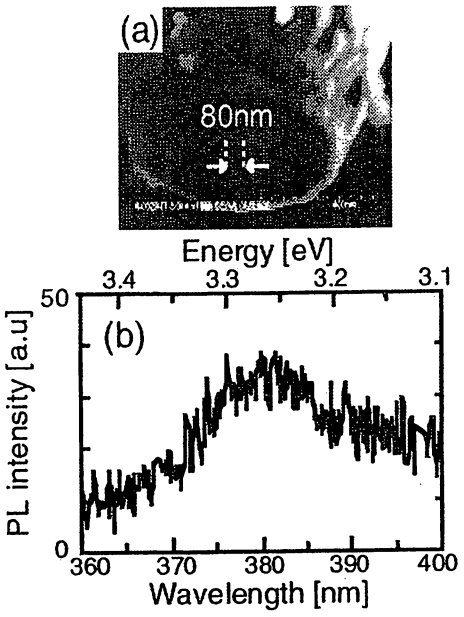

Fig. 2. (a) Apertured UV single tapered probe with D = 80 nm. (b) Near field PL spectra of polycrystalline ZnO dots [Fig. 1(a)].

The spatially resolved monochromatic photoluminescence image of the polycrystal ZnO dots was also observed with the apertured UV fiber probe with D of 80 nm [see Fig. 3(a)]. The detection wavelength is 380 nm with a spectral bandwidth of 5 nm. Figure 3(b) shows the cross sectional profile along the white dashed line in (a).

As shown in Fig. 3, one can find a number of emission spots from the individual ZnO dots. The spot sizes of positions X and Y are 160 nm and 240 nm, respectively, which are comparable to the size of the ZnO dots [see Fig. 1]. The difference in the PL intensity of the emission spots might be attributed to the crystallinity of the ZnO dots. Since Zn thin film deposited by PE-MOCVD is polycrystalline with a hexagonal close packed crystal lattice [6], the amount of the oxygen diffused into Zn film depends on the crystal orientation, which results in the difference in the crystallinity of ZnO dots. From these results, it can be supposed that the higher PL intensity of dot Y is related with a smaller density of defects and relatively higher crystallinity in the polycrystalline ZnO dots.

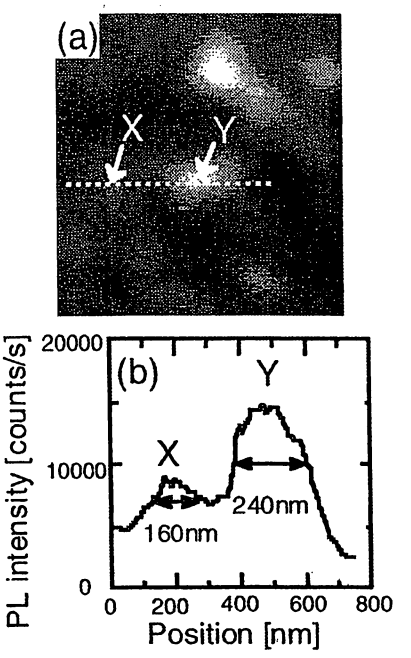

Fig.3. (a) Monochromatic photoluminescence image of the polycrystalline ZnO dots [Fig. 1(b)]. Image size is 2.5 μm×2.5 μm. (b) Cross sectional profile along the white dashed line in (a).

This successful first acquisition of the two-dimensional identification of the crystallinity with such nanometric spatial resolution is attributed to the high spatial resolution capability of the near field optical microscope. Furthermore, since the deposition techniques of ZnO reported here is applicable to NFO-CVD, it can be expected that such a high spatial resolution capability of the optical near field technique will be powerful to realize nanometric opto-electronic device with high crystallinity.

References

1. Z. K. Tang, *et al.*, APL 72, 3270 (1998).
2. D. M. Bagnall, *et al.*, APL. 73, 1038 (1998).
3. G. H. Lee, *et al.*, in Near-Field Optics: Physics, Devices, and Information Processing, Proc. SPIE 3791, 132 (1999).
4. *Near-field nano/atom optics and technology*, edited by M. Ohtsu, Chap. 3 (Springer Verlag, Tokyo, 1999).
5. Y. Yamamoto, *et al.*, APL. 76, 2173 (2000)
6. S. Cho, *et al.*, APL. 75, 2761 (2000)

P2-62

Optical near-field sample-probe interaction depending on excitation energy of matter

Suguru Sangu,[1] Kiyoshi Kobayashi,[1] and Motoichi Ohtsu[1,2]
[1] *ERATO, Japan Science and Technology Corporation*
687-1 Tsuruma, Machida, Tokyo, 194-0004 Japan
(tel.+81-42-788-6043, fax.+81-42-788-6031, e-mail:sangu@ohtsu.jst.go.jp)
[2] *Interdisciplinary Graduate School of Science and Engineering,*
Tokyo Institute of Technology
4259 Nagatsuta-cho, Midori-ku, Yokohama, Kanagawa, 226-8502 Japan

Abstract: Characteristics of optical near fields can be modified with a change of electronic excitation energy of microscopic matter. Our theoretical evaluation shows that this change affects contribution of several potential components with different interaction ranges.

With recent progress in nano-fabrication techniques, realization of nanometric functional devices and their integrated circuit has been expected. Optical near fields, localized in the microscopic regime and free from the diffraction limit, can assist to operate such devices.

Optical near fields in the nanometric regime might be mixed states consisting of photons and matter excitation. We have developed a quantum mechanical theory on optical near fields which produce an effective interaction between nanometric objects via photon-matter coupled modes, i.e., exciton-polariton modes [1,2]. As an effective interaction, the Yukawa function with several kinds of interaction ranges well describes characteristic size-dependence of near-field signal intensity [3]. This formulation also has advantages for treatment of quantum mechanical effects and may describe some phenomena inherent to the optical near fields.

In the previous study [3], we have mainly paid attentions to dependence on the size of microscopic objects. Optical near field, however, depends on material of the objects as well as the size. This is clear from the difference in images of various samples observed by optical near-field microscopy and spectroscopy. In this paper, effects of electronic excitation energy of the objects on signal intensity are evaluated theoretically, where nanometric sample and probe idealized by spheres are used. The interaction potential between nanometric sample and probe consists of localized component and oscillating one. Our calculation shows that the oscillating component is particularly varied according to a change in the excitation energy, in addition to the localized one.

Interaction potential between microscopic objects via optical near fields can be written in the dipole approximation as follows:

$$\begin{aligned} V(r) &= -\langle \Psi | \sum_{\alpha=A}^{B} \theta(z_\alpha)\hat{\mu}_\alpha \cdot \hat{D}(r_\alpha) | \Psi \rangle \\ &= -\frac{1}{2\pi^2} \sum_{\alpha\neq\beta}^{A,B} \int dk e^{ik\cdot(r_\alpha - r_\beta)} \\ &\times \left[\frac{K'_\alpha(k) K'^{*}_\beta(k)}{\Omega(k)+\Omega_\beta} + \frac{K'_\beta(k) K'^{*}_\alpha(k)}{\Omega(k)-\Omega_\alpha} \right], \end{aligned} \tag{1}$$

where μ_α and $\hat{D}$ denote a dipole operator in the microscopic object and displacement field operator rewritten by the exciton-polariton modes, $[\hat{\xi}(k), \hat{H}_{\text{bath}}] = \hbar\Omega(k)\hat{\xi}(k)$, $(\hat{\xi}^{\dagger}, \hat{\xi})$ being a creation and annihilation operators of exciton-polaritons. Resonance frequency of microscopic sample ($\alpha = A$) or probe ($\alpha = B$) is denoted by Ω_α. The exciton-polaritons and sample (probe) interact with each other with the coupling coefficient $K'_\alpha(k)$. For transformation into the second row in Eq. (1), projection operator method is used in which a few degrees of freedom are focused and the others are renormalized as an effective operator as described in Ref. [1].

In a nanometric object, a wave function has a discrete wavenumber depending on the size of the object. The exciton-polaritons are supposed to have the same wavenumber that is characterized by a reciprocal number of the size of the object. Applying effective mass approximation to exciton-polariton dispersion relation around this wavenumber, Eq. (1) is finally written as [3]

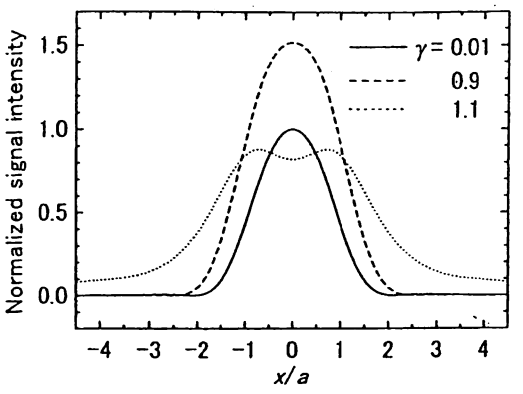

Fig. 1 Spatial distribution of signal intensity detected by spherical probe with the radius of 30 nm (equal to the sample radius) and the fixed height 10 nm. Solid, dashed, and dotted curves represent $\gamma = 0.01$, 0.9, and 1.1, respectively.

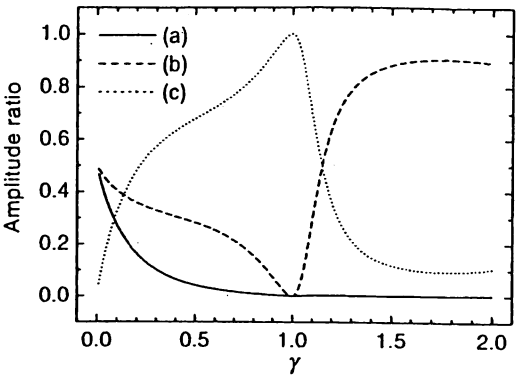

Fig. 2 Amplitude ratio of each component to the total at the probe height 10 nm. Solid, dashed, and dotted curves represent three components described in Eq. (2)

$$V(r) = \sum_{\alpha \neq \beta}^{A,B} \frac{\pi^2}{a_\alpha^2} \left[\frac{w_+(\gamma_{\alpha\beta}) e^{-\sqrt{1+\gamma_{\alpha\beta}}\pi r/a_\alpha}}{r} + \frac{w_-(\gamma_{\alpha\beta}) e^{-\sqrt{1-\gamma_{\alpha\beta}}\pi r/a_\alpha}}{r} + \frac{w_1(\gamma_{\alpha\beta}) e^{-2^{-1/2}(1+i)\pi r/a_\alpha}}{r} + \text{c.c.} \right], \quad (2)$$

$$\gamma_{\alpha\beta} = 2a_\alpha \Omega_\beta / \pi c,$$

where a_α represents the radius of sample (probe). $\gamma_{\alpha\beta}$ denotes the ratio of the electronic excitation energy of the sample (probe) to the exciton-polariton mass inversely proportional to the sample (probe) radius. From Eq. (2), the interaction potential consists of three components: (a) the localized component with fast decay, (b) the localized component with slow decay ($\gamma_{\alpha\beta} < 1$) or oscillating one ($\gamma_{\alpha\beta} > 1$), and (c) the damped oscillating component. The weight coefficient of each component is represented by $w_{\pm,1}(\gamma_{\alpha\beta})$. Exponents of the former two include the parameter $\gamma_{\alpha\beta}$, and thus, these components are related to the direct coupling between the sample and probe.

In order to take into account the effect of the finite sizes of sample and probe on signal intensity, we integrate the gradient of Eq. (2) over the probe and sample volumes. When we consider spherical sample and probe, the integral can be performed analytically. Figure 1 shows the spatial intensity profile with $\gamma = 0.01$, 0.9, and 1.1, where we assume the sample and probe with identical radii and rewrite the parameter $\gamma = \gamma_{\alpha\beta}$. In the regime of $\gamma > 1$, the profile changes drastically with long-tailed decay because the second component in Eq. (2) acts as a propagation mode. In order to evaluate contributions of each component, we show the amplitude ratio of each component to the total in Fig. 2, where the value of the envelope is taken in the components with spatial oscillation. From the ratio at $\gamma = 0.9$, we find that most of the interaction potential comes from the contribution of the component (c), which gives the FWHM of the signal intensity about the sample (probe) diameter. While $\gamma > 1$, the component (b) becomes large, which makes the long-tailed decay inversely proportional to the sample-probe distance. The central dip of the curve ($\gamma = 1.1$) in Fig. 1 is caused that the component (b) and (c) have opposite sign at the height of 10 nm.

These results can modify the contrast of the optical near-field images for various samples. Furthermore, the selective coupling to localized and oscillating components may be useful for nanometric optical devices leading a signal to an outer macroscopic portion and connecting to two or more portions.

[1] K. Kobayashi and M. Ohtsu, J. Microsc. **194** (1999) 249-254.

[2] K. Kobayashi, S. Sangu, H. Ito, and M. Ohtsu, Phys. Rev. A**63** (2001) 013806.

[3] S. Sangu, K. Kobayashi, and M. Ohtsu, J. Microsc. **201** (2001) Jan/Feb.

P2-67

Deposition of nano-meter size Zn dot by near-field optical CVD with nonresonant light

Tadashi Kawazoe[1], Yoh Yamamoto[2], and Motoichi Ohtsu[1),2)]

[1)]Exploratory Research for Advanced Technology (ERATO), Japan Science and Technology Corporation (JST), 687-1 Tsuruma, Machida, Tokyo 194-0004, Japan
Telephone:+81-42-788-6039, fax:+81-42-788-6031, e-mail: kawazoe@ohtsu.jst.go.jp

[2)]Interdisciplinary Graduate School of Science and Engineering, Tokyo Institute of Technology, 4259 Nagatsuta, Midori-ku, Yokohama 226-8502, Japan

Abstract: We demonstrate novel deposition of Zn dots with nonresonant light based on the unique properties of optical near field which are two-photon absorption, induced near-field transition, and direct coupling to dissociation mode.

Optical near field has been exploited in various application areas, such as high-resolution optical microscopy, high-density optical memory, atom manipulation, and so on [1]. Recently, we have shown the feasibility of chemical vapor deposition (CVD) of Zn dots by optical near field [2]. In this work, we employed high spatial resolution of the optical near field for the deposition. However, the optical near field has unexplored unique properties which have not been used in applications. In this presentation, we examine for the first time the near-field optical CVD of nano-meter size Zn dots with nonresonant light.

Figure 1 shows the experimental setup for the deposition by using optical near field. Second harmonics (λ=244 nm) of Ar^+ laser was used as resonant light source to the absorption band of diethylzinc (DEZn). Fundamental (λ=488 nm) of Ar^+ laser and He-Ne laser (λ=633 nm) were used as nonresonant light sources. The near-field fiber probe used for the deposition was a high throughput-type single tapered fiber probe which was fabricated by pulling and etching of a fiber with the pure silica core [1]. The cone angle of the fabricated fiber probe was 30 degrees with apex diameter of 30 nm. In order to investigate the deposition effect of nonresonant light, the fiber probe without the metal coating on it, that is a bare fiber probe, was used for the deposition. Therefore, the optical far field leaked to circumference of the fiber probe as shown in Fig.1. XYZ position of the near-field fiber probe was controlled by the piezo stage. Separation between the fiber probe and the sapphire substrate was regulated to several nanometers by using a shear-force technique [1]. The output laser power from the fiber probe was measured with a photo-diode placed behind the sapphire substrate. The sizes of the deposited Zn dots were measured using the shear-force microscope. During the deposition, the partial pressure of diethylzinc (DEZn) and the total pressure in the chamber were 100 mTorr and 3 Torr, respectively.

Figure 2 shows the shear-force images before (a) and after (b) the near-field optical CVD on the sapphire step substrate for the wavelength of 244 nm. The input laser power and the irradiation time were 1.6 μW and 60 s, respectively. Before the laser irradiation, the step structures of 0.4 nm height on the sapphire substrate are clearly observed in Fig.2 (a). After the irradiation, the sapphire step

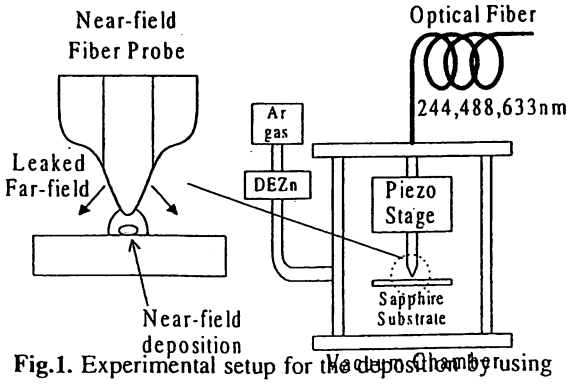

Fig.1. Experimental setup for the deposition by using optical near field.

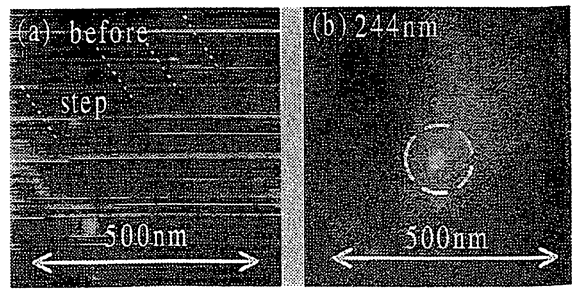

Fig.2. Shear-force images before (a) and after (b) the near-field optical CVD. The output laser power and the irradiation time for the deposition were 1.6 μW and 60 s with the wavelength of 244 nm.

disappears and the deposited Zn dot of 50 nm diameter appears at the center as marked within the broken circle, as shown in Fig.2 (b). This is because the emitted near field deposited the Zn dot directly under the apex. Further, since the fiber probe without metal coating emitted not only the near field at the apex but also the leaked strong far-field light, the leaked light also deposited Zn layer and concealed the surrounding step structures.

Figure 3(a) shows the shear-force image after the near-field optical CVD on the sapphire step substrate for the wavelength of 488 nm. The observed laser power and the irradiation time were 150 μW and 75 s, respectively. This wavelength offers higher energy than the dissociation energy of DEZn but it is still lower energy than the absorption edge of DEZn [3,4]. The DEZn gas has no absorption for this wavelength. However, the deposited Zn dot of 50 nm diameter appears at the center as indicated within the broken circle. On the other hand, the sapphire step does not disappear as observed for the case of 244 nm deposition completely. Thus, it is clear that the leaked 488 nm far-field light did not deposit Zn layer. For the wavelength of 633 nm, Zn deposition was not observed at all, because this wavelength has lower energy than both the dissociation energy and the absorption edge of DEZn.

Figure 3(b) shows the cross-sectional profile of the deposited Zn dots for 244 nm (solid curve), and 488 nm (broken curve). For 244 nm, the profile of the deposited Zn dot has tails of 4 nm height on the both side of the dot. The tails correspond to the deposition by the leaked far-field light. On the other hand, the profile of the Zn dot for 488 nm has no tails, since, in the case of the far-field optical CVD, Zn deposition using the wavelength longer than the absorption edge of DEZn is not possible [5].

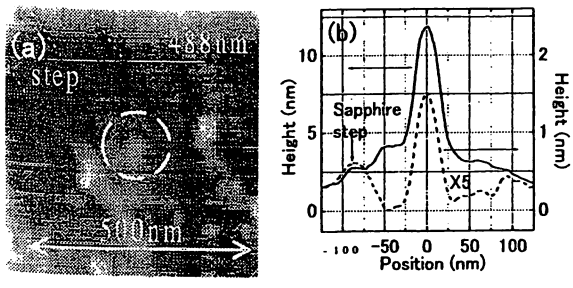

Fig.3. (a)Shear-force image after the near-field optical CVD for 488-nm light. The output laser power and the irradiation time were 150 μW and 75 s, respectively. (b) The cross-sectional profile of the deposited Zn dots for 244 nm (solid curve), 488 nm (broken curve).

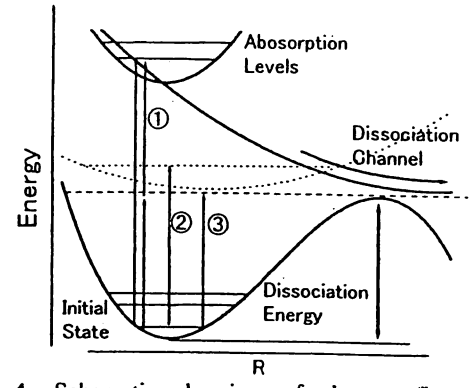

Fig.4. Schematic drawing of the configuration coordinate for the dissociation of DEZn

We discuss the possible DEZn dissociation and deposition mechanisms of the optical near field. For optical far field, photo-absorption and the predissociation cause the dissociation of DEZn. In contrast, for optical near field, the dissociation can take place even under the nonresonant condition. We show the possible mechanisms of the DEZn dissociation in Fig.4. The first is two-photon absorption process due to the high energy density of the optical near field at the top of the high throughput fiber probe (① in Fig.4). The second is the induced transition to the dissociation channel by the near-field fiber probe (doted curves and ② in Fig.4). The third mechanism involves the direct coupling between the optical near field and the dissociation molecular vibration mode (broken line and ③ in Fig.4). We have to investigate the near-field optical CVD in detail to clarify its deposition mechanism, for example, the energy density dependence, the dependence of the probe-substrate distance, and the photon energy dependence for the deposition rate.

We believe this novel deposition method has high potential for the application to the near-field optical CVD of gas sources for which the far-field optical CVD is unrealizable. Besides this approach gives unique advantage of the spatially controlled CVD.

References

1.M.Ohtsu, *Near-Field Nano/Atom Optics and Technology* (Springer, Tokyo, Berlin, Heidelberg, New York, 1998).

2.Y.Yamamoto, M.Kourogi, M. Ohtsu, V. Polonski, and G. H. Lee, Appl. Phys. Lett. **76**, 2173-2175 (2000).

3.P. F. Seidler, J. Phys. Chem. **98**, 2095-2100 (1994).

4.R. Larciprete and E. Borsella, Chem. Phys. Lett. **36**, 221-230 (1989).

5.M.Shimizu, H. Kamei, M. Tanizawa, T. Shiosaki and A. Kawabata, J. Crystal Growth **89**, 365-370 (1988).

P2-69

Mercury treatment of near field fiber probes for overcoming light leakage

H.N. Aiyer[1], T. Kawazoe[1], J. Lim[2], T.Shimizu[2]
and M. Ohtsu[1,2]
[1]ERATO Localized photon project
Japan Science and Technology Corporation
687-1-17/4F Tsuruma, Machida-shi,Tokyo 194-0004,
Japan
[2]Tokyo Institute of Technology, 4259, Nagatsuta,
Midori-Ku, Yokohama 226-8502, Japan
E-mail: hemant@ohtsu.jst.go.jp
Tel: +(81)42-788-6045
Fax: +(81)42-788-6031

Abstract:
The 'simple' mercury treatment on near field probe has realized 7% improvement of optical density of metal coating, ~ (¼) times decrease in optical leakage and 21% increase in optical damage threshold which reveals its potential usefulness.

In the recent, fast developing and much promising near field optical technology, a probe with the subwavelength aperture at the apex of a metal-coated glass fiber is the critical component [1]. Desirable properties of such aperture probes are high throughput ratio obtained with large cone angles, well defined circular aperture, high optical damage threshold and minimum/no light leakage [2,3]. The quality of metal coating on such a probe directly governs the extent of light leakage through the pinhole defects. Thus, smooth metal coating is most desired. Hitherto, various methods such as use of adhesion layer, protection coating preventing corrosion during aging, application of mixed metal coating have been reported for considerable improvement in the fiber probe properties [4,5]. Here, we report a novel approach of mercury treatment on near field fiber probes. Mercury treatment is performed by physically contacting the tip of previously Au coated chemically etched double tapered fiber probe onto a mercury droplet for a short time. Mercury is soluble in gold and forms a solid solution at ambient temperature [6]. Mercury on the gold surface is very mobile and adsorbs fast migrating to different grain boundaries closing the porous structure. Figs. 1(a) and (b) show the SEM images of as fabricated and the mercury treated plus F.I.B. drilled fiber probe respectively revealing smooth microstructure for Hg treated probes.

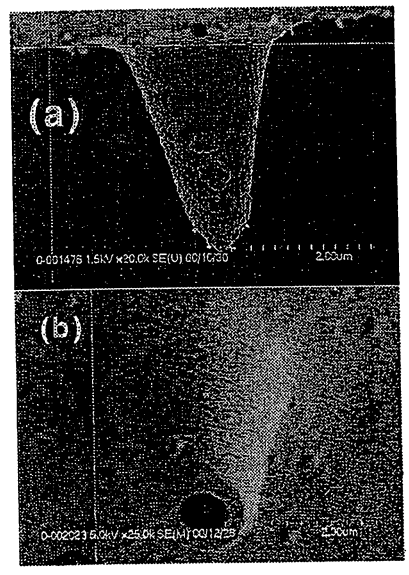

Fig.1 SEM images of (a) as fabricated gold coated and (b) FIB drilled and Hg treated near field fiber probes. (aperture diameter 600 nm)

The experimentally recorded absorption spectra for the thin gold film with thickness 695Å and for the mercury treated case showed improved optical response with ~ 7% increase in the optical density for 300-900 nm wavelength range. Ambient chemical stability of the mercury treated gold films has been investigated by identifying the nature of the surface species employing X-ray photoelectron spectroscopy using an incident X-ray energy of 1253.6 eV. XPS spectra were recorded for (a) untreated gold film and (b) mercury treated gold film (aged for 2 days) in the Au 4f and Hg 4f binding energy regions.

The bare gold film spectra showed the Au $4f_{7/2}$ and Au $4f_{5/2}$ peaks at the expected positions of 83.8 eV and 87.5 eV respectively. On mercury treatment, Hg 4f peaks appeared and the Au $4f_{7/2}$ peak showed a binding energy shift of 0.3 eV. This spectra also revealed some change and broadening of the peaks. These results indicate the chemical change upon mercury treatment which may be attributed to the formation of amalgamation phase. However, we rule out the oxidation effects as the observed B.E. shift is seen towards the lower B.E. range. Thus, the XPS observations confirm the chemical stability of the post mercury treatment gold films.

We confirmed the considerable improvement of light leakage on mercury treatment of apertureless near field fiber probes by conducting the damage threshold experiments. The light of Ar laser, 488 nm was focussed on freshly cleaved fiber of the same type as that under study. This fiber was then coupled to the near field probe using fiber splicer. The light leaked from the tip of the apertureless probe on varying the power of the focussed laser light was detected by a silicon photodiode. The effective optimum coupling efficiency in the present experiments was 15%.

Fig. 2 compares the typical result of such experiment performed on as fabricated, gold coated probe and that after the mercury treatment. The mercury treatment is seen to yield ~ (¼) times decrease in the optical leakage (at 280mW input laser power) and 21% increase in the optical damage threshold. SEM study showed the clear ripping of the metal coating on the fiber probe beyond the optical damage threshold as seen in Fig. 3. The extent of damage caused by coupling of overly high laser powers into the probe is much smaller for mercury treated probes (Fig.3b) in contrast with that for the as fabricated and gold coated probes. (Fig.3 a). This feature could be exploited for fabricating nanometric aperture by proper choice of input laser power.

Other performance aspects such as near field profile of mercury treated near field fiber probes are also explored. Mercury treatment approach giving smoother surface structure offers a simple technique to further improve the yield as well as the performance of near field probes.

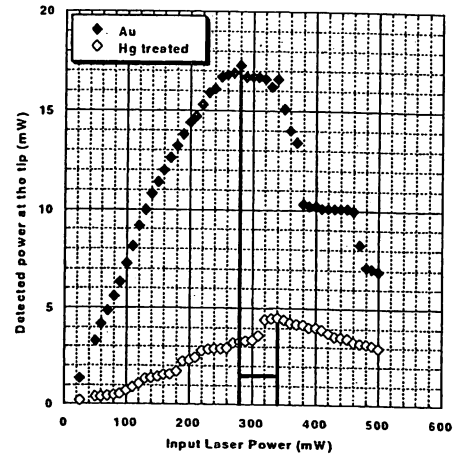

Fig.2 Variation of detected power at the tip of the Au coated apertureless near field fiber probe before and after the mercury treatment with the input laser power coupled at the other end.

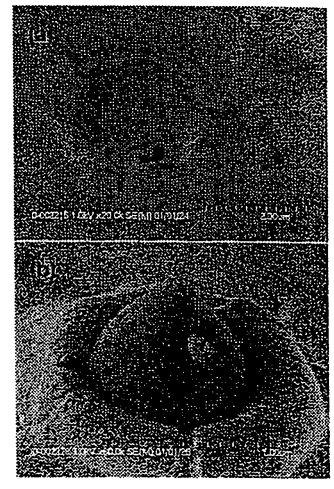

Fig. 3 SEM images of near field optical probe after coupling laser powers beyond the damage threshold. (a) As fabricated Au coated probe and (b) Hg treated case

[1] Near Field Nano/Atom Optics and Technology, edited by M. Ohtsu (Springer Verlag, Berlin, 1998).
[2] G.A. Valaskovic, M. Holton and G.H. Morrison, Appl. Opt.**34**, 1215 (1995).
[3] L. Novotny, D. Pohl and B. Hetcht, Opt. Lett., **20**, 970(1995).
[4] R.M. Stockle, N. Schaller, V. Deckert, C. Fokas and R. Zenobi, J. Microscopy, **194**, 378(1999).
[5] P. Hoffmann, B. Dutort and R.P. Salathe, Ultramicroscopy, **61**, 165(1995).
[6]A.W. Castleman Jr. and J.J. Conti, Phys. Rev. A,2,1975(1970).

WH2-5

Characterization of Silica Optical Fibers Based on Chemical Etching

Shuji Mononobe, Motoichi Ohtsu *

Special Research Laboratory for Optical Science
Kanagawa Academy of Science and Technology (KAST)

KSP East 408, 3-2-1 Sakado, Takatsu, Kawasaki 213–0012, JAPAN
Phone (+81) 44 8192075
Fax (+81) 44 8192072
E-Mail mononobe@net.ksp.or.jp

Abstract

We propose a method to characterize silica fibers with submicrometer–sized resolution. The method is based on etching in buffered hydrogen fluoride solutions and observing by a scanning electron microscope.

Summary

In developing a new optical fiber, one has to characterize the fiber by measuring its structural parameters such as a core diameter and a relative refractive index difference. For commercial multimode and single–mode fibers, two measurements called near field pattern [1] and side–view [2] have been known as effective methods, respectively. However, it is difficult to investigate special fibers having submicrometer–sized structure and a complex index profile by these methods due to the optical diffraction limit. In this paper, we propose a method [3] based on chemical etching [4–6] in order to characterize silica fibers with high resolution of submicrometer–size or less.

In the following, we describe the proposed method for a step index fiber with the GeO_2 doped silica core and pure silica clad. Firstly, the fiber is cleaved and etched in a buffered hydrogen fluoride solution (BHF) with a volume ratio of [40wt.%–NH_4F aqueous sol.]: [50wt.%–HF acid]: [H_2O] = 10:1:1. If the dissolution rate of the core and clad is represented by R_1 and R_2, respectively, at $R_1<R_2$, the core is protruded from the clad end with the taper angle α as shown in Fig. 1(a). Here, the foot diameter D_f of the protruded core corresponds to the core diameter. Secondly, to measure the taper angle α and core diameter, the etched fiber is observed with nanometric resolution by scanning electron microscopy (SEM). If the dissolution rates of the core and clad denoted as R_1 and R_2, the taper angle α is represented by

$$\sin\alpha = R_1/R_2. \quad (1)$$

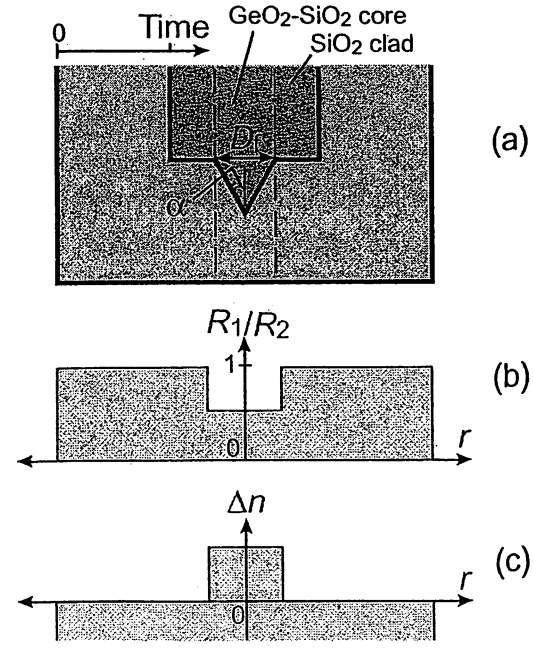

Fig .1 Cross–sectional profiles of (a) etched fiber, (b) dissolution rate ratio R_1/R_2, (c) and relative refractive index difference Δn.

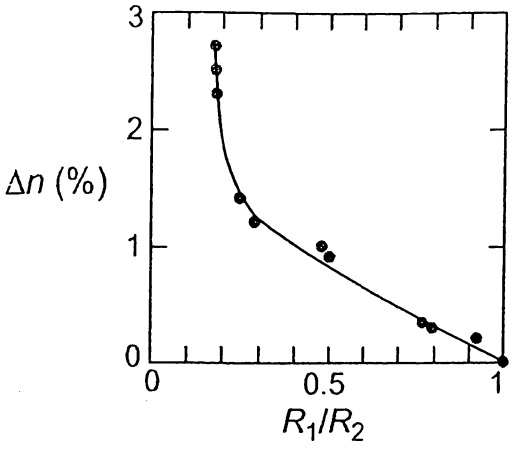

Fig. 2 Dependence of the relative refractive index difference Δn on the dissolution rate ratio R_1/R_2.

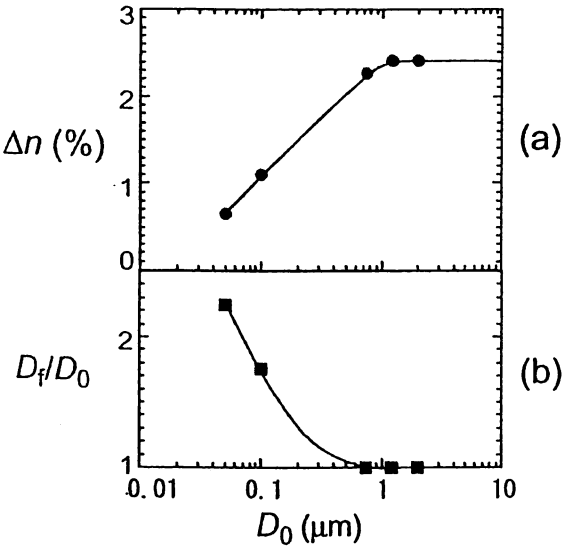

Fig. 3 Dependencies (a) the relative refractive index difference Δn and (b) the ratio of the core diameters D_f of and the linearly reduced diameter D_0. given by Eq. 2.

The right side of this equation depends on the relative refractive index difference Δn as shown in Fig. 2. Therefore, one can estimate the relative refractive index difference with nanometric resolution by using a value of α, Eq. 1, and the dependence of Fig. 2.

To demonstrate the proposed method, we estimated relative refractive index difference of GeO_2–doped fibers with a clad diameter of D_2=125μm and various core diameters in a region more than 0.1μm. These fibers were made by heating and pulling preform glass rods with a relative refractive index difference of Δn_0=2.4%. Figures 3(a) and 3(b) show the dependencies of the relative refractive index difference Δn and the ratio of the core diameter D_f and the linearly reduced diameter D_0 expressed by

$$D_0 = D_{P1} \cdot D_2/D_{P2}. \quad (2)$$

Here, D_{P1} and D_{P2} represent the core and clad diameters of the preform rod, respectively. In a region of D_0< 1μm, Δn is lowered from 2.4%, and the core diameter is increased from the diameter D_0. We consider that this increase attributes to germanium dispersion at heating and pulling. It is found that the proposed method is very effective in characterizing optical fibers with submicrometer–sized structure.

In conclusion, we proposed a method based on selective etching to characterize silica fiber, and then, demonstrated submicrometer–level resolution of the method.

* *Tokyo Institute of Technology, 226-8502 Yokohama, JAPAN*

1. D. Gloge and E. A. J. Marcatili, "Multimode theory of graded core fibers," Bell Syst. Tech. J., **52**, 1563 (1973).
2. Y. Hattori and A. Inoue, "Measurement of structural parameters of single–mode fiber by side–viewing method," OFC '88, 1998.
3. S. Mononobe et al., JP-Patent H11-108798.
4. S. Mononobe, Dr. Thesis, Tokyo Inst. of Technol., Yokohama, 1999 (in Japanese), http://www.kast.or.jp/Mononobe.pdf.
5. S. Mononobe and M. Ohtsu, "Probe fabrication," in Near–field nano/atom optics and technology, M. Ohtsu ed., Springer-Verlag, Tokyo, (1998), Chap. 3.
6. S. Mononobe and M. Ohtsu, J. Lightwave Technol., **14** (10), 2231 (1996).

Theoretical and experimental study on a near-field optical nano-switch

K. Kobayashi [(1)], T. Kawazoe [(1)], S. Sangu [(1)], J. Lim [(2)], and M. Ohtsu [(1),(2)]
(1) ERATO Localized Photon Project, Japan Science and Technology Corporation, 687-1 Tsuruma, Machida, Tokyo 194-0004, Japan
Telephone: +81 42-788-6036, fax: +81 42-788-6031, e-mail: kkoba@phtsu.jst.go.jp

(2) Interdisciplinary Graduate School of Science and Engineering, Tokyo Institute of Technology, 4259 Nagatsuta-cho, Midori-ku, Yokohama, Kanagawa 226-8502, Japan

Abstract: A near-field optical switch using quantum dots is proposed for ultrahigh density integration. Optical switching of sub-nanosecond speed is estimated. As a first step in verification, we experimentally obtained spatial and spectral distribution of nanometric dots with desirable sizes.

OCIS codes: (230.3990) Microstructure devices; (260.2160) Energy transfer

1. Introduction

Rapid growth rate in data communication has required higher speed and greater bandwidth from optical communication systems. This encourages accelerated study of miniaturization and integration of high-speed photonic devices that will ultimately be nanometric, as small as their electronic counterparts [1]. However, we have to overcome the diffraction limit of light and find a new principle of operation in order to achieve miniaturization of the devices on a nanometer scale.

A near-field optical technique combined with photochemical deposition is a promising solution of the issue. It permits highly controllable nanostructure fabrication as regards both size and position [2]. When nanometric quantum dots (QDs) as components are prepared by the technique, optical near fields, not propagating far fields, are responsible for data transmission and control of photonic devices.

It is very critical for devices controlled by optical near fields to solve the following problems: (a) to maintain signal directionality and (b) to avoid crosstalk between input and output signals, or channel signals. From this point of view, we propose a novel approach towards a nano-switch for both elementary and functional photonic devices, and investigate fundamental aspects of the device both theoretically and experimentally.

2. Proposed device and principle

The building blocks of the proposed device consist of three nanometric QDs as illustrated in Fig. 1. The discrete energy levels of each dot are described as

$$E_n = E_B + \frac{\pi^2\hbar^2}{2Ma^2}\left[n_x^2 + n_y^2 + n_z^2\right], \quad \left(n, n_x, n_y, n_z = 1,2,3,\ldots\right), \tag{1}$$

where the mass and size are denoted as M and a, respectively. When the sizes of dots 1, 2, and 3 are respectively chosen as $a/2$, $a/\sqrt{2}$, and a, two neighboring dots with the distance $r_{ij}\,(i,j=1,2,3)$ have the same excited energies denoted as E_1, E_2, and E_3 in Fig. 1. The energy level E_3 of dot 1, for example, specified by $(n_x,n_y,n_z)=(1,1,1)$, is resonant with states specified by both $(2,1,1)$ for dot 2 and (2,2,2) for dot 3. Dot 1 is coupled to the input light, which is transmitted by the inter-dot Yukawa interaction [3] to dot 2 that is connected to the output light. Dot 3 is coupled to the control light that governs the switching mechanism. When the control light is on, near-field interactions of dot 3 with the other dots are forbidden, since the level E_1 of dot 3 is occupied and the intra-dot relaxation time is much faster than the inter-dot transfer time. In contrast, when the control light is off, those interactions are allowed, which results in the population difference in dot 2 producing a difference in the transmission signal. It should be noted that the fast intra-dot relaxation time guarantees a single direction for the signal transmission, and that the frequency conversion from input to output avoids irrelevant crosstalk.

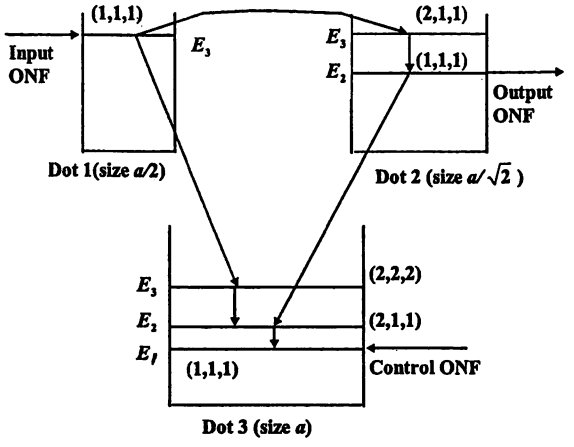

Fig. 1. Three-dot configuration as fundamental block of the proposed device. Optical near fields are abbreviated to ONF.

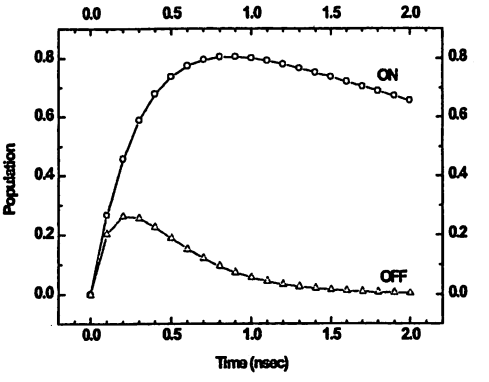

Fig. 2. Population of dot 2 as a function of time when control light is ON and OFF.

3. Theoretical analysis

In order to analyze dynamic properties of the device, we employ the following master equation:

$$\begin{cases} \dfrac{\partial P_n^j(t)}{\partial t} = -\left[\dfrac{1}{\tau_{n-1,n}} + U_n^{ij}\right] P_n^j(t) + U_n^{jk} P_n^k(t), \\ U_n^{ij} = \dfrac{Y_0}{\hbar} \dfrac{\exp\left[-m_{\text{eff}}(n) r_{ij}\right]}{m_{\text{eff}}(n) r_{ij}}, \end{cases} \tag{2}$$

where $P_n^j(t)$ represents the population of dot j to remain in the excited states E_n at time t. The intra-dot relaxation time from the E_n to the E_{n-1} level is denoted as $\tau_{n-1,n}$ while U_n^{ij} gnates the transfer rate due to the inter-dot Yukawa interaction. The strength and Planck's constants are shown as Y_0 and $\hbar$, respectively. The effective mass $m_{\text{eff}}(n)$ determines the interaction range between the E_n levels of the neighboring dots i and j, whose excitation energy is transferred. Under the initial condition of $P_{n=3}^{j=1}(0) = 1$ and otherwise $P_n^j(0) = 0$, we obtain the time evolution of the population of each dot.

We adopted CuCl dots for the following case study though any arbitrary material system is, in principle, suitable. These QDs have discrete energy levels due to quantum size effects, as a result of exciton confinement [4]. The energy levels are described as in Eq. (1), which means the energy structure reflecting each size of the QDs. Figure 2 shows an example of the time evolution of $P_{n=2}^{j=2}(t)$, where the largest dot size is assumed to be 10 nm and the distance between neighboring dots is 10 nm. The intra-dot relaxation time is set as 1 picosecond. The curve with circles represents the ON condition while the curve with triangles shows the OFF condition. We estimate from Fig. 2 that a near-field nano-switch can be operated within a few hundred picoseconds, and expect that it would, in principle, be applicable to other material systems like ZnO and GaAs.

4. Experimental results

In order to experimentally verify the switching mechanism and operation proposed, we need to surmount several kinds of difficulties. The first step is to identify a specific QD with a desirable size or energy, after observing the spatial and spectral distribution of QDs. Then it is necessary to verify the excitation energy transfer between two QDs, that is, to detect the desirable frequency conversion from ω_3 to ω_2. Finally we have to show the switching operation of the proposed device. Here we report experimental results on the first step, using CuCl QDs embedded in NaCl matrix. The spatial and spectral characteristics of the sample, as schematically drawn in Fig. 3(a), were investigated by using near-field optical microscopy and spectroscopy equipped with cryostat.

Figure 3(b) shows far-field and near-field photoluminescence spectra of a sample at 18 K that was excited by a He-Cd laser with a wavelength of 325 nm. The photoluminescence was detected by an optical near-field probe with a gold coating and an aperture diameter of 70 nm. The approach distance between the probe and the sample was 1 μm for the far-field detection while it was less than 10 nm for the near-field case. The far-field luminescence spectrum is inhomogeneously broadened by the size distribution of QDs while the near-field luminescence spectrum has the very fine structure that ideally corresponds to a vertical scan at a specific spatial position (see Fig. 3(a)).

Spatial distributions of QDs with energies of E_B and E_A are shown in Figs. 3(c) and (d), respectively. These values of E_B and E_A are respectively equivalent to the dot sizes of 3.4 nm and 4.8 nm, which correspond to a pair of dots 1 and 2, or dots 2 and 3. The spatial resolution of the images is close to the aperture diameter used. These results indicate that we have established how to identify QDs selected both spatially and spectrally.

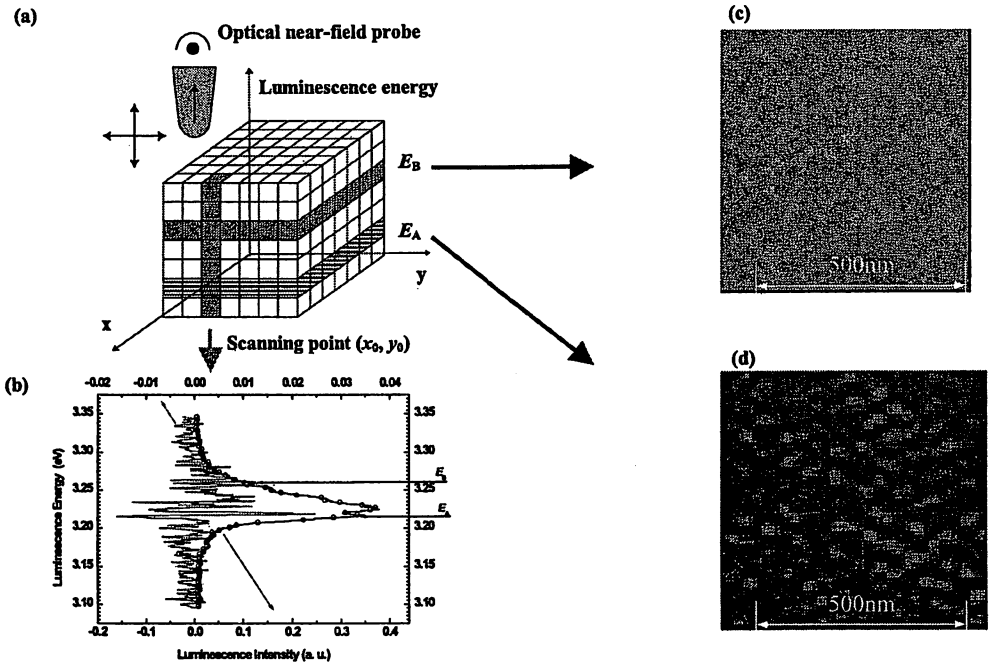

Fig. 3. (a) Spatial and spectral information of a sample, (b) luminescence spectra, (c) spatial distribution of QDs with E_B, and (d) with E_A.

5. Summary and future outlook

On the basis of the inter-dot interaction due to optical near fields and the fast intra-dot relaxation, we have proposed an optical nano-switch, and examined the fundamental properties of the device both theoretically and experimentally. We expect sub-nanosecond switching speed as a typical value from theoretical analysis based on the master equation with an incoherent transfer process. Towards experimental verification, a method for identifying both spatially and spectrally selected QDs has been established.

From the viewpoint of size and speed, the proposed approach is potentially superior, but there still remain several issues to be resolved as well as an experimental demonstration. The falling-off time should be improved, and moreover, optimum conditions for operation and materials should be investigated. It is also an important subject how to effectively interface the proposed device with external circuits.

References

1. For example, see G. A. Thomas et al., 'Physics in the whirlwind of optical communications,"Phys. Today 53, 30-36 (2000).
2. Y. Yamamoto et al., 'Fabrication of nanometric zinc pattern with photodissociated gas-phase diethylzinc by optical near field,"Appl. Phys. Lett. 76, 2173-2175 (2000).
3. K. Kobayashi et al., 'Near-field optical potential for a neutral atom,"Phys. Rev. A 63, 013806 (2001).
4. N. Sakakura and Y. Masumoto, 'Persistent spectral-hole-burning spectroscopy of CuCl quantum cubes,"Phys. Rev. B 56, 4051-4055 (1997).

P23

Nanometric quantum dots controlled by optical near fields: theoretical and experimental study

K. Kobayashi[(1)], T. Kawazoe[(1)], S. Sangu[(1)], J. Lim[(2)], and M. Ohtsu[(1),(2)]

[(1)] *ERATO Localized Photon Project, Japan Science and Technology Corporation, 687-1 Tsuruma, Machida, Tokyo 194-0004, Japan*
Telephone: +81 42-788-6036, fax: +81 42-788-6031, e-mail: kkoba@ohtsu.jst.go.jp
[(2)] *Interdisciplinary Graduate School of Science and Engineering, Tokyo Institute of Technology, 4259 Nagatsuta-cho, Midori-ku, Yokohama, Kanagawa 226-8502, Japan*

Optical near-field techniques have been applied to a variety of areas such as local excitation spectroscopy of a single molecules and a single quantum dots (QDs), and have been considered promising as enabling technologies for nanostructure fabrication with arbitrary shapes and high spatial accuracy far beyond the diffraction limit [1]. In fact, quantum wires and dots of Zn and ZnO on a nanometer scale have become possible by such a technique combined with photochemical deposition [2].

Once nanometric QDs are prepared as components, one can expect highly miniaturized photonic devices, where optical near fields, not propagating far fields, are responsible for data transmission and control of the devices. It is very critical for the devices to maintain signal directionality and to avoid crosstalk between input and output signals, or channel signals. From a theoretical viewpoint, a quantum-mechanical theory is required so that it can explicitly deal with interactions in a nanometric probe tip and sample system, which is coupled to a macroscopic bath system. Since conventional theories in near-field optics are unfortunately inadequate for the purpose, we try to develop a new approach to satisfy the conditions and to apply to nanometric photonic devices [3].

On the basis of the inter-dot interaction due to optical near fields and the fast intra-dot relaxation, we investigate an optical nano-switch using nanometric QDs, and examine the fundamental properties of the device both theoretically and experimentally. We expect sub-nanosecond switching speed as a typical value from theoretical analysis based on the master equation with an incoherent transfer process. We will also discuss a simple coherent population control of QDs. Towards experimental verification, a method for identifying both spatially and spectrally selected QDs has been established, and excitation energy transfer between two CuCl QDs has been examined. Such an excitation energy transfer is considered to be allowed only via optical near fields. We will report the current status of the experiment.

References

[1] M. Ohtsu et al., Proc. IEEE 88, 1499 (2000).
[2] Y. Yamamoto et al., Appl. Phys. Lett.76, 2173 (2000).
[3] K. Kobayashi et al., Phys. Rev. A 63, 013806 (2001).

Nanotechnology and nano/atom photonics by optical near-field

M. Ohtsu[a,b,c]

[a] Interdisciplinary Graduate School of Science and Engineering, Tokyo Institute of Technology

[b] Localized Photon Project, ERATO, Japan Science and Technology Corporation

[c] Near-field Photonics Group, Kanagawa Academy of Science and Technology

ABSTRACT

This paper reviews the recent progress of application of interactions between optical near-fields and nanoscale materials. Photochemical vapor deposition of nanometeric Zn and Al are realized by using an UV optical near-field. Deposition of nanoscale ZnO is also shown. Utilizing the very advanced potential of this technology, the concept of nano-photonic IC is proposed. The optical switching operation of a single InGaAs quantum dot is shown to be able to be used for nano-photonic devices. Nano-photonic switching operation utilizing optical near-field interaction is also proposed and related spectroscopy of CuCl quantum dots are demonstrated. High-density storage and read-out by optical near-field is also demonstrated. Atom manipulation by the optical near-field is reviewed briefly.

1. INTRODUCTION

As an introduction, three examples of technical trends and technical problems for the present and future optical industry are presented. (1) It has been estimated that the society of the year of 2010 requires the high-density optical storage and readout technology, with the storage density of 1 Tb/in^2 and data transmission rate of 1 Gbps. Though the DVD technology has improved its storage density, the value given above is more than 100 times higher than that of DVD . Since the mark-length for 1 Tb/in^2 is as short as 25 nm, writing such a small pit is far beyond the diffraction limit of light. (2) The progress of DRAM technology requires the drastic improvement of photo-lithography. It is estimated that the size of the fabricated pattern should be as narrow as 50 nm or even narrower. Though novel methods using excimer lasers, EUV, and SR light sources have been developed, this required linewidth is far beyond the diffraction limit of the methods using a conventional visible light source. (3) The progress of optical fiber transmission system requires the improvement of the photonic integration technology. It is estimated that the photonic matrix switching device should be sib-wavelength in its size in order to realize more than 1000 x 1000 element integration of the devices for the 5 Tbps switching capability in the year of 2010. Since the conventional photonic devices, e.g., diode lasers and optical waveguides have to confine the light in them, their minimum sizes are limited by the diffraction of light. Thus, the size required above is beyond the diffraction limit.

By the three examples shown above, it can be easily understood that a novel optical nanotechnology is required to go beyond the diffraction limit to support the science and technology of the 21st century. Near field optics can be used as such a novel one to meet this requirement. Near field optics deal with the local electromagnetic interaction between optical field and matters in a nanometric region. Due to the size-dependent localization and size-dependent resonance, optical near-field

ohtsu@ae.titech.ac.jp : phone +81-45-924-5455, fax +81-45-924-5599, http://uuu.ae.titech.ac.jp :
4259 Nagatsuta-cho, Mirodi-ku, Yokohama 226-8502, Japan

Optical Engineering for Sensing and Nanotechnology (ICOSN 2001), Koichi Iwata, Editor,
Proceedings of SPIE Vol. 4416 (2001) © 2001 SPIE · 0277-786X/01/$15.00

is completely free from the diffraction of light. Very primitive idea of near field optics as a super-resolution imaging tool has been proposed in 1928[1]. After about half a century of silence, basic research has been started early 1980 s by several groups in Europe, US and Japan almost independently. A short comment has been written on author s laboratory notebook of February 26, 1982, pointing out that *the chemical etching of fiber for fabricating a probe is not straightforward, and thus, requires a continuous effort to establish a nano-fabrication technology*[2]. However, after continuous efforts, study of near field optics showed a lot of progress. For example, the single string of DNA molecule has been successfully imaged. The linewidth of the image has been as narrow as 4 nm or even narrower[3]. By these progress, it can be claimed that a new field, i.e., so called nano-photonics has been started as a basic technology to support the society of the 21st century. Further, a novel field of atom-photonics has also been started, which controls the thermal and quantum motions of atoms precisely by the optical near-field[4,5]. This study can support a basic science of quantum electrodynamics and application to atom deposition. This paper reviews the recent progress of author s works on chemical vapor deposition, nano-photonic switching, optical storage/readout, and atom manipulation by optical near-field for nano/atom photonics.

2. CHEMICAL VAPOR DEPOSITION

There has been an interest in application to nano-structure fabrication because of the possibility of realizing nano-photonic integration[6]. For the realization of a device which uses the optical near-field as a carrier for signal transmission, various materials with nanometric size must be integrated laterally on a substrate. For this integration, we need an advanced nano-structure fabrication technique, able to realize spatially high resolution, precise control of size and position, and be applicable for various materials. Photo-enhanced chemical vapor deposition (PE-CVD) method has been attracting attention. Based on photochemical reaction, PE-CVD offers not only the possibility for the lateral integration of different in a truly single growth run[7,8] but also the option of chemical selective growth by varying the wavelength of the light source used. Since the optical near-field energy is concentrated within nanometric dimensions smaller than the wavelength of light[9,10], we are able to deposit various materials of nanometric dimensions by utilizing the photo-decomposition of chemical gases. The combination of optical near-field technology with the PE-CVD, i.e., a near-field optical CVD(NFO-CVD) thus appears to be the most suitable technology for the integration of nanometer scale elements, because it not only allows us to fabricate nanostructures but also gives dual advantage of *in-situ* measurement of the optical properties of the fabricated nanostructures.

2.1 Depositing zinc and aluminum

Let us discuss the deposition of Zn as an example of NFO-CVD by using a diethlzinc(DEZ) as a parent gas. As NFO-CVD is based on a photodissociation reaction, it is necessary for a reactant molecule to absorb photons with a higher energy than its dissociation energy. This molecule absorbs light with a photon energy higher than 4.59 eV ($\lambda < 270$ nm), and the photodissociation reaction occurs as: $Zn(C_2H_5)_2 + 2.256$ eV $\rightarrow ZnC_2H_5 + C_2H_5$, and $ZnC_2H_5 + 0.9545$ eV $\rightarrow Zn + C_2H_5$.Thus the second harmonic light (SH light) of an Ar^+ laser ($\lambda = 244$ nm) and an ArF excimer laser ($\lambda = 193$ nm) were used as the light source for photodissociation of DEZ gas. For the purpose of generating the UV optical near-field with sufficient power density to decompose DEZ gas, an UV fiber with transmission loss as low as 1.1 dB/m at 244 nm was used to fabricate a probe[11]. An UV probe was coated with 200 nm thick Al film after being tapered by chemical etching. The throughput of the probe was 1×10^{-4} and the power density at the probe tip with a sub-100nm aperture for 1 mW of incident UV light was as high as 1 kW/cm^2.

Figures 1(a) and (b) show two methods of NFO-CVD, i.e., prenucleation method and direct gas phase photodissociation method, respectively. Figure 2 shows the shear-force image of the loop-shaped Zn pattern on a glass substrate produced by the prenucleation method(Fig.1(a))[12]. The vacuum chamber was evacuated to below 10^{-5} Torr prior to the prenuclei fabrication stage, then filled with about 10 Torr of DEZ gas, maintaining the pressure for 20 min. Next, the chamber was re-evacuated to the pressure of 10^{-5} Torr, leaving a few adsorbed monolayer on the substrate surface. Prenucleation was performed by delivering the SH light on the substrate covered with adsorbed molecules using a probe. Nuclei of Zn were formed by the decomposition of DEZ gas adsorbed on the substrate with the optical near- field at the probe tip. In the growth stage after nuclei fabrication, DEZ gas was refilled in the chamber with a few Torr and the unfocused ArF excimer laser with the maximum energy of 10mJ was directly irradiated on the prenucleated substrate. Then growth proceeded only on the pre-existing nuclei. As this figure shows, the minimum width of the pattern is as small as 20 nm. The width achieved here is two orders smaller than the minimum width reported so far by conventional PE-CVD using a far-field light[13]. Since the measured width includes the resolution of a vacuum shear-force microscope(VSFM)[14] (depending on the shape of the used probe), the intrinsic width can be smaller than the value estimated from this figure. This method has the advantage of being free from the deposition at the probe tip, but otherwise has the drawback that the lateral integration of various materials is not easy due to using the propagating light in the second step.

We will now discuss the results from the direct gas phase photodissociation method(Fig.1(b))[15]. The advantage of this method lies in the possibility of selective deposition of various materials by changing parent gases, which is useful for lateral integration. One disadvantage of this method is that the probe tip is also gradually covered with the depositing materials while it is fabricating a nano-structure on the substrate. In our experience, however, this only becomes a problem after a few hours of operation, while only a few seconds are necessary to fabricate a nano-structure. It is therefore not a serious problem. In order to examine the effect of optical near-field energy on the growth, an experiment was performed by varying the illumination time at a constant gas pressure of 1 mTorr and an input SH light power of 15 mW. The value of the optical near-field energy was evaluated by measured SH light power $\times$ illumination time. It was confirmed that the dot size depends on the spatial distribution of the optical near-field in a direction lateral to the substrate surface, while depending on the optical near-field energy in the normal direction. One of the most attractive features of this technique is its high spatial resolution. The lateral size of the fabricated pattern depends on the spatial distribution of the optical near-field energy and its reproducibility also depends on the reproducibility of fabricating probes. Figures 3(a) and (b) show the shear-force image of dots and a cross sectional profile along the dashed line, respectively. Two dots with a diameter of 52 nm and 37 nm (FWHM of the cross-sectional profile) were fabricated at a very close distance of 45 nm. Since the measured diameter of the dot image includes the resolution of VSHM, the intrinsic diameter may be smaller than the value estimated from these figures.

The optical near-field has unexpected unique properties, which was examined for the first time by NFO-CVD of nanometer-sized Zn dots with nonresonant light[16]. In order to investigate the deposition effect by nonresonant light, the fiber probe without metal coating on it, i.e., a bare fiber probe, was used for deposition. Therefore, the far-field light leaked to circumference of the fiber probe. The solid curve in Fig. 4 shows the cross-sectional profile of a Zn dot on the sapphire step substrate deposited by using the 244 nm-wavelength light, i.e., the light resonant to the absorption spectrum. It has tails of 4 nm height on both side of the dot. The tails correspond to the deposition by the leaked far-field light. The broken curve in this figure shows the profile of the dot deposited by using the light of $\lambda = 488$ nm, i.e., the nonresonant light. This curve has no tails since, in the case of the far-field PE-CVD, Zn deposition using the nonresonant light is not possible[17]. We

discuss the possible mechanism of DEZ dissociation and deposition by the nonresonant optical near-field. In the case of using the far-field light, the dissociation of DEZ is induced by photo-absorption and predissociation. In contrast, in the case of using the optical near-field, the dissociation can take place even under the nonresonant condition. Its first reason is two-photon absorption process due to the high energy density of the optical near-field at the apex of the high throughput fiber probe. The second is the induced transition to the dissociation channel by the apex of the fiber. The third involved the direct coupling between the optical near-field and the dissociation molecular vibration mode. This nonresonant deposition method has high potential for the application to the NFO-CVD of gas sources for which far-field PE-CVD is unrealizable.

NFO-CVD also allows us to fabricate nanostructures of several metals (Al, Cr, W, etc.) as well as Zn. For example, Fig.5 shows shear-force image of five Al dots deposited on a sapphire substrate by dissociating the trimethylalminium(TMA) using the light of λ = 244 nm[18]. The TMA partial pressure and the light power incident into the fiber probe were 10 mTorr and 1mW, respectively. The FWHM of the dots are typically 25 nm, which is comparable to the apex diameter of the used probe. As demonstrated by the deposition of Zn and Al, various materials can be deposited selectively by only changing the reactant gases. Furthermore, there is no limitation in regard to substrate and deposited materials. Zn and Al were deposited on an insulator substrate like sapphire. These are the advantage of this technique. Another of the most attractive points of this technique is the possibility for *in-situ* lateral integration of nano-scale structures of different materials with ease, which is difficult in conventional technique. In order to demonstrate the possibility, Zn dots were deposited at the first step, under the DEZ pressure of 10 mTorr. As the second step, Al dots were deposited under TMA pressure of 10 mTorr after evacuating the deposition chamber to 5 x 10^{-6} Torr. Figure 6 shows the result, i.e., shear-force image of deposited Zn and Al dots at closely position on a sapphire substrate. The distance between the Zn and Al dots was as close as 100 nm[18].

2.2 Depositing zinc oxide

One of the advantages of this NFO-CVD is the fact that there is no limitation in regard to substrate and deposited materials. That is, nanostructure of oxides, insulators, and semiconductors are deposited as well as metals. As an example, let us demonstrate the nanofabrication by NFO-CVD of ZnO on a sapphire substrate as insulator [19]. As a preliminary experiment, ZnO films were deposited by the PE-CVD method by using a propagating far-field light. Here, we used the reaction between oxygen and DEZ conveyed by a carrier gas (Ar) into the chamber during the irradiation by the propagating SH light (λ =244 nm) of an Ar^+ laser. A (0001) sapphire was used as a substrate for the epitaxial growth of ZnO. The reaction chamber was filled with the reactant gases at the ratio of DEZ : O of 1 : 10 at a working pressure of 10 mTorr. The chamber pressure was maintained at 10 mTorr during the growth. In order to find the optimal growth conditions, the crystallinity, stoichiometry, optical transmission, and photoluminescence were evaluated.

The PE-CVD of ZnO was carried out for 10 min within a range of the substrate temperature from room temperature to 300 ℃. The energy density of the laser source and the spot size were 10 mW and 600 μm, respectively. Crystalline films were deposited at substrate temperatures over 100 ℃ and the films with c-axis oriented crystalline. For films deposited at a substrate temperature above 150 ℃, the atomic ratio of Zn : O was 1.00 : 1.00 within an accuracy of a few percent. The optical properties were also investigated. Transmission fell off steeply at around 380 nm, a characteristic of high-quality ZnO film. From the plot of the wavelength vs. the absorption coefficient, optical band gap energies ranging from 3.26 to 3.31 eV were estimated, which is identical to the value recorded for high-quality ZnO films[20]. The photoluminescence spectra were measured using the 325 nm line of a cw He-Cd laser. Figure 7 shows the emission spectra

measured at room temperature from films deposited at the substrate temperature from 150 ℃ to 300 ℃. The emission peak position is coincident with the expected energy of the free exciton, and a strong free exciton emission at 380 nm can be clearly observed even at room temperature[21,22]. This confirms that if we use PE-CVD method at a low temperature, a ZnO film emitting UV light at room temperature can be fabricated. This was the first observation of room temperature UV emission from ZnO films deposited by PE-CVD.

Under the growth conditions studied by the preliminary experiments mentioned above, the ZnO nanostructure fabrication was carried out by NFO-CVD. The fabrication was performed by introducing the SH light of an Ar^+ laser onto the sapphire substrate surface through the fiber probe. Figure 8 shows the VSFM image of fabricated nanometric scale ZnO. The dot was of a 200 nm diameter and a 5 nm height. The diameter is smaller than the wavelength of the irradiating light source. However, because this value includes broadening due to the resolution of VSFM, the real diameter should be much smaller than that observed.

3. NANO-PHOTONIC SWITCHING AND NANO-PHOTONIC INTEGRATION

Future optical transmission systems require an advanced photonic integrated circuit(IC) for increasing speed and capacity. To meet this requirement, its size should become much smaller than that of a conventional diffraction-limited photonic IC. The concept of such a nano-photonic IC is shown in Fig.9, where metallic wires, light emitters, optical switches, input/output terminals, and photo-detectors are all controlled by nano-scale single dots and lines[6]. These devices use the optical near-field as a carrier for signal transmission.

As has been demonstrated in the previous sections, the NFO-CVD constitutes a very promising tool for *in-situ* patterning of nanostructures for this integration because this technique exhibits extraordinarily high controllability and reproducibility in fabricating nanostructures at desired position. This has never been demonstrated by any other conventional self-organized growth technique for semiconductor nanostructures. What is excellent is that as it is based on a photodissociation reaction, selective growth of various materials, i.e., metals, insulators, and semiconductors, can be accomplished by the choice of light source. It allows us to realize a nano-photonic IC composed of nanostructures.

3.1 Optical Swithing by nonlinear absorption in a single quantum dot

In order to demonstrate, e.g., a nonlinear optical switching capability of a single quantum dot(QD), we measured the nonlinear absorption change in a self-assembled single InGaAs QD grown on a (100) GaAs substrate by gas-source molecular beam epitaxy[23]. The average QD diameter was 30 nm and the height was 15 nm. The QD density was about 2 x 10^{10} dots/cm^2. These QDs were covered with cap layers with a total thickness of 180 nm. As schematically explained in Fig.10 (a), a probe light (λ = 900 - 980 nm) was introduced into the back of the sample, and the transmitted light was collected and detected by a high throughput fiber probe with a double tapered structure[24] placed in the vicinity of the sample surface. When the sample was illuminated by a pump light(λ = 635 nm) passing through the fiber probe, carriers were generated in the barrier layer, and flew into the QDs. The ground states of the QDs were occupied by the carriers. The resultant reduction of the absorption of the QDs was measured by detecting the transmission change in the probe light. Experiments were carried out in a liquid helium cryostat, where a double modulation/demodulation technique was used for detecting very weak signals. Figure 10(b) shows an experimental result demonstrating a deep modulation of the transmitted probe light power due to irradiation of the pump light. This result confirms that a single QD works like an optical switch, and moreover, the switching operation can be detected by a conventional optical signal detection technique, which is

advantageous for application to nano-photonic IC.

3.2 Nano-photonic switch by optical near-field interaction between quantum dots

We have proposed another novel approach towards a nano-photonic switch for both elementary and functional photonic devices[25]. The building blocks of the proposed device consist of three nanometric QDs as illustrated in Fig.11. The discrete energy levels of each dot are described as

$$E_n = E_B + (h^2/8Ma^2)(n_x^2 + n_y^2 + n_z^2), \quad (n_x, n_y, n_z = 1, 2, 3, \text{---}) \qquad (1)$$

where the mass and size are denoted as M and a, respectively. When the sizes of dots 1, 2, 3 are respectively chosen as $a/2$, $a/\sqrt{2}$, and a, two neighboring dots with the distance r_{ij} (i, j = 1,2,3) have the same excited energies denoted as E_1, E_2, and E_3 in Fig.11. The energy level E_3 of dot 1, e.g., specified by $(n_x, n_y, n_z) = (1, 1, 1)$, is resonant with states specified by both (2, 1, 1) for dot 2 and (2,2,2) for dot 3. Dot 1 is coupled to the input light, which is transmitted by the inter-dot Yukawa interaction[26] to dot 2 that is connected to the output light. Dot 3 is coupled to the control light that governs the switching mechanism. When the control light is on, optical near-field interaction of dot 3 with the other dots are forbidden, since the level E_1 of dot 3 is occupied and the intra-dot relaxation time is much faster than the inter-dot transfer time. In contrast, when the control light is off, those interactions are allowed, which results in the population difference in dot 2 producing a difference in the transmission signal. It should be noted that the fast intra-dot relaxation time guarantees a single direction for the signal transmission, and that the frequency conversion from input to output avoids irrelevant cross-talk.

In order to analyze dynamic properties of the device, we solved the following master equations for the population $P_n^j(t)$ of dot j to remain the excited states E_n at time t. We adopted CuCl dots for the following case study though any arbitrary material system is, in principle, suitable. These QDs have discrete energy levels due to quantum size effects, as a result of exciton confinement[27]. The energy levels are described as in eq.(1), which means the energy structure reflecting each size of the QDs. Figure 12 shows an example of the time evolution of $P_{n=2}^{j=2}(t)$, where the largest dot size is assumed to be 10 nm and the distance between neighboring dots is 10 nm. The intra-dot relaxation time is set as 1 ps. The curve with circles represents the ON condition while the curve with triangles shows the OFF condition. We estimate from this figure that an optical near-field nano-switch can be operated within a few hundred picoseconds, and expect that it would, in principle, be applicable to other material systems like ZnO and GaAs.

In order to experimentally verify the switching mechanism and operation proposed, we need to overcome several kind of difficulties. The first step is to identify a specific QD with a desirable size or energy, after observing the spatial and spectral distribution of QDs. Then it is necessary to verify the excitation energy transfer between two QDs, i.e. to detect the desirable frequency conversion from ω_3 to ω_2. Finally we have to show the switching operation of the proposed device. Here we review experimental results on the first step, using CuCl QDs embedded in NaCl matrix. The spatial and spectral characteristics of the sample were investigated by using a near-field optical spectrometer[28]. The curves A and B of Figure 13(a) show the far-field and near-field photoluminescence spectra, respectively, of a sample at 15K that was excited by a He-Cd laser(λ = 325 nm). The far-field spectrum is inhomogeneously broadened by the size distribution of QDs while the near-field spectrum has the very fine structure that ideally corresponds to a vertical scan at a specific spatial position of the sample.

Spatial distributions of photoluminescence with energies X and Y are shown in Figs. 13(b) and (c), respectively.

These values of X and Y are respectively equivalent to the dot sizes of 4.8 nm and 3.4 nm, which correspond to a pair of dots 2 and 1, or dots 3 and 2. The spatial resolution of the images is close to the aperture diameter of the fiber probe used. These results indicate that we have established how to identify QDs selected both spatially and spectrally.

4. HIGH DENSITY OPTICAL STORAGE AND READOUT BY OPTICAL NEAR-FIELD

The use of an optical near-field for realization of a high-density optical storage system has attracted a great deal of attention. For realization of a high data transmission rate a super-resolution near-field structure[29] and a planar probe mounted on an optical slider[30] were proposed recently. Since these methods do not require shear-force feed-back, reading speed is increased without technical difficulties. However, since the incident light is focused by a lens in these systems, the intensity of the optical near-field generated on the subwavelength aperture is low. This section propose and demonstrate a new contact slider with a high throughput ratio of near-field intensity for realization high recording density and fast readout to the phase-change medium[31]. Schematics of the slider structure and the data storage system are illustrated in Fig. 14. A pyramidal silicon probe array is arranged on the rear pad of the slider. The advantages of such a slider are as follows: (1) The high refractive index of the silicon ($n=3.67$ at $\lambda = 830$ nm) leads to a short effective wavelength inside the probe, which results in higher throughput and smaller spot size than those of conventional fiber probes made of silica glass[32]. (2) The height of the pyramidal silicon probe array is fabricated to be less than 10 μm so that sufficiently low propagation loss in the silicon is maintained. Furthermore, the probe array has high durability because it is bonded to a thick glass substrate.(3) Compared with those of previously reported pyramidal probes fabricated by use of a focused ion beam[33] or by the transfer mold technique in a pyramidal silicon groove[34], ultrahigh homogeneity in the heights of the probes and pads can be obtained, since the flatness of the probe tip and the upper surface of the pads are determined by the uniformity of the thickness of silicon wafer. (4) Use of a probe array with many elements increases the total data transmission rate by parallel readout[34, 35]. In this system the incident light is spatially modulated by an electro-optics method, and the scattered light from a different probe can be read out as a time-sequential signal.

Since the key issue in realizing a pyramidal silicon probe array is high homogeneity in the heights of the probes, the probe array is fabricated from a (100)-oriented silicon-on-insulator (SOI) wafer. Figures 15(a) and (b) show an optical image of the contact slider and a scanning electron microscopic image of the pyramidal silicon probe array fabricated on the slider, respectively. The height dispersions of the probes and pads should be less than 10 nm, because these dispersions are determined by the uniformity of thickness of the SOI wafer. Here the slider is designed by use of the design criteria[36] for a contact-type hard-disk head so that its jumping height over the phase-change medium is maintained at less than 10 nm. Furthermore, since the phase-change medium is fragile, we designed the bank so that the contact stress becomes 100 times weaker than the yield stress of the magnetic disk at a constant linear velocity (CLV) of 0.3 m/s, corresponding to a data transmission rate of 10 MHz for a data density of 1 Tbit/in^2. To increase the readout speed 100 times, i.e., to realize a 1-Gbit/s data transmission rate for data density of 1 Tbit/in^2, we fabricated 100 probe elements on the inner part of the bank for parallel readout.

In recording and readout experiments with the fabricated contact slider, we compared signals transmitted through phase-change marks recorded with a single element of the probe array and focused propagating light. The experimental setup is shown in Fig. 16. The contact slider was glued to a suspension. The slider was in contact with a phase-change medium coated with a thin lubricant film (Fomblin Z-DOL). A laser beam ($\lambda = 830$ nm) was focused on one element of the probe array on the slider, where the frequency of the rectangularly modulated signal with 50% duty was changed from 0.16

to 2.0 MHz at a CLV of 0.43 m/s. Then the light transmitted through the recording medium was detected with an APD. We used an as-deposited AgInSbTe film as a recording medium. The optical recording powers for a pyramidal silicon probe with a mesa length L_m of 150 nm (see Figs. 1 and 17(a)) and a focused propagating light with an object lens (N.A.= 0.4) were 200 mW and 15 mW, respectively, which in both cases is the lowest recording power of which we are aware. The optical throughput of the pyramidal silicon probe with a 30-nm-thick aluminum coating is 7.5×10^{-2}, which is estimated from the ratio of the optical powers for near- and far-field recordings. Readout was carried out at a CLV of 0.43 m/s, and the constant reading optical powers for the pyramidal silicon probe and the focused propagating light were 20 mW and 3.6 mW, respectively. The resolution bandwidth was fixed at 30 kHz.

The dependence of the carrier-to-noise ratio (CNR) on mark length is shown in Fig. 17(b). In this figure one can see that shorter crystalline phase-changed marks beyond the diffraction limit were recorded and read out by an optical near field generated on the pyramidal silicon probe. The shortest mark length was 110 nm at a CLV of 0.43 m/s, corresponding to a data transmission rate of 2.0 MHz. This is, to our knowledge, the first phase-change recording reading with a contact slider. Since this slider has 100 elements in the probe array, we expect a 100-fold increase in the data transmission rate by parallel readout. Furthermore, a higher CLV can be expected, since we did not observe any damage on the probe tip or the recording medium after a series of experiments. The constant CNR of the pyramidal silicon probe seen in Fig. 17(b) might be due to the small spot size for recording reading and the narrow recorded mark width, which are as small as L_m of the pyramidal silicon probe. These results indicate that an increased CNR and decreases mark length will be achieved by means of tracking during readout. Furthermore, it is expected that the recording density can be increased to as high as 1 Tbit/in^2 by optimization of the interference characteristics of the guided modes in the pyramidal silicon probe[37].

5. SUMMARY

This paper reviewed the recent progress of application of interactions between optical near-fields and nanoscale materials. Photochemical vapor deposition of nanometeric Zn and Al were realized by using an UV optical near-field. Deposition of nanoscale ZnO was also shown. Optical near-field technology offers the opportunity of modifying surfaces and developing new nanostructures that may exhibit a quantum effect due to their extremely small size. Utilizing the very advanced potential of this technology, the concept of nano-photonic IC was proposed. The optical switching operation of a single InGaAs quantum dot was shown to be able to be used for nano-photonic devices. Nano-photonic switching operation utilizing optical near-field interaction was also proposed and related spectroscopy of CuCl quantum dots were demonstrated. High density storage and read-out by optical near-field was also demonstrated. By combining the technique reviewed here with atom manipulation by the optical near-field[5,38], further progress in depositing novel materials and operating more advanced photonic IC can be expected.

ACKNOWLEDGEMENTS

The author would like to thank Prof. H. Ito, Drs. M. Kourogi, Y. Yamamoto, H. Fukuda(Tokyo Inst. Tech.), Drs. K. Kobayashi, S. Sangu, T. Yatsui, T. Kawazoe, H. Aiyer, K. Totsuka, V. Polonski (ERATO), Drs. T. Saiki and S. Mononobe(KAST) for their collaborations and valuable discussions.

REFERENCES

1. E.A. Synge, Phil. Mag., 6, 356 (1928)

2. M. Ohtsu, *Near-Field Optics: Principles and Applications*, World Scientific, Singapore, 2000 (ed.by, X. Zhu and M. Ohtsu), pp.1-8
3.Uma Maheswari, S. Mononobe, K. Yoshida, M. Yoshimoto, and M. Ohtsu, Jpn. J. Appl. Phys., **38**, 6713 (1999)
4. H. Ito, T. Nakata, K. Sakaki, M. Ohtsu, K.I. Lee and W. Jhe, Phys. Rev. Lett., **76**, 4500 (1996)
5. M. Ohtsu, K. Kobayashi, H. Ito, and G.-H. Lee, Proc. IEEE, **88**, 1499 (2000)
6. M. Ohtsu, *Technical Digest of the 18th Congress of the International Commission for Optics*, SPIE, **3749**, 478 (1999)
7. E. Maayan, O. Kreinin, G. Bahir, J. Salzman, A. Eyal, and R. Beserman, *J. Crystal Growth*, **135**, 23 (1994)
8. D. Bauerle, *Appl. Surface Sci.*, **106**, 1 (1996)
9. M. Ohtsu, *Near-Field Nano/Atom Optics and Technology*, Springer-Verlag, Berlin, Tokyo, New York, 1998
10. M. Ohtsu and H. Hori, *Near-Field Nano-Optics*, Kluwer Academic/Plenum Publishers, New York, 1999
11. S. Mononobe, T. Saiki, T. Suzuki, S. Koshihara, and M. Ohtsu, *Opt. Commun.*, **146**, 45 (1998)
12. V.V. Polonski, Y. Yamamoto, M. Kourogi, H. Fukuda, and M. Ohtsu, *J. Microscopy*, **194**, 545 (1999)
13. D. Ehrlich, R.M. Osgood, Jr., and T.F. Deutch, *J. Vac. Sci. Technol.*, **21**, 23 (1982)
14. V.V. Polonski, Y. Yamamoto, J.D. White, M. Kourogi, and M. Ohtsu, *Jpn. J. Appl. Phys.*, **38**, L826 (1999)
15. Y. Yamamoto, M. Kourogi, M. Ohtsu, V. Polonski, and G.H. Lee, , *Appl. Phys. Lett.*, **76**, 2173 (2000)
16. T. Kawazoe, Y. Yamamoto and M. Ohtsu, The 4th Pacific Rim Conf. on Lasers and Electro-Optics, Makuhari, Japan, July 15-19, 2001, to be presented
17. M. Shimizu, H. Kamei, M. Tanizawa, T. Shiosaki and A. Kawabata, J. Crysta. Growth, **89**, pp.365-370 (1988)
18. Y. Yamamoto, T. Kawazoe, G.H. Lee, T. Shimizu, M. Kourogi and M. Ohtsu, The 4th Pacific Rim Conf. on Lasers and Electro-Optics, Makuhari, Japan, July 15-19, 2001, to be presented
19. G.H. Lee, Y. Yamamoto, M. Kourogi, and M. Ohtsu, *SPIE 44th Annual Meeting*, 3791-18, Denver, CO, July 18-23, 1999
20. T.Y. Ma, G.C. Park, and K.W. Kim, *Jpn. J. Appl. Phys.*, **35**, 6208 (1996)
21. Z.T. Tang, G.K.L. Wong, and P. Yu, *Appl. Phys. Lett.*, **72**, 3270 (1998)
22. D.B. Bagnall, Y.F. Chen, Z. Zhu, and T. Yao, *Appl. Phys. Lett.*, **70**, 2230 (1997)
23. T. Matsumoto, M. Ohtsu, K. Matsuda, T. Saiki, H. Saito, and K. Nishi, *Appl. Phys. Lett.*, **75**, 3246 (1999)
24. T. Saiki, S. Mononobe, M. Ohtsu, N. Saito and J. Kusano, *Appl. Phys. Lett.*, **68**, 2612 (1996)
25. K. Kobayashi, T. Kawazoe, S. Sangu, J. Lim and M. Ohtsu, OSA Integrated Photonics Research Topical Meeting, Monterey, Ca, June 11-13, 2001, to be presented
26. K. Kobayashi, S. Sangu, H. Ito, and M. Ohtsu, Phys. Rev. A., **63**, 013806 (2001)
27. N. Sakakura and Y. Masumoto, Phys. Rev.B, **56**, 4051 (1997)
28. T. Kawazoe, K. Kobayashi, J. Lim, Y. Narita and M. Ohtsu, Quantum Electronics and Laser Science Conf., Baltimore, Ma, May 6-11, 2001, to be presented
29. J. Tominaga, T. Nakano, and N. Atoda, Appl. Phys. Lett. **73**, 2078 (1998)
30. H. Yoshikawa, Y. Andoh, M. Yamamoto, K. Fukuzawa, T. Tamamura, and T. Ohkubo, Opt. Lett. **25**, 67 (2000)
31. T. Yastui, M. Kourogi, K. Tsutsui, M. Ohtsu, and J. Takahashi, Opt. Lett., **25**, 1279 (2000)
32. H. U. Dangebrink, T. Dziomba, T. Sulzbach, O. Ohlsson, C. Lehrer, and L. Frey, J. Microsc. (Oxford) **194**, 335 (1999)
33. F. Isshiki, K. Ito, and S. Hosaka, Appl. Phys. Lett. **76**, 804 (2000)
34. Y. J. Kim, K. Kurihara, K. Suzuki, M. Nomura, S. Mitsugi, M. Chiba, and K. Goto, Jpn. J. Appl. Phys. **39**, 1538 (2000)
35. T. Yatsui, M. Kourogi, K. Tsutsui, J. Takahashi, and M. Ohtsu, Proc. SPIE **3791**, 76 (1999)

36. M. Yanagisawa, A. Sato, K. Ajiki, and F. Watanabe, in *Tribology of Contact/Near-Contact Recording for Ultra High Density Magnetic Storage*, C.S. Bhatia nad A. K. Menon, eds., TRIB-Vol. 6 (American Society of Mechanical Engineers, New York, 1996), p. 25

37. M. Kourogi, T. Yatsui, and M. Ohtsu, Proc. SPIE **3791**, 68 (1999)

38. H. Ito, K. Sakaki, M. Ohtsu, and W. Jhe, *Appl. Phys. Lett.*, **70**, 2496 (1997)

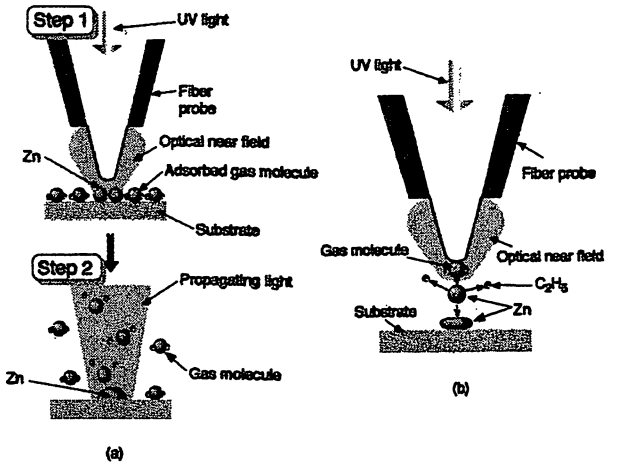

Fig.1
Principles of NFO-CVD. (a) Prenucleation method. (b) Gas phase direct photodissociation method.

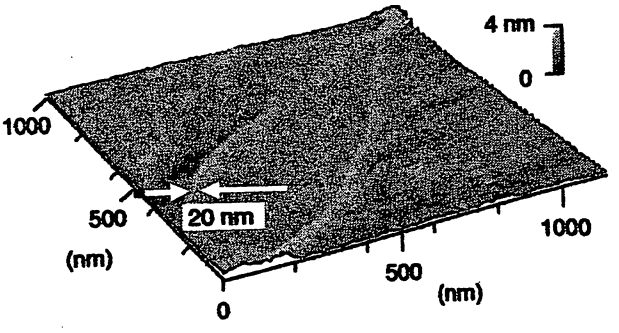

Fig.2
Shear-force image of a loop-shaped Zn deposited on a glass substrate by the prenucleation method.

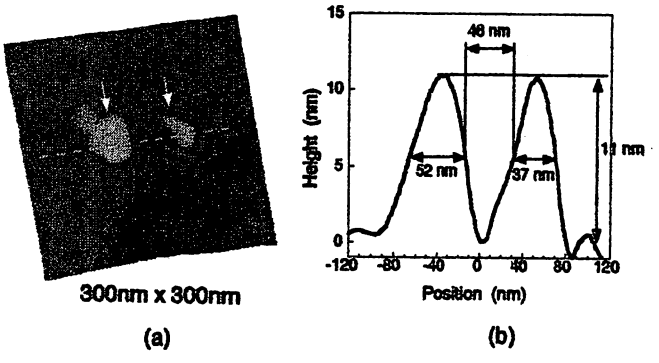

Fig.3
(a) Shear-force image of Zn dots. (b) Cross sectional profiles of the dots along the broken line in (a).

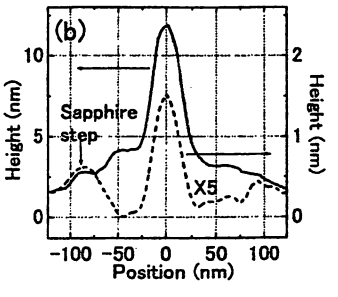

Fig.4
Cross sectional profiles of Zn dots deposited on a sapphire step substrate deposited by the light of λ =244nm(solid curve) and λ =488nm(broken curve).

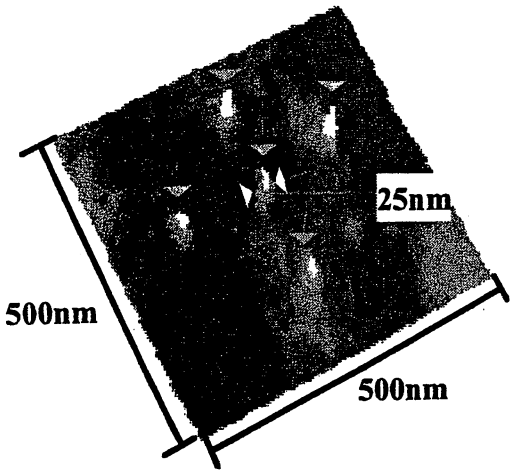

Fig.5
Shear-force image of five Al dots deposited on a sapphire substrate.

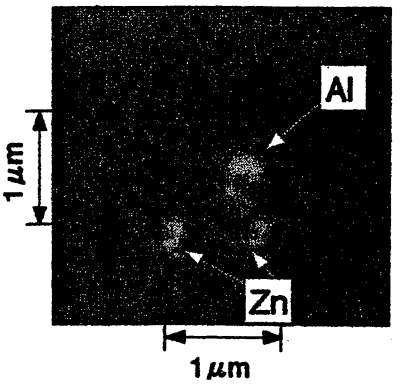

Fig.6
Zn and Al dots deposited closely on a sapphire substrate.

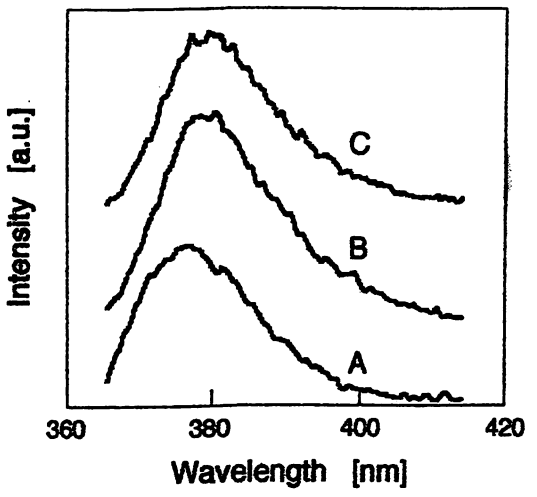

Fig.7
Photoluminescence spectra of ZnO films deposited at the substrate temperature of 150℃(A), 200℃(B), and 300℃(C). They were measured at room temperature.

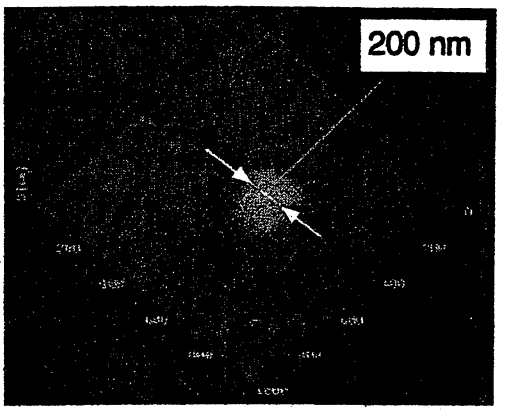

Fig.8
Shear-force image of a ZnO dot deposited on the (0001) sapphire substrate by NFO-CVD.

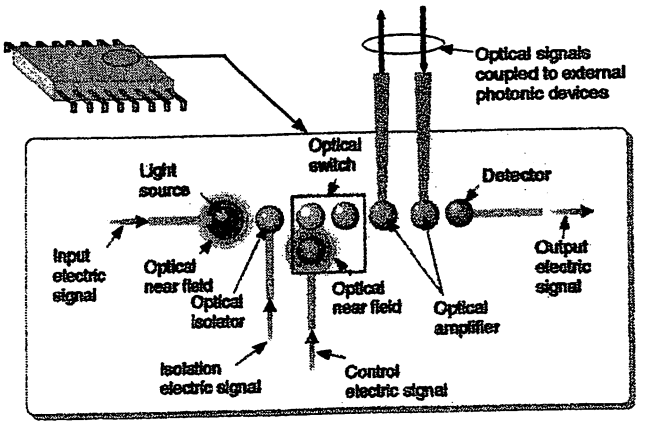

Fig.9
Concept of a planar nano-photonic integrated circuit.

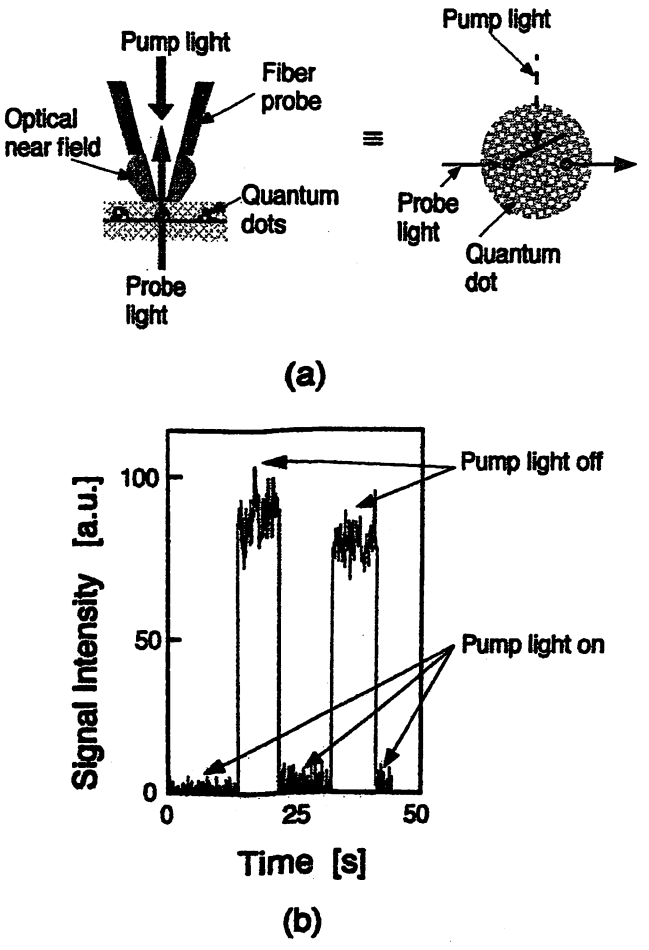

Fig.10
Saturated absorption spectroscopy of a semiconductor quantum dot. (a) Schematic explanation of the principle. (b) An experimental result of optical switching properties of a single InGaAs quantum dot.

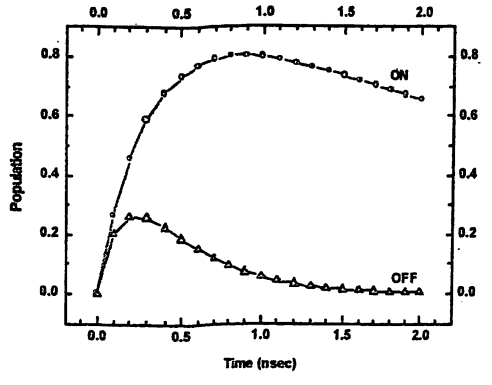

Fig.12
Population of dot 2 as a function of time when control light is ON and OFF.

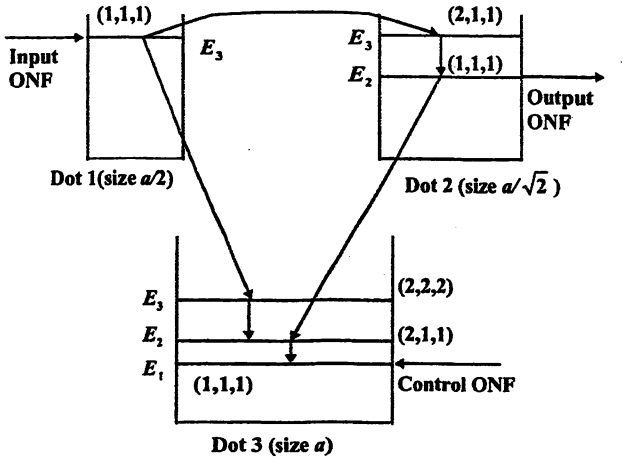

Fig.11
Three-dot configuration as fundamental block of the proposed device. Optical near-field is abbreviated by ONF.

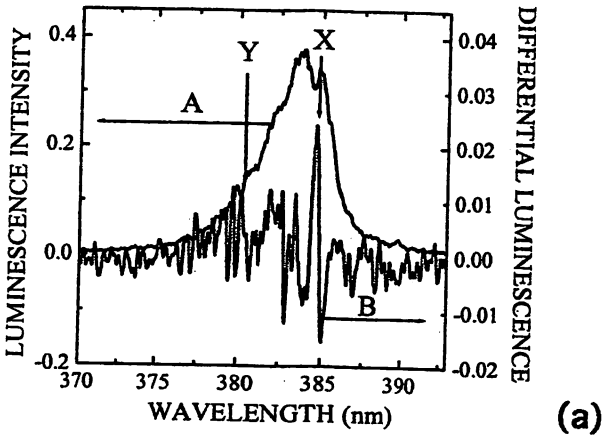

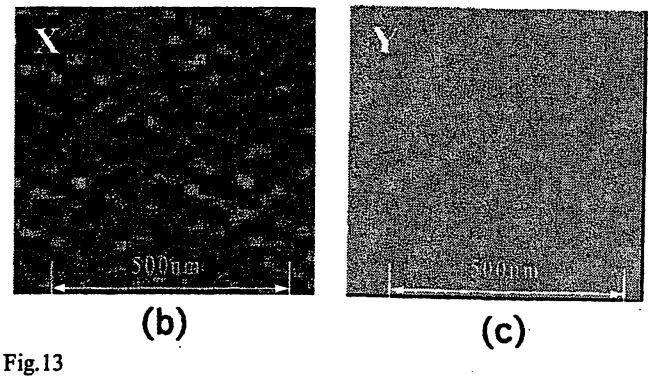

Fig.13
Spectral and spatial information of a sample. (a) Curves A and B show the far-field and near-field photoluminescence spectra, respectively, of CuCl quantum dots embedded in NaCl matrix at 15K. (b) and (c) Spatial distributions of the photoluminescence peaks X and Y, respectively, marked in (a). The spatial distributions for peaks X and Y correspond to the spatial distributions of the quantum dots with sizes of 4.3 nm and 3.4 nm, respectively.

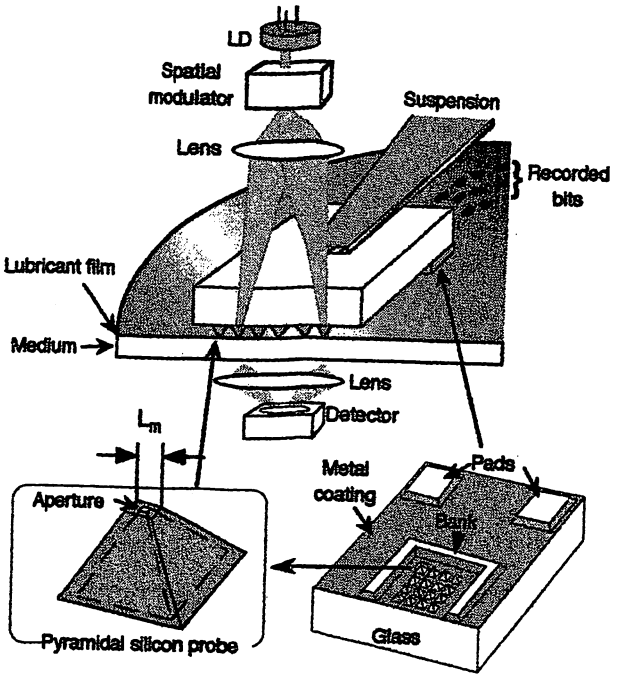

Fig.14
Schematic of the data storage/readout system with a contact slider and a pyramidal silicon probe array (L_m: mesa length).

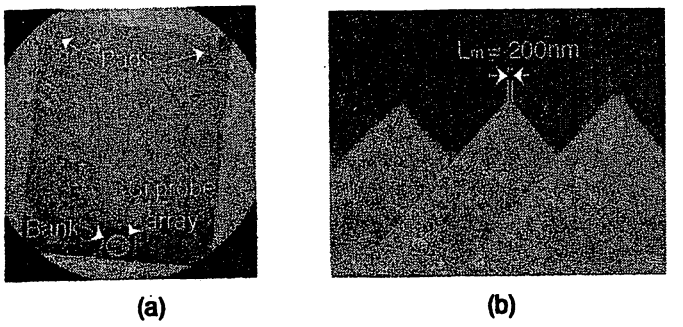

Fig.15
Optical image of the contact slider(a) and a SEM image of the pyramidal silicon probe array(b).

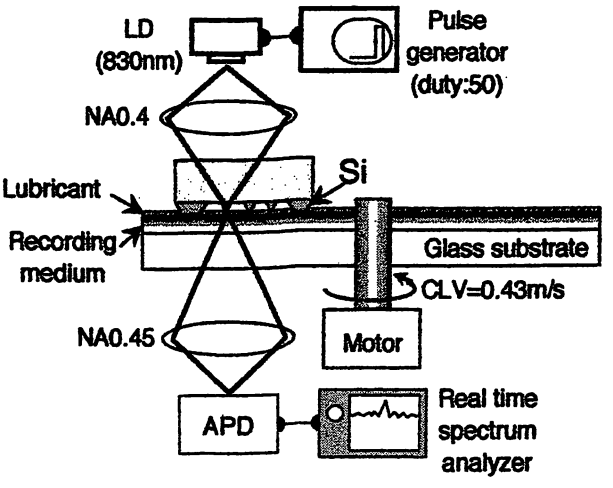

Fig.16
Experimental setup for phase-change storage/readout by the contact slider.

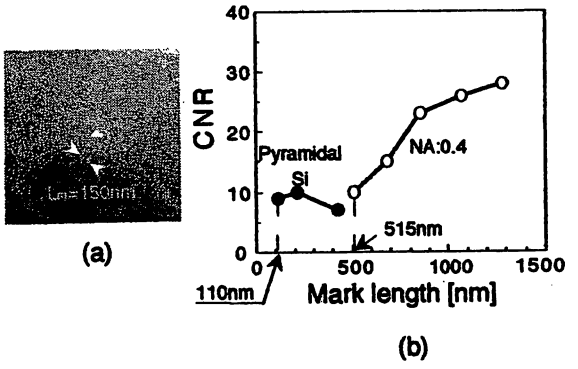

Fig.17
(a) Magnified SEM image of the pyramidal silicon probe tip used for storage/readout. (b) Dependence of the CNR on mark length for the optical near-field(closed circles) and propagating light focused by an objective lens(open circles).

Photochemical vapor deposition by optical near field toward nanometric photonic integration

M. Ohtsu

Tokyo Institute of Technology
ERATO Localized Photon Project, JST

We review recent progress of application of interactions between optical near-fields and nanoscale materials. Photochemical vapor deposition of nanometeric Zn and Al are realized by using an UV optical near-field. Deposition of nanoscale ZnO is also shown. Utilizing the very advanced potential of this technology, the concept of nano-photonic IC is proposed. Nano-photonic switching operation utilizing optical near-field interaction is also proposed and related spectroscopy of CuCl quantum dots are demonstrated.

QMN5 **5:15 pm**

A pyramidal silicon probe with an extremely high throughput and resolution for optical near field technology

T. Yatsui*, M. Kourogi**, and M. Ohtsu,*,**
**Ohtsu Project, ERATO, Japan Science and Technology Corporation 687-1 Tsuruma, Machida, Tokyo, Japan 194-0004; Email: yatsui@ohtsu.jst.go.jp; **Interdisciplinary Graduate School of Science and Engineering, Tokyo Institute of Technology, 4259 Nagatsuta, Midori-ku, Yokohama, Japan 226-8502*

For improvement in the performances of spatially resolved spectroscopy, optical data storage, and so on, we demonstrate here an extremely high throughput and resolution capability of a

pyramidal silicon probe. Since the high refractive index of the silicon (n= 3.67, @ λ = 830 nm) leads to a short effective wavelength inside the probe, which results in high throughput and spatial resolution compared to conventional fiber probes.[1]

The pyramidal silicon probe was fabricated from (100)-oriented silicon on insulator (SOI) wafer:

i. The SOI was bonded to the glass substrate by anodic bonding [Fig. 1(a)].
ii. After removing the silicon substrate, the oxide layer was patterned.
iii. The single tapered pyramidal probe was fabricated by anisotropic etching (40g:KOH + 60 g: H_2O + 40 g: isopropyl alcohol, 80°C) [Figs. 1(b) and (c)].
iv. The probe was coated with 30-nm thick aluminum [Fig. 1(d)].

Note that the pyramidal silicon probe with the mesa length (L_m) as short as 30 nm was realized by using this procedure.

By a probe-to-probe method,[2] we evaluated the throughput and resolution of the pyramidal silicon probe with L_m of 30 nm [P_A in Fig. 2(a)]. For comparison, we evaluated also an apertured fiber probe with aperture diameter (D) of 920 nm [P_B in Fig. 2(b)], which is equal to cut-off diameter (D_C) at λ = 830nm. As is described in detail in Ref. [2], the apertured probe with D = D_C has very narrow peak [full width at half maximum (FWHM) = 150 nm] due to the resonance interference between guided modes inside the tapered core and its throughput has been calibrated to be 10%. As a scanning probe, we used an apertured fiber probe with D of 50 nm (P_C in Fig. 2)

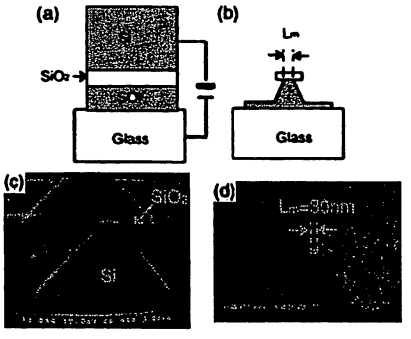

QMN5 Fig. 1. Schematic of the fabrication process of a pyramidal silicon probe. L_m :mesa length. SEM images of a pyramidal silicon probe: (c) bird's-eye view of the probe by the step (iii), (d) top view of the probe by the step (iv), respectively.

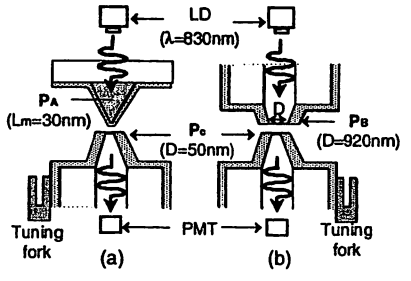

QMN5 Fig. 2. Probe-to-probe method.[2] The separation between the probes was maintaining within several nanometers with shear-force technique. P_A: pyramidal silicon probe with L_m = 30 nm, P_B: apertured fiber probe with D = 920 nm, P_C: apertured fiber probe with D = 50 nm.

Figures 3(a) and (b) show observed spatial distribution of the optical near field intensity for P_A and P_B. Curves A and B in Fig. 3(c) show the cross-sectional profile along the white dashed line in (a) and (b), respectively. One can find that the FWHM of the curve A is 85 nm (~ λ/10). Furthermore, the peak intensity for the curve A is as much as 25% that for the curve B. These results indicated that the pyramidal silicon structure led to high resolution (85 nm) and high throughput (2.5 %) simultaneously.

Since we have obtained a shortest mark length and a carrier-to-noise ratio of 110 nm and 10 dB, respectively, corresponding to a data transmission rate of 2.0 MHz using the pyramidal silicon probe with L_m = 150nm (λ = 830 nm),[3] the present results indicate that it will be easy to shorten the mark length to sub-100nm in order to improve the performances of ultrahigh density/speed optical data storage.

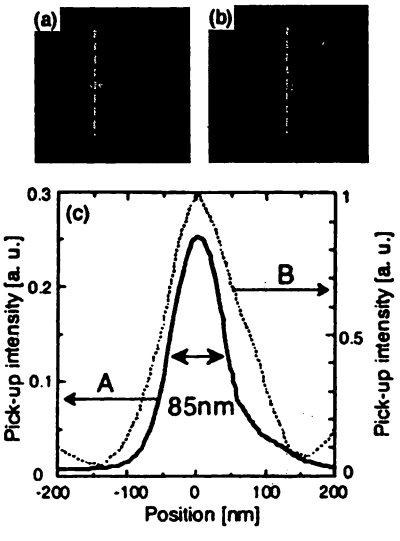

QMN5 Fig. 3. Spatial distribution of the optical near field intensity. (a) and (b) are for P_A (pyramidal silicon probe with L_m = 30 nm) and P_B (apertured fiber probe with D = 920nm), respectively. Image size is 1.5 μm × 1.5 μm. Curves A (solid line) and B (dashed line) in (c) are the cross sectional profile along the white dashed line in (a) and (b), respectively.

References

1. H.U. Dangebrink, T. Dziomba, T. Sulzbach, O. Ohlsson, C. Lehrer, and L. Frey, "Nano-slit probes for near-field optical microscopy fabricated focused ion beams," J. Microscopy, 194, Pt 2/3, 335–339 (1999)
2. M. Kourogi, T. Yatsui, K. Tsutsui, J. Takahashi, and M. Ohtsu, "Subwavelength-sized phase-change recording with a high throughput fiber probe" in Near-Field Optics: Physics, Devices, and Information Processing, S. Jutamulia, M. Ohtsu, and T. Asakura eds., Proc. SPIE 3791, 68–75 (1999).
3. T. Yatsui, M. Kourogi, K. Tsutsui, J. Takahashi, and M. Ohtsu, "High density/speed optical near-field recording/reading with a pyramidal silicon probe on a contact slider," Opt. Lett., 25, 1279–1281 (2000)

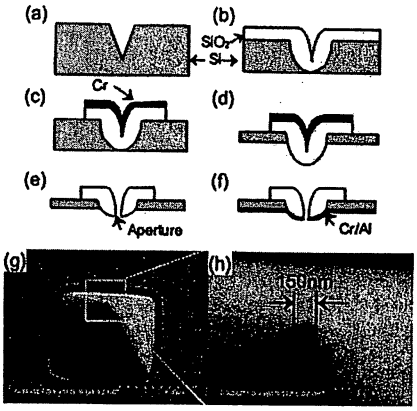

QTuE1 Fig. 1. Schematic of the fabrication process of a hollow probe.

QTuE1

High throughput capability of a microfabricated hollow probe for near field microscopy in ultraviolet region

T. Yatsui*, M. Ueda**, M. Kourogi*,**, and M. Ohtsu*,**, *Ohtsu Project, ERATO, Japan Science and Technology Corporation 687-1 Tsuruma, Machida, Tokyo, Japan 194-0004; Email: yatsui@ohtsu.jst.go.jp; **Interdisciplinary Graduate School of Science and Engineering, Tokyo Institute of Technology, 4259 Nagatsuta, Midori-ku, Yokohama, Japan 226-8502

For realizing high sensitivity in high spatially resolved spectroscopy in ultraviolet (UV) region, we demonstrate here high throughput capability of a hollow probe fabricated by the transfer mold technique in a pyramidal silicon groove. In comparison with the conventional fiber probe, the advantages of such a probe are:

1. Hollow structure leads to no optical absorption in the UV region inside the probe, which results in high throughput.
2. Hollow structure leads to no luminescence in the UV region inside the probe, which results in high signal to noise ratio in the illumination-mode near field spectroscopy.

The hollow probe was fabricated from (100)-oriented silicon wafer:[1]

i. After thermal oxidation and photolithography, the pyramidal tip structure was fabricated by anisotropic etching (34wt % KOH, 80°C). [Fig. 1(a)]
ii. 1-μm thick SiO_2 layer was thermally grown at 950°C. It is known that the thickness of oxide grown at low temperature at convex and concave corner is thinner than that on the plane surface. This effect is very important for making hole on the top of the tip at step (iv) [Fig. 1(b)]
iii. After depositing thin chromium film inside the groove [Fig. 1(c)], the Si wafer was etching until the appearance of the SiO_2 tip (TMAH, 80°C). [Fig. 1(d)]
iv. The wafer was dipped into the buffered-HF to form the aperture at the apex of the SiO_2 tip. [Fig. 1(e)]
v. The probe was coated with 2-nm-thick chromium film and 50-nm-thick aluminum film. [Fig. 1(f)]

Figures 1(g) and (h) show a round shape subwavelength aperture formed at the apex of the tip.

We evaluated the throughput of the hollow probe with aperture diameter (D) of 150 nm at λ = 325 nm by a probe-to-probe method (Fig. 2), using an UV single-tapered fiber probe.[2] We used the UV fiber probe with D and throughput (T_{Fiber}) of 80 nm (see SEM image in the inset of the Fig. 2) and 4.0×10^{-5}, respectively, for this evaluation.

Figure 3(a) shows an observed spatial distri-

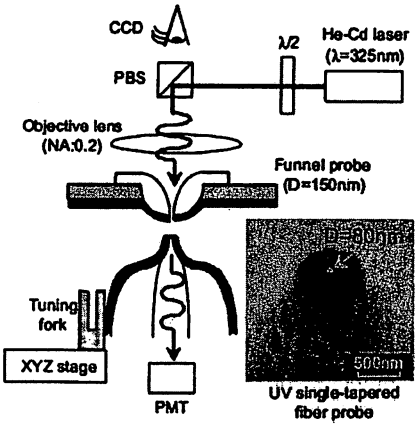

QTuE1 Fig. 2. Probe-to-probe method.[3] The separation between the probes was maintaining within several nanometers with shear-force technique.

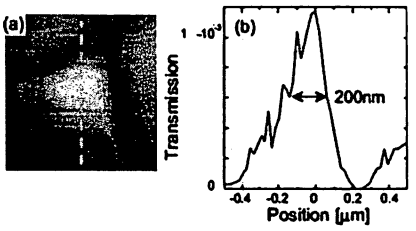

QTuE1 Fig. 3. Spatial distribution of the optical near field intensity. (a) Image size is 1.25 μm × 1.25 μm. (b) Cross sectional profile along the white dashed line in (a).

bution of the optical near field intensity at the aperture. Figure 3(b) shows the cross-sectional profile along the white dashed line in (a), where the transmission (T) is defined by

$$T \equiv \frac{\text{Pick - up intensity through the fiber}}{[\text{Input power}] \times T_{\text{Fiber}}}$$

The full width at half maximum of the curve is 200 nm, to which a part of the leaked light can contribute because of the thin coating. However, one can find that the throughput of the hollow probe is 1.2×10^{-3}. In comparison with that of the conventional UV fiber probe,[4] 10 times increase in the throughput was realized.

From these results, it can be expected that the microfabricated hollow probe is a possible candidate for realizing very high sensitivity in high spatially resolved spectroscopy in UV region.

References

1. P.N. Minh, T. Ono, M. Esashi, "Nonuniform silicon oxidation and application for the fabrication of aperture for near-field scanning optical microscopy," Appl. Phys. Lett., 75, 4076–4078 (1999).
2. *Near-field nano/atom optics and technology,* edited by M. Ohtsu, Chap. 3 (Springer Verlag, Tokyo, 1999).
3. T. Yatsui, M. Kourogi, and M. Ohtsu, "Highly efficient excitation of optical near-field on an apertured fiber probe with an asymmetric structure," Appl. Phys. Lett., 71, 1756–1758 (1997)
4. Y. Yamamoto, G.H. Lee, K. Matsuda, T. Shimizu, M. Kourogi, and M. Ohtsu, "Fabrication of and ultraviolet light-emitting functional probe with sub-micron size by photochemical vapor deposition," Opt. Rev., in press.

QTuE3

Second Harmonic Generation In Aluminum Coated Near-Field Fiber Probe

Tadashi Kawazoe,[1)] Takashi Shimizu,[2)] and Motoichi Ohtsu;[1),2)] [1)]*Exploratory Research for Advanced Technology (ERATO), Japan Science and Technology Corporation (JST), 687-1 Tsuruma, Machida, Tokyo 194-0004, Japan; Email: kawazoe@ohtsu.jst.go.jp;* [2)]*Interdisciplinary Graduate School of Science and Engineering, Tokyo Institute of Technology, 4259 Nagatsuta, Midori-ku, Yokohama 226-8502, Japan*

Second-harmonic generation (SHG) is a useful phenomenon not only for far-field spectroscopy but also near-field (NF) spectroscopy[1] to investigate material properties and to exploit nonlinear optical devices. However, investigation of SHG in the fiber probe has not yet been reported in spite of its potential application to frequency conversion, optical CVD by using UV light[2] and so on.

Figure 1 shows the cross-sectional profile of the employed fiber probe for SHG and schematic explanation of the probe-to-probe experiment for measuring the spatial distribution of the SH intensity by using the probe S. A triple-tapered fiber probe, employed for the ultraviolet region[3]

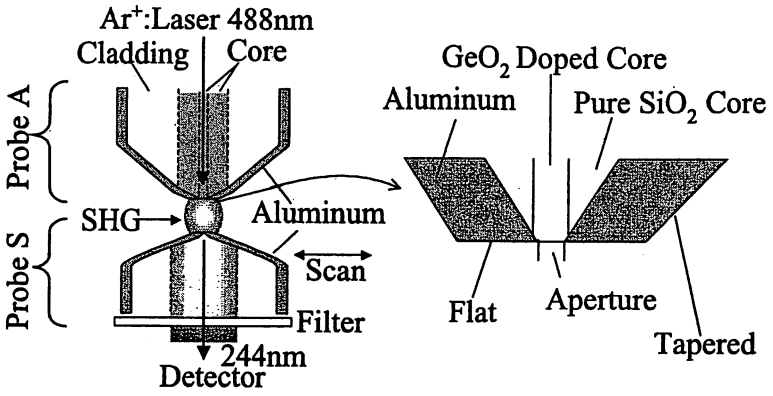

QTuE3 Fig. 1. Cross-sectional profile of the fiber probe for SHG (probe A) and the probe S for the probe-to-probe experiment.

was used as the probe A. The triple-tapered end was coated with 500 nm thick aluminum by vacuum evaporation. The probe S used for scanning was a single tapered fiber probe which was fabricated by pulling and etching of a fiber with the pure silica core and was coated with 500 nm thick aluminum. The apertures of the probes were created by using the focused ion beam technique. In the experiment, the Ar^+laser of 488 nm wavelength was used as the light source. The bandpass filter with the bandwidth of 10 nm was used to reject the fundamental signal.

We measured the SH intensity by using the cleaved fiber instead of the probe S in Fig. 1. Figure 2 shows the relation between the fundamental and the SH intensity where we used the fundamental signal from the probe as the reference for this measurement. The SHG intensity is proportional to the square of the fundamental intensity in the low intensity region. The solid line is a fit to the measured values in the unsaturated region. The SHG conversion factor R was obtained from the slope of the solid line for the aperture diameter of 100 nm, which was 2.0×10^{-11} cm^2/W. Such a surprisingly large value corresponds to that of a 5 mm thick KDP crystal in the far-field configuration.[4]

Figure 3 shows the top view of the SEM image (a) of the probe and the spatial distribution (b) of the SH intensity on the probe, respectively. In area A, a SH signal observed in the aperture was weaker than that recorded from both sides of the aperture coated with aluminum due to the large absorption of GeO_2 doped core for the SH light. In area B, the strong SH signal is emitted at the boundary between the flat and the tapered areas of the aluminum-coated probe. In a subwavelength-size fiber probe, the optical near field becomes dominant and it can excite the surface-plasmon polariton on the coated metal which is well known in the case of a flat metal surface.[5] We believe that the SHG enhancement at the fiber probe occurs due to the surface-plasmon effect on the coated metal.

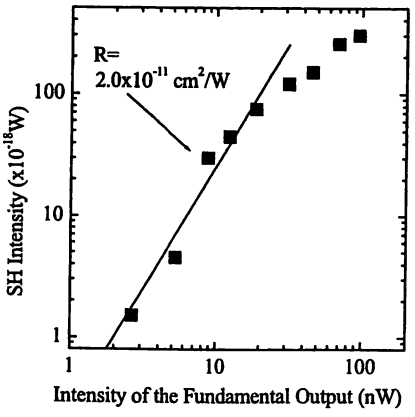

QTuE3 Fig. 2. Relation between the fundamental and SH intensities. Squares represent the experimental results. The solid line is fitted to them in the unsaturated region.

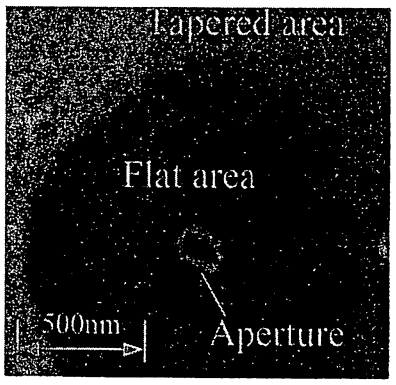

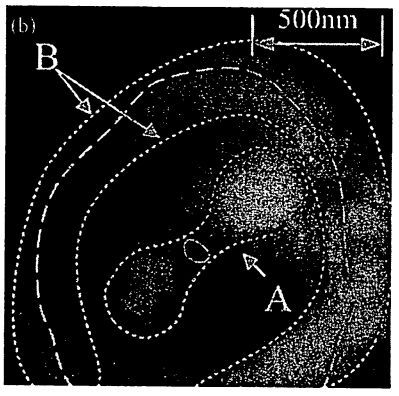

QTuE3 Fig. 3. (a) Top view of the SEM image of the aluminum coated probe. (b) Spatial distribution of the SH intensity on the probe A measured by the probe-to-probe experiment. Open and broken ellipses show the position of the aperture and the boundary between the flat and the tapered areas, respectively. Areas enclosed by a dotted dumbbell curve (area A) and a doted ellipses (area B) show the strong SH-emitting areas.

References

1. M. Ohtsu, *Near-Field Nano/Atom Optics and Technology* (Springer, Tokyo, Berlin, Heidelberg, New York, 1998).
2. Y. Yamamoto, M. Kourogi, M. Ohtsu, V. Polonski, G. H. Lee, "Fabrication of nanometric zinc pattern with photodissociated gas-phase diethylzinc by optical near field" Appl. Phys. Lett. 76, 2173–2175 (2000).
3. S. Mononobe, T. Saiki, T. Suzuki, S. Koshihara, M. Ohtsu, "Fabrication of a triple tapered probe for near-field optical spectroscopy in UV region based on selective etching of a multistep index fiber" Opt. Commun. 146, 45–48 (1998).
4. A. Yariv, *Introduction to Optical Electronics 3rd edition* (Holt, Rinehert and Winston, New York 1985), Chap. 8.
5. V. M. Agranovich and D. L. Mills, *Surface Polaritons, Electromagnetic Wave at Surface and Interface* (North-Holland, Amsterdam, New York, Oxford, 1982), Chap. 15.

OVERVIEW

M. OHTSU

Interdisciplinary Graduate School of Science and Engineering, Tokyo Institute of Technology, 4259 Nagatsuta-cho, Midori-ku, Yokohama 226-8502, Japan
E-mail: ohtsu@ae.titech.ac.jp

Three examples of technical problems for future optical industry are presented. It is pointed out that the near field optics is the most promising candidate to solve these problems. After briefly reviewing the history of near field optics, extended fields of research and development are described. As a concluding remark, future overlook is given.

1 Introduction

As an introduction of this article, three examples of technical problems for future optical industry are presented here. Firstly, it has been estimated that the society of the year of 2010 requires the high-density optical storage and readout technology, with the storage density of 1 Tb/in^2 and data transmission rate of 1 Gbps. Though the DVD technology has realized a high storage density, it is still 100 times lower than 1 Tb/in^2. Since the mark-length for 1 Tb/in^2 is as short as 25 nm, writing such a small pit is far beyond the diffraction limit of light(see Fig.1).

Secondly, the progress of DRAM technology requires the drastic improvement of photo-lithography by the year of 2010. It has been estimated that the linewidth of the fabricated pattern should be as narrow as 50 nm or even narrower(see Fig.2). Though novel methods using excimer lasers, EUV, and SR light sources have been developed, the required linewidth is far beyond the diffraction limit of these methods.

Thirdly, the progress of optical fiber transmission systems requires the improvement of the photonic integration technology. It has been estimated that the size of the photonic matrix switching device should be as small as 30 nm to realize the integration of 100 x 100 switching devices for the 5 Tbps switching capability in the year of 2010. Since the conventional photonic devices, e.g., diode lasers and optical waveguides have to confine the light in them, their minimum sizes are limited by the diffraction of light. Thus, the size required above is also far beyond the diffraction limit.

By the three examples demonstrated above, it can be easily understood that a novel optical technology is required to go beyond the diffraction limit to support the technology of the 21st century. Near field optics can develop such a technology to meet this requirement. It can also contribute to open new fields of optical science, physics, chemistry, biology, and so on.

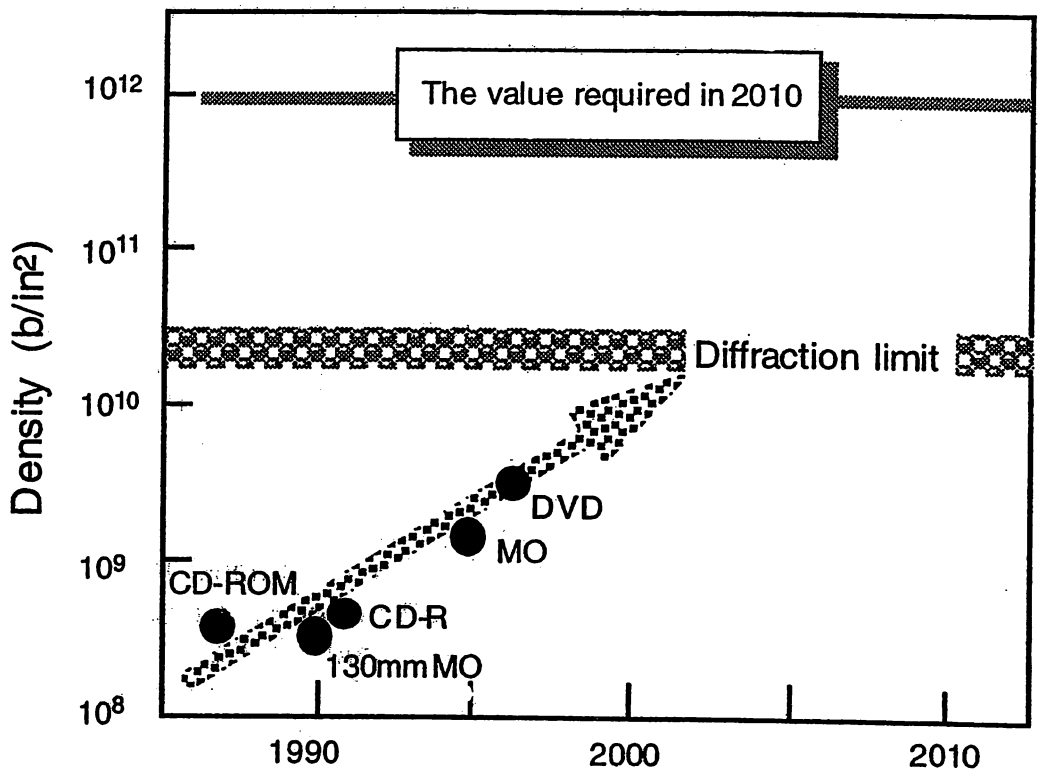

Figure 1. Increase in the optical storage density and diffraction limit of light.

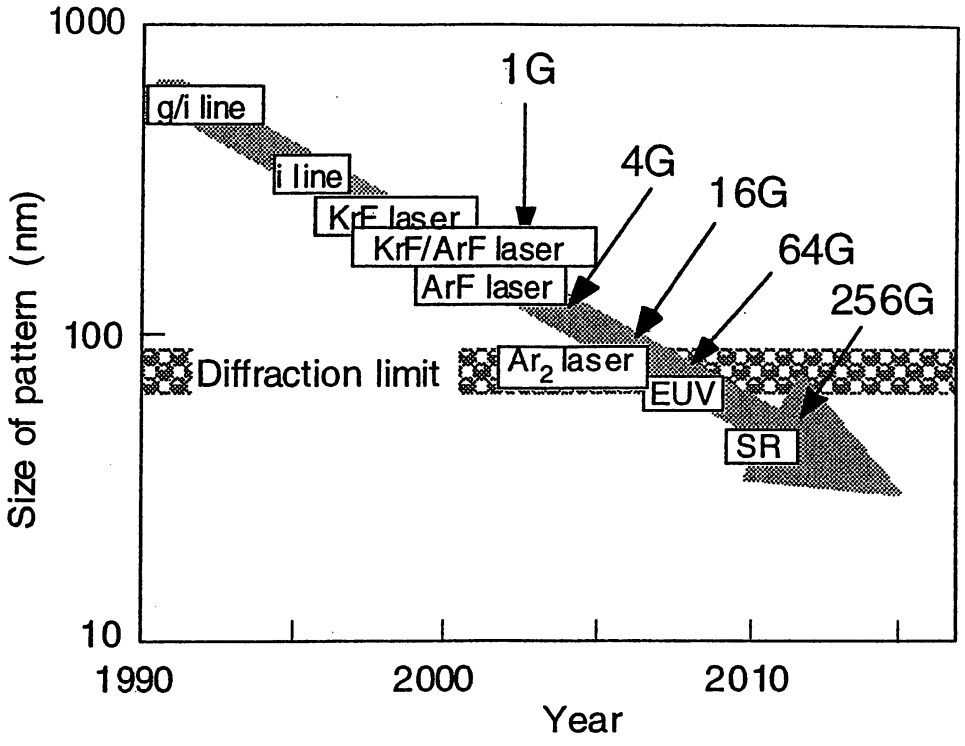

Figure 2. Decrease in the size of the pattern fabricated by phto-lithography and diffraction limit of visible light

2 Near field optics and technology

Near field optics deal with the local electromagnetic interaction between optical field and matters in a nanometric region. Optical near field generated on a nano-sized three-dimensional matter can be considered as the elementary excitation such as surface polariton and surface plasmon. Due to its size-dependent localization and size-dependent resonance, near field optics can open new fields of optical science and technology, which are free from the diffraction of light(see Fig.3).

A very primitive idea of near field optics has been proposed in 1928 in order to realize a super-resolution imaging[1]. After about half a century of silence, basic research has been started in early 1980 s by several groups in Europe, US, and Japan almost independently. Figure 4 shows a short comment written on my

laboratory notebook dated February 26, 1982, pointing out in Japanese that *the chemical etching of fiber for fabricating a probe is not straightforward, and thus, requires a continuous effort to establish a nano-fabrication technology.* However, after such a continuous effort, study of near field optics showed a lot of progress, and the number of research groups has been rapidly increased in the 1990 s. Though the Asian contribution to near field optics was not described, a brief history was reviewed in the proceedings of a small workshop on near field optics, being held in 1992, to which all the attendees were invited by the organizer[2].

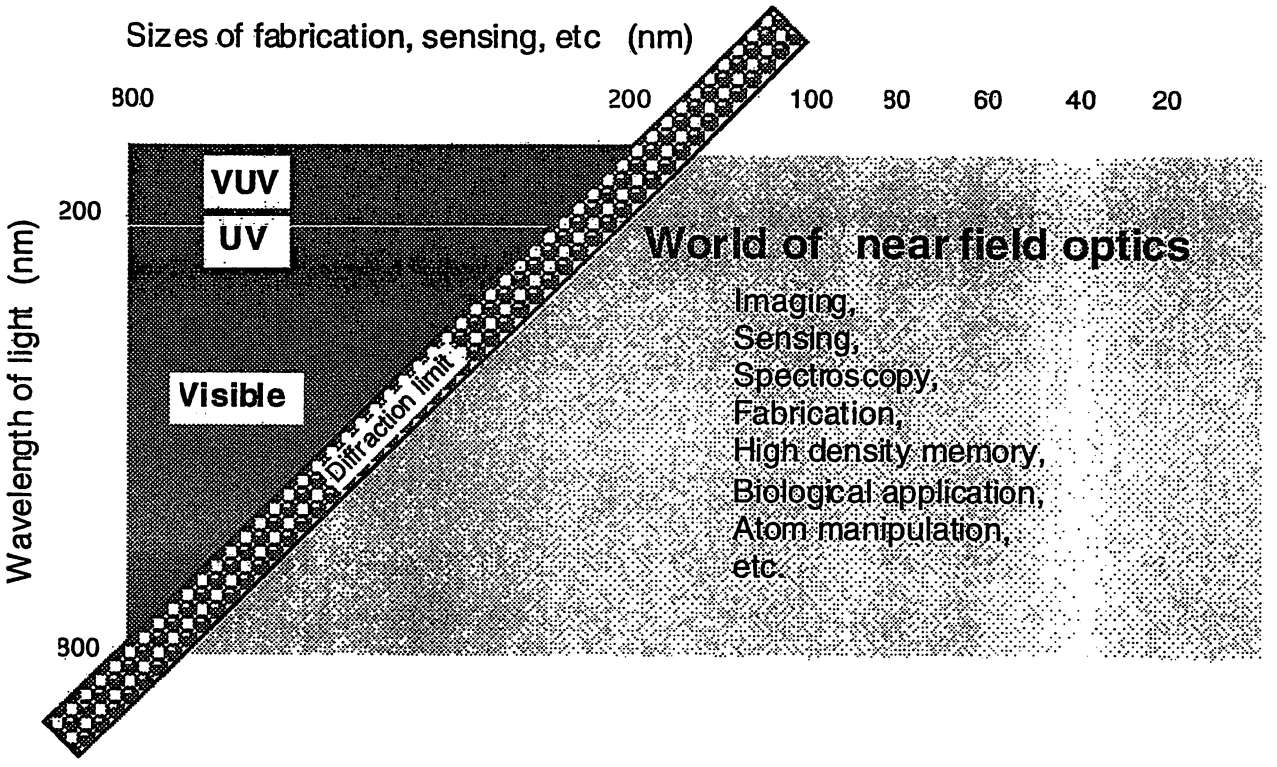

Figure 3. Conventional optics vs. near field optics

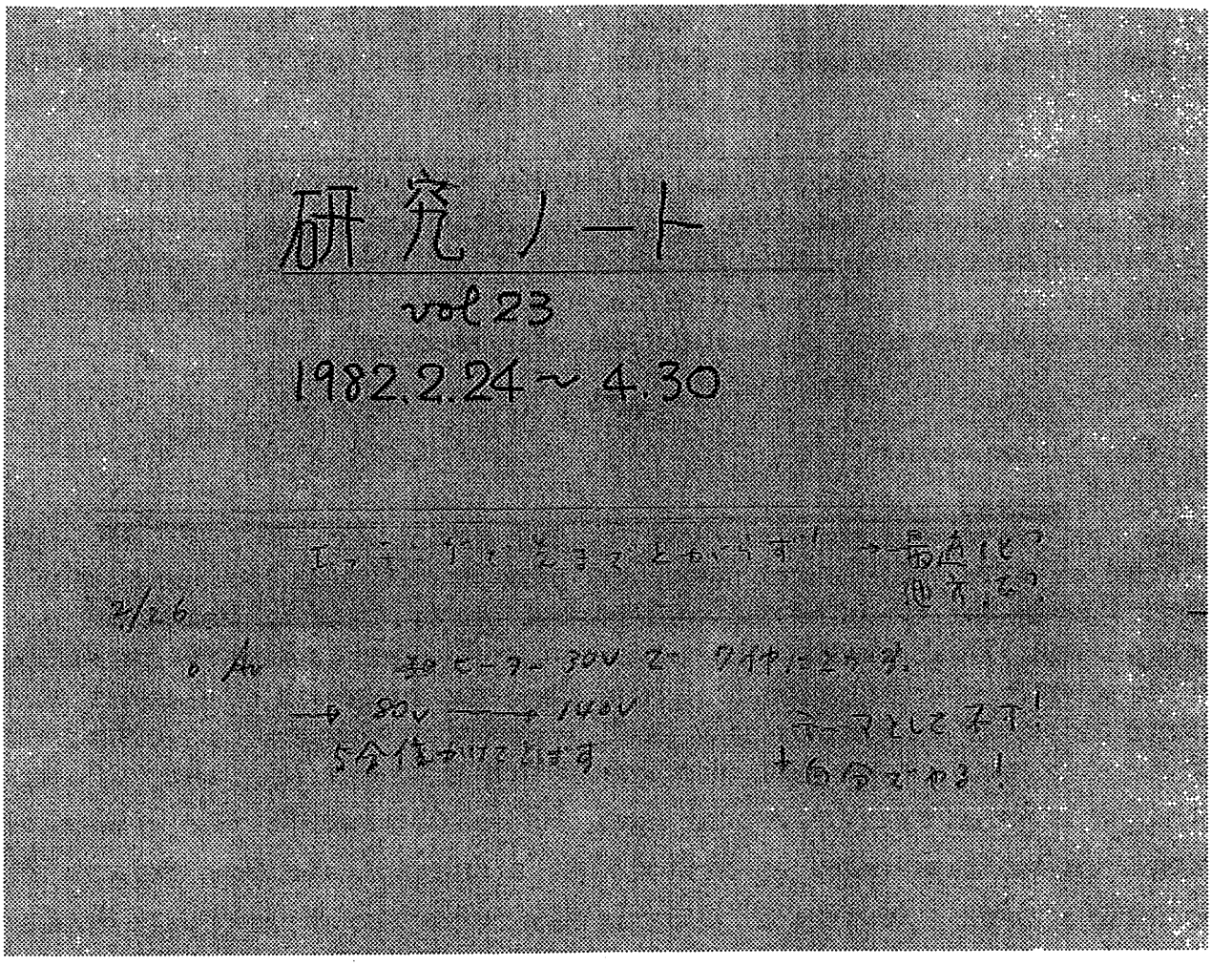

Figure 4. Author s laboratory notebook dated at February 26, 1982, which is written in Japanese.

It should be noted that essential application of near field optics is by no means the sensing and imaging because detecting the optical near field is a destructive process of the local electromagnetic field. Thus, it should be applied to fabrication and manipulation in a nanometric region. Based on this notice, study of near field optics has extended to probe fabrication, instrumentation, diagnostics of condensed matter, fluorescence imaging, single molecule detection, spectroscopy, industrial application(including optical storage, deposition, and lithography), surface plasmons, atom manipulation, and so on[3-6].

Recent progresses of optical near field imaging are remarkable, e.g., a single string of DNA molecule has been successfully imaged by an optically feedbacked collection-mode near field optical microscope even though fluorescence emission technique was not used. The linewidth of its image has been as narrow as 4 nm or even narrower[7]. Furthermore, photochemical vapor deposition using an UV optical near field has fabricated a pattern of Zn with the linewidth as narrow as 20 nm[8]. By these progresses, it can be claimed that a new field, i.e., so called nano-photonics has been started as a basic technology to support the society of the 21st

century. Further, a novel field of atom-photonics has also been started, which controls the thermal and quantum motions of atoms precisely by the optical near field[9]. It can open a new field of a basic science such as quantum electrodynamics, atom deposition, and so on.

For further developments of near field optics and technology, however, more efforts should be made to develop an intuitive theoretical model, advanced probe tips with higher resolution and higher throughput, fast mechanical components for driving the probe, sensitive photo-detection scheme, nano-sized material fabrication method, and relevant novel physical and chemical processes.

3 Concluding remark

It has been known that exponents have English names, e.g., 10^{-3}, 10^{-6}, 10^{-9}, and 10^{-12} are called as milli, micro, nano, and pico, respectively. The name micro-meter can be the origin of the conventional optical imaging instrument, i.e, micro-scope . This is because the conventional optics has attained the resolution of imaging to the diffraction limit, and thus, the image can be obtained even though the size of the specimen is as small as optical wavelength, i.e., in the order of one micrometer. It has been also known that exponents have also Chinese names, as is shown by Fig.5. Among them, 10^{-6} is called as 微. This is why the microscope has been called as 顯微鏡. As a reference, the first character 顯 represents a scope . and the last character 鏡 means a lens or mirror to be used to obtain the diffraction-limited image. Therefore, the English name micro-scope corresponds to 顯微鏡 perfectly.

However, near field optics has realized a diffraction-free imaging of a nanometer-sized specimen. Therefore, a near field optical microscope should be called as nano-scope . Since the Chinese name of nano (, i.e., 10^{-9}) is 塵 as is shown by Fig.5, the near field optical microscope should be called as 顯塵針 , where the last character 針 represents a needle, i.e., a probe tip generating or detecting the optical near field.

If further efforts can realize a pico-meter resolution in the future, such a ultrahigh resolution microscope will be called as a pico-scope . In this case, its Chinese name should be 顯漠？ because the Chinese name of pico (, i.e., 10^{-12}) is 漠 as is shown by Fig.5. I have used ？ as the last character because no one knows what kind of sensing head should be used to realize the picometer-resolution. It is neither a sharpened probe tip nor a lens. Instead of them, a completely novel tunneling head should be devised and used. It may be an atom, however, no one knows. It should be a remained question to be answered. Continuous efforts for further developments of near field optics and technology may find an answer.

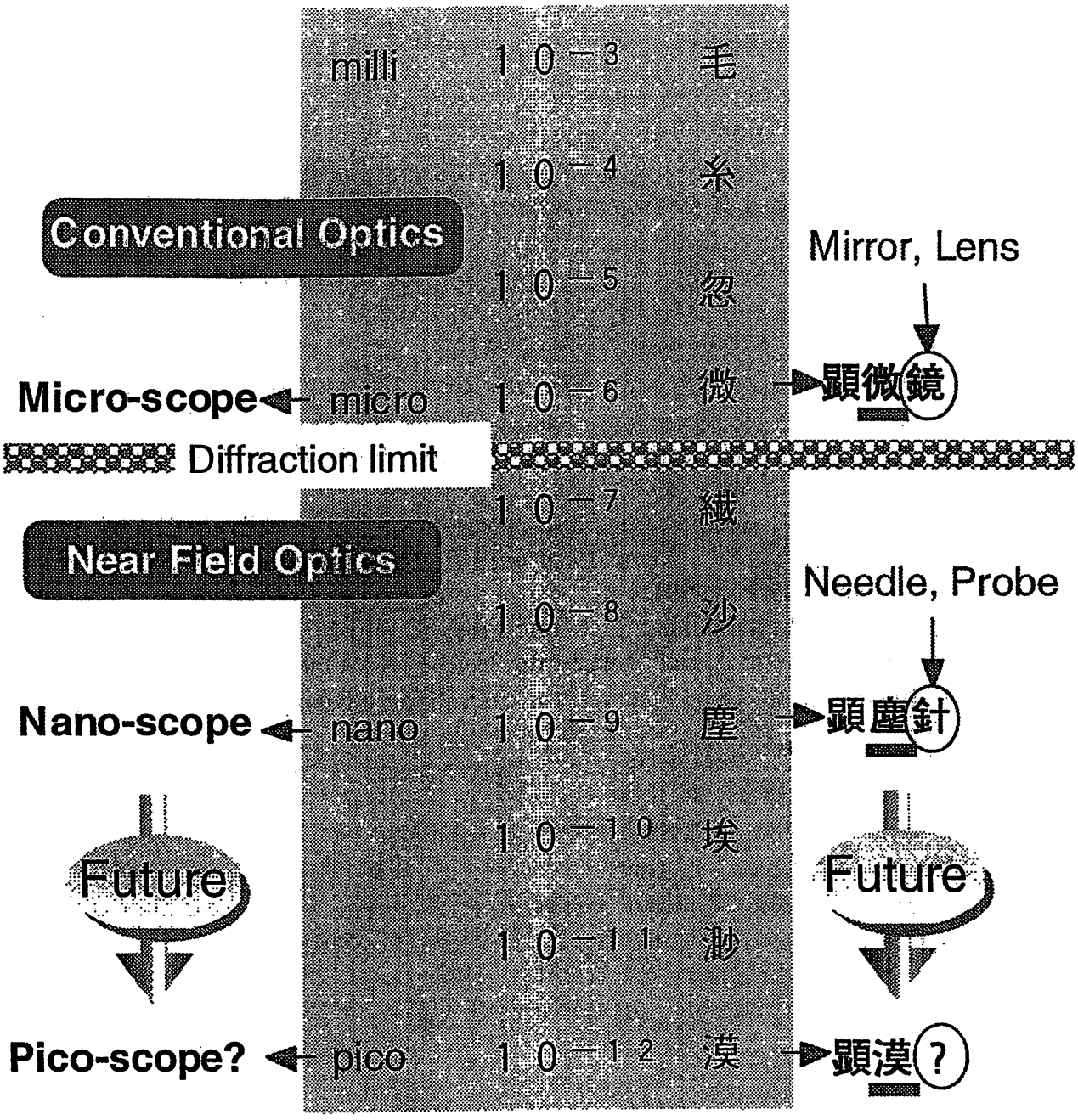

Figure 5. Correspondence between the English and Chinese name of several exponents.

4 Acknowledgements

The author thanks Prof. X. Zhu of Peking University, the editor of this book, to provide me with an opportunity to publish this short article.

References

1. E.A. Synge, A suggested method for extending microscopic resolution into the ultra-microscopic region, *Phil. Mag.*, **6** (1928) pp.356-362
2. D. W. Pohl, Some remark on the History of Near-Field Optics, in D.W. Pohl and D. Courjon(ed.) *Near Field Optics. Proceedings of the NATO Advanced Research Workshop on Near Field Optics, Arc-et-Senans, France, October 26-28, 1992* (Kluwer Academic Publishers, Dordrecht, 1993) pp.1-5
3. M.A. Paesler and P.J. Moyer, *Near-Field Optics: Theory, Instrumentation, and Applications* (Wiley, New York, 1996)
4. J.P. Fillard, *Near Field Optics and Nanoscopy* (World Scientific Publishing, Singapole, 1996)
5. M. Ohtsu, *Near-Field Nano/Atom Optics and Technology* (Springer-Verlag, Tokyo/Berlin/New York, 1998)
6. M. Ohtsu and H. Hori, *Near-Field Nano-Optics: From Basic Principles to Nano-Fabrication and Nano-Photonics* (Kluwer Academic/Plenum Publishers, New York, 1999)
7. Uma Maheswari Rajagopalan, S. Mononobe, K. Yoshida, M. Yoshimoto and M. Ohtsu, Nanometer Level Resolving Near Field Optical Microscope under Optical Feedback in the Observation of a Single-String Deoxyribo Nucleic Acid, *Jpn. J. Appl. Phys.*, **38** (1999) pp.6713-6720
8. V.V. Polonski, Y. Yamamoto, M. Kourogi, H. Fukuda and M. Ohtsu, Nanometric patterning of zinc by optical near-field photochemical vapour deposition, *J. Microscopy*, **194** (1999) pp.545-551
9. H. Ito, T. Nakata, K. Sakaki, M. Ohtsu, K.I. Lee and W. Jhe, Laser Spectroscopy of Atoms Guided by Evanescent Waves in Micron-Sized Hollow Optical Fibers, *Phys. Rev. Lett.*, **76** (1996) pp.4500-4503

FABRICATION OF A NEAR-FIELD OPTICAL PROBE BASED ON ELECTROLESS PLATING

Shuji Mononobe * and Motoichi Ohtsu †
Special Research Laboratory for Optical Science
Kanagawa Academy of Science and Technology (KAST)
KSP East 408-B, 3-2-1 Sakado, Takatsu, Kawasaki 213-0012, Japan
phone : +81-44-819-2075 fax : +81-44-819-2072
** e-mail : mononobe@net.ksp.or.jp http://home.ksp.or.jp/kast/en00.htm*
Kaoru Ishikawa , Hiroyuki Inaba, Hideo Honma
Graduate School of Engineering, Kanto Gakuin University, Yokohama 236-8501, Japan
http://member.nifty.ne.jp/honma-lab/ENGLISH.html

† M. Ohtsu is also with the *Interdisciplinary Graduate School of Science and Engineering, Tokyo Institute of Technology, Yokohama 226-8502, Japan.*

KEY WORDS : Electroless plating, Nickel, Near-field optics, optical fiber, Etching

Near-field optical microscopy employing a metallized probe has been widely applied to high resolution imaging of biological samples and spectroscopic study of optical and electronic devices. We have reported fabrication of several types of probe based on selective etching of a fiber and metal coating such as vacuum evaporation and sputtering. However, to use the probe for high resolution imaging, one has to remove metal covering an apex region of the probe mechanically or chemically [1, 2]. In this paper, we propose a new method based on selective metal coating of electroless plating to fabricate a near-field optical probe.

Figures 1 shows schematic diagram of the method. Here firstly, the fiber is tapered by dipping in a hydrogen fluoride solution mixed with a volume ratio of NH_4F: HF: H_2O = 10:1:1 for 90min. Secondly, the fiber is consecutively dipped in the 0.1g/ℓ-$SnCl_2$ aqueous solution and 0.05g/ℓ-$PdCl_2$ sol. and then, is activated due to the generated Pd-nuclei. Thirdly, electroless plating is performed in $NiSO_4$ based solution. Details of this method will be presented in the session. Figure 2 shows a scanning electron micrograph of the fabricated probe. The aperture diameter is <30nm.

In summary, we proposed a method based on electroless plating to fabricate a near-field optical probe and fabricated a with an aperture diamter less than 30nm.

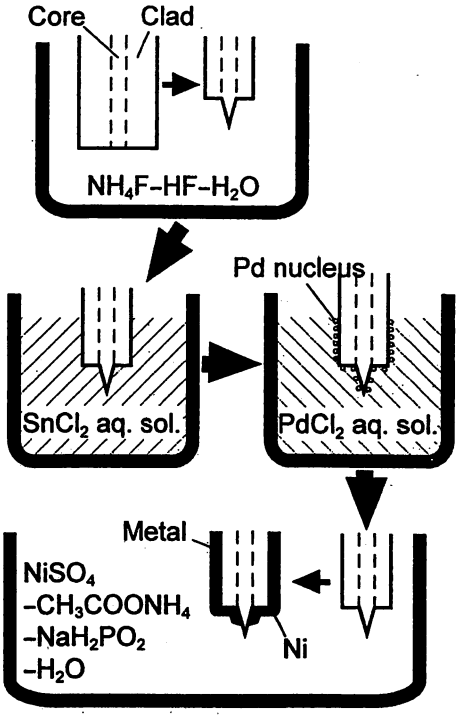

Fig. 1 Schematic diagram of an electroless plating method for fabricating a fiber probe.

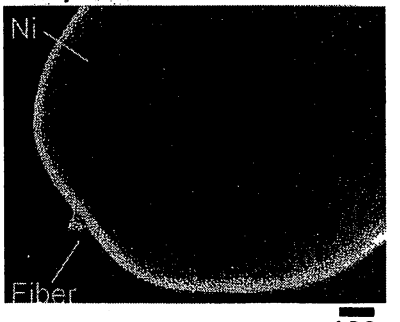

Fig. 2 Scanning electron micrograph of a nickel-coated probe.

REFERENCES

[1] S. Mononobe and M. Ohtsu, "Probe fabrication," in Near-field nano/atom optics and technology, M. Ohtsu ed., Springer-Verlag, Tokyo, (1998).
[2] S. Mononobe, Dr. Thesis, Tokyo Institute of Technology, Yokohama, 1999 (in Japanease), http://www.kast.or.jp/Mononobe.pdf.

CHEMICAL VAPOR DEPOSITION OF Zn AND ZnO DOTS WITH OPTICAL NEAR FIELD

Y. Yamamoto [a], G. H. Lee [b], V. V. Polonski [b], T. Shimizu [a], M. Kourogi [a,b], M. Ohtsu [a,b]

a. Interdiscriplinary Graduate School of Science and Engineering, Tokyo Institute of Technology, 4259 Nagatsuta, Midori-ku, Yokohama, 226-8502, Japan
Phone: +81-45-924-5476, Fax: +81-45-924-5599, E-mail: yoh@ae.titech.ac.jp
b. Japan Science and Technology Corporation, 687-1-17/4F Tsuruma, Machida, Tokyo, 194-0004, Japan

Introduction: Recently suggested technique of enhancing chemical vapor deposition by optical near field has proven to be a viable nano-fabrication tool [1]. This novel method underpins eventual realization of true nano-photonic devices, as it is capable of nano-scale precise positioning and selective thin film growth. Different sequence of layers, materials, size and dopant in a single growth run can be achieved, at the same time avoiding etching caused deterioration, in contrast to conventional nano-fabrication techniques. Due to the absence of conductivity requirements, one of methods most attractive features is a variety of applicable materials. In this work, we demonstrate deposition of nanoscale zinc (Zn) dots as a metal and zinc oxide (ZnO) deposit as a blue light emitting semiconductor.

Experimental: *Deposition* of Zn was performed by using photodissociation reaction of diethylzinc (DEZ) with second harmonic (SH) light (wavelength: 244nm) of argon ion laser. SH light was coupled with UV fiber probe [2], [3]. During deposition, separation between the substrate and the probe was maintained within several nanometers. Figure 1 shows the shear-force image of closely spaced two Zn dots deposited on a glass. We fabricated two dots with a full width at half maximum (FWHM) of 60nm and 70nm. The FWHM of the dots were comparable with aperture diameter of the used probe. The distance between the two dots was 100nm, close to the FWHM of the dots. Such a contiguous deposition capability is essential to use this technique for realizing a nano-photonic integrated circuit in which a size-dependent optical near field is transmitted from one dot to another. Figure 2 shows shear-force image of ZnO dot on a sapphire. Deposition of ZnO was performed by using the reaction between DEZ and oxygen during the irradiation by SH light. The FWHM of the dot is 200nm. However, because this includes the resolution of shear-force microscopy, real size should be significantly smaller than that observed. Blue and ultraviolet light, emitted even at room temperature, actualized ZnO nano-structure, fabricated under properly chosen growth conditions [4].

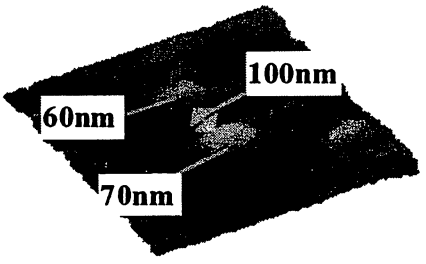

Fig. 1 Deposited Zn dots

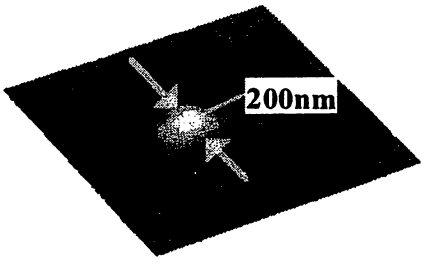

Fig. 2 Deposited ZnO dot

References

[1] V. V. Polonski, Y. Yamamoto, M. Kourogi, H. Fukuda, M. Ohtsu, "Nanometric patterning of Zn by optical near-field photochemical vapor deposition" J. Microscopy, **194**, 545-551(1999)
[2] M. Ohtsu (Ed.) Near-Field Nano/Atom Optics and Technology, Chapter 3, Springer-Verlag, Berlin (1998)
[3] Y.Yamamoto, V. Polonski, G. H. Lee, M. Kourogi, M.Ohtsu, "Fabrication of nanometric Zinc pattern with photodissociated gas-phase diethylzinc by optical near field", *Appl. Phys. Lett.*(To be published)
[4] G. H. Lee, Y. Yamamoto, M. Kourogi, M. Ohtsu, "Fabrication of ZnO nanostructure using near-field optical technology", *Proceedings of SPIE*, **3791**, 132-139 (1999)

Near-field photocurrent measurements of reverse-biased Si p-n junction

Hiroaki FUKUDA[1,2], and Motoichi OHTSU[1]

Tokyo Institute of Technology[1], RICOH Co.LTD.,[2]
4259, Nagatsuda, Midoriku-ku, Yokohama, Kanagawa 213-0002,Japan
phone : +(81)-45-590-1771 fax : +(81)-45-590-1904
e-mail : fukuda@rdc.ricoh.co.jp

Introduction

In recent years, near-field photocurrent measurement by using a near-field optical microscope has shown to be especially useful tool for the investigation of a p-n junction on a semiconductor devices [1,2]. In this paper, we reported the results of near-field photocurrent measurements of reverse-biased p-n junction on Si substrate. Furthermore, we estimate the dopant concentration of the p-n junction for the first time.

Experimental and results

The experimental configuration is shown in Fig. 1. The near-field probe with 300nm aperture diameter is fabricated by chemical etching technique. As excitation light source , Ar+ laser (λ =458nm) was coupled into the fiber probe. The photocurrent induced by the excitation light through the aperture is collected at electrodes. The surface of p-n junction is exposed by the etching of a passivation layer and a field oxide with reactive ion etching. Figure 2 shows the dependence of the FWHM of cross-sectional profile of the near-field photocurrent signals on the reverse-biased voltage. On increasing the reverse-biased voltage, the FWHM of Cross-sectional profiles of the near-field photocurrent signal becomes longer. Moreover, we analyze the FWHM behavior of these signals. As the result, the dopant concentration of the p-n junction is estimated as $5.2\times10^{16}cm^{-3}$.

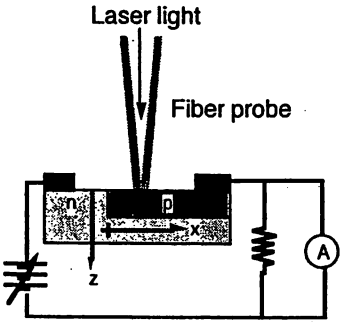

Fig.1 Experimental configuration

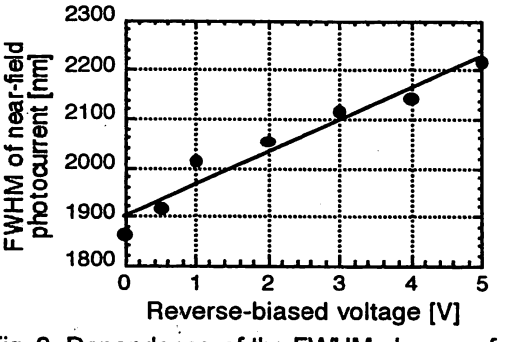

Fig. 2 Dependence of the FWHM change of the near-feild photocurrent signals on reverse-biased voltage

Summary

We demonstrated the near-field photocurrent measurements with reverse-biased p-n junction applied to the estimation of the dopant concentration of the p-n junction on Si substrate. The dopant concentration into Si substrate is estimated as $5.2\times10^{16}cm^{-3}$.

Acknowledgment

We thanks to Mr. Y. Kadota in RICOH Co. LTD., for the sample preparation of Si p-n junction and useful discussion.

References

[1] H.Fukuda; Y.kadota、and M.Ohtsu, "Estimation of the minority carrier diffusion length by near-field photocurrent measurement of p-n junction in Silicon using multiwavelength excitation", *Jpn. J. Appl. Phys.* Vol .38, L571-L573 (1999)
[2] M. Ohtsu, Near-field Nano/Atom Optics and Technology, Springer, Tokyo, (1998)

RECORDING/ READOUT/ ERASING ON PHASE-CHANGE OPTICAL MEDIA WITH APERTURED FIBER-PROBE

Nobuaki Toyoshima[a+], Toshiyuki Kawasaki[+], Masaya Ohtsuka[+], Jun-ichi Takahashi[+], Takashi Yatsui[*], Motonobu Kourogi[*], and Motoichi Ohtsu[*]

[+] R & D Center, RICOH Company, Ltd.,
16-1 Shinei-cho, Tsuzuki-ku, Yokohama, 224-0035 Japan
[*]Interdisciplinary Graduate School of Science and Engineering, Tokyo Institute of Technology,
4259 Nagatsuta, Midori-ku, Yokohama 226-8502 Japan
[a]e-mail: toyoshim@rdc.ricoh.co.jp

Keywords: fiber-probe, optical near-field storage, phase-change recording

Introduction

A near-field optical measurement system with an apertured fiber-probe was used to observe illumination-collection images of phase-change optical media after recording/erasing.

Experiments and Results

A near-field optical system in the illumination-collection mode (i-c mode) was used for recording, reading out and erasing. A fiber probe with an aperture of diameter 720 nm, and a diode-laser with a wave length of 785 nm were used. The system was used to record six spots on the surface of the medium, the six amorphous marks shown in Fig.1 were observed by using the same system. The six bright spots in the figure are the amorphous marks.
Marks recorded by a DVD disk tester were also observed by the system to estimate its optical resolution for readout. As shown in Fig.2, the bright spots that indicate amorphous marks appear periodically. The period of the marks is 400 nm, and the diameter of each is 230 nm. Two of the marks in the Fig.2 were erased by the optical system. As shown in Fig.3, two of the bright spots that indicate the periodic amorphous marks then became dark.

Conclusion,

Recording, readout, and erasing of phase-change optical media by using a near-field optical measurement system with an apertured fiber-probe have been demonstrated.

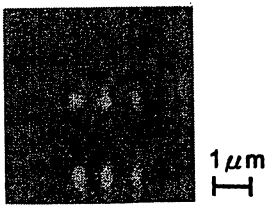

Fig.1 I-c mode image after recording.

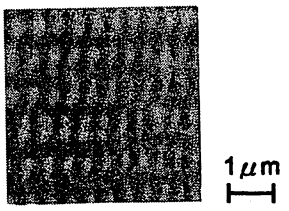

Fig.2 I-c mode image after recording by DVD disk tester.

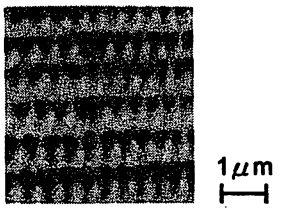

Fig.3 I-c mode image after erasing.

OPTICAL NEAR FIELDS AS PHOTON-MATTER INTERACTING SYSTEMS

Suguru Sangu,[(1)] Kiyoshi Kobayashi,[(1)] and Motoichi Ohtsu[(1),(2)]

(1) *ERATO Localized Photon Project, Japan Science and Technology Corporation, 687-1 Tsuruma, Machida, Tokyo, 194-0004 Japan*
e-mail: sangu@ohtsu.jst.go.jp
(2) *Interdisciplinary Graduate School of Science and Engineering, Tokyo Institute of Technology, 4259 Nagatsuda-cho, Midori-ku, Yokohama, Kanagawa, 226-8502 Japan*

Experimental and theoretical development of near field optics has mainly been devoted to visualizing microscopic objects far beyond the diffraction limit of light. However, it may advance micro- or nano-fabrication techniques because the optical near-field systems strongly depend on the coupling between photons and sample matter. In such systems, we have considered that an elementary excitation mode of exciton-polaritons well describes the optical near-field features. Starting from a quantum mechanical approach shown in Ref. [1], we give more rigorous formulation of effective potentials, where some additional parameters for characterizing the coupling properties are introduced.

The interaction potential consists of three components originated from exciton-polaritons coupled to microscopic (i) probe and (ii) sample, and (iii) macroscopic matter. Each term has characteristic interaction range depending on the excitation energies. Here we concentrate on the former two contributions because the last one can be regarded as a component related to far-field light. Figure 1(a) shows weight coefficient of the potential (i) as a function of the energy detuning, *i.e.*, difference between matter resonance energy and probe excitation energy. The positive and negative signs denote the repulsive and attractive potentials, respectively. The interaction between optical near fields and microscopic systems is strongly affected by their environment, such as probe and sample materials, size and shape, and the amount of the detuning. By controlling these factors, we can make various potentials desired for atom (molecule) trap and manipulation.

A numerical example of the total potentials is shown in Fig. 1(b), where we use a single atom as a sample interacting with the optical near field. Although potentials act attractively in most regime of the detuning, a potential with a negative minimum appears in the case with appropriate balance of the weight coefficients. Such a potential has a depth enough to trap the atom cooled at the kinetic temperature of several micro-Kelvin.

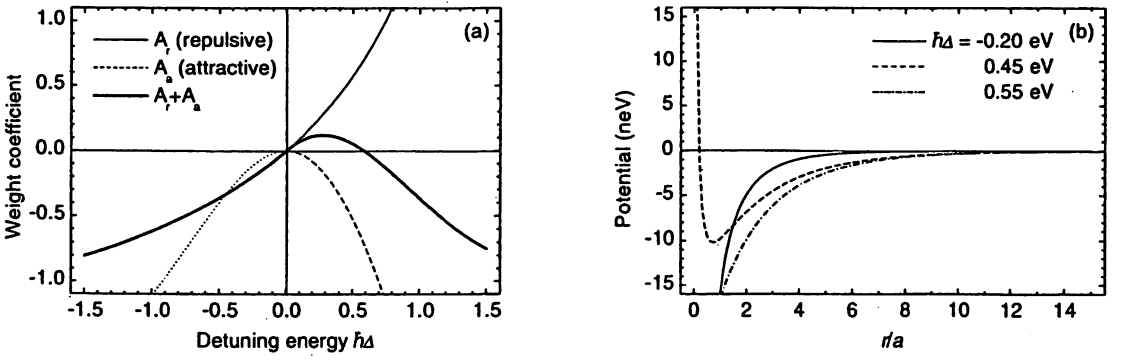

Fig. 1: (a) Weight coefficient of effective potentials. The dotted curve in the negative detuning represents a far-field component ignored in the potential. (b) Total effective potentials in the cases of the detuning, $\hbar\Delta = -0.20$, 0.45, and 0.55 eV.

Reference

[1] K. Kobayashi and M. Ohtsu, "Quantum theoretical approach to a near-field optical system", *J. Microscopy*, **194**, 249-254 (1999).

[I-3] REVIEW PAPERS

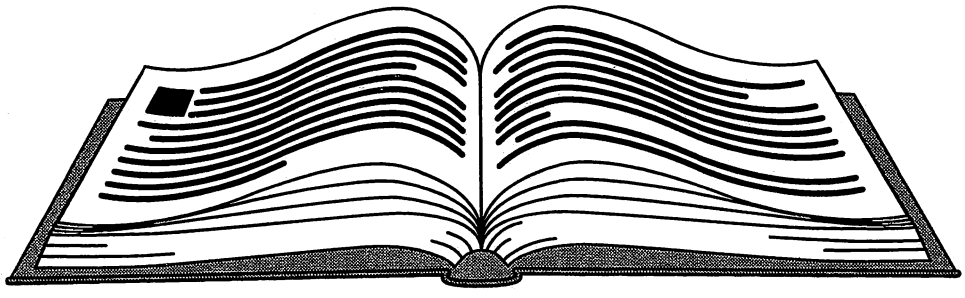

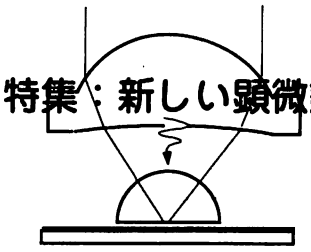

近接場光学顕微鏡の進展

大津元一

1. まえがき

半径aの小さな球(球Sと呼ぶ)を用意し，これに光を入射する。半径aは入射光の波長に比べずっと小さいものとする。入射光は球Sにより散乱するが(これを散乱光1と呼ぶ)，同時に球Sの表面には非伝搬の光(即ち物質表面に局在した光)があたかも球Sにまつわりついた薄い膜のように発生する。この光の膜の厚みは球Sの半径aとほぼ同じである。この光は「近接場光」と呼ばれている。

平板に開けられた小さな穴に発生する近接場光を使って顕微鏡を構成する提案は1928年にさかのぼる[1]。しかしその論理展開は波動光学の枠組みの中に留まっており，顕微鏡としての計測への応用のみを想定していた。従って近接場光の本質的特性について言及するものではなく，さらに分析，加工，操作などへの発展性を示唆するものではなかった。その後の半世紀の空白期の後に1980年代に入って近接場光の研究開発が始まったといってよい。即ち1982年に日本(東京工業大学)においてファイバを用いた先端部の鋭いプローブの開発が始まった[2,3]。その後1984年にはスイス(IBMチューリッヒ研究所)から石英結晶を流用したプローブを用い，近接場光学顕微鏡に応用する実験が発表された[4]。そして1986年には米国(コーネル大学)でも同様の研究発表があった[5]。1980年代の研究開発の方向は顕微鏡技術，走査プローブ顕微鏡技術の枠組みの中に留まっており，現に欧米ではその当時から現在に至るまで有機化学，生物などの試料を計測するための応用としての限定された研究分野に留まっている観がある。

しかし幸いなことに日本ではファイバプローブ開発を開始した1980年代初頭の時点ですでに近接場光の応用としては計測のみでなく，むしろ加工，操作が重要であることに着目されていた。そしてまず日本のファイバ製造技術の質の高さに支えられてファイバプローブ加工技術に著しい成果が得られ，ひきつづき顕微鏡に応用されてファイバプローブの優越性が実証された。この優れたプローブを使って，その後は分光分析，加工，光メモリ，さらには原子操作などへと体系的に発展し，現在に至っている[3,6,7]。

本稿では本特集号の趣旨に合わせるために近接場光の顕微鏡と分光分析への応用に的を絞って述べる。注意すべきはこの顕微鏡は全ての波動が持つ基本的性質である回折とは無縁で，光の回折限界を遙かに越えた高い分解能を有していることである。この点において本特集号の他の記事で扱う一連の顕微鏡とは一線を画している。

東京工業大学大学院 総合理工学研究科 教授(科学技術振興事業団ERATO局在フォトンプロジェクトリーダ，(財)神奈川科学技術アカデミー・光科学重点研究室第2研究グループリーダ) OHTSU, Motoichi
〒226-8502 神奈川県横浜市緑区長津田町4259

2. 近接場光学顕微鏡の原理

近接場光の測定には図1(a)に示すようにガラス製の光ファイバを尖らせたファイバプローブが使われている。すなわち図1(b)に示すように球S表面の近接場光の中にこのファイバプローブを差し込むと，その先端で近接場光を乱し，散乱光2が発生するが，ファイバプローブは透明なので，散乱光2の一部は先端からファイバプローブの中に入り込み，伝搬して出口に達する。そこに光検出器を置けばそのパワーが測定できる。一方，ファイバプローブの中に散乱光1が入り込むのを防ぐために，ファイバプローブの根本や周囲にアルミニウムや金などの不透明な金属膜を塗っておく。ここで不透明膜から突出している円錐状の透明な針の根元の半径a_fを光の波長以下にしておくと，突出している円錐部分は小さすぎ，散乱光1はファイバプローブの中に入り込めず，散乱光2だけを測定することができる。

以上で説明した測定法を応用したものが近接場光学顕微鏡である。すなわち図1(b)に示すようにファイバプローブを近接場光にさし込み，散乱光2のパワーを測定する。次にファイバプローブを近接場光の中で少し走査し，走査後の位置での散乱光2のパワーを再び測定する。これを繰り返し，測定した散乱光2のパワーの値をファイバプローブの位置に対してグラフに描くと，これは散乱光2のパワーの分布を表す地図になる。散乱光2は近接場光がもとになって発生したので，この地図は近接場光エネルギーの空間分布の形を表している。さらに近接場光は球Sがもとになって発生したので，この地図は球Sの形を表している。つまり，この地図は球Sの形の測定結果を表す顕微鏡の像ということができる。

ところでこの顕微鏡の分解能にはファイバプローブの先端の大きさaが影響する。つまり，近接場光のうち，いかに小さな部分からの散乱光2を測定するかによって決まる。従ってファ

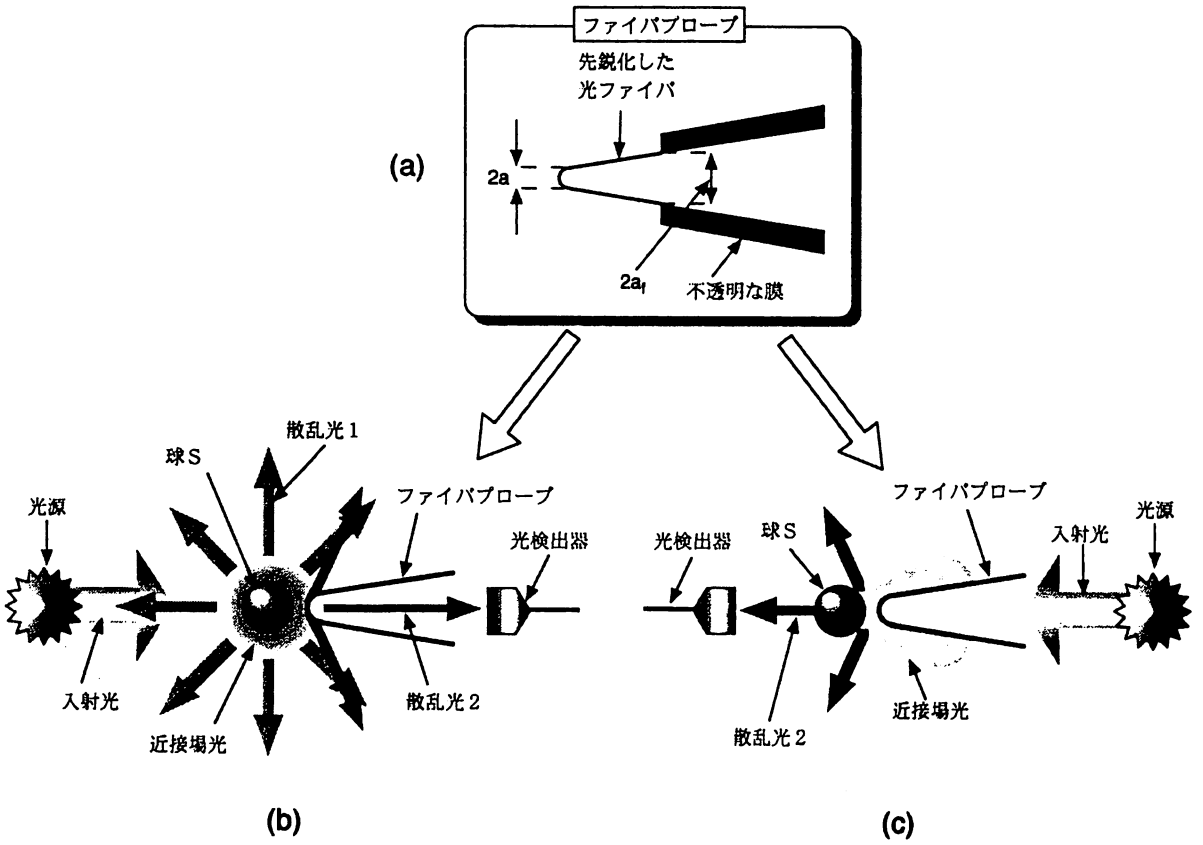

図1　ファイバプローブと測定モード。(a)ファイバプローブの構造。(b)集光モード。(c)照明モード。

イバプローブの先端が小さいほど，顕微鏡としての分解能が高くなるといえる。以上の分解能の議論は光源から出てきて球Sにあたる光の波長とは無関係なので，小さなファイバプローブを作ることができれば光の回折限界よりもずっと高い分解能の顕微鏡ができる。

さて今後の説明の都合上，図1(c)を掲げる。これを図1(b)とくらべると，光源と光検出器の位置が逆転していることが分かる。つまり光源からの光をファイバの後端から入れて，ファイバプローブ先端に近接場光を発生させ，これで球Sを照明する。そしてファイバプローブを少しずつ動かしながら，球Sからの散乱光2のパワーの測定値を先程と同様にグラフに記せば，やはり球Sの形を表す地図が描け，顕微鏡として働く。このようにして，ファイバプローブを小さな光源として使うこともできる。以上のようにファイバプローブを小さな光源のように使って球Sを照明する方法は「照明モード」と呼ばれており，これに対し図1(b)のようにファイバプローブで光を散乱させて集める方法は「集光モード」と呼ばれている。

3. ファイバプローブ技術

近接場光に関わる技術はファイバプローブが基本である。優れた性能のファイバプローブが無ければ優れた結果は決して得られない。ファイバプローブに要求される基本的性能は次の3つである。

Ⅰ．微小な近接場光を扱うのでその先端が小さいこと。

Ⅱ．微小な近接場光と伝搬光との間のインターフェース機能を有すること。

Ⅲ．近接場光に起因する光以外が光検出器に入射することを防ぐ機能を有すること。

現在使われているファイバプローブはこの3つの性能を向上させるように開発されている。まずその先端の曲率半径aを小さくすることで性能Ⅰを実現している。次に先端から根本へ至る円錐部分の形状を調節することで性能Ⅱを実現している。この調節の結果，集光モードと照明モードの場合，各々近接場光の測定効率，発生効率が向上する。

以上の性能Ⅰ，Ⅱを実現するためにガラス製の光ファイバを緩衝フッ酸溶液による化学エッチングにより溶解し，ファイバ中心部のコアを先鋭化している。これにより先端部の曲率半径aは2nm以下まで微小化し，性能Ⅰが実現している。また，エッチング条件を調節することにより各種のファイバプローブが実現している。なお先端の曲率半径aの値の小さなものは高分解能型として分類されている。特に性能Ⅱを向上させた高効率型のファイバプローブでは，たとえば照明モードにおける入射光から近接場光へのエネルギー変換効率は10%を超えるものが得られている[8]。二段テーパ型と呼ばれるものは高効率型のプローブの一種であるが[9]，二段テーパにすることにより先鋭化されたコアの根本から先端までの長さを短くし，高効率を実現している。5節の分光分析に使うためにコア先端はむしろ金属膜の中に埋め込み，プローブ先端を平面にしている。金属膜中心部の穴はしばしば開口と呼ばれ，その半径が図1(a)中のa_fに対応する。なお，このプローブの場合，分解能はa_fで決まるのではない。なぜなら埋め込まれたコア先端の曲率半径aの効果が残るからである。

さらに高分解能型と高効率型の複合型としての三段テーパ型[10]，およびファイバプローブ先端に発光する色素の分子などをつけ，溶液中のアルカリイオン濃度を測定する微小センサに応用するための機能型[11]などがある。また使用するファイバ素材を選ぶことにより，赤外，可視，さらには紫外[10]の領域で効率よく近接場光を発生するファイバプローブが開発されている。さらに最近ではガラスよりも屈折率の高い材料であるシリコン結晶基板を用い，これに半導体の微細加工技術を適用して高効率かつ高速走査可能なプローブの二次元配列[12]，さらには原子間

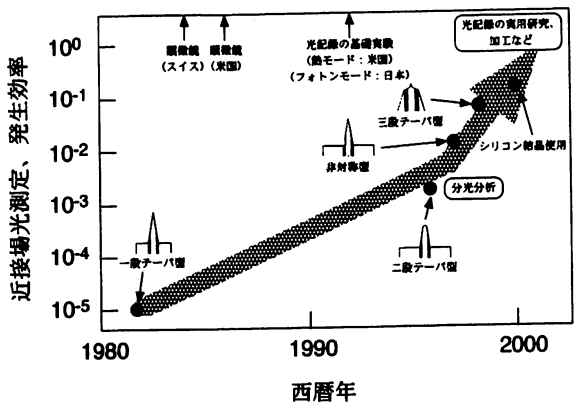

図2　ファイバプローブの近接場光測定、発生効率の増加のようす。

力顕微鏡のプローブ作製技術を流用したもの[13]などが開発されている。

性能Ⅲを実現するためには図1(a)にも示したように先鋭化コアの根本に不透明な金属膜を塗る。このようにすると集光モードの場合には散乱光1がファイバプローブの根本からファイバ本体に入り込むのを防ぐことができる。照明モードでは根本に到達した入射光がそのままファイバプローブから外へ放射されるのを防いでいる。

なお，ファイバプローブの代わりに走査トンネル顕微鏡用のプローブである金属針を用いる場合もある。この場合は上記の性能Ⅰは満たされる。また素材が金属であるので集光モードの場合，近接場光を乱し，散乱光を発生する効率は高い。ただし，上記の性能Ⅱ，Ⅲを満たす構造にはなっていないのが本質的な欠点である。この欠点をなくすために，先鋭化されたコア先端部が金属膜でおおわれているファイバプローブが開発された[14]。その根本は性能Ⅰを実現するために不透明な金属膜が塗られている。

以上のようなファイバプローブ開発により，近接場光測定，発生効率が著しく向上した技術的進歩の様子を図2に示す。

4.　近接場光学顕微鏡

4.1　基本的な測定例

ファイバプローブは先端曲率半径a，根本の断面半径a_f，先鋭の度合いを表す円錐角θの3つの寸法で表される形状を有するので，バンドパスフィルタの特性を有する。つまりファイバプローブにより近接場光学顕微鏡を構成すると，それにより測定できる試料の寸法はこのバンドパスフィルタの通過帯域内(，すなわちa～a_f)である。ここで集光モードの場合を考えてみると，円錐角θが小さい方が半径a_fの根本はファイバプローブ先端から遠くにあるので，この寸法a_fにおける近接場光測定効率はθが大きい場合とくらべ低くなっている。つまり鋭いファイバプローブの方が先端曲率半径aに相当する空間的分布の広がりをもつ近接場光のみをより選択的に測定することができる。このような選択性は明瞭度と呼ばれている。

照明モードの場合，ファイバプローブの先端には空間分布の寸法がa～a_fの近接場光が発生するので，a～a_fの寸法をもつ試料の形状を効率よく測定することができる。上記の明瞭度の他，散乱光1に対する近接場光の強度比(コントラスト)など，ファイバプローブが示す性能がファイバプローブの形状にどのように依存するかという議論は双極子間相互作用のモデルを用いて明らかにされている[15]。

さて，プローブを水平方向に走査する際，試料との鉛直方向間隔を一定に保つ必要がある。そのためにプローブ先端と試料表面との間の剪断応力の大きさを測定し，その測定値が一定となるようにプローブの鉛直方向位置を自動制御する。しかしこの場合，試料表面上空において剪断応力が一定値をとる等ポテンシャル曲面と近接場光のエネルギーが一定値をとる等エネルギー曲面とは互いに異なるので，剪断応力の等ポテンシャル曲面に沿ってプローブを走査するとき虚像が現れる。従ってプローブの鉛直位置制御の際には注意が必要である。

集光モードの近接場光学顕微鏡としての測定例を図3に示す[16]。これは生物試料であるDNAのひも状の一分子の測定結果である。この試料は超平坦サファイア基板の表面に固定されて

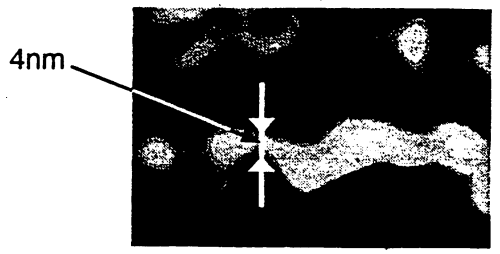

図3　DNAの単一分子を集光モードの近接場光学顕微鏡で観測した結果。

いる。得られた像の幅は4nmである。これは光源の波長の1/100以下の値であり，世界最高の分解能を示す図である。また，ここでは剪断応力などを用いず，その代わりに測定される近接場光のエネルギー値が一定に保たれるようにプローブと試料間の鉛直方向距離を自動制御しているので，この図は虚像ではない。この距離の値は1nm程度に保たれている。近接場光学顕微鏡によるとDNAおよび多種類の生体試料をこの図のように空気中で測定するだけでなく，水中で測定することもできる[17]。このような環境条件下での測定は従来の電子顕微鏡などでは不可能であった。なお，このような測定で得られる画像の特性，すなわち端部強調効果，像反転効果などは双極子間相互作用モデルによって考察されており，入射光の偏光方向，プローブの走査方向などに依存することが明らかになっている[18]。

4.2　分子間のエネルギー移動と近接場光測定への応用

発光する一つの分子を照明光源として使い，それに近接するもう一つの分子の像をどれだけ高い分解能で得るかという実験が古くから分子の分光分析の重要な課題として検討されている。この課題の究極の目標は分子寸法の分解能で分子を識別することである。最近では近接場光の方法を利用してこの課題に取り組む試みが始められている。本節ではこれについて概説する[15]。

二つの色素分子が近接している場合を考える。このとき第一の色素分子(これはドナーと呼ばれる)の発光スペクトルと第二の分子(これはアクセプターと呼ばれる)の吸収スペクトルとは周波数軸上で互いに重なるものとする。ここで入射光をドナーに吸収させると，励起されたドナーから双極子間相互作用によってアクセプターにエネルギーが移動する。この現象はエネルギー移動と呼ばれている[19,20]。この結果アクセプターは励起され発光するので，このエネルギー移動は特に放射エネルギー移動と呼ばれている。このエネルギー移動はドナーとアクセプターとがフェルスターの双極子間共鳴エネルギー移動半径R_0(通常は数nmの値をとる)と呼ばれる距離内に近づいたときのみ生ずるので[20]，アクセプター分子をプローブ先端に付着すればこの現象を近接場光測定に応用することができる。

より容易な方法として無放射エネルギー移動を利用した方法が考えられる。すなわちアクセプターの代わりに金属粒子をプローブ先端につける。たとえば3節末尾に述べたように先端が金属で覆われたプローブ[14]を用いれば良い。金属粒子がドナーに数nmの距離まで近づくと励起されたドナーのエネルギーは金属に移動する。ただし，金属はこのエネルギーを得て発光するのではなく，このエネルギーは熱として散逸する。従ってこの現象は無放射エネルギー移動と呼ばれている。その結果プローブを走査して得られるドナーの形状の画像は中心部が暗くなる。即ちあたかも明暗が反転した画像が得られる。

明暗が反転しない像を得るために，さらに進んだ方法が考案されている。すなわち図4に示したようにコア先端部が金属膜の中に埋め込まれたファイバプローブを使う方法である。ここでファイバプローブが図4(a)のように色素分子の真上にあるときは入射光によって励起された色素分子が発光し，それをファイバのコアを通して効率よく受光できる。しかし図4(b)のようにファイバプローブがわずかに横にずれるとドナーとしての色素分子からアクセプターとしての金属膜への無放射エネルギー移動が起こり，発光しない。以上よりファイバプローブを走査

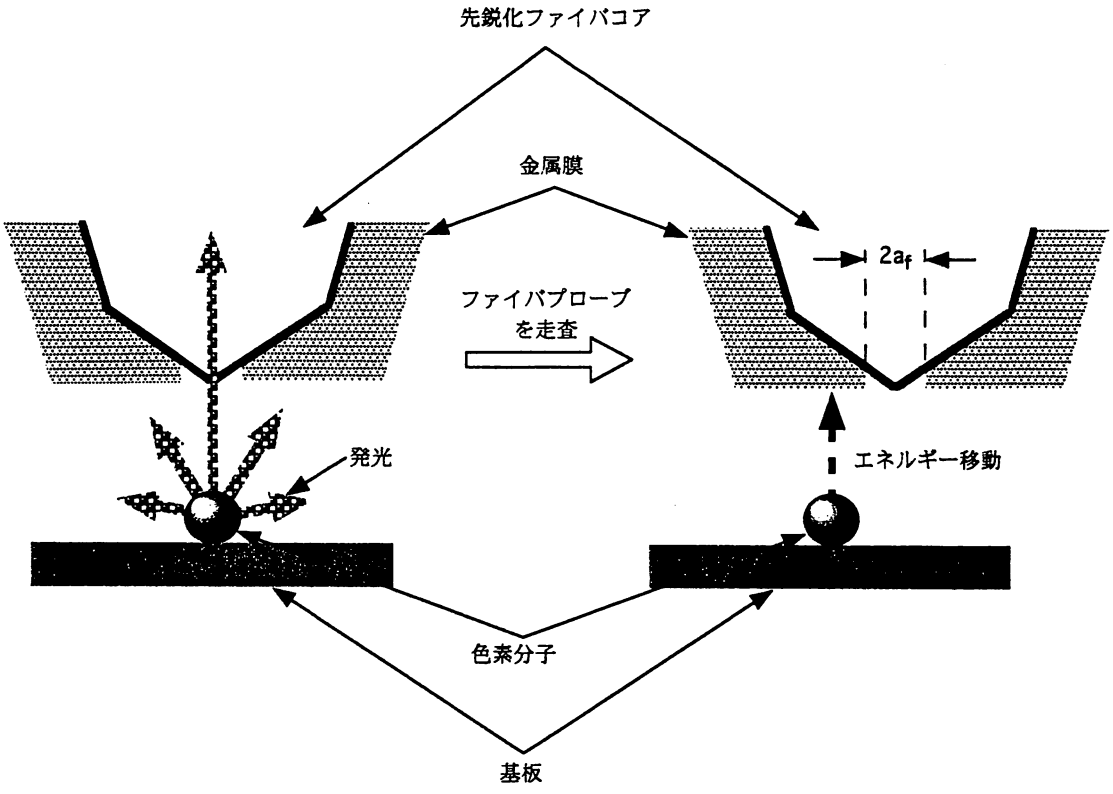

図4　集光モードの近接場光学顕微鏡への無放射エネルギー移動の応用の原理。(a)ファイバプローブが色素分子の真上にあり，色素分子が発光している場合。(b)ファイバプローブに塗布された金属膜が色素分子の真上にあり，無放射エネルギー移動が起こっている場合。

して測定した発光の強度の空間分布は金属膜を塗布している根本の直径$2a_f$程度の大きさを持つと推量できる。従って，効率の高いファイバプローブを作り，半径a_fの値を小さくすると微小な分子像が得られる。

この方法を用い，Cy5.5というシアニン系の色素の一分子からの発光像が測定されている[21]。ファイバプローブは図4に示したものと同等であり，$a_f = 10$ nmである。このとき得られた色素の発光像の直径は約15 nmになっており，これは直径$2a_f$の値とほぼ等しい。ただしこれらの直径の比較には注意が必要である。すなわちここで示したa_fの値はあくまでも電子顕微鏡で観察したときの値である。実際には金属膜の厚みが有限であり，ファイバのコアとの境界付近での金属膜厚は薄く，光を透過してしまう。すなわち光学的な直径$2a_f$の値は電子顕微鏡の像が示す値20 nmよりも大きいはずである。それでも色素の発光像の直径が15 nmとなったのはファイバのコアと金属膜との境界付近での無放射エネルギー移動に起因している。すなわち，ここで得られた画像の直径である15 nmという値は根本直径$2a_f$の光学的な値よりずっと小さい。図4と同様の例として，ファイバプローブを走査するとき，発光の強度や寿命がファイバプローブの位置の関数として変化することも観測されている[22]。

5. 分光分析

4節のような試料の形状測定の他に，試料に近接場光を照射した際に試料から発生する光のエネルギーの空間分布，発光スペクトルなどを測定することもできる。この測定は分光分析と

呼ばれている。その一例としてをInGaAs半導体の量子ドット(直径約30nm，高さ約15nm)の発光スペクトルが測定されている[23]。これは半導体基板の上に高密度で多数作られ，その上を薄い半導体の保護膜が覆っている。つまり保護層表面は平坦なので，それがよほど薄くない限りその上から量子ドットの形状を知ることはできない。

この試料表面に照明モードのファイバプローブを通して近接場光を照射すると保護膜に多数の自由電子が発生する。これらの電子が1μm程度の距離を走りながら，多数の量子ドットに注入される。各々の量子ドットに注入された電子は，量子ドットの寸法が非常に小さいために，離散的なエネルギー値しか取り得ない。注入された電子はその後さらにエネルギーを失うが，その際に発光する。このとき各量子ドットからの発光強度を同一のプローブを通して集光モードにより測定することができる。またその発光のスペクトルも得られる。図5は液体ヘリウム温度まで冷却された量子ドットの発光スペクトルの例であり，図中の破線で結んだ二つのピークは量子ドット内で電子が取り得る離散的な2つのエネルギー値に相当している。図6(a)は各量子ドットからの発光強度分布である。図6(b)には図5の発光スペクトルの測定結果をもとに，各量子ドットの中の電子の持つ離散的なエネルギー値を推定した結果を示している。以上のように高密度で配置された多数の量子ドットの各々に対し個別に発光スペクトルや発光強度分布を測定することは従来の光学的手法では不可能であったものである。なお，発光の測定の際，集光モードを使うことにより空間的分解能を著しく向上させているが，もともと発光強度は弱いのでこれを測定することは容易ではない。しかしこの目的のために3節に示した高効率型のファイバプローブが開発され[9]，測定が可能となった。さらに最近ではこのような量子ドットの発光スペクトル測定は室温でも可能となっている[24]。

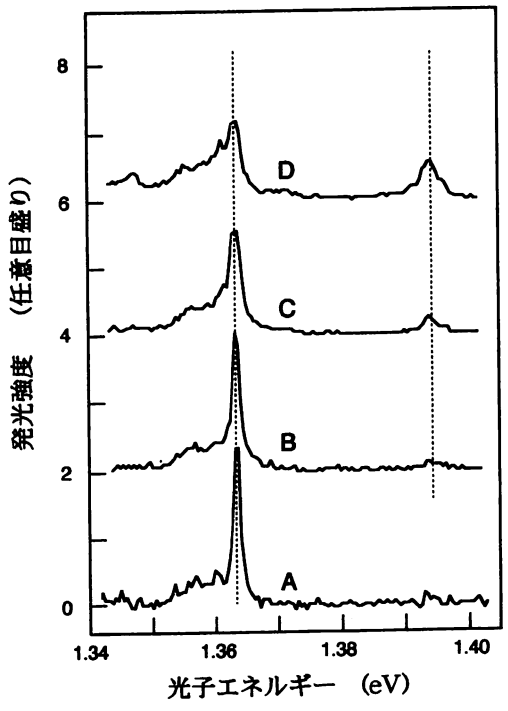

図5 低温での半導体の量子ドットからの発光スペクトル。曲線A，B，C，Dは励起用のレーザー光のパワー密度が各々1.3W/cm^2，5W/cm^2，14W/cm^2，28W/cm^{2}の場合。

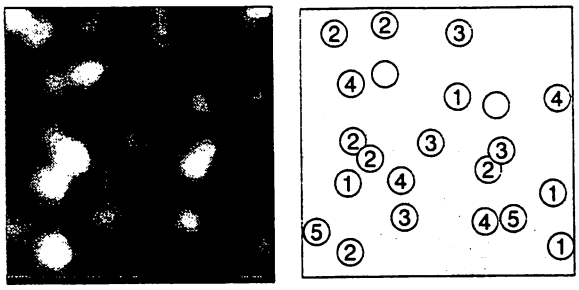

図6 各量子ドットからの発光強度の空間分布。(a)測定結果。画像の一辺は3μm×3μm。(b)各量子ドット中の電子のエネルギー値の推定結果。図中の白丸は(a)の量子ドットに対応し，それにつけられた数字1～5はエネルギー準位の番号を表す。数字1は基底準位を表す。2以上は励起準位を表し，数字が小さい方がエネルギー値が小さい。

この他の分光分析の例として，有機・無機材料のラマン分光測定[25]，半導体デバイスの評価への応用[26]などがある。なおこのような分光分析装置，およびそのためのファイバプローブは我が国の技術により世界で初めて市販されるに至っている[27]。

6. まとめ

本稿では顕微鏡計測と分光分析への近接場光の応用について述べた。顕微鏡は形状測定装置であるが，光子エネルギーを変えると分光分析ができ，構造についての知見を得ることができる。なお，近接場光の測定過程は試料とプローブとの間の近距離電磁相互作用を誘起することなので，この相互作用を強化すれば，以上のような計測，分析のみでなく物質の加工と操作とが可能になる。実はこのような加工，操作こそが近接場光の本質的な応用の方向なのである。すでに近接場光を用いたナノメートル寸法の光化学気相堆積[28,29]が実現しており，これはナノ光集積回路実現の基盤技術として進展している[3]。一方，近接場光を用いた超高密度光メモリも実用化を見据えて開発が進んでいる[30]。さらに基礎科学として原子操作なども試みられており[31]，今後は近接場光は単なる顕微鏡装置のための技術ではなくナノ・フォトニクス[3]と称する広い分野を開発する基盤技術として一層成長すると考えられる。

謝辞

本稿の内容に関して日頃より研究の推進にご協力頂いている科学技術振興事業団ERATO「局在フォトン」プロジェクト，小林潔，三宮俊，戸塚弘毅，川添忠，八井崇，H.アイヤー，S.M.イフティカの各博士，(財)神奈川科学技術アカデミー，物部秀二博士，東工大，伊藤治彦助教授，興梠元伸博士に感謝します。また，ご議論頂いた(財)神奈川科学技術アカデミー，斉木敏治博士に感謝します。

参考文献

1) E. A. Synge, "A suggested method for extending microscopic resolution into the ultra-microscopic region", Phil. Mag., vol.6, (1928) pp. 356-362

2) M. Ohtsu, "Overview", in *Near-Field Optics: Principles and Applications*, ed. by X. Zhu and M. Ohtsu, World Scientific, Singapore, New Jersey, 2000, pp. 1-8

3) 大津元一，「ナノ・フォトニクス」，米田出版，千葉，1999

4) D. Pohl, W. Denk and M. Lanz, "Optical stethoscopy: Image recording with resolution $\lambda/20$", Appl. Phys. Lett., vol. 44, no. 7 (1984) pp. 651-654

5) E. Betzig, A.Lewis, A. Harootunian, M. Isaacson and E. Kratschmer, "NEAR-FIELD SCANNING OPTICAL MICROSCOPY (NSOM) Development and Biophysical Applications", Biophys J., vol. 49, no. 1 (1986) pp. 269-279

6) M. Ohtsu(ed.), *Near-Field Nano/Atom Optics and Technology*, Springer-Verlag, Tokyo/Berlin, 1998

7) M. Ohtsu and H. Hori, *Near-Field Nano-Optics*, Kluwer Acacemic/Plenum Publishers, New York, 1999

8) T. Yatsui, M. Kourogi and M. Ohtsu, "Increasing throughput of a near-field optical fiber probe over 1000 times by the use of a triple-tapered structure", Appl. Phys. Lett., vol. 73, no. 15 (1998) pp. 2090-2092

9) T. Saiki, S. Mononobe, M. Ohtsu, N. Saito and J. Kusano, "Tailoring a high-transmission fiber probe for photon scanning tunneling microscope", Appl. Phys. Lett., vol. 68, no. 19 (1996) pp. 2612-2614

10) S. Mononobe, T. Saiki, T. Suzuki, S. Koshihara and M. Ohtsu, "Fabrication of a triple tapered probe for near-field optical spectroscopy in UV region based on selective etching of a multistep index fiber", Opt. Commun., vol. 146, (1998) pp. 1299-1301

11) K. Kurihara, M. Ohtsu, T. Yoshida, T. Abe, H. Hisamoto and K. Suzuki, "Micrometer-Sized Sodium Ion-Selective Optodes Based on a Tailed

Neutral Ionophore"", Anal. Chem., vol. 71, no. 16 (1999) pp. 3558–3566

12) T. Yatsui, M. Kourogi, K. Tsutsui, J. Takahashi, and M. Ohtsu, "High density/speed optical near field recording/reading with a pyramidal silicon probe on a contact slider," Optics Letters, 25, no. 17 (2000) pp. 1279–1281

13) P. N. Minh, T. Ono, and M. Esashi, "Nonuniform silicon oxidation and application for the fabrication of aperture for near-field scanning optical microscopy", Appl. Phys. Lett., vol. 75, no. 26 (1999) pp. 4076–4078

14) T. Matsumoto, T. Ichimura, T. Yatsui, M. Kourogi, T. Saiki and M. Ohtsu, "Fabrication of a Near-Field Optical Fiber Probe with a Nanometric Metallized Protrusion", Opt. Review, vol. 5, no. 6 (1998) pp. 369–373

15) M. Ohtsu (ed.), *Near-Field Nano/Atom Optics and Technology*, Springer-Verlag, Tokyo/Berlin, 1998, chapter 2

16) Uma Maheswari Rajagopalan, S. Mononobe, J. Yoshida, M. Yoshimoto and M. Ohtsu, "Nanometric Level Resolving Near Field Optical Microscope under Optical Feedback in the Observation of a Single-String Deoxyribo Nucleic Acid", Jpn. J. Appl. Phys., vol. 38, no. 12A (1999) pp. 6713–6720

17) M. Naya, R. Micheletto, S. Mononobe, R. Uma Maheswari and M. Ohtsu, "Near-field optical imaging of flagellar filaments of salmonella in water with optical feedback control", Appl. Opt., vol. 36, no. 7 (1997) pp. 1681–1500

18) 大津元一，河田聡編，「近接場ナノフォトニクスハンドブック」，オプトロニクス社，東京，1997，pp. 233 − 239

19) H. Kuhn, "Classical Aspects of Energy Transfer in Molecular Systems", J. Chem. Phys., vol. 53, no. 1 (1970) pp. 101–108

20) T. Förster, "Delocalized Excitation and Excitation Transfer", Section III-1, *Modern Quantum Chemistry*, Ed. by O. Sinanoglu, Academic Press, New York, 1965, pp. 93–138

21) N. Hosaka and T. Saiki, "Single molecule imaging in 30 nm range with illumination-collection mode NSOM", Abstrct of the 6th International Conference on Near Field Optics and Related Techniques, 27–31 Aug. 2000, Enschede, Netherlands, p. 172

22) X. S. Xie and R. C. Dunn, "Probing Single Molecule Dynamics", Science, vol. 265, 15 July (1994) pp. 361–364

23) T. Saiki, K. Nishi and M. Ohtsu, "Low Temperature Near-Field Photoluminescence Spectroscopy of InGaAs Single Quantum Dots", Jpn. J. Appl. Phys., vol. 37, no. 3B (1998) pp. 1638–1642

24) K. Matsuda, T. Saiki, H. Saito, K. Nishi, "Room-temperature photoluminescence spectroscopy on self-assembled $In_{0.5}Ga_{0.5}As$ single quantum dots by using highly sensitive near-field scanning optical microscope", Appl. Phys. Lett., vol. 76, no. 1 (2000) pp. 73–75

25) Y. Narita, T. Tadokoro, T. Ikeda, T. Saiki, S. Mononobe and M. Ohtsu, "Near-Field Raman Spectral Measurement of Polydiacetylene", Appl. Spectroscopy, vol. 52, no. 9 (1998) pp. 1141–1144

26) H. Fukuda, Y. Kadota and M. Ohtsu, "Estimation of the Minority Carrier Diffusion Length by Near-Field Photocurrent Measurement of p-n Junction in Silicon using Multiwavelength Excitation", Jpn. J. Appl. Phys., vol. 38, part 2, no. 5B (1999) pp. L571–573

27) ㈱日本分光カタログ，「走査型近接場光学顕微分光システム」，2000

28) V. V. Polonski, Y. Yamamoto, M. Kourogi, H. Fukuda and M. Ohtsu, "Nanometric patterning of zinc by optical near-field photochemical vapour deposition", J. Microscopy, vol. 194, no 2/3 (1999) pp. 545–551

29) Y. Yamamoto, M. Kourogi, M. Ohtsu, V. V. Polonski and G.H. Lee, "Fabrication of nanometric zinc pattern with photodissociated gas-phase diethylzinc by optical near field", Appl. Phys. Lett., vol. 76, no. 16 (2000) pp. 2173-2175

30) T. Yatsui, M. Kourogi, K. Tsutsui, J. Takahashi, and M. Ohtsu, "High density/speed optical near field recording/reading with a pyramidal silicon probe on a contact slider," Optics Letters, vol. 25, no. 17 (2000) pp. 1279-1281

31) 伊藤治彦，大津元一，「近接場光を用いた原子の制御」，光学，第28巻，第11号，(1999)，pp. 610 − 615

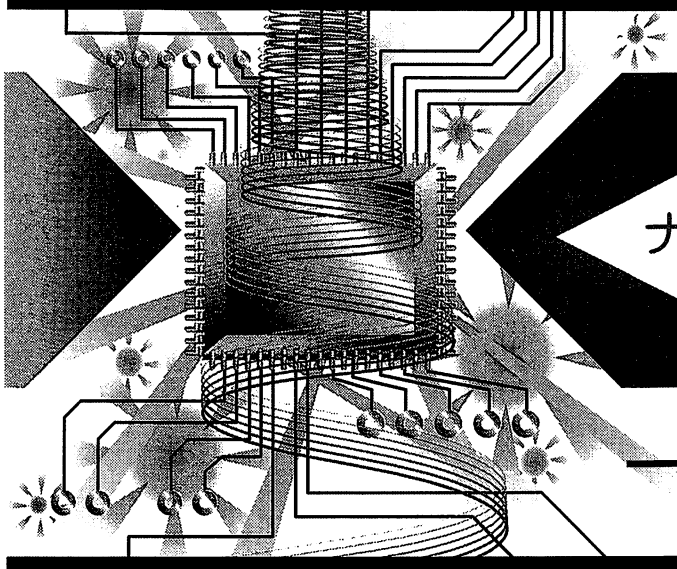

4

ナノフォトニクスとその展望

Nano-photonics and Its Overlook

大津　元一

1. まえがき

フォトニクスは光の利用技術であり，その代表例はディスプレイ，光メモリ，光通信などである．1960年に発明されたレーザにより人類は制御可能で優れた特長を持つ光を手にすることができ，それによりフォトニクスを発展させて現代社会の高度情報化の一翼を担ってきた．これを支える基盤部品は電子デバイスと光デバイスであり，その作製技術の一つとして光による加工が用いられ，通信，情報機器には半導体レーザ，ガラスファイバなどの光デバイスが組み込まれてきた．今や我が国のフォトニクス関連の産業規模は電子工業産業の約2割，すなわち約5兆円に達している．

ところで従来のフォトニクスはナノメートルの寸法を意味する「ナノ」の概念とは相いれない．なぜならば光の回折(用語)のために，光を使うとその波長より小さい物質を扱うことが原理的に不可能だからである（扱うことのできる最小寸法は回折限界(用語)と呼ばれる）．したがって光を使う限り図1に示すように数百nm以下の寸法の光技術，すなわち光デバイスのナノ寸法化は原理的に不可能であり，ナノ寸法のフォトニクスは実現しないことを意味する．

しかし21世紀の社会はこの実現を要求している．本稿ではこれを指摘し，更にそれを実現するための技術的ブレークスルー，すなわち，従来不可能とされてきたナノとフォトニクスの概念を結合させるナノフォトニクス[1]の進展について概説する．

大津元一：正員　東京工業大学大学院総合理工学研究科
E-mail　ohtsu@ae.titech.ac.jp
Nano-photonics and Its Overlook. By Motoichi OHTSU, Member (Interdisciplinary Graduate School of Science and Engineering, Tokyo Institute of Technology, Yokohama-shi, 226-8502, Japan).
電子情報通信学会誌　Vol.84 No.1 pp.26-32 2001年1月

2. 21世紀の社会の要求

本章ではフォトニクスの代表的な三つの例を取り上げ，21世紀，特に2010～2020年を目安とした将来の社会が要求する事柄とそれに関する問題点を列挙する．

（1）光メモリ

光メモリの記録密度は図2に示すように急速な進歩を遂げてきたが，それは回折限界（用語）との戦いであった．すなわち凸レンズで光ディスク面に光を絞ったときのスポット径の最小値は光の波長程度なので，これを小さくするために光源の短波長化が図られてきた．CDでは近赤外光，DVDでは赤色光が使われ，次世代DVDでは青色レーザを使うべく技術開発が行われている．しかし，光の回折による記録の高密度化の限界は20～30Gbit/in^{2}とされている．一方，光メモリ技術の将来動向予測をまとめた「光テクノロジーロードマップ報告書」(情報記録分野)[2]によると今後は社会的背景の変化，生活スタイルの変化にこたえるため情報需要量が一層増大すると予測されている．例えば2010年には各家庭で必要となる光メモリの記録密度は1Tbit/in^2（再生速度としては100Mbit/s）と見積もられている．この値は回折限界より数十倍大きく，このことは1bitの情報を記録するための加工の寸法として25nm程度まで小さくしなくてはならないことを意味している．したがって従来の光メモリ技術では原理的に実現不可能な値である．ただしこの値が実現すれば2010年における光メモリと磁気ディスクを合わせたメモリ産業市場は世界全体で30兆円以上の大きな規模になるとともに，新たな周辺産業を形成すると期待される．

（2）光通信システムと光デバイス

現在の光通信システムを支える光デバイスは半導体レーザ，光導波路などであるが，これらのデバイスの中

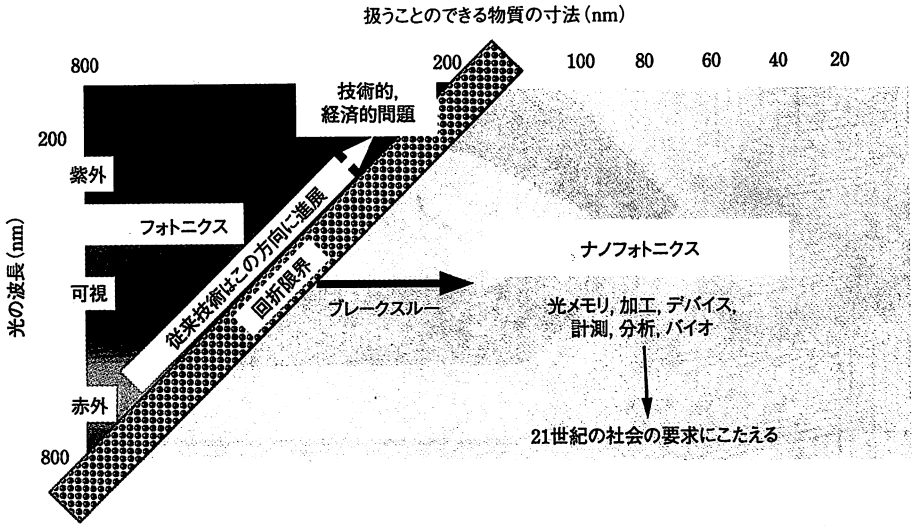

図1　フォトニクスとその回折限界　　ナノフォトニクスは回折限界を打破し，21 世紀の社会の要求にこたえる．

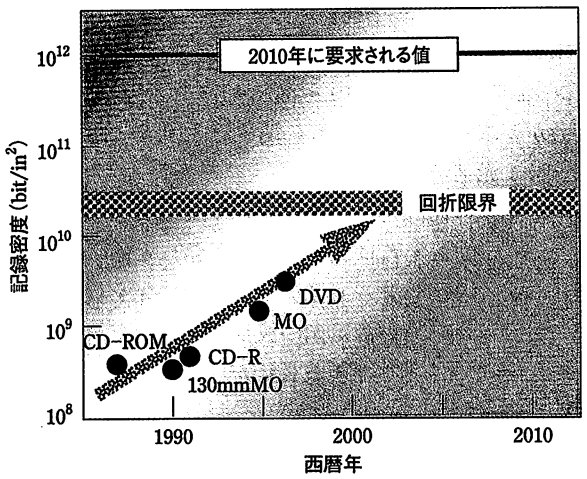

図2　各種の光メモリの記録密度の進歩の様子　　光の回折による高密度化の限界値は 20 ～ 30Gbit/in^2 であるが，2010 年に社会が要求する値はその数十倍の 1Tbit/in^2 である．

に光を閉じ込めるためにその寸法を 100～1,000 μm 程度にしている．これは電子集積回路中の各デバイスの寸法に比べて非常に大きい．これらの光デバイスを回折限界まで微小化しても 1μm 程度が限度である．このように現在の光デバイスは寸法の微小化に限界があり，それに伴って動作電圧やしきい値の低減という省エネルギーの面でも問題を抱えている．一方，「光テクノロジーロードマップ」(情報通信分野)[3]によると，光通信システムでは長距離国際統合網において 2010 年には 10Tbit/s (10,000km)の通信容量が必要とされる．この要求に対しては既存のデバイス技術の高度化により対応可能と考えられているが，2020 年代になると，急増するインターネット情報などの授受のために小型で高効率の新しいデバイス（1,000 × 1,000 の光スイッチ用デバイス，数 mV で駆動可能な低電圧光変調器，低駆動電力の光源など）の開発が必要となる．そのためにはデバイスの寸法は 20 ～ 50nm まで小さくする必要がある．しかしこの値は回折限界を超えており，現状の技術で実現することは不可能である．

（3）　微細加工

光を用いた微細加工の代表例であるリソグラフィーは被加工物に所望の光学像を縮小投影し，その像を被加工物に転写して所望の集積回路を作る技術であり，これは 1980 年代からの一貫した DRAM の高集積化に牽引されて発展してきた．加工寸法の最小値は回折限界のために光の波長程度に制限されるので，これまでの微細加工技術は主に加工用の光源の短波長化によって進展してきた．そして我が国の産業界では共同・統合化，国家予算の導入による共同研究を積極的に進め，1 Gbit の DRAM 製造の研究以降，ArF エキシマレーザ，F_2 レーザや極端紫外光源を用いたリソグラフィー技術を開発してきている．しかしながら，これらの短波長化は光源をはじめとして多くの周辺装置の更新を余儀なくされ，結果として膨大な設備投資を必要としている．一方，大きな規模を堅持する市場の獲得競争は激化の一途をたどったため過当競争となり，高水準の利益を生み出しにくい状況を生じてきている．更に我が国の産業界では予想をはるかに上回る DRAM の価格低下による業績不振のた

用　語　解　説

回折　光がその波長程度の寸法を持つ穴を通り抜けると，広がろうとする性質．

回折限界　回折のために光を凸レンズで集光してもそのスポット径は波長程度以下にはならず，したがって波長程度以下の寸法の小さな領域に光を閉じ込めることができない．この閉込めの下限を回折限界という．

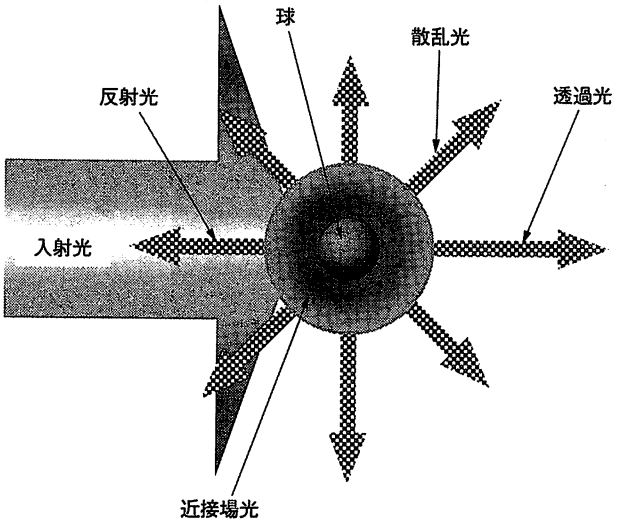

図3 近接場光の発生の様子　微小物体に光を照射すると透過，反射，散乱光とともに光の薄い膜，すなわち近接場光が発生する．

めに，CPU などの高付加価値半導体に支えられた米国，通貨と人件費の点で有利な韓国・台湾に対抗し得るだけの投資力が薄れつつある．この状況を打破するためには従来技術路線にない安価な量産加工技術の登場が待望される．

以上の三つの例をもとに考えると，21 世紀の社会は数十 nm の寸法の微小な光を発生し，それを用いた微小な技術を要求していることが分かる．しかし従来のフォトニクスで用いられている光を使う限り，回折限界のためにこの要求にはこたえられない．すなわち，上記三つの例に示される要求は回折限界のかなたにある．3. では回折限界を打破し，これらの要求にこたえる新技術，すなわちナノフォトニクスについて展望する．

3. ナノフォトニクスによる限界打破

3.1 近接場光の発生と使用

従来のフォトニクスに使われている光は光源から発し，その後は光源とは独立に空間を伝搬する電磁波である．回折はそのような波の基本的性質であり，それに起因する回折限界は打破できないと考えられてきた．しかし最近，近接場光と呼ばれる光を使うことによりこれが打破された．

近接場光の発生と検出のより詳しい説明は文献にゆずり[4]，ここでは現象論的に説明する．図3に示すように，入射光の波長に比べずっと小さい直径を持つ球に光を照射すると入射光の多くは透過，反射，散乱して伝搬していくが，同時に球表面には表面波，すなわち近接場光が発生する．そのエネルギーの値は球面から遠ざかるに従い急激に減少する．すなわち，球表面に近接したところにエネルギーが集中した光なのでこれは近接場光と呼ばれている．つまり非常に薄い光の膜であるが，その膜の厚みは球の直径程度であり，波長よりずっと小さい．この近接場光を使った技術がナノフォトニクスである．

近接場光を発生させるための微小な球の代りに最近ではガラスファイバを素材として図4に示すように先端の曲率半径が数 nm 以内に針のように尖ったプローブ（ファイバプローブと呼ばれている）が開発された．そしてこのファイバプローブ後端から光を入射し，先鋭化された先端部に近接場光を発生させ計測，構造分析などが行われている[4]．更に最近では近接場光のエネルギーを利用して光メモリ，加工などが行われるようになり，まさにナノフォトニクスが急進展している．例えば光メモリの記録の寸法，再生の空間分解能，加工の精度は近

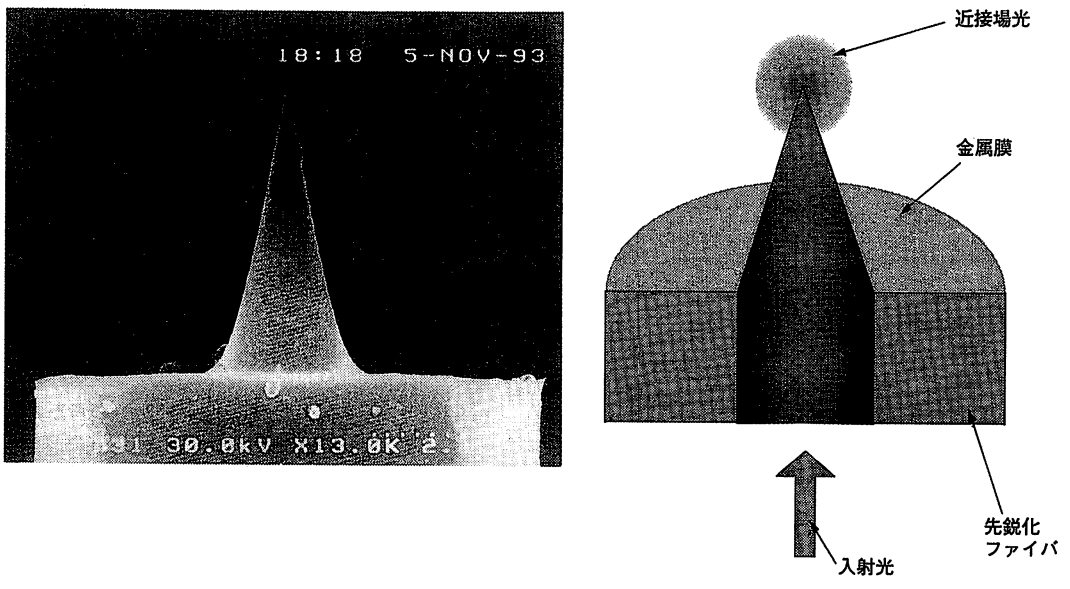

図4 ファイバプローブとその先端に発生する近接場光　左は先鋭化ファイバの電子顕微鏡写真（写真の横幅は 8.9 μm に相当）．この先鋭化ファイバを用いて作製したファイバプローブの先端に近接場光が発生する．

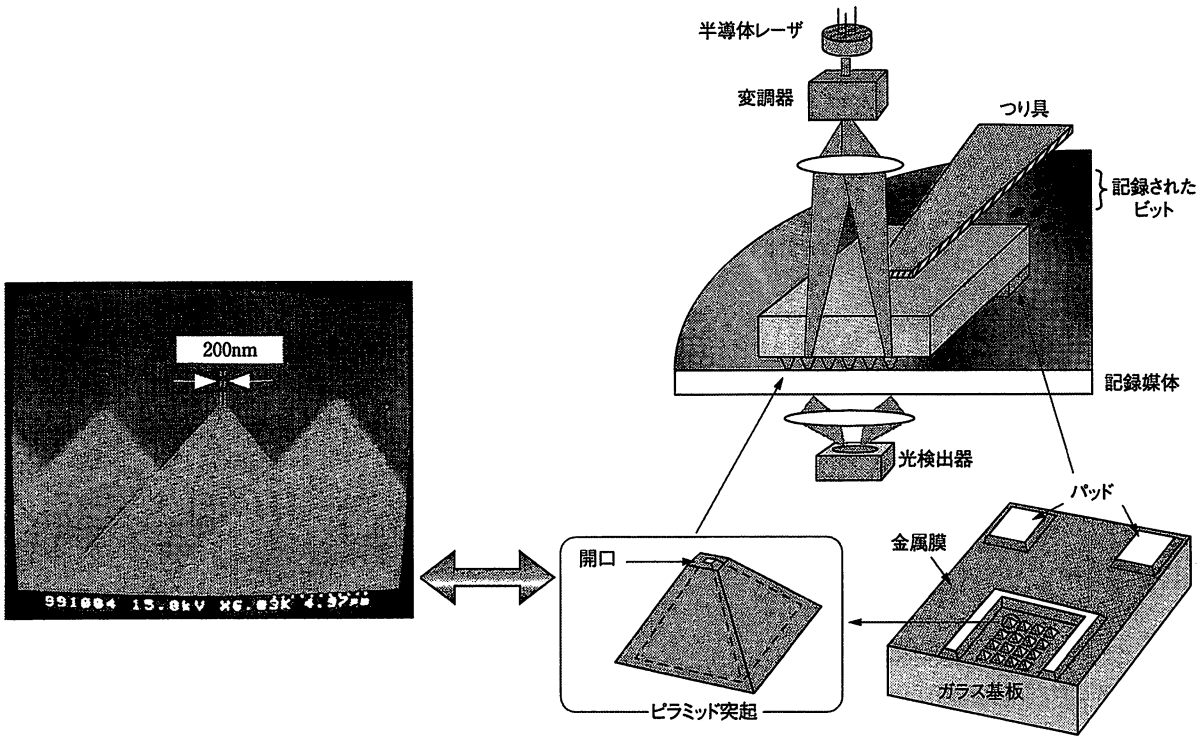

図5　ピラミッド突起状二次元アレーを用いた光記録再生　記録媒体上にシリコン製作のピラミッド突起（左の電子顕微鏡写真）を滑らせ，突起先端の近接場光で記録再生する．

接場光の空間的寸法，言い換えるとファイバプローブの先端の寸法によって決まり，それは回折限界を超えて波長よりもずっと小さな値であるから，2. で記した21世紀の社会の要求にこたえる可能性がある．現にこの可能性を実証する研究開発が活発に行われている[5]．以下ではこれらについて記す．

3.2　光メモリ

近接場光により記録するにはファイバプローブ先端の近接場光を記録材料に照射して材料表面の構造変化，形状変化を誘起させる．再生には近接場光による形状計測を行う．近接場光による記録密度及び記録の最小寸法はプローブ先端寸法によって決まり，記録密度 1Tbit/in^2 に相当する記録寸法（25nm）を実現することは原理的には既に可能となっている．実用化のための問題点はソフトウェアとハードウェアにかかわっており，かつこれらは相互に関連している．特にハードウェアに関しては記録再生速度，記録再生ヘッドの安定走査，記録材料の開発などの技術的問題点が抽出されている．

この状況下で既に記録再生ヘッドのデバイス，記録媒体，メカトロニクス，ソフトウェア，標準化などの各課題を有機的に関連付けた技術開発方針が詳細に検討され，産業的戦略とともに技術開発の段階に入っている．実用化の際の形態としては密閉型（従来のハードディスクドライブと同様の装置外形を有し，薄型・小型化によりすえ置型の端末や携帯端末など広範囲の端末機器に使用），パッケージ型（従来のパッケージ型光ディスクの発展型としてテラバイト級の廉価な脱着可能な記録媒体を提供）の二つが考えられており，両型とも ROM を経て RAM の実現に至るべく，開発が始まっている．

Super-RENS（Super-resolution near-field structure）と呼ばれ，記録媒体上に作りつけた非線形光学薄膜に伝搬光を照射したときに自己形成される微小開口により近接場光記録再生する方式，シリコン基板加工によるピラミッド突起状二次元アレー（図5），などによる記録再生が行われ，更には面発光レーザを用いた記録再生ヘッドの開発など，ファイバプローブによる点接触型から平面積層型へと脱却した近接場光技術が進展している．これらの方法は固侵レンズ（Solid immerion lens）のよう

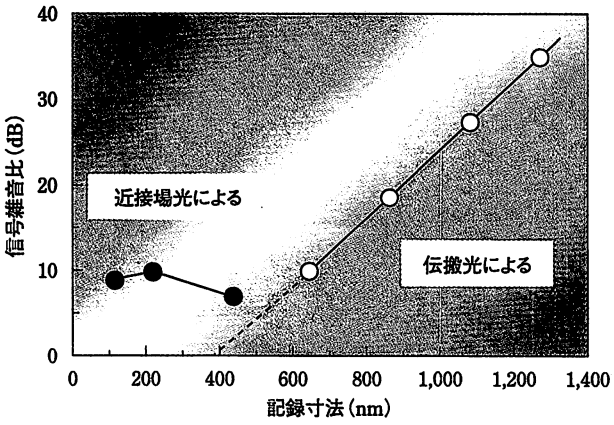

図6　近接場光による記録寸法と再生時の信号雑音比との関係　従来から用いられている伝搬光では記録寸法が約 400nm になると再生不能．しかし近接場光では 100nm 程度になっても再生可能．

に光学の枠組みの中にとどまり回折限界に律則された方法に比べ，性能及び将来の発展性の点で優れている（以上の個別技術の詳細は文献（5）とそれに引用された各文献を参照されたい）．これらのうちピラミッド突起状二次元アレーの中の一つの突起を用いた記録再生の予備実験の結果を図6に示す．これはAgInSbTeの相変化媒体に記録再生した結果で，再生の信号雑音比を記録寸法に対して示してある．従来から用いられている伝搬光では回折限界のために記録寸法が約400nm以下になると再生不可能になるのに対し，近接場光では100nm程度まで小さくなっても再生可能であり，1 Tbit/in^{2}に相当する記録寸法25nmに向けた可能性が示されている．

3.3 微細加工

近接場光を使って既存のデバイス用の加工が試みられているのと同時に，2.で記した要求にこたえるために近接場光を使って動作する新しい高機能デバイスの加工が提案されている．このような新デバイスの例は3.2に記した超高密度光ディスクメモリと3.4に記すナノ寸法の光集積回路であり，これらの製作は既存の加工技術では不可能で，近接場光による加工が必須である．以下にはこれらの事情に注意しながら加工に関する現状を概説する[5]．

（1） 既存のデバイスの製作にかかわる加工

ファイバプローブを用いてリソグラフィー用フォトレジストへの露光が行われ，数十nmの幅のパターンが描画されている．また，短パルス光を用いたアブレーション，一括露光可能なスタンプ光リソグラフィーなどの技術が開発されている．

（2） 近接場光で動作する新デバイスの製作にかかわる加工[6]

3.4で概説するように半導体量子ドットなどの微粒子表面に近接場光を発生させ，それを情報キャリヤとして信号伝達する光トンネルデバイス，そのための発光，スイッチング，受光デバイスからなるナノ寸法の光集積回路が提案されている．その製作には金属，誘電体，半導体などの異種材料を共通の半導体基板の上の希望する位置に，希望する寸法で作りつけなければならない．量子サイズ効果を援用するにはその寸法は約30nm以内，加工精度は数nm以内の必要がある．これらの要求にこたえる方法として，紫外域の近接場光を用いた光化学気相堆積が行われている．現在までに亜鉛金属の幅20nmの曲線（図7 (a)），微粒子（図7 (b)），青色発光する酸化亜鉛の微粒子（図7 (c)）などがガラスやサファイア基板上に堆積されている．使用する有機金属気体とそれを光解離するための光源の組合せにより，亜鉛のほかにアルミニウムなどの金属，絶縁体，更には化合物半導体の堆積が可能とされている．

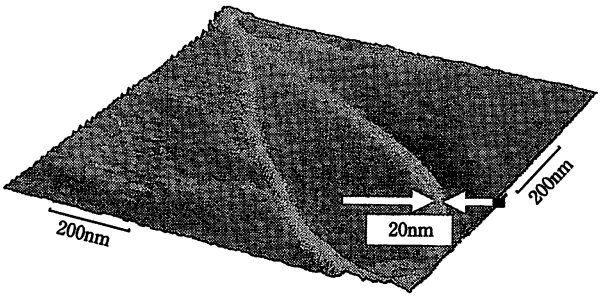

(a) ガラス基板上の亜鉛の楕円ループ状の細線

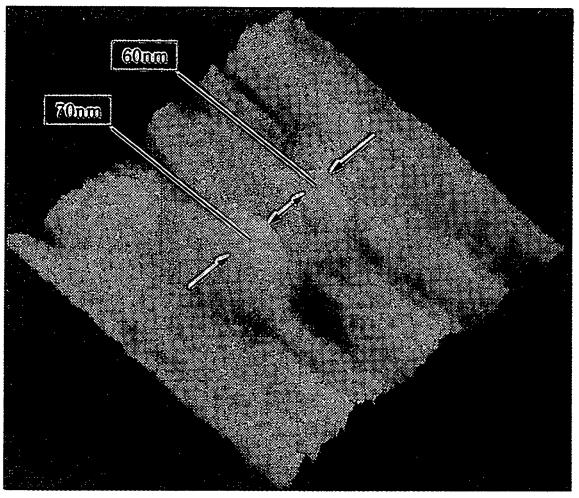

(b) ガラス基板上の近接した亜鉛の二つの微粒子

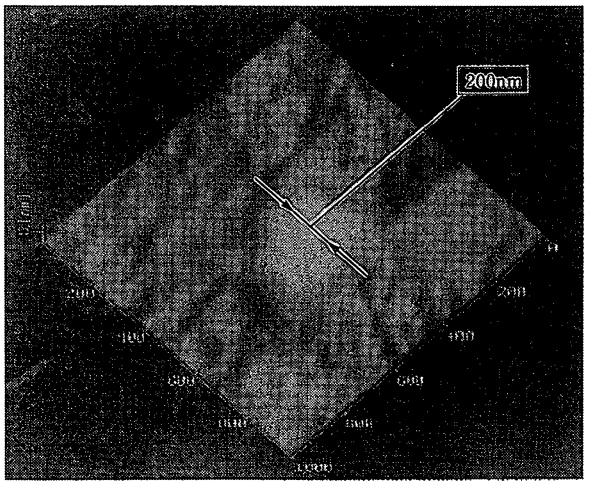

(c) サファイア基板上の酸化亜鉛の微粒子

図7 堆積された微小パターン

3.4 ナノ寸法の光集積回路

近接場光を用いれば従来の光技術では不可能であったナノメートル寸法の新しい光デバイスの開発が可能となり，2.（2）に記した要求にこたえることができると期待される．そのためにナノ寸法の微小な光デバイスとその集積化のための単一量子ドットによる発光デバイスの提案，スイッチング機能の検証実験が既に行われ，更には3.3で述べたようにこれらのデバイスを製作するための光化学気相堆積法の開発が進んでいる．例えば，図8に示すように，金属の細線（図7 (a)），発光半導体ド

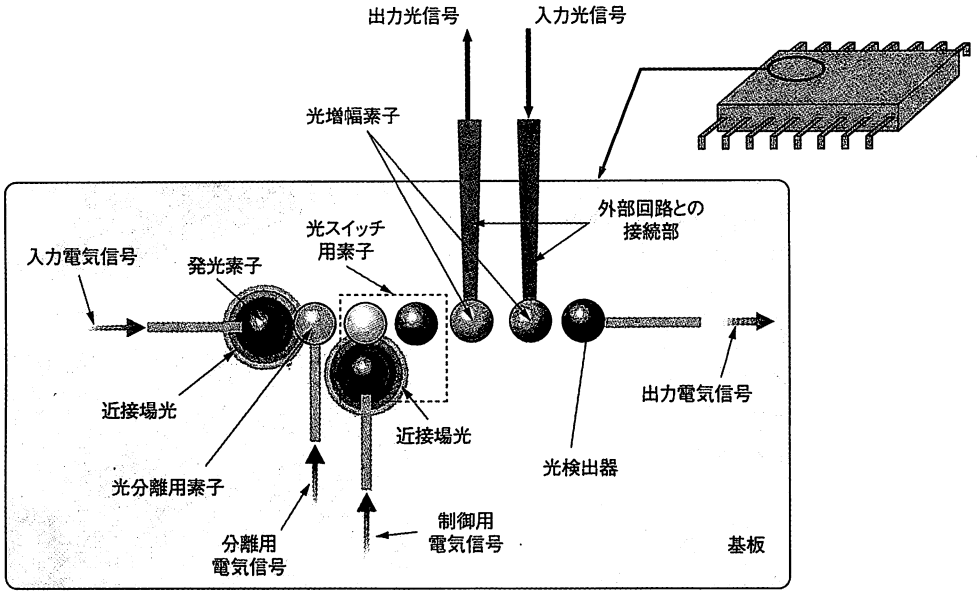

図8 ナノ寸法の光集積回路の構成　共通基板の上に堆積した微粒子に発光，増幅，変調，受光機能を持たせ，近接場光のエネルギーを授受して信号処理・伝送する．

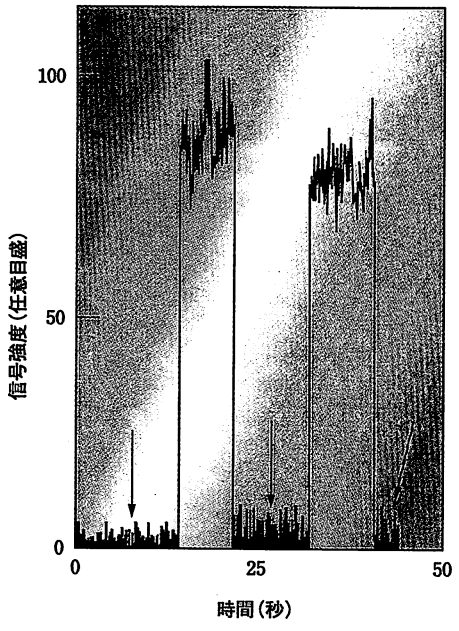

図9 InGaAs 半導体の単一量子ドットによる光スイッチ機能の実験結果　矢印のところでは制御用の光を入射しているので，スイッチが開かれており，信号が伝送されていない．

ト（図7(c)）などを共通基板の上に堆積させれば，半導体微粒子に電流を流し，エレクトロルミネッセンス発光させ，更には増幅，変調，受光する機能を持つナノメートル寸法デバイスが可能となる．これは微粒子により近接場光を発生させ，そのエネルギーを授受することにより機能する．

そのためには，各微粒子の寸法は量子サイズ効果が期待できる程度（約 30nm 以内）であること，近接場光のエネルギーを授受するために微粒子間隔は微粒子の寸法程度まで近づいていること，の二つの条件が必要である．

これが実現すれば，半導体レーザや光導波路などから構成される従来の光集積回路に比べて寸法が各々百分の一～千分の一のナノフォトニクス用の光集積回路となり得る．この2条件を満たすデバイスは 3.3 で記した近接場光による加工方法により実現可能と期待されている．実際に図7(b)に示すように Zn の二つの微粒子がその直径程度まで近接して希望する位置に堆積されている．一方，近接場光による光スイッチ機能については図9に示すように既存の半導体（InGaAs）の単一量子ドットに対して確認されている[5],[6]．

なお，図8の微小な光集積回路を周辺の巨視的な回路と連結して使うために，これらの回路との接続方法，更に集積回路内部での各微粒子間での近接場光信号の逆流の回避，などの動作原理に関する研究が進んでいる．また，光集積回路の信号処理速度，消費電力，などについても検討が始められている．

このようなナノ寸法の光デバイスに至る前段階での試みも行われている．すなわち半導体量子井戸の中の励起子によるポラリトン波動を利用してナノ寸法の光導波路を作り，干渉型の光スイッチを構成する方法[7]，金属細線を光導波路として利用する方法[8]などである．

4. ま と め

本稿では既存のフォトニクス技術には回折限界があること，21 世紀の社会の要求はこれを超えた高度なものであることを示した．そして，回折限界を打破しこれらの要求にこたえるために近接場光を利用したナノフォトニクスが進展している様子を概説した．これはフォトニクスがカバーする多くの部分を革新し得る技術であり，そのもたらす成果は大きい．例えば光メモリの記録密度

1Tbit/in^{2}は巨大な値であり，これを活用するためには超高密度，大容量光メモリに対する製作者，使用者のとらえ方の発想転換さえ要求されている．

ナノフォトニクスは単なるフォトニクスの微小化にとどまらず，情報，バイオ，フォトニクス，エレクトロニクスを融合した新概念である．ただし，まだ歴史が浅いため未熟な点も多い．今後のナノフォトニクスの技術はその形態を少しずつ修正しながら，社会の要求にこたえられるように進展していくと考えられる．

文　　献

（1） 大津元一，ナノ・フォトニクス，米田出版，千葉，1999.
（2） (財) 光産業技術振興協会編，光テクノロジーロードマップ報告書（情報記録分野），(財) 光産業技術振興協会，東京，1998.
（3） (財) 光産業技術振興協会編，光テクノロジーロードマップ報告書（情報通信分野），(財) 光産業技術振興協会，東京，1998.
（4） M.Ohtsu and H. Hori, Near-field Nano-optics, Kluwer Academic/Plenum Publishers, New York, 1999.
（5） 大津元一，“近接場光学技術とその展開，” 精密工学会誌，vol.66, no.5, pp.661-666, May 2000.
（6） 大津元一，“ナノ領域の光加工とその応用，” 応用物理，vol.68, no.4, pp.431-434, April 1999.
（7） T. Katsuyama and K. Ogawa, “Excitonic polaritons in quantum-confined systems and applications to optoelectronic devices,” J.Appl. Phys., vol.75, no.12, pp.7607-7625, June 1994.
（8） J.Takahara, S.Yamaguchi, H.Taki, A. Morimoto, and T.Kobayashi, “Guiding of One-Dimensional Optical Beam with Nanometer Diameter,” Opt. Lett., vol.22, no.7, pp.475-477, April 1997.

大津　元一（正員）

昭48東工大・工・電子卒，昭53同大学院博士課程了．同年東工大助手．以来，光エレクトロニクス，近接場光学の研究に従事．現在，同大学教授．工博．昭63日本IBM科学賞，平10井上学術賞各受賞．著書「ナノ・フォトニクス」など．平10～現在，科学技術振興事業団，創造科学技術推進事業，「局在フォトン」プロジェクトリーダー兼任．

ITのハードウェア技術を支える光ナノテクノロジー

東京工業大学大学院　総合理工学研究科　大津　元一

1. まえがき

IT（Information Technology）の普及のためには社会構造，ソフトウェア技術，ハードウェア技術などが足並みをそろえて進歩することが必要である。ハードウェア技術とは情報記録や情報通信であり，これらに光技術が深く関与している。特に情報記録のための光メモリー技術は従来より日本の産業界が世界をリードしていることは周知の通りである。一方，ITなる言葉が広まる以前に財団法人光産業技術振興協会が産官学の協力のもとに策定した光技術のロードマップの報告書によると，たとえば次の要求がある。

①情報記録分野：産業構造就業環境変化，ゆとり社会の実現，在宅勤務化，快適労働追求，生活情報の大容量化などにより，2010年には光メモリーの記録密度1Tbit/in^2，再生レート100Mbit/sが必要[1]。

②情報通信分野：地域インターネットバックボーンのパケット転送系の高速化，大容量化のためにには，光スイッチの入出力チャンネル数は2015～2020年には1000×1000が必要[2]。

しかしこれらの要求は大胆な値であることに気づく。なぜなら，①に関しては，もし記録ピットが円形の場合，その直径が25nm程度まで小さくならなくてはならないことを意味する。これは光の波長よりもずっと小さい値である。②に関しても同様であり，従来と同一寸法の基板の上に複数の光スイッチング素子を集積する場合，各素子の寸法はやはり光の波長以下にしなければならない可能性が大きい。しかしこれらの寸法は光のもっている基本的性質である回折による限界のために実現できない。したがってこれを実現するためには回折限界を越えた光のナノ寸法化技術，すなわち光ナノテクノロジーが必要となる。21世紀冒頭に出版される本誌のなかの一記事として，本稿ではこの光ナノテクノロジーについて論ずる。

2. 開発の必要性

将来の社会が前節に示した要求をつきつけている以上，それに応える技術を生み出すのが研究者，技術者の使命である。たとえば①については光源の短波長化によって高密度化が推進され，すでに数Gbit/in^{2}が達成されているが，これまでの記録密度の増加の進度を外挿すると今後数年で回折限界（約30Gbit/in^2）に達することが分かっている。一方ハードディスク技術では熱限界とされていた数10Gbit/in^{2}を越え，研究室レベルでは100Gbit/in^{2}が実現している。また，米国では中長期的なイニシアティブの確保を目指した研究開発が進行中であるし，東アジア諸国でも急速に技術力を向上させている。したがって①の実現が急務であるが，これが実現すればまさにITを支える基盤技術となると共にコンテンツ産業などの周辺産業の発展と雇用の促進，関連電子・機械産業などへの幅広いシナジー効果などが実現する。

①を実現するための技術的問題ははソフトウェア，記録媒体，記録再生システム，記録再生ヘッドのデバイスなど多岐にわたるが，すでにそれらは具体的に抽出されている[3]。このように問題が具体的に抽出されたこと自体が大きな進歩といえる。これらの問題を解決するに際して，技術者の心理としては往々にして既存技術を修正し，利用してその延長上で考えたくなる。なぜなら既存の設備や技術ノウハウが使えるからである。しかし回折限界と1Tbit/in^{2}との間には数10倍の差があり，既存

技術の延長線上にはない。そこで新概念，新技術への挑戦が必要となる。

3. 近接場光による光メモリー

前節の光メモリーの実現には光ナノテクノロジーが必要となる。しかしこれは従来の光技術の常識から考えると矛盾することを意味している（なぜなら回折限界のために「光」と「ナノ」とは原理的に相容れないからである）。この矛盾を解消するために光の小さな粒である近接場光を用いた方式が研究されている。この方式はハードディスクのような密閉型と光メモリーのようなパッケージ型の両方の利点を取り入れた新形態をとると考えられている（最近のハードディスクではモーターを内蔵した脱着可能型さえも出現している。たとえば東芝製のモバイルHDD，IBM製のmicrodriveなど）。

近接場光の研究はスイス，フランス，米国，日本で1980年代初頭に開始された[4]。しかしナノテクノロジーを標榜しながらも，欧米ではその必須素子であるプローブ開発を軽視し，また応用としては計測である顕微鏡分野に留まった。一方幸いなことにわが国ではプローブ開発技術に正面から取り組み，1980年代後半以降は分光，メモリー，加工など，本稿の議論に通じる光ナノテクノロジーの基盤を開発した。現時点ではこの分野の研究人口と研究成果については質，量ともにわが国が世界を先導している（これは2000年8月に開催された近接場光学国際会議でのわが国からの発表の質と量の高さとして如実に現われている[5]）。現在ではこのような先行性のために，さらには欧米にはメモリー，加工に対応する研究が立ち上がっていないために欧米から発表される学術論文にわが国の論文が引用されないという奇妙な現象さえ目につくようになっている。

このような状況下で光メモリーの研究が進んでおりコンタクト型ハードディスクのようにスライダーヘッドのアレイを用いた方式[6]，このアレイとして面発光レーザーを利用する方式[7]，これらとは異なり媒体の非線形光学特性を利用しプローブ走査を不要とするSuper-Rensと呼ばれる方式[8]など，すべて日本製の技術が生まれており，今後の進展が期待されている。

4. 光デバイスのナノ寸法化とその作製

②のための既存の光デバイスはレーザー，光導波路などである。しかしこれらも光の回折限界のためにナノ寸法化は不可能であり，新概念に基づく光デバイスが必要であることを意味する。たとえば光スイッチについては現状の干渉計型光導波路の形態に変わるものとしてマイクロマシン技術によるデバイスが提案されている[9]。その先にはナノ寸法の新奇な光デバイスが必要となるであろう。そこで最近では半導体の単一量子ドットにより近接場光のエネルギーを授受する光スイッチ動作の確認[10]，既存の光デバイスとナノ光デバイスとをつなぐインターフェイスとしてのプラズモン導波路[11]，数100nm寸法の干渉計型光導波路の形態を有するポラリトンスイッチ[12]などが提案されている。さらに動作原理については近接場光と量子ドットとの間の局所的電磁相互作用を利用した光スイッチが提案されており[13]，今後の進展が期待される。

ただしこのような試みを実用化に結びつけるには微小物質の加工技術が必要である。これらの寸法は数10nmであり，複数の微粒子の形状を制御して必要とする位置に作製する必要がある。さらに必須なことは近接場光のエネルギーを授受するために，隣り合う微粒子の間隔が微粒子寸法程度まで小さいことである。この加工は既存の加工では不可能で，光リソグラフィー技術の進展に頼っても不可能である。しかし最近近接場光による加工可能性が示された[14),15]。この方法は隣り合う微粒子の間隔をナノ寸法まで小さくすることなど，既存の装置では到底不可能な加工形態を実現している。

5. 今後なすべきこと

光ナノテクノロジーは光技術のパラダイムシフトである。その実現のためには既存の技術ノウハウから脱却する決意が必要である。あたかも「高級な装置を使って高性能の真空管を作っても，その技術からはトランジスターは決して生まれない」と言われたことに通じる。このパラダイムシフトの実現とともにその成果を国際的に認めさせる自己主張をすることが必須である。私事になるが，筆者らは1982年ごろには近接場光学用のプローブデバイスの研究に着手していたが[16]，この先駆性は存外国際的には広く知られていない。この経験から筆者は，日本人は欧米人の数倍の質，量で自己主張（論文出版，国際会議発表も含めて）しないと国際的には認知されにくいと自省している。池上，松倉両氏による「光エレク

トロニクスと産業」の第1.6節には「そのターニングポイントは1980年にブライトン（英）で開催された半導体レーザー国際会議であった。こともあろうに，日本の優れた長波長レーザーの論文はすべて，当時は口頭発表よりはランクの低いとみなされていたポスターセッションに集められたのである。理由は，（英語力に問題のある）日本人研究者から長波長レーザーについての情報を得るには，ポスターセッションの方が好ましい…」とあった[17]。これは日本人の口頭発表の際のアピール力の低さ（特に米国人はあたかも舞台俳優のように発表する），英語力の低さを象徴している。一方第1.8節には「日本の企業の研究所は，すぐれた研究者と金を湯水のように投入した。…，半導体レーザーの埋込み構造は当時の結晶成長技術の世界では『クレイジー』といわれたが，安定動作のできるデバイス作りのきっかけとなった。」ともあり，これは原理が既知の場合，日本人はそれを改良，実現する技術力が高いことを意味している。

関連する諸兄に対する無礼を覚悟で指摘すると，日本人研究者は上記と同様の口頭発表の際のアピール力の低さ，英語力の低さを3節で述べた近接場光学国際会議でも十分に発揮したといえる[5]。しかし幸いなことに原理と理論[18]にまで踏み込んだ研究の質の高さとともに技術力の高さは明らかに他国に比し優位性を示していた。この優位性を支えに光ナノテクノロジーに関して今後なすべきは上記の欠点を改善すること，および自己主張して成果を国際的に正当に認めさせることである。

自己主張は国際会議の公正な運営，新技術の国際的標準化などに際し日本の要望を通すために必須であり，これは国を挙げてすべきである。もともと日本人は照葉樹林帯に属する小さな国土で農耕を営み，そこに養われた文化によって培われた強烈な共同体意識，慎み深さを美徳としている。これに対し欧米人は乾燥落葉樹林の大平原地帯に生まれ育った。特に米国は共同体がなく個人としての才覚のみによってのみ安んじて生活する多民族国家なのでその人々はゴーゲッター（Go-getter：出ていって奪い取る人）であり，自己主張なしには生きていけない。村落，地区共同体，ギルド，いくつかのコミュニティーを経過して生きるのが普通であった欧州人は日米の中間にあるといってよいが，それでも自己主張の必要性は日本の比ではない[19]。学術論文の査読と発表形態，国際会議での発表形態，特許制度などはすべてゴーゲッターとしての欧米の文化に根ざしており，日本人はこれらになじまない。日本人の文化に根ざした品格を高く保ちながら自己主張するという矛盾した命題に取り組むことが必須である。

ノーベル賞，オリンピック，アカデミー賞などはゴーゲッターとしての欧米の自己主張の文化から生まれた栄誉形態である。したがって日本人は先駆的業績を挙げたり個人で自己主張しただけではこの栄誉に浴することはできない。これらは国を挙げた自己主張により勝ち取るものであり，これが今後なすべきことなのである。

参考文献

1) (財)光産業技術振興協会編：「光テクノロジーロードマップ報告書―情報記録分野―」，(財)光産業技術振興協会，p. 18 (1998)
2) (財)光産業技術振興協会編：「光テクノロジーロードマップ報告書―情報記録分野―」，(財)光産業技術振興協会，p.34 (1998) およびその改訂として同協会編，「オプトニューズ」，Vol. 116, pp. 7～10 (2000)
3) (財)光産業技術振興協会編：「極限光インフォニクス技術に関する調査研究報告書」，(財)光産業技術振興協会，pp. 50～74 (2000)
4) 大津元一：「ナノ・フォトニクス」，米田出版，pp. 46～50 (1999) および上記3)のp. 129
5) Conference Program on 6th International Conference on Near Field Optics and Related Techniques, 27–31 August 2000, Enschede, Netherlands
6) T. Yatsui, M. Kourogi, K. Tsutsui, M. Ohtsu, and J. Takahashi: "High-density-speed optical near-field recording-reading with a pyramidal silicon probe on a contact slider", Opt. Lett., Vol. 25, No. 17, pp. 1279～1281 (2000)
7) S. Shinada, F. Koyama, K. Suzuki, K. Goto, and K. Iga: "Near-field Analysis of Micro-Aperture Surface Emitting Laser for High Density Optical Data Storage", Opt. Rev., Vol. 6, No. 6, pp. 486～488 (1999)
8) J. Tominaga, T. Nakano and N. Atoda: "An Approach for Recording and Readout beyond the Diffraction Limit with an Sb Thin Film", Appl. Phys. Lett., Vol. 73, No. 15, pp. 2078～2080 (1998)
9) 羽根一博：「光通信用マイクロマシン」，電気学会誌，第120巻，第11号，pp. 683～686 (2000)
10) T. Matsumoto, M. Ohtsu, K. Matsuda, and K. Nishi: "Low-temperature near-field nonlinear absorption spectroscopy of InGaAs single quantum dots", Appl. Phys. Lett., Vol. 75, No. 21, pp. 3246～3248 (1999)
11) J. Takahara, S. Yamaguchi, H. Taki, A. Morimoto, and T. Kobayashi: "Guiding of One-Dimensional Optical Beam

with Nanometer Diameter", Opt. Lett., Vol. 22, No. 7, pp. 475～477 (1997)
12) T. Katsuyama and K. Ogawa: "Excitonic polaritons in quantum-confined systems and applications to optoelectronic devices", J. Appl. Phys., Vol. 75, No. 12, pp. 7607～7625 (1994)
13) 小林潔，川添忠，大津元一：「近接場光スイッチの提案」，第61回応用物理学会学術講演会・講演予稿集，講演番号3p-D-5，p. 899（平成12年9月）
14) V. V. Polonski, Y. Yamamoto, M. Kourogi, H. Fukuda, and M. Ohtsu: "Nanometric pattering of zinc by optical near-field photochemical vapour deposition", J. Microscopy, Vol. 194, No. 2/3, pp. 545～551 (1999)
15) Y. Yamamoto, M. Kourogi, M. Ohtsu, V. Polonski, and G. H. Lee: "Fabrication of nanometric zinc pattern with photodissociated gas-phase diethilzinc by optical near field", Appl. Phys. Lett., Vol. 76, No.16, pp. 2173～2175 (2000)
16) M. Ohtsu: "Overview", Near-field Optics: Principles and applications, ed. by X. Zhu and M. Ohtsu, World Scientific, Singuapore, 2000
17) 池上徹彦，松倉浩司：「光エレクトロニクスと産業」，共立出版，pp. 5～9 (2000)
18) K. Kobayashi and M. Ohtsu: "Quantum theoretical approach to a near-field optical system", J. Microscopy, Vol. 194, No. 2/3, pp. 249～254 (1999)
19) 会田雄次：「人生の探求」，大和出版，pp. 135～219 (2000)

近接場光によるナノ領域堆積

*科学技術振興事業団，創造科学技術推進事業，大津局在フォトンプロジェクト
**東京工業大学大学院総合理工学研究科
李　謹炯*,[1]・山本　洋**
興梠　元伸*,**・大津　元一*,**

1. まえがき

高度情報化社会の実現のためには光通信システムや光情報処理システムのいっそうの高速化，大容量化が必要であり，そのためには今後これらのシステムを構成する光デバイスの寸法を数十 nm まで小さくして高速化，高密度集積化を図らなければならない．しかし，光は回折のために光波長以下の寸法の領域に局在することが原理的に不可能であるため，従来の光デバイスの寸法は光の波長以下にはなり得ない．このことはナノメートル寸法の光デバイスを動作させるには新概念が必要であることを意味している．

一方，従来の代表的な微細加工技術である光リソグラフィーの精度も光の回折により制限されている．すなわち，その加工精度は光波長程度である．したがって上記のナノメートル寸法の光デバイスの製作には，より高精度な加工技術の開発が必要である．

以上のようなナノメートル寸法の光デバイスの製作，およびその動作のために近接場光（物質表面の非常に薄い領域に存在する電磁場．そのエネルギーは光波長より小さなナノメートル寸法の領域に集中している）を使うことが試みられている[1]．

本稿では近接場光を用いる微細加工の方法，特に光化学気相堆積法について紹介する．これは堆積する元素を含む原料ガスを光エネルギーで解離し，微細なパターンを直接堆積する方法で，工程が単純で，低損傷性，多種材料の二次元集積化が容易，低温プロセス，基板と堆積物質の組み合わせにきびしい制約がないことなどの長所がある．近接場光を用いてこれを行うことにより，光波長以下の寸法の微細なパターンの製作が単一工程で可能となる．さらにナノメートル寸法の光デバイスの製作への応用が期待される．次章では金属原子である亜鉛（Zn）の堆積とその酸化物である酸化亜鉛（ZnO）の堆積とについて紹介する．

2. 近接場光を用いた光化学気相堆積法

真空容器中に設置されたファイバープローブ先端に発生する近接場光を使ってジエチル亜鉛ガスを光解離させ，ガラス基板上に亜鉛を堆積させた．プローブの走査は近接場光学顕微鏡システムを用いて行われた．

ジエチル亜鉛の分子は 4.59 eV（λ=270 nm）以上のエネルギーをもつ光子を吸収し，解離するので，この値以上の光子エネルギーを有し，十分なパワーをもつ紫外域の近接場光が必要となる．紫外域の光源として Ar^+ レーザーの第二次高調波（λ=244 nm）および ArF エキシマレーザー（λ=193 nm）を使用した．

ファイバープローブ先端に十分なパワー密度をもつ近接場光を発生させるため，純粋シリカガラス製のコアを有する紫外域用のファイバーを開発し，波長 244 nm の光の伝送損失を 1.1 dB/m まで減少させた（光通信用の従来のファイバーでは約 96 dB/m）．このファイバーを用いて選択化学エッチングによりプローブを製作した[2]．その結果，直径 100 nm の開口を有するプローブ先端での近接場光のパワー密度は 1 mW の紫外光入力に対して 1 kW/cm^2 に達した．これは亜鉛の微小パターンを短時間で堆積するために十分大きな値である．堆積用の基板とプローブの距離はせん断応力を用いて制御した[3]．

二通りの堆積方法が試みられた．以下ではこれらについて記す．

2.1 前期核形成法

工程は次のとおりである．（1）真空容器にジエチル亜鉛ガスを満たし，数分維持してから排気すると基板表面に吸着層が残る．その吸着層を近接場光で光解離し，堆積の前期核として少数個の亜鉛原子を堆積させる．このとき，プローブを走査することにより多様なパターンの製作が可能である．（2）プローブを基板から避難させた後，ガスを再び真空容器に満たし，ArF エキシマレーザーからの紫外域の伝搬光を直接基板表面に照射すると光解離された亜鉛が選択的に前期核の上に堆積され，パターンが成長する．

この方法によりガラス基板上に堆積しただ円ループ状の亜鉛パターンを図 1 に示す[4]．この図では堆積に使われたプローブをせん断応力顕微鏡用のプローブとして再び用い，形状を観察した結果を示している．パターンの高さは 4 nm であり，これは 50 層の亜鉛原子に対応する．矢印で示す位置での幅は 20 nm であり，この値は同じ光源からの伝搬光を用いた従来の光化学気相堆積法により製作されたパターンの幅の最小値の 1/40 である[5]．ただし，観察された幅の値にはせん断応力顕微鏡のために使われたプローブの形状に依存する分解能が含まれているので，より高分解能の測定を行えばさらに小さな値が得られるはずである．

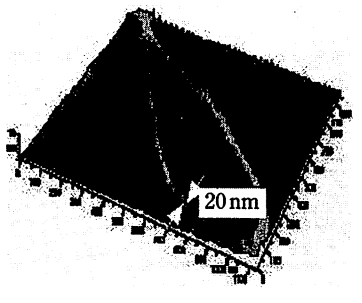

図 1　前期核形成法によりガラス基板上に堆積しただ円ループ状の亜鉛のパターンのせん断応力顕微鏡像．

[1] 現在：韓国 東義大学校 新素材工学科

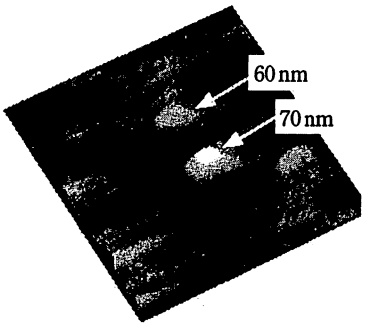

図2　直接気相分解法により堆積した二つの亜鉛ドットのせん断応力顕微鏡像.

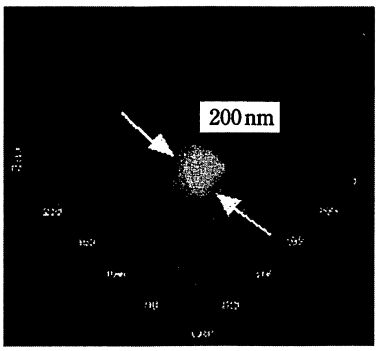

図3　サファイア基板上に堆積した酸化亜鉛ドットのせん断応力顕微鏡像.

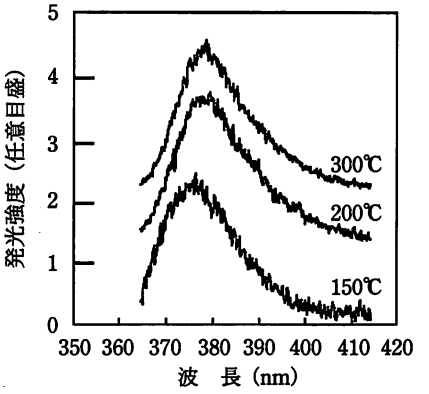

図4　伝搬光を用いてサファイア基板上に堆積した酸化亜鉛の青色室温発光スペクトル．図中の数値は堆積の際の基板温度.

2.2　直接気相分解法

ジエチル亜鉛ガスを真空容器に満たし，プローブ先端からの近接場光を用いてこのガスを直接解離し，亜鉛を堆積させる方法である．この方法は堆積中に原料ガスを交換することによって多様な物質の堆積ができ，二次元集積化に有効であるという利点をもつ.

図2にはこの方法によりガラス基板上に堆積した二つのドット状の亜鉛パターンのせん断応力顕微鏡像を示す[6]．二つのドットの直径はおのおの60 nm，70 nmであった．ただしこれらの値も前節の図1の場合と同様せん断応力顕微鏡の分解能の影響を受けている．したがって真の値はこれより小さい．なお，図1ではプローブと基板との間隔の制御により開口径以下の幅のパターンが実現しているので，これを応用すればさらに小さい寸法のパターンが製作可能と考えられる．一方，ドットの高さは光のエネルギーに比例しており，高精度に制御することができた．すなわち，高さは光エネルギーの増加とともに5 nm/μJの割合でほぼ線形に増加した．また堆積時間は数秒－数分と短く，この時間内ではプローブ先端に堆積する亜鉛の厚みは十分薄く，したがって光学的に十分透明であるため，プローブを汚染することはまったく問題にならなかった．一方，この図にも示すように二つのドットをその直径の値程度，すなわち100 nmまで近接して堆積することができた．このように本方法はドットの堆積位置に関する制御性もきわめて高い.

なお前節および本節の方法では，金属のみでなく絶縁体，半導体などが堆積可能と試算されている．これは，光化学反応を利用しているので基板と堆積物質の組み合わせに対するきびしい制限がないからである．この適用範囲の広さを示す例として，直接気相分解法によりサファイア基板上に堆積した酸化亜鉛(ZnO)のドットのせん断応力顕微鏡像を**図3**に示す.

ここでは真空容器にジエチル亜鉛ガスと酸素とを導入し，近接場光により解離した亜鉛を酸化させることにより酸化亜鉛を堆積させた．このときサファイア基板は150℃以上に加熱した．ドットの直径の測定値は200 nmであるが，これはせん断応力顕微鏡の分解能によって決まる広がりを含んでおり，真の値はさらに小さい.

なお，予備実験として伝搬光を用いて同一条件下で酸化亜鉛の薄膜を堆積したところ，これはC-軸優先方位を示し，XPSを用いた組成分析によると亜鉛と酸素の原子比が1である高品質の結晶性を示した．さらに，**図4**に示すようにHe-Cdレーザー(λ=325 nm)の光励起により励起子からの青色室温発光(λ=380 nm)が観察された．これらの結果から推定すると近接場光により堆積したナノメートル寸法の酸化亜鉛ドットからも青色室温発光が期待される.

3. むすび

近接場光を用いた光化学気相堆積法により，数十ナノメートル寸法の金属，絶縁体，半導体が基板上の必要な位置に，必要な大きさと形状で堆積できることを述べた．この方法によりナノメートル寸法の金属の細線，発光体，変調機能を有する微粒子などを製作することができれば従来の光技術では不可能であったナノメートル寸法の光デバイス，光集積化の実現が可能となると期待される．すでにこの可能性が指摘されるとともに[7]，InGaAsの単一量子ドットに対する飽和吸収分光法による光スイッチング動作が確認されている[8].

1) 大津元一：応用物理 **68**, 431 (1999).
2) S. Mononobe, *et al.*: Opt. Commun. **146**, 45 (1998).
3) E. Betzig, *et al.*: Appl. Phys. Lett. **60**, 2484 (1992).
4) V. Polonski, *et al.*: J. Microscopy **194**, 545 (1999).
5) D. J. Ehrlich, *et al.*: Appl. Phys. Lett. **38**, 946 (1981).
6) Y. Yamamoto, *et al.*: Appl. Phys. Lett. **76**, 2173 (2000).
7) M. Ohtsu: *Technical Digest of 18th Congress of the International Commission for Optics*, USAC/ICO, SPIE vol. 3749, 498 (1999).
8) T. Matsumoto, *et al.*: Appl. Phys. Lett. **75**, 3246 (1999).

分類番号　11.2, 11.7

Nanometric area deposition by optical near-field. Geun-Hyoung LEE*, Yoh YAMAMOTO**, Motonobu KOUROGI*,** and Motoichi OHTSU*,**.
*Ohtsu localized photon project, ERATO, Japan Science and Technology Corp.
**Interdisciplinary Graduate School of Science and Engineering, Tokyo Institute of Technology.
E-mail: ghl@ohtsu.jst.go.jp

研究最先端

光ファイバーの選択エッチングとその応用
(近接場光学顕微鏡用プローブ作製)

財団法人神奈川科学技術アカデミー　光科学重点研究室
物部 秀二，大津 元一*

Selective etching of optical fibers and their applications
(Fabrication of fiber probes for near-field optical microscopy)

Shuji Mononobe, Motoichi Ohtsu
Special Research Laboratory for Optical Science, Kanagawa Academy of Science and Technology

光ファイバーの選択エッチングはコアとクラッドの溶解速度比によって特徴付けられ，高い形状制御性と再現性を持つ光ファイバー微細加工プロセスとしての側面を持つ。我々はこれを近接場光学顕微鏡用プローブ作製に応用し，プローブ技術を体系化することに成功している。

1. はじめに

石英ガラス製の単一モード光ファイバーを弗化水素を含む水溶液に浸漬すると，ファイバーが溶解しその直径が減少すると共に，コア領域が陥没（あるいはテーパー化）する様子が観測される。このような光ファイバーの選択エッチングは不純物が添加されたコアガラスの溶解速度がクラッドのそれよりも大きい（あるいは小さい）ために生じる。近年，これを近接場光学顕微鏡用プローブの作製[1,2]，光ファイバーの評価[3]，ファイバー型マイクロレンズアレイの作製[4]に応用するための研究が行われ，その結果，近接場光学顕微鏡用プローブ技術が飛躍的に向上した。特に選択エッチングの発展型である多段屈折率型ファイバーの複合選択エッチングは実用技術[5]として注目されている。本稿では光ファイバーの選択エッチングについて詳述し，その近接場光学顕微鏡用プローブ作製への応用について概説する。

〒213-0012　川崎市高津区坂戸 3-2-1 KSP 東棟 408-B
TEL 044-819-2075
FAX 044-819-2072
E-mail: mononobe@net.ksp.or.jp

2. 光ファイバーの選択エッチング

図1 (a)(b)はそれぞれ緩衝弗化水素水溶液(BHF) 中にある光ファイバーのコアが陥没する工程とテーパー化する工程の説明図である。ここで，R_1, R_2 はコアとクラッドの溶解速度であり，2つの溶解速度分布に示されるように，(a)では $R_1 > R_2$, (b)では $R_1 < R_2$ である。r_1, r_2 はコアとクラッドの半径を表す。ϕ は陥没部の角度であり，d, θ, L_{TC} はそれぞれテーパー部の先端径，角度，長さである。また，T と τ はそれぞれ陥没工程のエッチング時間とテーパーの先端径を零にするための最小エッチング時間を表す。幾何学的関係から，先鋭角 ϕ, θ，テ

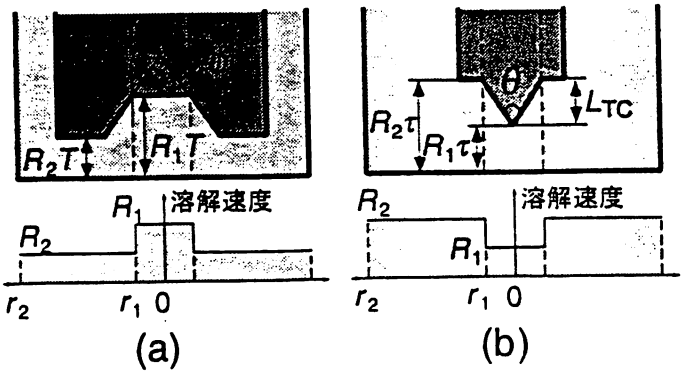

図1 選択エッチングに基づく(a)陥没工程と(b)テーパー化工程の説明図。r_1, r_2, コアとクラッドの半径；R_1, R_2, コアとクラッドの溶解速度；ϕ, 陥没部分の角度；θ, テーパー部分の角度（先鋭角）；τ, 先端径がゼロになる時間；L_{TC}, テーパー部分の長さ。

ーパー部長さL_{TC}，最小エッチング時間τはそれぞれ次のように表される。

$$\sin(\phi/2)=R_2/R_1 \quad (R_2<R_1) \qquad (1)$$

$$\sin(\theta/2)=R_1/R_2 \quad (R_2>R_1) \qquad (2)$$

$$L_{TC}=(r_1-d/2)/\tan(\theta/2) \qquad (3)$$

$$d(T)=2r_1(1-T/\tau) \quad (T<\tau) \qquad (4)$$

$$d=0 \quad (T>\tau) \qquad (5)$$

$$\tau=(r_1/R_1)[(R_1+R_2)/(R_2-R_1)]^{1/2} \qquad (6)$$

(2)式から，テーパー化工程の先鋭角はコアとクラッドの溶解速度比によって決定されることが分かる。

今，二酸化ゲルマニウム添加石英コアと純粋石英クラッドを持つコア半径$r_1=1\,\mu m$，比屈折率差$\Delta n=2.5\%$の分散補償ファイバー[6]を40 wt% NH_4F水溶液：50 wt% HF酸：H_2O =10:1:1の体積比で混合された25度CのBHFに1時間浸漬すると，図2の電子顕微鏡写真に示されるような先端径$d<10$ nm，先鋭角$\theta=20$度のテーパー化ファイバーが高い再現性をもって得られる。さらにNH_4F水溶液の体積比Xとして変化すると，図3(a)に示されるように$X>1.7$において180度から20度の範囲で先鋭角が制御され，$X<1.7$では陥没工程となる。また，Xを10に固定し，先鋭角と比屈折率差の関係を調査すると図3(b)に示すようなような単調減少となる。比屈折率差は二酸化ゲルマニウム添加量とほぼ比例関係にあるので，これはファイバーの最小先鋭角が二酸化ゲルマニウム添加量によって決定されることを意味する。一方，フッ素添加石英クラッドと純粋石英コアからなるファイバーに関して，先鋭角の依存性を同様に調査すると，図4(a)(b)に示すような結果となる。これらより，フッ素添加石英クラッドと純粋石英コアを持つファイバーの先鋭角はBHFの濃度に関して一定であり，比屈折率差(またはフッ素の添加量)のみによって決定されることが分かる。

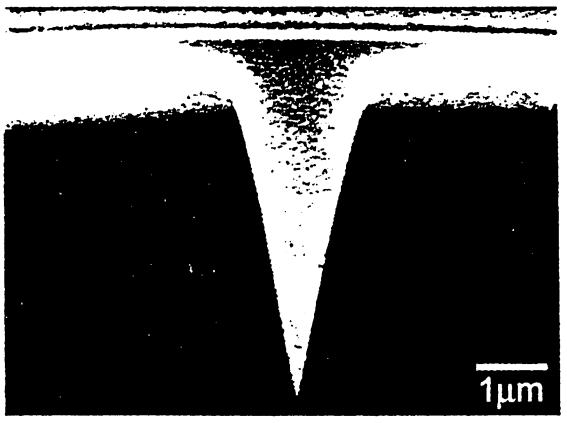

図2 テーパー化された分散補償ファイバーの先端部分の電子顕微鏡写真。$\theta=20$度。

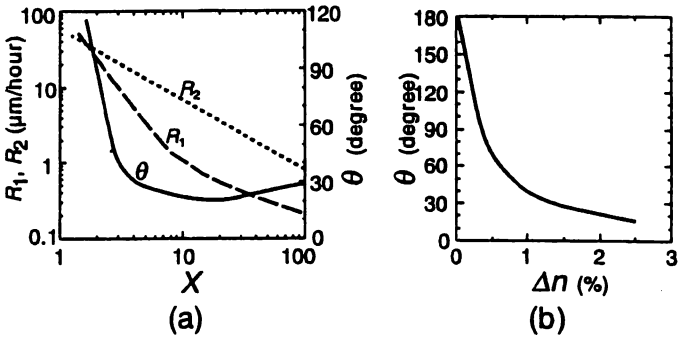

図3 二酸化ゲルマニウム添加石英コアと純粋石英クラッドを持つファイバーの先鋭角 θ の(a)NH_4F 水溶液の体積比 X と(b)比屈折率差 Δn に対する依存性。(a)において $\Delta n=2.5\%$, (b)では $X=10$.

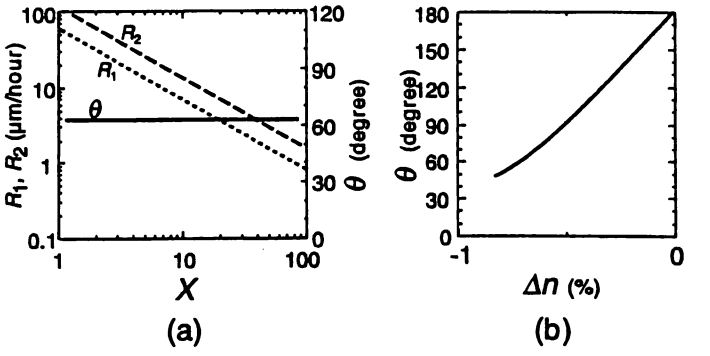

図4 フッ素添加石英クラッドと純粋石英コアを持つファイバーの先鋭角 θ の(a)X と(b)比屈折率差 Δn に対する依存性。(a)において $\Delta n=-0.7\%$, (b)で $X=10$.

3. 近接場光学顕微鏡用プローブへの応用

近接場光学顕微鏡はプローブが微小光源として働く illumination モード，プローブが試料の近接場光を散乱・検出する collection モード，プローブが光源と散乱体の両方として機能する illumination-collection モードの3つの顕微鏡方式に大別される。illumination モードのためには金属平板で形成される微小開口が理想形状のプローブとして考えられる。しかし，実際には試料上を衝突なしに走査しなければならないことを考慮して，テーパー化ファイバーの側面を金属化しその先端を微小開口に仕立てた金属コートファイバープローブがよく用いられている。テーパー化ファイバーの金属化には真空蒸着やスパッタリング等が用いられる。詳細に関しては文献[2]を参照されたい。

先鋭角等の構造パラメーターやプローブ形状は顕微鏡の明るさを決定する重要な要素であり，前述の選択エッチングに基づく形状制御によって高い透過効率（開口径 200 nm に対して $<10^{-2}$）を示す2重テーパー化プローブが実現されている。さらに，筆者は3つの顕微鏡方式と使用波長帯に関するプローブの最適化のため，三重テーパー化プローブ，Protrusion 型プローブ，金属-誘電体-金属コートプローブ，単一モード多モードファイバープローブ，純粋石英コアを持つファイバープローブからなる応用指向プローブ群[2]を提唱し，二酸化ゲルマニウム添加石英，純粋石英，フッ素添加石英からなる多段屈折率型光ファイバーの複合選択エッチングによりその作製に成功している。また，これらのプローブを用いて，単一 DNA 分

子のイメージング[7]，InGaAs単一量子ドットの発光測定[8]，ラマン分光[9]，ポリシラン分子の紫外発光イメージング[10]が行われた。

4. まとめ

光ファイバーの選択エッチング工程に関する幾何学的考察と実験の結果を示し，不純物添加石英ガラスの溶解速度について議論した。さらに，その近接場光学顕微鏡用プローブへの応用についてまとめた。

参考文献

1) 物部秀二 他，“近接場光学用プローブの作製法”，精密工学会誌，**66**(5)，667-670，2000.
2) 物部秀二，学位論文，東京工業大学，1999; http://www.kast.or.jp/Mononobe.pdf.
3) 物部秀二 他，特開平 11-108798.
4) 本望宏 他，信学技報 OPE94-64, 79-84, 1994.
5) http://www2.odn.ne.jp/kawaguchi-opt/
6) 西村正幸，“波長多重用光ファイバー”，Oplus E, **216**, 143-148, 1997.
7) R. Uma Maheswari, et al., “Nanometer level resolving near field optical microscope under optical feedback in the observation of a single-string deoxvribo nucleic acid” Jpn. J. Appl. Phys., **38**, 6713-6720, 1999.
8) T. Saiki et al., “Low temperature near-field photoluminescence spectroscopy of InGaAs single quantum dots”, Jpn. J. Appl. Phys., **37**, 1638-1642, 1998.
9) Y. Narita et al., “Near-field Raman spectral measurement of polydiacetylene”, Appl. Spectroscopy, **52**, 1141-1144, 1998.
10) S. Mononobe et al., “Fabrication of a triple tapered probe for near-field optical spectroscopy in UV region based on selective etching of a multisptep index fiber”, Opt. Commun., **146**, 45-48, 1998.

[II] PAPERS IN OTHER FIELDS

profilometer—a configuration" Appl. Opt. Vol. 37, pp. 4137–4142, 1998.
2. P. Akinson and J.P. Woodcock, *Doppler ultrasound and its use in clinical measurement* (Academic London, 1982) Chap. 2 and Chap. 3, pp. 72–115.
3. S.C. Lin and T.G. Giallorenzi, "Sensitivity analysis of the Sagnac-effect optical fiber ring interferometer," Appl. Opt. Vol. 18, pp. 915–931, 1979.

CWN3 **5:15 pm**

Ultra-high scanning speed optical coherence tomography using optical frequency comb generators

Motonobu Kourogi[1,2,3], Bambang Widiyatmoko[3], Seok-Jeong Lee[1], Motoichi Ohtsu[1,2,4], *[1]Interdisciplinary Graduate School of Science and Engineering, Tokyo Institute of Technology, 4259 Nagatsuta, Midori-ku, Yokohama 226-8502, Japan, Kanagawa Academy of Science & Technology; [2]KSP east building R 408, 3-2-1 Sakado, Takatsu-ku, Kawasaki-shi, Kanagawa 213-0012 Japan; [3]Optical Comb Project, Japan Science and Technology Corporation, G-2 Building Room 1106, Tokyo Institute of Technology, 4259 Nagatsuta, Midori-ku, Yokohama 226-8502, Japan; [4]ERATO Localized Photon project, Japan Science and Technology Corporation, 687-1 Tsuruma, Machida-shi, Tokyo 194-0004, Japan; email: kourogi@ae.titech.ac.jp*

Optical coherence tomography (OCT) has been used to study the geometry and internal structure of objects. It is based on a Michelson interferometer with an optical broadband source. This method has to change the optical path length of a reference arm to match with that of a sample arm. However, since its reference mirror must be continuously moved for depth scans, it requires a long time because it is limited by mechanical movement speed. The reported maximum speed for longitudinal scans is 21 m/s using a rotating cube and prism.[1]

We proposed an ultra high scanning speed OCT using two optical frequency comb generators (OFCG)[2] without any moving parts. Our system includes OFCG1 in the object arm and OFCG2 in the reference arm of usual interferometer instead of a moving a reference mirror. OFCG1 and OFCG2 are modulated with the different modulation frequencies having a frequency difference Δf. The time intervals between output pulses of OFCG1 are shorter than those of OFCG2. Let the output pulses of OFCG1 be t_0, t_1, ... and those of OFCG2 be t_0', t_1', ... Output pulses of OFCG2 are progressively delayed by Δt with respect to the OFCG1 pulses. If the optical path length is same, pulses t_0 and t_0' will interfere with each other. With different optical path length e.g. when the difference in optical path length is $c\Delta t$, pulses t_1 and t_1' will interfere each other simultaneously at a goal because of high temporal coherence of the output pulses of OFCG. Therefore, corresponding set of pulses from both OFCG's interferes each other automatically even for different optical path length.

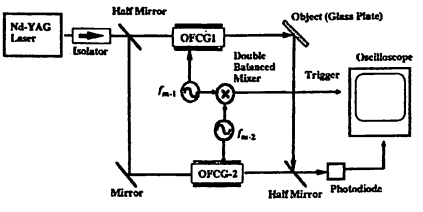

CWN3 Fig. 1. Experimental setup of depth scanning measurement for a glass plate

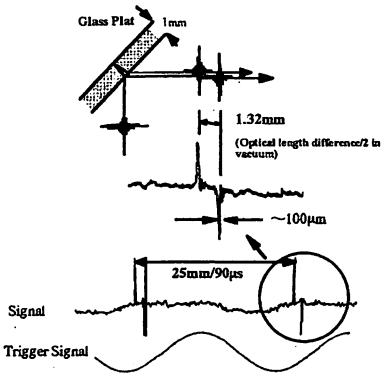

CWN3 Fig. 2. Experimental results of glass thickness measurement.

An experiment has been performed for depth scanning with 1mm glass plate as an object in the configuration of Fig. 1. The light source is a monolithic Nd-YAG laser (1319nm,200mW). OFCG1 and OFCG2 were driven with modulation frequencies of 6.20233 GHz and 6.202319 GHz, respectively, i.e., the frequency difference Δf is 11kHz and corresponds to 275 m/s of the scanning speed of depth. The one way optical path length from a front surface of a slide glass to the back surface was 1.32mm at incidence angle of 45°. Considering incidence angle of 45° the thickness of a slide glass was about 1 mm as shown in Fig. 2. It agrees well with the range of resolution since the depth resolution is approximately 100μm. The scanning speed as high as 10 km/s was observed in our experiment which is mainly limited by electronics means bandwidth.

In summary, we proposed an ultra-high scanning speed OCT by using two OFCG's. The experiment achieved the resolution of about 100μm and depth scanning speed above 10 km/s.

References

1. J. Ballif, R. Gianotti, Ph. Chavanne, R. Walti, RP. Salathe, "Rapid and scalable scans at 21 m/s in optical low-coherence reflectometry", Optics Letters. Vol.22, No. 11, p757–759, 1997.
2. M. Kourogi, K. Nakagawa, and M. Ohtsu, "Wide-Span Optical Frequency Comb Generator for Accurate Optical Frequency Difference Measurement,", IEEE J. Quantum Electron., Vol.29, No. 10, p2693–2701, 1993.

Invited Paper

Past, Present, and future of optical comb generation.

Motonobu Kourogi[1,2,3], Motoichi Ohtsu[1,3]

1) Interdisciplinary Graduate School of Science and Engineering, Tokyo Institute of Technology, 4259 Nagatsuta, Midori-ku, Yokohama 226-8502, Japan.
2) Optical Comb Project, Japan Science and Technology Corporation, 1106,G2, in Tokyo Institute of Technology.
3) Kanagawa Academy of Science & Technology , KSP east building R 408, 3-2-1 Sakado, Takatsu-ku, Kawasaki-shi, Kanagawa 213-0012, Japan.

ABSTRACT

We review here the historical development of an optical comb generation technology. In 1991, an optical comb as wide as 1THz was generated for the first time for the purpose of the optical frequency measurement, and the difference frequency between two lasers was measured. The measured difference frequency was only 500GHz at that time. However, measurable difference frequency has been increased by thousand times in nine years. Finally, absolute frequency measurement of laser has become possible.

1. INTRODUCTION

Accurate frequency measurements of lasers are required for the various applications such as high-resolution spectroscopy, measurements of fundamental physical constants, frequency-division-multiplexed communication network and so on. Though the frequency measurements of microwave oscillators can be accurately realized, the frequency measurements of lasers have not been straightforward because the frequency of lasers is as high as 1THz-1PHz. One must overcome this difficulty and realize the accurate control of the frequencies of lasers to meet the requirements of future opto-electronics. For this purpose, an optical difference frequency measurement system using an optical frequency comb (OFC) generator has been developed over past twenty years [1-46]. Finally, absolute frequency measurement of laser has become possible by using an OFC generator designed with a femtosecond mode-locked laser.

We review here the historical development of an OFC generation technology with main focus on our OFC generator. The OFC generator was based on Electro-Optic (EO) modulator. We begin the article with the outline of OFC history, then describe an OFC generator based on EO modulator and a method of expanding span of OFC generation by using self-phase modulation in optical fiber. We also discuss several unique techniques for use of an OFC in order to get high signal-to-noise ratio, and propose a novel application with two OFC generators.

2. OUTLINE OF OFC HISTORY

The first idea/proposal of basic principle of OFC was reported by J.N.Eckstein et.al [1]. In this paper, authors mentioned An actively mode-locked laser has an important advantage over a passive interferometer. If all modes are properly phase locked, their spacing is rigidly determined by the modulation frequency and is not affected by the exact resonator length, by phase shift in mirror coating.". At the end of 1980's, sinusoidal and pulse modulation techniques for generating optical frequency reference combs [2], optical comb synthesis using optical feedback[3] and a frequency comb with a double acousto-optic modulator were proposed [4,5]. S.N.Bagayev proposed frequency measurement using a mode-locked color center laser [6]. However, to the best of our knowledges, there have not been any reports regarding OFC for frequency measurement reaching optical frequency.

Laser Frequency Stabilization, Standards, Measurement, and Applications, John L. Hall, Jun Ye, Editors,
Proceedings of SPIE Vol. 4269 (2001) © 2001 SPIE · 0277-786X/01/$15.00

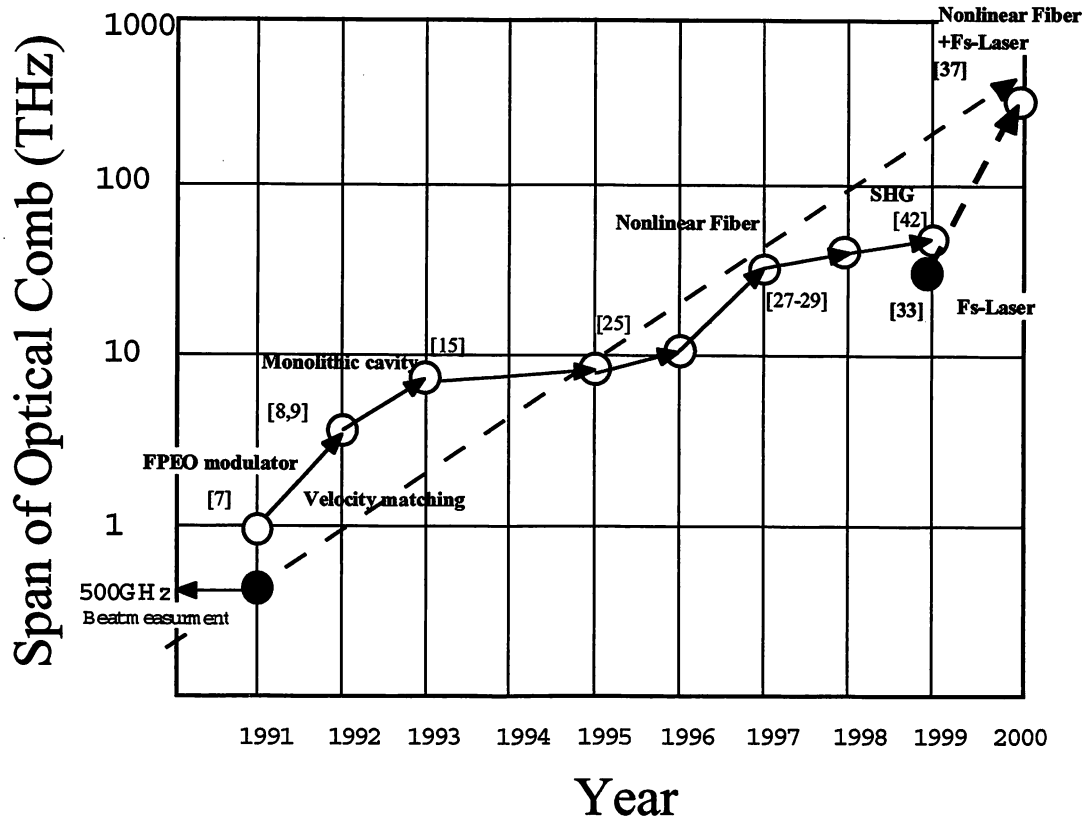

Figure 1: Development of the span in OFC generation.Circles:Span of OFC.Filled circles Measured frequency difference.

In 1991, an optical comb [7], which is based on principle as EO modulators for the purpose of forming ultrashort optical pulses [47], was generated for the first time for the purpose of the optical frequency measurement, and the difference frequency between two lasers was measured. Figure 1 shows the progressive development of the span(or frequency difference measurement) in OFC generation since the first report of measured difference frequency only 500GHz. There has been significant improvement about thousand times in past nine years and today over 300THz difference frequency measurement is possible. Finally, absolute frequency measurement of laser has become possible by use of a mode-locked OFC generator [33-41].

There are three methods of the OFC generation, which are distinguished by the use of

1. External modulation.
2. Supercontinuum generation using self-phase modulation (SPM) inside optical fiber.
3. Stabilized mode-locked laser.

In the first stage of development, the method 1 was used. The OFC generator was developed by many improvements such as novel configuration of the modulator beat detection technique and so on. In the second stage, the two methods 1 and 2 were combined to achieve several times improvement, i.e., SPM in optical fibers was applied to the output of a modulator. An OFC span of 30THz was obtained by SPM. This lead to five times increase in the frequency span of a conventional OFC.

Finally methods 2 and 3 were combined for further ten improvement by using a well stabilized femto-second TiSa: mode locked laser, and a well-designed optical fiber. This was sufficiently broad to contain any fundamental and its second harmonic frequencies of the laser, and this enabled the measurement of the absolute frequency of the laser through the measurement of frequency difference between them.

3. OFC GENERATORS USING FP EO MODULATOR.

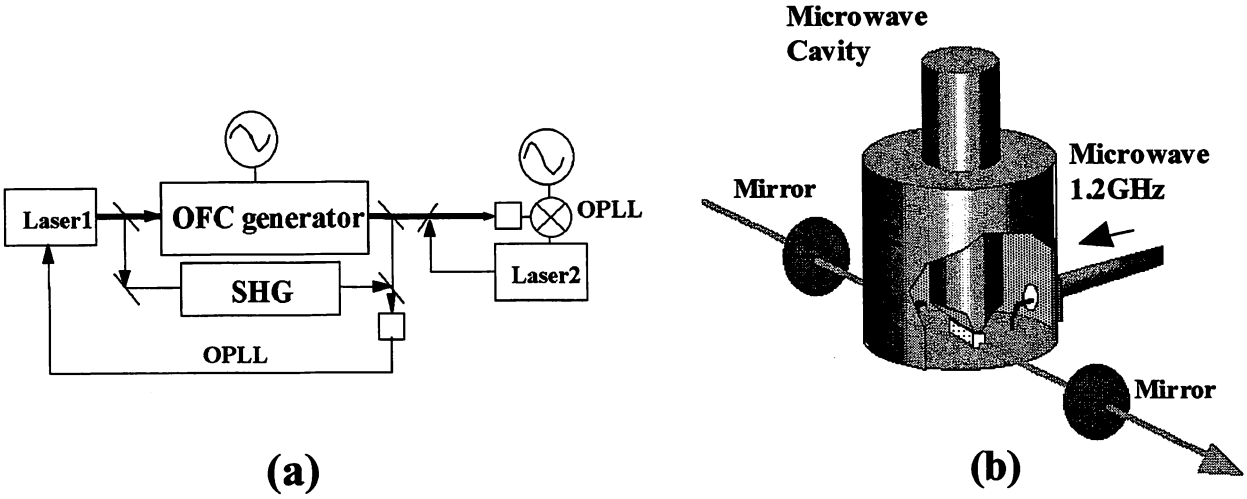

Figure 2: (a) Proposed optical frequency synthesizer [46].(b) The first OFC generator.

The first OFC generator [7] was derived from the Fabry-Perot Electro-Optic (FP EO) modulator which had been proposed for forming ultrashort optical pulses in 1972 [47]. Purpose of this work was to realize highly accurate optical frequency measurement in 1.5 μm wavelength region, and realization of an optical frequency synthesizer. In Fig.2 , the optical frequency synthesizer proposed by us [46] and the first OFC generator are shown. It consists of an efficient $LiNbO_3$ EO phase modulator installed in an optical FP cavity with the modulation frequency being a harmonic of the free-spectral-range. The EO modulator was developed by installing a $LiNbO_3$ crystal inside a coaxial microwave cavity. The modulation frequency was only 1.2GHz. The microwave was amplified up to 10W. This afforded the deep modulation of the light resonating in the FP cavity. By using the OFC generator, we have demonstrated the frequency difference measurement from carrier up to 500GHz. Although this value was not sufficiently large if one compare with recent results, this value was comparable with the frequency difference measurement using metal insulator-metal diode [48].

In 1992, an OFC generator employing velocity matching [49] modulator was realized [8,9]. This method resulted in large modulation frequency of OFC generator increasing the span to several THz. We demonstrated a frequency difference measurement up to 0.5 THz was realized with signal-to-noise ratio exceeding 60dB. The heterodyne optical phase locking with a heterodyne frequency of 0.5 THz in which the residual phase error variance was less than 0.01 rad^2. N.C.Wong at al., also realized an OFC generation and phase locking of an optical parametric oscillator at 665GHz [10]. Accurate optical frequency atlas of the 1.5μm bands of acetylene has been mapped by using this OFC generator [11]. Using a Rb two-photon transition at 0.778 μm as an absolute frequency reference, the absolute frequencies of 90 transitions of $^{12}C_2H_2$ and $^{13}C_2H_2$ were determined in the wavelength range from 1.515 to 1.55 μm with an uncertainty of approx.10^{-9}. Hydrogen-Deuterium 1S-2S isotope shift and absolute optical frequency of the cesium D2 line were measured accurately by using an OFC generator [12,13]. In 1998, two methods for measuring large optical frequency differences: an OFC generator and an optical frequency interval divider chain, which divides a frequency gap successively by two until it becomes accessible to a radio-frequency counter have been compared [14]. By locking two diode lasers to two modulation sidebands of an OFC generator, 1 THz apart, and measuring this interval with a chain of four phase-locked interval dividers, the accuracy of the two techniques within an experimental limit of 6.8×10^{-15} was obtained.

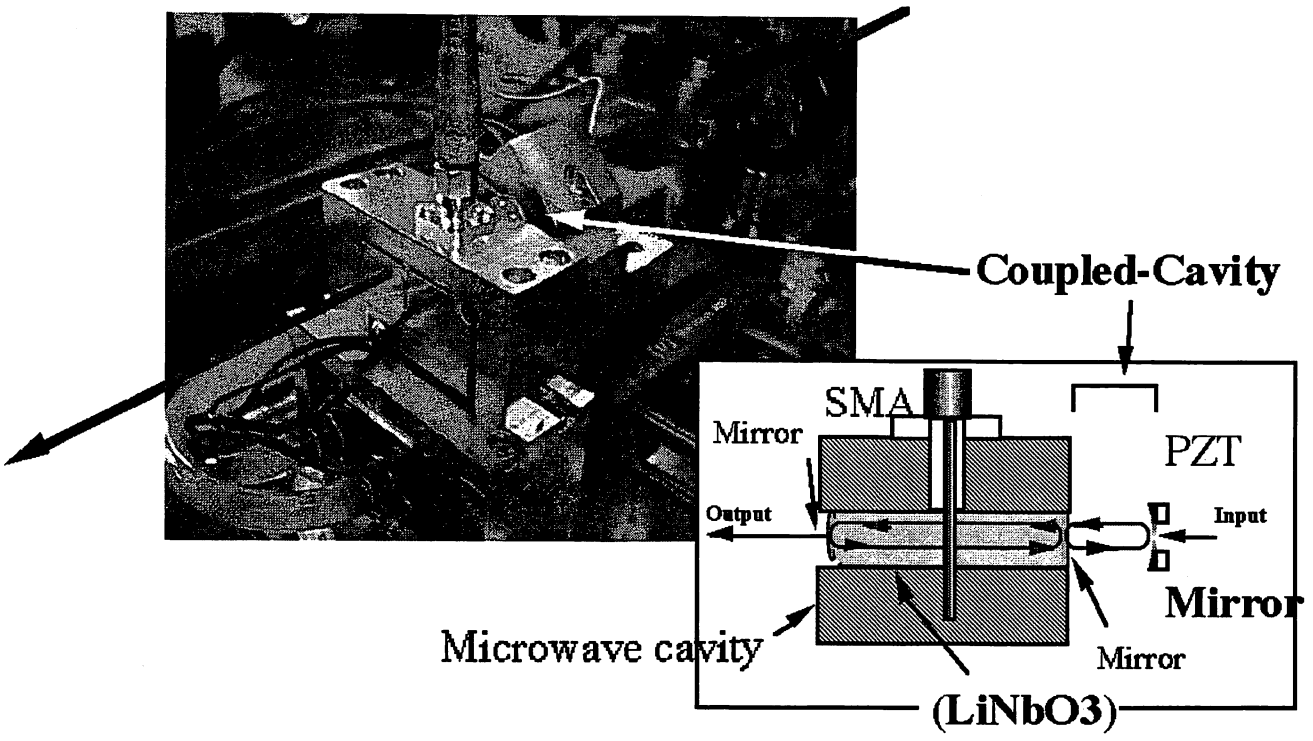

Figure 3: Recent monolithic OFC generator with a coupling cavity.

In order to increase the power transferred to high-order sidebands from the OFC generator, many methods were proposed [15-24]. The two main modifications are:

1. An OFC generator with a monolithic cavity [15].

2. An OFC generator with a coupled-cavity. The original design was proposed and demonstrated by A.Morimoto et.al., [50] while A.S.Bell, et.al., also demonstrated in experimentaly [16].

We employed these features in our OFC generator as shown in Fig.3. The feedback loop for stabilization of cavity in an OFC generator was same as shown in [17]. We chose the way to get the very high finesse of the FP cavity by applying a monolithic cavity structure to the EO modulator with the reflection coatings on both ends. By this way, we could achieve finesse as high as 600. Furthermore, by using it with a coupled-cavity, which works as a window for the incident light and a high reflection mirror for the sidebands, the transmission of the OFC generator can be increased up to 30%. By such approach, all the sidebands inside the span of the OFC can be used [18].

For optical communications, a waveguide type OFC generator was proposed and demonstrated [19-24]. Modification of modulation signal superimposing with the higher harmonic wave was shown. The measurable difference frequency span was increased to about two times that obtained by normal modulation [22].

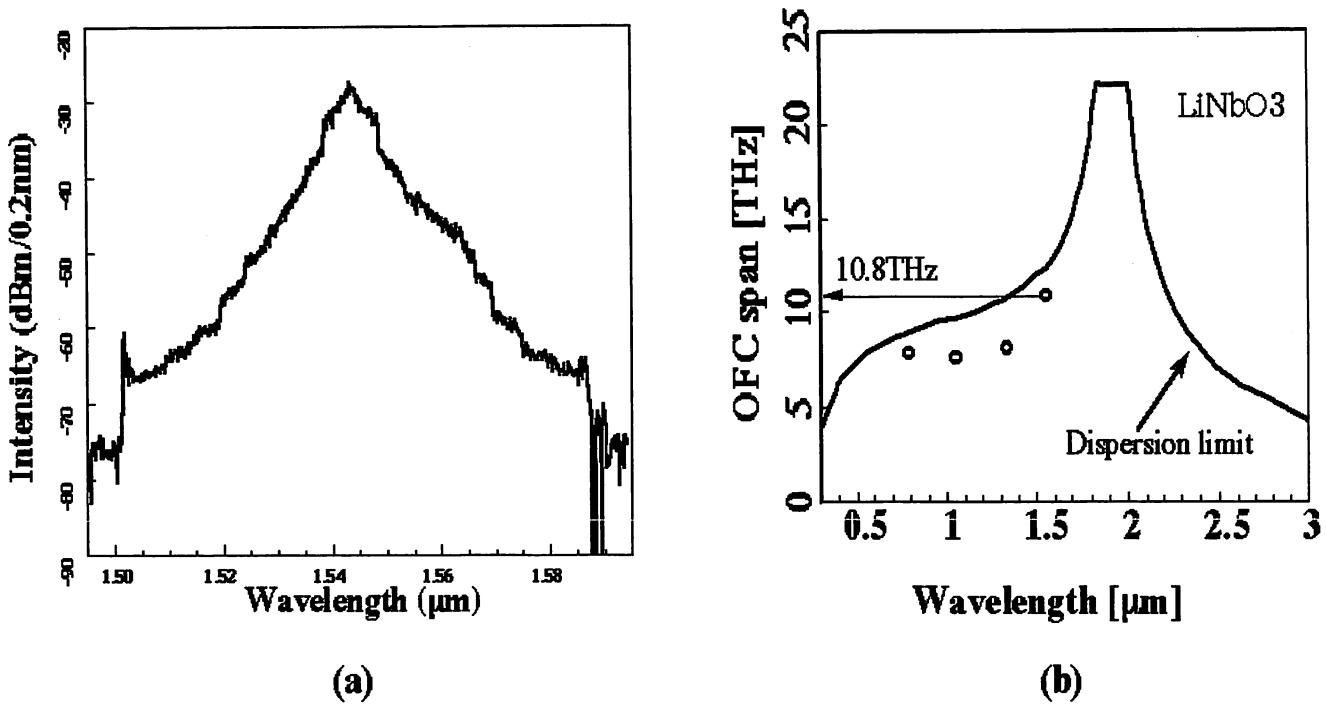

Figure 4: (a)Examples of the spectral envelopes of OFC .(b)Dispersion limit of the span of OFC.
Solid line is the result of theoretical calculation. Open circles are experimental results.

Examples of the spectral envelopes of OFC are shown by Fig.4(a) where the laser wavelength was 1.5μm. Since the modulation frequency was 6GHz which is twice the free-spectral-range of the monolithic cavity and is smaller than the resolution, curve in this figure show the spectral envelopes of the OFC. Since the output of the OFC generator is a Lorentzian pulse train, the spectral shape has exponentially decaying sidebands. The output of OFC generator has decaying sidebands with stepwise discontinuities on the both sides of the spectrum due to the group velocity dispersion of EO crystal ($LiNbO_3$) [25]. The span as wide as 10.8 THz is obtained, which is limited by the group velocity dispersion of the material. When the finesse of the monolithic cavity including the EO modulator is sufficiently high, the limit of the frequency difference measurement is governed by the dispersion [51]. Though dispersion compensation for OFC generation is proposed and demonstrated [26], OFC generation over 10 THz was not realized. This might be owing to the extra loss of dispersion compensation devices.

4. SELF-PHASE MODULATION INSIDE AN OPTICAL FIBER FOR EXPANDING THE SPAN OF OFC.

Although the span of currently available OFC has been expanded beyond 10THz, it is still limited to about 5% of the carrier frequency. For further increase, one has to solve problems such as limited mirror reflection bandwidth, incident microwave power limit to prevent damage to the EO modulator and group velocity dispersion of the EO crystal. Self-phase modulation (SPM) [52] inside optical fiber is very powerful method for expansion of span of OFC.

In 1997, to solve these problems, we have applied the SPM in an optical fiber to the OFC [27-29]. Since output of OFC generator is optical pulses, SPM can be applied for the comb in a nonlinear medium in which a refractive index depends on the optical power. Since this process is the same as supercontinuum generation [53,54], we believed that more than one octave span of OFC generation could be realized [55]. It is also important to note that the power-dependent modulation index is readily increased by the use of a small fiber core. We carried out an experiment at 1.5 μm wavelength region. We considered that optical fibers in this wavelength have low loss and low dispersion because the material dispersion of the fiber can be compensated by the structural dispersion.

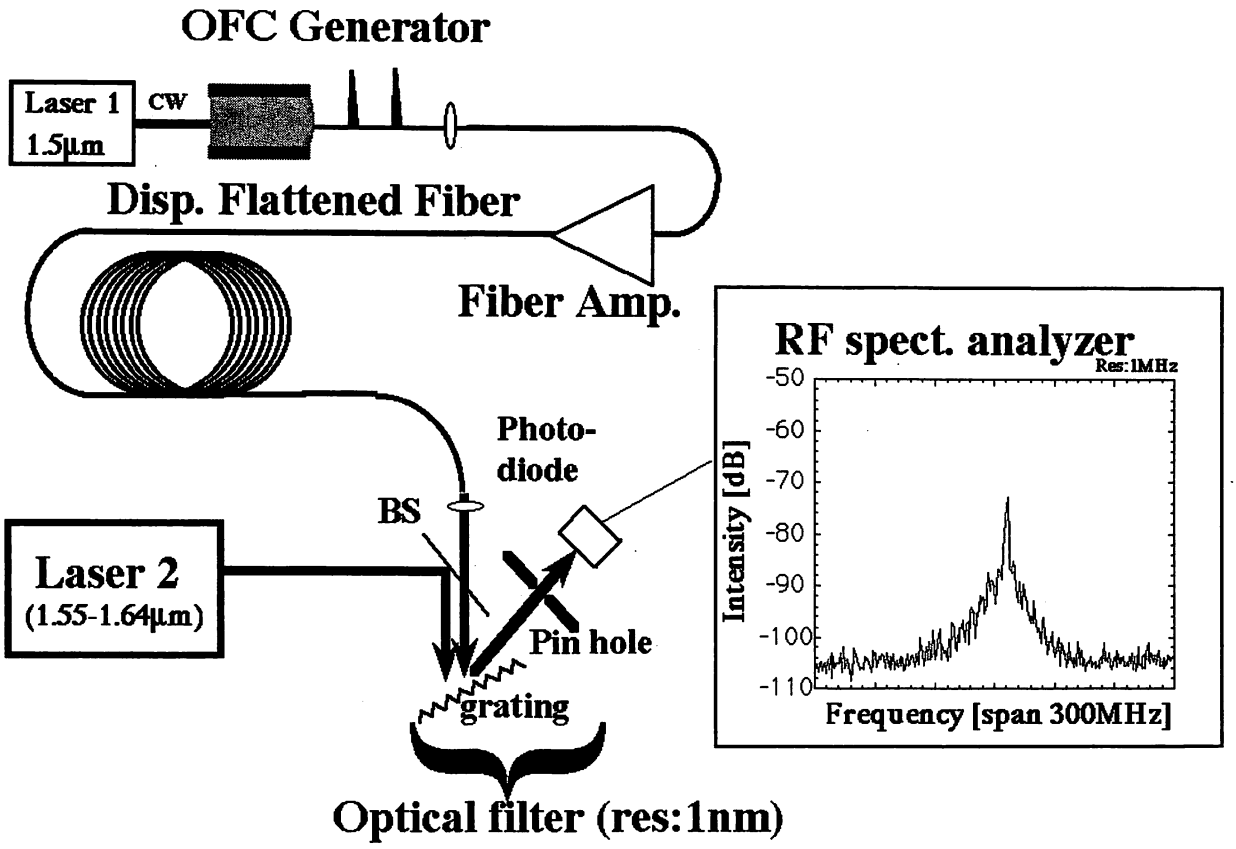

Figure 5: Experimental setup for expansion of a span of OFC by using self-phase modulation inside optical fiber and applying a heterodyne detection. Lasers: Extended cavity laser diode. Disp.Flattened Fiber: 1km length dispersion flattened optical fiber. BS: beam splitter. The inset shows rf-spectra of a beat signal between Laser2 and the comb. The offset frequency from the carrier is 12THz.

The experimental configuration used in the first experiment is shown by Fig.5. The laser beam (4mW) from a 1.54 μm extended cavity laser diode was introduced into the OFC generator. Its output was introduced into a 1km-long dispersion-flattened-fiber(DFF) [56] via an erbium-doped optical fiber amplifier (EDFA). The DFF has an anomalous-dispersion of 0.12 ps/km/nm.The EDFA increased the average OFC power to 50mW which corresponds to peak power of pulses as high as several W. Since SPM under the anomalous-dispersion supports the formation of a soliton, we can expect efficient spectral broadening by the pulse compression of the higher order solitons.

The spectral envelopes of OFC are shown in Fig.6, in which three curves are the spectral envelopes observed with a monochromator with a resolution of 1 nm. Curve A shows the spectral envelope of the output from the OFC generator. The spectral envelopes of curve A exceeded the width of the gain profile of EDFA as shown in curve B that is after being passed through EDFA. The curve C shows that the envelope was extended to a span as large as 30THz with power more than 1nW. The value of 30 THz corresponds to 5000 sidebands, and is about 5 times larger than the span of OFC obtained without a fiber. The measurable difference frequency reached 15% of the carrier frequency.

The optical spectrum from the DFF in the vicinity of several sideband frequencies was heterodyne-detected using an additional laser diode (Laser 2) acting as a local oscillator, a fast InGaAs pin photodiode, and an rf-spectrum analyzer. The Laser 2 output was combined with the comb using a beam splitter. Two lasers were used as Laser 2 for large frequency difference measurements. Because the comb power is much higher than the power of Laser 2, we used a grating and a pinhole as a filter to remove the amplitude noise of the comb. The spectral width of 1nm around the sideband was coupled into the PD. The beat signal was amplified, and its spectrum was measured with an rf-spectrum analyzer.

The inset of Fig.5 shows the heterodyne detected spectrum of the beat signals when the frequency offset from the carrier was 12 THz (1.645μm)[29]. The output power was 50mW and the envelope spectrum of the comb was similar to curve C of Fig. 6. The beat signals were measured with a resolution bandwidth of 1MHz. The intensities are normalized to the shot noise limit produced by Laser 2. The signal-to-noise ratio (SNR) was 32 dB in 1MHz resolution bandwidth. The floor of the beat spectrum, which was 16 dB higher than the shot noise limit, was due to beat noise between the second laser and the spontaneous emission noise around the sideband. The linewidths of the beat spectra were less than a few MHz at the -3dB point. Since the linewidth of the laser was 1MHz, we could not observe linewidth broadening less than 12THz offset. Accuracy of OFC generation in optical fiber was high [30]. The measured beat spectra proved the coherent nature of this process. However the noise floor of the beat signals within 100MHz around the carrier increased with the offset frequency because of higher order multiplication of several additional noise. The noises of these beat signals were given by the beat noise.

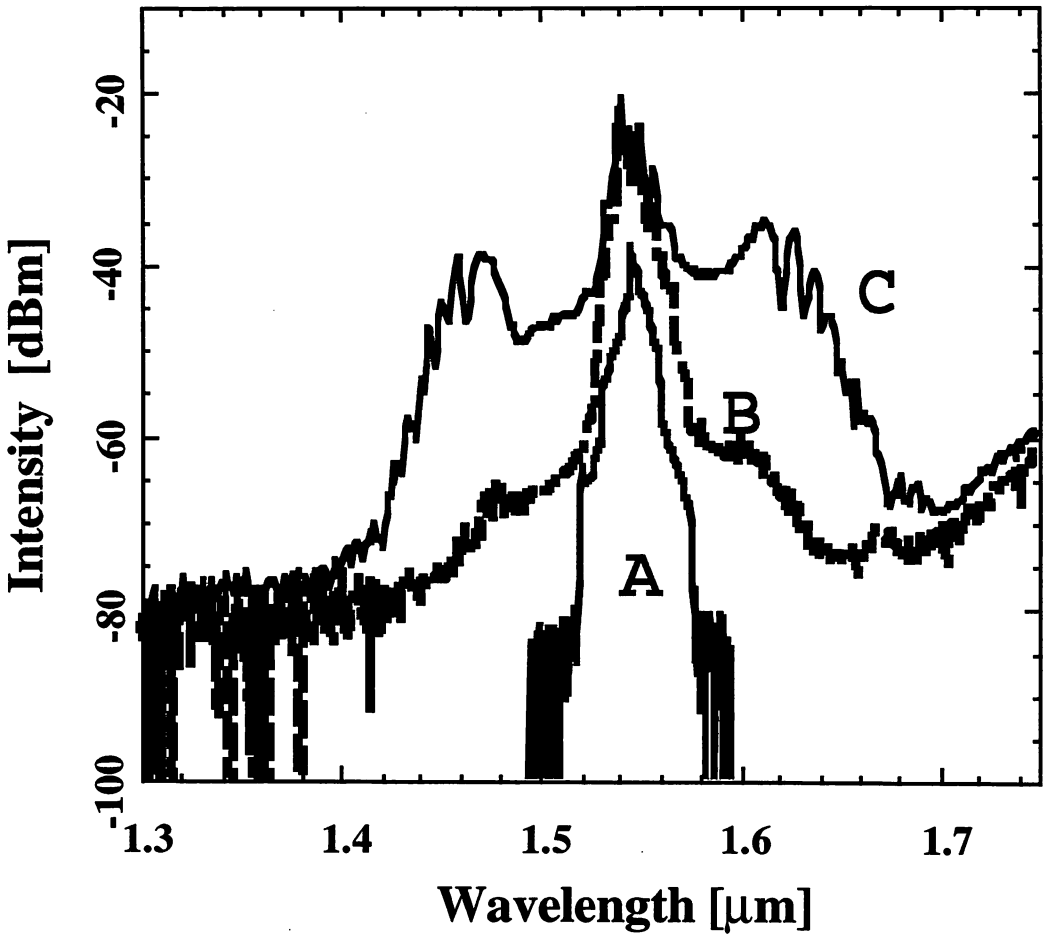

Figure 6: Spectral envelope of OFC. A and B: before and after passed through the EDFA, respectively. C: after passed through the DFF with amplified power of 50mW.

We have used the SPM technique for a high-resolution spectroscopy [31]. In this work, we measured the frequency difference of 14THz between the carrier frequency of the OFC and other laser. It means that all of the sidebands in 30THz span can be used. Much larger span of OFC can be expected by increasing the optical power and improving the characteristics of DFF. Though significantly larger span of OFC was realized by employing larger optical power [32], span of the measurable frequency did not increase.

In order to get much wider span of a comb, it is important to use high peak power fundamental comb before amplification, as the main source of noise for the comb generated in the optical fiber is the amplified spontaneous emission noise. In this context, low repetition rate mode locked laser has advantages. It has very large peak power without use of optical amplifier. Furthermore, recent progress of mode-locked laser has realized very stable modes of a mode-locking laser.

In 1999, Udem et.al., stabilized the modes of a comb of optical frequencies emitted by a mode-locked femtosecond-laser and used it as a ruler to measure differences [33-35]. Their work showed that the modes of a mode-locked laser are distributed uniformly in frequency space within the experimental limit of 3.0 parts in 10^{17} and that the mode separation equals the pulse repetition rate within the experimental limit of 6.0 parts in 10^{16}. They applied these techniques to determine the absolute frequencies of the cesium D1 line at 335 THz (895 nm), the hydrogen 1S-2S transition at 2466 THz (121 nm) and the frequency of a methane stabilized He-Ne Laser at 88.4 THz (3.39 μm) as well as the isotope shift of the 1S-2S frequency. In 2000, Prof.J.L. Hall and Prof. T.W. H nsch used self-phase modulation inside optical fiber for expansion of span of OFC generated from a mode-locked laser [37-41] . The OFC is sufficiently broad to contain fundamentals and its second harmonic frequencies of the laser, enabling the carrier-envelope phase control of femtosecond mode-locking laser and the measurement of the frequency difference between them, thus the absolute frequency measurement of the laser was realized. Recent results can be seen in this conference.

5. METHODS FOR EXPANDING THE MEASURABLE DIFFERENCE-FREQUENCY

Idea to use an OFC as tools for frequency difference measurements is based on the fact that generated sideband from electro-optic modulator has same coherency with the carrier frequency. The basic principle is the use of the generated sidebands from OFC generator with the carrier frequency ν_1 as local oscillators to measure the frequency difference between the Laser 1 and Laser 2 with frequencies ν_1 and ν_2 , respectively. Even if the difference frequency is higher than the response frequency of photo diodes, the value of the difference frequency $\nu_1 - \nu_2$ can be determined by measuring the frequency difference $\Delta\nu$ between K-th generated sideband of laser 1 and the laser 2 i.e., $\nu_1 - \nu_2 = \Delta\nu + K f_m$, where f_m is the modulation frequency of the OFC generator. In this case, the span is limited by the one sideband power, since shot noise limit depends on the lower power of the two beams which relates with beat generation, and the signal to noise level of the beat signal depends on the power of the one sideband. As reported, the measurable span can be increased by modulation frequency (f_m) and or increase in the K value, i.e., increase in the OFC span. Here we describe the other approach to use combs for high signal to noise ratio and wider span.

In a different approach, the expanded comb was used to generate second harmonic OFC. The span of second harmonic combs was two times wider than that of the fundamental comb. In 1998, we tried to expand the combs by this method. 50 THz level was realized using multi period periodically poled $LiNbO_3$. We could measure 22 THz difference frequency from carrier [42]. To our knowledges, this was the first report of SHG of OFC.

Further, when two laser beams are inserted into two OFC generators which are driven by same frequency, and when the beat signal is observed between two beams from OFC generators, many sidebands can create the beat generation. In this case, the signal to noise ratio of the beat signal depends on the total power of the sidebands which related to beat generation, and the increase in signal to noise ratio. In 1995, this method was proposed and demonstrated [43] and optical phase locking using this method was demonstrated [44]. A combination of SHG comb and beat signal between two OFC s is presently being used for carrier-envelope phase control of femtosecond mode-locked laser [37].

All the methods reviewed above can be realized if the two combs are overlapped with each other. If two combs do not overlap or if laser 2 leaves from the comb span, frequency difference can be measured by promoting the nonlinear frequency conversion i.e., second harmonic generation and the sum frequency generation of the two combs [45]. Combination of two nonlinear processes of SHG and SFG will be useful to measure the difference frequency which is the second laser excess out from OFC span. In this case the sum frequency between laser 2 and a part of comb in the range of phase matching bandwidth will generate the beat signal with the second harmonic of a part of the comb. This requires matching of the pulse of SHG comb and SFG comb.

For studying this process, the sum frequency generation between OFC and continuous wave (CW) laser at 1.55μm was done using 19.4 μm poled period of periodically poled $LiNbO_3$. The 19.4 μm period coincides with the second-harmonic phase matching around 1.55 μm of wavelength and also coincidences with sum frequency phase matching between laser 2 and part of OFC to produce the SFG comb at the center frequency 0.776 μm. The SHG comb and SFG comb were confirmed through the observation of the beat signal between them. As a comparison we also measured the beat signal between the fundamental comb and laser, and we confirmed that the span of SFG comb to be wider than the SHG comb. With the use of SFG and SHG comb, the observed signal to noise ratio of the beat signal was 5dB higher than that obtained fundamental comb. This is because using fundamental comb, the beat signals resulted from laser and one sideband. However, when using SHG/SFG comb, the beat signal is generated through many pairs sideband of the SHG comb and SFG comb, and hence the signal will be increased.

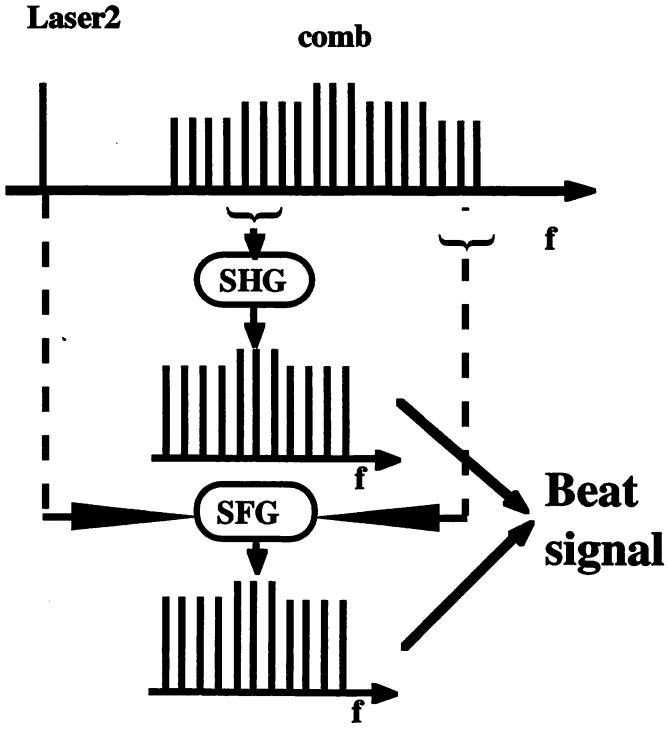

Figure 7: Illustration of beat signal generation using SHG and SFG process

6. NOVEL APPLICATIONS OF OFC GENERATOR

In future, an optical frequency comb is expected to contribute to both the developments of basic physics as well as the industrial applications, such as optical communications. Further, it will be used not only for the frequency control of the light but also for the active control of the waveform. For example, femto-second comb generator can be applied for generation of ultra short optical single-cycle pulse[37]. For optical reflectometry, frequency-shifted feedback laser which generates chirped frequency comb output [57] is an interesting application.

For the purpose of industrial applications, we believe that a waveguide type OFC generator is suitable for optical communications, and identification of order of sideband is important. It can be realized using two comb generators with different modulation. Such a double waveguide optical frequency comb generator shown in Fig.8. The relative modulation frequency of two OFC generators in this device will be easily controlled .The idea of a double comb generators is also seen

in a recent report by D. Weide., et.al., which proposed and demonstrated spectroscopy with two electronic terahertz comb generators [58].

Recently, we considered the other possible applications of such a double optical frequency comb generator for, e.g., optical coherence tomography(OCT).

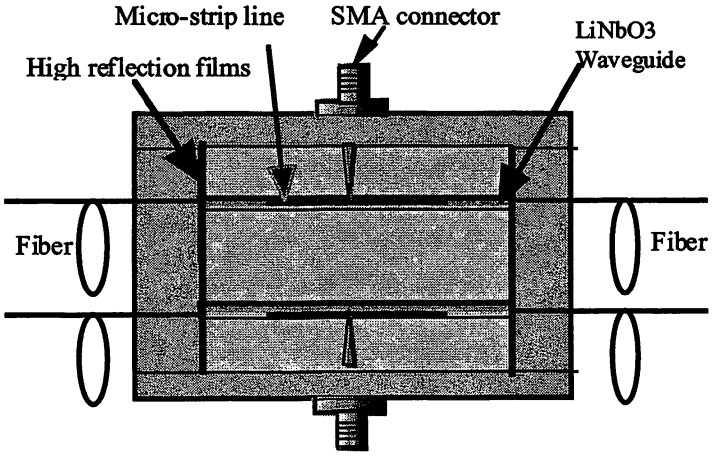

Figure 8: Double waveguide optical frequency comb generator.

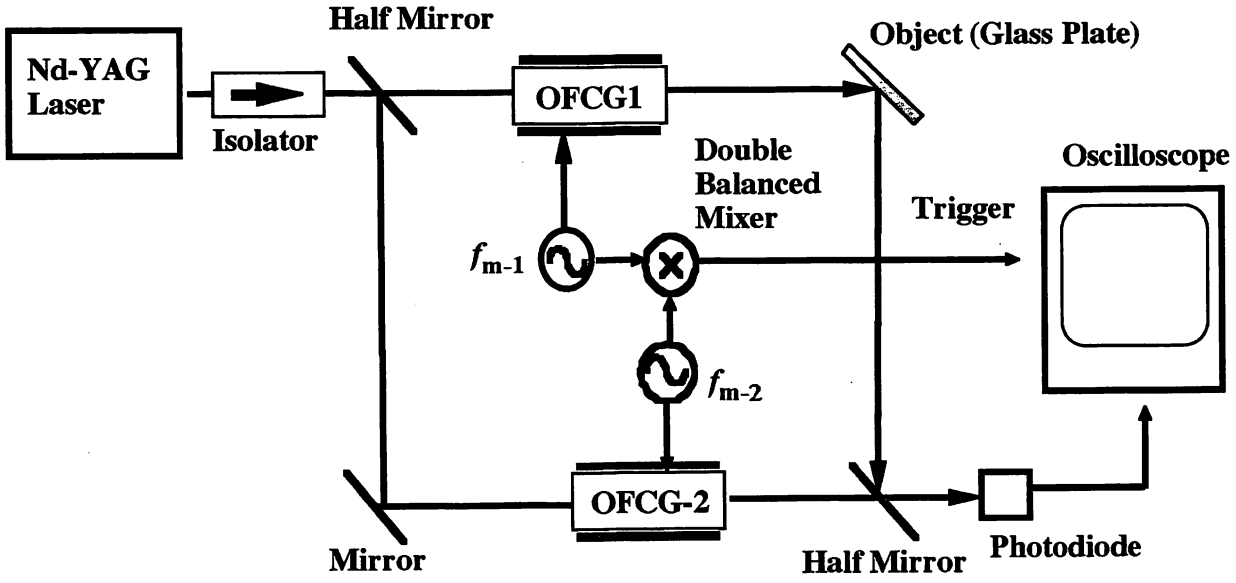

Figure 9: Experimental setup of depth scanning measurement for a glass plate. OFCG's:OFC generators.

OCT has been used to study the conformation and structure of objects. It is based on a Michelson interferometer with an broadband optical source. This method exploits the change the optical path length of a reference arm to match with that of a sample arm. However, since its reference mirror must be continuously translated for depth scans, it requires a long time because it is limited by the mechanical translation speed. The reported maximum speed for longitudinal scans is 21m/s using a rotating cube and prism [59].

We propose here an ultra high scanning speed OCT using two OFC generators(OFCG) without any moving parts. Our system includes OFCG1 in the object arm and OFCG2 in the reference arm of usual interferometer instead of translating a reference mirror. OFCG1 and OFCG2 are modulated with the different modulation frequencies having a frequency difference Δf. The time intervals between output pulses of OFCG1 are shorter than those of OFCG2. Let the output pulses of OFCG1 be t_o, t_1, t_2,... and those of OFCG2 be t_o', t_1', t_2',... Output pulses of OFCG2 are progressively delayed by Δt with respect to the OFCG1 pulses. If the optical path length is equal, pulses t_o and t_o' will interfere with each other. With different optical path length e.g. when the difference in optical path length is $c\Delta t$, pulses t_1 and t_1' will interfere with each other simultaneously at a goal because of high temporal coherence of the output pulses of OFCG. Therefore, corresponding set of pulses from both OFCG's interfere with each other automatically even for different optical path length.

An experiment has been performed for depth scanning with 1mm glass plate as an object in the configuration of Fig.9. The light source is a monolithic Nd-YAG laser (1319 nm, 200 mW). OFCG1 and OFCG2 were driven with modulation frequencies of 6.20233 GHz and 6.202319 GHz, respectively, i.e., the frequency difference Δf is 11kHz and corresponds to 275m/s of the scanning speed of depth. The one way optical path length from a front surface of a slide glass to the back surface was 1.32mm at incidence angle of 45°. Considering incidence angle of 45 ° the thickness of a slide glass was about 1mm as shown in Fig.10. It agrees well with the range of resolution since the depth resolution is approximately 100 μm. The scanning speed as high as 10km/s was observed in our experiment which is mainly limited by the electronics bandwidth.

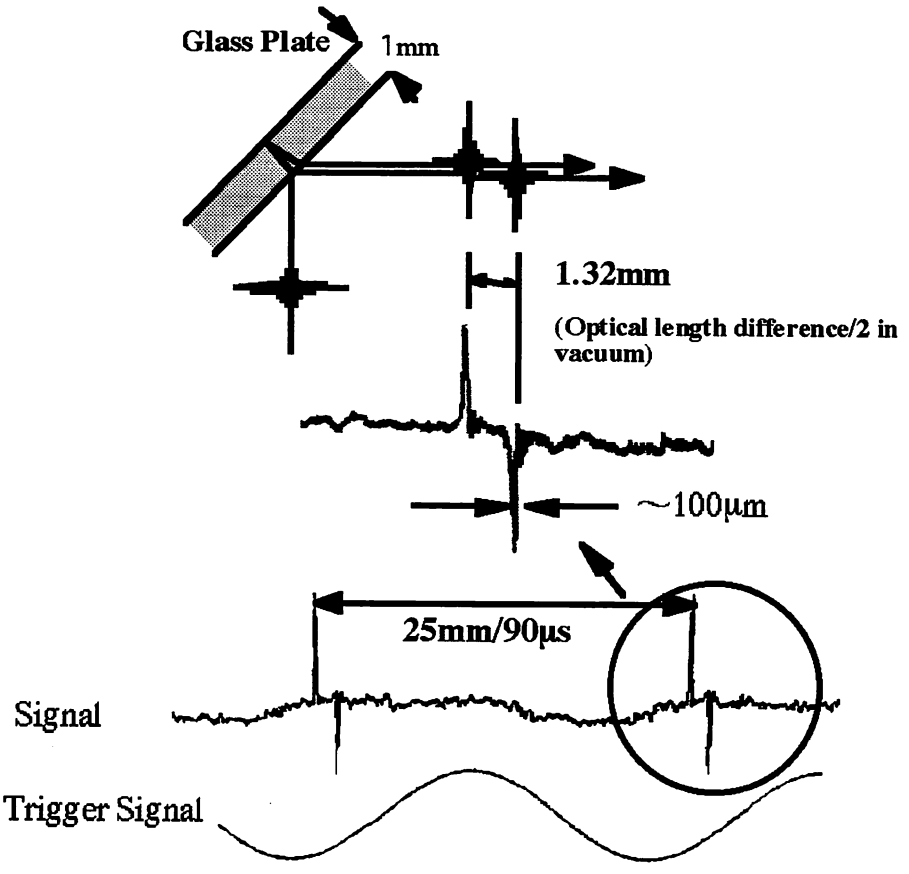

Figure 10: Experimental results of glass thickness measurement.

7. SUMMARY

We reviewed the historical development of the optical comb generation technology. In 1991, we introduced a method using an OFC generated by a conventional EO modulation technique. A THz optical comb was generated for the first time for the purpose of the optical frequency measurement, and the difference frequency between two lasers was measured. The measured difference frequency was 500GHz. After that, the self-phase modulation inside optical fiber was used for the next ten times increase. As a result, the span of the obtained OFC could be increased up to several 10THz.
The measurable difference frequency has been increased by thousand times in past nine years and has presently reached over 300THz with a stabilized femto-second mode-locked laser and self-phase modulation the optical fiber. Finally, absolute frequency measurement of laser has become possible.

In future, the optical frequency comb is expected to contribute not only to the development of basic physics but also to the industrial applications, such as optical communications. Besides, it can be employed for both the frequency control of the light and the active control of the waveform.

REFERENCES

1. J.N.Eckstein, A.I.Ferguson, and T.W. H nsch, Phys. Rev. Lett. No.13, pp.3568(1978)
2. T. G.Hodgkinson, and P. Coppin, , Electron. Lett., Vol.25 ,No.8, pp.509-510(1989)
3. J.P.Shevy and T.G.Hodkinson, Electron. Lett., Vol.26,No.1,pp.28-30(1990)
4. P. Jessen, M.Kristensen, Appl. Opt.vol. Vol.31 ,No.24, pp.4911-4913(1992)
5. M.W.Phillips,G.Y.Liang and J.R.M.Barr,Opt. Commun., Vol.100 ,No.5,6, pp.473-478 (1993)
6. S.N.Bagayev, V.P.Chebotayev,V.M.Klementyev and O.I..Pyltsin,Tenth International Conference on Laser Spectroscopy, M.Ducloy, eds, World Science, pp.91-98(1991)
7. M.Kourogi,K.Nakagawa,C.H.Shin,M.Teshima and M.Ohtsu, in Pro.CLEO Baltimore, paper number CThR57(1991)
8. M. Kourogi, K. Nakagawa, and M. Ohtsu, in Pro. IQEC, Vienna , paper number TuM5(1992)
9. M. Kourogi, K. Nakagawa, and M. Ohtsu, IEEE J. Quantum Electron., Vol.29 ,No.10,pp.2693-2701 (1993)
10. L. R. Brothers, D. Lee and N.C. Wong, Opt. Lett., Vol. 19 ,No.4,pp.245-247(1994)
11. K. Nakagawa, M.de Labachelerie, Y.Awaji, M. Kourogi, T. Enami, and M. Ohtsu, Opt. Lett., Vol.20,No.4, pp.410-412 (1995)
12. A.Huber, Th.Udem, B.Gross, J.Reichert,M.Kourogi,K.Pachucki,M.Weitz, and T.W.H nsch,Phys.Rev.Lett., Vol.80,No.3,pp.468-471 (1998)
13. T.Udem, J.Reichert, T.W. H nsch, and M.Kourogi, Phys. Rev. A. Vol.62,No.3, (2000)
14. Th. Udem, M. Kourogi, J. Reichert, and T. W. H nsch, Opt. Lett., Vol.23 ,No.17, pp.1387-1389 (1998)
15. M. Kourogi, T. Enami, and M. Ohtsu, IEEE Photon. Technol. Lett., Vol.6 ,No.2, pp.214-217 (1994)
16. A.S.Bell,G.M.Mcfalane, E.Riis and A.I.Ferguson , Opt. Lett.,Vol.20 ,No.1,pp.1435-1439(1995)
17. Go. Keang-P and J. M. Kahn , IEEE Photon. Technol. Lett., Vol.5 ,No.6, pp.721-725(1993)
18. M. Kourogi, T.Enami, and M. Ohtsu, IEEE Photon. Technol. Lett.,8 ,No.12, pp.1698-1700 (1996)
19. T. Saitoh, M. Kourogi, and M. Ohtsu, IEEE Photon. Technol. Lett., Vol.7 ,No.2, 197-199 (1995)
20. T. Saito, E.Duran, M. Kourogi, and M. Ohtsu, IEEE Photon. Technol. Lett.,8 ,No.2, pp.287-289 (1996)
21. T. Saito, M. Kourogi, and M. Ohtsu IEEE Photon. Technol. Lett., Vol.8 ,No.10, pp.1379-1381 (1996)
22. T. Saito, M. Kourogi, and M. Ohtsu, IEEE Photon. Technol. Lett., Vol.8 ,No.11, pp.1543-1545(1996)
23. E Durand, T.Saitoh, M. Kourogi, and M. Ohtsu, IEEE Photon. Technol. Lett., Vol.8 ,No.1, pp.163-165 (1996)
24. T.Saito,S.Mattori,S.Kinugawa,K.Miyagi,A.Taniguchi,M.Kourogi and M.Ohtsu, IEEE J.Lightwave Technol.,16 ,No.5,pp.824-832(1998)
25. M. Kourogi, B. Widiyatomoko, Y. Takeuchi, and M. Ohtsu, IEEE J. Quantum Electron., Vol.31 ,No.12,pp.2120-2126 (1995)
26. L.R.Brothers, and N.C Wong, Optics lett., Vol.22 ,No.13, pp.1015 -1018 (1997)
27. M.Kourogi, K.Imai, B.Widiatmoko, and M.Ohtsu, LEOS Summer Topical Meeting. August, IEEE, Piscataway, NJ, USA,97TH8276. p23-24(1997)

28. K. Imai, M. Kourogi, and M. Ohtsu, IEEE J. Quantum Electron., Vol.34 ,No.1, pp.54-60 (1998)
29. K. Imai, B. Widiyatmoko M. Kourogi, and M. Ohtsu, IEEE J. Quantum Electron., Vol.35 ,No.4, pp.559 -564 (1999)
30. K. Imai, Y. Zhao, M. Kourogi, B. Widiyatmoko, and M. Ohtsu, Opt. Lett., Vol.24 ,No.2, pp.214-216 (1999)
31. C. Ishibashi, M. Kourogi, K. Imai, B. Widiyatmoko, A. Onae, and H. Sasada,Opt. Commun., Vol.161 ,No.4, pp.223-226(1999)
32. K. Imai, M. Kourogi, and M. Ohtsu, in proc.CLEO/Pacific Rim,Chiba Japan, July,p113,ThA1(1997)
33. Th,Udem, J,Reichert. R,Holzwarth, T,H nsch. and M,Kourogi, in proc. of the Annual Frequency Control Symposium.2, pp.620-625(1999)
34. Th. Udem, J.Reichert, R.Holzwarth, T.W. H nsch, Phys. Rev. Lett. Vol.82,No.18, pp.3568-3571(1999)
35. Th. Udem, J.Reichert, R.Holzwarth, T.W. H nsch, Opt. Lett., Vol.24 ,No.13, pp.881-883(1999)
36. J.Reichert, R.Holzwarth, TH.Udem, T.W. H nsch, Optics communications. Vol. 172 ,No.1, pp.59-69(1999)
37. D.J.Jones, S.A.Diddams,J.K.Ranka,A.Stentz,R.S.Windeler,J.L.Hall,S.T.Cundiff,Science, Vol.288 ,No.28,April, pp.635-639(2000)
38. S.A.Diddams, D.J.Jones, J.David , Jun Ye, Steven T. Cundiff, Steven, J.L. Hall, J.K.Ranka, R.S. Windeler, R.Holzwarth, Th.Udem, T.W. H nsch, Phys. Rev. Lett. Vol.84 ,No.22, pp.5102-5106 (2000)
39. S.A.Diddam, D.J.Jones,Jun Ye,T.M.Fortier, R.S.Windeler, S.T.Cundiff, T.W. H nsch, John LHall, Optics and photonics news. Vol.11 ,No.10, pp.16-24 (2000)
40. Jun Ye, John L. Hall, S.A. Diddams, Opt. Lett.,. Vol.25 ,No.22, pp.1675 -1678(2000)
41. D.J.Jones, S.A.Diddams, M.S.Taubman, S.T.Cundiff, Long-Sheng Ma, J. L. Hall, Opt. Lett.,Vol.25 ,No.5, pp.308 –309(2000)
42. B.Widiyatmoko, K. Imai , M. Kourogi, and M.Ohtsu,Opt. Lett., Vol.24 ,No.5, pp.315-317(1999)
43. M. Kourogi, B. Widiyatomoko, and M. Ohtsu, IEEE Photon. Technol. Lett., Vol. 8 ,No.4, pp.560-562 (1996)
44. B. Widiyatmoko, M. Kourogi, and M. Ohtsu ,IEEE Photon. Technol. Lett., Vol.11 ,No.4, ,pp.460-462(1999)
45. M.Kourogi, Workshop on Optical Frequency Measurement, Synthesis and Stability,Perth, Western Australia September 30 to October 4, invited(1998)
46. M.Kourogi, Thesis in Japanease, January. Tokyo Institute of Technology (1993)
47. T.Kobayashi, T.Sueta , Y.Cho and Y.Matsuo, Appl. Phys. Lett., Vol.21 ,No.8, pp.341-343 (1972)
48. R.E.Drullinger,K.M.Evenson,D.A.Jennings,F.R.Petersen,J.C.Bergquist and Lee Burkins, Appl. Phys. Lett., Vol.2,No.2, pp.137-138(1983)
49. B.Y.Lee, T.Kobayashi, A.Morimoto and T.Sueta, in Proc. CLEO, Baltimore, May, paper number CTuR4(1991)
50. A.Morimoto, A. Shibagaki and T.Kobayashi, in Proc. CLEO, Baltimore, May, paper number CThS84(1993)
51. T.Kobayashi, A.Morimoto ,T.Fujita, K.Amano,T.Uemura and T.Sueta, Ultrafast Phenomena V(1986)
52. G.P. Agrawal."Nonlinear Fiber Optics".ACADEMIC PRESS, Inc., (1989)
53. T.Morioka, S.Kawanishi., K.Mori, and M.Saruwatari. Electron. Lett., Vol.30,No.10, pp.790-791, (1994)
54. H.Nishioka, W.Odajima, K.Ueda, and H.Takuma.Opt. Lett., Vol.20, No.24, pp.2505-2507, (1995)
55. Y.Kubo, H.Kanamori, H.Yokota, and S.Tanaka. In Conf. Proc. ECOC'90, pp.505-508(1990)
56. L.F. Mollenauer, R.H. Stolen, J.P. Gordon, and W.J. Tomlinson. Opt. Lett., Vol.8, pp.289-291, (1983)
57. K.Nakamura, T. Miyahara, and H. Ito, Appl. Phys. Lett., Vol.72 , No.21,pp.2631-2634(1998)
58. D.W.Weide,J.Murakowski, and F.Keilmann,IEEE transactions on microwave theory and techniques. Vol.48, No.4, pp.740 –744(2000)
59. J.Ballif, R. Gianotti, Ph. Chavanne, R. Walti, R P. Salathe, Opt. Lett.,.Vol.22, No.11, pp.757-759(1997)

Generation of Expanded Optical Frequency Combs

Motonobu Kourogi[1,2], Kazuhiro Imai[1],
Bambang Widiyatmoko[1], and Motoichi Ohtsu[1,2]

[1] Tokyo Institute of Technology
4259 Nagatsuta, Midori-ku, Yokohama 226-8502, Japan
[2] Kanagawa Academy of Science and Technology
KSP East Building, Room 408,2-1,Sakado 3-chome, Takatsu-ku,
Kawasaki 213-0012, Japan
kourogi@ae.titech.ac.jp

Abstract. We present a method to expand optical frequency combs (OFC) using self-phase modulation in an optical fiber. The initial OFC is generated using a resonant electro-optic modulator and exhibits a span of less than 10 THz. The span of a broadened OFC can reach up to 50 THz in the 1.5 μm wavelength domain. Second-Harmonic Generation (SHG) of this OFC has also been demonstrated. The span of a second-harmonic comb can also reach up to 50 THz but in the 0.8 μm region. We also demonstrate an innovative method to make frequency-difference measurements between two laser signals when the difference frequency between the lasers is larger than the span of the OFC.

1 Introduction

Accurate frequency measurements of lasers are required for various applications, such as frequency-division-multiplexed communication networks, high-resolution spectroscopy, or measurements of fundamental physical constants [1,2]. Although one can make very accurate measurements of the frequency of microwave oscillators, the measurement of laser frequencies is not so straightforward, because laser frequencies fall in the range of 1 THz to 1 PHz (10^{12} to 10^{15} Hz) where normal electronic frequency-counting techniques are not applicable. One must overcome this difficulty and realize accurate control of the frequencies of lasers so that future optical electronics can be developed.

For this purpose, an optical difference frequency-measurement system using an Optical Frequency Comb (OFC) generator based on a Fabry–Pérot Electro-Optic (FPEO) modulator has been proposed and demonstrated [3,4,5,6,7,8,9,10,11]. By applying an OFC to frequency difference measurements between two lasers, it is possible to measure frequency differences up to as high as several terahertz. The measurement accuracy has been compared with other methods of optical difference frequency measurement, e.g. Optical Parametric Oscillator (OPO) [12] or optical frequency interval dividers [13,14]. It was shown that the accuracy of both methods was better than the experimentally measurable limit of 6.8×10^{-15} [14].

A. N. Luiten (Ed.): Frequency Measurement and Control,
Topics Appl. Phys. **79**, 315–335 (2001)

When one uses an OFC Generator (OFCG) in conjunction with a tunable laser, one can create a stable and coherent light source that is tunable over 10 THz, i.e. the basis to an optical frequency synthesizer or an optical frequency sweep generator [15]. For this application, the tuning range of the optical frequency synthesizer depends on the span of the OFC that can be generated from a standard laser.

Recently, we have applied the output of a conventional electro-optic OFCG to an optical fiber for the purpose of expanding the span by Self-Phase Modulation (SPM) in the fiber [16]. An OFC span of 50 THz was obtained by SPM in the fiber using a high-intensity pulse train from a conventional OFCG [17]. This is a frequency span expansion by five times that of a conventional OFC. It is expected that, by further development of this technique, even wider spans will be available. If an OFC is sufficiently broad to contain both the fundamental and the second-harmonic frequencies of some laser, one could directly measure the frequency difference between the first and second harmonic, and thus clearly determine the absolute frequency of the laser.

Here we will describe a study of OFC generation that includes a review of the generation of the OFC with a conventional OFCG, the expansion of the comb by the SPM principle, as well as a proposal for a method to make frequency-difference measurements larger than the span of the OFC. In Sect. 2, we explain the basics of an OFC, and show an OFCG based on an FPEO modulator. In Sect. 3, we show an expansion of the OFC span by SPM in optical fiber and we discuss the frequency fluctuations of the OFC. In Sect. 4, we give a method to make frequency-difference measurements between two lasers that are separated in frequency by more than the span of the OFC.

2 Conventional OFCG Based on EO Modulators

Frequencies of electromagnetic waves can be measured by relative measurement. In order to measure the relative frequency between a standard frequency and a frequency under test, the heterodyne frequency between them is measured. When the relative frequency exceeds the bandwidth of the counter, a comb generator can be advantageously used.

For microwave-frequency applications, a comb generator generates a monopulse train with a constant repetition frequency which is locked to the standard, as shown by Fig. 1(a). When a Fourier transformation is applied to this signal, the spectrum of this pulse train becomes a comb shape, as shown by Fig. 1(b) where the frequency difference between adjacent sideband components is constant. Therefore the frequency of each sideband component is a multiple of the standard frequency. Even if the difference between the standard frequency and the frequency under test is larger than the bandwidth of the heterodyne detection, the measurement of the frequency difference between one sideband of the comb and the frequency under test is possible.

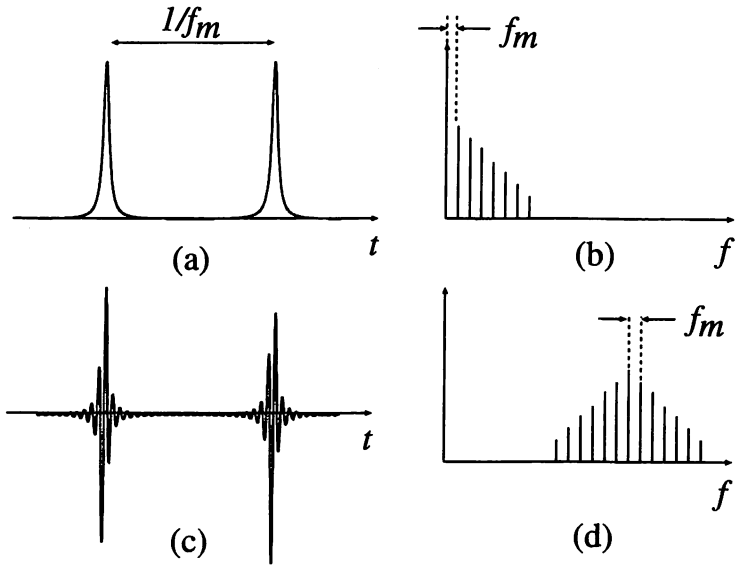

Fig. 1. Waveforms and spectral shapes of combs; (**a**) and (**b**) for the microwave; (**c**) and (**d**) for the light, respectively

For optical applications, the generation of the monopulse train with a constant repetition frequency as shown by Fig. 1(b) is not practical. However, it is possible to generate the envelope pulse shown by Fig. 1(c). When transformed by the Fourier operator, the spectrum of this envelope pulse train becomes a frequency comb centered at the carrier frequency (see Fig. 1(d)). In order to make each sideband component of the comb the equivalent of a frequency standard, the frequency of the carrier must be stabilized and the carrier linewidth must be sufficiently narrow to be able to detect a heterodyne signal with high sensitivity. One solution for this problem is to use an external modulator such as the OFCG. By modulating a narrow-linewidth stabilized laser whose frequency is known, each sideband component of the comb becomes a potential frequency standard.

2.1 Optical Frequency Comb Generator (OFCG)

Figure 2(a) shows a conventional OFCG that can generate a wide-span OFC. Such modulators can also be used for the purpose of short optical-pulse generation [11]. It consists of an efficient electro-optic (EO) phase modulator installed in an optical Fabry–Pérot (FP) cavity. The modulator is driven by a microwave signal that is a harmonic of the cavity's Free-Spectral-Range (FSR). The OFCG can realize deep modulation of the light which is in resonance with the FP cavity. The waveform of the output becomes an optical pulse train with a Lorentzian shape whose repetition frequency is twice that of the modulation. The pulse width is expressed by $\frac{1}{2Ff_m\beta}$, where F is the finesse of the FP cavity, β is the modulation index of the single pass EO modulator, and f_m is the modulation frequency.

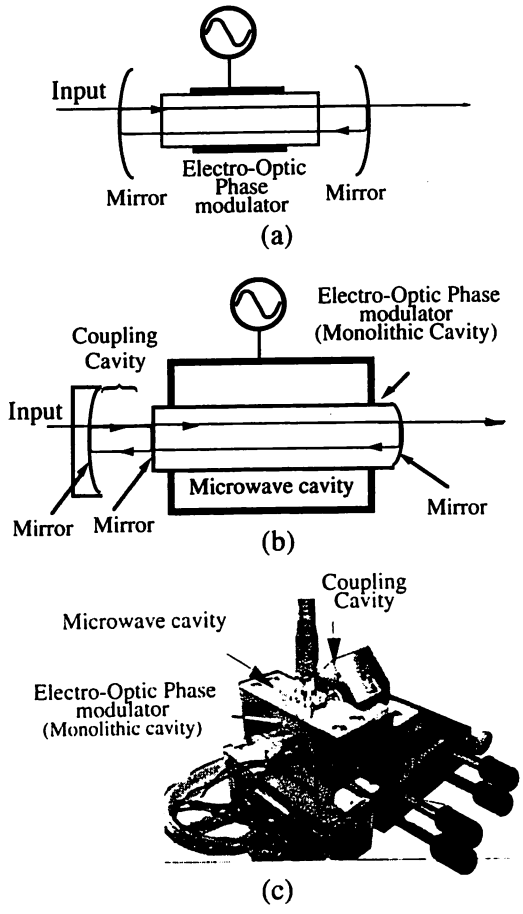

Fig. 2. OFC generator: (**a**) conventional type; (**b**) monolithic type with a coupling cavity; (**c**) Photograph of (**b**)

In order to increase the power transferred to high-order sidebands, a high finesse FP cavity including a highly efficient modulator is required. So, in order to get the highest possible finesse, we have chosen to create a monolithic cavity structure [4] by placing high-reflection coatings on both ends of the EO modulator. By this method, we could achieve a finesse of 400–600. Furthermore, by using it with a coupled-cavity [7], which works as a window for the incident light and a high-reflection mirror for the sidebands, the transmission of the OFCG can be as high as 25%. In Figs. 2(b) and (c) a monolithic-type modulator with a coupling cavity is shown. For all the experiments in this chapter, we used this OFCG.

Examples of the spectral envelopes of an OFC are shown Fig. 3 where the laser wavelength was 1.5 μm. The modulation index was 0.7 rad, and the finesse of the monolithic cavity was about 600. The OFC modulation frequency is 6 GHz, which is twice the FSR of the monolithic cavity. Since this modulation frequency is less than the resolution of the spectrometer, the curves in Fig. 3 show the spectral envelopes of the OFC. Curve A shows the spectral envelope of the output when the monolithic cavity was locked to the

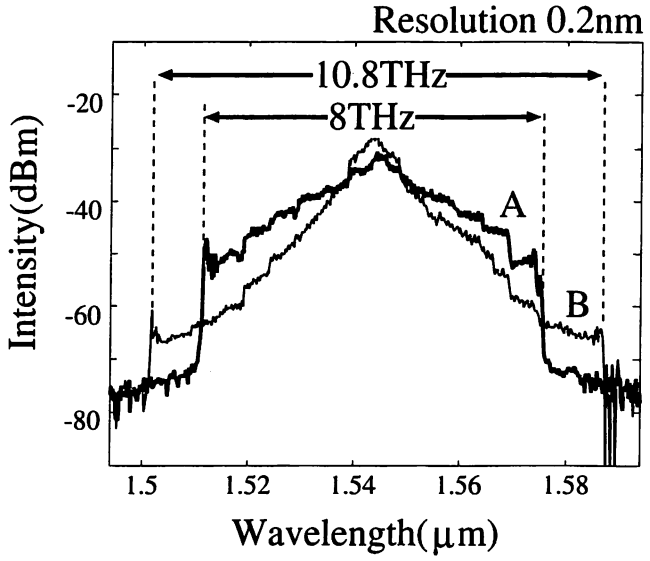

Fig. 3. Spectral envelopes of OFCs generated with a conventional OFC generators. See text for discussion of curves A and B

laser frequency. Since the output of the OFCG is a Lorentzian pulse train, the spectral shape is approximately that of exponentially decaying sidebands. The output of a general OFCG demonstrates these decaying sidebands in addition to stepwise discontinuities on the both sides of the spectrum due to the group velocity dispersion of an EO crystal ($LiNbO_3$) used as a modulator [5]. In the case of curve A the spectral width is limited by material dispersion of the EOM to about 7.7 THz. When the monolithic cavity was locked to the point slightly offset from the exact laser frequency, the OFC span can be increased to 10.8 THz, as shown in curve B. Nonetheless, the span is still limited by the group velocity dispersion of the modulator material.

2.2 Dispersion Limit

When the finesse of the monolithic cavity, including the EO modulator, is sufficiently high, the limit of the frequency-difference measurement is governed by crystal dispersion. The dispersion limit of the span of the optical comb is given by

$$2\sqrt{\frac{2\beta c}{\pi D\lambda_o^2 L_c}},$$

where $D \equiv \frac{\lambda_o}{c}\frac{\partial^2 n_e}{\partial \lambda^2}$ is the material dispersion of the crystal used for the EO phase modulator, λ_o is the wavelength of incident laser to the OFCG, c is the speed of light in a vacuum, n_e is the refractive index of the EO crystal, and L_c is the length of the crystal [5]. In accordance with this, we can calculate the dispersion limit of the span of the optical comb on Fig. 4 as a function of wavelength of laser. The theoretical result is in good agreement with the

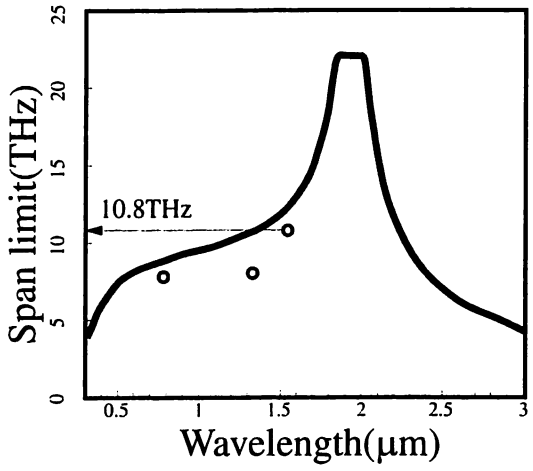

Fig. 4. Dispersion limit of the span of OFC. *Solid line* is the result of theoretical calculation; *open circles* are experimental results

measured results. When operating the OFCG in the 1.8 μm wavelength range, the group velocity dispersion of the crystal becomes small. In this situation, higher-order terms of the dispersion can govern the limit of the span of the comb.

2.3 Additive Phase Noise Characteristics of the OFC

Acoustic, electrical, and temperature fluctuations disturb the creation of the sidebands of an OFC. Imperfect control of the coupling cavity creates amplitude noise. Imperfect control of the resonant condition of the OFCG produces additional phase noise on the the k sideband, where k is the frequency multiplication factor. To create the k sideband, the resonant light needs to make $k/(2\beta)$ round trips in the cavity (see Appendix B of [5]). Therefore the phase noise intensity due to fluctuations of the monolithic cavity is $(\frac{k}{2\beta})^2$ times for the k sideband over the first-order sidebands. Furthermore, any noise from the microwave generator is also multiplied the factor k. In a frequency-multiplication process the total noise intensity grows as k^2. In Sect. 5 of [1], it is pointed out that this will lead to carrier collapse, in which case the carrier frequency of high-order sidebands would be buried in the noise.

Despite this expectation, it is important to note that we have never observed this type of behavior in experiments with our conventional comb generator. The is because there is a mechanism which suppresses phase noise in the comb generation process. In order to create the kth sideband ,the resonant light has to make $\frac{k}{2\beta}$ round trips in the cavity. During this circulating period, the phase noise of the microwave source is averaged. Since one round trip time in the cavity is $\frac{1}{FSR}$, the averaging time is expressed by $\tau = \frac{k}{2\beta FSR}$. Therefore, it is understood that even though the noise of the microwave generator is multiplied and added to the phase of the optical sideband component, it

is filtered with a cutoff frequency expressed by $\frac{\beta FSR}{\pi k}$. This is the mechanism which suppresses phase noise in the comb generation process.

3 Expansion of the OFC Span

Although the span of currently available OFCs has been expanded to more than 10 THz, this is only about 5 percent of the carrier frequency. For further increases, one needs to solve problems such as limited mirror reflection bandwidth, limits to the microwave modulation power because of potential thermal damage to the EO modulator, and group velocity dispersion of the EO crystal.

To circumvent these problems, we have applied the output of the OFCG to a fiber. In transmission through the fiber the comb undergoes Self-Phase Modulation (SPM) [18]. Since the output of an OFCG is a series of optical pulses, SPM can be applied to the comb by a nonlinear medium in which a refractive index depends on the optical intensity. Since this process is the same as super-continuum generation [19,20], a span of more than 100 THz is potentially available [20]. We carried out an experiment in the 1.5 μm wavelength region as optical fibers have low loss as well as low dispersion in this range. This low dispersion arises from a compensation of the material dispersion of the fiber by structural dispersion. It is important to note that the power-dependent modulation index can be readily increased by the use of a small fiber core. This indicates a potential to even further expand the OFC span.

3.1 Experiment

The experimental configuration is shown in Fig. 5. The laser beam (4 mW) from a 1.54 μm extended cavity diode laser was introduced into the OFCG. Its output was introduced into a 1-km-long Dispersion Flattened Fiber(DFF) [21] via an Erbium-Doped optical Fiber Amplifier (EDFA). The DFF has an anomalous dispersion of 0.12 ps/km/nm and a mode field diameter of 6.1 μm. The EDFA increased the average OFC power to between 50 mW and 250 mW,

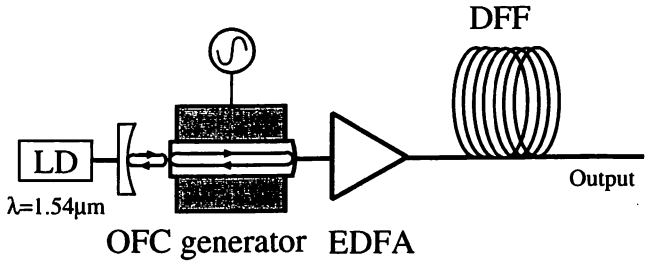

Fig. 5. Experimental setup. LD: Extended cavity laser diode. EDFA: optical fiber amplifier. DFF: 1 km length of dispersion-flattened optical fiber

which corresponds to a peak pulse power of between 2 W and 10 W. Since SPM, in the anomalous-dispersion regime, can support the formation of a soliton, we can expect efficient spectral broadening by the pulse compression of the higher-order solitons [22]. Curves C and D in Fig. 6 are spectral envelopes of the OFC after passing through the DFF with an output power of 50 mW and 250 mW respectively.

The initial OFC was generated by an OFCG as described earlier with a span similar to that shown by curve A in Fig. 3. The shortest pulses are obtained when the monolithic cavity is exactly locked to the laser frequency, even though curve B in Fig. 3 exhibits a larger spectral width. We have monitored the output from the EDFA with an autocorrelator. The full width at half maximum of the autocorrelation signal was 2.0 ps. Since this width is predicted to be twice the output of the OFCG (assuming a Lorentzian pulse shape), the full width at half maximum of the output pulse from EDFA is predicted to be 1.0 ps. Although the width of the output pulse from an OFCG, calculated by $1/(2Ff_{\mathrm{m}}\beta)$, predicts a pulse duration of 200 fs for the experimental conditions described, the dispersion of the EOM distorted the pulse shape and hence broadened the pulse.

The spectral envelopes of OFC are shown on Fig. 6. The curves were observed with the aid of a monochromator with a resolution of 1 nm. Curve A shows the spectral envelope of the output from the OFCG. It was not mandatory to maximize the span of the OFCG for these experiments as the spectral envelope of the OFCG exceeded the gain profile of the EDFA (as shown in curve B) even for a medium span. Curve D shows that the envelope was extended to a span as large as 50 THz with power more than 1 nW. (We choose the 1 nW level since this is the required power for a beat

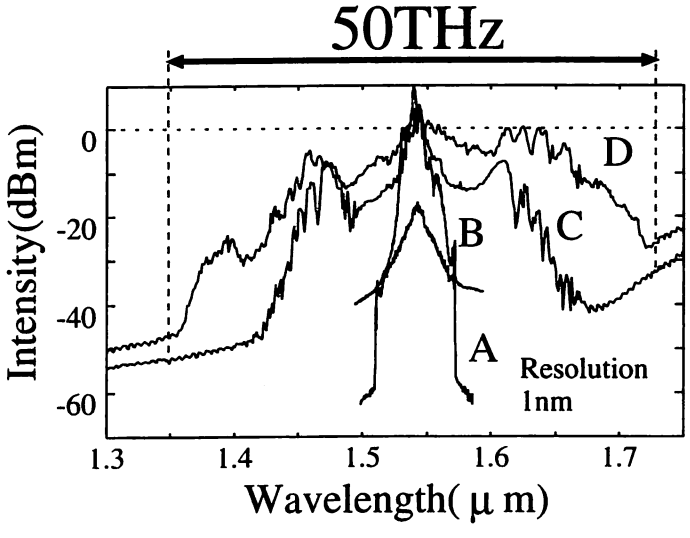

Fig. 6. Spectral envelope of an OFC. Curves A and B: before and after the comb has passed through the EDFA. Curves C and D: after comb has passed through the DFF with amplified power of 50 mW and 250 mW respectively

measurement with high signal-to-noise ratio.) A span of 50 THz would contain 8000 sidebands, and is about five times larger than the span of OFC obtained without fiber. The difference frequency between the two ends of the OFC reaches 25% of the carrier frequency.

We have used this broad OFC for high-resolution spectroscopy [23]. In this work, we measured frequency differences of up to 14 THz between the carrier frequency of the OFC and another laser. An even larger span OFC can be expected by employing larger optical power and improving the characteristics of the DFF.

Curve C on Fig. 6 is symmetric with a characteristic three-peak structure, as is predicted by numerical simulations. The side peaks are formed around 80 nm (9 THz) away from carrier. The peaked structure is caused by a higher-order group velocity dispersion in the optical fiber.

We have also observed effects that make the spectrum asymmetric in curve D, such as stimulated Raman scattering. Spectral broadening of the OFC was not observed when the output of EDFA was launched in the opposite direction of the fiber. This indicates that the dispersion characteristic of the other end of the fiber was significantly different. In addition, the width of the OFC obtained in the experiment was larger than that expected from the theoretical result, although the three-peak structure was in agreement with the numerical simulations. These discrepancies might be due to the fact that we ignored variations in the dispersion characteristics along the fiber, which are caused by the core diameter variations around the designed value. The group velocity dispersion characteristic of DFF is varied by the core diameter variations through the structural dispersion. The intensity of the side peaks in the three-peak structure is lower and the width of each peak is broader. This broadening is thought to be caused by a dispersion variation of the fiber because the exact position of the side lobes depends on the dispersion.

3.2 Noise Analysis

The spectral broadening of a pulse train is a result of four-wave mixing between the different comb modes, which means that the mode separations of the generated sidebands are maintained. However, any practical spectral broadening process also contains other noise sources, such as spontaneous emission from the optical amplifier, laser noise and microwave oscillator noise. Since these noise sources can increase the phase noise intensity through the intensity-dependent refractive index, they will degrade the quality of the generated sidebands. In this section we describe the experimental results of beat signal measurements between the comb and other single-mode lasers. Applying a heterodyne detection method we have investigated the contribution of these noise sources and, furthermore, proved the coherent nature of the nonlinear process.

Figure 7 shows the experimental setup for the beat signal measurement. The optical spectrum from the DFF in the vicinity of several sideband fre-

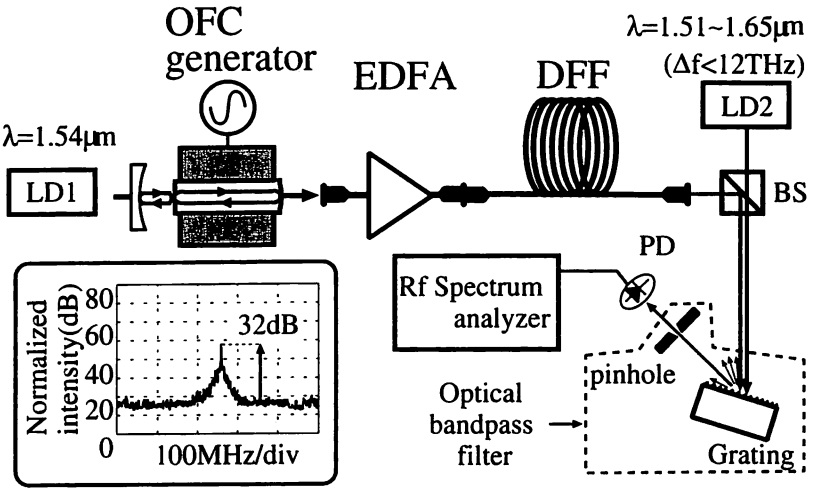

Fig. 7. Experimental setup. BS: beam splitter. The inset shows rf-spectra of a beat signal between LD2 and the comb. The offset frequency from the carrier is 12 THz. The intensities are normalized to shot noise produced by LD2

quencies was heterodyne-detected using an additional Laser Diode (LD2) acting as a local oscillator, a fast InGaAs pin Photo-Diode (PD) and an RF spectrum analyzer. The LD2 output is combined with the comb using a beam splitter. Two lasers were used as LD2 for large frequency-difference measurements. The total tunable range of the two lasers was between 1.51 μm and 1.65 μm in wavelength, and the maximum frequency offset from LD1 was 12 THz. Because the comb power is much higher than the power of LD2, we used a grating and a pinhole as a filter to reduce the amplitude noise of the comb, and to select the correct part of the comb. A spectral width of 1 nm around the appropriate sideband was coupled into the PD. The beat signal was amplified, and its spectrum was measured with an rf-spectrum analyzer.

The inset of Fig. 7 shows the heterodyne-detected spectrum of the beat signals when the frequency offset from the carrier was 12 THz (1.645 μm). The output power was 50 mW and the envelope spectrum of the comb was similar to curve C of Fig. 6. The beat signals were measured with a resolution bandwidth of 1 MHz. The intensities are normalized to the shot noise limit produced by LD2. The SNR was 32 dB in a 1 MHz resolution bandwidth. The noise floor of the beat spectrum, which was 16 dB higher than the shot noise limit, was due to beat noise between the second laser and the spontaneous emission noise around the sideband. The linewidths of the beat spectra were less than a few megahertz at the −3 dB point. Since the linewidth of the laser was 1 MHz, we could not observe linewidth broadening less than 12 THz offset. The measured beat spectra proved the coherent nature of the process. However, the noise floor of the beat signals within 100 MHz around the carrier increased with the offset frequency because of higher-order multiplication of several additional noises.

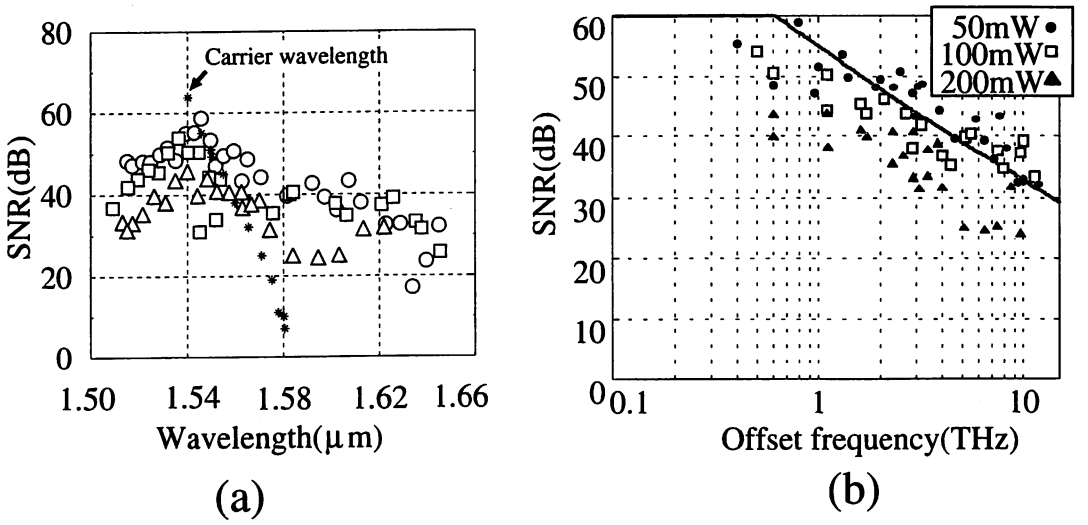

Fig. 8. Dependence of the SNR on the offset frequency from carrier as a function of the average output power of EDFA. *circles*, *squares* and *triangles* show the measured SNR for 50 mW, 100 mW and 200 mW; respectively. *stars* gives the SNR obtained from a conventional OFCG. (**a**) wavelength dependence; (**b**) frequency dependence

Figure 8(a) shows the dependence of the SNR on the offset frequency from the carrier for several average output powers of EDFA: Circles, squares and triangles show the measured SNR for the EDFA power of 50 mW, 100 mW and 200 mW respectively. The noises of these beat signals were given by the beat noise. Stars show the SNR measured with a conventional OFCG without SPM. Because of the shot-noise-limited SNR of the conventional OFC, the SNR decreased exponentially, corresponding to the exponentially decreasing sideband intensity. The maximum measured offset frequency was 5 THz, which was observed with a SNR of 10 dB. The decrease of the SNR as a function of offset frequency was much slower than an equivalent measurement with a conventional OFCG. This is because the variation of noise intensity was also similar to the measured spectral profile. However, the SNR of the comb produced by SPM also decreased gradually with offset frequency, and decreased also with the average power. The decrease in the SNR was measured as 20 dB per decade at each EDFA power level (see Fig. 8(b)).

3.2.1 Noise Sources

Potential noise sources for a comb expanded with an optical fiber include:

- Amplified Spontaneous Emission (ASE) noise
- noise of the modulation signal
- imperfect control of both cavities in the OFCG
- laser noise
- environmental perturbations such as acoustic pressure and temperature
- spontaneous emission noise produced in the parametric amplification process.

Although spontaneous emission due to the parametric process will determine the limit of SNR of the SPM sidebands, the contribution was found to be negligible when compared with ASE from the EDFA. Carrier collapse is particularly important for higher-order sidebands in SPM, because the noise amplitude is multiplied by the same factor as the sideband order, and the mechanism which suppresses phase noise in the OFCG does not occur in the optical fiber. The carrier can thus collapse because of phase noise in the rf modulation signal, or because of fluctuations in the cavity length, or because of amplitude fluctuations at the fiber input.

ASE noise was added to the amplified comb at a level 30 dB higher than the shot-noise limit because of the amplifier gain of 23 dB and a noise figure of 7 dB for 50 mW output power. The noise spectrum is uniform over a wide frequency range of the EDFA. The ASE noise imposes white noise on both the amplified sidebands and the additionally generated sidebands in DFF. This can be see on the inset of Fig. 7. Since the higher orders of the fiber-generated sidebands are generated with a higher multiplication factor, the SNR decreases with increasing sideband order. This simple consideration shows that the SNR of sidebands should decrease by approximately 20 dB per decade, at least while linewidth broadening due to carrier collapse is not significant. Thus a large span and a high SNR of the initial comb are required for high-power and high-quality OFC generation.

Since the kth sideband of the OFCG output has a phase deviation which is k times as large as the phase deviation of the rf signal, the mixing products between the sidebands in an optical fiber maintain the phase deviations in proportion to the order of the sideband. Though there is a mechanism which suppresses phase noise in the comb generation process in a monolithic cavity (see Sect. 2.3), this mechanism is not effective with the beat signal generated from sidebands more than 1 THz away from the carrier. This is because these sidebands are generated by repetition of four-wave mixing among the different sidebands less than 1 THz of the comb originally generated by OFCG. The measured relative intensity in the phase noise pedestal at the 12 THz beat signal (see inset in Fig. 7) was larger than that of 1 THz beat signal, showing that the phase noise around the beat signal increased with sideband order. In the measured beat signals, the intensity in the foot of the beat signals increased by the same factor.

The phase deviation due to fluctuations of the monolithic cavity increases in proportion to the order of the sideband, and this instability of the OFCG affects the measured beat spectrum, especially with large offset frequency. Therefore fluctuations of monolithic cavity of the OFCG will also cause carrier collapse due to the large phase deviations. We have confirmed that the phase pedestal was broadened by imperfect control of the monolithic cavity. The procedure of this mechanism is explained in Appendix B of [5].

Fluctuations of the front coupling-cavity causes amplitude fluctuations of the comb. We found that the measured beat signal included large-amplitude

fluctuations. Because the spectral broadening effect depends on the output power, small input power fluctuations introduce large fluctuations in the sideband power. When the power fluctuation at the output of the OFCG was 20% of the average power, sideband intensity at 7 THz offset from carrier varied by more than 10 dB. The intensity fluctuation was reduced to less than 3 dB when the output power fluctuation was reduced to a few percent of the average power by stabilization of the front cavity.

The amplitude noise of the laser incident upon the OFCG, which is small compared with its phase noise, produces phase noise through the intensity-dependent refractive index in the fiber. In addition, the phase noise of this laser is converted to amplitude noise by its passing through the monolithic cavity of the OFCG. The amplitude noise increases the phase noise of sidebands by SPM. We compared two beat signals which were obtained before and after SPM at 1 THz offset frequency. Sidebands in the beat signals, which were generated by unwanted phase modulation, were enhanced by 20 dB after SPM with 50 mW average power. The noise in the foot of the beat signals was larger than that of conventional OFCG even around the carrier frequency. Therefore the phase noise of the comb is increased in the combination of the OFCG and SPM.

Figure 9 shows a beat spectrum measured with a frequency difference of 14 THz between the carrier frequency of the OFC and a 1.66 μm laser [23]. Although the SNR was still 20 dB in bandwidth of 1 MHz, the linewidth of the beat spectrum was broadened to 8 MHz. Since both lasers were modulated to lock the frequency to an absorption line of reference gas, and the short-term stability of rf modulation signal for OFCG was unknown, we could not identify the dominant noise source that caused this carrier collapse.

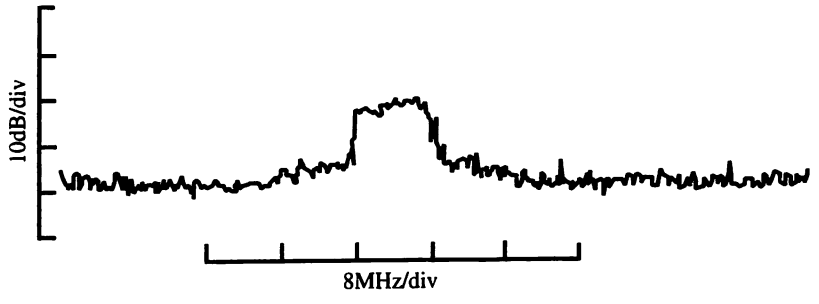

Fig. 9. RF-Spectrum of beat signal between a 1.54 μm laser diode and a 1.66 μm laser diode. The offset frequency from the carrier was 14 THz and the resolution bandwidth was 1 MHz

3.3 Accuracy of the OFC

Long-term stability of the sidebands is essential for optical frequency measurement using an OFC. Acoustic noise [24] and the temperature and inten-

sity dependence of the refractive index [25] of the optical fiber may induce output frequency fluctuation in the SPM process. In practice, a long optical fiber is used to enhance the SPM effect. A temperature change of 1°C per hour may result in a 2 Hz shift at 1.5 μm carrier frequency. Here we show the experimental results of frequency-variation measurements of SPM-induced sidebands in optical fibers. Since the accuracy of a conventional OFC has been demonstrated, we compare the frequency of an SPM sideband with that of a conventional OFC.

The experimental apparatus is shown in Fig. 10. The laser input to the OFCG was amplified to about 30 mW in an EDFA in front of the OFCG. After passing through the EDFA, the OFC span was increased to more than 30 THz by SPM in a dispersion-flattened optical fiber. The inset of Fig. 10 shows a schematic explanation of the spectrum comparison during different processes. A common reference laser LD2 was used to mix with a sideband in the OFC directly after the OFCG and produced a beat signal at frequency f. A second beat signal at $f + \mathrm{d}f$ was produced when LD2 was mixed with the same sideband after the EDFA and DFF, where $\mathrm{d}f$ is the frequency drift due to the environmental condition change in the SPM process. Then the frequency difference $\mathrm{d}f$ between these two signals was measured using a frequency counter.

We measured a frequency difference between a sideband and the output of LD2 (1.7 THz), and the frequency difference between the carrier of the OFC and the output of LD2 (0 Hz). These frequency differences were measured both before and after it had passed through the optical fiber and EDFA. The two beat signals had an SNR of more than 40 dB with a 1 MHz bandwidth.

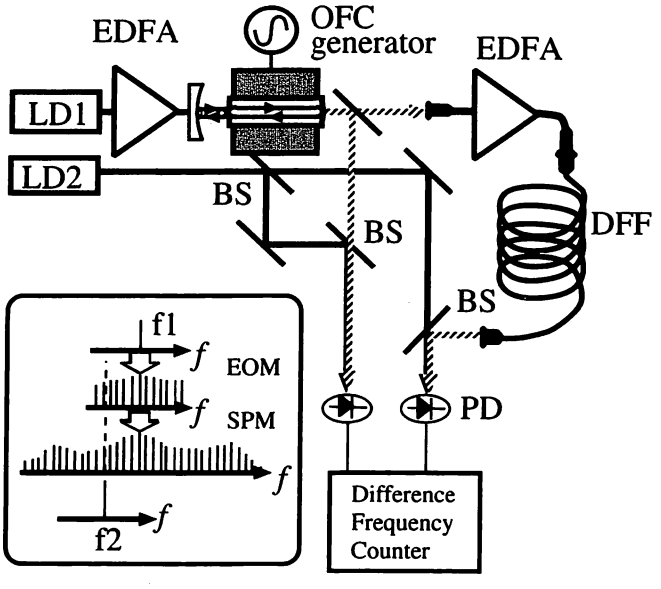

Fig. 10. Experimental setup for comparison of two combs generated by electro-optic modulation and SPM. DBM: Double Balanced Mixer. The inset shows a schematic explanation of the frequency comparison

Since the intensities of the SPM sidebands are sensitive to the output power of the conventional OFCG, the output power fluctuation could cause incorrect counting. The output power fluctuations of the OFCG were stabilized to less than approximately 5% of the average power, by increasing the bandwidth of the OFC coupling-cavity control.

Figure 11 shows the square root of Allan variance of the measured frequencies. The open circles give the frequency difference between LD2 and the comb carrier as measured before and after the EDFA and DFF stages, where we measured the frequency difference without the OFCG as a reference and the average power propagating in the fiber was sufficiently small to suppress SPM. The closed circles give the equivalent measurement for the 1.7 THz sideband. Since the experimental setup is similar to the delayed self-heterodyne method, fluctuations of the carrier frequencies of each of the lasers were measured in addition to the thermal or acoustic fluctuations of the sidebands. The measured Allan variance depends on both the linewidth of the lasers, and the time delay due to the optical fiber. The solid line is the result of a theoretical calculation assuming 1 km of optical fiber and the typical FM noise of a laser diode, which consists of $1/f$ noise up to 100 kHz and white frequency noise beyond 100 kHz. The measured results were in good agreement with the theoretical result between $10\,\text{ms} \leq \tau \leq 5\,\text{s}$. The effects of temperature variation of the fiber were observed for $100 \leq \tau \leq 200\,\text{s}$, which lifted the frequency instability to around 1 Hz. These integration times correspond approximately to the period of the temperature variation caused by air conditioning. We believe that the main frequency fluctuation of the SPM sidebands originated from temperature drift, even though the spectral broadening due to SPM was efficient.

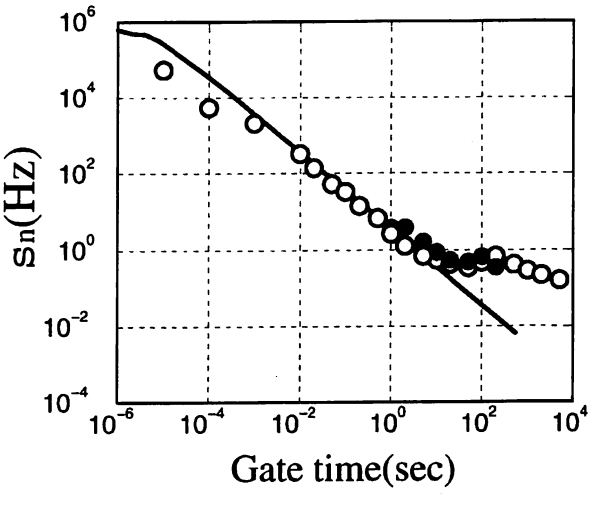

Fig. 11. Square root of Allan variance σ_ν of the frequency difference without (*open circles*) and with (*closed circles*) OFCGs. The *Solid line* is the result of theoretical calculation which was derived by assuming typical frequency fluctuations of the laser diode

Although the measured frequency shift suggests that the sideband frequencies drifted after the SPM process in optical fibers, the accuracy of sideband separations is still very high. The effect on the difference frequency measurement is manageable. The frequency fluctuations can be suppressed by controlling the temperature around the long fiber, or can be canceled by an external phase modulator such as acousto-optic modulator (AOM) [24,26].

4 A Method of Frequency Difference Measurement by Using Second Harmonic Generation

For increased expansion of the OFC span, we propose employing nonlinear optical-frequency conversion processes e.g. second harmonic generation (SHG), Sum Frequency Generation (SFG) and Difference Frequency Generation (DFG) of the OFC. An OFC that has been amplified has a wide frequency span, short pulse duration, and high peak power. These properties are well-matched to a nonlinear-frequency conversion process. A Periodically Poled Lithium Niobate (PPLN) crystal was pumped by an OFC having a span of 25 THz to yield an SHG comb having a total span of 50 THz (see Fig. 12). The detail of the experiment is given in [27].

We have already used this SHG comb to measure a difference frequency between two lasers separated by 22 THz. As shown in Fig. 13(a), the expanded OFC was incident upon two PPLN crystals with period of 19.2 μm and 21.4 μm respectively. PPLN 1 has been use to generate a SHG comb at around 0.778 μm and PPLN 2 to generate a SHG comb at around 0.826 μm.

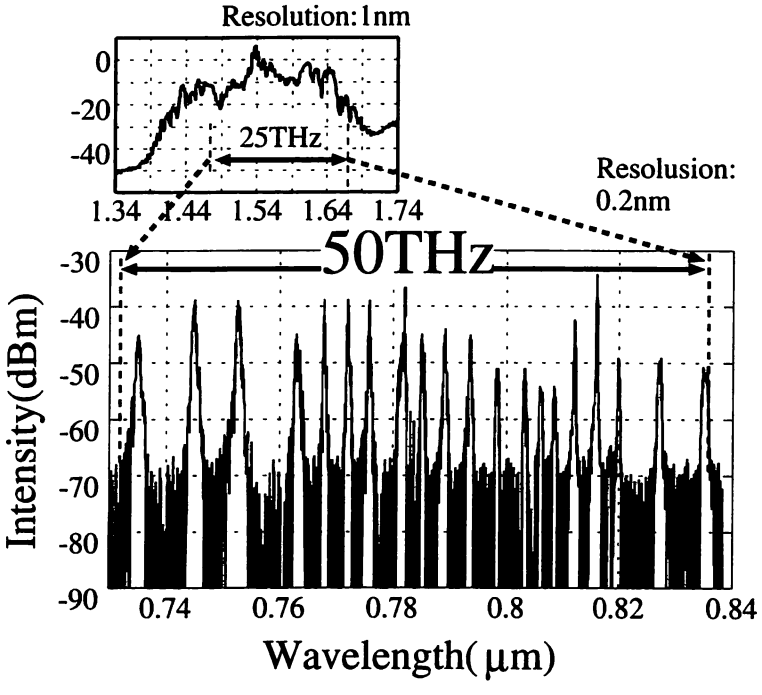

Fig. 12. SHG generation of an OFC

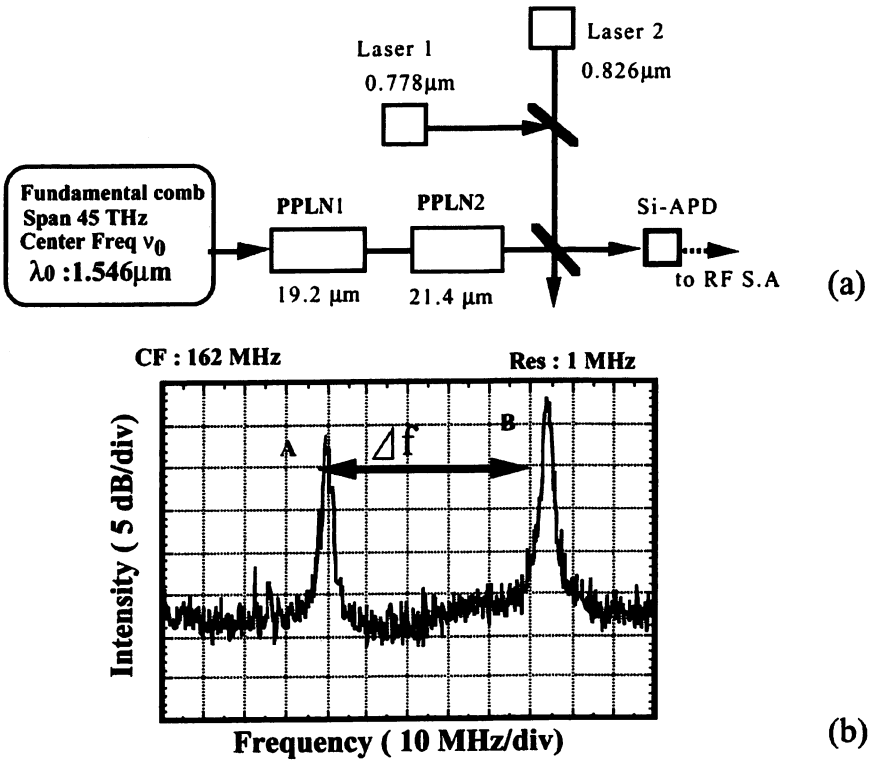

Fig. 13. Measurement of the difference frequency between two lasers separated by 22 THz: (**a**) experimental setup; (**b**) beat spectrum between SFG comb and two lasers

Both the SHG combs were combined with laser 1 and laser 2, which define the frequency interval that we wish to measure. Both laser 1 and laser 2 were chosen as extended cavity diode laser in order to be able to tune the laser frequency continuously. The wavelength of two lasers was 0.7782 μm and 0.8265 μm respectively. Figure 13(b) shows the beat spectrum between laser 2 and the SHG comb (A) and between laser 1 and the SHG comb (B) observed using an rf spectrum analyzer with 100 MHz span and 1 MHz resolution bandwidth. This beat frequency was changed to 38.7 MHz for beat A and 3.64 MHz for beat B when the frequency modulation was shifted 10 kHz. From this value, the frequency difference between laser 1 and laser 2 is 22.057 THz. Only half the span of the SHG comb is used for this measurement, and so it appears possible to measure frequency differences up to 50 THz.

Using this SFG technique, we can develop a method for frequency difference measurements that allows measurement of frequency differences that are even larger than the span of the comb. The concept is based on the beat generation between two OFCs generated by SFG and SHG. This concept is similar to that of the optical frequency divider stage [13]; however, in the proposed setup no phase-locked lasers are required.

Figure 14 shows the experimental apparatus. The OFC was amplified to 180 mW average power using a fiber EDFA. After amplification, we combined the OFC with LD2 (1.532 μm of wavelength and 15 mW of power). The differ-

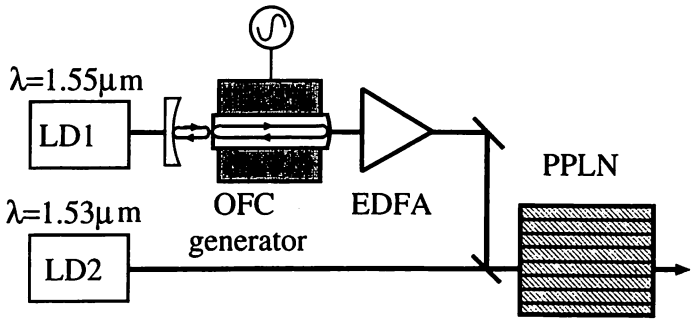

Fig. 14. Experiment setup. EDFA: erbium-ytterbium-doped fiber amplifier. PPLN: periodically poled lithium niobate

ence frequency ($\delta\nu$) between LD1 and LD2 was 3.1 THz. The combined laser beams were incident on a 19.6-μm-period, 19-mm-long bulk PPLN crystal, which was chosen for second-harmonic phase matching of radiation of wavelengths near 1.56 μm. A lens focused the combined beam into the PPLN crystal to get a spot size of about 80 μm. The PPLN crystal period is simultaneously phase-matched for sum frequency generation between LD2 and a part of the OFC to produce the SFG comb at 0.776 μm of center frequency. We confirmed that the second harmonic of LD2 was not generated using the crystal.

Figure 15 (curve A) shows the spectrum of a part of the combined beam of the amplified fundamental comb and LD2 spectrum. The span of amplified OFC is limited by the bandwidth of the EDFA, which was about 4.5 THz. Figure 15 also shows the SHG comb spectrum when LD2 is off (curve A) and when LD2 is on (curve B). It is shown that the span and power of curve B was broader then that of curve A, because the SFG comb is also generated

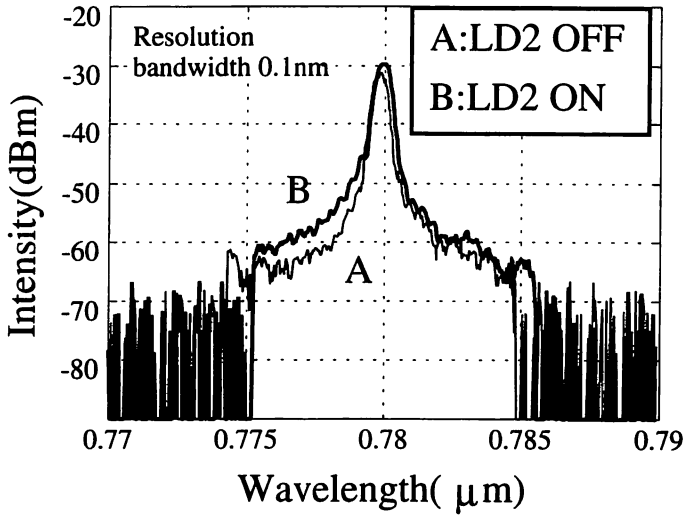

Fig. 15. Spectral envelope of amplified SHG comb when LD2 was off (A) and LD2 was on (B), observed by using an optical spectrum analyzer with 0.1 nm resolution

together. To confirm the SHG comb and SFG comb, we observed the beat signal between them using Si-APD. As a comparison we also measured the beat signal between the fundamental comb and the laser using a Ge-PIN photodiode.

Figure 16 shows the beat signal between the laser and the fundamental comb (curve A), as well as the beat between the SHG comb and SFG comb (curve B), monitored by a spectrum analyzer with 1 MHz resolution. It shows that the SNR is increased by about 5 dB using an SHG comb. This improvement in SNR arises because many pairs of sidebands of the SHG and SFG comb can contribute to the output beat signal. In the case of the fundamental beat signals, only one laser and one sideband can contribute to the beat signal. Thus we see that a wideband and efficient nonlinear crystal can significantly increase the SNR.

In principle, this technique allows frequency-difference measurements between two laser signals which differ in frequency by three times the span of the comb.

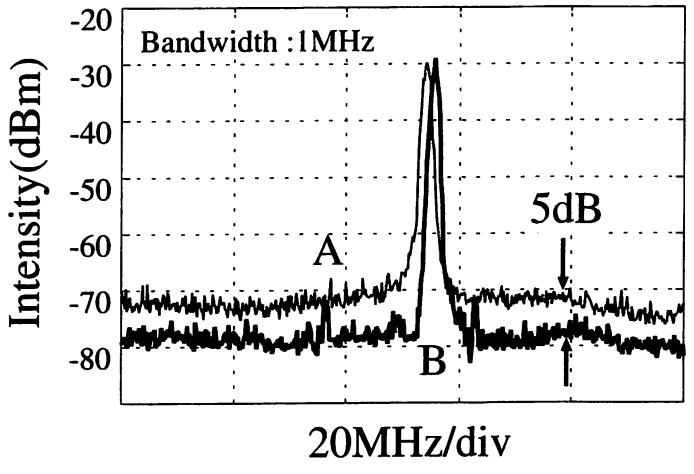

Fig. 16. Measured beat spectrum between laser and fundamental OFC (A) and beat spectrum between SFG comb and SHG comb (B). Span and resolution bandwidth was 100 MHz and 1 MHz respectively

5 Summary

We have introduced a method of expanding an OFC, was generated by a conventional EO modulation technique, by applying it to an optical fiber. The expansion arises from SPM of the signal in the fiber core. As a result, the span of the obtained OFC maybe as large as 50 THz. We have measured the frequency accuracy of the optical sideband generated by this SPM process. Frequency fluctuations and drift of both the carrier frequency and sidebands at 1.7 THz away from the carrier were experimentally determined.

The square root of Allan variance was increased to $\sim 1\,\mathrm{Hz}$ at a gate time of 100 s. It was found that these frequency fluctuations were mainly caused by temperature variations in the fiber, which could be managed by using a temperature controller and an external phase controller. Second-harmonic generation of an OFC was also demonstrated. The span of the second harmonic comb could reach up to 50 THz in the 0.8 μm wavelength range. We have also demonstrated a method that allows frequency-difference measurements between two signals that differ in frequency by more than the span of the OFC.

Acknowledgment

The authors would like to thank Dr. M. Ohnishi, Sumitomo Electro Industry, for discussions about the optical fiber.

References

1. M. Ohtsu (Ed.): *Frequency Control of Semiconductor Lasers* (Wiley-Interscience, New York 1996)
2. A. Huber, Th. Udem, B. Gross, J. Reichert, M. Kourogi, K. Pachucki, M. Weitz, T. W. Hänsch: Hydrogen–deuterium $1S$–$2S$ isotope shift and the structure of the deuteron. Phys. Rev. Lett. **80**, 468-471 (1998)
3. M. Kourogi, K. Nakagawa, M. Ohtsu: Wide-span optical frequency comb generator for accurate optical frequency difference measurement. IEEE J. Quantum Electron. **29**, 2693–2701 (1993)
4. M. Kourogi, T. Enami, M. Ohtsu: A monolithic optical frequency comb generator. IEEE Photon. Technol. Lett. **6**, 214–217 (1994)
5. M. Kourogi, B. Widiyatomoko, Y. Takeuchi, M. Ohtsu: Limits of Optical Frequency Comb Generation due to the Material Dispersion. IEEE J. Quantum Electron. **31**, 2120–2126 (1995)
6. M. Kourogi, B. Widiyatmoko, M. Ohtsu: 3.17 THz frequency-difference measurement between lasers using two optical frequency combs. IEEE Photon. Technol. Lett. **8**, 560-562 (1996)
7. M. Kourogi, T. Enami, M. Ohtsu: A coupled-cavity monolithic optical frequency comb generator. IEEE Photon. Technol. Lett. **8**, 1698–1700 (1996)
8. T. Saito, M. Kourogi, M. Ohtsu: A waveguide-type optical-frequency comb generator. IEEE Photon. Technol. Lett. **7**, 197–199 (1995)
9. T. Saito, M. Kourogi, M. Ohtsu: Expansion of span-width of an optical frequency comb using a higher harmonic wave modulation. IEEE Photon. Technol. Lett. **8**, 1379–1381 (1996)
10. A. S. Bell, G. M. Macfarlane, E. Riis, A. I. Ferguson: An efficient optical frequency comb generator. Opt. Lett. **20**, 1435–1437 (1995)
11. T. Kobayashi, T. Sueta, Y. Cho, Y. Matsuo: High-repetition-rate optical pulse generator using a Fabry-Perot electro-optic modulator. Appl. Phys. Lett. **21**, 341–343 (1972)
12. S. Slyusarev, T. Ikegami, S. Ohshima, E. Sakuma: Frequency measurement of accurate sidebands of an optical frequency comb generator. Opt. Commun. **135**, 223–226 (1997)

13. H. R. Telle, D. Meschede, T. W. Hänsch: Realization of a new concept for visible frequency division: phase locking of harmonic and sum frequencies. Opt.Lett. **15**, 532–534 (1990)
14. T. Udem, M. Kourogi, J. Reichert, T. W. Hänsch: Accuracy of optical frequency comb generators and optical frequency interval divider chains. Opt.Lett. **23**, 1387 –1389 (1998)
15. W. Wang, M. Ohtsu: Generation of frequency-tunable light and frequency reference grids using diode lasers for one-petahertz optical frequency sweep generator. IEEE J. Quantum Electron. **31**, 456–467 (1995)
16. K. Imai, M. Kourogi, M. Ohtsu: 30-THz span optical frequency comb generation by self-phase modulation in an optical fiber. IEEE J. Quantum Electron. **34**, 54–60 (1998)
17. K. Imai, M. Kourogi, B. Widiyatmoko, M. Ohtsu: Beat signal measurement of 12 THz separated lasers by using self-phase modulation in optical fiber. In: 1998 Conf. Lasers and Electro-optics, San Francisco, OSA Tech. Dig. **6**, 472–473 (1998) paper CThY4
18. G. P. Agrawal: *Nonlinear Fiber Optics* (Academic, New York 1989)
19. T. Morioka, S. Kawanishi, K. Mori, M. Saruwatari: Nearly penalty-free, < 4 ps supercontinuum Gbit/s pulses generation over 1535–1560 nm. Electron. Lett. **30**, 790–791 (1994)
20. H. Nishioka, W. Odajima, K. Ueda, H. Takuma: Ultrabroadband flat continuum generation in multichannel propagation of terrawatt Ti:sapphire laser pulses. Opt. Lett. **20**, 2505–2507 (1995)
21. Y. Kubo, H. Kanamori, H. Yokota, S. Tanaka: Dispersion flattened single-mode fiber for 10,000 km transmission system. Proc. ECOC'90, 505–508 (1990)
22. L. F. Mollenauer, R. H. Stolen, J. P. Gordon, W. J. Tomlinson: Extreme picosecond pulse narrowing by means of soliton effect in single-mode optical fibers. Opt. Lett. **8**, 289–291 (1983)
23. C. Ishibashi, M. Kourogi, K. Imai, B. Widiyatmoko, A. Onae, H. Sasada: Absolute frequency measurement of the saturated absorption lines of methane at the 1.66 μm region. Opt. Commun. **161**, 223–226 (1999)
24. L.-S. Ma, P. Junger, J. Ye, J. L. Hall: Delivering the same optical frequency at two places:accurate cancellation of phase noise introduced by an optical fiber or other time-varying path. Opt. Lett. **19**, 1777–1779 (1994)
25. T. Yoshino, K. Kurosawa, K. Itoh, T. Ose: Fiber-Optic Fabry-Perot interferometer and its sensor applications. IEEE J. Quantum Electron. **18**, 1624–1633 (1982)
26. M. Kourogi, K. Imai, B. Widiyatmoko, M. Ohtsu: Accurate relative frequency cancellation between two independent lasers. Opt. Lett. **24**, 16–18 (1999)
27. B. Widiyatmoko, K. Imai, M. Kourogi, M. Ohtsu: Second-harmonic generation of optical frequency comb at 1.55 μm using a periodically poled lithium niobate. Opt. Lett. **24**, 315–317 (1999)

【平成12年度光学論文賞受賞論文紹介】

興梠元伸氏の論文紹介

大津　元一
（東京工業大学大学院総合理工学研究科）

興梠元伸氏は平成5年3月に東京工業大学大学院総合理工学研究科博士後期課程を修了，同大学院助手として奉職し現在に至っている．また平成11年より科学技術振興事業団新規事業志向型研究開発成果展開事業「超高精度多周波数光パルス発生器」プロジェクトリーダーを兼任している．興梠氏は大学院在籍中から一貫してレーザー光の周波数，位相制御の研究に従事しており，特に光周波数コム発生器（OFCGと略記）を中心としてすぐれた業績をあげている．今回受賞された論文 “Continuous tuning of an electrically tunable external-cavity semiconductor laser,” Opt. Lett., **25**, No. 16 (2000) 1165-1167 は音響光学素子を用いて共振器モードの位相を制御するという新しいアイデアにより外部共振器型波長可変半導体レーザーの連続周波数可変を初めて可能にした結果を報告したものである．

外部共振器型波長可変半導体レーザーは計測，通信などに広く使われており，外部共振器をモノリシック集積化した半導体レーザーなども開発されている．しかしこれらは複数の共振器間のモード間干渉のために連続波長可変が不可能であった．特に複数の共振器長を機械的に変化させる場合には波長掃引速度はきわめて遅い．それに対し，この論文では上記のように響光学素子を用いて共振器モードの位相を制御することにより連続波長可変を可能にした．かつ，この制御は電気的なので波長掃引は著しく高速化でき，したがって本方法の先駆性，優秀性はきわめて高い．

本論文は上記のOFCGを用いた光周波数シンセサイザーに用いる光源を開発した成果を発表したものである．興梠氏は共振器内電気光学変調器を用いたOFCGの発明者であり，その後ファイバーの分散効果，非線形光学効果を利用して研究を発展させ，周波数コムのスパンとして世界最高値50 THzを実現している[1,2]．これはドイツのマックスプランク研究所でのリドベルグ定数の精密測定[3]，さらには最近国際的に活発化しているフェムト秒レーザーによるOFCG，スーパーコンティニウムの研究の先駆となったものである[4]．さらにこれらの研究は大規模計測システムを必要としていた旧来の光周波数精密測定をデスクトップ化する大きなきっかけにもなった．これらの興梠氏の一連の業績は国際的に高く評価され，解説論文，招待講演などにより多数公表されている．

さらに最近では興梠氏は通信，光CTなどへの応用のためにOFCGをモノリシック集積化し，この技術をもとにベンチャー起業をも試みている．特に光CTについては深さ掃引速度が10 km/sに達する超高速システムを実現している．

以上のように本論文の優秀性のみでなく，研究者としての高い独創性を有する興梠氏が今回光学論文賞の対象となったことはまことに喜ばしい．論文賞審査委員会の各位に深く感謝するとともに，今後は興梠氏がさらにすぐれた研究業績をあげられるよう期待する．

文　献

1) 興梠元伸，大津元一：“広スパン光周波数コムの発生と応用”，応用物理，**67** (1998) 551-554.
2) M. Kourogi, B. Widiyatmoko, K. Imai, T. Shimizu and M. Ohtsu: “Accurate relative frequency cancellation between two independent lasers”, Opt. Lett., **24** (1999) 16-18.
3) P. F. Schewe and B. P. Stein: “Physics News in 1999,” *A Supplement to APS News* (1999) p. 5.
4) D. J. Jones, S. A. Diddams, J. K. Ranka, A. Stentz, R. S. Wideler. J. L. Hall and S. T. Coundiff: “Carrier-envelope phase control of femtosecond mode-locked lasers and direct optical frequency synthesis,” Science, **288** (2000) 635-639.

[III] Published Books

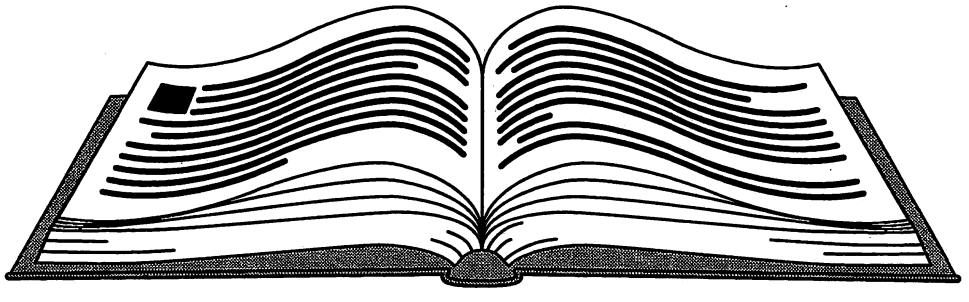

ADOP Advances in Optoelectronics

OPTICAL AND ELECTRONIC PROCESS OF NANO-MATTERS

Edited by

Motoichi OHTSU

Tokyo Institute of Technology, Yokohama

KTK Scientific Publishers / Tokyo

Kluwer Academic Publishers
Dordrecht / London / Boston

Preface

Sizes of electronic and photonic devices are decreasing drastically in order to increase the degree of integration for large-capacity and ultrahigh-speed signal transmission and information processing. This miniaturization must be rapidly progressed from now onward. For this progress, the sizes of materials for composing these devices will be also decreased to several nanometers. If such a nanometer-sized material is combined with the photons and/or some other fields, it can exhibit specific characters, which are considerably different from those of bulky macroscopic systems. This combined system has been called as a mesoscopic system. The first purpose of this book is to study the physics of the mesoscopic system.

For this study, it is essential to diagnose the characteristics of miniaturized devices and materials with the spatial resolution as high as several nanometers or even higher. Therefore, novel methods, e.g., scanning probe microscopy, should be developed for such the high-resolution diagnostics. The second purpose of this book is to explore the possibility of developing new methods for these diagnostics by utilizing local interaction between materials and electron, photon, atomic force, and so on.

Conformation and structure of the materials of the mesoscopic system can be modified by enhancing the local interaction between the materials and electromagnetic field. This modification can suggest the possibility of novel nano-fabrication methods. The third purpose of this book is to explore the methods for such nano-fabrication.

Several articles on mesocopic systems have reviewed their physics, diagnostics, and fabrication separately from the viewpoint of electronic interaction. Some of them are the reviews on the application of scanning tunneling microscopy. In contrast with them, the unique feature of this book is to introduce the concept of nano-optics, i.e., near field optics into discussions on mesoscopic systems.

Intensive discussions on the three purposes presented above, including the methods of scanning tunneling microscopy, near field optics, and atomic

force microscopy, have been made by the 17 members of a working group in the Institute of Electrical Engineers of Japan from April 1996 to March 1998, to which I have served as chairman. This book summarizes the main topics of the discussion, where most of the co-authors have been the members of this working group. Chapters 1–5 are devoted to physics. Chapters 6, 7, and 9–11 are for diagnostics, and Chapter 8 is for fabrication. Among them, reviews on electronic systems are dealt with in Chapters 2–6, and 11. Those topics on near-field optical systems and on atomic force systems are mentioned in Chapters 6–8 and in Chapters 9–11, respectively. All the chapters are carefully organized so that the readers can obtain a deep understanding on the contents. I hope that this book will enable undergraduate and graduate students, junior scientists, and engineers to systematically study the physics, diagnostics, and fabrication of nano-sized materials and devices.

M. Ohtsu
March, 2000

Contents